BIOLOGY AND MEDICINE DIVISION ANNUAL REPORT 1985

LBL--20345

DE86 012736

Lawrence Berkeley Laboratory
University of California
Berkeley, California 94720

This work was supported by the Office of Health & Environmental Research of the United States Department of Energy under Contract DE-AC03-76SF00098. Portions of this work were also supported by the National Institutes of Health, Department of Health and Human Services; the National Aeronautics and Space Administration; the Nuclear Regulatory Commission, the Veterans Administration, International Business Machines Corporation (IBM Instruments), and the Electric Power Research Institute. Contracts and grants are listed in Appendix A.

CONTENTS

Lipoproteins

Structural Biology

INTRODUCTION

In looking back at the introduction to last year's report, I can only wistfully say that at that time I had hoped that the financial stresses of a shrinking budget would be behind us before now. Unfortunately that has not proved to be the case. This has been the year of the "deficit crisis" and Gramm-Rudman. As a result, the federal funding of research has continued to be a serious problem. Nevertheless, we have managed to hold our own and to contribute in a very respectable fashion to the world of science. Let me express my heartfelt thanks and appreciation to all our staff. You have weathered significant tribulations while maintaining your sense of proportion and commitment to good science.

During the past year the Donner Pavilion program on the treatment of arteriovenous malformations in the brain has chalked up very significant successes. The disease control rate has been high and objective measures of success using cerebral angiography have been established. This program along with the Research Medicine program on brain disease have received very wide public exposure, including a successful appearance before a House Committee hearing. The new high resolution positron emitting tomographic imager has been demonstrated to operate successfully.

The NMR imaging program is now in full swing, with projections for development of magnets with fields up to 10 tesla as a goal for the future. This imaging program, particularly the high-field aspects, is coordinating nicely with the laboratory program in magnetic field effects on animals.

In the Radiation Biophysics program, the availability of higher mass ions up to uranium has allowed us to carry out cell and tissue studies in a radiation domain that is entirely new. Using uranium beams, investigators have already made new and exciting findings that are described in the body of the report.

To increase the effectiveness of our mutagenesis-carcinogenesis group, now formally named "Cellular and Molecular Biology," we have consolidated nearly all of the investigators concerned in one building—Building 934, which is more or less affectionately called the "Dymo Building" after its former occupants.

Our Division staff continues to provide outstanding service to the investigators, particularly at a time when our volume of new proposal submissions has increased dramatically. I wish to extend to all of them my particular thanks.

Also, "welcome aboard" to our new staff members. I believe you will enjoy your participation in our programs and contribute to our continuing high-quality science.

Edward L. Alpen

SECTION 1. RESEARCH MEDICINE

INTRODUCTION

The Research Medicine Group has continued to develop and apply new instruments and procedures for evaluation of the physiological state of normal and pathological processes of major diseases such as aging and atherosclerosis. Cancer, of course, is a continuing challenge, but in this area we focus on the use of noninvasive methods to aid the heavy-ion radiotherapy program. The two major tools we are developing in this quest to understand disease mechanisms are emission tomography and nuclear magnetic resonance (NMR). Emission tomography involves the injection of radioactive isotopes bound to chemicals that go to specific regions of the body, depending on the normal or abnormal metabolic activity in the region of interest. NMR is used to learn about physical and chemical composition of body tissues as well as enzyme activities that might be specific for disease.

Our approach is to make pictures of normal and abnormal body function. An example of this comparison appears in the Alzheimer's disease study reported in this section.

We are strongly focused on noninvasive methods for mapping body metabolism because basic principles of science dictate that energy changes must precede anatomical changes. Thus, we believe metabolic images are more sensitive than anatomic images for evaluation of disease problems.

Accomplishments of the Research Medicine Group over the last year are:

1. Establishment of a new method for brain-blood-flow measurements in Alzheimer's disease and stroke.
2. Development of a method for labeling human blood platelets so that early signs of stroke can be detected.
3. Development of a method for evaluation of coronary artery disease using positron tomography and a rubidium-82 generator device developed at LBL.
4. Installation of two new medical research NMR magnets for *in-vivo* studies of human metabolism in normal subjects and patients with early aging or atherosclerosis.
5. Discovery of a remarkably abnormal behavior of platelets when in blood with high cholesterol.

Research Medicine (at a glance).

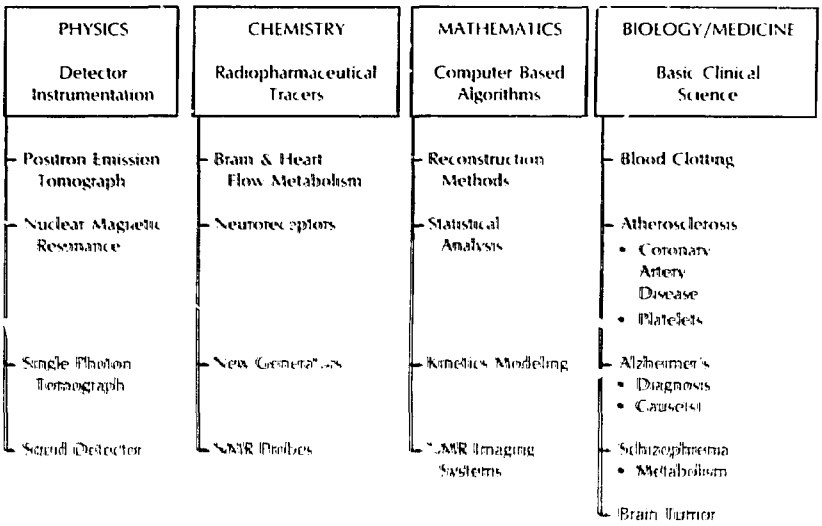

EVALUATION AND USE OF IODINE-122 BRAIN BLOOD FLOW RADIOPHARMACEUTICALS

Chester A. Mathis, Thornton Sargent III, Thomas F. Budinger, Yukio Yano, William J. Jagust, Alexander Shulgin, Natalia Kusubov, and Kathleen M. Brennan

The development of positron emission tomography (PET) has provided a quantitative brain imaging device that can help correlate such physiological parameters as brain blood flow, blood volume, oxygen metabolism, glucose metabolism, protein incorporation, and receptor site densities and affinities. The accurate measurement of brain blood flow would be of considerable value in the understanding of the pathophysiology of various brain diseases, including Alzheimer's disease, stroke, and radiation necrosis. When brain blood flow is measured in concert with one or more of the other cerebral functional indicators, therapeutic decisions concerning the medical treatment of patients with brain disorders can be made on the basis of more precise diagnosis.

The radiopharmaceuticals presently used to assess brain blood flow must be produced at the PET facility because of the short half-lives of their radionuclides. We have investigated the possibility of using the $^{122}Xe/^{122}I$ generator system to provide a radionuclide that can be produced at a regional cyclotron and shipped to PET imaging centers without on-site cyclotrons. The 20-hour half-life of the ^{122}Xe parent makes this generator system attractive for widespread use, and the 3.6-min half-life of ^{122}I results in a low radiation dose to the patient. In addition, repeat studies can be performed under changed physiological conditions because the injected activity will have disappeared in 20 min. We have previously described a generator that we load with about 200 mCi of ^{122}Xe and from which we are able to remove 25–100 mCi of ^{122}I every 20 min for 2 days.[1]

We have investigated several compounds that can be labeled with ^{122}I and have evaluated their potential usefulness as brain blood-flow agents. One class of compounds is the iodo-dimethoxy-N,N-dimethylamphetamines, and we have studied several ^{122}I-labeled amphetamine derivatives in animals.[2,3] Another compound is a substituted diamine (termed HIPDM) that previously has been labeled with ^{123}I and used in single-photon gamma camera studies of brain blood flow.[4] Clinical trials with ^{123}I-labeled HIPDM have demonstrated the usefulness of this agent to detect flow defects sometimes not seen with x-ray computed tomography. We are interested in PET application of ^{122}I-HIPDM because single photon imaging devices have decreased resolution compared to PET systems and the 13-hr half-life of ^{123}I limits repeat studies with ^{123}I-HIPDM.

In collaboration with Dr. Hank F. Kung of the Veteran's Administration Medical Center, Buffalo, N.Y., the rapid labeling of HIPDM with ^{122}I (Fig. 1) has been investigated. We have labeled HIPDM with ^{122}I rapidly (2 min) and in high yield (70%). The radiopharmaceutical was ready for injection about 4 min after removal of ^{122}I from the generator, and preliminary studies in animals indicated its potential usefulness for human brain blood flow studies.

The results of our first patient study with ^{122}I-HIPDM are shown in Fig. 2. The patient had suffered a stroke three years previously and x-ray CT scans had shown some deficits in the frontal area of the brain. As seen in Fig. 2, ^{122}I-HIPDM uptake in the left frontal region (right side of the photo) is markedly diminished. Later PET images were taken following the injection of a radiolabeled sugar compound, ^{18}F-FDG, which showed decreased metabolic function in the same brain region (Fig. 2). The dynamic uptake and retention of ^{122}I-HIPDM and ^{18}F-FDG in different brain regions were determined and the data are shown (Fig. 2). It can be seen that the ^{18}F-FDG uptake in the stroke area was about 50% that of the normal contralateral side; the uptake and retention of ^{122}I-HIPDM in the stroke area was about 40% that of the unaffected side. Quantitative measurements of brain blood flow, metabolism, and blood volume in stroke

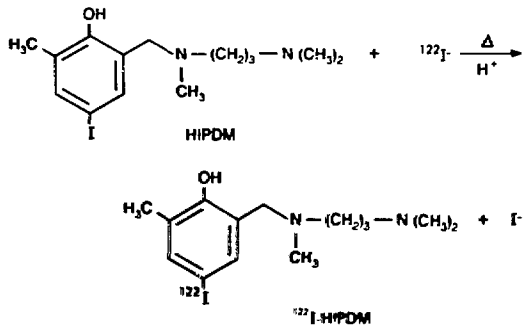

Fig. 1. Exchange labeling of HIPDM with ^{122}I-iodide to produce ^{122}I-HIPDM. (XBL 851-8149)

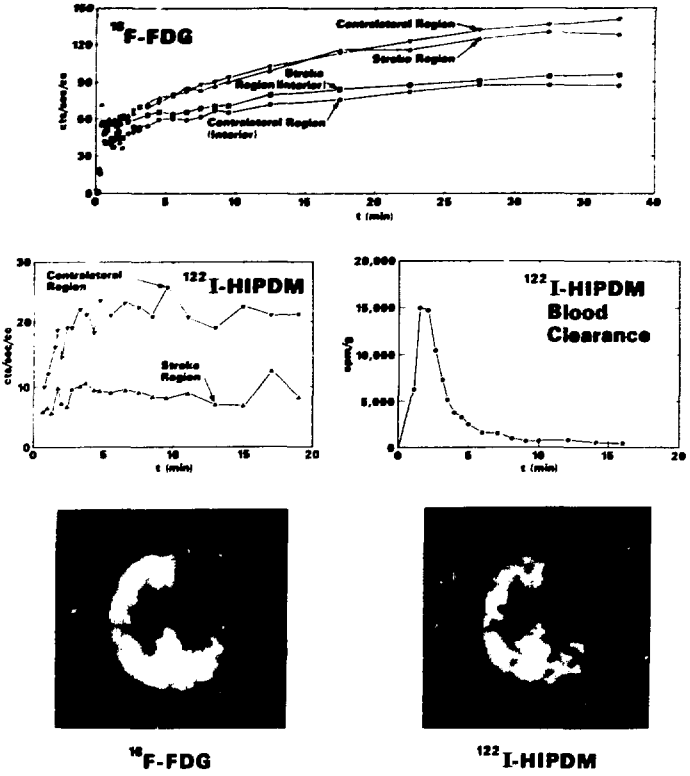

Fig. 2. ^{122}I-HIPDM and ^{18}F-FDG in a patient with a left frontal stroke three years previously. PET images are as labeled at bottom. Dynamic PET data for ^{18}F-FDG are plotted in the top panel and ^{122}I-HIPDM data from the cortical areas only are shown in the middle left panel. ^{122}I blood clearance data are shown in the middle right panel.
(XBB 859-7141A)

patients such as the one shown in Fig. 2 will help guide therapeutic interventions such as hyperbaric oxygen treatment and cerebral bypass surgery. We are collaborating with Dr. Philip Weinstein of the VA Hospital, San Francisco and the Neurosurgery Department, UCSF in following stroke patients before and after medical treatment to assess their progress.

Preliminary studies such as the one shown in Fig. 2 demonstrate the potential usefulness of the ^{122}I-radionuclide for PET studies. Work is underway to critically evaluate characteristics of HIPDM and the iododimethoxyamphetamines, which are important in their ability to accurately measure brain flow. These include the extent of metaboiic breakdown during the uptake study, and the fraction that is extracted into the brain. When these comparative studies have been completed, we will choose the best agent for development as the brain blood-flow radiopharmaceutical to be used in our research on brain dysfunction and for clinical procedures. We are also investigating the application of the ^{122}I-radiolabel to other compounds such as albumin to measure brain blood volume and to fatty acid derivatives to assess heart function. The short half-life of the ^{122}I-radionuclide permits extraction from the generator every 20–30 min, so that it can be used to label different compounds. These radiopharmaceuticals may be used in concert to measure several functional parameters in the same patient.

REFERENCES

1. Yano, Y., Budinger, T.F., Mathis, C.A., Singh, M., Moore, D., and Jones, R. Development of radionuclides and radiopharmaceuticals for

positron emission tomography. Biology and Medicine Division Annual Report 1983–1984, LBL-18393 (1985).
2. Mathis, C.A., Sargent III, T., Shulgin, A.T., Yano, Y., Budinger, T.F., and Lagunas-Solar, M. Synthesis and evaluation of meta-substituted I-122-labeled dimethoxy-N,N-dimethylamphetamines for brain imaging. *J. Nucl. Med. 26*, P69 (1985).
3. Mathis, C.A., Sargent III, T., and Shulgin, A.T. Iodine-122-labeled amphetamine derivative with potential for PET brain blood-flow studies. *J. Nucl. Med. 26*, 1295 (1985).
4. Kung, H.F., Tramposch, K.M., and Blau, M. A new brain perfusion agent: [I-123] HIPDM: N,N,N'-trimethyl-N'[2-hydroxy-3-methyl-5-iodobenzyl]-1,3-propanediamine. *J. Nucl. Med. 24*, 66 (1983).

DYNAMIC PET STUDIES OF GLUCOSE UPTAKE IN ALZHEIMER'S DISEASE

William J. Jagust, Robert P. Friedland, Ronald H. Huesman, Bernard M. Mazoyer, Yukio Yano, Chester A. Mathis, Kathleen M. Brennan, Brian Knittel, and Thomas F. Budinger

Studies utilizing positron emission tomography (PET) with [^{18}F]fluorodeoxyglucose (FDG) in the investigation of cerebral glucose metabolism in Alzheimer's disease (AD) have been underway at the Donner Laboratory for several years. Alzheimer's disease is the most common degenerative brain disease of adulthood, and as such is responsible for 50 to 60% of all cases of progressive mental deterioration, or dementia, in adult life. We have previously found that Alzheimer's disease is characterized by glucose hypometabolism in the temporal and parietal cortex.[1] These findings are consistent in all the AD patients we have studied, and the pattern of regional cerebral hypometabolism is now found to be useful in the clinical evaluation and diagnosis of elderly patients with impaired cognition. In fact, we have evaluated several patients with communicating hydrocephalus, a potentially reversible dementia caused by accumulation of cerebrospinal fluid in the cerebral ventricles, which is treatable by a surgical shunting procedure. This diagnosis, however, is often difficult to confirm because patients with hydrocephalus frequently cannot be distinguished from patients with AD. We found that patients who improved following surgery did not demonstrate the typical AD pattern of temporoparietal hypometabolism, thus suggesting that PET's ability to exclude AD may be useful in selecting patients for surgery.[2]

Recent work has involved the correlation of these metabolic abnormalities with clinical features of AD. Thus, we have observed differences in metabolism in left and right hemispheres that correlate with behavioral features of the disease and age at onset.[3,4] In addition, we have found that the new methods of NMR and high-resolution x-ray techniques cannot detect the disease.[5]

PET, however, is not limited to the evaluation of regional rates of glucose metabolism, but can also be used to investigate more basic physiologic processes through the use of tracer techniques with mathematical modeling. The kinetics of glucose metabolism can be represented by a three-compartment model (Fig. 1, top) with three rate constants[6]; k1 represents transport of glucose from blood to brain, k2 is the reverse transport, and k3 represents the phosphorylation of glucose by the enzyme hexokinase. Because dephosphorylation occurs very slowly in brain, if at all, its rate constant, k4, is not modeled.

The tracer [^{18}F]fluorodeoxyglucose (FDG) is utilized in these studies. Between 5 and 10 mCi of activity are injected in the patient. Subsequently, blood is collected at frequent intervals from a hand vein for 60 minutes in order to derive a description of the variation of blood activity with time. Concurrently with this, the Donner 280-crystal tomograph acquires data from the brain. Because of the high temporal resolution of the instrument we are able to acquire data rapidly, thus providing a good description of the time-course of brain activity. Through the use of a nonlinear iterative least squares fitting procedure, we are able to fit the brain and blood time-activity curves to the three-compartment model in order to derive the rate constants for glucose transport and phosphorylation.

Results in 11 patients with Alzheimer's disease and 6 healthy elderly control subjects are presented

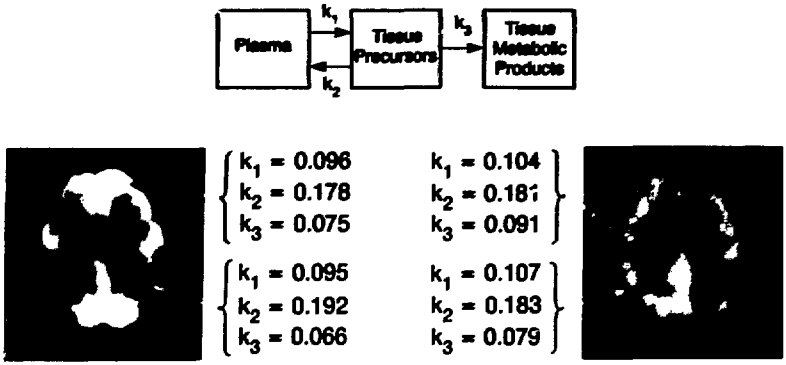

Fig. 1. *Top: The three-compartment model representing forward and reverse transport (k_1 and k_2) and phosphorylation (k_3) of glucose. Bottom: Rate constants from Alzheimer patients (left) and control subjects (right). Data represent regional values for frontal and temporoparietal cortex of each group.* *(XBB 850-10104)*

in Fig. 1, bottom. Rate constants have been calculated for regions of frontal, temporoparietal, occipital, and entire cortex. Values shown here are those for the mean of left and right frontal and temporoparietal cortex for Alzheimer and control subjects. These results are not significantly different from each other because of the large variability of the populations. When ratios are constructed of the individual rate constants in frontal temporoparietal, and occipital cortices divided by the same rate constant in entire cortex, this variability is reduced. We then find that the ratio of k3 for temporoparietal cortex to k3 for entire cortex is smaller in the Alzheimer patients than the controls ($p < 0.02$).

We can also calculate metabolic rates using the kinetic data. The local cerebral metabolic rate for glucose (LCMRglc) is given by the steady-state equation (k1 × k3)/(k2 + k3) times the plasma glucose concentration. Using this method, we find that LCMRglc is significantly lower ($p < 0.05$) in temporoparietal cortex in the Alzheimer patients.

These results, in addition to demonstrating that the temporoparietal cortex is most severely involved in AD, provide new evidence that helps to localize the site of the physiological lesion. The findings of normal k1 and k2 in all cortical regions suggest that glucose transport is normal in the illness. The lower k3, which is the rate constant for the hexokinase reaction, implicates the phosphorylation process as the factor limiting glucose metabolism in AD. It remains to be determined whether this occurs because of an actual abnormality in the enzyme or its kinetics, or that the results reflect a normal physiologic process occurring in fewer normally functioning cortical neurons.

REFERENCES

1. Friedland, R.P., Budinger, T.F., Ganz, E., et al. Regional cerebral metabolic alterations in dementia of the Alzheimer type: positron emission tomography with [^{18}F]fluorodeoxyglucose. *J. Comput. Assist. Tomogr. 7*, 590–598 (1983).
2. Jagust, W.J., Friedland, R.P., Budinger, T.F. Positron emission tomography with [^{18}F]fluorodeoxyglucose differentiates normal pressure hydrocephalus from Alzheimer-type dementia. *J. Neurol. Neurosurg. Psychiat. 48*, 1091–1096 (1985).
3. Friedland, R.P., Budinger, T.F., Koss, E., and Ober, B.A. Alzheimer's disease: anterior-posterior and lateral hemispheric alterations in cortical glucose utilization. *Neurosci. Lett. 53*, 235–240 (1985).
4. Koss, E., Friedland, R.P., Ober, B.A., Jagust, W.J. Lateral hemispheric asymmetries of glucose utilization are different in early and late onset Alzheimer-type dementia. *Am. J. Psychiatr. 142*, 638–640 (1985).
5. Friedland, R.P., Budinger, T.F., Brant-Zawadzki, M., and Jagust, W.J. The diagnosis of Alzheimer-type dementia: a preliminary. comparison of positron emission tomography and proton magnetic resonance. *JAMA, 252*, 2750–2752 (1984).
6. Sokoloff, L., Reivich, M., Kennedy, C., et al. The [^{14}C]deoxyglucose method for the measurement of local cerebral glucose utilization: theory, procedure, and normal values in the conscious and anesthetized albino rat. *J. Neurochem. 28*, 897–916, (1977).

HUMAN MYOCARDIAL STUDIES WITH ^{82}Rb AND PET

Thomas F. Budinger, Yukio Yano, Julia A. Twitchell, Kathleen M. Brennan, Stephen E. Derenzo, and Ronald H. Huesman

Since 1978 we have been perfecting a method for the early detection of atherosclerosis leading to heart attacks. Each day an estimated 3400 Americans, more than two each minute, suffer a heart attack. While most heart attacks are not fatal, they frequently occur in subjects who are not under physicians' care or who do not know they have a problem.

Our method employs positron emission tomography (PET) for production of pictures reflecting the integrity of blood flow to heart muscle. This procedure is believed to be far more definitive and practical than coronary angiography because the PET method shows the actual muscle capillary perfusion, whereas coronary angiography done through catheterization shows only narrowing of the coronary arteries, which is not strictly indicative of compromised heart muscle flow. After six years of development, including the improvement of the Donner 280-crystal PET device, we discovered a new procedure providing important results.

The new protocol for the examination of heart patients before and after exercise using ^{82}Rb and positron emission tomography (PET) has now been successfully completed on four patients. Short-lived ^{82}Rb (76-sec half-life) is available from a small portable generator (developed at LBL in 1968), which eliminates the need for a cyclotron.

The patient is exercised briefly on a treadmill with a cardiologist in attendance. ^{82}Rb is injected at a point of peak exercise when, in our judgement, exercise can be continued for another 60 seconds. At the end of exercise the patient is positioned in the tomograph at the appropriate transverse section, predetermined by a transmission image taken prior to exercise. A static image is acquired over the ensuing 5-minute interval. The patient is allowed to rest and another ^{82}Rb study is performed 15 or 30 minutes later.

Of the patients studied, one had an inferior posterior wall infarction and had been studied by coronary artery angiography. The rubidium study was made to ascertain if there was a margin of viable tissue in the region of this previous infarction that might benefit from angioplasty. We ascertained that such was the case because the exercise image showed a greater volume of diminished rubidium uptake than was the case during rest. Based on this study, the patient received an angioplasty.

Two patients had septal wall lesions demonstrated on thallium and angiography studies. Their ^{82}Rb studies showed a remarkable differential uptake of rubidium in the septal and left ventricular wall regions before and after exercise. Results from one of these studies are shown in Figs. 1 and 2. We observed that the compromised muscle, which has limited blood flow, receives even less blood relative to the normal muscle during exercise. However, after exercise there is a rebound flow (hyperemia) in the compromised muscle. This leads to reversal in the ratio of uptake of Rb between the compromised and normal muscle.

These results are new findings, which have not been observed before because no isotope studies involving separate injections before and after exercise had been done. The reason is that radionuclides previously used do not have the short half-life of ^{82}Rb which enables the before- and after-excercise studies to be done.

These observations have given us strong evidence that we now have a very sensitive method for detection of coronary artery disease that entails radiation doses to the patient no greater than those received from routine back x rays.

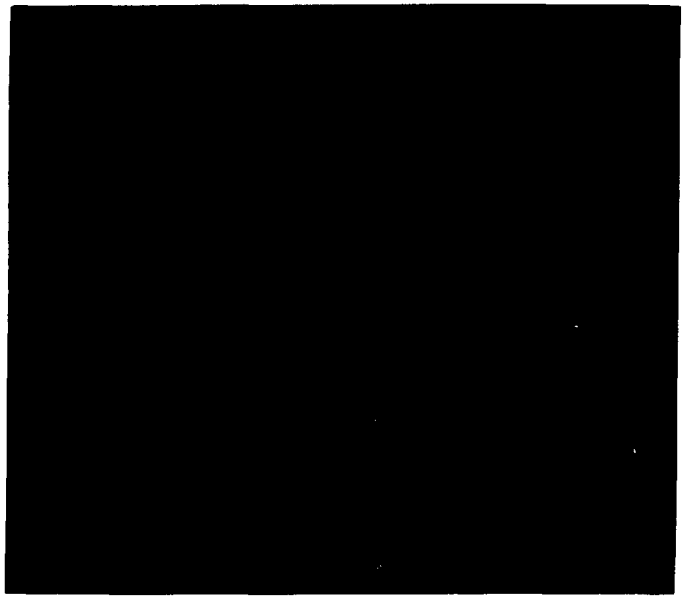

Fig. 1. Left shows decreased septal uptake during exercise. This area shows "rebound" blood flow increase after rest. This pattern of decreased-then-increased rubidium accumulation relative to the accumulation in normal heart muscle is a new finding. *(CBB 858-6389)*

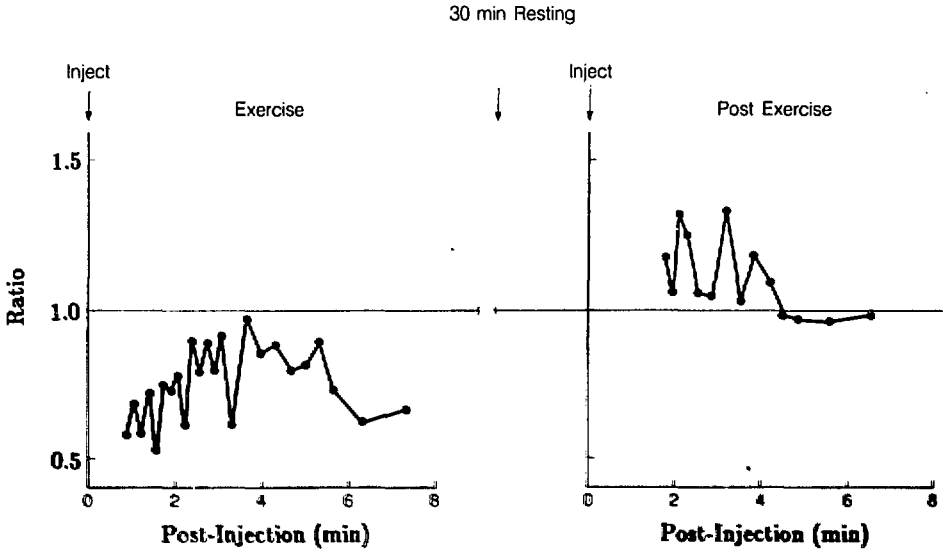

Fig. 2. Ratio of ^{82}Rb accumulation in the septum to the left myocardial wall 60 sec to 420 sec after injection in a patient with a septal defect. *(XBL 859-10749)*

POSITRON EMISSION TOMOGRAPHY OF FDG IN SCHIZOPHRENIA

Thornton Sargent III and Natalia Kusubov

Research groups studying schizophrenia at several laboratories have reported reduced frontal blood flow, reduced frontal glucose metabolism, and enlarged ventricles in the brains of patients with this disorder. We have used the Donner dynamic positron emission tomograph (PET), which has the spatial and temporal resolution to quantify metabolism of the brain more accurately than other instruments, to study fluorodeoxyglucose labeled with fluorine-18 (18-FDG) in six patients with schizophrenia and six normal controls in a collaborative study with the Palo Alto Veteran's Administration Medical Center. This radiopharmaceutical has been widely used and studied; it is taken up by the brain and phosphorylated by the same mechanisms used for glucose metabolism, but at the step after phosphorylation the metabolism is arrested. Thus, the quantitative localization of the positron-emitting fluorine-18 provides a quantitative image of regional glucose uptake. A mathematical model describing the metabolism has been derived by other workers, utilizing the compartment model shown in Fig. 1. Solution of the model to obtain values for k_1, k_2, and k_3 requires, in addition to rapid blood sampling to obtain the input function, rapid dynamic sampling of appearance of the radioactivity in the brain. The Donner PET imaging system is unique in its ability to obtain rapid sampling and thus obtain the k's for any desired brain region in each patient. Other laboratories use the mean values from a few normal subjects to solve an operational equation that provides the local cerebral metabolic rate (lCMR) for various brain regions. In this method the static values of fluorine-18 concentration seen by PET 40 minutes after injection are used in what is known as the operational equation, a complex function incorporating many assumptions, including the average k values to calculate lCMR. By use of our dynamic PET imaging capabilities we are able to calculate a glucose metabolic rate (GMR) from the equation

$$GMR = \frac{k_1 k_3}{k_2 + k_3} Cp \quad ,$$

where C_p is the plasma glucose concentration. The dynamic brain uptake data and the blood input function are used to calculate the k's by an iterative least squares fitting program on our VAX 780 computer, for all regions of interest chosen in the brain.

All of the patients had been withdrawn from medications for two weeks prior to the 18-FDG study. One important difference between our study and that of other laboratories that reported reduced frontal uptake in patients with schizophrenia was that our subjects were all given an auditory vigilance task during the study. The purpose of this was to have all subjects in the same cognitive state, so that any differences seen could be attributed to underlying pathophysiogy rather than to variability of cognition. We did not observe any differences between patients and controls in relative uptake in the static 40-min FDG images in any brain region that we examined, which included the frontal lobes, the peri-sylvian, temporal-parietal and occipital cortex. However, in the four patients and three normals in whom we were able to measure the dynamic uptake data and solve the compartment model, we found differences in the values for the rate constants of Fig. 1. All three rate constants, k_1, k_2, and k_3 were lower on the average in the patients with schizophrenia. These differences reached statistical significance for k_3 in specific regions of the brain, mostly on the right side, as shown in Fig. 2. The 18-FDG images of patients and normal controls were not visually different; the image in Fig. 2 is one from a patient in which individual regions of the cortex, for which calculations were made, are outlined in white.

Although this is too small a group of patients on which to base conclusions, differences in k_3 were statistically significant in several brain regions; the means of k_1 and k_2 were also lower in the patients, but did not reach statistical significance. In spite of these overall lower values, the calculated GMR values were not lowered to the same degree due to the nature of the equation for GMR and the operational equation for lCMR, as shown in Table I. That is, since k_3 appears in both the

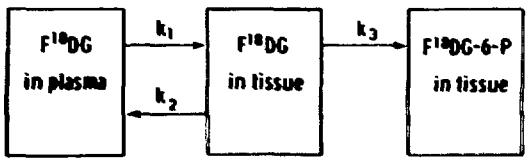

Fig. 1. *Compartment model for 18-FDG transport in brain.*
(XBL 8511-8572)

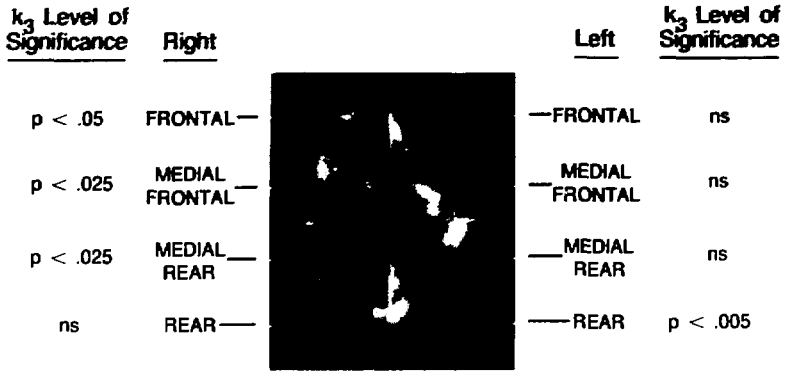

Fig. 2. *^{18}FDG concentration (in white) in transverse section of brain of a patient with schizophrenia; normal controls were not visually different. White outlines are regions for which k's were calculated, and the level of significance (t-test) between normals (n = 3) and patients (n = 4) for each region is shown in the side columns (ns = not significant).* *(XBB 850-10176)*

numerator and denominator, if it is reduced and k_1 and k_2 are also reduced, the value of GMR obtained from the equation is relatively insensitive to such changes in the k's. Thus it appears possible that there may be differences in glucose transport and metabolism in the brain that are not as apparent from simple static measurements used for lCMR calculations, or even from the GMR. The physiologic association customarily made is that k_1 represents 18-FDG uptake by the cell from circulating blood and that k_3 is the rate of phosphorylation. Our results suggest that these rate parameters may change in schizophrenia, although probably as a result of some other basic pathophysiology, and we will study further patients to provide a better statistical basis for these observations.

Table 1. Mean values of transport parameters calculated for patients and controls.

	Mean values for all cortical regions		
	Normal controls	Unmedicated patients	Percent difference
k_1	0.124	0.107	−13.7%
k_2	0.196	0.173	−11.7%
k_3	0.0996	0.0727	−27.0%
GMR	3.40	3.32	−2.3%
lCMR	3.84	3.25	−15.3%

GALLIUM-68 LABELED PLATELETS AND POSITRON EMISSION TOMOGRAPHY FOR DETECTING VASCULAR LESIONS

Yukio Yano, Kathleen M. Brennan, Mohindar Singh, Julia A. Twitchell, Dorothy A. Carpenter, Elizabeth M. Mazoyer, Shirley N. Ebbe, Kanu Dalal, Ronald H. Huesman, Chester A. Mathis, and Thomas F. Budinger

The enthusiasm for platelet accumulation studies is based on substantial evidence that platelet deposition at sites of arterial injury play a central role in arteriothrombosis and atherogenesis. The technique of platelet labeling and imaging, particularly using high resolution positron-emission tomography, may permit the evaluation of localized platelet deposition on vascular lesions. Imaging capable of assessing platelet activity and distribution would be invaluable in the evaluation of platelet

dynamics associated with high risk for stroke and in following the kinetics of platelet accumulation noninvasively in the body for detecting clinical complications of atherosclerosis before embolization occurs.

Human and animal platelets have been labeled with ^{67}Ga, ^{68}Ga, ^{99m}Tc, and ^{111}In for imaging studies. ^{111}In-labeled platelets demonstrate normal functional characteristics of the more traditional ^{51}Cr platelets. ^{111}In-labeled autologous platelets have been used to detect carotid atherosclerosis in man, to measure thrombogenicity of arterial grafts and to identify sites of peripheral balloon angioplasty. However the use of ^{111}In-platelet imaging is limited to a dose of only 300 μCi due to the radiation dose from the 67-h half-life of ^{111}In. Furthermore the ^{111}In activity from platelets in the general circulation causes interference in normal single projection imaging. A solution to these problems might lie in the use of platelets labeled with generator-produced ^{68}Ga, a positron emitter with a half-life of 68 min. Using proper instrumentation for positron imaging, the sensitivity for detection of ^{68}Ga-labeled platelets can be 10 or more times greater than for single-photon imaging. Of equal importance is the fact that due to the short-half life of ^{68}Ga a dose 10 or more times greater than ^{111}In can be injected. Thus ^{68}Ga-labeled platelets should provide a sensitivity of 100 times more than the ^{111}In-platelet procedure. In addition, cross-sectional positron tomographic methods are able to provide quantitative data with a resolution of 2.5 mm, which is not available with single-photon imaging.

GALLIUM-68 LABELLED PLATELETS AND ANIMAL STUDIES

From work reported last year it was found that ^{68}Ga complexed to the lipophilic ligand mercaptopyridine-N-oxide (^{68}Ga MPO) gave the best platelet labeling results of 43–63% with both human and rabbit platelets.

The platelets used in these studies were separated by centrifugation from 35–45 ml of rabbit blood collected in Squibb modified acid citrate dextrose. The platelet-rich plasma (PRP) was separated from the red cells; then the platelets were separated from the PRP by centrifugation. The separated platelets were suspended in saline and incubated with the ^{68}Ga MPO complex. After centrifugation, the free ^{68}Ga was removed in the supernatant, and the ^{68}Ga-labeled platelets were resuspended in saline for intravenous infusion into scraped-aorta rabbit models for PET imaging and tissue distribution studies of the ^{68}Ga platelets.

The ^{68}Ga-labeled platelets were evaluated in animal studies using New Zealand white rabbits weighing 3–4 kg. The scraped-aorta rabbit models were prepared about 10–20 min before intravenous injection of the ^{68}Ga-labeled platelets. An embolectomy catheter was introduced intrafemorally and pushed to the aorta arch. The bulb was inflated to about the same pressure each time, and the aorta was scraped three times before the catheter was removed.

The ^{68}Ga platelets were administered intravenously, and whole body PET images (Fig. 1) were obtained with the Donner 280 bismuth germanate (BGO) detector positron tomograph. The animals were sacrificed, and the percent uptake of the injected tracer was determined for selected tissues as well as for the normal and scraped aorta. Enface autoradiography of the aortic wall was also used to demonstrate the regional uptake of the labeled platelets on the exposed media smooth muscle layer. Normally, intimal endothelium protects the medial layer from platelet adherence and degranulation. The removal of the endothelial layer from the vessel was confirmed by the uptake of Evans blue dye on the aortic wall when the dye was injected 30 min before sacrifice. The percent uptake of the injected dose (ID) of ^{68}Ga platelets in selected organs and aorta is seen in Table 1.

The spleen has the greatest concentration of the ^{68}Ga platelets with a range of 1.9-6.1%/g. Rabbit #3 data were excluded because of acute trauma to the aorta due to over-inflation of the balloon cathether. Using the carotid arteries and the proximal aorta for normal aortic uptake ($n = 8$) gives 0.04 ± 0.01% ID in normals. For the scraped aorta ($n = 3$) there was 0.15 ± 0.06% of ID in damaged aorta. Nearly four times more uptake occurred in the damaged endothelium of the aorta compared to the normal. The lung uptake has a wide range from 0.13 to 1.30% ID. In some animals the lungs were abnormally enlarged and showed infiltration with granular clusters. It is known that trauma or endotoxins can cause pulmonary platelet aggregation. The damaged aorta showed staining with Evans blue dye and about four times the radioactivity compared to the normal aorta as determined by autoradiography and densitometer measurements.

Platelet viability, i.e., the ability to recirculate, is a stringent test of the integrity of labeled platelets. Survival of labeled platelets also gives an estimate of the permanence of the attachment of the radioisotope to platelets. Longer-lived ^{67}Ga ($t_{1/2}$ = 3.2 d) was treated identically to ^{68}Ga and labeled to

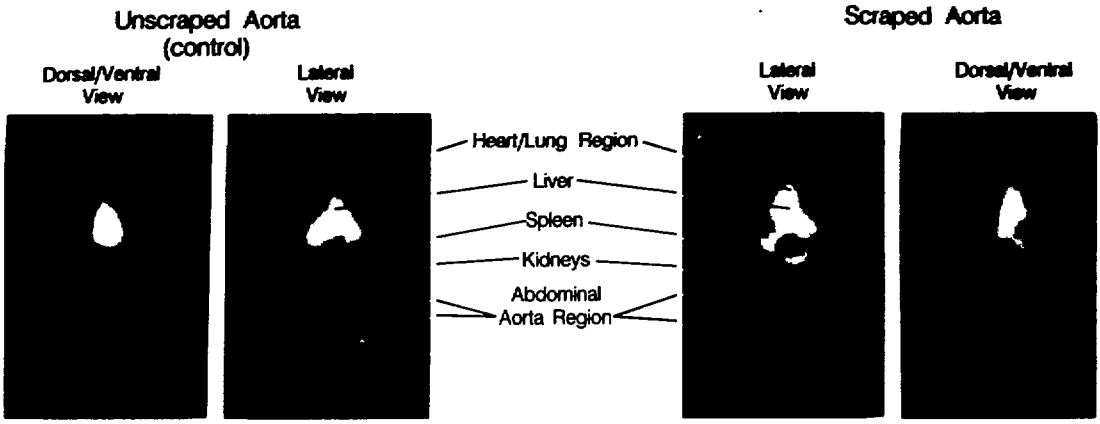

60–70% Labelling Efficiency of Ga^{68} MPO onto Platelets
Final Platelet Suspension for Injection:

5–10 Million Platelets/cc
4–5 cc Injected into Rabbit
~1 mCi Ga^{68} activity

Fig. 1. *^{68}Ga platelet imaging in scraped-aorta rabbit model by positron emission tomography whole-body scans.* *(XBB 840-7350A)*

Table 1. Uptake of ^{68}Ga platelets (% injected dose/gram tissue).

	When aorta scraped	Carotid arteries	Proximal aorta	Distal aorta	Spleen	Heart	Lung	Kidney cortex	Liver
Rabbit #1	20 min *before* inj	0.03	0.03	0.11	4.65	0.06	0.13		0.23
Rabbit #2	Immediately *before* inj	0.05	0.05	0.22	1.89	0.07	0.50	0.10	0.21
Rabbit #3	Immediately *after* inj	0.02	0.09	4.88[b]	10.24	0.11	0.44	0.10	0.28
Rabbit #4	Immediately *after* inj	0.02	0.04	0.13	3.02	0.03	0.31	0.05	0.33
Rabbit #5	Control *not* scraped	0.04	0.04	0.06	6.06	0.14	1.30	0.08	0.28

$$\text{Average Uptake Ratio } \frac{\text{Scraped distal aorta}}{\text{Normal proximal aorta}}^{a} = 3.77$$

[a]Does not include distal aorta from Rabbit #3.
[b]Distal aorta on Rabbit #3 was very damaged.

rabbit platelets to determine the recovery and survival after intravenous injection into normal rabbits. Results were compared to ^{51}Cr-labeled platelets and are presented in Table 2.

These results demonstrate the feasibility of labeling viable rabbit platelets with ^{67}Ga or ^{68}Ga. Their survival *in vivo* is similar to that of ^{51}Cr-labeled platelets.

Table 2.

Isotope	Medium	1-hour recovery (%)	Survival, days (extrapolated)	n
^{51}Cr	plasma	50–100	3–4	7
^{51}Cr	saline	60–100	4	5
^{67}Ga	saline	43–104	3–4	19

ABNORMALITIES OF BLOOD PLATELETS IN RABBITS WITH DIETARY HYPERCHOLESTEROLEMIA AND ATHEROSCLEROSIS

Elisabeth Mazoyer, Kanu Dalal, Dorothy Carpenter, Kathleen Brennan, Tamlyn Yee, Bernard Mazoyer, Robert Leven, and Shirley Ebbe

Atherosclerosis is a common disease that accounts for extensive morbidity and mortality in human beings, but its causes and pathogenesis are not well understood. Currently available diagnostic procedures usually permit diagnosis of the disease only when it is far advanced. Because of the difficulty in detecting and studying early vascular lesions in human beings, animal models have been used for development of better diagnostic procedures and study of etiologic factors. This report will describe some aspects of our preliminary observations of rabbits that were fed a high cholesterol diet to induce atherosclerosis.

Rabbits were fed a diet consisting of 1% cholesterol and 4% peanut oil. At two-week intervals, complete blood counts, serum cholesterol, platelet volume, and platelet lipids and protein were determined. After 2 to 3 months on the diet, the survival of homologous platelets labeled with ^{51}Cr was measured. The animals were then killed, and their aortas were removed and examined grossly and microscopically.

Hypercholesterolemic rabbits developed pronounced atherosclerotic lesions of the aorta (Fig. 1). On microscopic sections, the lesions showed subendothelial infiltration with a substance that stained with the lipid-specific stain, oil red O. One of the purposes of this project was to develop an animal model that would be appropriate to use for testing the feasibility of noninvasively imaging vascular lesions by positron emission tomography or other techniques. The reproducible and rapid development of vascular lesions makes this a useful animal model for detection of substances that interact with lipid-laden vessel walls.

It is thought that blood platelets may play a role in the production of atherosclerotic lesions by interacting with the vessel wall in areas where the endothelium is damaged. However, studies by others of the aortas of monkeys that were fed an atherogenic diet indicated that platelet adherence to the vessel wall occurred late in the course of diet-induced atherosclerosis relative to the subendothelial accumulation of lipid. In addition to their proposed role in the pathogenesis of vascular lesions, the possibility that blood platelets themselves may be abnormal in hypercholesterolemia

Fig. 1. Luminal surface of thoracic aorta from a normal rabbit (above) and a rabbit fed a high cholesterol diet for about 2 months (below). (XBB 850-9571)

has been reported. Functional abnormalities may differ in different species, but they indicate that platelets may be hyperreactive to stimuli that induce aggregation. Platelet abnormalities do not appear to result from exchange of plasma lipids. Rather, the platelets are probably abnormal when produced by the megakaryocytes in hypercholesterolemic subjects. These reports by others support our findings that the platelets in hypercholesterolemic rabbits are not only chemically abnormal but are small in size.

Rabbits fed the high cholesterol diet rapidly developed hypercholesterolemia, with serum cholesterol increasing to about 1500 mg% after 8 weeks (normal = <100 mg%). After 2 weeks on the diet, platelet counts gradually increased, so that after 8 weeks, they were about 70% greater than those of control rabbits. The difference between diet and control animals was amplified by the fact that platelet counts of control animals (also bled every 2 weeks) declined during the course of the experiments; the reason for this decline is not evident. Platelet volumes were measured by three different methods: 1) platelets in samples of whole blood were electronically sized in an instrument with a hydrodynamically focused aperture tube; 2) platelets in platelet rich plasma were sized by Coulter counter, and the possible contribution of lipid droplets to the result was eliminated by correcting each result by "sizing" samples of platelet poor plasma; and 3) platelets separated from plasma by Stractan gradient were sized by Coulter counter. Absolute values for platelet volumes varied somewhat depending on the method, but the differences between platelets from control and diet rabbits were found with all three methods. After 2 weeks, platelets of animals fed a high cholesterol diet were consistently smaller than those of controls. The difference was due to two factors: a pronounced decrease in size of platelets in hypercholesterolemic rabbits and a moderate increase in size in controls. After 8 weeks, the average volume of platelets of diet rabbits was about 70% that of controls.

Even though the platelets were smaller than controls, they contained more lipid (1575 vs. 737 $\mu g/10^9$ platelets) and more protein (2330 vs. 1768 $\mu g/10^9$ platelets). The lipid increase was due to an increase in free cholesterol and was associated with a reduction in total phospholipid. The molar ratio of free cholesterol to total phospholipid was increased (3.5 vs. 0.5). The significance of these changes to platelet function, prostaglandin metabolism, and fatty acid composition of platelets is under investigation.

The survival of normal homologous platelets in hypercholesterolemic rabbits was normal, suggesting that the observed platelet abnormalities were not due to damage inflicted by circulation through atherosclerotic vessels. Preliminary observations suggest that the survival of the small, biochemically abnormal platelets produced by the hypercholesterolemic rabbits may be shorter than normal. Studies of the kinetics of production and destruction of platelets are continuing.

Platelet and vascular abnormalities are prominent under the experimental conditions described. However, it is clear that these conditions do not accurately mimic human atherosclerosis. Rabbits tolerate the diet for no more than 3 months. They gradually become anemic with acanthocytosis and reticulocytosis, and develop fatty infiltration of their livers and other tissues. The possibility that the platelet abnormalities may represent an enlightening caricature of more subtle changes that have been described in other species encourages further study.

IN VITRO MATURATION OF BONE MARROW MEGAKARYOCYTES

Robert M. Leven, Marilyn Yee, and Cheryl Lynn Tanguay

The maturation of bone marrow megakaryocytes is being studied in order to understand the mechanisms by which platelet formation is controlled in normal animals and in conditions of induced thrombocytopenia. Present studies are investigating the effect of plasma from thrombocytopenic rabbits on megakaryocyte morphology. It has been shown that a fraction of plasma from thrombocytopenic rabbits can stimulate thrombopoiesis *in vivo*, but no direct effect of this factor, called thrombopoietin, on mature megakaryocytes has previously been demonstrated.

For these experiments megakaryocytes are isolated from suspensions of bone marrow cells. A

combination of density gradient centrifugation and velocity sedimentation is used to prepare megakaryocytes that are purified up to 900-fold compared to the starting material (Fig. 1). The cells are maintained in liquid culture for up to 48 hours with little loss of viability.

To prepare crude thrombopoietin, citrated plasma is collected from control rabbits and from experimental rabbits 4 hours postinjection of anti-platelet antiserum. Platelet count and hematocrit are measured to ensure that the animals are thrombocytopenic without any anemia. The plasma is fractionated by ammonium sulfate precipitation. The fraction of proteins that precipitates between 60% and 80% saturation is collected, solubilized, dialyzed and concentrated. This fraction from the plasma of control animals or thrombocytopenic animals is added at one tenth volume to cultures with isolated megakaryocytes.

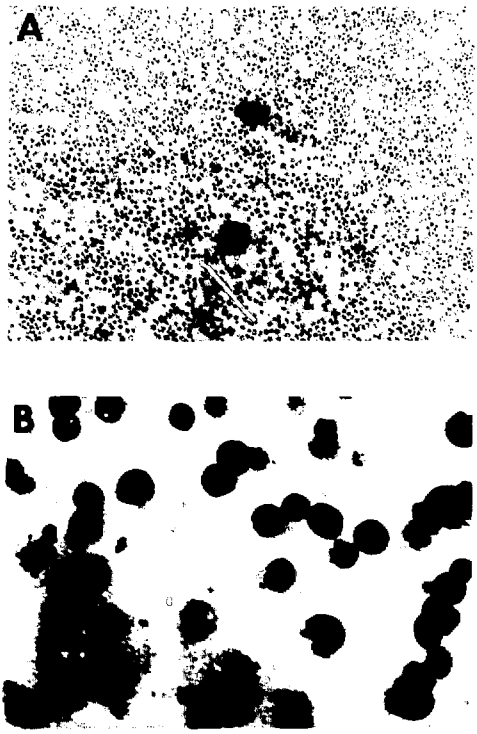

Fig. 1. A) Mouse bone marrow suspension stained for acetylcholine esterase. Megakaryocytic cells stain, while only the nuclei of other cell types are visible. B) Purified megakaryocytes stained for acetylcholine esterase. The cell suspension contains almost all megakaryocytes with few contaminating cells. ((A) XBB 850-9099, (B) XBB 850-9100)

Normal megakaryocytes, when isolated in liquid culture, are spherical (Fig. 2). After 12–18 hours incubation with the thrombocytopenic plasma fraction, 5%–7% of the cells form many long cytoplasmic extensions (Fig. 3). The cytoplasm becomes attenuated and may actually fragment. It has been postulated that the formation of cytoplasmic processes may be an important step leading to platelet formation, but although in our culture conditions there is some cytoplasmic fragmentation, it remains to be shown if true platelets are formed.

The cytoskeletal basis for the stimulation of megakaryocyte morphogenesis is also under investigation. Colchicine and vincristine, which disrupt microtubules, inhibit the effect of the thrombocytopenic plasma. Unexpectedly, cytochalasin B, which disassembles microfilaments, seems to mimic the effect of the thrombopoietin preparation, causing almost all of the megakaryocytes in the culture to form cytoplasmic processes (Fig. 4). Therefore it appears that intact microtubules are required for the effect of the thrombocytopenic plasma on megakaryocyte morphology, while the role of microfilaments remains obscure.

The possible role of cyclic AMP in this stimulation is also of interest. Drugs that affect cyclic AMP metabolism have been shown to profoundly alter the morphology of platelets and megakaryocytes. We have found that the phosphodiesterase inhibitor isobutylemethylxanthine can reverse the stimulation of cytoplasmic process formation if it has not progressed too far. The very long processes are not affected, while shorter ones retract.

These studies show that a still poorly defined factor in the plasma of thrombocytopenic rabbits,

Fig. 2. Isolated megakaryocytes in liquid culture. Prior to addition of the thrombocytopenic plasma fraction all cells are spherical. (XBB 850-9095)

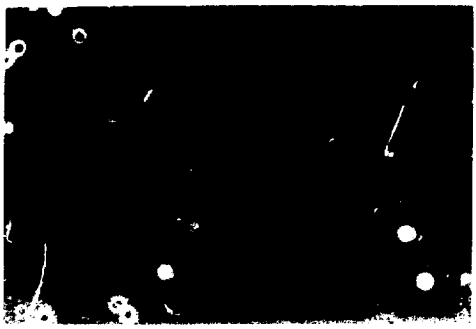

Fig. 3. Isolated megakaryocytes incubated with the thrombocytopenic plasma fraction for 18 hours. The formation of cytoplasmic processes and the attenuation of the cytoplasm are apparent in the center cell. (XBB 850-9096)

Fig. 4. Isolated megakaryocytes incubated for 18 hours in the presence of the thrombocytopenic plasma fraction and 10 µg/ml of cytochalasin B. Many more cells react, and the cytoplasm begins to fragment. (XBB 850-9097)

but not normal rabbits, is capable of stimulating morphological change in megakaryocytes thought to be similar to that which occurs during platelet formation *in vivo*. This implies that a possible mechanism by which animals compensate for thrombocytopenia could be through the direct action of a humoral agent on mature megakaryocytes, stimulating their platelet forming activity. This is in contrast to control of platelet formation by an increase in the number or maturation rate of megakaryocyte precursor cells, a very different mechanism of altering thrombopoiesis.

RELATIONSHIP BETWEEN MEGAKARYOCYTE SIZE AND PLOIDY IN MICE DURING RECOVERY FROM ACUTE IMMUNOTHROMBOCYTOPENIA

Shirley Ebbe, Tamlyn Yee, Dorothy Carpenter, and Elizabeth Phalen

Megakaryocytes in the bone marrow are normally polyploid cells, and the final size of a megakaryocyte is determined by its ploidy. Since the size of a megakaryocyte determines the cytoplasmic mass that fragments into platelets, ploidy is also a determinant of the mass of platelets producted by a megakaryocyte. When the level of blood platelets is experimentally perturbed, megakaryocyte ploidy and size are adjusted to change the rate of platelet production in the direction of normalizing the platelet count; these changes occur together with changes in the number and maturation rate of megakaryocytes. These findings show that there is a feed-back mechanism by which the rate of production of platelets is regulated by their number in the blood.

Macromegakaryocytosis occurs in response to depletion of blood platelets, and the ploidy distribution of megakaryocytes shifts to higher values. The present experiments were done to determine if the shift in ploidy accounts for all the macrocytosis or if size changes would occur within ploidy groups. The size and ploidy of individual mouse megakaryocytes of a defined morphological class were compared from 4 hours to 4 days after thrombocytopenia was produced by an injection of guinea pig antimouse platelet serum (APS). The areas of post-DNA synthetic mature (stage III) megakaryocytes were measured in bone marrow smears stained with Wright and Giemsa stains. The smears were destained, restained by the Feulgen technique, and the ploidy of the same cells was measured by two-wavelength microspectrophotometry. Small segmented nuclei were measured as 2N reference cells.

Of 781 normal stage III megakaryocytes, 0.1% were 4N, 8.7% 8N, 72.1% 16N, 18.0% 32N, and 1.0% 64N. From 8 to 64N, mean size increased by

a factor of 1.4–1.6 between ploidy groups, but there was a considerable amount of overlap of sizes between ploidy groups. Four hours after a single injection of APS, platelet counts of the mice were less than 5% of normal, and recovery from the thrombocytopenia occurred gradually over several days. Changes in ploidy distribution of stage III megakaryocytes occurred on days 2–3 after the injection of APS and were maximal at day 2.5 (1.4% 8N, 47.2% 16N, 45.8% 32N, 4.2% 64N, and 1.4%128N). The mean size of megakaryocytes of all ploidy groups paralleled the proportion of 32N and 64N cells, indicating that ploidy was a major determinant of overall megakaryocyte size. Mean size of all stage III megakaryocytes was maximally increased to 155% of normal on day 2.5. In one experiment, 32N megakaryocytes were 22% larger than normal 32N megakaryocytes ($p < 0.005$) 2 days after injection of APS, showing that megakaryocyte size may increase out of proportion to ploidy in some cases. However, in three experiments there was no change in size within ploidy groups (Fig. 1).

These results show that the main cause of macrocytosis of megakaryocytes in response to the stimulatory effect of acute thrombocytopenia is a shift to higher nuclear DNA content. Size may occasionally increase within the 32N ploidy group, suggesting that this group of cells may be more responsive to the demands imposed by acute thrombocytopenia than the others. The mechanism of macrocytosis within the 32N group is not known, but it may be related to the acceleration of maturation that occurs in response to platelet depletion.

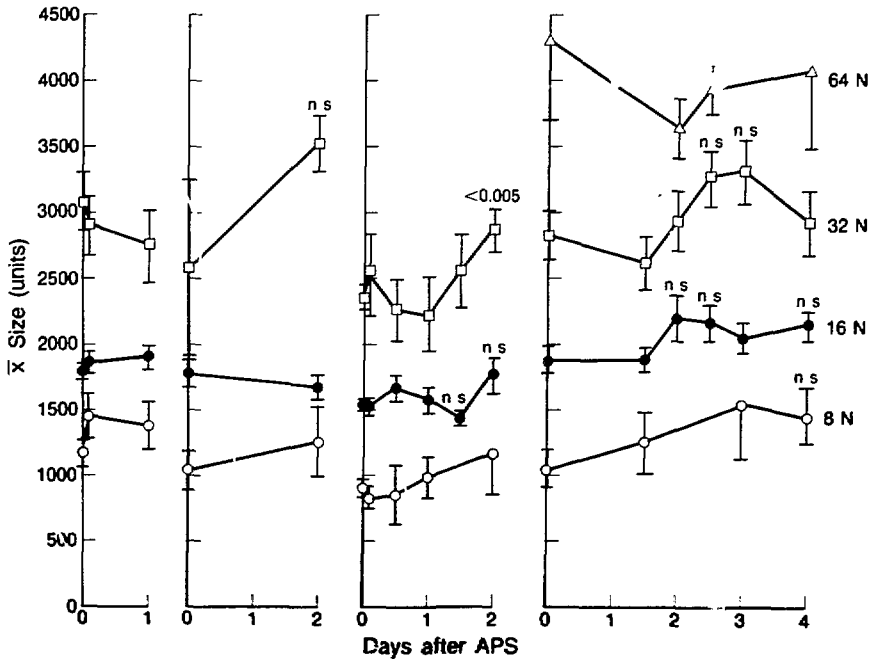

Fig. 1. The results of four experiments in which sizes and ploidy of individual stage III (mature, platelet-producing) megakaryocytes were measured after acute thrombocytopenia was produced by a single injection of APS. The ordinates show the average sizes of megakaryocytes within each ploidy group; the abscissas show time after injection of APS. Changes in size that were not statistically significant (Student's test, $p > 0.05$) are designated as "ns" (not significant). In the third experiment, 32N megakaryocytes were significantly larger than 32N megakaryocytes of uninjected controls 2 days after injection of APS. (XBL 858-8440)

THROMBOCYTOPOIETIC RESPONSE TO IMMUNOTHROMBOCYTOPENIA IN NUDE MICE

Shirley Ebbe, Jack Levin, Kathleen Miller, Tamlyn Yee, Francine Levin, and Elizabeth Phalen

It is known that platelet production is regulated by feed-back mechanisms that are, in turn, regulated in part by the level of circulating platelets. Thus induction of immunothrombocytopenia in normal mice by injection of heterologous antiplatelet antibodies, is followed by compensatory increases in megakaryocytopoiesis and platelet production to correct the platelet deficit. A humoral thrombopoietin appears to account for this stimulation of thrombocytopoiesis, but the cellular mechanisms responsible for determining the level of thrombopoietin are unknown.

Hemopoietic tissues contain cells that form colonies of differentiated cells when cultured with appropriate conditioning medium *in vitro*. The precursors of the colonies are thought to be committed stem cells for the individual types of myeloid cells, and they include those that form megakaryocytes (Meg-CFC), granulocytes and macrophages (GM-CFC), and erythrocytes (BFU-E and CFU-E). Conditioning medium for Meg-CFC is commonly prepared from mitogen stimulated T lymphocytes, thus introducing the possibility that T lymphocytes may have a role in meditating the regulation of platelet production *in vivo*. It has been further suggested that the thrombocytopoietic stimulatory effects of acute immunothrombocytopenia could be partly mediated by T cell activation by the antigen-antibody reaction that follows the injection of preformed heterologous antiplatelet serum (APS). In either case, nude mice (nu/nu) should show abnormalities of thrombocytopoiesis or the response to acute platelet depletion, since, in addition to being hairless, nu/nu mice are deficient in T lymphocytes. The present experiments were done to determine if thrombocytopoiesis would be abnormal in T cell deficient nu/nu mice or if they would respond to thrombocytopenia differently than normal (nu/+) controls.

Untreated nude mice had normal platelet and megakaryocyte counts, indicating that unperturbed platelet production was normal. They had a slight but significant anemia and significantly fewer bone marrow cells than nu/+ mice. Their spleen cells showed a normal mitogenic response, as determined by tritiated thymidine incorporation, to lipopolysaccharide (a B lymphocyte mitogen), but none to phytohemaglutinin (PHA) or concanavalin A (Con A) (both are T lymphocyte mitogens), thus confirming a deficiency of T cells in nu/nu mice.

Megakaryocyte and platelet responses to an injection of APS were the same in nu/nu and nu/+ mice: acute thrombocytopenia was followed by increased megakaryocytes in the bone marrow (137–155% of normal on day 2), macromegakaryocytosis (megakaryocyte size was 150–178% of normal on day 2), and rebound thrombocytosis (platelet counts were 168–212% of normal on days 5 and 6). These results showed that stimulation of megakaryocytopoiesis and platelet production in response to acute thrombocytopenia was normal in nude mice. Meg-CFC were increased in nude mice 4 to 5 days after APS or an injection of normal guinea pig serum (NGpS) to 3× controls in the spleen and 2× controls in the bone marrow. GM-CFC showed a 6-fold increase in the spleen on days 5 and 6 after APS and no increase in the marrow. Neither CFC increased in nu/+ mice. Marrow BFU-E did not change. Nude spleen cells showed no response to either T cell mitogen on days 2, 4, and 5 after APS or NGpS. However, weak responses occurred sporadically at 6 days after APS to ConA, 4 hours after NGpS to ConA, and 6 days after NGpS to both ConA and PHA.

Thrombocytopoiesis was normal in undisturbed nu/nu mice, and stimulation of platelet production in response to acute immunothrombocytopenia was the same in nu/nu and nu/+ mice. Therefore, it is unlikely that T cells play an important role in these processes. Sporadic weak T cell mitogenic responses in nu/nu mice did not correlate with thrombocytopoietic activity. Increases in megakaryocyte number and size and platelet production occurred independently of changes in numbers of Meg-CFC, GM-CFC, or marrow BFU-E.

DEVELOPMENT OF RADIONUCLIDES AND RADIOPHARMACEUTICALS FOR EMISSION COMPUTED TOMOGRAPHY

Yukio Yano, Chester A. Mathis, Stephen M. Moerlein, Mohindar Singh, Reese Jones, and Thomas F. Budinger

Our objective is to develop methods for the production of radionuclides and for the radiolabeling of biochemical substrates to investigate human physiology and metabolism noninvasively by emission-computed tomography.

Our approach is to use radioisotope generators or cyclotrons to obtain relatively short-half-life positron or single-photon emitters. Generators provide a readily available supply of short-lived radionuclides at a low cost while cyclotrons provide the radionuclides of carbon, nitrogen, oxygen, fluorine, bromine, or iodine that can be incorporated into biochemical compounds or analogues.

RADIOISOTOPE GENERATORS

Generators for short-lived positron emitters such as 68-*min* ^{68}Ga, 76-sec ^{82}Rb, and 3.6-*min* ^{122}I are listed in Table 1. The ^{82}Sr/^{82}Rb generator was reloaded every three months with 200 mCi of ^{82}Sr obtained from Los Alamos National Laboratory. The generator routinely provided 20–60 mCi doses of ^{82}Rb for PET studies of myocardial blood flow in heart patients or changes in the permeability of the blood-brain barrier in patients with brain tumor or radiation therapy necrosis. Validation studies of myocardial blood flow measurements with ^{82}Rb were done with ^{15}O water and radiolabeled microspheres.

The ^{68}Ge/^{68}Ga generator was used to obtain ionic ^{68}Ga for labeling platelets and low density lipoproteins (LDL) for PET studies of thrombosis and atherosclerosis in cardiovascular disease.

^{68}Ga was attached to LDL via a bifunctional chelating agent, DTPA. Low pressure gel column chromatography and HPLC were used to preparatively separate and analyze ^{68}Ga LDL for uptake studies in the healing endothelium of the scraped aorta rabbit model. The biological viability and radiolabeling yield of ^{68}Ga LDL were dependent upon maintaining a concentration of 15–20 mg LDL/ml of plasma.

^{68}Ga EDTA was used to measure cerebral blood volume and blood-brain barrier breakdown in Alzheimer's type dementia. ^{68}Ga EDTA was also used to study brain tumor patients for radiation therapy necrosis.

The ^{122}Xe/^{122}I generator work was continued with ^{122}I-radioiodinated amphetamine analogues to measure regional cerebral flow in patient studies utilizing PET.

For broader applications in nuclear medicine, a ^{99}Mo ($t_{1/2}$ = 2.78d)/^{99M}Tc($t_{1/2}$ = 6h) generator was used to obtain high specific concentration ^{99m}Tc (20–100 mCi/ml saline) and to utilize the ideal 140-keV photons of ^{99m}Tc for imaging studies with an improved single-photon emission-computed tomography (SPECT) system now in operation at Donner Laboratory.

A new complexing agent thiocaprolactam (TCL) and 8-hydroxyquinoline (oxine) were studied for ^{99m}Tc labeling. Various concentrations of ligand (0.400–3.0 mg) were evaluated with stannous ion or sodium borohydride ($NaBH_4$) reduction of Tc VII. HPLC analysis and octanol/aqueous buffer partition coefficients were determined for the ^{99m}Tc complex prior to platelet labeling studies. In concentrations of 400–500 μg both oxine and TCL gave 70–100% complex formation when $NaBH_4$ was used to reduce Tc VII to Tc V. The octanol/saline buffer partition coefficient was about 12 for ^{99m}Tc oxine and about 6 for ^{99m}Tc TCL.

The ^{99m}Tc complex of oxine and thiocaprolactam was incubated with separated rabbit platelets in saline alone and in platelet-poor plasma (ppp):

Table 1. Generators for positron emitters.

Parent	Half-life	Decay mode (%)	Daughter	Half-life	Decay mode (%)	Gammas (MeV) (%)
^{68}Ge	275 d	EC(100)	^{68}Ga	68 m	β^+(88),EC(12)	1.08(3.5)
^{82}Sr	25 d	EC(100)	^{82}Rb	75 s	β^+(96),EC(4)	0.73(9)
^{122}Xe	20.1 h	EC(100)	^{122}I	3.6 m	β^+(77)	0.56(14)

saline. The platelet labeling yields with 10-min incubation at room temperature were 10% for ^{99m}Tc oxine in saline and 24% for ^{99m}Tc thiocaprolactam in saline: ppp (1:1).

We continued our studies of lipophilic compounds to serve as carriers for the single-photon emitter ^{99m}Tc. We determined complex formation by HPLC analysis and lipophilicity by octanol partition. The following ligands were studied: diethyldithiocarbamate, pyrolidinedithiocarbamate, 2-(2-pyridyl) benzimidazole, 1-(2-methoxyphenyl) piperazine, and 2-mercapto-4-methyl- pyrimidine. Some of these ^{99m}Tc-labeled compounds were evaluated in animal studies to determine their usefulness as tracers for blood flow to the brain, heart, and lungs.

CYCLOTRON PRODUCED RADIONUCLIDES

The Lawrence Berkeley Laboratory 88-Inch Cyclotron was used to produce Ci quantities of ^{11}C CO_2 and CH_3I for the synthesis of palmitic acid, methionine, and choline. ^{15}O-labeled water was produced in 100-mCi batches for use as a freely diffusible tracer for blood-flow measurements in the heart and brain. We continued to explore the production of 98-min ^{75}Br by the proton irradiation of an isotopically enriched ^{76}Se target of SeF_6. ^{75}Br may be a useful positron label for high specific activity receptor ligands.

The Crocker Nuclear Laboratory cyclotron at U.C. Davis produced ^{18}F fluorodeoxyglucose on a weekly basis for studies of glucose metabolism in brain and heart. Further modifications in the chemical synthesis of ^{18}FDG using ^{18}F-acetyl hypofluorite increased the labeling yield and radiochemical purity of the product. About 80 mCi of ^{18}FDG results from a 30 μA-hr irradiation with a proton beam.

The radiochemical yields of nine N,N-dimethyl-2-(substituted phenyl) isopropylamines (amphetamine analogues) were determined following reaction with ^{18}F-acetyl hypofluorite in a 0.1 M HCl solution at room temperature. The *meta*-dimethoxy substituted amphetamines gave the highest radiofluorination yields (24-32%, at EOB). Purification of the ^{18}F-labeled amphetamines was achieved in 10–20 min. 5-^{18}F-2,4-dimethoxy-N,N-dimethylamphetamine (5-^{18}F-2,4-DNNA) was utilized to determine brain and lung uptake in rats. Positron-emission tomography studies were conducted in a dog to determine the dynamic brain uptake and retention of this agent.

We continued to use the Medi-Physics CS-22 cyclotron to produce ^{18}F fluoride by the irradiation with protons of an ^{18}O-enriched water target. The target is filled and emptied remotely from a hot laboratory adjacent to the cyclotron vault. The enriched water target and the ^{18}F-fluoride are captured in a trap that serves as a vessel for the evaporation of the water and as a reaction vessel for incorporating ^{18}F into radiopharmaceuticals for ligand receptor binding studies in the brain.

NEW INSTRUMENTATION FOR HIGH RESOLUTION, DYNAMIC, THREE DIMENSIONAL IMAGING OF POSITRON LABELED COMPOUNDS IN THE HUMAN BODY

Stephen E. Derenzo, John L. Cahoon, Ronald H. Huesman, Tony Vuletich, and Thomas F. Budinger

600-CRYSTAL HIGH RESOLUTION POSITRON TOMOGRAPH

This new tomograph has 600 bismuth germanate scintillation crystals that encircle the head in a close-packed ring. The patient sits in an adjustable chair during the study (Fig. 1). After administration of a positron-labeled compound, the distribution of the tracer is measured as a function of time by recording coincidences between detectors in opposite groups of the ring, and performing a mathematical process called computed tomography. The crystals are small (3 mm × 10 mm) and the in-plane resolution is 2.5 mm. The resolution along the patient axis can be varied from 0.5 mm to 5 mm by adjusting a lead shielding ring. The electronics employ many high-speed emitter-coupled logic (ECL) circuits for rates of 1,000,000 transmission events per sec and 100,000 emission events per sec. In addition, the pulse height windows and timing for all 600 detectors are adjusted by computer control.

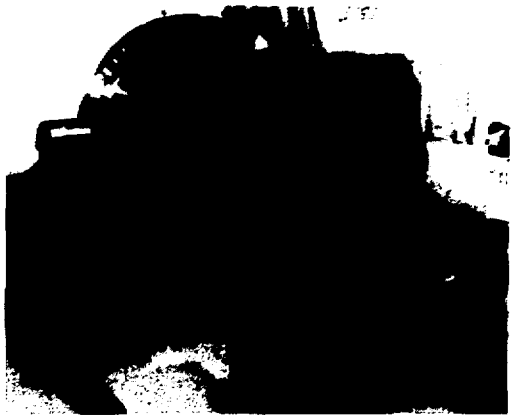

Fig. 1. Donner ultrahigh resolution 600-crystal positron tomograph with patient chair. (CBB 852-1304)

STATISTICAL PROPERTIES OF COMPARTMENTAL MODEL PARAMETERS EXTRACTED FROM DYNAMIC POSITRON EMISSION TOMOGRAPHY EXPERIMENTS

Bernard M. Mazoyer, Ronald H. Huesman, Thomas F. Budinger, and Brian L. Knittel

The determination of physiological properties (such as tissue blood flow, metabolic rates, receptor activity, and substrate turnover or clearance) relies on accurate measurements of the response of a tissue or organ system to an input. The input might be an injected radioactive tracer of biological activity in nuclear medicine imaging procedures, or a pulse sequence in nuclear magnetic resonance studies. Over the past years a major focus of research in physiologic studies employing tracers has been the computer implementation of mathematical methods of kinetic modeling for extracting the desired physiological parameters from tomographically derived data. We have recently completed a study of factors that affect the statistical properties of compartmental model parameters extracted from dynamic positron emission tomography (PET) experiments.

PARAMETER ESTIMATION USING DYNAMIC PET DATA

A dynamic PET experiment can be generalized as follows (see Fig. 1): a single intravenous injection of a radionuclide is performed, and the time course of the activity, a(t) (which we will refer to as the model residue function), in some region of interest in the tomographic slice, is recorded. The input function, $x_1(t)$, is usually measured by acquiring venous or arterial blood samples, but could be acquired by tomographic sampling under some conditions. A mathematical model is used to represent the physiological behavior of the tracer in the region of interest; for example

$$a(t) = h(p) * x_1(t) \quad , \tag{1}$$

where h(p) is the impulse response of the system, which depends on a parameter vector p, and * denotes the convolution operation. A 3-compartment model such as used in ^{18}F-fluorodeoxyglucose (FDG) experiments is the reference system in our study. In this model, the activity in the region of interest is

$$a(t) = s\{f_v x_1(t - \tau) + (1 - f_v)[x_2(t) + x_3(t)]\} \quad , \tag{2}$$

where s is a concentration-activity scaling factor, f_v is the fractional volume of tissue comprising blood

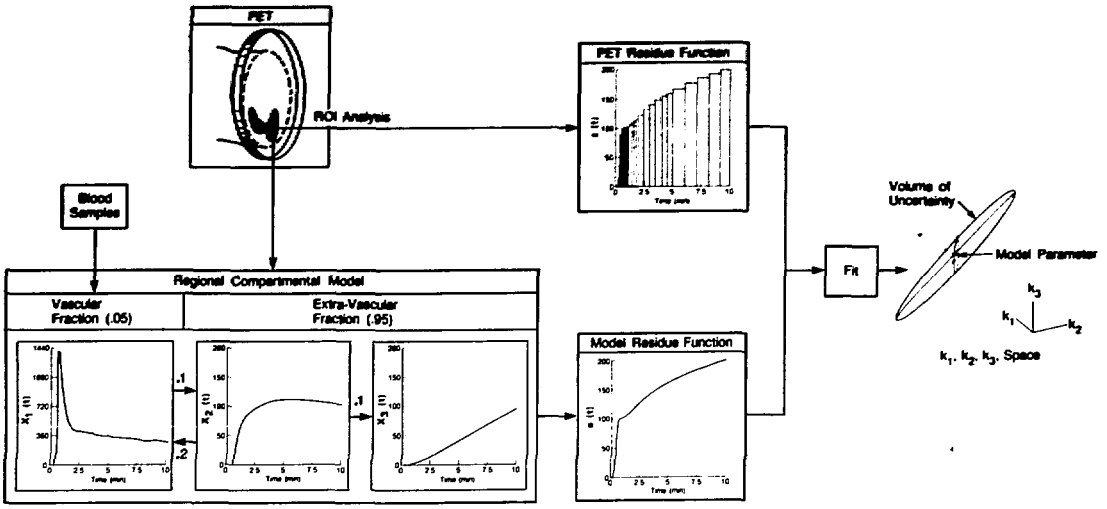

Fig. 1. Flow-chart of a dynamic FDG-PET experiment. The fit provides estimates of the compartmental model parameters and of their accuracies in terms of a covariance matrix. On the right is the uncertainty elipsoid corresponding to the covariance matrix of k_1, k_2 and k_3. *(XBL 855-8292)*

capillaries, and τ is the sample delay time which depends on the blood sampling site and method (e.g., the longer the catheter the larger τ).

Actually, the tomographic device provides a series of measures of mean values of a(t) over time intervals ($[t_{i-1}, t_i]$, i = 1,...,n) which can be modeled as

$$z_i = y_i + e_i \quad , \tag{3}$$

$$y_i = \frac{1}{t_i - t_{i-1}} \int_{t_{i-1}}^{t_i} a(t)dt \ , \ i = 1,2,...,n \ , \tag{4}$$

where the y_i are the theoretical model values for the data, and the z_i, which we will refer to as the PET residue function, represent the actual data with statistical fluctuations given by the e_i.

Using any of the available procedures to fit y (the vector of y_i) to z (the vector of z_i) will provide a parameter vector estimate $\hat{p}$. Two kinds of information are useful in order to assess the quality of this estimate: the bias in its mean,

$$b = E(\hat{p}) - p \quad , \tag{5}$$

and its covariance matrix,

$$COV(\hat{p}) = E\{(\hat{p} - E\{\hat{p}\})^2\} \quad , \tag{6}$$

where $E\{.\}$ stands for the mathematical expectation of a random variable. The bias gives a measure of the accuracy of $\hat{p}$, and we have investigated the biases resulting from

- using a mid-point interpolation instead of a true integral model to compute the y_i in Eq. (4),
- using a wrong model to describe the data, such as fixing (and not fitting) the parameter f_v and τ to wrong constant values, and
- using venous (instead of arterial) blood-tracer data as input function.

The covariance matrix of $\hat{p}$ as defined in gives a measure of the precision of $\hat{p}$ and can be estimated as

$$COV(\hat{p}) = (S^T\Sigma^{-1}S)^{-1} \quad . \tag{7}$$

The matrix $S = (s_{ij})$, called the sensitivity matrix, denotes the derivative of y relative to p,

$$s_{ij} = \frac{\partial y_i}{\partial p_j} \ , \ i = 1,2,...,n \ , \ j = 1,2,...,r \ , \tag{8}$$

(r equals the number of parameters), and Σ is the data covariance matrix. Equation (7) clearly shows how the data statistical uncertainties are propagated to the parameter estimate uncertainties through the

matrix S. The determinant of COV($\hat{p}$) is proportional to the volume of the parameter confidence region and provides a criterion for evaluating the effects of factors on parameter estimate precision. The principal parameters of interest in dynamic PET experiments are the rate constants (k_1, k_2, k_3 for our model), because they represent the physiological process under study. The parameters f_v and τ are necessarily included in the model because of the nature of the data acquired in PET experiments. For this reason, we shall use the determinant, Δ, of the covariance matrix of only k_1, k_2 and k_3 as a measure of merit for the various protocols and input functions. Because p also includes f_v and τ, this matrix is a submatrix of COV($\hat{p}$). In subsequent figures we will plot a normalized form of this quantity denoted by $\mathscr{D}$, and defined as:

$$\mathscr{D} = \left(\frac{\Delta}{(k_1 k_2 k_3)^2} \right)^{1/6} . \qquad (9)$$

$\mathscr{D}$ can be interpreted as a mean coefficient of variation for the k's. We have investigated the effects on $\mathscr{D}$ of various experimental factors over which the experimenter has control, which are

- the tracer injection duration, which will condition the input function shape, and
- the tomographic data collection protocol, e.g., the number and time series of images.

SIMULATIONS AND RESULTS

Patient blood data were acquired using a fast venous injection into the arm and a typical sampling procedure to provide a function used for the standard or reference input data, $x_1(t)$. Given $x_1(t)$, a set of values for the parameter vector $p = (k_1, k_2, k_3, f_v, \tau)^T$, and the sequence of t_i (the sampling protocol), the exact values of the y_i are computed using Eqs. (4) and (2). We approximate the e_i (the random errors on the y_i) as n uncorrelated normal distributions with zero means and variances given by:

$$\sigma_i^2 = \frac{y_i}{(t_i - t_{i-1})} , \; i,j = 1,2,\ldots,n . \qquad (10)$$

Different sampling protocols have been tested, some of which are currently used by various groups (see Tables 1a and 1b). Also, a set of blurred-input functions (and the corresponding residue functions) were generated by convolving the reference input function with unit area rectangular functions of durations 10, 30, 60 and 120 sec. These blurred-input functions are used to evaluate the effects of prolonging the intravenous injection.

Table 1a. Sampling strategies with various initial frame durations and constant study durations (2400 sec).

Protocol number	Initial frame duration (sec)	Sampling strategy (no. of frames × frame duration)
1	1	60×1 − 6×10 − 6×30 − 35×60
2	2	60×2 − 4×30 − 12×180
3	5	24×5 − 12×15 − 10×60 − 5×300
4	30	10×30 − 10×60 − 5×300
5	60	5×60 − 5×120 − 5×180 − 2×300
6	180	10×180 − 2×300

Table 1b. Sampling strategies with various study durations. The initial frame durations are kept constant for each of the three groups of protocols, and correspond to the initial sampling rates of protocols 1, 4 and 6 of Table 1a.

Initial frame duration (sec)	Sampling strategy (no. of frames × frame duration)	Study duration (sec)
1	95×1 − 12×2	119
	60×1 − 6×10 − 31×6	306
	60×1 − 6×10 − 6×30 − 35×9	615
	60×1 − 6×10 − 6×30 − 35×26	910
	60×1 − 6×10 − 6×30 − 35×43	1505
	60×1 − 6×10 − 6×30 − 35×60	2400
	60×1 − 6×10 − 6×30 − 35×77	2995
	60×1 − 6×10 − 6×30 − 35×94	3590
30	6×30	180
	10×30	300
	10×30 − 5×60	600
	10×30 − 10×60	900
	10×30 − 10×60 − 2×300	1500
	10×30 − 10×60 − 5×300	2400
	10×30 − 10×60 − 5×300 − 1×600	3000
	10×30 − 10×60 − 5×500 − 2×600	3600
180	5×180	900
	7×180	1260
	9×180	1620
	10×180	1800
	10×180 − 1×300	2100
	10×180 − 2×300	2400
	10×180 − 1×400	3000
	10×180 − 6×300	3600

SOURCES OF PARAMETER INACCURACIES

The biases resulting from fitting values computed using a midpoint interpolation to data generated using the integral model are shown in Table 2. Notice that bias amplitude increases with the initial scan duration and injection duration.

Table 2. Biases (in % of the parameter true value) in the mean of parameter estimates resulting from the use of a non-integral model.

	Sharp-input function			Blurred-input function		
Parameter	Prot. 1	Prot. 4	Prot. 6	Prot. 1	Prot. 4	Prot. 6
k_1	0.02	1.7	9.9	0.002	5.7	7.3
k_2	0.002	2.8	11.4	0.003	9.3	10.
k_3	0.005	0.32	7.	0.04	1.7	9.3
f_v	0.6	1.3	62.	0.01	34.	94.
t_o	0.06	50.	100.	0.08	67.	170.

Values were obtained by fitting the non-integral model using two different input functions (the sharp reference and a blurred function obtained by convolving the reference with a unit area rectangular function of 60-sec duration), and three PET data protocols (1, 4 and 6 of Table 1a with initial frame duration 1, 30 and 180 sec). Notice that since a one-second time scale was used to generate the data, no significant biases are observed for protocol 1 (sampling rate = 1/sec).

Table 3 shows that significant biases are generated for the fit parameters when wrong values are used for the parameters not fitted. The bias values can be predicted using a first order expansion of the fitting criterion, and Table 3 gives the first order derivatives of the parameters k_1, k_2, k_3 considered as functions of the parameters f_v and τ. Notice that k_1 and k_2 are more sensitive than k_3 because they are more correlated with f_v and τ, and that biases are independant of the data collection protocol.

Assuming that circulation can be roughly modeled as a convolution by a square function, we fit the model with the 10-second input function to the data generated with the sharp reference input. Table 4 shows that significant biases are generated. This effect is more important for protocols with faster initial data collection rates, and may be explained by the fact that the model is sensitive to inaccuracies in the input function measurements at early times through the blood contribution [represented in Eq. (2) by $f_v x_1(t - \tau)$]. Protocols with lower initial sampling rates are less sensitive to this contribution, because the averaging of the blood contribution over a relatively long time interval makes this average value more stable with respect to the shape of the input function.

EFFECTS OF EXPERIMENTAL DESIGN ON PARAMETER PRECISION

Effects of various sampling rates at early times and various injection durations on parameter esti-

Table 3. Normalized partial derivatives of fit parameters (k_1, k_2, k_3) relative to constant parameter f_v and τ.

	Sharp-input function A		
	Protocol 1	Protocol 4	Protocol 6
$\frac{f_v}{k_1}\,\partial k_1/\partial f_v$	−0.33	−0.34	−0.38
$\frac{\tau}{k_1}\,\partial k_1/\partial \tau$	0.059	0.067	0.12
$\frac{f_v}{k_2}\,\partial k_2/\partial f_v$	−0.61	−0.64	−0.7
$\frac{\tau}{k_2}\,\partial k_2/\partial \tau$	0.11	0.13	0.25
$\frac{f_v}{k_3}\,\partial k_3/\partial f_v$	−0.065	−0.07	−0.85
$\frac{\tau}{k_3}\,\partial k_3/\partial \tau$	0.028	0.036	0.076

Normalized derivatives (in relative value) are given for protocols 1, 4, and 6 with initial frame durations 1, 30, 180 sec respectively (see Table 1a) and the sharp reference input function. These derivatives can be used to predict the basis of fit parameter estimates when using wrong constant values for other parameters. For example setting f_v to 0.04 instead of 0.05 and τ to 11 instead of 10 sec will generate a value of k_1 overestimated by 7.2% (−20% × −0.33 + 10% × 0.059) for protocol 1.

Table 4. Biases (in % of the true parameter value) in the mean of parameter estimates due to arm venous blood sampling instead of true capillary sampling.

	Blurred-input function A		Blurred-input function B	
Parameter	Protocol 3	Protocol 4	Protocol 3	Protocol 4
k_1	4.3	0.6	9.7	3.3
k_2	8.1	1.0	18.	5.5
k_3	0.2	0.1	0.4	0.5
f_v	9.4	3.0	49.	16.
τ	21.	47.	40.	118.

Venous sampling was simulated by convolving the sharp reference input function (assumed to represent the true brain capillary tracer concentration) with unit-area rectangular functions of (A) 10- and (B) 30-sec durations. The PET data were generated with the reference residue curve sampled with protocol 3 and 4 (initial frame duration 5 and 30 sec respectively) of Table 1a.

mate precision are shown in Fig. 2. Note that only small improvement is gained by using initial frame durations smaller than 30 seconds, and that use of fast injection provides only small gains in parameter precision. Notice that for each injection duration, the fastest sampling rate always provides the more precise parameter estimate but that an optimal input function seems to exist for the protocols with an initial sampling of 30 seconds or larger.

Figure 3 decribes the effects of the total study duration for three different protocols. For each protocol, the initial frame duration is kept constant while additional information is added using later images. Only small improvements in $\mathscr{D}$ as well as in k_3 precision are obtained by setting the total study duration to values larger than 40 minutes for the set of rate constants encountered in FDG experiments. The precision of k_1 and k_2 do not change significantly.

CONCLUSION

We have shown that it is important to include the parameters f_v and τ in the model and to account for the integration process inherent in emission tomography data when fast data collection is impossible. We have also found that higher rates of injection and higher rates of data collection lead to more precise parameter estimates. However, for the range of rate constants encoutered in PET studies with ^{18}FDG, insignificant differences were found between protocols with initial scan durations less than 30 seconds. Moreover, we have shown that in the absence of arterial blood data, the use of venous blood data as an input function leads to biases for fast data collection protocols. We are currently developing methods for retrieving arterial tracer time activity functions from venous blood data.

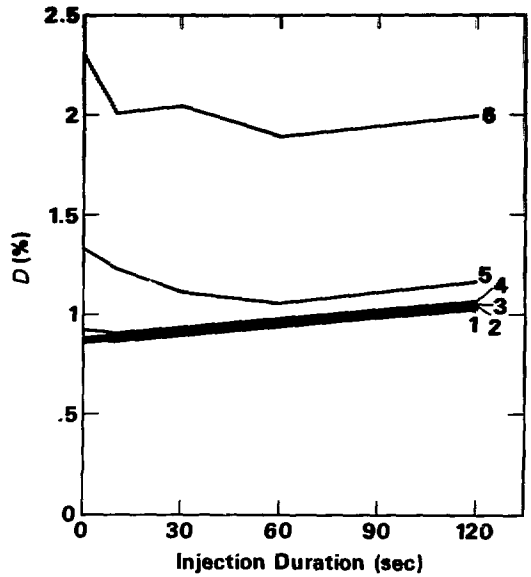

Fig. 2. Comparison of experiments using the six different sampling protocols of Table 1a as a function of the injection duration: normalized determinant of k_1, k_2, k_3 covariance matrix ($\mathscr{D}$). *(XBL 855-8288)*

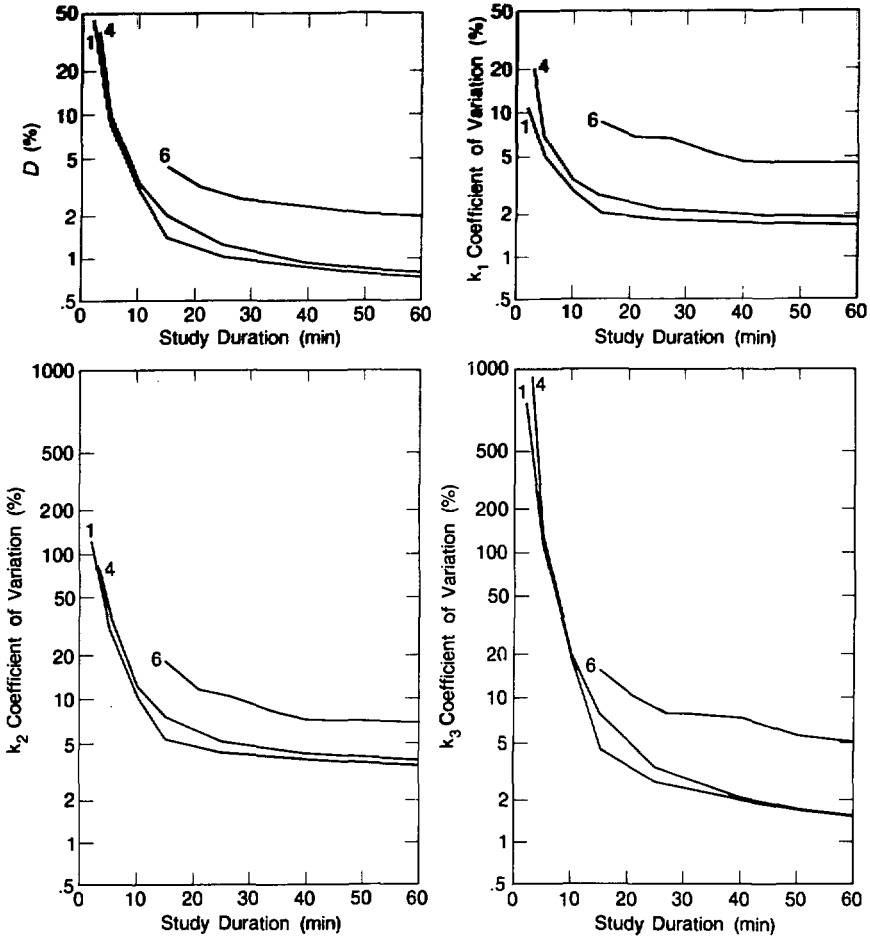

Fig. 3. Comparison of experiments as a function of the study duration using the protocols of Table 1b; a: normalized determinant of k_1, k_2, k_3 covariance matrix ($\mathfrak{L}$); b,c,d: coefficient of variation of k_1, k_2 and k_3 respectively.
(XBL 855-8291)

DEAD TIME CORRECTION AND COUNTING STATISTICS FOR POSITRON TOMOGRAPHY

Bernard M. Mazoyer, Mark S. Roos, Ronald H. Huesman, and Thomas F. Budinger

A correction for loss of events due to dead time in dynamic positron emission tomography has been studied. The model employs a paralyzing dead time to describe the behavior of a tomograph over the range of event rates normally encountered in patient studies (up to 200,000 events/sec/detector layer).

The Donner 280-Crystal Positron Tomograph is characterized by a dead time of 1.8 μsec/event for observed count rates of less than 200,000 events/sec. The dead time correction factor is 1.8 at 180,000 events/sec.

The correction is applied to projection data and to region-of-interest analysis of dynamic PET studies

and formulae for the covariances between corrected projection data and between counts in regions of interest in different images from the same dynamic study are established. At 180,000 events/sec, the variance of the actual (corrected) number of events in a region containing 3.34 × 10^5 actual events is predicted from the model to be 3.86 × 10^6 events^2, which is more than 10 times the variance that would be expected from a naive assumption of Poisson statistics (Fig. 1). These statistical results are verified experimentally.

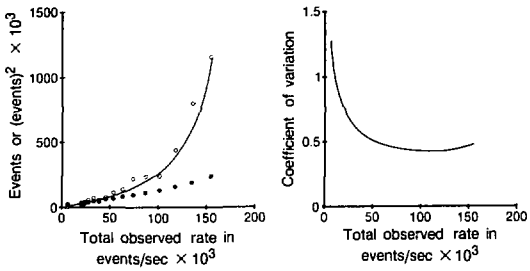

Fig. 1. Statistics for corrected number of events as a function of the total observed count rate. a) Sample mean (•) and variance (○); predicted variance (solid line) using propagation of errors in the dead time model. b) Predicted coefficient of variation. *(XBL 846-7197A)*

The necessity and importance of dead-time correction in dynamic PET is shown by an example of an observed error of 25% in myocardial flow if dead-time compensation is not applied (Fig. 2).

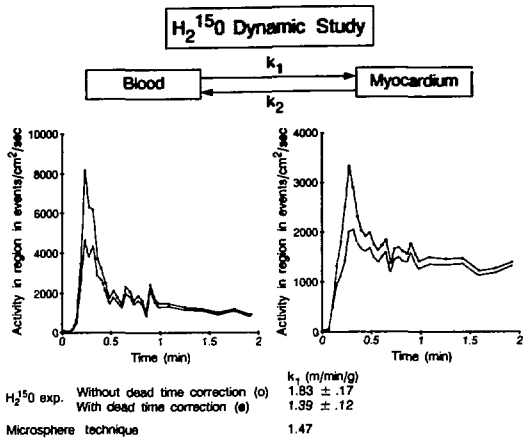

Fig. 2. Input (left) and residue (right) curves from an $H_2{}^{15}O$ dynamic study with (•) and without (○) correction for dead time. Using the microsphere technique, the flow value (ml/min/g tissue) was measured to be 1.47; the flow values derived from the $H_2{}^{15}O$ experiment were 1.83 before and 1.39 after correction for dead time. The correction factor at the time of the peak of the input curve was 1.8 for a 180,000 events/sec total observed count rate. *(XBL 846-7195A)*

BIOLOGICAL EFFECTS OF STATIC MAGNETIC FIELDS

Thomas F. Budinger, Kay S. Bristol, Dorothy A. Carpenter, Patricia A. Garbutt, Priscilla D.C. Wong, and Chi-Kwan Yen

A retrospective epidemiological study on the health effects, if any, of stationary and alternating magnetic fields produced by man-made devices such as cyclotrons, bubble chambers, and proton synchrotrons was started in 1977 and is now completed. The magnetic fields to which the workers were exposed are as high as 2 tesla (2×10^4 gauss) for a few hours and as low as a few times the natural earth magnetic field (5 gauss) for long durations.

Two quite different exposure environments can be distinguished: the alternating field and the static field environments. This particular study is focused on the effects of steady magnetic fields and low-frequency alternating fields. The induced-current effects of alternating fields on the human body with a conductivity of approximately 0.25 S/m are reasonably well known, or at least there is a biophysical basis for analysis and prediction. On the other hand, the influences of static or very low frequency fields on human subjects exposed over long time periods are neither known nor theoretically predictable.

The objectives were the acquisition of low-exposure data that can be used to evaluate any risks to the population incidentally exposed to environmental increases in magnetic fields as well as the acquisition of high-exposure data to be used

in determining allowable exposure standards for the technical personnel working at magnetic facilities.

The study involves 792 scientists and technician who have been occupationally exposed to fields of at least 5 G in strength for 8000 G-hr during their working careers. The criterion is based on a typical exposure of a cyclotron worker for about a year and a half. The study includes acquisition of medical data from 792 exposed subjects as well as from 792 controls matched for sex, age, race and socioeconomic status from seven national laboratories in North America. Listed below are the institutions that participated and the number of subjects studied, which are matched by the number of controls.

1. Lawrence Berkeley Laboratory (LBL), 354
2. Brookhaven National Laboratory (BNL), 159
3. National Magnet Laboratory at MIT (NML), 6 (combined with FNAL)
4. Argonne National Laboratory (ANL), 66
5. Fermi National Accelerator Laboratory (FNAL), 71
6. Stanford Linear Accelerator Center (SLAC), 101
7. Oak Ridge National Laboratory (ORNL), 41

The studies of the latent effects from acute and very high exposures involve subjects who have worked in fields greater then 400 G at facilities such as the calutrons at Berkeley (California) and Oak Ridge (Tennessee) during World War II. In addition, individuals involved in calibrating large magnets and individuals exposed to very high fields around bubble chambers are included in this high-field exposure population.

The number of individuals with diseaes from 20 catagories are shown for exposed and control populations in Fig 1. No significant increase or decrease in the prevalence of diseases was found. Of the 792 subjects, 198 had 0.3 T or higher exposures for 1 hour or longer, and no difference was found between this group and the remainder of the exposed populations or the matched controls. There were no trends in the data suggestive of a dose-response (Fig. 2). Major advances made over the last two years involve a quality check on the data, including chi-square analysis of different portions of the population in a search for biases. A sound test of the data completed recently was an evaluation of whether there is a greater prevalence of respiratory conditions in those individuals who were smokers vs. the nonsmokers. Evaluations relative to subject age, etc., have also been completed. The report on this work should be published by January 1986.

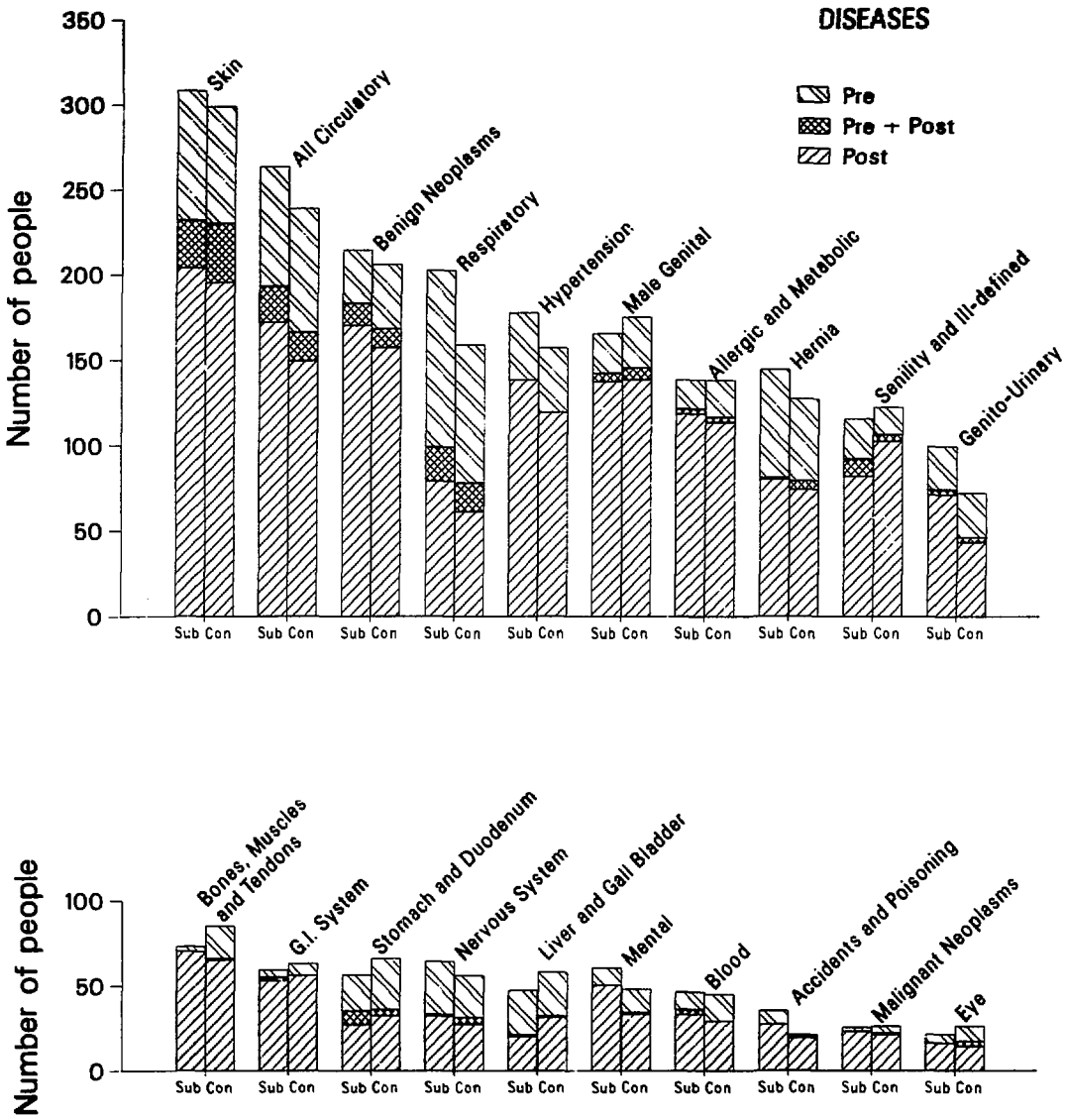

Fig. 1. Disease frequency for exposed subjects (sub) and controls (con). Bars are divided for disease occurrences pre-, pre- and post-, and post-employment in the exposure or control environments. *(XCG 858-384)*

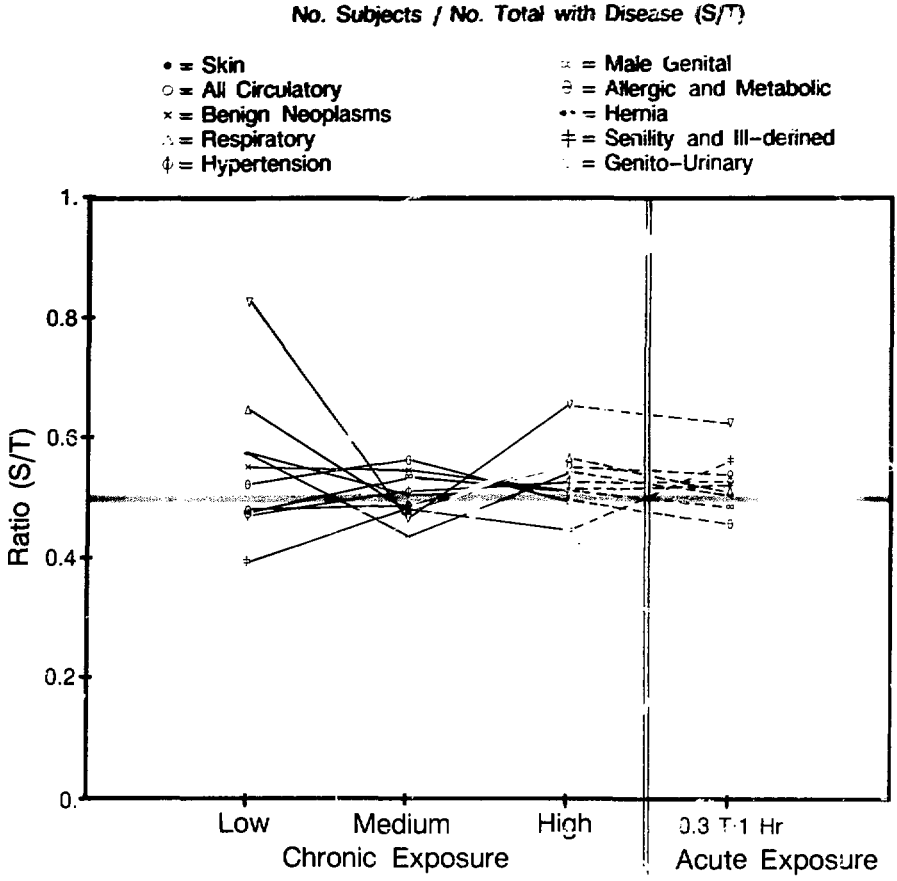

Fig. 2. Post-employment disease ratios as a function of exposure.
(XBL 847-7746)

APPENDICES

Section 2. DONNER PAVILION

INTRODUCTION

The biomedical program at Donner Pavilion continues to apply nuclear medicine research to the diagnosis and radiosurgical treatment of life-threatening central nervous system (CNS) disorders, for example, intracranial arteriovenous malformations, which affect approximately one million Americans. In the clinical research program, stereotactic Bragg-peak radiosurgery, using narrow beams of heavy charged particles, demonstrate superior biological and physical characteristics in brain over x rays, and γ rays, and protons, namely, improved dose distribution in the Bragg peak, sharp lateral and distal borders, and less multiple scattering and range straggling for the same residual range in CNS tissues. CNS tissue response and alteration of cerebral blood-flow dynamics related to heavy-ion Bragg-peak radiosurgery is being investigated using three-dimensional treatment planning and quantitative neuroradiological imaging, including stereotactic cerebral angiography, x-ray computerized tomography (CT), magnetic resonance imaging (MRI), cine-CT, xenon x-ray CT and positron emission tomography (PET). Based on the evaluation and treatment with stereotactically-directed narrow beams of heavy charged particles in over 160 clinical patients, using extensive clinical and neuroradiological follow-up, it appears that stereotactic heavy charged-particle radiosurgery can obliterate intracranial arteriovenous malformations (AVMs) or protect against recurrent hemorrhage with reduced morbidity and mortality. The clinical research program continues in collaboration with Stanford University and the University of California San Francisco.

Also under study are the physical properties of narrow heavy-ion beams for improving methods of dose delivery and dose distribution and for establishing clinical RBE/LET and dose-response relationships for human CNS tissues. The biophysics research program continues to examine the cellular basis of radiation-induced injury—cellular response and cell proliferation kinetics—in defined cell populations of the mammalian brain. Studies include the hierarchical organization and glial cell kinetics and the radiation response to cytotoxic insult, primarily the proliferative kinetics of the subependymal plate and the pathogenesis of early and late delayed radiation injury in brain, and CNS repair and regeneration after exposure to narrow beams of charged particles. The proliferative capacity of the mature glial cells and their ability to modulate responses to injury are of importance in CNS disease and healing processes. Neuroglial cells may enhance or decrease the regenerative capacity of neurons and the reformation of their interconnections with appropriate target cells. Furthermore, these altered capacities of neuroglial cells may also affect myelin renewal and remyelination processes following heavy charged-particle radiation injury.

STEREOTACTIC HEAVY ION BRAGG PEAK RADIOSURGERY

Jacob I. Fabrikant, John T. Lyman, Kenneth A. Frankel, Mark H. Phillips, Edward L. Alpen, Neela B. Manley, Richard P. Levy, Myrtle L. Foster, Frederick W. Yeater, George J. Hampton, Maureen H. Morford, and Barbara Modlinski

CLINICAL RESEARCH

To date, the Donner Pavilion program has evaluated and treated over 160 neurological patients with intracranial vascular disorders, using stereotactic heavy charged-particle Bragg peak radiosurgery. Most lesions have been deep, surgically inaccessible arteriovenous malformations in the brain. Patient selection and management are based on defined human subject protocols; patients are placed into one of three radiosurgical treatment groups: stereotactic heavy charged-particle radiosurgery, flow-directed embolization of accessible feeder vessels followed by stereotactic radiosurgery, or ligation or excision of accessible feeder vessels followed by stereotactic radiosurgery. The aim of flow-directed embolization and/or surgical ligation of feeder vessels is to decrease the size and to shape the AVM for stereotactic radiosurgery using narrow heavy-ion beams. More than half of our patients are treated solely with stereotactic radiosurgery; more than one-third undergo surgical ligation of accessible feeder-shunts prior to radiosurgery; and a small number undergo prior embolization procedures.

All patients are followed frequently, both clinically and radiologically, after radiosurgical treatment; about two-thirds have now had 24-month follow-up and extended follow-up to 5 years is now done on a regular basis. Clinical objectives are to achieve changes in the intracerebral hemodynamic condition, resulting in elimination of subarachnoid or parenchymatous brain hemorrhage and a decrease in progressive or fixed neurological deficits, in frequency of seizures, and in subjective complaints, including frequency and intensity of headaches. Preliminary observations in the first 96 patients thus far treated to the end of 1984 indicate that these objectives are being achieved. The first 66 patients have been evaluated clinically to the end of 1984: 45 patients have improved neurologically, 16 patients demonstrated no change, and 5 have worsened (Table 1). The follow-up periods for the remaining patients are too short to draw firm conclusions at this time, but the general pattern of clinical response continues. There have been four cases of intracranial hemorrhage occurring since radiosurgery; two of these patients were cured of their AVM and two died as a result of the hemorrhage. This complication rate falls well below the probability of hemorrhaging in a population of untreated deep AVM patients. There have been no patients with known late delayed radiation injury in the brain.

Table 1. Stereotactic radiosurgery cerebral arteriovenous malformations: Results.

		Symptoms				Angiography		
Year	Pts	Imp	NC	Prog	SAH	Comp	Part	NC
1980	2	2/2	0/2	0/2	0/2	0/1	1/1	0/1
1981	5	3/5	1/5	1/5	0/5	0/4	2/4	2/4
1982	16	12/16	4/16	0/16	1/16	1/12	7/12	4/12
1983	30	18/28	8/28	2/28	2/28	5/16	10/16	1/16
1984	43	10/15	3/15	2/15	1/15			
Totals	96	45/66	16/66	5/66	4/66	6/33	20/33	7/33

Pts = patients; Imp = improved; NC = no change; Prog = progressively worsened; SAH = subarachnoid hemorrhage; Comp = complete obliteration; Part = partial obliteration; NC = no change.

Hemodynamic and anatomic changes in cerebral vessels are examined by cerebral angiography. The hemodynamic changes are manifested by a decrease in blood flow through the pathologic cluster of abnormal blood vessels with a decrease in size of the feeding arteries, shunts and draining veins; anatomic changes include progressive decrease in the size of the AVM until stabilization, or total disappearance. The hemodynamic changes occur successively and are usually observed before the morphologic changes. The results of the yearly follow-up cerebral angiographic studies in the initial patients examined to date demonstrate complete obliteration of the AVM has occurred in about 20% of the patients; partial obliteration has occurred in two-thirds of the patients; no change has occurred in the remaining patients. Hemodynamic changes with attendant decrease in blood flow through the AVM has been seen to occur in about 80% of patients thus far investigated.

PHYSICS RESEARCH

The new beamline configuration for stereotactic cerebral irradiation with the Bragg ionization peak of the helium-ion beam (230 MeV/u) has been developed at the 184-Inch Synchrocyclotron. The modified beam has a 14.7-cm range in water to the Bragg peak with very sharply delimited lateral and distal borders. The practical limits on beam diameter range from 6 mm to 40 mm. The unmodulated Bragg peak maximum dose is greater than three times the entrance dose and the width of the peak at 80% of the maximum is 8 mm. The range can be modulated by a rotating acrylic variable-thickness absorber to increase the width of the high-dose region to 40 mm. The maximum range of the helium-ion beam (230 MeV/u) is greater than that of the Harvard and Uppsala proton beams, and more energy degradation is necessary to obtain the same residual range. Since the nuclear charge and mass of helium are greater than those of the proton, the multiple scattering and the range straggling can be less for the same residual range in tissues. Studies are in progress at the Bevalac to develop beam characteristics of heavier charged particles, such as carbon ions and neon ions, for stereotactic Bragg-peak radiosurgery in the brain; such parallel beams of monoenergetic heavy ions with small uniform transverse profile and modified Bragg peak have physical characteristics with unique advantages for achieving much improved dose distribution and dose localization with multiple port delivery.

Our present procedures use the modulated or unmodulated helium-ion beam at the 184-Inch Synchrocyclotron. We are currently planning stereotactic heavy-charged-particle radiosurgery at the Bevalac to take advantage of the heavier charged-particle beams, namely, carbon-12 (308 MeV/u), and neon-20 (425 MeV/u) and a new helium beam line. The advantages of these heavier ions over helium ions and protons include narrow beams with less range straggling and less multiple scattering for the same residual range in tissues, and improved dose distribution in the Bragg peak, with very sharp lateral and distal borders, and with greater sparing of adjacent critical structures in the brain.

Chatterjee and his colleagues are exploring the use of radioactive beams, e.g., carbon-11 and neon-19, at the Bevalac for localizing the region where heavy-ion beams are deposited in tissue. If the majority of the deposited beam particles in tissues do not leave the region of deposition, then imaging the distribution of radioactivity can serve to measure the stopping power of brain tissue and to check the adequacy of beam delivery in radiosurgery. A special coincidence camera has been built at LBL to image the distribution of the short-lived positron-emitting beam particles in human tissues. The stopping region of a small radioactive beam can be determined within a few seconds with an accuracy better than 1 mm when the dose delivered by the beam is about 0.02 Gy. The application of this new nuclear medicine procedure to stereotactic radiosurgery of intracranial vascular disorders is presently being explored.

Heavy Charged-Particle Treatment Planning

Narrow beams of heavy charged particles provide improved physical dose distributions due to the relatively small amount of multiple scattering and by the rapid fall-off of dose with depth beyond the end of the Bragg peak. The same physical requirements make stringent demands on the accurate assessment and compensation of inhomogeneities without which precision radiosurgery with focal charged-particle beams cannot be accomplished. Our method for treatment planning for stereotactic charged-particle radiosurgery continues to develop, and involves a sequence of stages using stereotactic neuroradiological procedures (namely stereotactic cerebral angiography, stereotactic computerized tomography (CT) and magnetic resonance imaging), AVM-target contouring, reconstruction of CT data and angiographic mapping, conversion of CT data to relative stopping power values, three-dimensional reconstruction of isoeffective central-axis depth distributions for dose-distribution calculations and aperture-compensator fabrication. Cerebral angiographic and CT data used for target contouring and conversion to relative stopping power values are transferred to the VAX-11/780 computer system; multiple-entry angles and beam ports are chosen to confine the high-dose Bragg ionization peak to the contoured target of the AVM and the arterial feeders/shunts, while carefully protecting adjacent critical structures in the brain (Fig. 1). The development of pixel-by-pixel treatment planning for heavy charged-particle radiosurgery permits design of collimator apertures for entry portals and selection of the appropriate range and modulation of the heavy-ion beam, thereby providing isoeffect and physical dose-distributions on reconstruction CT images (Fig. 2).

Noninvasive Imaging Research

Neuroradiological and nuclear medicine procedures are used to investigate three areas of brain

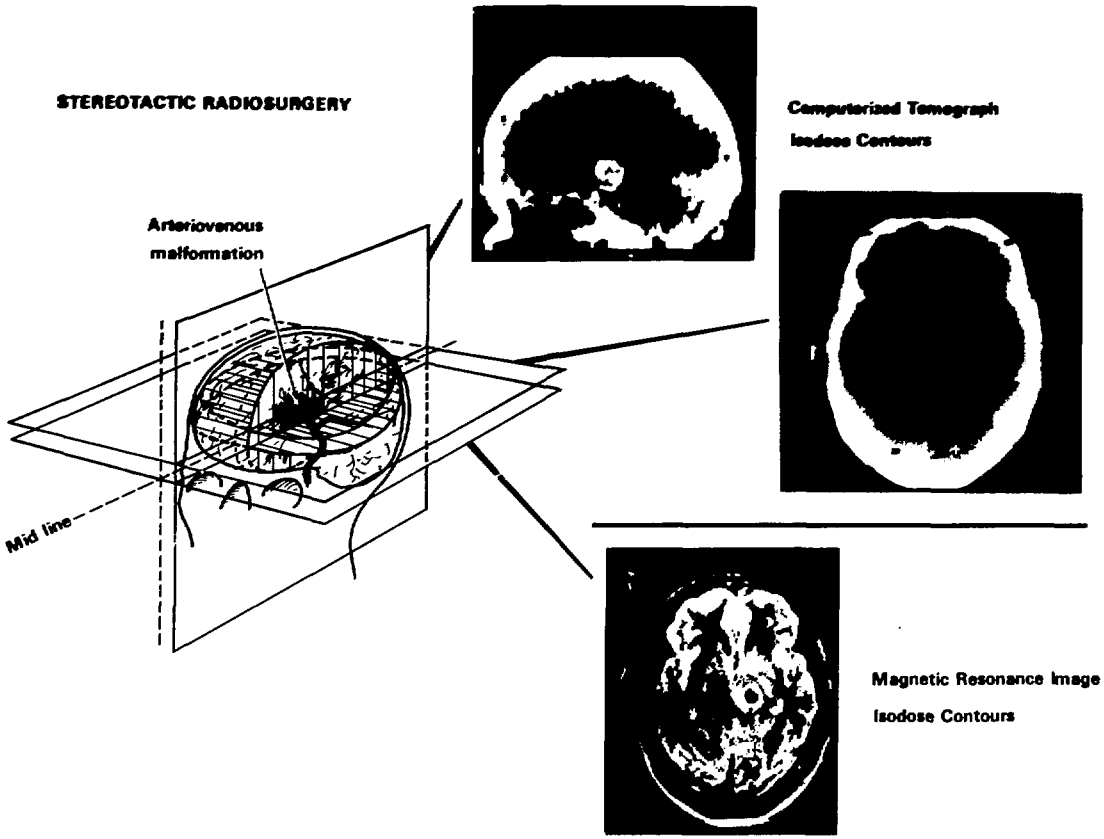

Fig. 1. The physical basis for stereotactic heavy-charged-particle Bragg-peak radiosurgery treatment planning for intracranial vascular disorders integrates information from the stereotactic cerebral angiogram (left), the stereotactic CT scans (upper right, right) and the magnetic resonance image (lower right). The data are used for target contouring and conversion to relative stopping power values. Multiple-entry angles and beam ports are chosen to confine the high-dose Bragg ionization peak to the contoured target of the arteriovenous malformation, while protecting adjacent critical structures in the brain. (CBB 843-1469)

structure and function and the effects of focal irradiation with heavy-ion beams: hemodynamic function and cerebral blood flow, alteration of structure and function and homeostatic control, myelin maintenance, and injury and repair in irradiated brain tissue.

Cerebral Angiography. Stereotactic cerebral angiography is carried out before stereotactic radiosurgery in order to determine the precise size, shape and location of the treatment target volume for heavy charged-particle Bragg-peak radiosurgery. Following irradiation, cerebral angiography is done at 12-month intervals on all patients, up to a period of 5 years. The arteriographic changes being examined include hemodynamic changes, e.g., decrease in cerebral blood flow, in the size of arterial feeders/shunts and in draining veins, and morphologic changes, for example progressive decrease in size of AVM until stabilization or total disappearance (Fig. 3).

The hemodynamic changes occur successively and are frequently observed before the morphologic alterations. In a few cases, the effects of the irradiation appear to occur early; nevertheless, in the majority of patients who have had angiograms within 6 months of radiosurgery, no changes are visible. In some patients, particularly those with very large cerebral AVMs, no visible changes have occurred after 2 years. In several patients, before

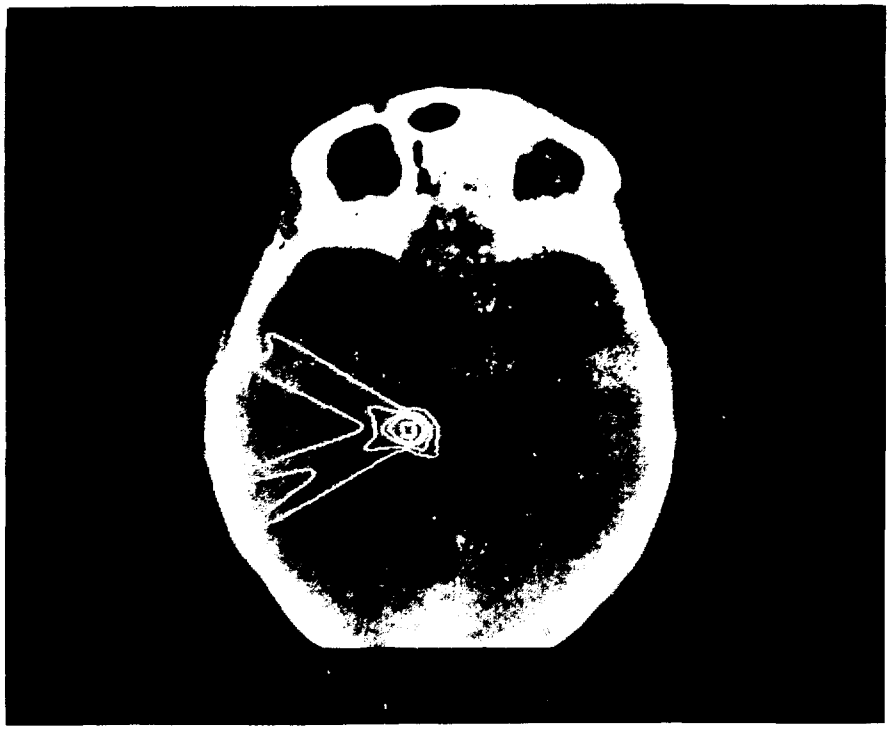

Fig. 2. Isodose contour, stereotactic heavy charged-particle Bragg-peak radiosurgery of a brain stem AVM in a 42-year-old female. The helium-ion beam was collimated by an 8-mm circular aperture. Treatment was carried out using four coplanar ports in 1 day to a volume of 250 mm³ within the brain stem; treatment dose, 45 GyE.
(XBB 853-1740)

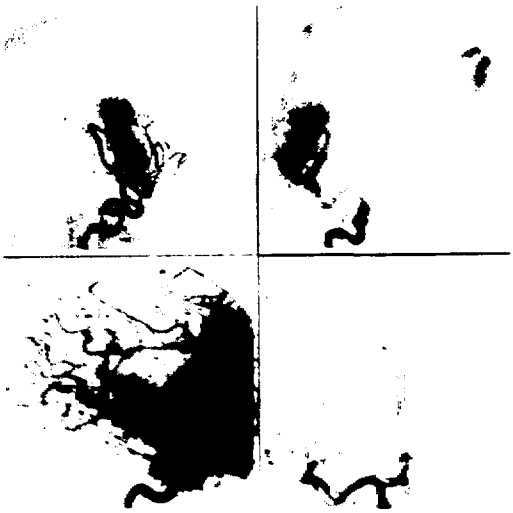

gross morphologic changes in the AVM can be determined, hemodynamic changes are noted: the cerebral blood flow rate through the malformation appears to decrease with time, with concomitant decrease in the size of the feeding arteries and outflow veins. In most patients, where response has occurred, the angiograms initially show a marked decrease in the size of the AVM due to partial obli-

Fig. 3. *Patient is a 39-year-old female with recurrent seizures and progressive motor and sensory changes due to a steal phenomenon resulting from a right cerebral (parietal) AVM. Upper: Cerebral angiogram (lat. and AP) demonstrates the size, shape, and location of the AVM and the feeding vessels arising from the branches of the middle cerebral artery. The anterior cerebral artery and its branches do not fill. Lower: Cerebral angiograms (lat. and AP) 1 year after stereotactic helium-ion Bragg-peak radiosurgery (dose, 45 GyE). There has been complete obliteration of the AVM with redistribution of the normal blood flow. There is now filling of the anterior and posterior cerebral arteries and their branches.* ***(XBB 853-2094)***

teration of the malformation within the first year; some stabilize, and progression to complete obliteration may or may not occur. Total obliteration, in cases where it is documented angiographically, usually occurred within 1 to 2 years after treatment. Since early filling of a small vein may be the only indication of a persistent shunt, complete obliteration of the AVM can be confirmed only by angiography.

X-Ray Computerized Tomography. Stereotactic CT scanning has become the basis for pretherapeutic diagnostic confirmation, for assessing AVM contour information, for transferring the angiographic data into three-dimensional format for treatment planning, and for conversion of CT data to relative stopping power, i.e., relating CT numbers on a pixel-by-pixel basis and water-equivalent pathlength per pixel. This provides the basis for heavy charged-particle radiosurgery treatment planning. The high-resolution scans are necessary for establishing the relationship of the AVM to critical brain structures, such as the brain stem, by relating the CT sections corresponding to the coordinates obtained on the stereotactic angiogram. Stereotactic CT is essential for evaluating and treating cryptic AVMs; these are small vascular malformations that are not detectable by means of routine cerebral angiography, but that are identified by pathological examination as a cause of spontaneous cerebral hemorrhage. CT may reveal possible delayed radiation necrosis, hemorrhage or infarct as well. Initially, serial CT scans were obtained on all patients every 3 to 6 months to assess response to radiosurgery and potential focal radiation injury to the brain resulting from charged-particle beam irradiation. However, no early or late changes in the brain were seen during the first 2 years of scanning in any patients. Accordingly, because such frequent scanning was considered clinically unnecessary and expensive, we have now limited serial scanning to yearly intervals for the first 5 years unless more frequent examination is clinically warranted.

Cine-Computerized Tomography. Cine-CT scanning has been carried out on five AVM patients (in a collaborative program with the Division of Neuroradiology, University of California San Francisco). We are examining the extent to which cine-CT scanning can determine cerebral blood flow through vascular disorders. In cine-CT scanning, iodinated contrast agent is injected and then two or four contiguous slices with subsecond rate exposures are obtained. Following the scan sequence, cerebral blood flow dynamics can be computed through a region of interest as a function of time (Fig. 4). By scanning through various regions of the body, it is possible to compute such quantities as the percentage of cardiac output that the arteriovenous malformation receives. Such information should prove useful in measuring the temporal and morphologic responses of cerebral blood flow through brain tissue following stereotactic radiosurgery.

Magnetic Resonance Imaging. We have begun MRI studies before and following radiosurgical treatment. Currently, all nonsurgical patients at Stanford

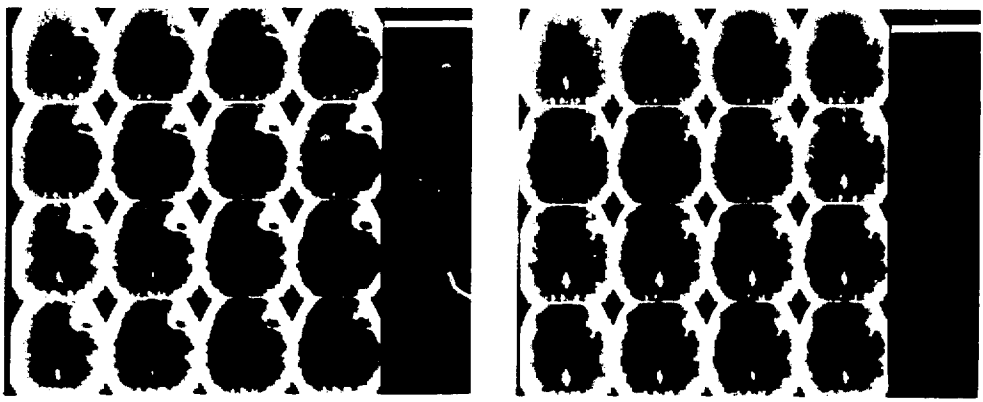

Fig. 4. Cine-computerized tomographic study of a patient with an intracranial AVM. Iodinated contrast medium is injected and two to four contiguous CT slices are then obtained with subsecond rate exposures. Following the scan sequence, cerebral blood flow dynamics can be computed through a region of interest as a function of time.
(XBB 852-1032)

University Medical Center have been selected for study, primarily on the basis of location and size of lesion. Changes of edema and scarring surrounding the AVM have been noted as early as 5 months following radiosurgical treatment, with a concomitant decrease in cerebral blood flow through the pathologic cluster of vessels. These MRI studies are aimed at determining and evaluating brain tissue tolerance, the mechanisms of radiation injury and repair, the examination of cerebral blood flow (Fig. 5), and the processes of myelination and myelin renewal, in relation to dose, dose-fractionation, heavy charged particle, and temporal patterns of radiation response. Furthermore, we are exploring the application of MRI to stereotactic heavy charged-particle treatment planning; the early results appear promising.

Xenon Computerized Tomography. Blood shunting through the AVMs in the brain, due to high-volume, high-flow changes, can cause focal or generalized neurological deficits by the vascular steal phenomenon where tissue perfusion in the adjacent brain is decreased. The obliteration of the AVM may be associated with decrease in neurological deficits and recovery. There is evidence that such deficits can regress, and that improved perfusion can, at times, reverse the cerebrovascular steal. However, little is known about the pathophysiology and cerebral blood flow dynamics of AVMs and the effect of this altered brain tissue perfusion. We are presently studying patients with AVMs who are undergoing stereotactic radiosurgery (collaborative program with Stanford University Medical Center Departments of Radiology and Surgery) using stable xenon computerized tomography to quantitate the temporal pattern of tissue response and cerebral blood flow following heavy-ion radiosurgery. The results of xenon-CT studies provide a detailed mapping for quantifying altered cerebral perfusion in brain tissue adjacent to and remote from the AVM (Fig. 6). Reduction in cerebral blood flow occurs in both cerebral hemispheres and is most severe when the AVM is large or has a major intracranial arterial supply, and is most pronounced in brain tissue adjacent to the AVM. It has been demonstrated that, following partial or complete vascular obliteration of an AVM, cerebral blood flow is decreased, whereas blood flow in adjacent and remote brain tissue increases. Neurological improvement may occur as a result of reduction in the vascular steal phenomenon because of obliteration of the pathologic cluster of shunts following stereotactic radiosurgery.

BIOPHYSICS RESEARCH

Synthesis and Maintenance of Myelin. One of the major problems in the neurosciences is the extreme cell heterogeneity of the brain. The CNS tissue is composed largely of three types of highly characteristic cells—neurons, astrocytes, and oligodendroglia — that are recognized by their size and distinctive morphology. The architecture of the brain and

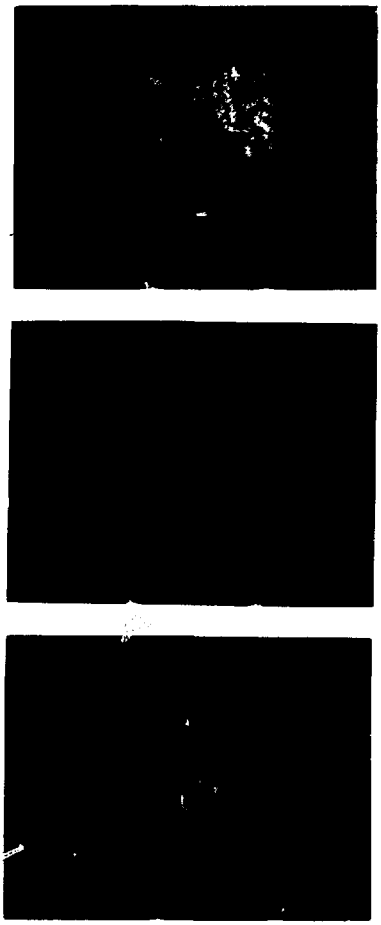

Fig. 5. Magnetic resonance image demonstrating regional perfusion kinetics and brain blood-flow transit in a patient with a large brain stem arteriovenous malformation. The vascular region of interest selected is defined (upper panel) and characterized (middle panel), and blood flow alterations are quantitated as a function of time through the offending vascular lesion (lower panel). (In collaboration with Dr. Peter Valk, Research Medicine Laboratory.) *(XBB 851-960)*

Fig. 6. Xenon-computerized tomographic imaging of an intracranial AVM in a 49-year-old male with significant steal phenomenon involving the left cerebral (parieto-occipital)cortex. The scan demonstrates cerebral blood flow dynamics and alterations of brain tissue perfusion involving the immediate area of the AVM and diminished perfusion in the entire ipsilateral cerebral cortex. (XBB 852-1629)

its hierarchical structure are such that all three cell populations, together with the vascular structures, intertwine to form a highly integrated tissue. This complex tissue also contains populations of cells with different biochemical and metabolic characteristics; this has made biochemical studies on defined cell types in intact normal brain tissue virtually impossible, despite the distinct functions of these cells. The problem of cellular heterogeneity in the brain is accentuated when the brain is abnormal. The abnormalities may include changes in the size, shape, or architecture of the cells or the cell populations so that their characteristic morphology or metabolic function may be altered, for example, when brain cells undergo radiation injury leading to early and late delayed effects. In order to overcome the difficulties in defining changes in cells or their membranes in the highly integrated brain tissue, we have begun to develop techniques to isolate and maintain defined brain cell populations in short-term tissue culture in order to provide information about the specific abnormalities and to assess potential cell-specific properties for use as indicators of cell damage. We have begun studying specific membrane components in isolated purified populations of defined cell types from the brain. We are particularly interested in myelin, the membrane essential for normal functioning of the nervous system, with special emphasis on oligodendrogial function and synthesis of myelin and its breakdown, and its response to charged-particle irradiation.

Induction and Repair of DNA Damage

Capillary Endothelium. The late delayed radiation effects in the brain are considered vascular in origin and associated with vascular endothelial injury and functional disturbances, leading to ischemia, cell death and necrosis. Late radiation effects on the capillary endothelium in irradiated mammalian brain have been described and have been studied with respect to dose and temporal patterns of change; however, the mechanisms leading to these changes are not known. To clarify the sequence of events in the mammalian brain following charged-particle irradiation, we are examining the endothelial cells early after irradiation with low and moderate doses. The induction of and *in-vivo* repair of DNA strand breaks, a very sensitive index of early radiation effects, is being studied in rat and mouse brain cerebral and cerebellar capillary endothelial cells after helium-ion (230 MeV/u) and neon-ion (425 MeV/u) irradiation *in vivo* (doses: 2–15 Gy). A microscope photometer method that measures the unwinding of DNA is used. Single endothelial cell nuclei are stained with the fluorescent dye acridine orange and the intensity of the red fluorescence (from single-stranded DNA) relative to the green fluorescence (from double-stranded DNA) is used as a measure of DNA strand breaks. Initial observations demonstrate that most DNA strand breaks in cerebral and cerebellar capillary endothelial cells are repaired within 30 minutes post-irradiation with low-LET radiation, with a linear dose-effect relationship. This appears to obtain, as well, for DNA strand breaks in single endothelial cells in cerebrum and cerebellum exposed to high-LET charged-particle beams (Fig. 7). We are continuing to investigate dose-effect relationships for helium-ion, carbon-ion, and neon-ion irradiation, the radiation

Fig. 7. *DNA strand breaks in capillary endothelium in the irradiated mouse brain. The microscope photometer method used measures the unwinding of DNA; the fluorescent dye technique provides a measure of single-stranded and double-stranded DNA lesions reflecting the damage to the genome of these target cells of the brain. Upper: unirradiated; Lower: irradiated. (In collaboration with Dr. Kirsten Rosander, Swedish National Defense Research Institute.)* *(XBB 851-796-A)*

response (DNA strand breaks) *in vivo*, the response vs. time after irradiation, and the kinetics of short-term and long-term repair of DNA strand breaks (in collaboration with Dr. Kirsten Rosander, Swedish National Defense Research Institute).

DNA Damage and Biological Dosimetry. The repair kinetics of radiation-induced DNA strand breaks demonstrate three components: an initial fast rate of repair, followed by a slow rate of repair, and delayed or long-term repair associated with residual and irrepairable breaks. We are developing a method of assaying for DNA strand breaks in the Simian virus 40 genome, irradiated intracellularly, and are attempting to apply the technique to biological dosimetry *in vivo* for study of narrow heavy-charged particle beams. The method uses an electro-optical effect to measure conformation changes in phage DNA, and the number of strand breaks is thereby obtained (Fig. 8). For a radiation of a given quality, this information yields the dose applied, or it can be used to compare the RBE of different radiation fields. This will prove valuable as we examine heavier ion beams for the treatment of brain disorders. Furthermore since the target volume of viral DNA is very small, and because it is difficult to assay DNA lesions in the large mammalian genome, dose distribution can also be mapped in order to understand biological effects and tolerances. As we move to the *in-vivo* isolation and maintenance of brain cell populations, the method may be adapted for understanding radiation response of different brain structures *in vivo*, with applications to improved treatment and to evaluate the potential of heavier charged particle beams and beam delivery systems in clinical research.

Brain Cell Population Kinetics. In the young adult CNS, the subependymal plate of the lateral ventricles in the brain appears to be the only tissue that is actively proliferating. The relatively high rate of proliferation may be a continuous source of progenitor or stem cells for new glial cells, both for glial cell renewal in normal conditions or during regeneration after cytoxic injury. Based on experimental observations of quantitative analysis of changes in time of counts of various cell types, a model of glial cell renewal and differentiation can be proposed, based on original cytologic criteria established by Leblond: four characteristic nuclear patterns—small dark, small light, large dark, and large light nuclei—define stages of cell proliferation and differentiation and migration patterns of glial

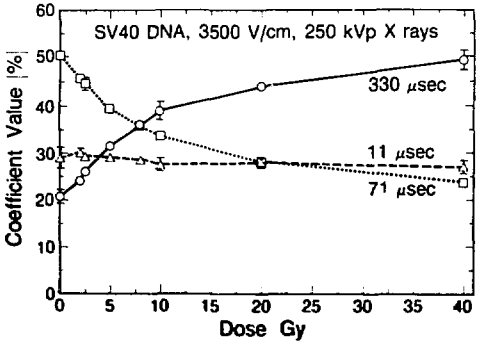

Fig. 8. *Decay curve coefficients as a function of radiation dose (in Gy) for SV40 DNA strand breaks (3500 V/cm) for low-LET radiation (250-kVp x rays). The method has proven to be reliable and reproducible in the dose ranges of clinical importance in stereotactic radiosurgery.* *(XBL 8511-8598)*

cell precursors and their progeny. Following injection of tritiated thymidine, initially only large dark nuclei are labeled, these apparently divide promptly to become small dark cells. Small dark cells represent a stem cell pool in the subependymal plate; they appear to be glial cell precursors and young oligodendrocytes. These cells transform into cells with small light nuclei, which are glial cell precursors that migrate in the brain. About 20% of the small light cells transform to large light nuclear cells, as precursors of astrocytes.

The subependymal plate cells undergo prompt radiation-induced injury. The cellularity of the plate is depressed following exposure to low-LET radiation, and the mitotic activity is strongly reduced for doses up to 45 Gy, but recovery appears to be dose dependent, e.g., after 40 Gy no recovery occurs and cell population counts are depressed, whereas after lesser doses, control levels are reached after a few months. It has been observed that following irradiation the dark cells disappear rapidly and the light cells do not; this suggests that the light cells remaining represent a glial stem cell pool with relatively slow turnover times, whereas the dark cells comprise a rapidly proliferating stem cell population. This observation is consistent with the view that the dark cells represent a stem cell population in the subependymal plate and is responsible for recovery after high-LET exposure (Fig. 9).

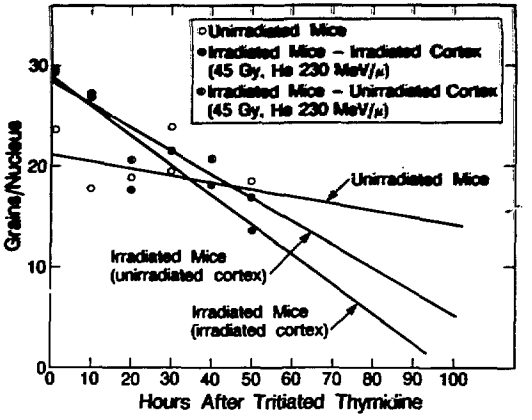

Fig. 9. The nuclear grain counts in subependymal plate cells in the mouse brain following 45 Gy (helium ions, 230 MeV/u) are plotted as a function of time after injections of tritiated thymidine 66 hr after exposure. Linear regression analysis demonstrates a profound shortening of the population doubling times compared with the unirradiated controls; the unirradiated half of the cerebral cortex in irradiated mouse, however, shows the same temporal pattern of cellular response. Population doubling times of subependymal cells are: irradiated mice (irradiated cortex), ~44 hr; irradiated mice (unirradiated cortex), ~56 hr; unirradiated mice, ~139 hr. (XBL 8511-8597)

SECTION 3. PHYSIOLOGY

INTRODUCTION

During the past year the name of the Environmental Physiology Group was changed to Physiology Group in order to reflect more accurately the nature of its programs. Limited research on environmental issues such as ozone toxicity is still being performed by scientists within the Physiology Group. However, the primary research emphasis is on elucidating cellular and tissue regulatory mechanisms, and on assessing the perturbations of biological control mechanisms that occur in response to pathogens, toxic chemicals, and radiation.

This year's annual report for the Physiology Group contains a discussion of research progress in programs related to the endocrine and hematopoietic systems, hematozoan infections, nonionizing radiation bioeffects, and transuranium element clearance techniques. It includes summaries of the research programs of two new investigators, Paul H. Silverman and Robert P. Liburdy, who joined the Group in the latter half of 1984. Silverman is a specialist in the field of parasitology and Liburdy in the field of microwave radiation bioeffects. The following is a summary of highlights of the Physiology Group programs described in this year's annual report.

Two of the major effects of advanced malarial infections are a severe anemia and immunosuppression. The research reported by Silverman et al. suggests that both syndromes may be due to the depletion of hematopoietic stem cells in response to malarial infection. Studies with three species of murine malaria have shown that the marrow content of pluripotential stem cells measured in a spleen-colony assay (CFU-S) was significantly reduced during advanced stages of parasitemia in mice. The interesting finding was made that the level of biologically active serum erythropoietin (Ep) increases in the infected hosts in parallel with the onset of severe anemia. This observation suggests that the decreased level of CFU-S may lead to a depletion of erythroid progenitor cells that can respond to Ep. Along with the decrease in CFU-S, a marked decrease in marrow cellularity and a significant splenomegaly were observed. The latter finding indicates that the spleen alone is not able to satisfy the hematopoietic requirements of malaria-infected mice. Another interesting finding by Silverman et al. was the observation that nonspecific stem cell stimulation by endotoxin conferred some degree of protection in mice against the lethal effects of malarial infection.

Additional new information on the molecular basis of the dyserythropoiesis that accompanies malarial infection is described by Schooley and Kullgren. They have compared the rate of DNA synthesis following exposure to Ep of spleen cells from mice made anemic by malarial infection and by injection of phenylhydrazine, a drug that destroys mature erythrocytes. The spleen cells from phenylhydrazine-treated mice exhibited a burst of DNA synthesis in response to Ep, whereas the spleen cells from malaria-infected mice did not. It was also found that the addition of conditioned medium from cultures of malaria-infected spleens to cultures of spleen cells from phenylhydrazine-treated mice inhibited the response of the latter to Ep. This finding indicates that a molecular inhibitor produced by cells from malaria-infected mice may prevent the normal response of erythroid precursor cells to Ep, and thereby cause the anemia associated with this disease.

Using two sublines of CBA mice whose cells can be distinguished by the presence of two district alloenzymes of phosphoglycerate kinase (PGK-A and PGK-B), Brecher has been studying the fate of transfused bone marrow cells. The research described in this year's report was designed to answer the specific question of whether pluripotential bone marrow stem cells divide symmetrically to form a clone of mature cells. In order to maintain a pool of pluripotential stem cells, the symmetric division of a committed stem cell into differentiated daughter cells would require its replacement by a new uncommitted stem cell. This process has been termed the clonal succession of pluripotential stem cells. By transfusing small inocula of marrow cells containing PGK alloenzyme markers, Brecher was able to demonstrate that the clonal succession process does not occur in the simple manner

described above. Instead, his data indicate that each single stem cell must produce a pool of pluripotential stem cells before it loses its capacity for self-renewal through the production of differentiated daughter cells.

Two papers describing endocrine research by Clemons and her colleagues also appear in this year's report. In the first paper, she describes tests on antisera used for the radioimmunoassay (RIA) of Ep. In order to be useful for Ep RIA, it was found that an antiserum must also exhibit binding affinity for Ep in a relatively insensitive *in vivo* assay technique using plethoric mice. However, among different antisera with this property, there was no correlation between Ep neutralizing capacity *in vivo* and the binding affinity for ^{125}I-labeled Ep in the *in vitro* RIA. Various antisera prepared against human urinary Ep were also found to have differing affinities for Ep from rats, mice and sheep. In another series of experiments, the RIA procedure was used to compare the binding affinities of antisera for two samples of purified human urinary Ep and one sample of human Ep prepared by recombinant DNA techniques. One of the chemically purified human Ep samples had the highest binding affinity for antiserum, but when the three different Ep samples were heated briefly at pH 5.5, their binding to antiserum was identical and higher than that observed for any of the unheated samples. This finding suggests that heat treatment may unmask Ep immunologically reactive sites, possibly through an effect on the carbohydrate moiety of Ep.

Previous studies by Clemons demonstrated that the exposure of rats for one day to an atmosphere containing 1 ppm of ozone leads to a significant decrease in the levels of circulating thyroid hormones. Because high levels of thyroxine serve to potentiate the toxic effects of ozone, it was hypothesized that the decrease in thyroid hormone levels may represent an adaptive mechanism in the exposed animals. In this year's report, Fitzsimmons and Clemons describe the results of polyacrylamide gel electrophoretic studies designed to test the binding of thyroxine to serum proteins in ozone-exposed rats. It was found that a one-day exposure to 1 ppm of ozone increases the number of binding sites for thyroxine on pre-albumin molecules by about 30%. This change in pre-albumin binding capacity correlates well with the previously determined decrease in the level of circulating thyroxine in rats exposed to 1 ppm of ozone.

An analysis of the biological effects of magnetic fields and radiofrequency radiation form an integral part of the Physiology Group's research program. Studies on cellular, tissue, and animal responses to high-intensity magnetic fields are described in this year's report by Tenforde et al. A variety of sensitive electrical recording techniques have been used in this program to detect magnetically-induced alterations in physiological functions that involve ionic conduction processes, such as those in the cardiovascular, nervous, and visual systems. A description is given in this year's report of studies on visual processes in the retinas of cats and monkeys exposed to high-intensity stationary magnetic fields. By recording the electrical activity of the retina following photon absorption, it was demonstrated that no significant visual alterations occurred in six cats and three monkeys during exposures to magnetic fields with graded intensities up to 1.5 tesla. Several studies of physiological parameters and their circadian variations in rodents exposed to a 1.5-tesla magnetic field are also described in this year's report. Using an exposure system with an array of noninvasive monitoring devices, it was demonstrated that none of seven simultaneously measured circadian variables was significantly perturbed by a high-intensity magnetic field. New research findings with a superconducting magnet are also described in the report by Tenforde et al. This magnet achieves an ultrahigh field level of 9 tesla, and it is being used to study mechanisms of magnetic field interactions that cannot be analyzed using conventional electromagnets that reach a maximum field strength of approximately 2 tesla. Of particular interest are the responses of molecular systems such as biological membranes that have a high degree of diamagnetic anisotropy. A new phenomenon discovered during initial experiments with the 9-tesla magnet is a magnetically-induced change in the permeability properties of model liposome membranes. At temperatures close to the thermal phase transition point, liposome unilamellar membranes exhibit a significant increase in solute permeability in the presence of an applied magnetic field. This new finding has important implications for magnetic field interactions with cellular membranes.

In another series of experiments with liposomes, Liburdy has investigated the use of microwaves to stimulate the release of a chemotherapeutic drug encapsulated in unilamellar liposome vesicles. As described in this year's report, the release of tritiated cytosine arabinofuranoside (^{3}H-ARA-C) can be triggered by microwave exposure, thus indicating the feasibility of using this technique for targeted drug delivery *in vivo*. The microwave

stimulation of ^{3}H-ARA-C release is not a result of liposome disruption, since radioisotopically labeled phospholipid molecules are not lost from the liposome membrane in response to microwave exposure. In other experiments, Liburdy has characterized the effects of temperature and the chemical environment of liposomes in modifying the microwave-stimulated release of encapsulated solutes. He has observed that components of blood plasma and a high oxygen tension potentiate the microwave effect on liposome permeability. In contrast, an inhibitory effect on microwave-induced solute release is exerted by ascorbic acid, mercaptoethanol, or an anaerobic environment.

Durbin and collaborators from the LBL Materials and Molecular Research Division and the UC Berkeley Department of Chemistry have been studying several classes of chelating agents with appropriate molecular dimensions for the efficient binding of Pu(IV). The long-range goal of this program is to develop a set of chelating agents that are effective in accelerating the elimination of actinides and chemically similar metals from the body, while simultaneously having a low biological toxicity. In this year's report, progress is described in the testing of four newly synthesized ligands for their ability to promote the excretion of Pu(IV) from mice. Two of these agents are promising as Pu(IV) chelating agents when administered by the oral route. In addition, the results of dose-effect studies are described for the hydroxypyridinone oxide derivative of desferrioxamine, which is the most effective Pu(IV) chelating agent developed thus far. Another chelating agent, a tetrameric carboxy(catechoylamide) ligand, was studied for its effectiveness in removing Pu(IV) that is recirculated from the liver and other soft tissues. It was shown that multiple daily injections of this ligand can promote the long-term clearance of residual Pu(IV) by directing the recirculated plutonium to an excretion pathway.

HEMOPOIESIS AND MALARIA

Paul H. Silverman, John C. Schooley, and Lynn J. Mahlmann

The World Health Organization has viewed with increasing concern the continued spread of malaria since failure of the eradication campaigns of the post World War II era. These campaigns were based heavily on the use of insecticides to control the mosquito vector and on antimalarial drugs to treat the infection (Fig. 1). Unfortunately, development of resistance to insecticides by the mosquitos and resistance to the antimalarials by the parasite combined with administrative instability in the affected countries led to a breakdown in malaria control. It is estimated that 1.8 billion people are now in need of some form of protection from the disease. Children are particularly at risk. In Africa alone, more than a million deaths in children are attributed to malaria annually because of the direct and indirect effects of this disease. Even a slight parasitemia induces immunosuppression and creates an increased susceptibility to other infectious organisms. Recent optimism about the development of a malaria vaccine presupposes that the target population is immunologically intact. However, evidence from clinical studies on the use of well-established vaccines (e.g., tetanus, pertussis, etc.) in areas where malaria is prevalent suggest that these populations are immunologically impaired.

The work reported here suggests that the anemia and immunosuppression characteristic of malaria may be due to the depletion of hemopoietic stem cell populations. The hematopoietic stem cell is the ultimate source of all red blood cells, white cells, and immune lymphocytes (Fig. 2). A decrease in stem cells might result in perturbations of all clonal progeny. This work then suggests the basis for new strategies to achieve protection from and treatment of malaria and other related protozoan parasite diseases.

Anemia is a major complication of malaria and contributes to the morbidity and mortality effects of the disease. The causes of anemia have been variously ascribed to 1) destruction of red cells by the parasites, 2) autoimmune phenomena that result in enhanced nonspecific erythrophagocytosis, and 3) gross dyserythropoiesis leading to impaired red cell production that continues for several weeks, even after the parasitemia has been chemotherapeutically controlled.

Numerous studies over the past 20 years have indicated that mechanisms of red cell destruction and autoimmune responses are, by themselves, inadequate to account for the severity and extent of anemia caused by malaria. As a result of a

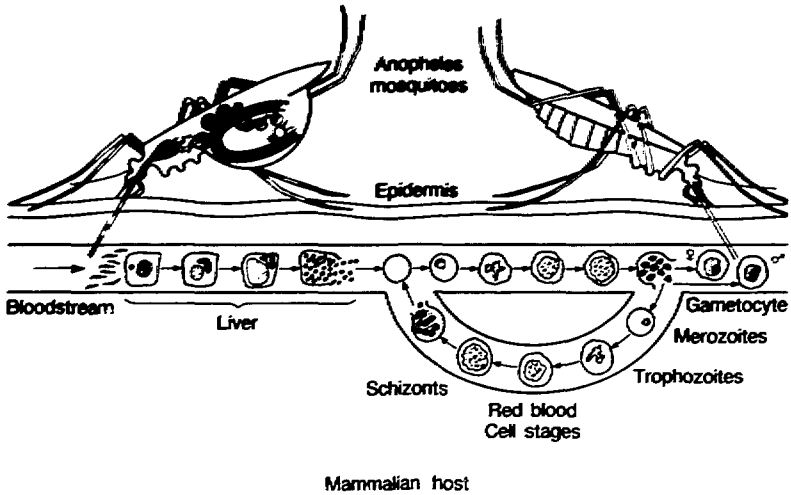

Fig. 1. Malaria lifecycle. *(XBL 8510-8505)*

number of human studies, Weatherall and his coworkers[1] concluded that, "It is becoming apparent that severe dyserythropoiesis with minimal hemolysis plays a major role in the anemias of *Plasmodium falciparum* infection....".

Another aspect of malaria infection concomitant with anemia is immunosuppression. Malaria has been observed to induce a state of immunological hyporesponsiveness to homologous (malaria) and heterologous organisms (measles, gastroenteritis, and respiratory infections). Immunological hyporesponsiveness is associated with both acute and chronic human *P. falciparum* malaria.

Efforts to elucidate the mechanisms of malaria-induced immunosuppression have been largely limited to clinical observations and studies that have focused on peripheral blood effector cells. The studies have focused, in particular, on T and B lymphocytes, monocytes, and macrophages, and have tended to suggest that splenic macrophages play a central role in regulating immune hyporesponsiveness. However, it is clear that the regulatory mechanism of immunosuppression cannot be compartmentalized to the spleen because immune responses to antigens administered peripherally are also blunted.

Some workers have suggested that immunosuppression is due either to impairment of the progenitor cells of granulocytes/macrophages or an imbalance of the competition between erythropoietic and immune cell lineages, which are all derived from a common pluripotent stem cell (CFU-s).

Although there is much that is unknown about the processes involved in the renewal and differentiation of hemopoietic stem cells, there is general agreement that the sequence of events leads unidirectionally from a pluripotent cell to a committed mature cell with specialized function and eventual death. It is also apparent that the pluripotent stem cell must renew itself, achieving an effective state of immortality. Several models have been proposed for the regulation of stem cell renewal and

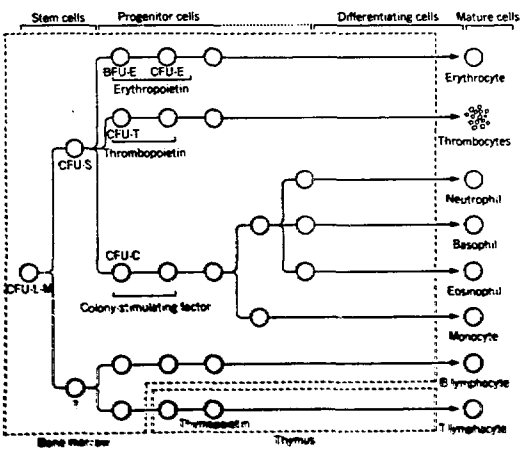

Fig. 2. Scheme of hematopoietic cell differentiation. BFU, burst-forming unit; CFU, colony-forming unit; -C, culture; -E, erythroid; -L-M, lymphoid-myeloid; -S, spleen, -T, thymoid.
(XBL 852-1427)

differentiation. The preponderance of data favor a stochastic model in which the decision to self-renew or to differentiate into a committed progenitor is a random process, not under the influence of external factors. The process might be positionally affected and may lead to committed lines or to the random loss of lineage potentials.

In unstressed homeostatic animals or humans, the great majority (90%) of hemopoietic stem cells are in a quiescent state. Normally only a few stem cells are active in the hemopoietic system, generating between 5 and 15 cell clones. Each progenitor cell line is capable of proliferation in response to systemic needs. For example, hypoxia stimulates the production of the hormone erythropoietin, which acts on erythroid progenitor cells to give rise to a population of erythrocytes. Other clones give rise to megakaryocytes, polymorphonuclear leukocytes, and lymphocytes under the influence of specific hormones. Although no specific activator or regulator for pluripotent stem cells has been identified, a number of nonspecific substances have been shown to increase the number of CFU-s undergoing proliferation.

Schooley and Lin[2] observed that an acute and continuing demand for erythrocytes may result in a depleted population of bone marrow stem cells. During stress, the proliferation of CFU-s and the intermediate populations of unipotent cells derived from CFU-s are increased. However, the resulting stem cells may have a limited capacity to renew or to develop certain cell lineages. In the context of these interacting and interdependent cell regulatory mechanisms, there exists a possible explanation for the concommitant anemia and immunosuppression associated with malaria infection.

ERYTHROPOIETIN PRODUCTION DURING MALARIA

The effects of infection with three species of murine malaria (*Plasmodium berghei, P. chabaudi adami, and P. vinckei vinckei*) were determined on the plasma levels of erythropoietin (Ep), the hormone responsible for regulating erythrocyte production. A polycythemic mouse bioassay and a radioimmunoassay were used to follow plasma titers of Ep during the course of infection. The potential capacity of Ep production was assessed by exposing infected mice for 5 hours in a decompression chamber equivalent to a 22,000-foot altitude (6706 m)(pO_2 = 67.1 torr).

As exemplified by the results for *P. berghei* (Fig. 3), Ep production increases as the infection progresses until maximum capacity is reached during peak parasitemia. The Ep plasma concentration, which is increased in the early stages of malaria infection, is increased even more when the mouse is exposed to hypoxia, indicating that the tissues producing the hormone are not maximally stimulated. During the later stages of infection, the Ep plasma levels are not further increased by an hypoxic exposure, suggesting that the Ep generating system is stimulated maximally. It is possible that the sites of production of Ep are different at later stages of infection with extrarenal sites, such as the liver, becoming involved.

The temporal pattern of Ep production and increase in production capacity in response to infection with *P. berghei, P. vinckei* and *P. cha-*

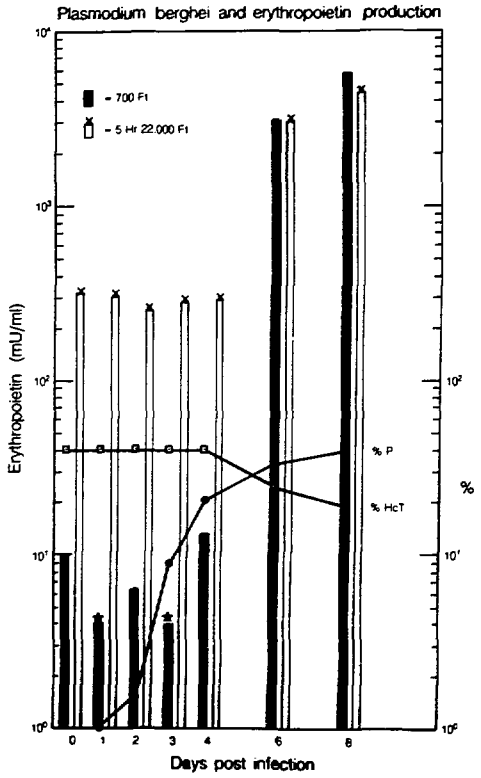

Fig. 3. Parasitemia (P), hematocrit (HCT) and erythropoietin (Ep) levels during the first 8 days of inoculation of female Swiss Webster mice with Plasmodium berghei. On day 0 each mouse was injected with 1 × 10^6 P berghei i.v. Plasma samples were collected from 8 to 15 mice per day for subsequent Ep determination by RIA. Bar graphs represent Ep titers before (■) and after (□) hypoxic stimulus. (✱) Ep levels on days 1 and 3 were estimated because the titers were below the threshold of sensitivity of the RIA which is about 5 mU/ml. (XBL 854-9533)

baudi were similar. The results, which are based on a bioassay method that assesses the biological function of Ep, confirm that an amount of active Ep is present in the vascular circulation adequate to stimulate the differentiation and proliferation of erythroid committed progenitor cells. The data suggest that the lack of an adequate erythropoietic response during malaria infection must be due to a failure of the erythroid progenitor cells (BFU-e, CFU-e) to respond to Ep, or a decreased production of erythroid progenitors, and/or a diminished production of CFU-s.

BONE MARROW STEM CELL KINETICS DURING MALARIA

Bone marrow cells from donor mice when transplanted into lethally irradiated syngeneic recipients will form macroscopic cell colonies in the spleen of the recipient mouse. After 7 days, the number and type of the newly formed colonies (as determined by histological examination) provide qualitative and quantitative data on the pluripotent stem cells derived from the donor. Since the spleen colony assay was introduced over 25 years ago, several workers have demonstrated that each of the spleen colonies in the recipient mouse is derived from a single pluripotent cell. Experiments in this laboratory did not reveal any statistical difference between spleen colony assays counted on days 8, 9 or 10 after transplantation. The spleen colony assay results reported here are based on the widely accepted standard of counts made on day-8 post-transplantation.

The status of CFU-s in mice infected with murine malaria was examined at peak parasitemias as well as during the course of infection. The data presented here are representative of the results obtained (Table 1). A minimum of four but usually five infected donor mice were used as sources of bone marrow cells, aliquots of which were transplanted into each of 10 lethally irradiated recipient mice for spleen colony assays.

FEMORAL CELLULARITY

Determinations of the total number of nucleated cells in the femurs of mice infected with *P. berghei* and *P. vinckei* indicated, consistently, that a marked depletion (40–60%) occurs in the later stages of the disease (Table 1). It is highly probable that the results reported here are minimal estimations of the actual proportional reduction because of the evidence of osteoclasia that was apparent in the femurs of the infected mice. Femoral bones from infected mice were very brittle.

STEM CELL KINETICS

Changes in CFU-s populations were measured as a proportion of the nucleated bone marrow cells and in relation to the total cellularity of the femoral contents. Observations made during the early phases of infection with *P. berghei* and *P. vinckei*

Table 1. Results of the spleen colony assay using BALB/c female mice. Depending upon the time postinoculation and level of parasitemia, 0.5–1.0× 10^5 nucleated bone marrow cells pooled from the femurs of each donor mouse was injected i.v. into 10 syngeneic recipients. Spleen colonies were observed on day 8 after transplantation. The mean spleen colony counts (± SEM) represent n = 40 for P. berghei days 5 and 11, n = 50 for P. berghei day 14, P. vinckei day 7 and n = 70 for uninfected controls. Femoral cellularity was determined by Coulter Counter (Hieleah, Florida) on suspensions of bone marrow cells which were freed of erythrocytes by antiserum treatment (Zap-Oglobulin II, Coulter Diagnostics).

Donor N	Post-inoculation (Day)	Parasitemia (%)[a]	Cells/femur (×10^6)[a]	CFU-s (×10^{-6}BMC)[a]	CFU-s/Femur[a]	Femoral cellularity (% Normal)[a]	Femoral CFU-s (% Normal)[a]	Hematocrit (%)[a]	Body weight (g)[a]	Spleen weight (g)[a]
Uninfected controls										
7	—		14.2 ± 0.90	275 ± 10	3870 ± 140	—	—	47 ± 0.04	20.7 ± 0.19	0.10 ± 0.01
Plasmodium berghei										
4	5	8.3 ± 2.6	9.9 ± 0.76	473 ± 20	4590 ± 190	70 ± 6.9	119 ± 6.4	48 ± 0.65	20.2 ± 0.55	0.25 ± 0.01
4	11	32 ± 3.1	6.4 ± 0.99	149 ± 7.0	990 ± 73	45 ± 7.5	26 ± 2.1	20 ± 3.0	15.8 ± 0.92	0.74 ± 0.12
5	14	55 ± 5.6	8.6 ± 0.63	105 ± 7.0	897 ± 63	61 ± 5.9	23 ± 1.8	24 ± 1.0	13.8 ± 0.23	0.65 ± 0.08
Plasmodium vinckei vinckei										
5	7	65 ± 3.3	6.1 ± 0.57	312 ± 10	1880 ± 94	43 ± 4.8	49 ± 3.0	24 ± 0.92	18.5 ± 0.21	0.64 ± 0.02

[a] $\bar{x}$ ± SEM

BMC – bone marrow cells

CFU-s – pluripotent stem cells

indicated early enhanced proliferation of stem cell populations. However, in the late stages of infection with murine malaria, stem cell depletion dropped to less than 25% of the normal (Fig. 4). It is important to note that the degree of CFU-s depletion during late stages of infection is greater than the depletion observed for the total femoral cellularity. The differences in the response of the two cell populations suggest that factors affecting stem cell renewal and differentiation may be different, or are affecting different target cells in the bone marrow.

Whether the parasite-induced factors are acting on one or more constituents of the bone marrow cell population is difficult to assess from these experiments. However, the net effect of a depleted hemopoietic stem cell population is of considerable importance to the potential outcome of the infection. Stem cell suppression might result in reduced capacity to generate blood cells to meet physiologic needs and for survival itself. All of the main disease characteristics of malaria could result from, or be exacerbated by, stem cell depletion. Erythrokinetic studies indicate that an unstressed human requires more than 2.0×10^6 new red cells each *second* to replace senescent erythrocytes. The effects of suppressed production of new erythrocytes by CFU-s inhibition might theoretically account for half the anemia observed in the mouse on day 14 postinoculation with *P. berghei*. Whatever the degree of contribution to anemia caused by CFU-s depletion, it is apparent that perturbation of progenitor cell production will enhance the anemia caused by parasite induced red cell destruction and delay recovery of erythropoiesis after cure has been achieved chemotherapeutically. Because of the random nature of the pluripotential stem cell renewal and differentiation, it is probable that suppression of stem cell production of one cell lineage is accompanied by depression of all cell lineages. Thus, an inevitable outcome of stem cell depletion will be reduced production of megakaryocytes, granulocytes, and lymphocytes, resulting in thrombocytopenia, leuckocytopenia, and immunodepression, all of which occur during malaria and infection with other hematazoa (e.g., trypanosomes, *Babesia*, and *Anaplasma*).

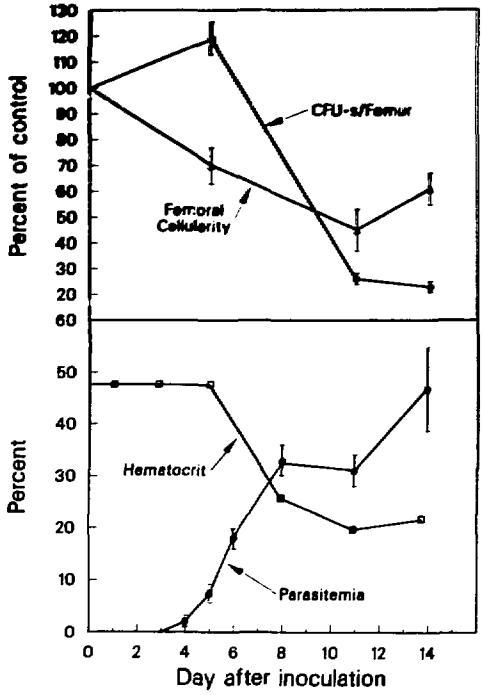

Fig. 4. Changes in femoral cellularity and bone marrow stem cell (CFU-s) populations following inoculation of Balb/c female mice with 1×10^5 Plasmodium berghei injected i.v.
(XCG 858-377)

NONSPECIFIC IMMUNITY

Support for the concept that parasite-induced perturbation of stem cell renewal and progenitor cell production is a characteristic of hematozoan infection is provided by observations that a wide variety of known stem cell stimulators induce resistance to hematozoa infections. If stem cell depression is an important factor in malaria pathogenesis, then stem cell stimulation should ameliorate the virulence of malaria infection. This prediction is borne out by reports that various intact bacteria (*Cornybacterium, Brucella, Listeria,* and *Salmonella*) and bacterial cell wall components such as endotoxins (lipopolysaccharides), when injected prior to infection, induce a degree of nonspecific protection that varies from reduction in parasitemia to prevention of lethal effects. It is well established that when endotoxins from bacterial cell walls are injected into mice there is a rise in the number of pluripotent hemopoietic stem cells and progenitor cells in both the bone marrow and spleen. This rise peaks approximately 5 to 7 days after injection of the endotoxin.

We tested the concept of stem cell and progenitor cell stimulation as an effective inducer of resistance to the lethal effects of murine malaria. A series of injections of 5, 10, and 15 μg *E. coli* lipopolysaccharide-W were interspersed with mild

hypoxia to stimulate stem cells and erythroid progenitor cells for 5 days prior to infection with a virulent inoculum of *P. vinckei* (Fig. 5). The results indicate that the combination of stem cell and erythroid progenitor cell stimulation confers significant protection. Indeed, after all controls and unprotected mice had died by day 15, the protected survivors resolved the infection by day 22, and 2 weeks later, when challenged with another infective inoculum, showed either no or only a transient parasitemia.

THE ROLE OF THE SPLEEN

Splenomegaly has long been recognized as a characteristic response to malaria and other parasitic infections. As our results indicate, the size of the spleen may increase 7 times over normal during the course of the infection (Table 1). The increase in weight of the spleen may be due to the splenic migration of cells from the bone marrow as well as proliferation of cells located in the spleen. As impressive as is the remarkable increase in spleen cellularity, it remains to be demonstrated whether it is capable of replacing the hemopoietic functions of the bone marrow when it is depleted of a substantial portion of pluripotent stem cells. The obvious fact that the enlarged spleen does not meet the hemopoietic needs of the malaria-infected mouse suggests that it is not functionally equivalent to the bone marrow.

The discovery that murine malaria induces substantial depletion of bone marrow pluripotent stem cells is of practical and theoretical importance. It suggests that through appropriate use of stem cell stimulators, alone or in conjunction with specific antigens, the immunological status of affected populations might be significantly improved. This approach might enhance immune responses to vaccines in endemic malarial areas as well as improve the general nonspecific immune response in malaria-infected persons to heterologous infections.

The theoretical importance of a stem cell suppressor mechanism is considerable. Since malaria organisms are not known to invade

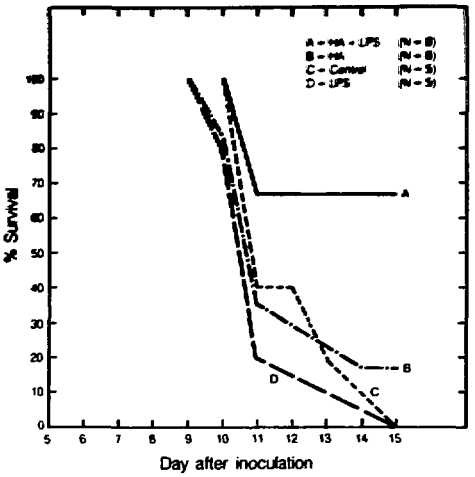

Fig. 5. Cumulative survival of female Swiss Webster mice that were infected with 1 × 10⁵ Plasmodium vinckei inoculated i.v. after various treatments: (A) i.p. injection on days 1, 4, and 6 with 5, 10, and 15 μg E. coli lipopolysaccharide-W and held in a decompression chamber equivalent to high altitude (HA) of 22,000 ft for 5 hours on days 0, 3, and 5. (B) Held in a decompression chamber equivalent to 22,000 ft for 5 hours on days 0, 3, and 5. (C) Control group. (D) I.p. injection on days 1, 4, 6 with 5, 10, and 15 μg lipopolysaccharide-W (E. coli 0127: B_8, Difco Labs.). *(XBL 854-9534)*

nucleated bone marrow cells *in vivo*, it is probable that the stem cell suppression is accomplished by a diffusable product of the infection process. Elucidation of how the stem cell is affected by malaria, directly or indirectly, may lead to new insights in the physiology of stem cell renewal and differentiation.

REFERENCES

1. Weatherall, D.J., Abdalla, S., and Pipparo, M.J. *Malaria and the Red Cell.* Ciba Symposium, Pittman, London, p. 74–97 (1983).
2. Schooley, J.C., and Lin, D.H.Y. *Regulation of Erythropoiesis.* A.S. Gordon, M. Condorelli, C. Peschle, Eds., Il Ponte, Milan, pp. 52–66 (1972).

MALARIAL DYSERYTHROPOIESIS: A POSSIBLE ROLE FOR INTERLEUKIN 1?

John C. Schooley and Birgitta Kullgren

Malaria is a mosquito-borne parasitic disease that has afflicted mankind since antiquity. Various methods for eradication of the mosquito and new drugs to treat infected individuals raised hopes that ultimate victory against this dreaded disease was near. Yet these hopes have not been realized. Mosquitos have developed resistance against various pesticides, and the malarial parasite has developed resistance against many of the new drugs. In 1961 only 50,000 cases of malaria were reported in India, but by 1977 slightly more than 30 million individuals had the disease. Today, the disease afflicts 200–400 million persons in tropical and subtropical areas, and it is the major cause of early childhood mortality. Persons surviving the disease are often anemic, and this contributes to the debilitating aspects of the disease.

Anemia—the lack of an adequate mass of functioning erythrocytes in the circulating blood—may result from numerous causes related to an increased destruction or a decreased production of erythrocytes. The malarial parasite invades the erythrocytes and reproduces within them during one stage of its life cycle, during which considerable destruction of erythrocytes occurs. Infected individuals, however, are often anemic even when the parasite is no longer present in their erythrocytes, implying that erythrocyte production must also be abnormal in this case.

In healthy individuals erythrocytes live 120 days. Therefore 1/120th of the total circulating erythrocyte mass must be produced each day if a steady state is to be maintained. It can be calculated that about 1 to 2 million erythrocytes are made per second in a healthy individual. The regulation of this day-to-day production, as we have previously demonstrated, is achieved by the hormone erythropoietin, which is a glycoprotein produced in the kidney and other tissues. It appeared possible that the anemia in malaria infection might relate to inadequate erythropoietin production.

Similar malaria-like organisms also infect rodents, birds, reptiles, and amphibians. We have studied the effect of a number of different rodent malarias that mimic various clinical aspects of human malaria. Within a few days after infection with *Plasmodium berghei, P. vinckei, or P. chabaudi,* the blood erythrocytes contain the malarial parasite, a pronounced splenomegaly develops, and the animal becomes severely anemic. The severity of the disease and its mortality depend upon the infecting organism.

In collaboration with Paul Silverman and Lynn Mahlmann, we determined the serum concentration of erythropoietin during infection. In addition, we determined whether the serum erythropoietin levels were increased if a hypoxic exposure was imposed on the infected mouse. It is well-known that hypoxia stimulates erythropoietin production. These data have been presented elsewhere in this report, and we will only emphasize our conclusion that the anemia of malaria is not due to a lack of erythropoietin production. Indeed, the erythropoietin-generating tissues are apparently working maximally soon after the anemia is evident. These results suggested that the anemia might result from the failure of the infected animal to produce within its hematopoietic tissues the appropriate cell populations that respond to erythropoietin.

During the last 30 years a large body of experimental evidence indicates that all of the blood cells—the erythrocytes, platelets and various types of granulocytes and lymphocytes—are derived from a pluripotential "stem cell." This pluripotential cell, which is a slowly proliferating cell, gives rise to more rapidly proliferating progenitor cell populations that are unipotential or possibly bipotential. The agents regulating differentiation, such as erythropoietin, thrombopoietin, and CSF (the regulator of granulocyte production), interact with these unipotential precursor populations and produce the morphologically recognizable blood cells. The scheme of this hierarchical concept of the development of blood cells is shown in Fig. 2 of the preceding report by Silverman, Schooley and Mahlmann.

Consideration of this proposed scheme for the production and interrelationships of the various types of hematopoietic progenitor cells clearly indicates that the lack of mature blood cells of a particular cell line may result from numerous changes. For example, the humoral agents regulating the production of one cell line may stimulate the pluripotential progenitor to produce more of the direct precursor of this line, and therefore fewer CFU-S are available to produce the early progenitors of other cell lines, and marked increases in lymphocytopoiesis may inhibit the production of erythroid cell progenitors. As mentioned, our collaborative experiments indicate that the CFU-S population is

depressed in malaria-infected mice. We do not know as yet, however, whether these CFU-S are proliferating more rapidly than usual and producing increased numbers of the unipotential progenitor populations or whether the surviving CFU-S maintain their normal slow proliferative rate. Some preliminary observations suggest the former possibility is correct; that is, the CFU-S are proliferating more rapidly than in the normal mouse.

If a single-cell suspension is prepared of the spleen of mice made severely anemic by injections of phenylhydrazine—a drug that destroys mature red cells—and incubated with various concentrations of erythropoietin for 22 hours, the subsequent 2-hour uptake of ^{3}H-thymidine into cells synthesizing DNA is increased as shown in the upper curve of Fig. 1 (Control). A log-dose response to the hormone is observed. In contrast, if a spleen cell suspension is prepared from spleens taken from mice infected with malaria but with an anemia equivalent to that induced by phenylhydrazine injection, the addition of erythropoietin does not induce a significant increase in DNA synthesis. This suggests that erythropoietin-responding cells are decreased in the spleen of the malaria-infected mouse. Conditioned media (CM) from cultures of malaria-infected spleens or from cultures of normal spleens to which the malaria organism has been added are collected after 24 hours and the cells and parasites removed. These CM were then added to cultures of spleen cells obtained from phenylhydrazine-injected mice and the ability of Ep to induce DNA synthesis determined. The addition of both of these CM almost completely inhibited the action of erythropoietin on cells normally responsive to the hormone (bottom two curves of Fig. 1). Those erythropoietin-responsive cells that are induced to synthesize DNA by addition of erythropoietin are composed of BFU-E and CFU-E precursor populations of erythroid cells. We conclude that an inhibition of the early stages of erythropoiesis contributes to the dyserythropoiesis of malaria infection. The nature of this soluble hormonal agent is unknown, and its characterization forms the basis for future work. We believe that the unknown substance may be interleukin 1 (IL-1) since we know from other experiments that IL-1, a product of activated macrophages, and interleukin 2 (IL-2), a product of T-lymphocytes, also inhibit the action of erythropoietin in this system. We therefore advance as a working hypothesis the scheme shown in Fig. 2 to account for our observations.

The malaria organism of the parasitized erythrocyte or its products interact with macrophages

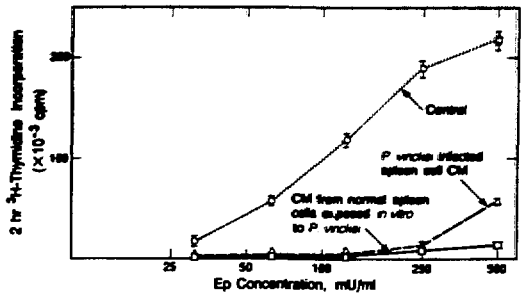

Fig. 1. Inhibition of the erythropoietin-induced stimulation of DNA synthesis of splenic cells, measured by the 2-hour incorporation of ^{3}H-thymidine, by conditioned media (CM) from cultures of normal spleen cells incubated with P. vinckei for 24 hours or cultures of spleen cells infected with P. vinckei.
(XBL 8510-8519)

inducing the production of IL-1. IL-1 stimulates T-cells to produce IL-2. IL-1 and IL-2 inhibit the action of erythropoietin on erythropoietin-responsive cells (BFU-E and CFU-E). Activated macrophages also produce tumor necrotic factor (TNF), and evidence indicates that TNF inhibits the development of adipocytes. Adipocytes of the

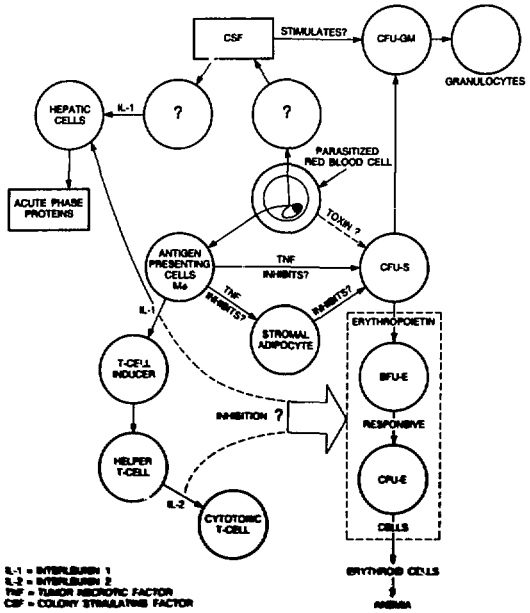

Fig. 2. Schematic presentation of the proposed role of IL-1 in the development of the dyserythropoiesis of malaria infection.
(XBL 859-8453A)

bone marrow stromal population are necessary for bone marrow growth and development, and their absence would inhibit ultimately the growth of erythroid cells. Experiments in collaboration with Paul Silverman are in progress to explore this aspect of the role of TNF in malaria. It is also possible that the malaria parasite generates some agent toxic to CFU-S. The malaria parasite may trigger some mononuclear cell to produce CSF via an endotoxin-like action, and this increased CSF may also stimulate macrophages and other cells to produce IL-1. We have found that CSF is markedly increased in the serum of mice infected with malaria. Lastly, IL-1 stimulates hepatic cells and initiates the acute-phase response.

The acute-phase response is a systemic reaction to inflammation or tissue injury that is characterized by complex changes that include fever, increase in white blood cells, increased breakdown of muscle, altered carbohydrate and trace metal metabolism, and a pronounced change in hepatic protein synthesis. The hepatic production of some blood proteins is increased, and the production of others is decreased. Humans with malaria infection often have some of these acute-phase responses; however, a more thorough study of the kinetics of these changes during experimental malaria infection is desirable. Evidence has been accumulating that these changes in hepatic protein synthesis are mediated by IL-1.

Very recent work indicating that IL-1 can stimulate hepatic cells pretranslationally to increase the production of acute-phase proteins (serum amyloid A, etc.) and inhibit albumin synthesis. Thus, the possibility that IL-1 directly inhibits erythropoiesis appears reasonable. Whether IL-1 inhibits erythropoietin-receptor synthesis or the synthesis of some key protein of the earliest proteins involved in erythroid differentiation or masks the erythropoietin-receptor is the subject of future work. This preliminary work provides some exciting insights into possible mechanism responsible for the anemia of malaria. The possibility that IL-1 and/or IL-2 may be involved in other diseases that exhibit an elevated serum level of erythropoietin with an anemia, such as aplastic anemia, opens some very exciting new approaches to investigate.

SEEDING OF SINGLE HEMOPOIETIC STEM CELLS AND SELF RENEWAL OF COMMITTED STEM CELLS

George Brecher

The fate of transfused bone marrow cells can now be followed more readily and in greater detail than with the older cytogenetic method. This is due to the availability of a subline of CBA mice with two alloenzymes of phosphoglycerate kinase (PGK A and B). By using mice that have only the A enzyme as donors in B hosts (or vice versa), cells of donor origin can be identified in the recipient. Because PGK is present in the cytoplasm of all body cells, one can determine the percentages of cells of donor origin in red cells, white cells, and platelets of the peripheral blood. (The cytogenetic method could only identify the donor origin of dividing cells in the marrow.)

The new methodology is available in our laboratory thanks to a Director's grant in 1981 that enabled us to obtain the new strain of mice and to acquire the necessary experience in the electrophoretic quantitation of the enzymes. Recently we have used the new methodology to explore the question of clonal succession, an unsolved problem of stem-cell kinetics. There is extensive evidence that the cell in transfused marrow that seeds in the recipient and is responsible for repopulation of an irradiated marrow is a pluripotential stem cell. However, the initial steps of the development of stem cells committed to production of a single cell line, e.g., red blood cells, is not known. When a pluripotential stem cell divides and produces two daughter cells committed to a single cell line, it necessarily loses its ability to function as a pluripotential stem cell. It is possible that a pluripotential stem cell may undergo an asymmetric division and produce one pluripotential stem cell to replace itself and one committed stem cell, thus maintaining a stable number of pluripotential stem cells. It has been argued that this type of differentiation would require an excess number of divisions and that each pluripotential stem cell divides symmetrically, producing a clone of mature cells. Having

done so, it must be replaced by a new pluripotential stem cell, hence the notion of clonal succession.

In collaboration with H.S. Micklem of the University of Edinburgh, we have succeeded in transfusing both single cells and two to five proliferating cells into animals whose own stem cells had been killed by irradiation. The PGK enzyme is sex linked. Hence female mice heterozygous for PGK A and B contain either A or B enzymes in any individual cell. When we gave a small inoculum of 50,000 AB marrow cells, only 4 of 20 recipients survived, but all 4 had only PGK A enzyme in their peripheral blood cells. (The fact that the single enzyme in the host was A is explained by the normal ratio of PGKA/PGKB in CBA mice being 70:30. A single cell seeding is thus much more likely to be A than B.) The results indicate that the survivors received a single pluripotential stem cell capable of proliferating. The chances of two or three cell seedings all being A (or B) can be shown to be less than 10%. The loss of 16 out of 20 animals that received 50,000 cells confirms that the average of cells seeded and proliferating was 1 or fewer, resulting in a high proportion of recipients receiving no pluripotential stem cells. The survivors among the recipients of 50,000-cell inocula have now been observed for many months and show no deterioriation in their blood picture. It must be concluded that there is no clonal succession in the simple form originally proposed. At a minimum, the single stem cell must have laid down a reservoir of pluripotential stem cells before losing its capacity for self-renewal through differentiation and maturation.

After transfusion of 100.000 AB marrow cells, all of 20 lethally irradiated recipients survived. There were two animals with only PGK A enzyme in the peripheral blood cells, suggesting that the average number of seeded stem cells was about two, when the expectation of all seeded cells being A is of the order of 10%. There was a striking variation between animals in the ratios of A:B enzymes in the RBC and platelets of the recipients of 100,000 cells compared with the similarity of the ratios after 10,000,000 cells were given (Fig. 1.) In addition, the A/B ratios of red blood cells and platelets differed more markedly over time in the recipients of 100,000 cells than in those that had been given 10,000,000 cells. Similar observations have been made on the A/B ratios of granulocytes as well as T and B lymphocytes by Micklem. The

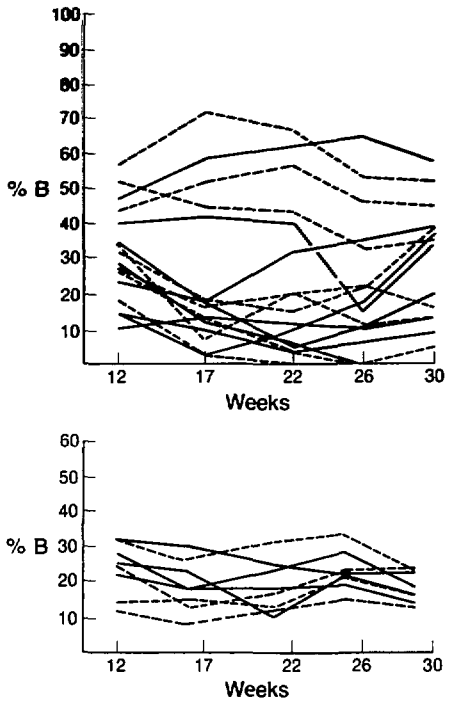

Fig. 1. Percent of B enzyme in the red blood cells (_____) and platelets (------) following transfusions of AB marrow cells. Note the great variation among curves following transfusions of 100,000 cells (upper graph) compared with the marked similarity among curves following transfusions of 10,000,000 cells (lower graph). *(XBL 8511-8582)*

most likely explanation for this observation is the production of committed stem cells that have significant self-renewal. The alternative, that pluripotential stem cells produce committed stem cells of different lineages at different rates and that these rates vary appreciably over time appears unlikely. Apart from the complexity of such a scheme, it should be recalled that many of the animals that received 100,000 cells started out with only two pluripotential stem cells and that there is evidence that the A:B ratio of pluripotential stem cells is maintained during self-renewal.

The findings are of interest, because continued self-renewal of committed stem cells has not been demonstrated previously. The implications for our views of stem cell kinetics are being studied.

CHARACTERIZATION OF ANTISERA TO ERYTHROPOIETIN AND IMMUNOLOGICAL DIFFERENCES BETWEEN ^{125}I LABELED HUMAN URINARY AND RECOMBINANT ERYTHROPOIETIN

Gisela K. Clemons

The maintenance of a normal number of circulating red blood cells and hemoglobin that is optimal for oxygen transport to body tissues is dependent on the hormone erythropoietin (Ep). Erythropoietin assays comprise bioassays that measure the hormone effect in the whole animal or the *in-vitro* action on tissues or whole cells and radioimmunoassays (RIA) that determine the interactions with antibodies raised against the hormone. The advantage of the bioassay in the whole animal is that it measures the biological activity of the hormone. However, these assays usually have a low sensitivity. The sensitivity of bioassays has been improved recently thanks to the introduction of *in-vitro* methods. These use signals generated by erythropoietin in whole cells, such as fetal mouse liver cells or spleen and bone marrow cells derived from phenylhydrazine-treated mice and rabbits. While these assays have the sensitivity required, they are still subject to effects of nonspecific factors in serum, plasma, or crude Ep, a feature of all bioassays from which the RIA appears to be free.

The essential requirements for the development of a radioimmunoassay are specific antibodies to the hormone, the availability of the pure hormone for labeling, a standard reference preparation, and a technique to separate the antibody-bound and nonantibody-bound hormone after a given incubation period.

The first requirement is the preparation of antisera to Ep that are sensitive and specific for this purpose. In order for a polyclonal antiserum to be useful, it must be specific for the hormone of interest and have a reasonable titer, i.e., a high dilution at which the labeled antigen binds such that antibodies to other substances cause no interference. The biological and immunological properties of some antisera are shown in Table 1. These antisera were obtained by immunization with crude urinary Ep extract with an activity [in units (U)] of 20 U/mg protein. Boosters were either the same preparation or purified Ep with activities of either 8,000 or 29,000 U/mg. For the initial immunization, each rabbit received 200 U Ep, and booster shots were given at 100 U per animal.

The neutralizing capacities of these antisera were tested in the polycythemic mouse assay, and they appear to be proportional to the purity of the antigen used for immunization, ranging from 25 U/ml with only crude human urinary erythropoietin (HUE) to greater than 1,000 U/ml with highly purified Ep. However, this cannot be generalized because Rabbit #139 was also a contributor to Pool I, and the neutralizing capacity of Pool I may be lower because it was diluted with antisera from other rabbits not having this high quality. No correlation was found between the purity of the antigen used, the neutralizing capacity *in vivo*, and the possible use for binding of ^{125}I-Ep in an immunological assay. But in order for an antiserum to be useful for the development of an RIA, it apparently has to have some neutralizing capability, as tested in the *in-vivo* assay, because we have found that nonneutralizing antisera do not bind labeled Ep.

Based on titration curves, a radioimmunoassay is dependent upon the competition between labeled and unlabeled antigen for binding sites on

Table 1. Biological and immunological properties of erythropoietin antisera.

Specific activity of antigen used for immunization (U/mg)	Boosters (U/mg)	I.D.	Neutralizing capability *in vivo* (U/ml)	Final dilution to bind 40% ^{125}I-Ep
20	20	Pool I	25	1: 5,000
20	8,000	139-18	300	1: 50,000
20	29,000	313-6-30	500	1: 50,000
20	29,000	318-6-30	600	1: 50,000
20	29,000	233-6-30	700	1: 50,000
20	29,000	314-6-30	1,000	1: 40,000

the antibodies. Dilutions of antisera were chosen to bind 40% of the label. Use of excess antibody results in loss of sensitivity because all binding sites must be occupied before unlabeled Ep can compete with the tracer. The suitability and sensitivity of each antiserum for radioimmunoassay use was determined at three dose levels of unlabeled human, rat, mouse, and sheep Ep (Fig. 1). This RIA established that only two of the antisera tested had any significant competition between labeled and unlabeled Ep, AS 139-18, and Pool I. In addition, these two antisera also neutralize Ep's from several species.

Some competition could be obtained at the highest dose of human Ep (100 mU/ml) using two antisera made with highly purified antigen, but the possible "sensitivity" of the assays would lie considerably above that of the polycythemic mouse assay, and very little, if any, competition with animal Ep's could be established. Since only antisera with the steepest slopes are suitable for sensitive assays, it appears from these data that for obtaining good polyclonal antisera for radioimmunoassay purposes the use of highly purified erythropoietin does not seem to be necessary, and may be even undesirable.

The second requirement for the radioimmunoassay is the availability of the hormone in the pure form and its ability to accept a radioactive label. Erythropoietin was purified to a specific activity of 70,000 U/mg in Dr. Eugene Goldwasser's laboratory, and he made some of it available for distribution through the National Institutes of Health. This material was obtained from urine of anemic patients. Recently two other pure Ep preparations have become available for labeling. One was also purified from human urine by Dr. Gerald Krystal (Terry Fox Laboratory, Vancouver,

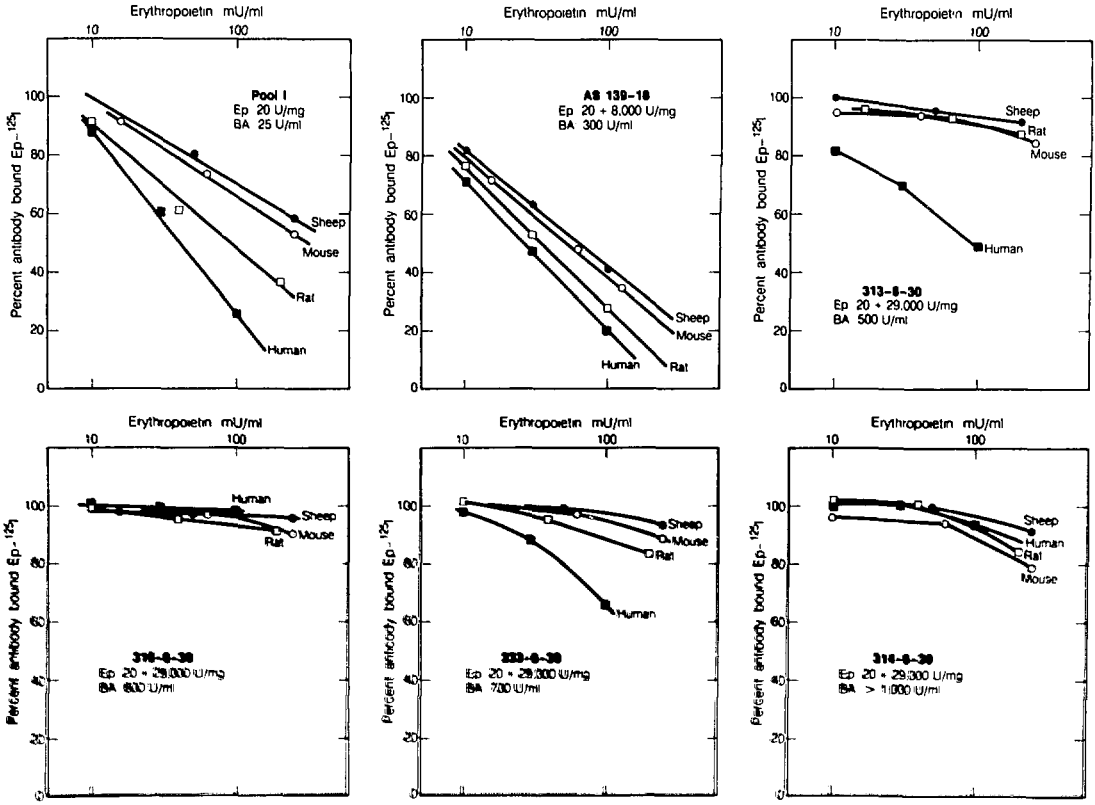

Fig. 1. Suitability and Crossreactivity of labeled and unlabeled erythropoietin with various antisera.

(KBL 854-9961)

Canada), and the other is recombinant Ep distributed by Amgen Company, Thousand Oaks, California.

The three preparations were iodinated in our laboratory, using an identical procedure for all, and the labels were tested in the RIA as described by the late Joseph Garcia (LBL). The specific activities of the labeled erythropoietins were comparable (Table 2). Four standard curves of each, human and mouse Ep, and internal standards were tested in quadruplicate. The second International Reference Preparation for human Ep was obtained from the National Institute of Biological Standards, Mill Hill, England, and the mouse standard was a previously bioassayed serum preparation from animals exposed to 24 hours of hypoxia. As can be seen from Table 2, the highest binding to the antibody was obtained with Goldwasser's Ep, and the bindings for the other two preparations were significantly lower. As can be seen from Fig. 2 there was no immunological difference between the two labeled Ep's that were purified from urine (G and K). However, the label obtained with A-Ep differed such that it appears to have a slightly higher affinity to the antibody than the respective unlabeled standard preparations. This resulted in a shift of the curves to the right and reduced the sensitivity slightly. However, the determinations of the internal standards for each species of immunoreactive Ep were comparable among all three labeled preparations.

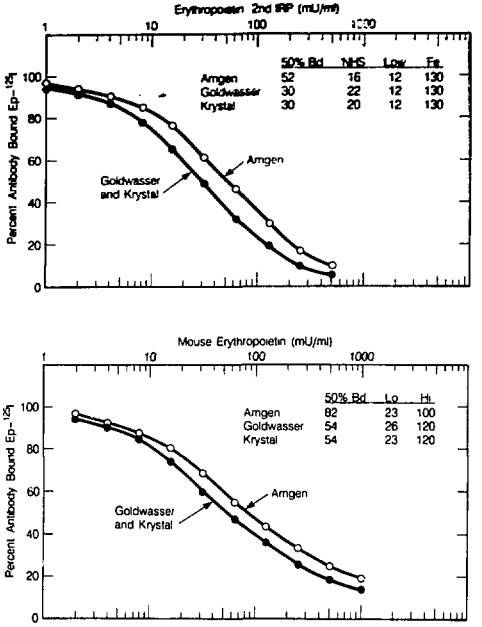

Fig. 2. Differences between recombinant (A) and human urinary erythropoietin (G and K). *(XBL 855-8294A)*

Table 2. Comparison of RIA quality controls using three highly purified Ep preparations.

	G[a]	K[a]	A[a]
Specific activity of ^{125}I-Ep (μCi/μg)	195	170	200
Total binding to antibody (%)	35	21	22
50% Total Binding (mU/ml):			
Human	30	30	52
Mouse	54	54	82
Internal Standards (mU/ml):			
Human:			
Normal human serum pool	22	20	16
Anephric pool	12	12	12
Iron-deficient pool	130	130	130
Mouse:			
Low pool	26	23	23
High pool	120	120	120
Total binding after heat treatment (%)	NT[b]	32	52

[a] G = Goldwasser, K = Krystal, A = Amgen
[b] NT = not tested

We then compared the effect of heat treatment on human urinary and recombinant Ep. Two fractions from the immunologically active ^{125}I-Ep peak of A-Ep and K-Ep were pooled each, acidified to pH 5.5, boiled 5 minutes, the pH readjusted and the labels repurified. Both preparations were tested in the RIA under conditions identical to those before. Heat treatment had two significant effects: The total binding to the antibody for both labels increased significantly, and the immunological differences observed between the two urine-derived Ep's and the recombinant Ep had disappeared and the standard curves were superimposable. The higher binding can be utilized to increase the sensitivity of the RIA further by being able to use the antiserum at a higher dilution than previously.

So far we have not been able to detect an immunological difference between renal (or plasma) and urine-derived Ep either in the human or in other mammalian species. This comparison of uri-

nary and recombinant Ep is the first instance in which the antiserum does discriminate between preparations. Since it has been established that the amino acid sequence in both the urinary and recombinant Ep is identical, the difference observed has to lie in the carbohydrate moiety. It is not presently known whether the degree of glycosylation in recombinant Ep is identical to native Ep, but brief boiling appears to unmask the immunologically reactive site(s).

PERIPHERAL CHANGES OF THYROID HORMONE BINDING TO SERUM PROTEINS AFTER SHORT TERM OZONE EXPOSURE

Sherry L. Fitzsimmons and Gisela K. Clemons

Previous studies have shown a profound decrease in the levels of circulating thyroxine (T4), triiodothyronine (T3), and thyroid stimulating hormone (TSH) in serum of rats exposed to relatively low levels of ozone for a short period (1 ppm × 24 hr). This decrease is thought to represent an alteration of the hypothalamic set point that regulates thyroid hormone homeostasis at the level of the central nervous system.

Ozone is an environmental pollutant, a product of photochemical smog, that causes pulmonary injury and edema. It was found that high levels of thyroxine administered to rats potentiates the toxic effects of ozone, thus decreasing their survival. Thyroidectomized rats, however, are less susceptible to ozone toxicity. Therefore, this reduction of thyroid hormone levels in the normal animal measured after ozone exposure may be be an adaptive mechanism of the organism. Previous studies have suggested that ozone induces a total suppression of the hypothalamic-pituitary-thyroid axis by lowering the set point at the level of the central nervous system. However, this can only partially explain the reduction of thyroid hormone levels since rats administered exogenous T4 also showed a reduction in their circulating levels after short-term ozone exposure. Inhalation of ozone appears to also induce peripheral changes in serum that lead to the reduction of measurable thyroid hormone levels.

Most of the circulating thyroid hormones in the blood are bound to binding proteins. A very small fraction of thyroxine (T4), which represents also the metabolically active hormone, remains in the unbound or free state (0.025%). This free hormone is available for peripheral deiodination into triiodothyronine (T3), the biologically more potent of the thyroid hormones. The binding of T4 to serum binding proteins serves to maintain a large reservoir of readily available hormone and to prevent the otherwise rapid excretion of this small hormone. In both humans and rats, there exist several binding proteins that are characterized by different affinities and binding capacities for T4. In humans, 75% of T4 is bound with a very high affinity and specificity to thyroid binding globulin (TBG), 15% of circulating T4 is bound less tightly to thyroxine binding pre-albumin (TBPA), and the remaining T4 is bound with a low specific activity to the abundant protein, albumin. In the rat the majority of the circulating T4 is bound quite specifically to TBPA, with less than 10% bound to a TBG-like protein.

These three binding proteins can be separated on the basis of their size and electrophoretic mobility using native polyacrylamide gel electrophoresis. Serum samples were incubated with a tracer quantity of ^{125}I-T4 and electrophoresed overnight, and the resultant dried gels were later autoradiographed. The autoradiogram revealed three radioactive regions corresponding to the three T4 binding proteins. Since the majority of the T4 is bound to TBPA in the rat, we determined the binding characteristics of this protein and any alterations induced by short-term ozone exposure.

The binding constants of TBPA can be determined using polyacrylamide gel electrophoresis. Varying concentrations of unlabeled T4 were incubated with serum samples containing tracer quantities of labeled hormone in order to compete for the binding sites on the TBPA molecules. From the experimental data and a Scatchard plot the binding constants were determined. The affinity of TBPA for T4 is given by the slope of the line, while the binding capacity of TBPA corresponds to the x-intercept. Since ozone is capable of oxidizing various side chain residues of amino acids, and it has been shown to have denaturing effects on albumin and tyrosine *in vitro*, it was hypothesized that an alteration in the binding affinity of TBPA for T4

could lead to an early disappearance of the hormone from the circulation.

Control and experimental animals were housed in identical chambers for the duration of the experiments. The experimental animals were exposed to 1 ppm ozone for 24 hours, while the control animals received normal air. Serum from each group was collected and incubated with appropriate quantities of labeled and unlabeled hormone. All samples were electrophoresed under identical conditions using a slab gel apparatus and were later autoradiographed. Examination of the autoradiogram showed that the binding of T4 by rat TBG had been abolished after short-term ozone exposure, since the labeled hormone migrated only in two bands (Fig. 1). The Scatchard analysis for both sera is shown in Fig. 2. The affinity of TBPA for T4 is given by the slope of the line. There does not appear to be a significant difference in the affinity

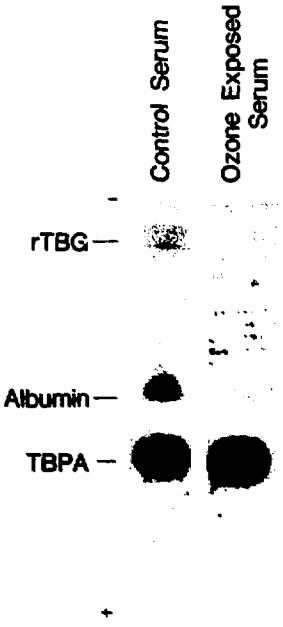

Fig. 1. Effect of short term ozone exposure on the binding of T4 to serum binding proteins. 5 µl of serum from normal air (left) and ozone exposed (right) were electrophoresed for 18 hours after a 2-hour incubation with ^{125}I-thyroxine.

(XBB 850-9234)

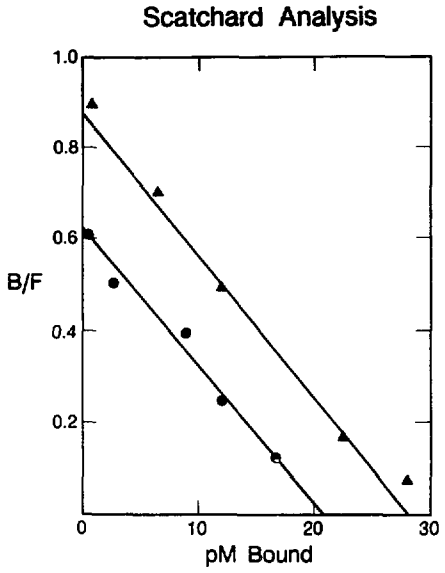

Fig. 2. Scatchard plot of ^{125}I-thyroxine binding to thyroxine binding prealbumin (TBPA). • = rat exposed to normal air and Δ = rats exposed to 1 ppm × 24 hours ozone. Bound and free T4 were separated using polyacrylamide 8% gel electrophoresis. Values have been corrected for nonspecific binding.

(XBL 8510-8547)

of TBPA for T4 as a result of short-term ozone exposure. The apparent affinity constant for this protein in the presence or absence of ozone is 3.5 × 10^8 M, which denotes a high degree of specificity for the hormone. Although the affinity of TBPA does not seem to be reduced in those animals previously exposed to ozone, there is a significant increase in the binding capacity of TBPA in these animals as represented by the x-axis intercept in the Scatchard plot. This suggests an increase in the number of unoccupied binding sites. This could be either the result of increased levels of circulating TBPA, or the previously bound T4 was being removed from the circulation as the result of ozone exposure, creating more available binding sites. The latter seems to be the more plausible explanation since the 30% increase in the binding capacity corresponds to the decreased levels of the circulating T4 leveis observed in animals after short-term exposure to ozone.

BIOLOGICAL EFFECTS OF MAGNETIC FIELDS

Thomas S. Tenforde, Cornelius T. Gaffey, Robert P. Liburdy, and Lynette Levy

High-intensity magnetic fields are used in several newly developing energy technologies (fusion reactors, magnetohydrodynamic generators, superconducting magnetic energy storage rings), research facilities (accelerators, bubble chambers, superconducting spectrometers), industrial operations (chemical separation processes, electrosteel production), and medicine (nuclear magnetic resonance imaging and *in vivo* spectroscopy). Because of the increasing number of applications of strong magnetic fields, a program is being carried out to evaluate the potential health effects of this form of nonionizing radiation. Both laboratory animals and selected cellular and tissue systems are being used to detect alterations in physiological functions during acute and chronic exposures to high-intensity magnetic fields. The initial work in this program involved studies with stationary magnetic fields produced by electromagnets at intensities up to 2 tesla (1 T = 10^4 gauss). During the past year, a new superconducting magnet was installed that is capable of producing fields up to 9 T for biological research with cells, tissues and small mammals. These investigations will provide essential data for assessing the potential health effects associated with the use of ultrahigh magnetic fields (in the 2 to 10 T range) in medical applications of nuclear magnetic resonance.

ELECTROPHYSIOLOGICAL MEASUREMENTS

A major area of research in this program has been the use of sensitive electrical recording techniques to detect functional alterations in the cardiovascular, neural, and visual systems during exposure to high-intensity magnetic fields. The physiological functions of these systems involve ionic conduction processes that are potentially sensitive to electrodynamic interactions with large stationary magnetic fields. Our investigations in this research area include 1) the use of noninvasive radiotelemetry to monitor cardiac electrical activity during the chronic exposure of rats to a 1.5-T stationary magnetic field, 2) study of blood flow characteristics in rats and dogs during exposure to magnetic field intensities that exceed the threshold for producing measurable magnetohydrodynamic effects, 3) recording the bioelectric activity of isolated neurons and the central nervous system during exposure to field intensities up to 1.5 T, and 4) measurement of the photically-elicited electrical responses of the retina in cats and monkeys during exposure to fields of graded intensity up to 1.5 T. During the past year, data acquisition was completed in the fourth of these research areas, and the experimental results will be described briefly in this report.

The influence of strong magnetic fields on visual phototransduction was studied by using corneal contact electrodes to record the transient electrical signals that originate in the retina following photon absorption. This electrical activity, known as the electroretinogram (ERG), consists of two prominent signals of opposite polarity. The first of these signals, the A wave, is a brief negative potential. The second major signal in the ERG is a large positive potential, the B wave, which has a duration in excess of 100 msec. The relative magnitudes and durations of the A and B waves are shown in the top ERG trace in Fig. 1, which was

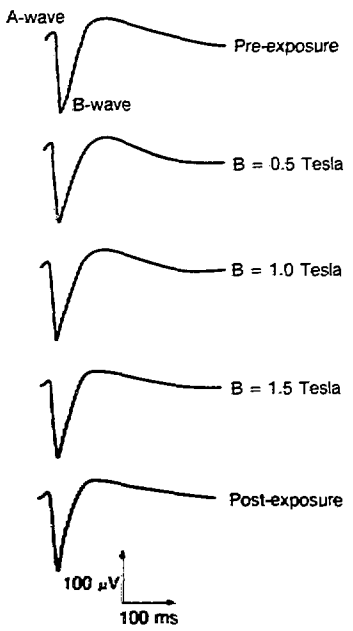

Fig. 1. *Electroretinogram traces recorded in vivo from a cat during exposure to stationary magnetic fields with graded intensities up to 1.5 T. The magnitudes and durations of the A-wave and B-wave signals were unaffected by exposure to the field.*
(XBL 8510-8549)

recorded *in vivo* from a cat's eye subjected to a short pulse of white light following a 30-min dark adaptation period. Although the origins of the eye's electrical activity have not been determined previously, experiments with intracellular microelectrodes indicate that the A wave originates from the outer segments of the photoreceptor cells and the B wave from the synaptic region of the bipolar cells.

A total of three monkeys (*Macaca*) and six cats (*Felis domestica*) were used for visual response studies during exposure to stationary magnetic fields with graded intensities up to 1.5 T. After dark adaptation, the ERG was recorded following 10-μsec white light flashes with relative intensities of 1, 4, 16, 48, and 80, where the highest intensity flash was 240 lumen/m^2/sec. As demonstrated by the ERG data presented in Fig. 1 for a cat, there was no measurable change in either the A or B wave signals of the nine animals studied during exposure to fields up to 1.5 T. Ophthalmic examinations of all the subjects and electrical measurements of flicker-fusion frequencies in five animals also indicated no effects of the magnetic field exposure.

ANIMAL PHYSIOLOGY AND CIRCADIAN REGULATION

Noninvasive techniques have been used for the continuous monitoring of physiological and behavioral variables in rodents exposed to a 1.5-T stationary magnetic field. The parameters being measured include heart rate, core body temperature, respiration, nutrient consumption, body mass, excreta, and locomotor activity. The circadian waveforms of these variables are sensitive indicators of stress, and they were therefore studied to detect physiological and behavioral alterations in rodents exposed to a 1.5-T field for periods up to 10 days.

One set of three experiments completed during the past year utilized an exposure chamber and physiological monitoring systems designed and fabricated at LBL for the simultaneous recording of seven circadian variables. A schematic diagram of the exposure chamber and transducers is shown in Fig. 2. Groups of 40 female LAF-1 mice were housed in an aluminum cage with a floor area of 0.37 m^2 that was placed within the homogeneous field region of an electromagnet operated at 1.5 T. The cage was supplied with uniform lighting at an intensity of 155 cd/m^2, and a steady flow of conditioned air at a temperature of 22.0 ± 0.5°C and a relative humidity of 50% ± 10%. Six strain gage monitors provided continuous data on the following parameters: 1) total body mass, 2) center-of-mass coordinates of the entire rodent population as an index of migratory locomotor activity, and 3) climbing activity registered on an exercise bar. Respiratory rate was assessed by infrared measurements of the carbon dioxide content of air emerging from the cage outlet port. The rodents were fed a complete nutrient diet in liquid form on an *ad lib* basis, and their nutrient consumption was measured volumetrically. Urine and feces excretion were monitored gravimetrically from the contents of a collecting tray located below the honeycomb aluminum floor of the exposure chamber. A wire mesh covering the excreta collecting tray was used to separate the feces and urine, and the urine samples were preserved in a frozen state for subsequent chemical analysis. Data from the various transducers and environmental monitoring devices were recorded continuously on magnetic tape at 5-min intervals throughout experiments of 50 to 60 days duration, and the circadian waveforms of physiological and behavioral parameters were analyzed using a CDC 7600 computer.

Figure 3 shows the circadian waveforms in respired carbon dioxide, body mass, and two measures of activity based on the weight applied to a triangular exercise bar and the time rate of change of the center-of-mass coordinates of the rodent population. Circadian waveforms with large amplitudes were also measured for nutrient consumption and urine and fecal excreta. The data shown in Fig. 3 were continuously recorded at 5-min intervals during five serial days. The animals were maintained in a free-running circadian state throughout this period by imposing constant dim illumination. Various mathematical models of circadian oscillations have been used to generate best-fit curves for these data using a least-squares analysis. For the smoothly varying circadian parameters such as respired carbon dioxide and body mass, a cosine function provides an optimal fit based on the criterion of minimizing the sum of the squares of residuals between the measured data and the best-fit curve. For circadian variables with superimposed stochastic fluctuations, e.g., the two measures of locomotor activity shown in panels (C) and (D) of Fig. 3, alternate models such as a piecewise-linear approximation provide a fit of the data that is equally as good as the conventional cosine analysis procedure. The smooth curves shown in Fig. 3 represent the best-fit cosine functions for the four circadian variables, along with the 95% confidence intervals. It is evident from the parameters of the best-fit curves that in the free-running circadian state, i.e., in the absence of external time cues, the periods of the circadian waveforms in physiological

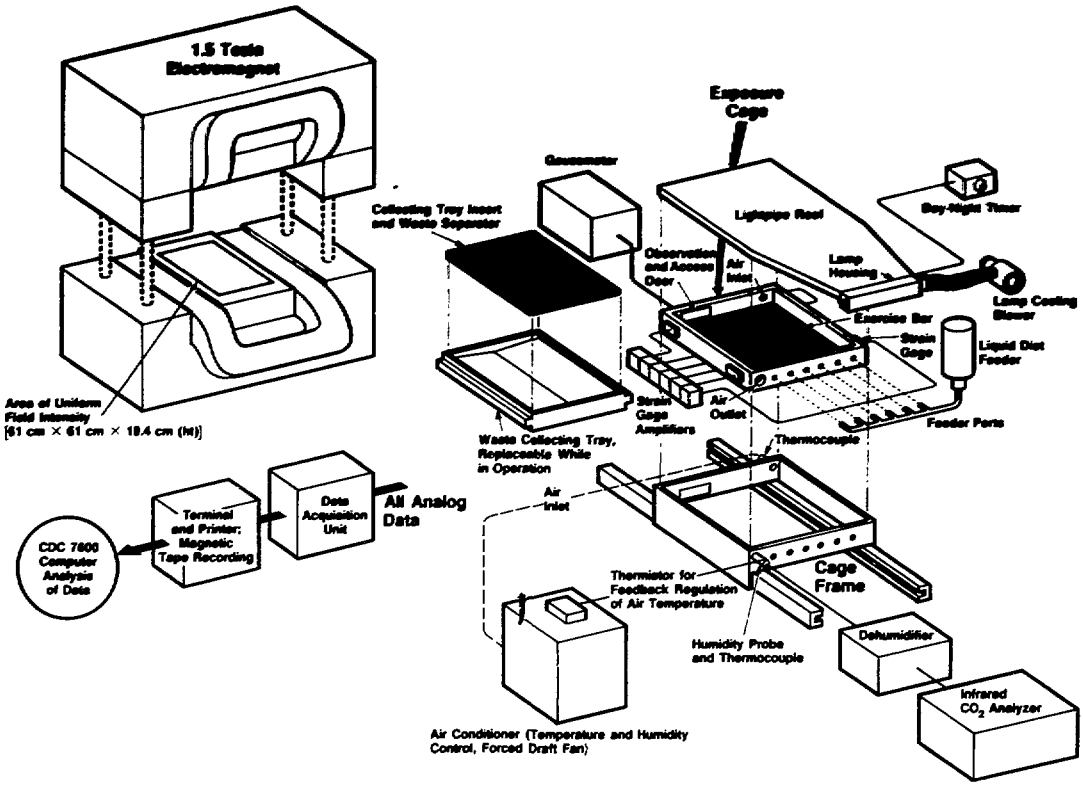

Fig. 2. Schematic diagram of the exposure chamber, transducer system, and environmental monitors used in experiments to detect magnetic field effects on physiological and behavioral variables in mice. (XBL 849-7946)

and behavioral variables range from approximately 25 to 26 hours. When a strong time cue such as a daily light/dark schedule is imposed, these circadian variables become entrained within 5 to 10 days and exhibit periods close to 24 hours.

In the first two long-term experiments designed to test for physiological and behavioral effects of a 1.5-T stationary magnetic field, the seven circadian variables under study were measured noninvasively for a continuous two-month period throughout which the rodent population was maintained in an entrained state by an imposed 12-hr-light/12-hr-dark diurnal cycle. Following a pre-exposure control period, the field was applied either continuously for 5 days or intermittently in an 8-hr-on/16-hr-off daily cycle for 10 consecutive days. The circadian variables were continuously monitored before, during, and after each application of the magnetic field. In the third long-term experiment, rodents were maintained in a free-running circadian state by imposing constant dim illumination in the exposure chamber. Circadian waveforms were measured before, during, and after the application of a 1.5-T field for 10 consecutive days in a 8-hr-on/16-hr-off diurnal cycle. As a positive test for entrainment, the rodents were then subjected to a daily 8-hr-dark/16-hr-light cycle for 20 consecutive days. Both parametric and nonparametric analyses of the extensive data obtained in these three experiments indicated that exposure to a high-intensity magnetic field had no effect on the circadian waveforms of the seven simultaneously measured physiological and behavioral variables. In addition, no entraining influence of the field was observed when the animals were maintained in a free-running circadian state during the third experiment. An imposed diurnal light/dark cycle was found, however, to produce a rapid entrainment of

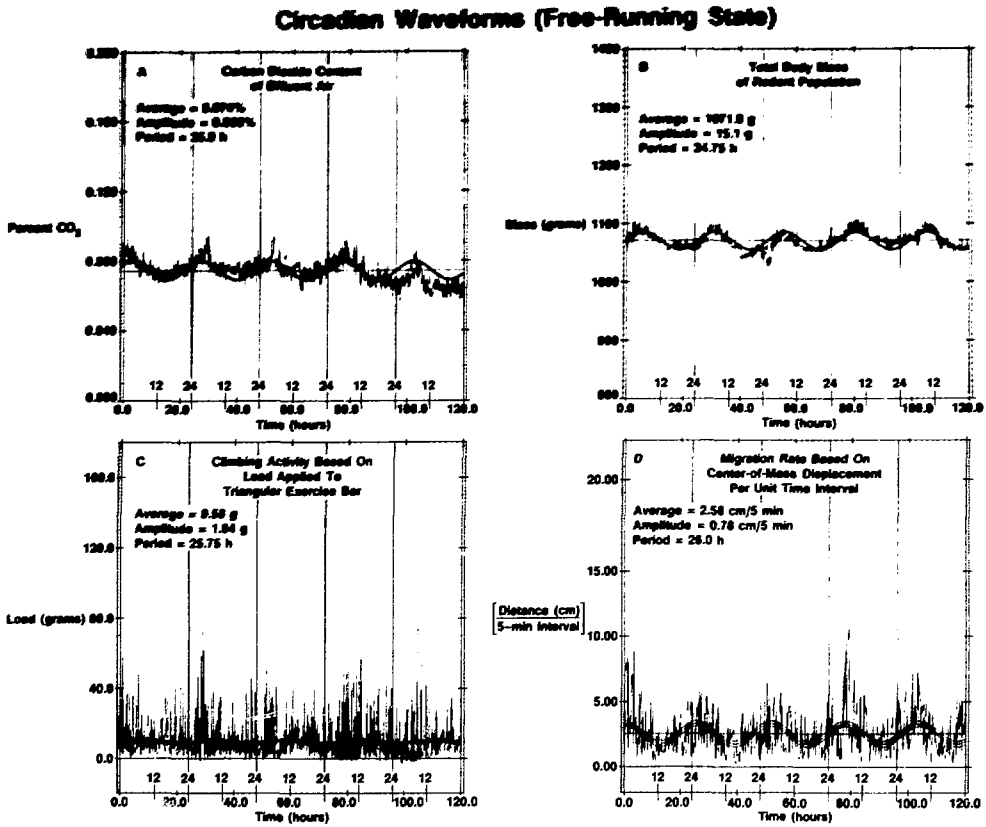

Fig. 3. Circadian waveforms in respired carbon dioxide, body mass, and two independent measures of locomotor activity measured for a population of 40 female LAF-1 mice. The mice were maintained in a free-running circadian state by imposing constant dim illumination in the exposure chamber shown in Fig. 2. The three smooth curves superimposed on each set of circadian data represent a cosine function fit by a least-squares analysis technique, along with the upper and lower bounds of the 95% confidence interval. The amplitude and period of the best-fit cosine function are listed for each of the four circadian variables. *(XBL 848-7916)*

all the circadian variables under study. Our observation that no significant circadian alterations occur in response to a high-intensity stationary magnetic field is in distinct contrast to a large number of earlier publications which reported that physiological regulation and circadian timing in rodents and other animal species are influenced by relatively weak magnetic stimuli.

SUPERCONDUCTING MAGNET RESEARCH

A new 9-T superconducting magnet from Oxford Instruments, Ltd. was installed at LBL in the Fall of 1984. This magnet has a 7.25-cm bore suitable for biological studies of cellular and tissue specimens and small laboratory animals. Following installation, the magnet was subjected to detailed performance tests and field mapping using a nuclear magnetic resonance (NMR) probe, a search coil, and an axial Hall-effect probe. All three independent methods of field detection gave consistent results when compared at a field level of 7.5 T. As shown in panel (A) of Fig. 4, the stationary magnetic field in the central 20-cm region of the 73.6-cm long cylindrical bore is homogeneous, and large spatial gradients up to 60 T/m are present in the end regions of the bore. NMR measurements on a D_2O sample were performed in the central 6-cm region of the bore, and the field homogeneity in the middle of this region was found to be better

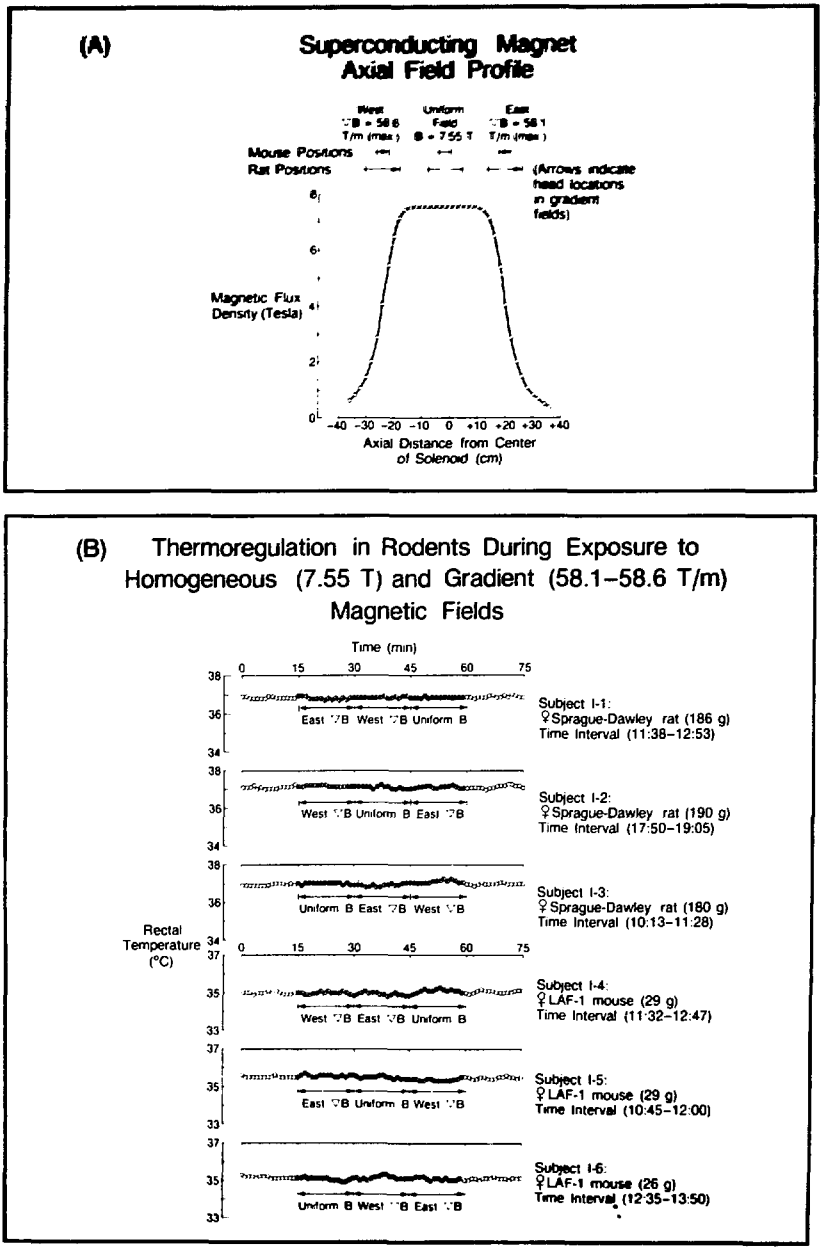

Fig. 4. (A) Magnetic field profile measured with a search coil along the central axis of the superconducting magnet being used for biological research. The positions of mice and rats in the uniform central field and in the ascending and descending gradient regions are shown by brackets. (B) Rectal temperatures recorded at 1-min intervals are shown for six rodents subjected to 45-min exposures to the uniform and gradient fields produced by the superconducting magnet. The exposures were preceded and followed by 15-min recordings of the rectal temperature in the absence of a magnetic field. (XBL 856-8362)

than one part in 75,000. Following the completion of this detailed field characterization, biological experiments were initiated to study the effects of ultrahigh magnetic fields on ionic conduction processes in the cardiac and nervous systems, on cyclosis in plant cells, on the thermoregulatory system of rodents, and on the structural and functional properties of artificial lipid membranes. Research results in the last two of these areas will be described in this report.

Two recent reports from Germany have indicated that thermoregulation in humans and in laboratory animals is significantly influenced by uniform magnetic fields and by strong spatial gradients of magnetic fields. Gremmel et al.[1] reported changes up to 5°C in human skin temperature studied by infrared thermography during exposure to stationary fields of 0.2 to 1.5 T intensity. Both increases and decreases in temperature were observed, and these results were qualitatively confirmed in laboratory studies with cats. Sperber et al.[2] subsequently reported similar changes in rodents exposed to stationary fields with intensities ranging from 0.4 to 8.0 T. In the strong magnetic field gradients near the end of a superconducting magnet bore, these investigators observed both increases and decreases in skin and rectal temperatures. The temperature changes were reported to begin within 5 min, and reached a maximum magnitude of approximately 2.4°C after 2 to 3 hours of exposure to a magnetic field. When the field was turned off, the skin and rectal temperatures slowly returned to their pre-exposure values within 2 hours. Sperber et al.[2] proposed that orientational effects of strong magnetic fields on biologically important macromolecules may be the basis for the apparent loss of thermoregulatory capacity observed in their experiments.

Because these results, if confirmed, would have major implications for the safety of NMR imaging with human subjects, an effort was made to reproduce the reported effects in rodents subjected to large uniform magnetic fields and high magnetic field spatial gradients. Both pigmented LAF-1 mice and albino Balb/c mice were used in these experiments, the latter strain being identical to the mice used by Sperber et al.[2] in their earlier experiments. In addition, albino Sprague-Dawley rats were used as test subjects in our experiments. The positions of the adult female mice and rats in the uniform field and the gradient fields are indicated in panel (A) of Fig. 4. The unanesthetized animals were placed with minimal restraint in lucite holders, and rectal temperatures were recorded with a nonmagnetic copper/constantan thermocouple coated with plastic.

Three series of experiments were carried out to determine whether the thermoregulatory capacity of rodents was influenced by high-intensity magnetic fields. In the first experiment, shown in panel (B) of Fig. 4, three Sprague-Dawley rats and three LAF-1 mice were exposed for consecutive 15 min intervals to the uniform central field and the ascending and descending gradient fields. The order of presentation of the uniform and gradient fields was randomized for the six animals. The interval of 15 min was longer than the time reported by Gremmel et al.[1] and Sperber et al.[2] to produce a measurable rectal or skin temperature change. An analysis of variance of the data obtained in these experiments showed that no statistically significant change occurred in rectal temperature in response to magnetic field exposure. This result was independent of the field uniformity or the time of day during which the exposures were made. Exposures to a strong magnetic field gradient for periods of 1 to 3 hours were also carried out with two Sprague-Dawley rats, two LAF-1 mice, and six Balb/c mice. The results of these experiments are presented in Fig. 5. An analysis of variance again showed no significant change in the rectal temperature of any of the ten rodents during the magnetic field exposure. This result was also independent of the time of day during which the animals were exposed to the field. These studies with a total of 16 animals clearly indicate the absence of effects of a high-intensity magnetic field on the thermoregulatory capacity of laboratory animals, in distinct contrast to the earlier results obtained by two other groups of investigators.

In another area of superconducting magnet research, the influence of ultrahigh magnetic fields on the structure and permeability properties of lipid membranes was studied using liposomes with a well defined molecular composition. Diamagnetically anisotropic assemblies of molecules such as membrane phospholipids experience an orientational torque in strong magnetic fields and adopt a spatial configuration that minimizes their free energy state in the field. For thin nematic liquid crystals, stationary fields in the range of 0.1 to 1.0 T have been shown to significantly alter the rate of solute transport as a consequence of magneto-orientation of the lipoidal constituents. In our experiments, 200-μm liposome vesicles bounded by a phospholipid bilayer containing saturated fatty acyl chains were used as test specimens. The dipalmitoylphosphatidyl choline (DPPC) moieties in

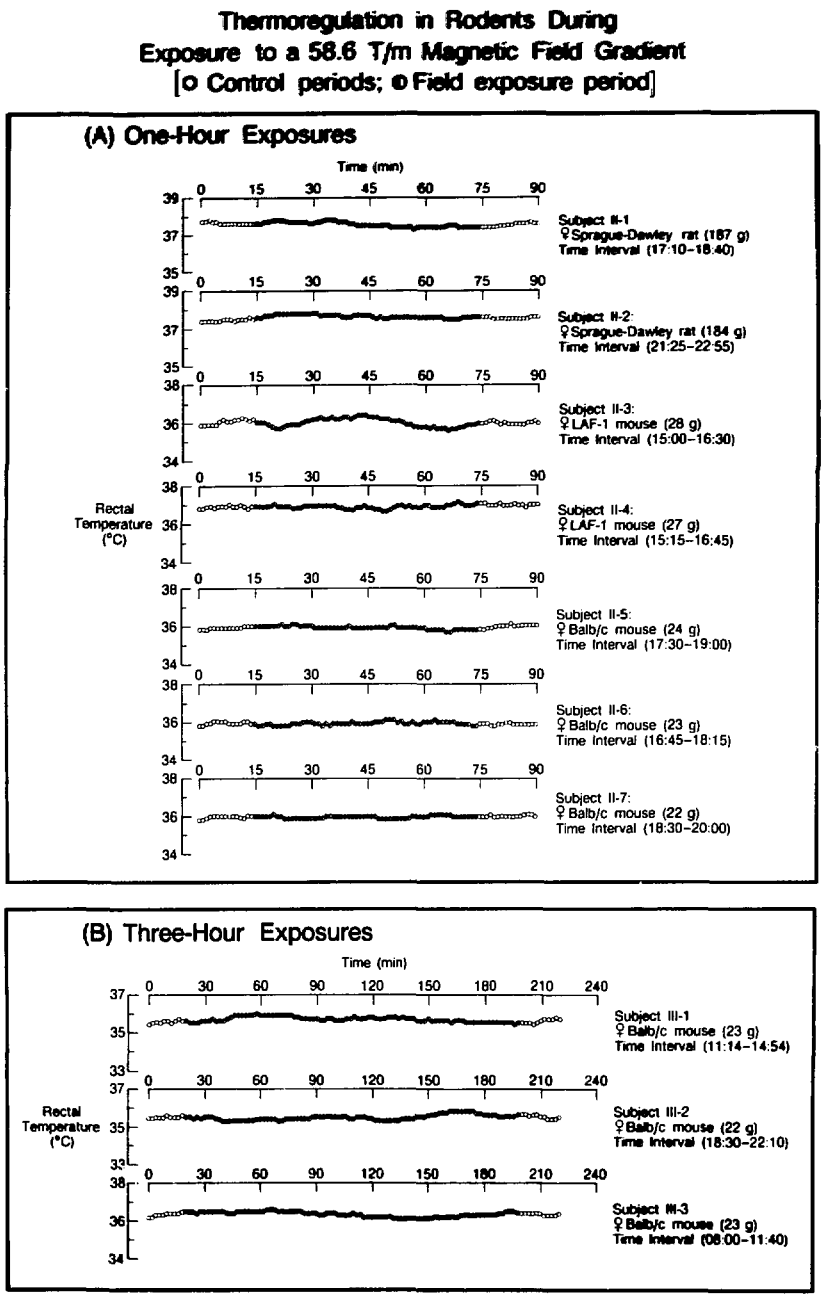

Fig. 5. (A) Rectal temperature recordings are shown for seven rodents exposed to a 58.6 T/m magnetic field gradient for 1 hr. The median field strength at the midpoint of the exposed subjects was 4.16 T. The continuous 1-hr exposure was preceded and followed by 15-min recordings of the rectal temperature in the absence of a magnetic field. (B) Rectal tempeature recordings are shown for three Balb/c mice exposed for 3 hr to a 58.6-T/m gradient field. ***(XBL 856-8363)***

the liposomal membranes were radiolabeled with ^{14}C, and the inner compartment of the vesicles contained ^{3}H-labeled cytosine arabinoside (^{3}H-ARA-C: M.W. = 243). The release of ^{3}H-ARA-C from these liposomes has recently been shown to be stimulated by 2450-MHz microwaves, as described by R.P. Liburdy in this annual report. In experiments with the new superconducting magnet, the release of ^{3}H-ARA-C and ^{14}C-DPPC was measured following exposures that ranged in duration from 1 min to 18 hr at graded field intensities from 0.001 to 7.5 T. At each field level, the release of trapped ^{3}H-ARA-C solute and ^{14}C-DPPC membrane phospholipids was determined over a temperature range of 4°C that bracketed the thermal phase transition which occurs at 40.5°C. The temperature of the liposome samples was maintained with an accuracy of 0.08°C at each of the specified temperatures over this range, and control samples were assayed for release of ^{3}H-ARA-C in parallel with the samples exposed to a magnetic field. At temperatures below 40°C and above 41°C, the release of ^{3}H-ARA-C solute was identical in the exposed and control liposome samples. However, in the pre-phase transition region from 40.0 to 40.5°C, an accelerated release of trapped solute was observed in samples exposed to stationary magnetic fields greater than 0.01 T. This magnetic field effect on liposome permeability is rapid, and a difference between the exposed and control liposome samples of 30% of the total maximal release of ^{3}H-ARA-C was observed within one minute. As shown in Fig. 6, exposures at field levels between 0.001 and 7.5 T revealed that this permeability effect has a sigmoidal dependence on the magnetic flux density. The 50% effect level is 0.015 T, with a 95% confidence interval of 0.0065 to 0.0349 T. Experiments were also conducted with liposomes exposed to magnetic fields produced by samarium-cobalt permanent magnets. As shown in Fig. 6, 0.40-T fields produced by the permanent magnets and the superconducting magnet produced a comparable release of ^{3}H-ARA-C at 40.5°C. The observed change in permeability to ^{3}H-ARA-C was also shown not to result from disruption of the liposomes, since there was no accelerated release of ^{14}C-DPPC from the liposome membranes at any of the magnetic field strengths that were used in these studies.

These liposome studies indicate that a stationary magnetic field of 0.015 T or greater can significantly increase passive solute transport in phospholipid bilayers maintained at or near the membrane phase transition temperature. Lipid clustering which occurs at pre-phase transition temperatures may predispose membrane phospholipids to diamagnetic orientation in a magnetic field, and thereby trigger a phase transition enabling drug release. This finding represents a totally new phenomenon that potentially has important implications for magnetic field interactions with cellular membranes.

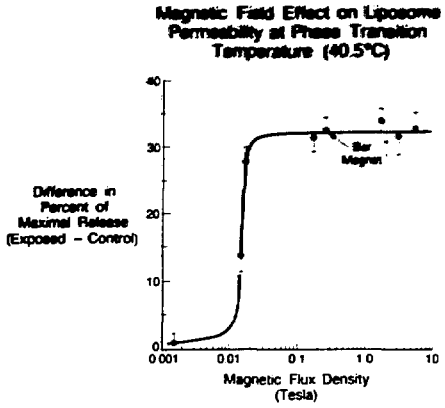

Fig. 6. The release of ^{3}H-ARA-C from liposomes is shown as a function of magnetic field strength from 0.001 to 7.5 T. Exposures of liposome samples were made in a superconducting magnet for 15 min at 40.5°C, and the solute permeability change is expressed as the difference in percent of maximal release observed between the field-exposed and control samples. The dependence on magnetic field strength of the permeability increase is sigmoidal with a 50% effect occurring at 0.015 T. The data point labeled as Bar Magnet corresponds to a 0.40-T exposure made with a pair of samarium-cobalt permanent magnets. Error bars represent 1 S.E. (XBL 859-8500)

REFERENCES

1. Gremmel, H., Wendhausen, H., and Wunsch, F. Biologische Effekte statischer Magnetfelder bei NMR-Tomographie am Menschen. Wiss. Mitt. Univ. Kiel, Radiologische Klinik (1983).
2. Sperber, D., Oldenbourg, R., and Dransfeld, K. Magnetic field induced temperature change in mice. *Naturwiss. 71*, 100–101 (1984).

MICROWAVE STIMULATED DRUG RELEASE FROM LIPOSOMES

Robert P. Liburdy

Recent results from our laboratory raise the important question of whether proteins, phospholipids, or both are responsible for the phenomenon of microwave-induced cation permeability we observe in the erythrocyte and in the lymphocyte.[1-3] To determine if phospholipids in membranes are influenced by microwaves we have constructed liposomes devoid of proteins and examined their permeability in a microwave environment.[4] These studies demonstrate that microwaves stimulate the release of an aqueous chemotherapeutic drug from liposome vesicles and indicate that liposomes should be useful model systems for the study of biological membrane responses to nonionizing radiation. In addition, this technology may prove useful as an *in-vivo* drug-delivery modality.

Liposome vesicles containing tritiated cytosine arabino-furanoside (^{3}H-ARA-C, mol wt = 243) were prepared using the reverse phase evaporation process from two highly purified and completely saturated phospholipids, dipalmitylphosophatidylcholine (DPPC) and dipalmitylphosphotidylglycerol (DPPG); this technique forms large unilamellar vesicles 2000 Å in diameter. Trace amounts of ^{14}C-DPPC were used to enable monitoring of membrane disruption. Exposures to microwaves (2450 MHz, 60 mW/g, 10 min) were accomplished using a waveguide apparatus that controls and monitors sample temperature to 0.05°C.[1-3] Release of drug and membrane phospholipid in response to microwaves were determined by monitoring each radioisotope in the supernatant obtained after pelleting exposed liposomes (170,000 × g, 1 min).

Release of ^{3}H-ARA-C and ^{14}C-DPPC from liposomes as a function of exposure temperature is shown in Fig. 1. A characteristically sharp increase in drug release (^{3}H-ARA-C) occurs at 40°C for sham-exposed liposomes with essentially no membrane phospholipid release; this occurs at the membrane phase transition temperature, T_c. In saline a 60% maximal release occurs in contrast to 80% in plasma; thus a plasma component(s) facilitates drug release from these liposomes at T_c. Significantly, microwaves are observed to stimulate drug release at temperatures as low as 33°C and 25°C for liposomes in saline and plasma, respectively. This stimulation of drug release is remarkable because it occurs at temperatures well below T_c, where these

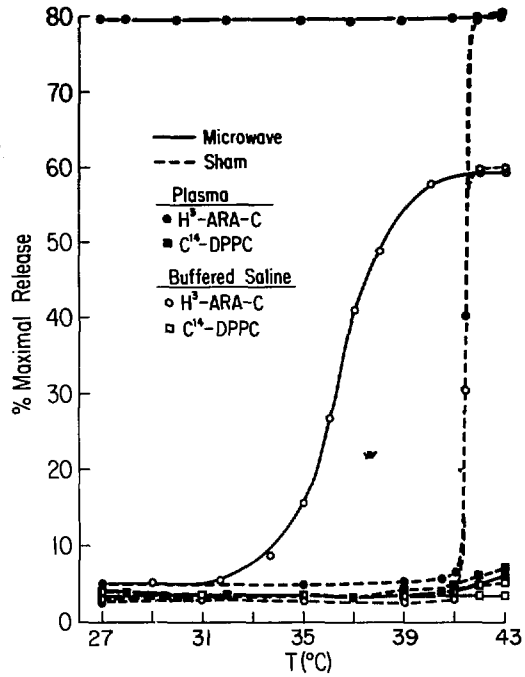

Fig. 1. Microwave-stimulated drug release from liposomes. Drug release curves for liposomes heated by microwaves (60 mW/g, 10 min) and by conventional means; effects in buffered saline and plasma. Tritiated cytosine arabinofuranoside ([^{3}H]-ARA-C) was encapsulated into the aqueous compartment and [^{14}C]-DPPC into the lipid membrane. (XBL 8411-8034)

liposomes are normally not leaky. In contrast, microwaves do not result in release of membrane phospholipid(^{14}C-DPPC), indicating that gross membrane structure is not altered. These data are consistent with a mechanism of action in which microwaves induce the formation of a pore, and this could occur if an apparent membrane phase transition is triggered during exposures.

Since pO_2 varies considerably *in vivo*, the effect of oxygen on this liposome response to microwaves was investigated. Figure 2 shows heat release curves for exposures at pO_2 = 760 mm Hg(100% oxygen), 0 mm Hg(100% nitrogen), and 150 mm Hg(atmospheric air). Oxygen is seen to markedly potentiate the microwave effect while having no

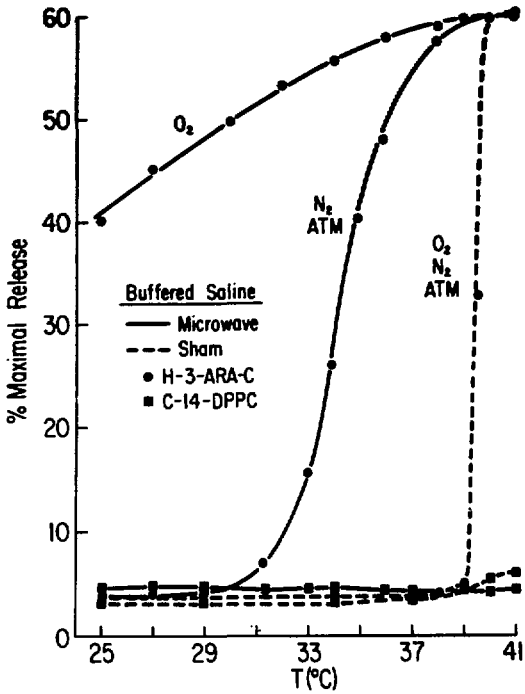

Fig. 2. Effect of oxygen on microwave-stimulated drug release. Liposomes were exposed as in Fig. 1 with the exception that prefiltered O_2 and N_2, as well as atmospheric air (ATM), were used as vehicles to mix the sample volume and maintain pO_2 during exposures. *(XBL 8411-8032)*

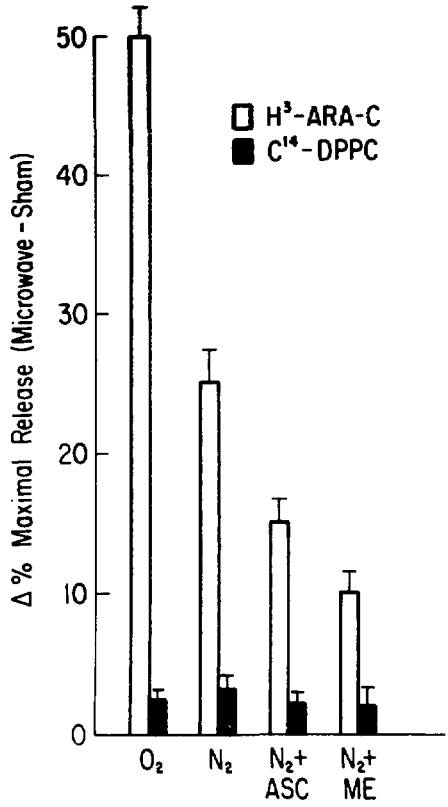

Fig. 3. Effect of antioxidants on microwave-stimulated drug release. Exposures at 37°C as in Fig. 2. Ascorbic acid or mercaptoethanol was present at a 5× and 1× mole ratio of antioxidant to lipid, respectively. Mean ± S.D., n = 7.
(XBL 8411-8031)

effect on drug release from sham-exposed liposomes. This indicates that oxygen significantly facilitates permeability of liposomes in the presence of microwaves. The low level of ^{14}C-DPPC released from the liposome membrane also indicates that oxygen plus microwaves does not act to disrupt bilayer integrity. This permeability increase is therefore consistent with a pore-formation event.

Free-radical formation can lead to lipid peroxidation and an increase in liposome permeability[3]; thus the influence of oxygen on microwave-stimulated drug release might be mediated through free-radical formation. To test this hypothesis liposomes were microwave-treated at 37°C in the presence of 100% oxygen, 100% nitrogen, or 100% nitrogen plus two different free-radical scavengers, ascorbic acid (ASC) and mercaptoethanol (ME). Figure 3 indicates that a significant reduction in drug release is observed for nitrogen compared to oxygen, as observed for 37°C in Fig. 2. Significantly, in the presence of either free radical scavenger drug release is further reduced. This strongly suggests that free-radical formation may play a role in the oxygen effect.

The above results demonstrate that microwaves can interact with phospholipids in membrane bilayers to increase liposome permeability below T_c. This phenomenon occurs in the absence of membrane protein and does not involve gross bilayer disruption; this latter fact suggests that a pore-formation event occurs. One way microwaves might accomplish this is by *physically* exciting phospholipid rotational/vibrational motion to trigger a phase transition[4]; phospholipid acyl chains are reported to exhibit rotational motion with relaxation frequencies in the microwave range during phase transitions. Although the exact molecular mechanism responsible for microwave-stimulated drug release is at present unknown, this interaction is

modulated by *chemical* factors. Both plasma and oxygen potentiate drug release, whereas antioxidants inhibit it. This latter observation strongly suggests that free-radical formation plays a role in modulating this interaction.

REFERENCES

1. Liburdy, R.P., and Fanek, Jr., P.F. Microwaves and the cell membrane. II. Temperature, plasma, and oxygen mediate microwave-induced membrane permeability in the erythrocyte. *Radiation Research 102,* 190–205 (1985).
2. Liburdy, R.P., Penn, A., Nesta, D., and Vanek, Jr., P.F. Microwaves alter cation transport and induce protein shedding in the lymphocyte. *Federation Proceedings 43,* 908 (1984).
3. Liburdy, R.P. and Penn, A. Microwave bioeffects in the erythrocyte are temperature and pO_2 dependent: Cation permeability and protein shedding occur at the membrane phase transition. *Bioelectromagnetics 5,* 283–291 (1984).
4. Liburdy, R.P. and Magin, R.L. Microwave-stimulated drug release from liposomes. *Radiation Research 103,* 266–275 (1985).

NEW SEQUESTERING AGENTS FOR THE ACTINIDES: EFFECTIVENESS FOR REMOVAL OF Pu FROM MICE OF HYDROXAMIC ACID DERIVATIVES OF DTPA, EDTA AND DESFERRIOXAMINE AND AN N-CENTERED TRIS(CATECHOYLAMIDE) LIGAND; GRADED DOSAGES OF DESFERRIOXAMINE PYRIDINONE OXIDE (desferriHOPOCAM); PROTRACTED ADMINISTRATION OF 3,4,3-LICAM(C)

Patricia W. Durbin, Nylan Jeung, Kenneth N. Raymond,*† David L. White,‡ Steven J. Rodgers† and Petra Turowski†

INTRODUCTION

The purpose of this program is to develop biological data needed to guide the design of safe effective chelating agents that will accelerate elimination of actinides and chemically similar metals from the body. Macromolecules have been synthesized containing multiple catechoylamide (CAM), hydroxamate (X), hydroxypyridinone (HOPOCAM) and carboxyl (C) functional groups, either all the same structure [e.g., the tetrameric carboxycatechoylamide, 3,4,3-LICAM(C)] or of more than one structure (e.g., desferriHOPOCAM, which contains three hydroxamate and one hydroxypyridinone oxide groups). All those functional groups, in a variety of molecular arrangements, form stable complexes with Pu(IV) and Fe(III) at pH 7.4 and promote significant excretion of circulating Pu(IV) in mice and dogs.[1–4] Three-dimensional models of all the ligands designed and synthesized in this laboratory demonstrate that Pu(IV) can be fully coordinated at the appropriate bond angles and distances by the octadentate ligands (e.g., desferriHOPOCAM, Fig. 1) and Fe(III), by the hexadentate ligands (e.g., TRENCAM, Fig. 2).

This report consists of three parts: 1) the initial screening of four new ligands for their ability to promote excretion of circulating Pu(IV), 2) the effectiveness of desferriHOPOCAM at reduced dosages, and 3) tests of the ability of 3,4,3-LICAM(C) to remove deposited Pu(IV) from mice.

METHODS

The test of effectiveness for promoting excretion of newly injected (circulating) ^{238}Pu(IV) in mice has been described.[1,2] Briefly, groups of five mice each receive an intravenous injection (i.v.) of 9250 Bq/kg ^{238}Pu(IV) in 0.2 ml of citrate buffer. One hour later, 30 μmole/kg of ligand is injected intraperitoneally (i.p.) in 0.5 ml of saline. The mice are killed 24 hr after the Pu injection, frozen, and dissected after partial thawing. The ^{238}Pu in skeleton, tissues, and separated excreta is determined by counting the ^{234}U L x rays.

The effect of desferriHOPOCAM dosage on its ability to promote excretion of circulating Pu was investigated by varying the dosage in the 24-hr test

*Materials and Molecular Research Division, LBL.
†Dept of Chemistry, University of California, Berkeley.
‡University of California Medical Center, San Francisco.

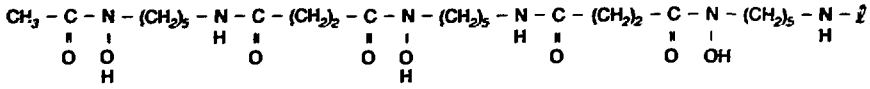

Abbreviation	ℓ	X	Molecular formula and (weight)
DFOM	$-CH_3-SO_3H_2$	–	$C_{26}H_{52}N_6O_{11}S$ (657)
DesferriCAM	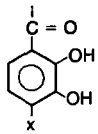	H	$C_{32}H_{52}N_6O_{11}$ (697)
DesferriCAM(C)	Same as above	$-CO_2Na$	$C_{33}H_{51}N_6O_{13}Na$ (763)
DesferriHOPOCAM	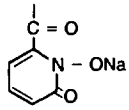	–	$C_{31}H_{51}N_7O_{11}Na$ (721)
Toluyl-DesferriX	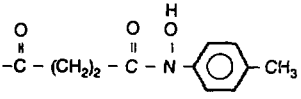		$C_{36}H_{59}N_7O_{11}$ (765)

Fig. 1. *Octadentate derivatives of desferrioxamine. Official IUPAC names have been requested.*

(XBL 8511-11426)

of ligand potency just described.[5] The ability of 3,4,3-LICAM(C) to remove Pu deposited in the target organs was investigated by administering 30 μmole/kg of ligand 24 hr after the Pu injection; Pu-injected controls received one saline injection; mice were killed 24 hr later (48 hr after the Pu injection). The ability of prolonged administration of 3,4,3-LICAM(C) to promote excretion of deposited Pu was investigated by giving 13 daily injections of 30 μmole/kg of ligand starting 24 hr after the Pu injection; Pu-injected controls received daily injections of saline; all mice were killed 14 days after the Pu injection.

Effectiveness of New Ligands

Desferrioxamine is a selective hexadentate ligand that forms stable Pu(IV) and Fe(III) complexes, but it is slow acting. Addition of a catechoyl or carboxycatechoyl group to DFO to form desferriCAM or desferriCAM(C) (Fig. 1) greatly enhanced both the rate of removal of Fe(III) from transferrin (Tf) (Ref. 6) and the excretion of Pu from mice (see Table I and Ref. 4). A fourth hydroxamate group was added to the terminal N of DFO through an amide linkage to prepare toluyl-desferriX (Fig. 1) to learn whether enhanced kinetic

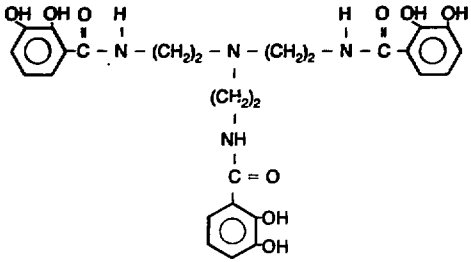

TRENCAM

Abbreviation	Molecular formula and weight
TRENCAM	$C_{27}H_{30}N_4O_8$ (554.6)

Fig. 2. *Catechoylamide trimer centered on N. Official IUPAC name has been requested.* *(XBL 8511-11425)*

capability would also be conferred by conversion of DFO to a tetrahydroxamate ligand. The toluyl-hydroxamic acid DFO derivative was prepared because suitable starting materials were available. It is sparingly soluble, and the standard 30 μmole/kg dosage was administered to mice as a suspension. As shown in Table 1, toluyl-desferriX promoted net Pu excretion in 24 hr (treated − control) of 15.2% injected dosage (ID). It was more effective than desferriCAM, which is even less soluble, but it was not as effective as an equimolar amount of unsubstituted DFOM. The partitioning of Pu excretion (70% in urine and 30% in feces) resembled DFO. Acute toxicity will be examined, and Pu excretion will be retested at the limiting concentration of the ligand.

TRENCAM (Fig. 2) is an enterobactin analogue consisting of three catechoyl amide groups attached to a central N atom. It is a sterically flexible molecule with a high affinity for Fe(III) that should also form stable Pu(IV) chelates. Unsubstituted TRENCAM is sparingly soluble, and the standard dosage of 30 μmole/kg was administered to mice as a suspension. Excess Pu excretion was 24.2%

Table 1. Effect of desferrioxamine (DFO) containing a fourth hydroxamate group on distribution and excretion of ^{238}Pu(IV) in mice.

	Percent of injected ^{236}i u ± S.D. at 24 hr[a,b]						
	Tissues					Excreta	
	Liver	Skeleton	Kidneys	Residual soft tissue	Body content	Urine	Feces and GI contents
Test ligand							
Toluyl-desferriX	39 ± 7.5	26 ± 5.2	1.6	8.5 ± 2.3	76	17	6.9
Similar ligands[c]							
DesferriCAM	43 ± 3.7	31 ± 2.3	3.1	8.6 ± 2.2	86	7.5	6.5
DesferriCAM(C)	11 ± 2.0	13 ± 1.2	0.9	3.0 ± 0.4	27	28	45
Baseline ligand[c]							
DFOM	19 ± 13	20 ± 11	1.8	4.5 ± 1.4	46	40	15
^{238}Pu-Injected Control[c]							
24-hr	49 ± 8.3	32 ± 7.9	2.0	7.7 ± 2.0	92	4.7	4.1
1-hr	30 ± 7.4	24 ± 4.4	2.7	37 ± 7.1	94	1.1	4.8

[a] S.D. = $[\Sigma dev^2/(n-1)]$. Where S.D. is not shown, samples from each 5-mouse group were pooled for ^{238}Pu analysis. Results for each experiment were normalized to 100% material recovery; discrepancies are due to rounding.

[b] Ligand was administered (30 μmole/kg, i.p.) at 1 hr and mice were killed at 24 hr after injection (i.v.) of ^{238}Pu(IV) citrate.

[c] Previously published (Refs. 1,2,4).

ID (Table 2), about the same as for the benzene-centered tris(catechoylamide)s, MECAM and MECAM(S).[2] TRENCAM was not as effective for Pu removal as the soluble, more acidic hexadentate ligands—the sulfonated linear tris(catechoylamide), 3,4,3-LICAM(S), or the benzene-centered tris(hydroxypyridinone), HOPO-MECAM. Investigation of acute toxicity and retesting of Pu excretion at a reduced dosage are planned.

One of the goals of this research is development of an orally effective removal agent for Pu(IV) and (or) Fe(III). The Ca or Zn salts of DTPA (Fig. 3), which are used clinically to treat actinide contamination, are not well absorbed from the GI tract and are usually administered by i.v. injection. In general, a large fraction of Pu chelated by ligands with a low net negative charge tends to be eliminated by the liver and GI tract.[4,4] Such ligands are also likely to be better absorbed from the GI tract and effective when administered by mouth. To that end, two of the four terminal acetic acid groups of DTPA or EDTA were replaced by bis(isopropyl)hydroxamic acid, which reduced the net negative charge of the ligands and increased their metal-binding capacity. Bis(isopropyl)DTPA-DX and bis(isopropyl)EDTA-DX (Fig. 3) were administered to mice as the tri- and di-sodium salts, respectively. Because of the known ability of DTPA to bind essential Ca and Zn, Pu removal by the Ca and Zn complexes of bis(isopropyl)DTPA-DX was also investigated.

Net Pu excretion promoted by the Na, Ca, and Zn forms of bis(isopropyl)DTPA-DX and by bi(isopropyl)EDTA-DX was 66.3, 66.3, 57.2, and 8.8% ID, respectively (see Table 3). The Na and Ca forms of bis(isopropyl)DTPA-DX promoted slightly more, and the Zn form slightly less Pu excretion than the baseline ligand, $CaNa_3$-DTPA (net Pu excretion 61.2% ID). While nearly all of the Pu-DTPA chelate is excreted by the kidneys, 53 to 68% of the Pu excretion promoted by the dihydroxamic acid derivatives was via the GI tract. All three forms of bis(isopropyl)DTPA-DX will be tested for acute toxicity, and the Zn complex will be investigated for dosage effectiveness, ability to remove deposited Pu, and oral activity.

Dosage Effectiveness of desferriHOPOCAM

To date, the most effective ligand prepared for Pu removal is the hydroxypyridinone oxide derivative of desferrioxamine, desferriHOPOCAM (Fig. 1).

Table 2. Effect of an N-centered tris(catechoylamide) ligand on distribution and excretion of ^{238}Pu in mice.

	Percent of injected ^{238}Pu ± S.D. at 24 hr[a,b]						
	Tissues					Excreta	
	Liver	Skeleton	Kidneys	Residual soft tissue	Body content	Urine	Feces and GI contents
Test ligand							
TRENACAM	31 ± 9.2	27 ± 12	2.1	6.8 ± 0.6	67	12	21
Similar ligands[c]							
MECAM	18 ± 3.4	33 ± 3.8	4.6	7.9 ± 1.3	63	13	24
3,4-LICAM(C)	17 ± 1.6	17 ± 2.8	9.0	5.2 ± 1.2	48	52	
3,4,3-LICAM	18 ± 3.4	26 ± 5.2	4.3	5.1 ± 0.8	53	9.4	35

[a] S.D. = $[\Sigma dev^2/(n-1)]$. Where S.D. is not shown, samples from each 5-mouse group were pooled for ^{238}Pu analysis. Results for each experiment were normalized to 100% material recovery; discrepancies are due to rounding.

[b] Ligand was administered (30 μmole/kg, i.p.) at 1 hr and mice were killed at 24 hr after injection (i.v.) of ^{238}Pu(IV) citrate.

[c] Previously published (Ref. 2).

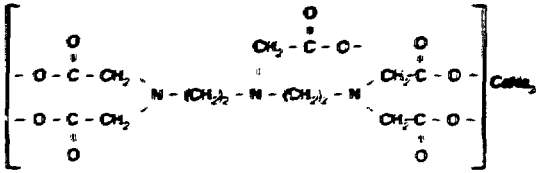

DTPA – Ca Na_3

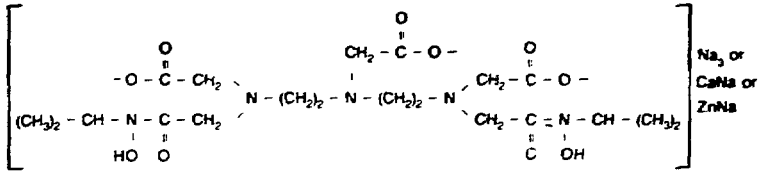

Bis(isopropyl)DTPA-DX

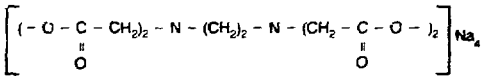

EDTA – Na_4

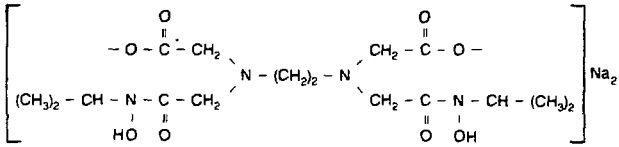

Bis(isopropyl)EDTA-DX-Na_2

Fig. 3. *(XBL 8511-11427)*

Abbreviation	*Molecular formula and weight*	*IUPAC name*
DTPA-$CaNa_3$	*$C_{14}H_{18}N_3O_{11}CaNa_3$ (497.4)*	*Calcium disodium (diethylenetrinitrilo)pentaacetate*
Bis(isopropyl)DTPA-DX-Na_3	*$C_{20}H_{34}N_5O_{10}Na_3$ (573.5)*	*Trisodium diethyletrinitrilo-N,N',N''-triacetic-N,N''-di(isopropylacetichydroxamate)*
Bis(isopropyl)DTPA-DX-CaNa	*$C_{20}H_{34}N_5O_{10}CaNa$ (567.6)*	*Calcium sodium diethylenetrinitrilo-N,N',N''-triacetic-N,N''-di(isopropylacetichydroxamate)*
Bis(isopropyl)DTPA-DX-ZnNa	*$C_{20}H_{34}N_5O_{10}ZnNa$ (592.9)*	*Zinc sodium diethylenetrinitrilo-N,N',N''-triacetic-N,N''-di(isopropylacetichydroxamate)*
EDTA-Na_4	*$C_{10}H_{12}N_2O_8Na_4$ (380.2)*	*Tetrasodium (ethylenedinitrilo)-tetraacetate*
Bis(isopropyl)EDTA-DX-Na_2	*$C_{16}H_{28}N_4O_8Na_2$ (451)*	*Disodium ethylenedinitrilo-N,N'-diacetic-N,N'-di(isopropyl-acetichydroxamate)*

Table 3. Effect of poly(aminohydroxamatocarboxy) ligands on distribution and excretion of ^{238}Pu in mice.

	Percent of injected ^{238}Pu ± S.D. at 24 hr[a,b]						
	Tissues					Excreta	
	Liver	Skeleton	Kidneys	Residual soft tissue	Body content	Urine	Feces and GI contents
Test ligands							
Bis(isopropyl)DTPA-DX-Na_3	8.4 ± 3.2	12 ± 2.8	0.3	3.8 ± 0.2	25	32	43
Bis(isopropyl)DTPA-DX-CaNa	7.1 ± 1.2	14 ± 0.6	0.6	3.3 ± 0.7	25	35	40
Bis(isopropyl)DTPA-DX-ZnNa	12 ± 1.5	17 ± 3.3	0.7	4.9 ± 0.7	34	21	45
Bis(isopropyl)DTPA-DX-N...	50 ± 3.7	24 ± 3.9	1.3	5.5 ± 1.7	83	12	5.6
Baseline ligand[c]							
DTPA-$CaNa_3$	16 ± 2.8	11 ± 1.2	0.4	3.8 ± 1.5	30	70	

[a] S.D. = $[\Sigma dev^2/(n-1)]$. Where S.D. is not shown, samples from each 5-mouse group were pooled for ^{238}Pu analysis. Results for each experiment were normalized to 100% material recovery; discrepancies are due to rounding.

[b] Ligand was administered (30 μmole/kg, i.p.) at 1 hr and mice were killed at 24 hr after injection (i.v.) of ^{238}Pu(IV) citrate.

[c] Previously published (Ref. 1).

The net Pu excretion promoted in 24 hr by the standard dosage of 30 μmole/kg was 77.1% ID; acute toxicity in mice appears to be low.[4] The dosage effectiveness curve for this ligand is shown in Fig. 4. The discontinuous line provides comparison with the more carefully studied tetracatechoylate, 3,4,3-LICAM(C).[5] Significant Pu removal was observed at dosages as low as 0.3 μmole/kg, and additional Pu removal probably can be achieved with dosages greater than 30 μmole/kg. The slope (m) of a straight line fitted by least squares [m = −35.2% ID in body/$\log_{10}$(μmole/kg of ligand)] is the same as that for the parent compound, DFOM [m = −35.9% ID in body/$\log_{10}$(μmole/kg of ligand)]. The curve for desferriHOPOCAM is displaced towards lower dosage, and for removal of equal fractions of circulating Pu from the body, desferriHOPOCAM is about 30 times more effective than DFOM. The effect of delayed administration of desferriHOPOCAM is under investigation, and study of its oral effectiveness and Pu excretion under protracted administration are planned. The properties of this ligand indicate that it is a good candidate for investigation in a larger animal.

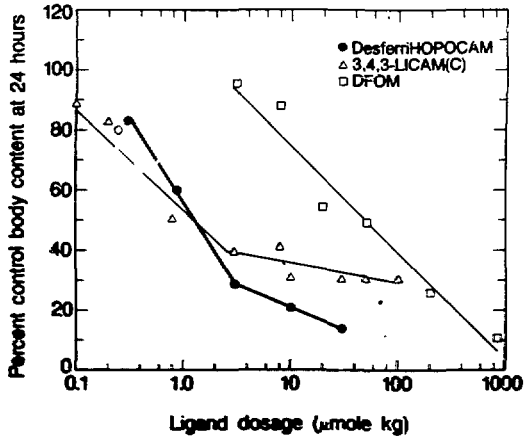

Fig. 4. Effect of desferriHOPOCAM dosage on retention of ^{238}Pu in mice. (XBL 8511-11423)

Removal of Deposited Pu by 3,4,3-LICAM(C)

Within 24 hr after i.v. injection of Pu(IV) citrate in adult mice about 90% of the Pu remaining in the body is deposited in the liver and skeleton.[7] Elimination of the liver Pu begins immediately, mainly by way of biliary secretion into the GI tract; a small variable fraction is recirculated. Pu recirculated from soft tissues and liver augments skeletal Pu by about 20% during the first few days after injection. If a ligand that reacts with metals only in the body fluids is administered 24 hr after the Pu, it can be

expected at a minimum to react with undeposited Pu remaining in the body fluids and Pu released and recirculated from soft tissues and liver but not yet redeposited. If the residence time of the ligand is sufficiently long, and it is effective at low concentration, most of the recirculated Pu can be intercepted and the early skeletal increase prevented.

The tetrameric carboxy(catechoylamide) ligand, 3,4,3-LICAM(C), was shown to be effective for removal of circulating Pu at low dosage and to be of low toxicity.[2-4] The potential of 3,4,3-LICAM(C) as a clinically useful Pu removal agent was explored further by investigating removal of deposited Pu by one administration or 13 daily administrations of 30 μmole/kg of 3,4,3-LICAM(C).

Single Administration 24 hr after Pu. Two groups of five mice each were injected i.v. with Pu; 24 hr later excreta were collected and the ligand was injected: the mice were killed at 48 hr and excreta were again collected. The pooled results are shown in Table 4. One group of five Pu-injected control mice was killed at 2 days postinjection; the distribution of Pu in their tissues is given in Table 4. Excreta were also collected at 1 and 2 days after

Table 4. Effect of 3,4,3-LICAM(C) on ^{238}Pu(IV) deposited in mice: single or protracted administration.

	Percent injected ^{238}Pu ± S.D.[a,b]				
	3,4,3-LICAM(C)[b]		^{238}Pu-injected controls		
	2-day	14-day	24-hour[d]	2-day[b,c]	14-day[b]
Liver	38.1 ± 3.6	6.3 ± 2.4	49 ± 8.3	42.7 ± 5.2	9.7 ± 4.6
Skeleton	29.0 ± 4.0	20.4 ± 3.9	32 ± 7.9	34.5 ± 5.1	29.7 ± 6.2
Kidneys	1.2	1.3	2.0	0.51	0.6
Residual soft tissue	6.6 ± 1.0	5.6 ± 0.6	7.7 ± 2	6.2 ± 0.7	4.4 ± 0.9
Retained in body	74.7 ± 4.3	33.7 ± 3.6	92	84.0 ± 3.5	44.5 ± 3.5
Urine, day 1	4.0	5.6	4.7	5.5	6.0
2	3.4	3.6		1.0	0.6
3		1.8			0.4
4,5,6		2.9			0.6
7,8		1.5			0.4
9,10		1.1			0.1
11,12,13		1.0			0.3
14		0.7			0
Total	7.4	18.2	4.7	6.5	8.4
Feces, day 1	2.8	2.9	4.1[e]	2.4	2.4
2	15.1[e]	11.6		7.1[e]	3.4
3		5.8			6.5
4,5,6		14.4			15.1
7,8		5.5			7.8
9,10		4.3			5.3
11,12,13		2.8			5.3
14		0.6[e]			1.2[e]
Total	17.9	47.9	4.1	9.4	47.0

[a] See footnote a, Table 1.

[b] Ligand was administered (30 μmole/kg, i.p.) once (2-day group) or daily for 13 days (14-day group) starting at 24 hr, and mice were killed at 48 hr (2-day group) or at 14 days (14-day group) after injection (i.v.) of ^{238}Pu(IV) citrate.

[c] Control excreta data at 2 days p.i. are averages for five 5-mouse groups studied from 2 to 14 days after ^{238}Pu injection; 2-day tissue data are for one 5-mouse group normalized to 84% ID retained.

[d] Previously published (Refs. 1,2).

[e] Includes GI contents.

Pu injection from four groups of longer-term Pu-injected control mice; the control urine and fecal data in Table 4 are grand means of all five sets of control excretion data. Net Pu excretion by the mice given 3,4,3-LICAM(C) at 24 hr was 9.4% ID. The mean body content of the ligand-treated group, 74.7 ± 4.3% ID, was significantly less ($p < 0.01$, Ref. 8) than that of the Pu-injected control group, 84.0 ± 3.5% ID. The Pu contents of both liver and skeleton were reduced by the ligand, but the differences from the appropriate control values were not statistically significant. Both urinary and fecal excretion of Pu were increased by the single ligand injection, to two to three times the quantities excreted by the controls.

Protracted Administration of 3,4,3-LICAM(C). Mice tolerated 13 injections of 3,4,3-LICAM(C) well; body weight, appetite, behavior, and irritability were not different from saline-injected controls, and no grossly visible lesions were found at autopsy. The Pu content of the skeleton and the whole body were significantly different from the controls (see Table 4). Between days 2 and 14, daily administration of 3,4,3-LICAM(C) promoted an excess Pu excretion of 10.6% ID. Nearly all the excess Pu excretion was renal. The urinary and fecal excretion rates of the control and ligand-treated mice are shown in Fig. 5. If fecal Pu excretion is derived mainly from clearance of the liver via bile, then it appears that the action of 3,4,3-LICAM(C) is to slightly accelerate Pu clearance from the liver, thereafter diverting chelated Pu to renal excretion and precluding additional Pu accumulation in the liver. Under the influence of daily 3,4,3-LICAM(C) urinary excretion of Pu was six to seven times greater than for the control mice.

Even after 13 ligand injections, urinary Pu excretion was still 0.3 to 0.4% ID/day suggesting that the more rapidly clearing (or renewing) compartments in soft tissues (other than liver) and skeleton had not been exhausted, and additional reduction might be achieved by further prolonging the ligand treatment. It has often been suggested that the main action of chelating agents that do not enter cells is to prevent redeposition by diverting recirculated Pu to excretion. The parallel urinary excretion rate curves for the ligand-treated and control mice lend support to that hypothesis. For metals like Pu that are not efficiently excreted, the physiological rates at which they are transferred out of the target organs are masked by continual redeposition of recirculated metal. If an effective Pu-binding agent like 3,4,3-LICAM(C) were administered to Pu-injected animals continuously for an extended period, diverting a large fraction of recirculated Pu to excretion, it should be possible to measure the true turnover rates of Pu in the major target organs.

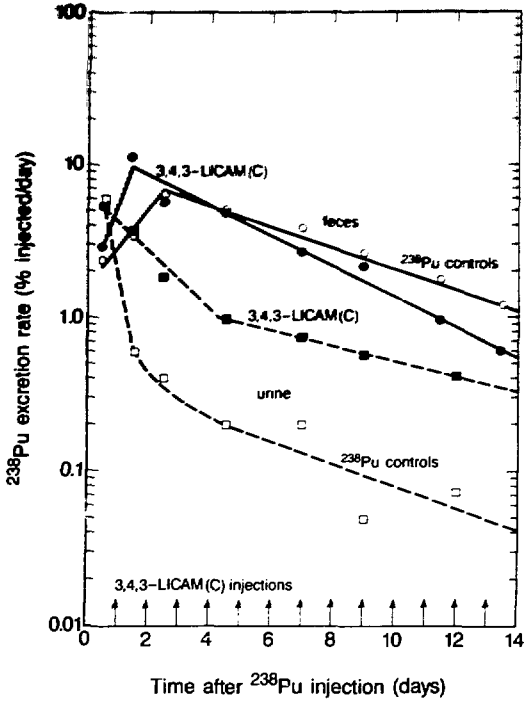

Fig. 5. Effect of protracted administration of 3,4,3-LICAM(C) on rates of ^{238}Pu excretion in urine and feces of mice.
(XBL 8511-11424)

REFERENCES

1. Durbin, P.W., Jones, E.S., Raymond, K.N., and Weitl, F.L. Specific sequestering agents for the actinides: 4. Removal of ^{238}Pu(IV) from mice by sulfonated tetrameric catechoyl amides. *Radiat. Res. 81*, 170–187 (1980).
2. Durbin, P.W., Jeung, N., Jones, E.S., Weitl, F.L., and Raymond, K.N. Specific sequestering agents for the actinides: 10. Enhancement of ^{238}Pu elimination from mice by poly(catechoylamide) ligands. *Radiat Res. 99*, 85–105 (1984).
3. Lloyd, R.D., Bruenger, F.W., Mays, C.W., Atherton, D.R., Jones, C.W., Taylor, G.N., Stevens, W., Durbin, P.W., Jeung, N., Jones, E.S., Kappel, M.J., Raymond, K.N., and Weitl, F.L. Removal of Pu and Am from beagles and

mice by 3,4,3-LICAM(C) or 3,4,3-LICAM(S). *Radiat. Res. 99*, 106–128 (1984).

4. Durbin, P.W., Jeung, N., Rodgers, S.J., White, D.L., and Raymond, K.N. New sequestering agents for the actinides: acute toxicity and effectiveness for removal of Pu from mice of derivatives of desferrioxamine and of poly(hydroxypyridinone) ligands and their ferric and zinc complexes. Biology Medicine Division Annual Report 1983–1984, Lawrence Berkeley Laboratory report LBL-18393, pp. 59–64 (1985).
5. Durbin, P.W., Jeung, N., Jones, E.S., Raymond, K.N., and Weitl, F.L. Plutonium removal from mice by poly(catechoylamide) ligands, Ca-DTPA, desferrioxamine B, and Tiron: effect of ligand dosage. Biology and Medicine Division Annual Report 1982–1983, Lawrence Berkeley Laboratory report LBL-16840, pp. 43–47 (1984).
6. Rodgers, S.J. and Raymond, K.N. Ferric ion sequestering agents. 11. Synthesis and kinetics of iron removal from transferrin of catechoyl derivatives of desferrioxamine B. *J. Med. Chem. 26*, 439–442 (1983).
7. Durbin, P.W. and Jeung, N. Kinetics of plutonium deposition in the mouse. Division of Biology and Medicine Annual Report 1982–1983, Lawrence Berkeley Laboratory report LBL-16840, pp. 56–59 (1984).
8. Fisher, R.A. Statistical Methods for Research Workers. Hafner Publishing Co., New York (1954).

SECTION 4. RADIATION BIOPHYSICS

INTRODUCTION

The Radiation Biophysics Group has an interdisciplinary approach to the understanding of the deleterious and beneficial effects of a broad array of ionizing radiations. The Bevalac accelerator is a unique source of accelerated heavy particles, from protons to uranium ions, and our group is the central core of a worldwide effort. In this effort, the Department of Energy supports the accelerator and some fundamental biophysical studies. Our cell, tissue, and tumor radiobiology programs and controlled cancer therapy studies with heavy ions are sponsored by the National Cancer Institute. Since fast heavy ions are part of interplanetary space radiation, our space radiobiology program is important for achieving the goals of NASA.

Most of the biological effects of ionizing radiations are ultimately due to macromolecular changes in genetic material and consequent alterations in inherited and acquired characteristics of cells. The studies reported in this section are organized into five sections. These are: Physics of Interactions between Fast Charged Particles and Matter, Molecular Studies, Cellular and Tumor Radiobiology, Tissue Effects of Heavy Charged Particle Beams, and Heavy-Ion Therapy and Related Physics and Biology.

Studies of physical interactions between fast charged particles and matter are essential for the measurement and understanding of particle fields. Walter Schimmerling and associates have made progress in quantitating the complex particle fragmentation events and multiple elastic collisions that determine the pathways of particles in biological material, and Jorge Llacer has provided new instrumental methodology for these purposes.

The heavy particles allow the delivery of ionizing radiation deep in the body with localization more precise than is possible with other radiations. The use of protons and of helium ions (see Castro et al.) has led to important advances in the therapy of local cancer, for example, of certain tumors of the eye and of otherwise incurable tumors near the spinal cord. The beam localization properties have also allowed rapid advances in the treatment of arteriovenous malformations in the brain. For these reasons we have initiated a new study to find the particle beams that are particularly suited to the delivery of high localized doses with maximum sparing of surrounding normal tissue. These presently appear to be carbon ions.

Other investigators are involved with studies at the molecular level. The manner in which ionizing radiations produce alterations in DNA is mediated by diffusion-controlled free radical interactions. Aloke Chatterjee, John Magee, and their coworkers are developing an important new theoretical approach to this problem. They can model the kinetics of elementary interactions that occur using three-dimensional representations of DNA molecules immersed in water. With their approach it is possible to follow the fate of water radicals and the detailed free radical chemistry of DNA. Viral DNA is being used *in vitro* to study the influence of the chemical milieu on the yield of DNA lesions.

In studies of cellular and tumor radiobiology, it is shown that heavy ions are more efficient than x rays in producing cell transformation as well as cell lethality. At very high linear energy transfers, the lethal effects predominate. The maximum effectiveness for cell transformation occurs at a linear energy transfer of well above 100 keV/μm. Accelerated iron nuclei transform with peak efficiency, and these particles are also prominent in space radiations. Tracy Yang and Mantong Mei, a scientist visiting from mainland China, have devised experiments that allow one to test the effects of specific chemical and physical environments on these cell changes, and also permit one to study the effects of heavy ions on gene expression.

Eleanor Blakely et al. have a systematic program for investigating the role of antioxidant enzymes in modifying the expression of radiation damage and repair during the course of the cell division cycle. This study is being conducted in collaboration with the Armed Forces Radiobiology Research Institute. Blakely found that the activity of these enzymes rapidly rises in the period immediately following cell division in unirradiated cells and that this rise coincides with an increased resistance to x-ray radiation injury. In certain genetically abnormal cell lines, the antioxidant enzyme levels are significantly reduced; these cell lines are correspondingly much more sensitive to radiation injury than normal cell lines.

Using special chromosome condensation techniques that require cell fusion to permit visualization of interphase chromatin, Edwin Goodwin has experimentally demonstrated that when single fast heavy ions penetrate the G_1-phase cell nucleus, the particles can produce multiple chromatin breaks. X rays, electrons, or ultraviolet radiation can only rarely produce multiple chromatin lesions, and only when large doses are administered. The interactions between the multiple chromatin breaks during the course of repair (and misrepair) processes, appear to explain the high carcinogenic potency and lethality of heavy ions.

The group is collaborating with scientists from the National Institute of Radiological Science at Chiba, Japan. Hiroshi Ohara and our group have investigated chromosome aberrations produced by heavy ions in human blood cells and cell killing effects in cultured human squamous cell carcinoma cells from lung.

Synchronized mammalian cells are used in a systematic study of the role of protein synthesis in the repair of DNA injury. The use of temperature-sensitive mutants helped to establish the relationship of protein synthesis during the DNA replicating S phase to delays and disturbances in cell progression. A current phase of this work is reported by Polly Chang, who has shown that inhibition of protein synthesis in exponentially growing cells can disrupt the development of thermotolerance.

Michael Nusse from Johann Wolfgang Goethe University in West Germany collaborated with Stanley Curtis in a study of the induction of micronuclei in mammalian cells following exposure to heavy charged-particle beams. The micronuclei originate from chromatin fragments that rejoined in a stable configuration; their presence is a measure of the degree of radiation injury and in some cell strains of the degree of sensitivity to radiation.

Stan Curtis also has a program of studying tumor cell killing and kinetics after exposure to heavy particle beams. The data indicate that the rhabdomyosarcoma tumor cells repair a considerable amount of potentially lethal damage following both low- and high-LET radiation, but that this repair cannot be detected in the absence of repair inhibitors because it is so rapid. Repopulation studies after x-ray doses show that tumor cells accumulate in G_1-phase.

The physical properties of red blood cell membranes change in a very sensitive manner relating to the chemical and macromolecular composition of blood serum. Such relationships are under continued investigations by Howard Mel and associates.

The study of tissue effects of heavy charged-particle beams continues in our group. The dose that can be delivered in the radiation therapy of cancer is limited by the possible occurrence of irreparable injury to normal tissues in the path of the therapy beam. Edward Alpen and group are focusing their interest on two different systems: the kidney and the spinal cord. The development of late effects is of particular interest. Alpen is using a system developed in collaboration with the Gray Laboratory in England for assessing kidney function in mice. He has quantitated the dose dependence of late injury occurring after fractionated doses of helium ions. With Adrian Rodriguez another set of studies is focusing on spinal cord injury.

John Ainsworth is reporting the consequences of acute heavy-ion injury to stem cells in bone marrow. Of particular interest is the finding that repair of heavy-ion injury appears to leave some permanent damage in the hemopoietic system, as evidenced by the lack of full recovery of the red corpuscle series. Ainsworth is also reporting progress on short- and long-term lethal effects caused by exposures to charged heavy-ion particles, a study undertaken in order to clarify the hazards of space radiations.

Heavy-ion therapy and related physics and biology continues as a major effort of our group. Joseph Castro is leading a group dedicated to therapeutic investigations with heavy-ion beams. In this effort he is further supported by the Radiation Oncology Department of the UCSF Medical School and by the Northern California Oncology Group. Gratifying results have been achieved in treatment of ocular tumors, particularly melanoma of the retinal choroid, and of tumors adjacent to the spinal cord. Other cancers of interest are pancreatic carcinoma, some classes of lung carcinoma, and prostate carcinoma.

John Lyman describes a quantitative system that can be used to estimate complications that might arise as a consequence of localized or generalized therapy.

Aloke Chatterjee et al. have for some years worked on the use of radioactive beams for accurately localizing the Bragg peak of beams used in therapy. This approach is uniquely possible when heavy ions are used. The first radioactive beam studies have been carried out in cancer therapy patients during the current year. This method promises to significantly improve our

abilities to accurately localize therapy beams and thus to protect sensitive adjacent structures in patients.

The cell biology group has been collaborating with the therapists in order to assess the sensitivity of human skin for late radiation injury and in quantitating the radiobiological responses to beams in uveal melanoma. The group is also engaged in an ambitious program to improve therapy-beam delivery by wobbling and scanning the high-energy particle beams. Curtis is reporting the status of radiobiological studies with such beams.

In summary, the use of heavy particle beams is instrumental in learning basic molecular and cellular biology of the cell response and cell transformation processes. Application of these beams to cancer therapy has already been extremely useful in special classes of patients, and further heavy-ion studies appear to be important to the progress of biomedical science.

Physics of Interactions between Fast Charged Particles and Matter

HIGH ENERGY HEAVY ION BEAMS USED IN BIOLOGY AND MEDICINE: MEASUREMENT OF PARTICLE DISTRIBUTIONS IN THE FRAGMENTATION TAIL OF A 670 A MeV NEON BEAM STOPPING IN WATER

Mervyn Wong, Walter Schimmerling, Marwin Rapkin, and Jerry Howard

When a beam of high-energy heavy ions passes through matter, the beam fragmentation products penetrate more deeply than the original ions. As a consequence, in heavy-ion radiotherapy, vital organs located behind and in close proximity to the tumor volume to be treated receive a significant fraction of the absorbed dose. Therefore, it is important to measure the beam quality in the distal portion of the Bragg curve, where only fragments contribute. We have performed a measurement of this contribution at the Bevalac biomedical facility with a 670 A MeV neon beam.[1]

Fragments emerging from a 33-cm water absorber, which is sufficiently thick to stop the beam, were detected with a spectrometer consisting of a coaxial array of solid-state detectors. A schematic of the experimental setup is shown in Fig. 1. The beam enters from the right of the diagram. There are two sets of ion-implanted silicon detectors. Two fully depleted silicon detectors, T_1 and T_2 (~200 μm thick and 1.9 cm in diameter) are mounted ~1 m apart. These two detectors provide the time-of-flight (and hence velocity) measurement of the fragments. The energy deposition of particles traversing the spectrometer is measured in D_1, D_2, and D_3, each being ~3 mm thick. Particle identification is achieved through correlation of velocity and energy deposition measurements. A detailed description of the apparatus is given in Ref. 2.

The charge of each particle for the case where dE/dx does not vary significantly inside the detector

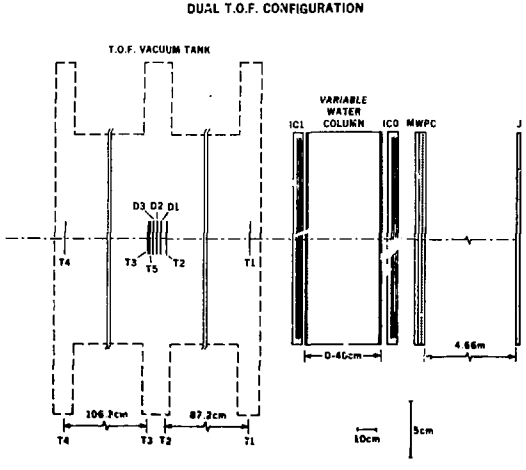

Fig. 1. Schematic layout of the experimental apparatus. There are three sets of detectors: 1) ion chambers IC_1, IC_0 are used to measure the Bragg curve at high beam intensity; 2) T_1, T_2, and T_3, T_4 are fully depleted silicon detectors providing separate time-of-flight (and hence velocity) measurements of the fragments; 3) D_1, D_2, and D_3 are silicon detectors used to measure the energy deposition of particles traversing the spectrometer. Particle identification is achieved through correlation of velocity and energy deposition measurements. (XBL 8310-11900)

can be calculated using the expression

$$Z^2 = \left[\frac{\Delta E}{\Delta x}\right]_{obs} / \left[\frac{dE}{dx}\right]_p \qquad (1)$$

where ΔE is the energy deposition in the detector and $(dE/dx)_p$ the proton stopping power calculated at the measured velocity v. The charge spectrum obtained in this way, using the energy deposition measured in D_1, is shown in Fig. 2a. In the present experiment amplifier gains and discriminator thresholds were set such that emphasis was placed on detection of the high-LET fragments. A wider range of sensitivity was obtained with detector D_2, as shown in Fig. 2b, where partial detection of helium is observed.

Equation (1) is an approximation that becomes less accurate for particles stopping in the detector, such as O and F (and, possibly, some residual primary beam particles). The increased asymmetry in the Z^2-distribution of these particles may be attributed to this cause. Further work is in progress to refine the analysis for the stopping particles.

The individual velocity spectrum for each fragment species can be projected out by applying cuts to the charge spectra. As an example, Fig. 3 shows the projected oxygen velocity spectrum. Given the Z^2 and the measured velocity, the LET for each particle can be calculated. The water-equivalent LET spectrum for oxygen obtained in this way is shown in Fig. 4. Plots, such as are shown in Figs. 3 and 4, can be displayed on-line during data acquisition.

The dose per incident particle due to fragments emitted into the ~0.8° angle subtended by the spectrometer, can be calculated using:

$$\text{Dose}(Z) = \frac{1}{A}\,\frac{1}{n_{inc}} \int \frac{dn(Z)}{dL}\, L\, dL \qquad (2)$$

where:

n_{inc} = number of incident beam ions,

$n(Z)$ = number of particles of charge Z, corrected for computer dead time losses,

$dn(Z)/dL$ = differential LET spectrum (using $L \equiv$ LET), and

A = area of geometry-defining D_1 detector (2.84 cm^2);

Table 1 summarizes the results for the contribution of each fragment to the total dose. The uncertainties result from an estimate of the overlap between the tails of the Z^2 distribution for the neighboring charges.

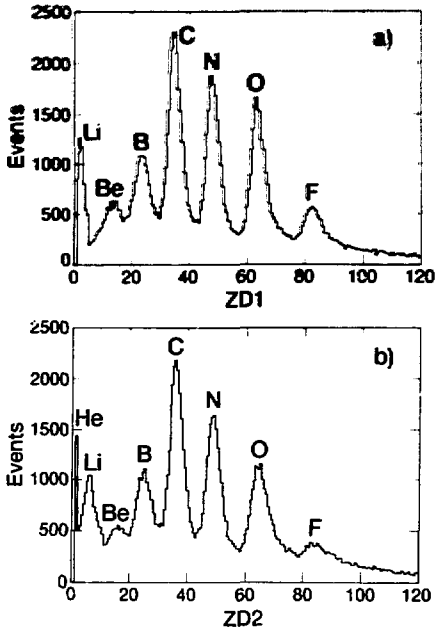

Fig. 2. Measured fragment charge-squared spectra for a 670-MeV/A neon beam incident on 33 cm of water. Shown are the spectra obtained for the two detectors D_1 and D_2, respectively (XBL 8510-8536)

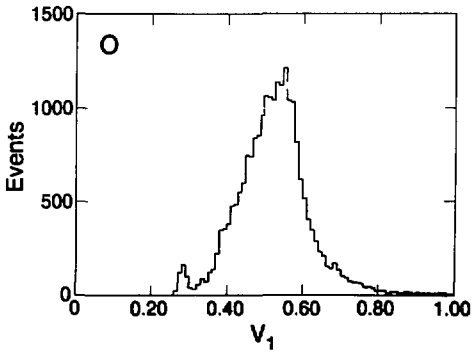

Fig. 3. Measured velocity spectrum of oxygen fragments. Velocity is expressed as a fraction of speed of light. (XBL 8510-8537)

The contribution to the total dose from the low-LET particles helium and hydrogen is expected to be small. If we assume ~6% combined contribution from these, as suggested by transport calculations,[3] the percentage contribution to the total

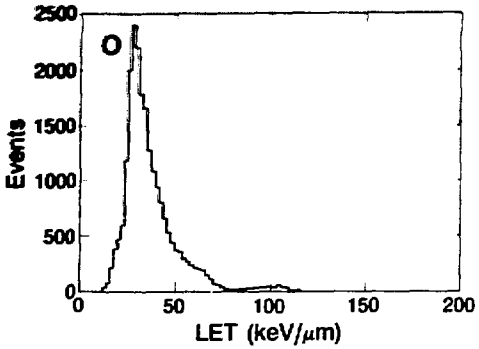

Fig. 4. The water-equivalent LET spectrum for oxygen derived from the charge and velocity measurements as discussed in the text. Such spectra can be displayed on-line during data acquisition. (XBL 8510-8538)

Table 1. Neon 670-MeV/nucleon dose at Bragg tail (33.01 cm H_2O).

Element	Z	Dose (Gy/incident ion)	% of total dose at tail	% of peak dose
F	9	$(1.55 \pm 0.30) \times 10^{-10}$	21.6 ± 4.3%	~6.3%
O	8	$(2.10 \pm 0.21) \times 10^{-10}$	29.3 ± 2.9	8.5
N	7	$(1.29 \pm 0.13) \times 10^{-10}$	18.0 ± 1.8	5.2
C	6	$(1.07 \pm 0.11) \times 10^{-10}$	14.9 ± 1.5	4.3
B	5	$(0.43 \pm 0.09) \times 10^{-10}$	6.1 ± 1.2	1.8
Be	4	$(0.20 \pm 0.04) \times 10^{-10}$	2.8 ± 0.6	0.8
Li	3	$(0.10 \pm 0.02) \times 10^{-10}$	1.4 ± 0.3	0.4
He	2		6.0 (assumed)	1.7
H	1		6.0 (assumed)	
				~29.0%

dose from each fragment is given by the second column of Table 1. The third column expresses these results as a fraction of the dose deposited at the Bragg peak. It is seen that the nuclear fragments fluorine, oxygen, nitrogen, and carbon completely dominate the high-LET contribution. The total dose contribution from all fragments amounts to ~29% of the peak dose, which support earlier predictions made on the basis of transport theory.[3]

REFERENCES

1. Wong, M., Schimmerling, W., Rapkin, M., Howard, J. High-energy heavy ion beams used in biology and medicine: Measurement of particles distributions in the fragmentation tail. Radiation Research Society, 33rd Annual Scientific Meeting, Los Angeles, May 5–9, 1985 (Abstract HF-3).
2. Schimmerling, W., Rapkin, M., Wong, M., Howard, J., Kaplan, S.N., Spieler, H.G., Jarrett, B.V. and Walton, J.T. Physical Characterization of Heavy-Ion Beams. Biology and Medicine Division Annual Report, Lawrence Berkeley Laboratory report LBL-16840, p. 77 (1984).
3. Wong, M., Schimmerling, W., Civello, J., Howard, J., Wilson, J.W., Townsend, L.W. and Bidasaria, H.B. Transport of High-Energy Heavy Ions through Extended Matter. Biology and Medicine Division Annual Report, Lawrence Berkeley Laboratory report LBL-16840, p. 85, (1984).

MULTIPLE COULOMB SCATTERING OF HEAVY IONS

Mervyn Wong, Mark Phillips, Walter Schimmerling, Don L. Murphy, and Cornelius A. Tobias

Multiple scattering processes affect dosimetry, performance, effectiveness, and resolution in the use of heavy-ion beams in radiotherapy (dose localization, critical structures, beam delivery systems), radiobiology (loss of particles to sample), radiological imaging (limits of resolution), and radioactive beams (optimization of target thickness). On the other hand, hardly any experimental data on heavy-ion multiple scattering exist. We have therefore initiated at this laboratory a systematic experimental investigation of heavy-ion multiple scattering with a variety of beams and targets.

The experimental method is summarized in Fig. 1. The angle between the incoming particle trajectory and the outgoing scattered particle trajectory is measured in three dimensions. The equipment consists of four sets of position-sensitive silicon detectors (PSD's), each set providing information on one pair of coordinates (x,y). The target is located between PSD sets 2 and 3. With the target removed, straight-through (collinear) tracks are used to measure the alignment and spatial resolution of the detectors. This experimental configuration measures the multiple scattering in the target only,

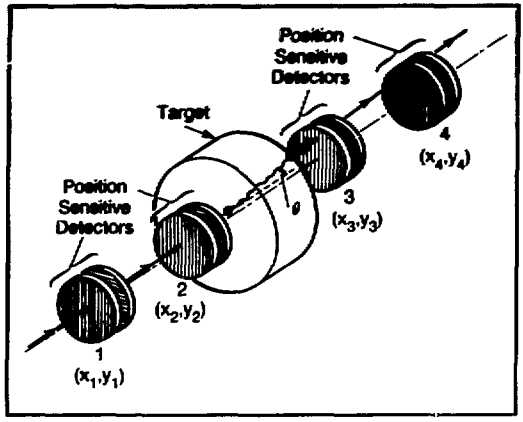

Fig. 1. Schematic diagram of experimental method to measure heavy-ion multiple scattering. Position-sensitive detectors 1 and 2 measure the incoming particle trajectory, detectors 3 and 4 the outgoing scattered particle trajectory. All detectors are lithium-drifted silicon. From the reconstructed particle trajectories, the target multiple scattering angle θ is determined. With the target removed, straight-through tracks serve to measure detector alignment and spatial resolution. (XBL 8510-8550)

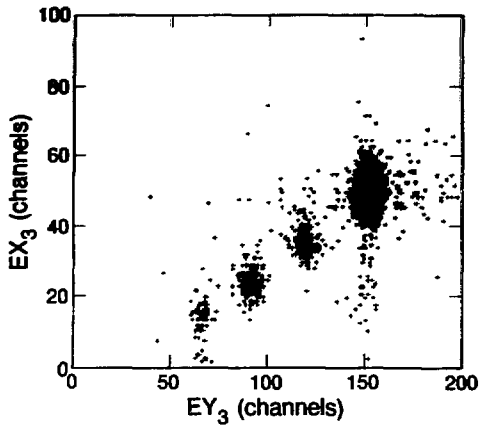

Fig. 2. Correlation in energy loss measured by two adjacent detectors downstream of a 10-cm water target for incident 670-MeV/A neon ions. Events in the upper right hand cluster correspond to primary beam particles and were selected as the outgoing particles for this experiment. Events in the other clusters correspond to projectile fragments. (XBL 8510-8548)

independent of beam collimators, absorbers, etc., placed upstream of it.

Each detector provides, on an event-by-event basis, measurement of particle energy loss in the detector. Eight separate detectors yield eight independent measurements of energy loss, and this information can be used to identify the incoming and outgoing particles.

Initial runs have been made with neon and iron beams in Cave II of the Biomed complex. Figure 2 shows the correlation in energy-loss measured by two adjacent detectors downstream of a 10-cm water target for incident 670-MeV/A neon ions. Events in the upper-right cluster correspond to primary beam particles. Events in the lower clusters are those in which the primary beam particle has changed identity as it traversed the target. Events wherein the identity of the primary particle is preserved during the scattering process, i.e., *elastic* multiple scattering, are selected in each measurement.

Figures 3a, b, c, and d show results for the scattering of 600-MeV/A Fe ions on a 1-cm thick brass target. Shown are the profiles for the coordinates (x_3, y_3) and (x_4, y_4) for the downstream PSD's 3 and 4. These profiles can be compared with measurements made with the same beam on a 5-cm thick Lucite target and with no target (straight throughs). Table 1 shows preliminary results for the full width at half-maximum of the emerging beam. For each coordinate dimension, the width increases monotonically, as is expected. Further, the *sensitivity* to measuring the difference in the amount of scattering from different materials is exhibited. We see that a difference in width of 5% from Lucite to brass can be detected.

High precision differential measurements of multiple scattering are planned to permit comparison with theoretical calculations of this fundamental electromagnetic process. For thin targets, we anticipate interesting interference effects with nuclear elastic scattering. In addition, for thick targets, we expect nuclear fragmentation processes to affect the angular distributions, especially for large angles.

Table 1. Full width at half-maximum (cm) for emerging, 600-MeV/a Fe beam.

	No target	Lucite (5 cm)	Brass (1 cm)
x_3	1.90	2.26	2.50
y_3	1.91	2.18	2.26
x_4	1.90	2.14	2.26
y_4	1.89	2.18	2.26

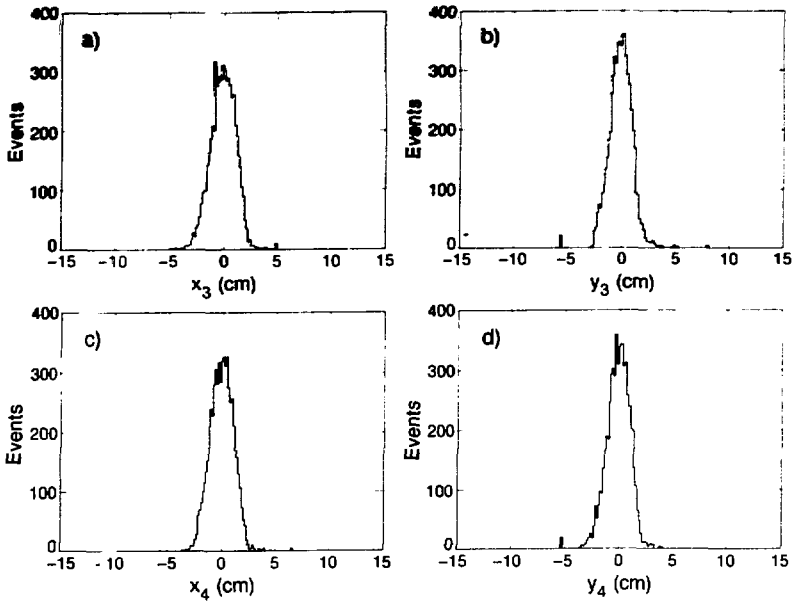

Fig. 3. Profiles for the (x_3,y_3) and (x_4,y_4) coordinates for the scattering of 600-MeV/A iron ions on a 1-cm thick brass target. *(XBL 8510-8535)*

^{16}O AND ^{56}Fe EXCITATION FUNCTIONS

John P. Wefel,* T. Gregory Guzik,* Henry J. Crawford,† Walter Schimmerling, Peter J. Lindstrom,† Douglas E. Greiner,† and T. James M. Symons†

The sources of radiation in space are the radiation trapped in the earth's magnetic field, solar particle radiation, and galactic cosmic rays. Man-made radiation may also be present. The cosmic radiation is fairly constant in time, both in its intensity and its composition. Solar flares have a cyclical activity; the particulate radiation dose cannot be predicted on a time scale greater than hours or days. The radiation field to which a space worker is exposed in the course of a mission will also vary greatly, depending on the geomagnetic location, shielding by the spacecraft or other structures, and the extent of extra-vehicular activities (EVA's).

Radiation dosimetry in space has a predictive function because the dose to space workers must be estimated before they are exposed, but it also has an archival function because the actual exposures must be known after they have occurred. Measurements of these exposures are not likely to be sufficient because of the temporal and spatial variations involved and because of the limitations of personnel dosimeters in measuring radiation quality. For this reason, space radiation dosimetry is likely to rely increasingly on calculations that are based on fundamental physical quantities, e.g., cross sections, cosmic-ray spectra, and so forth.

The energy spectra of the heavy elements in galactic cosmic rays increase from low energies to a broad maximum around 200–400 MeV/A, and then decrease with energy per nucleon approximately as $(E/A)^{-2.6}$. Thus, the energies of galactic cosmic rays fall well into the range accessible at the Lawrence Berkeley Laboratory Bevalac. In this energy region, the ranges of heavy nuclei in matter

*Louisiana State University
†Nuclear Science Division, LBL

(15–35 g/cm^2) become comparable to their mean free path for nuclear interactions. As a consequence, a significant fraction of the relativistic heavy-ion flux will undergo nuclear reactions in thick absorbers, e.g., shielding materials or tissue. When these reactions can take place anywhere in a thick absorber, it is necessary to know these quantities as a function of particle energy for all particles present. In the present context, the first problem to be solved is the measurement of the probability for emission of a given fragment, at a given energy, into a given angle, i.e., inclusive differential cross sections, and of the probability for any reaction of an incident projectile leading to its disappearance, i.e., total reaction cross sections.

Transport calculations of HZE particles depend fundamentally on a knowledge of inclusive fragmentation cross sections, i.e., the probability that the projectile suffers an interaction leading to a fragment (generally contained in a forward angle of ~3°) and residual particles. There are also interesting problems in astrophysics that depend on such cross sections.

The measurement of these cross sections can be somewhat simplified by an experimental design that does not require detection of the residual particles (i.e., an inclusive experiment). A program to measure excitation functions (differential inclusive cross sections as a function of projectile energy) using hydrogen as a target, has been initiated at LBL in collaboration with colleagues from Louisiana State University (LSU).

The experimental arrangement is shown schematically in Fig. 1. The beam leaves the accelerator ring and is magnetically steered through a beam transport system to the target. A series of scintillation counters monitor the beam position and intensity. Different targets are mounted on a remotely controlled drive that can change targets without breaking the seal on the vacuum tank. The fragments from beam interactions in the target appear in the cave, spread out according to their emission angle from the interaction site. A particle identification telescope is mounted in the cave such that it can be positioned within the main beam or at any desired angle on either side of the main beam. At large angles with respect to the beam, the high momentum tail of the momentum distribution can be examined in detail.

The particle identification telescope, shown in Fig. 2, consists of a stack of solid-state detectors in which the particles are brought to rest to determine their atomic mass. The telescope consists of three pairs of position-sensitive detectors (PSD's) and 30 5-cm-thick lithium-drifted silicon detectors. The

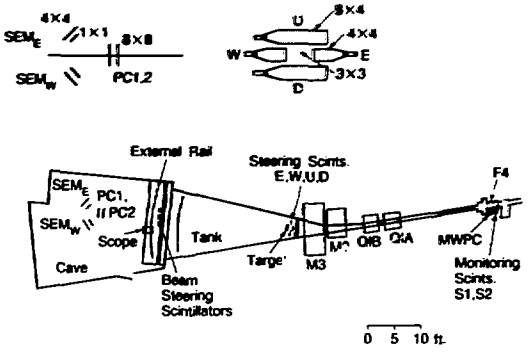

Fig. 1. Schematic diagram of the experiment arrangement for Experiment 683H showing the beam monitoring.

(XBL 8510-8534)

total thickness of the telescope is sufficient to bring to rest heavy fragments from the interaction of approximately 375-MeV/A ^{16}O nuclei. The PSD's are employed to localize each event, in order to give fine positioning and to measure the trajectory through the stack to correct for events entering or leaving the sides of the telescope. All detectors are parallel to each other within ± 3°. An external pulser circuit into each preamplifier allows for individual calibration of the amplifier gains. The external pulser provides a monitor of each of the signal processing chains throughout the experiment.

The advantages of the arrangement shown in Fig. 1 are 1) minimum material along the beam line between target and telescope, 2) good spatial separation to measure the angular distribution of the fragments, 3) a well understood mass-determining technique, and 4) capability to use high beam rates for the large angles at which the telescope is outside of the main beam. The disadvantage is that the arrangement assumes a constant

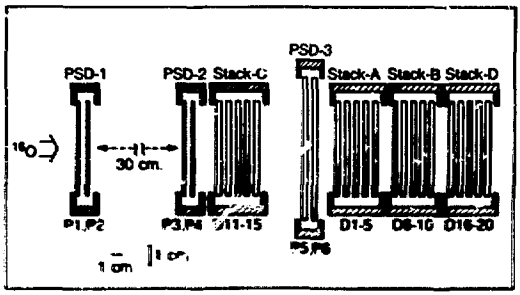

Fig. 2. The solid state detector telescope

(XBL 8510-8583)

beam location, i.e., stability of the magnets along the B4C line, and of magnets M2 and M3 in particular. We are working on methods to ensure accurate beam positioning.

An initial data-taking run was performed in March 1984. The data analysis is still in progress, but preliminary results, discussed below, indicate that the experimental technique can give the needed high-quality data. Unfortunately, there were problems with the beam delivery system and the magnet power supplies during the March run that limited the amount of data per beam hour that could be obtained. Solutions have been found for these difficulties, and the beam time needed to acquire the data to meet our objectives has been scheduled for April 1986.

Our first run employed a 225-MeV/A ^{16}O beam to study fragmentation in targets of carbon and polyethylene plus a blank target holder. Runs were taken at 0°, 0.5°, 0.75°, 1.0°, 1.75° and 2.75° to the beam direction. Figure 3 shows an example of the mass histograms derived from this initial data set. The top portion shows the isobaric mass histograms of $A \geq 10$ while the lower plot shows the results for carbon. Note that mass peaks for ^{10}C through ^{14}C are resolved but the abundance of ^{10}C is, as expected, quite low. From the figure the isotopic mass resolution is of the order of 0.2 mass units. This should improve as energy resolution and trajectory information is refined. Figure 4 shows preliminary results for the angular distribution of the carbon fragments produced by the incident oxygen beam in the carbon target.

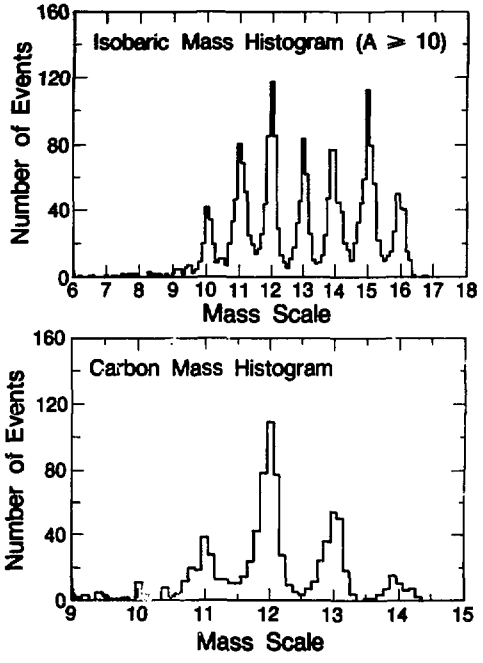

Fig. 3. Mass histogram obtained at 1.75° to the beam direction. The top portion shows the isobaric plot for $A \geq 10$ and the lower part shows the mass distribution for the element carbon.
(XBL 8510-8531)

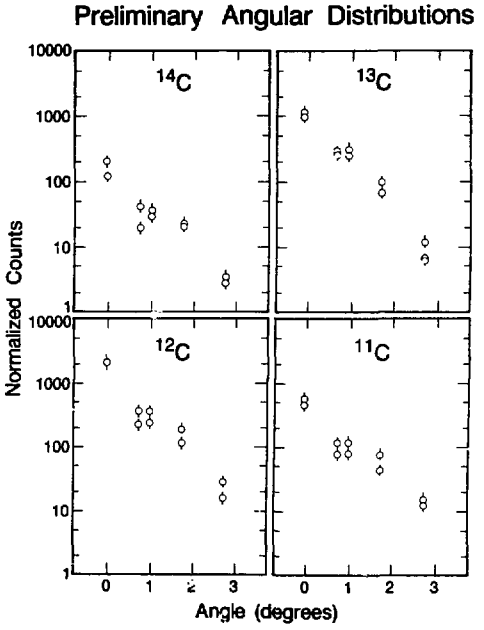

Fig. 4. Preliminary results for the angular distribution of carbon isotopes from oxygen fragmenting in a carbon target.
(XBL 8510-8532)

BERKLET UPGRADE: IMPROVED DETECTION OF LOW LET PARTICLES IN HIGHLY FRAGMENTED HEAVY ION BEAMS

Jorge Llacer,* Julius J. Almasi, and Cornelius A. Tobias

The BERKLET is a simple solid state detector telescope that was developed to measure the LET and the relative number of particles of different atomic numbers in heavy-ion beams under conditions of complex primary beam fragmentation.[1] It consists of a thin silicon radiation detector that measures the LET of individual incoming particles followed by a thick germanium detector where the particles stop and deposit their residual energy. The data from the BERKLET is displayed in a two-dimensional histogram of LET and residual energy that, with some limitations, determines the atomic number of the particles in a beam. Track and dose-average LET values can be calculated for individual particles or for groups of particles, and particle velocities can be approximated.

We have recently made BERKLET measurements in neon-20 beams for the purpose of determining accurately the contribution to beam characteristics from low-LET particles in the fragmented beams. The frequency and LET range of this component of the beams could not be determined with the early design of the BERKLET. During the past year, we have been able to redesign the silicon detector in the telescope to allow for routine measurement of the low-LET part of the beam concurrent with measurement of complex high-LET components.[2]

The original silicon detector consisted of a single wafer of 300-μm thickness divided into two regions, a center "active" region, (Fig. 1, left) surrounded by a "guard" region that provided signals for the logic operations and that defined the area over which the measurement was being made. The edges of silicon detectors give erroneous results and have to be collimated electronically. The LET ratio of a silicon particle near its stopping point and that of a fast proton is of the order of 2500:1. The dynamic range of such measurements creates a difficulty. Even with a specially-designed event discriminator that would perform well under such a wide range of operating conditions, we had a problem with electronic interference between the two regions of the detector. When a heavy ion would traverse the guard region, a small signal would be induced in the "active" region. That signal would

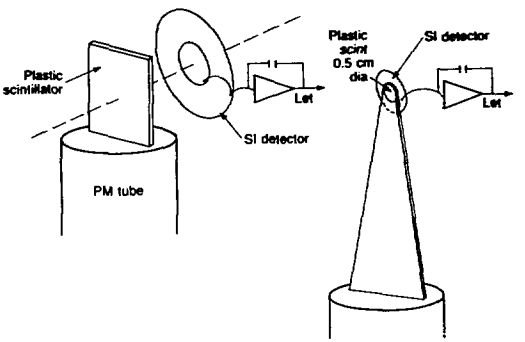

Fig. 1. Test design of new LET detector configuration and new final design. *(XBL 857-11241)*

appear to the electronic circuits as a light particle. There was no way, then, to determine whether a small signal was from a real particle or if it was an induced signal from a high-LET event in the guard region.

To correct the problem, we have devised a new first detector consisting of a thin small-diameter plastic scintillator (Fig. 1, right) followed by a 300-μm silicon detector, without a guard ring. By requiring a coincidence measurement from each of the two detectors, we define the active region of the LET detector without cross-interference, and we obtain an added advantage: the discriminator thresholds of both the plastic scintillator and of the silicon detector can be lowered until the respective noise sources are exposed. When we require a coincidence between the two detectors, the noise disappears for all practical purposes, and the signals of the very low-LET particles can be unambiguously discriminated.

A preliminary experiment has been completed to test the new design with our available equipment. A thin plastic scintillator was placed in front of the original silicon BERKLET detector, and in spite of the incorrect geometry, we have been able to analyze the results successfully. Figure 2 shows a comparison of Bragg ionization measurements made in a neon-20 beam with either the standard ionization chambers (solid line) or the BERKLET (circles). We studied the configuration of absorbers in the beam used for the cancer therapy trials, without

*Engineering Division (Instrument Science and Engineering Department), LBL.

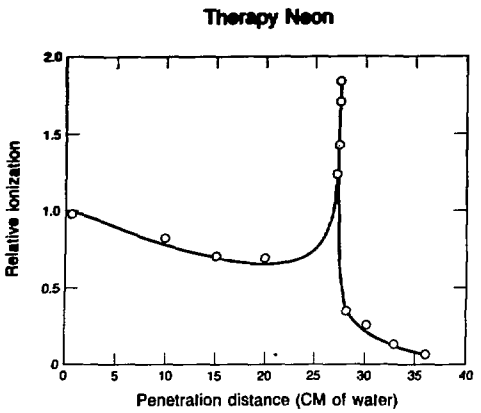

Fig. 2. Bragg curve comparison: ion chamber vs. BERKLET for therapy neon beam, without range modulation filter.
(XBL 857-11238)

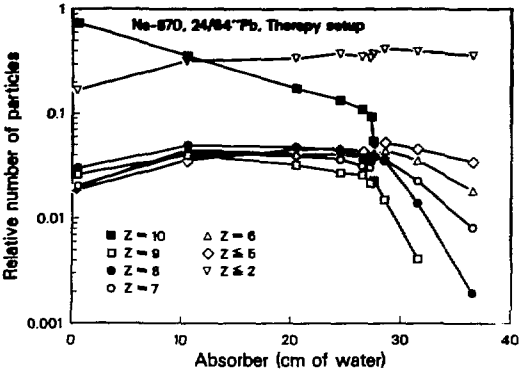

Fig. 3. Relative number of particles vs. H_2O thickness depth o penetration in water for the same neon beam of Fig. 2.
(XCG 855-215)

the range modulating ridge filter. The BERKLET results are obtained from the measured number of particles of a given atomic number and their average LET value, and include particles with LET values as low as 0.17 keV/μm.

Figure 3 shows the relative number of particles in the beam as a function of the thickness of water absorber. The presence of large numbers of low-LET particles, ($Z \leq 2$ in the figure) is confirmed, although their contribution to the total dose is small. Their presence causes little change to the calculation of the dose-average LET, but modifies considerably the track-average LET values. We expect that the completion of the modifications to the BERKLET will permit rapid optimization of clinical heavy-ion beams and also will allow an analysis of particle-beam composition and track-structure effects on biological systems, which can be compared to time-of-flight measurements of particle distributions.

REFERENCES

1. Llacer, J., Tobias, C.A., and Holley, W.R. On-line characterization of heavy-ion beams with semiconductor detectors. *Med. Phys. 11*(3), 266–278 (1984).
2. Llacer, J., Tobias, C.A., and Almasi, J.J. Low LET particles in heavy ion beams, Radiation Research Society Meeting, May 5–9, 1985, Los Angeles, California. (Abstract).

CARBON PROTON BEAM COMPARISONS

Cornelius A. Tobias, Eleanor A. Blakely, William T. Chu, Bernhard A. Ludewigt, and Julius J. Almasi

Based on research with proton beams at Harvard[1–3] and helium beams at Berkeley,[4–6] there has been a general recognition of the value of highly localized particle beams for therapy. The treatment of ocular melanoma, juxtaspinal tumors, pituitary and AV-malformations are examples. A committee of the American College of Radiology has reviewed this matter recently.[7] As a result, a number of laboratories are planning to propose the construction of proton accelerators; however, we have not been able to find any direct comparisons of protons and heavy ions under strictly identical conditions.

Based on theoretical considerations and on results obtained from two preliminary Bevalac

experiments, we have tentatively confirmed our hypothesis that carbon and neon beams are potentially better for beam localization than protons or helium ions of comparable range. When a small beam is used, multiple scatter broadens the beam as it penetrates an absorber. The scattering for carbon beams is about $\sqrt{12}$ times less than for proton beams. The same can be said for the straggling. The end result is that the Bragg peak/plateau ratio is reduced for protons much more than for carbon, and the proton beam is physically broadened. Figure 1, which is a plot of Bragg peaks from Bevalac carbon (308 MeV/u) and proton (155 MeV/u) beams extracted at energies that yield 15 cm penetration into tissue equivalent material, illustrates this point. The small circular data points were taken with a large (2.0-cm diameter) beam downstream of a 1-cm collimator. The solid square symbols represent Bragg data taken with a small (0.4-cm diameter) beam downstream of a 1-cm collimator. The carbon Bragg curves of the large and small beams are identical, while clear differences are shown between the large and small diameter proton beams. The Bragg peak of the smaller diameter proton beam is degraded in comparison to the larger diameter proton beam.

The same point is obvious from Fig. 2. Two linear arrays of polaroid beam spots are shown, the top set from a 20-rad (plateau dose) carbon exposure, the lower set from an 8-rad proton exposure. Water-filled tissue culture flasks were sandwiched between the polaroids during the exposure. The most extreme left polaroids are in the entrance plateau of the beam. The most extreme right polaroids are in the Bragg peak. At this depth, the carbon beam is still well-defined while the proton beam is not.

Further experiments are planned with Bevalac protons and carbon-ion beams to evaluate the importance of multiple scattering to the successful delivery of sharply-defined and narrowly-collimated dose distributions at clinically significant depths of penetration for the treatment of eye tumors and brain lesions.

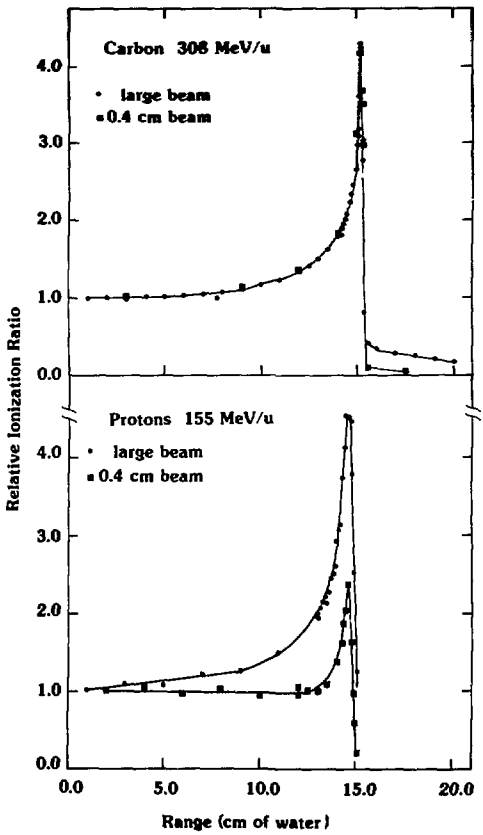

Fig. 1. Comparison of Bragg ionization curves from large beam (2-cm diameter) and narrowly collimated (0.4-cm diameter) proton (155 MeV/u) and carbon (308 MeV/u) Bevalac beams.
(XBL 853-3340)

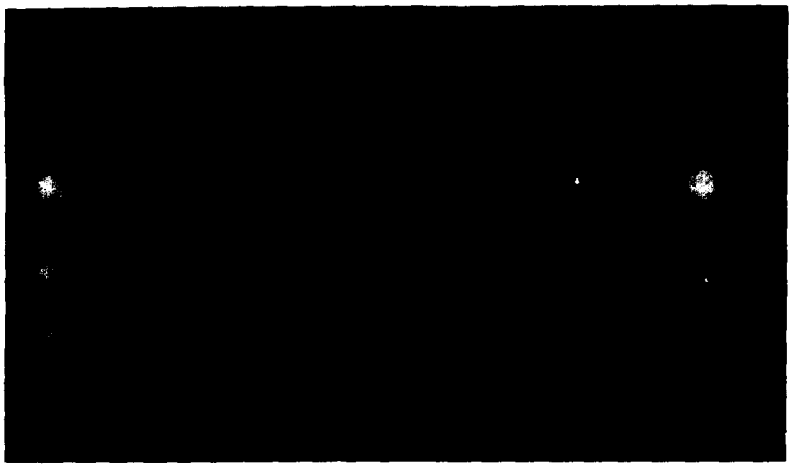

Fig. 2. Polaroid beam spots from a 20-rad (plateau dose) carbon 308-MeV/u exposure and an 8-rad (plateau dose) proton 155-MeV/u exposure. The description of the experiment can be found in the text. (XBB-858-6040)

REFERENCES

1. Munzenrider, J.E. Proton therapy at Harvard. *Pion and Heavy-Ion Radiotherapy, Preclinical and Clinical Studies* (L.D. Skarsgard, Ed.) 363–372, July 1981.
2. Koehler, A.M. Use of protons in radiotherapy. In *Proceedings of the Symposium on Pion and Proton Radiography,* National Accelerator Laboratory, Batavia, Illinois, pp. 63–88 (1971).
3. Verhey, L.J., and Munzenrider, J.E. Proton beam therapy. *Ann. Rev. Biophys. Bioeng.* (in press).
4. Saunders, W.M., Castro, J.R., Quivey, J.M., Chen, G.T.Y., Lyman, L.T., and Collier, J.M. Clinical experience with heavy-ion beams at Lawrence Berkeley Laboratory, *Pion and Heavy-Ion Radiotherapy: Preclinical and Clinical Studies* (L.D. Skarsgard, Ed.) 373–394 (July 1981).
5. Castro, J.R., and Quivey, J.M. Clinical experience and expectations with helium and heavy-ion irradiation. *Int. J. Radiat. Oncol. Biol. Phys. 3,* 127–131 (1977).
6. Phillips, T.L., Fu, K.K., and Curtis, S.B. Tumor biology of helium and heavy ions. *Int. J. Radiat. Oncol. Biol. Phys. 3,* 109–113 (1977).
7. *Cancer Treatment Symposia,* Vol. 1 (Robert E. Wittes, Ed.) pp. 1–191 (1984).

Molecular Studies

DETECTION OF RADIATION INDUCED LESIONS AT THE MOLECULAR LEVEL

Ruth J. Roots, Gianfranco Grossi, and Cornelius A. Tobias

We have begun studies of radiation-induced changes in specific genes of mammalian cells, in particular with respect to genetic changes in cells transformed by high-LET radiation. Alterations in the protooncogenes are associated with neoplastic growth characteristics. In normal cells, certain protooncogenes function in DNA synthesis control, as for example the c-myc gene, while others may code for gene products that are components of growth factors or growth factor receptors.

To screen for genetic abnormalities following radiation, gene location is compared in normal and

transformed cells. Secondly, gene expression levels are measured in normal and transformed cells.

Figure 1 shows the karyotype of male muntjac cells. There are three pairs of chromosomes plus the Y chromosome. This cell line was chosen in preliminary work because of the low diploid chromosome number; primary cultures of normal diploid hamster embryo cells are now used. Chromosome spreads were made of cells harvested from mitotic selection. Following fixation of the cells, metaphase spreads were made, and the chromosomes were then G-banded.

We have chosen to study genetic changes in the c-myc protooncogene following radiation-induced cell transformation. Other protooncogenes may also be studied, but we have elected to begin our screening process with c-myc. The *in-situ* hybridization technique of the hybridization of a ^{3}H-labeled v-myc probe to chromosome spreads used in combination with chromosome banding can be used to identify the c-myc locus. This technique can, therefore, be used to identify gross abnormalities in a specific gene locus. It is expected that c-myc is present as a single copy. The *in-situ* hybridization technique that we are using is, however, capable of locating single-copy gene sequences. The value of the *in-situ* hybridization technique is that a gene locus can be assigned to a specific band on a specific chromosome.

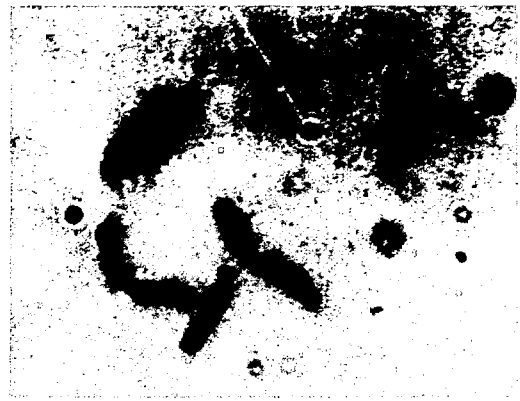

Fig. 1. Karyotype of the Muntiacus muntjak male deer cell (2N−7) showing G-banding patterns. (XBB 854-2848)

The results of *in-situ* hybridization of ^{3}H-labeled v-myc (1.5 kbp) to unirradiated muntjac chromosome spreads are shown in Fig. 2A and 2B. The autoradiogram Fig. 2A was obtained from a one-week's exposure to the emulsion, while Fig. 2B is from a two-week's exposure. The v-myc hybridization appears to be on chromosome number 1; however, we have not yet made a systematic study of grain localization to identify the exact band position, and we regard these data as preliminary.

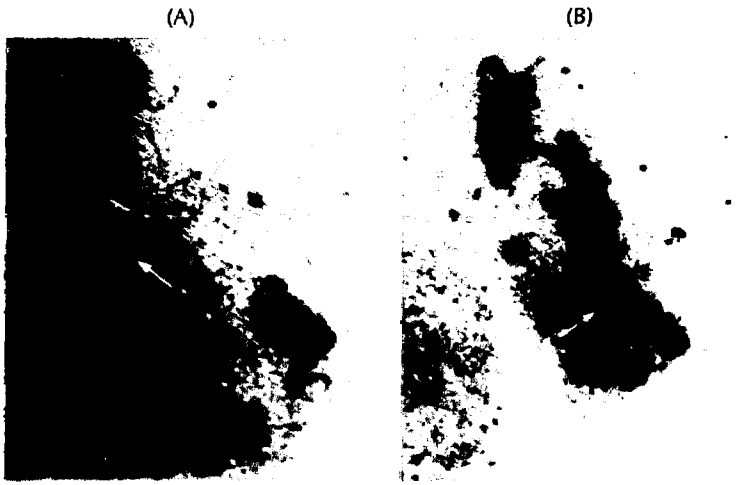

Fig. 2. In situ hybridization of ^{3}H-labeled v-myc to unirradiated muntjac chromosome spreads. (A) 1-week exposure; (B) 2-week exposure. (XBB 854-3535A)

PRODUCTION OF STRAND BREAKS IN DNA BY WATER RADICALS: A THEORETICAL STUDY

Aloke Chatterjee, John L. Magee, Patrice Koehl, and William Holley

Starting with the physical phenomena of energy deposition by ionizing radiation, we are attempting to develop an understanding of the mechanisms of radiation damage in living cells. Such an understanding is essential for 1) better protection against radiation as an environmental hazard, 2) an intelligent use of radiation as a diagnostic tool, and 3) treatment optimization for cancer patients undergoing radiation therapy.

The initial phase of energy deposition in a cell ($\sim 10^{-16}$ sec), leads to a series of physicochemical ($10^{-16} - 10^{-12}$ sec), chemical ($\sim 10^{-12} - 10^{-6}$ sec), and biochemical ($10^{-9} - 10^{-3}$ sec) changes that eventually produce observable biological (seconds to years) damage. For a better understanding of the mechanisms of radiation damage these changes must be correlated both qualitatively and quantitatively and an effective research program must include coordinated theoretical and experimental studies. Obviously the task is a difficult one and a major effort is needed to achieve this goal. We have initiated such a program with the participation of physicists, chemists, and biologists working in a collaboration.

The human cell is a highly organized and complex system, and although we understand a great deal about its response to various kinds of damage by ionizing radiation, there are many phenomena that still remain obscure. It was therefore decided that at the initial phase of our effort a much simpler system should be used. This simpler system must, of course, be relevant and mimic the actual living cell in terms of radiation damage. Simian virus (SV40) DNA in dilute aqueous solution with Tris as a buffer seemed to meet our requirements and was chosen for the initial studies.

Just like DNA in a cell, the SV40 DNA molecule in aqueous solution can be damaged by two different mechanisms: indirect effect and direct effect. The indirect effect generally means that radiation interacts with the surrounding water molecules, creating hydroxyl radicals that eventually damage the DNA. In contrast, damage due to the direct effect is caused by the direct deposition of energy in the DNA molecule. We have made significant progress in understanding indirect effects with respect to SV40 DNA and this is the subject of this article. The direct effect is under investigation and progress will soon be the subject of another report.

Although we have made a large number of experiments with different qualities of radiation using SV40 DNA solutions, our primary focus is on the theoretical development of this system. Experimental results are necessary for verification of the models introduced in the development. Understanding requires both theoretical and experimental aspects.

There are four main stages in our theoretical approach:

(1) Simulation of the SV40 DNA molecule through a computer code according to its stereochemical parameters obtained from x-ray diffraction studies.
(2) Location of the hydroxyl (·OH) radicals around the DNA as they are created in the tracks of the ionizing radiation.
(3) Following of each ·OH by simulation of its diffusive motion in the medium and calculation of its reactions.
(4) Use of computer graphics as an aid in the qualitative understanding of the diffusion and reaction processes mentioned above.

The calculation of the reactions of the OH radicals is the most important and difficult task. There are three reaction channels:

(1) Reaction with the other water decomposition products: ·H, e_{aq}^-, H_3O^+ and other ·OH's.
(2) Reaction with the Tris buffer.
(3) Reaction with the DNA molecule.

When an ·OH radical reacts with a DNA molecule, it can either react with the ribose phosphate backbone or with the bases. If it reacts with the ribose moiety a strand break results and if both strands are broken close to each other then there is a double strand break. Reactions of ·OH with the bases do not lead to strand breaks, but other biological effects, such as mutation, base release, etc., are expected.

We have simulated the diffusion of ·OH by a Monte Carlo code that we developed. A result of our code is shown in Fig. 1 for a case where a ·OH

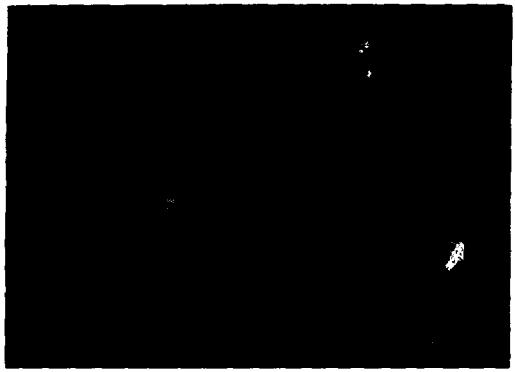

Fig. 1. Computer calculation of the diffusive motion of an ·OH radical that reacts with the ribose moiety of a DNA molecule. The radical is formed by the action of a 14-MeV electron at the extreme left of the figure and its subsequent motion is indicated. Radicals formed at the same position have an infinite variety of patterns of motion and from many calculated paths we have selected one that leads to reaction with the DNA. The reactive sites on the ribose moieties of the DNA are indicated by spheres; the reactive sites on the bases have much larger reaction radii and the overlapping reaction sphere are indicated by the pattern of small dots. Other possible reactions of the ·OH radical are with other water radicals (e^-_{aq}, ·OH, ·H) or with the buffer. Actually for most of the many possible diffusive paths the radical moves away from the DNA and reacts with a buffer molecule (Tris). (CBB 857-5204)

interacted with a sugar molecule on the DNA backbone. This particular radical could have gone in any direction with equal probability. There is no rule that it must go toward the DNA. The part of the SV40 DNA molecule represented in the same figure is in its B form and its stereochemical parameters have been obtained from x-ray diffraction patterns.

Through a large number of trials in our VAX computer we have obtained some meaningful average quantities that could be checked with experimental measurements. For example, we have been able to calculate the D37 (dose required to produce damage in 63% of the DNA molecules) for single-strand breaks for a 14-MeV electron beam, 500-MeV/n and 10-MeV/n neon beams. When compared with experiments, the agreement is quite reasonable and gives us a confidence in our approach. For 14-MeV electron irradiation, it has been determined that about 80% of ·OH radicals attack the bases and about 20% of them interact with the sugar molecules.

The next stage is to introduce more complexities by adding histones and other proteins along with the DNA. We also expect to bring in enzymes that have the capability to repair strand breaks as found in cells. When we understand to a reasonable degree the processes involved in repair chemistry we hope to be ready to deal with the complexities of a cell.

A STEREOCHEMICAL MODEL FOR THE REACTIONS OF DNA WITH THE HYDROXYL RADICAL

William R. Holley, Patrice A. Koehl, Aloke Chatterjee, and John L. Magee

INTRODUCTION

Ionizing radiation creates damage in DNA molecules in aqueous solution by two mechanisms: either the DNA itself absorbs the energy and suffers the damage directly (direct effect), or the molecules of water absorb the energy and the radiation products formed react with the DNA (indirect effect). For dilute aqueous solutions of viral DNA the damage is mainly indirect, and the OH radical is generally believed to be the major contributor to the production of strand breaks on the DNA.

It has been experimentally demonstrated that the rate constants for the reactions of the various radical species with DNA are, in general, much lower than those for reactions with the isolated monomer unit. In order to understand the mechanisms of this effect, we have studied separately the action of OH on DNA and on isolated bases from a theoretical point of view.

The system we have chosen for study is dilute aqueous solutions of Simian Virus 40 DNA. Tris buffer is used to maintain proper DNA conformation and as a scavenger of OH radicals. This system is convenient because there is a reliable method for experimental determination of the

strand breaks occurring after irradiation, and the average migration distance (150 Å) for OH radicals in low Tris buffer concentration (10^{-2} mole l^{-1}) is in the domain of interest for a mammalian cell (90 Å).

In the theoretical investigations discussed here the diffusion of OH and its reactions with a sugar or a base are assumed to follow the Smoluchowski theory. Two particles A and B diffusing in a solution are considered as having reacted with unit probability if they come within a distance R_{AB}, called the "reaction radius," of each other. We attribute to each sensitive site on the DNA a reaction radius that can be calculated from known values for the rate constants.

CALCULATIONS

Using the stereochemical parameters of the DNA, obtained from crystallographic data, a 3D representation of the sensitive sites of the DNA is constructed. Nucleotides are built using the coordinates of each atom, and 2,000 different base pairs are constructed as shown in Figure 1. OH radicals formed by the radiolysis of the water are uniformly created in 3D three-dimensional space around this molecule, and their diffusion is simulated by a Monte Carlo technique. Each radical is followed separately till it reacts, either with another radical or with a Tris molecule, or with the DNA. We keep a record of how many radicals have reacted with a sugar moiety and how many have reacted with a base. The reaction probability P_r is then calculated as the ratio of successful events to the total number of events, and from P_r the average number of reactions per kilorad and the corresponding D_{37} value are calculated.

The case of the isolated ribose or base has also been considered. It is simpler because there is only one reaction radius, but the overall calculation procedure remains the same. A typical base is simulated as a central point surrounded by a sphere whose reaction radius has been determined to be 4 Å from experimentally observed rate constants. The diffusion of the radicals and their reactions are studied with the procedure described above.

In the theoretical analysis of the diffusion process it is well known that there is an extended region of influence around a particle beyond the "reaction radius" that affects the local concentration of interacting particles. A time-dependent rate constant can be introduced to take this effect into account. Suitably averaging this rate constant over time yields an "effective" rate constant that can be compared with experiment.

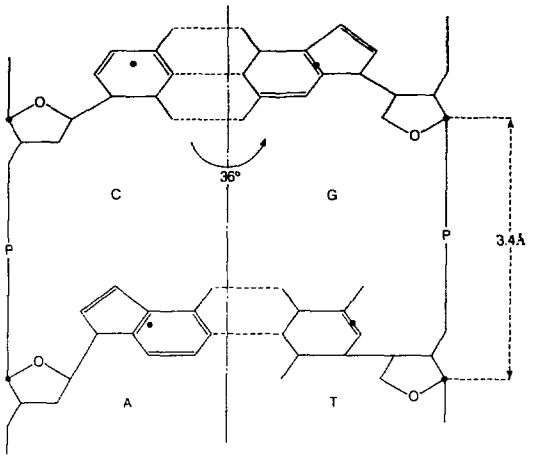

Fig. 1. Two consecutive base pairs of a DNA molecule taken from a stereochemical model are presented here. The guanine cytosine stack has been rotated through 36° and projected on the plane containing adenine-thymine. The reaction centers that we use have been indicated by dots. (XBL 858-3355)

RESULTS

Table 1 summarizes the values found for the time-averaged rate constant of OH-base reactions for different buffer concentrations. For the isolated monomer all these values are around 6×10^9 l mole^{-1} s^{-1} as expected. The variation of the effective rate constant $k_{OH-base}$ with buffer concentration is explained by the effects of the time-dependent rate constant; the higher the buffer concentration the shorter the average OH lifetime and the more important are the enhanced contributions of the time-dependent rate constant at short times to the effective rate constant.

Table 1. Effective rate constants for OH-Base and for OH-DNA reactions.

C_s (mole l^{-1})	$k_{OH-Base}$ (l mole^{-1} s^{-1})	$k_{OH-DNA}/Base$ (l mole^{-1} s^{-1})
10^{-3}	5.9×10^9	3.6×10^8
5×10^{-3}	6.0×10^9	4.4×10^8
10^{-2}	6.0×10^9	5.2×10^8
2×10^{-2}	6.2×10^9	5.9×10^8
4×10^{-2}	6.5×10^9	7.0×10^8
8×10^{-2}	6.8×10^9	8.4×10^8

A time-varying rate constant theory for reactions with DNA has not yet been formulated, but in terms of an effective time-averaged rate constant we find the values for k_{OH-DNA} *per base* summarized in the last column of Table 1. These results show a strong dependence on scavenger concentration, again reflecting the effects of an extended region around the DNA where the local concentration of interacting radicals is affected by the DNA molecule itself. Here the effects are even more pronounced than in the isolated monomer case because the interacting region is much larger, due to the combined effects of nearby reaction sites.

Another feature to be noted is that the effective rate constants *per base* from the DNA calculation are reduced by a factor of 10 or more compared to the values assumed for the individual reaction sites or obtained in the isolated monomer calculation. The reason for this reduction is that each reaction site in the polymer is shielded by nearby sites that intercept some of the OH radicals preventing their subsequent reaction with the site in question. The overall interaction rate is thereby reduced and the corresponding reaction rates are lowered in agreement with experimental results.

Cellular and Tumor Radiobiology

NEOPLASTIC CELL TRANSFORMATION BY HEAVY ION RADIATION

Tracy Chui-hsu Yang, Laurie M. Craise, Mantong Mei, and Cornelius A. Tobias

The major objective of the present project is to understand the potential carcinogenic effects of cosmic rays and the mechanisms of radiation-induced cell transformation. During the past several years, we have studied the relative biological effectiveness of heavy ions with various atomic numbers and linear energy transfer (LET) on neoplastic cell transformation and the repair of transformation lesions induced by heavy ions in mammalian cells.[1] All these studies, however, were done with high dose rate. For risk assessment, it is extremely important to have data on the low-dose-rate effect of heavy ions. Recently we initiated some dose-rate studies with high-LET iron particles and observed an enhancement effect of low dose rate.

For x and gamma rays, many biological effects, e.g., cell killing, are dose-rate dependent. The effects of low dose rate are usually smaller than those of high dose rate. The effect of gamma rays on cell transformation has also been found to be dose-rate dependent. For a given dose, the transformation frequency of low dose rate is lower than that of high dose rate.[2] In contrast to low-LET radiation, there are some data to show that low-dose-rate fission neutrons can enhance the cell transformation significantly.[3] At present, there is no satisfactory explanation for the enhancement effect of a low dose rate of neutrons on neoplastic cell transformation. Because fission neutrons have a mixed-LET spectrum, it is unknown how the enhancing effect depends on LET and what its mechanisms are. The capability of the Bevalac in accelerating heavy ions with various charges to different energies provides an opportunity to study the dependence of enhancement effect on LET. With confluent cultures of the C3H10T1/2 cell line, we have recently initiated some studies on the low-dose-rate effect of high-LET particles on cell transformation. Figure 1 shows the results obtained for cell killing. There was no significant difference between cells irradiated with low- and high-dose-rate iron particles (600 MeV/u; ~200 keV/μm). For cell transformation, however, confluent cells irradiated with 2-rad/min iron particles gave a significantly higher transformation frequency than those irradiated with 100-rad/min iron beam, as shown in Fig. 2. The enhancement effect was greater at lower doses than at higher doses. For example, the transformation frequency for 50 rad of low dose rate iron particles was about the same as that for 100 rad of high dose rate. The transformation frequency of dose 175 rad of low dose rate was, however, no higher than that for 250 rad of high dose rate.

These results, although preliminary, indicate that high-LET heavy ions may enhance cell transformation at low dose rate as fission neutrons. We

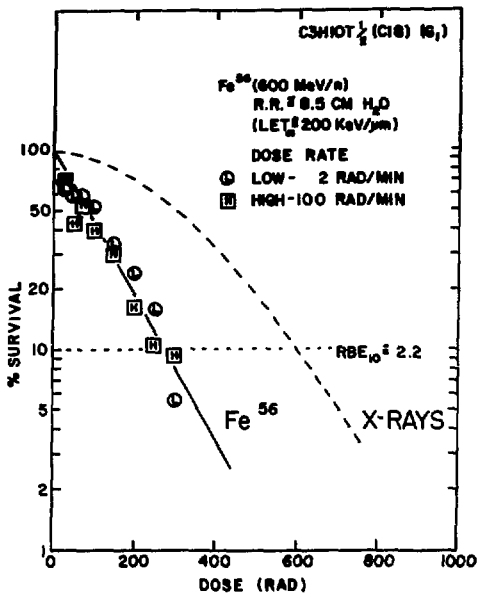

Fig. 1. Dose response curves for confluent C3H10T1/2 cells irradiated with 2-rad/min or 100-rad/min iron particles (600 MeV/u; 200 keV/μm). (XBL 859-3858)

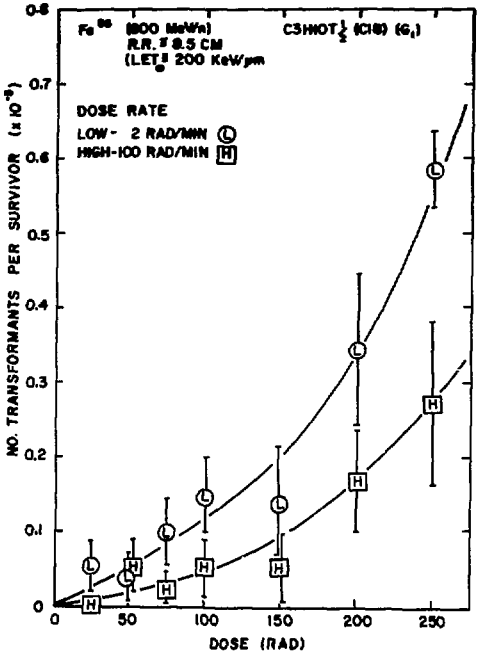

Fig. 2. An enhancement effect of a low dose rate of iron particles on cell transformation. Confluent C3H10T1/2 cells irradiated with a low dose rate (2-rad/min) showed a significantly higher transformation frequency than those exposed to high-dose-rate iron particles (100 rad/min). (XBL 859-3859)

are continuing to investigate the low-dose-rate effects of heavy ions with various LETs on cell transformation and will study the role of repair and track structure in the enhancement effect. Information collected from these studies should help us in understanding the fundamental mechanisms of the low-dose-rate effect of ionizing radiation.

REFERENCES

1. Yang, T.C., Craise, L.M., Mei, M., and C.A. Tobias. Neoplastic cell transformation by heavy charged particles. *Radiat. Res. 104* (1985) (in press).
2. Han, A., Hill, C.K., and Elkind, M.M., Repair of neoplastic transformation damage following protracted exposure to ^{60}Co gamma rays. *Br. J. Cancer 49*, Suppl. 4, 91–96 (1984).
3. Hill, C.K. Buonagurs, F.M., Myers, C.P., Han A., and Elkind, M.M. Fission-spectrum neutrons at reduced dose rates enhance neoplastic transformation. *Nature 298*, 67 (1982).

CHEMICAL MODIFICATION OF NEOPLASTIC CELL TRANSFORMATION BY HEAVY ION RADIATION

Tracy Chui-hsu Yang, Laurie M. Craise, Mantong Mei, and Cornelius A. Tobias

The objective of this project is to obtain quantitative data on the chemical modification of neoplastic cell transformation by heavy-ion radiation, using in-vitro cell transformation technique. The specific aims are 1) to test the potential effects of various chemicals on the expression of cell transformation, and 2) to systematically collect information on the mechanisms of expression and progression

of cell transformation by ionizing radiation. Our recent experimental studies with DMSO, 5-azacytidine, and dexamethasone suggest that DMSO can effectively suppress the neoplastic cell transformation by high-LET radiation and that some nonmutagenic changes in DNA may be important in modifying the expression and progression of radiation-induced cell transformation.

Experimental observations on the modulation of radiation cell transformation indicate that the process of neoplastic cell transformation is a complicated one and includes at least two different states: induction and expression. The induction is a relatively short one and may be complete after one cell division. The expression stage, however, will usually take several weeks and can be modulated by various physical and chemical agents. In our laboratory we have observed and reported earlier that fungizone (amphytericin B), an antibiotic for fungus, and dimethyl sulfoxide (DMSO) can decrease the frequency of cell transformation by x rays.[1,2] Even many days after x-irradiation, the presence of a low concentration of DMSO can significantly inhibit the neoplastic cell transformation by radiation. It was unknown, however, whether DMSO would have a similar effect on cells irradiated with high-LET radiation. Recently we did cell transformation experiments with energetic iron particles (300 MeV/u; ~500 keV/μm) and found a significant decrease of cell transformation frequency in cells irradiated and treated with 0.5% DMSO for 1 week, starting 10 days after irradiation (Fig. 1). DMSO appears, therefore, very effective in suppressing the cell transformation by low- and high-LET radiation.

How DMSO suppresses the expression of radiation-induced cell transformation is an interesting question. There are several possible mechanisms: 1) altering the cytoplasmic membrane structure and functions, 2) acting on DNA to induce cell differentiation, and 3) reducing cellular free radicals that may promote the expression of cell transformation. For a better understanding of the mechanisms, we have investigated the potential effects of various chemicals on neoplastic cell transformation. These chemicals are known to act specifically on certain cellular organelles or macromolecules. The experimental results from studies with DMSO, 5-azacytidine, and dexamethasone are shown in Fig.

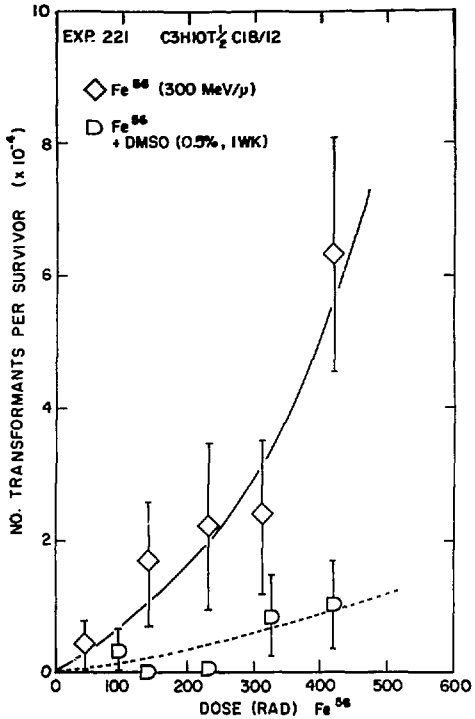

Fig. 1. Effect of 0.5% DMSO on transformation of cells irradiated with ^{56}Fe. (XBL 846-2450)

2. Both DMSO and 5-azacytidine caused a significant decrease of transformation frequency. The dexamethasone, however, showed no effect on the cell transformation by silicon ions (320 MeV/u; ~88 keV/μm). It has been reported that the possible targets for 5-azacytidine and dexamethasone are DNA and cell membrane receptors, respectively.[3,4] The effect of DMSO and 5-azacytidine on the progression of cell transformation is interesting because neither chemical has been found to be mutagenic at the concentrations we used. Our results indicate that some nonmutagenic changes in the cellular DNA can interfere with the expression and progression process. The mechanism of progression and expression of transformation, however, may be quite complicated; further studies are needed for a complete understanding of these processes.

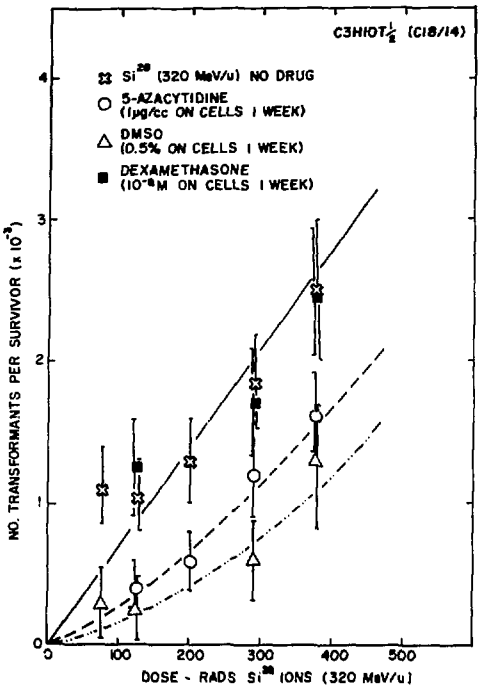

Fig. 2. Effect of various drugs on transformation of ^{28}Si irradiated C3H10T(1/2) cells. *(XBL 854-1988)*

REFERENCES

1. Yang, T.C., and Tobias, C.A. Neoplastic cell transformation by energetic heavy ions and its modification with chemical agents. *Adv. Space Res. 4*, 207–218 (1984).
2. Yang, T.C. and Tobias, C.A. Mechanisms of radiation-induced neoplastic cell transformation. *Proceedings of Berkeley Conference in Honor of Jerzy Neyman and Jack Kiefer.* Vol. 1. L.M. LeCam and R. A. Olshen, Eds. Wadsworth, Inc., pp. 343–366 (1985).
3. Chiu, P., and Blau, H.M. 5-Azacytidine permits gene activation in a previously noninducible cell type. *Cell 401, 417-424 (1985).*
4. Roberts, A. S., Anzano, M. A., Lamb, L. C., Smith, J.M., and Sporn, B.M. Antagonistic actions of retinoic acid and dexamethasone on anchorage-independent growth and epidermal growth factor binding of normal rat kidney cells. *Cancer Res. 44*, 1635–1641 (1984).

CELL AGE DEPENDENT VARIATIONS IN OXIDATIVE PROTECTIVE ENZYMES

Eleanor A. Blakely, Polly Y. Chang, Leora Lommel, and Cornelius A. Tobias

Oxidative stress caused by reactive oxygen intermediates (ROI) can be produced in mammalian cells by ionizing radiation as well as by several radiomimetic agents (e.g., peroxides, etc.). Mammalian cells possess enzymes capable of enzymatically detoxifying both oxygen radical species and hydrogen peroxide, resulting in a decrease in ROI and a restoration of the homeostatic milieu of the cell. Most mammalian cells exhibit distinct cell-cycle-dependent structure in their survival response to oxidative stress, although a molecular mechanistic explanation for this age response is unknown. We have reported that there are significant differences in the early G1-phase age response of human T-1 cells to either low-LET radiation (225-kVp x rays) or to Bragg-peak neon ions (425 MeV/u).[1] As illustrated in Fig. 1, the cells are initially sensitive to x rays in early G_1-phase, but then become increasing resistant until approximately 4.5 hours postmitosis when they again become radiosensitive. In contrast, the survival response of the synchronized cell populations at equivalent cell killing after Bragg-peak neon ions indicates an initial radioresistance that decreases continuously as the cells enter S-phase.

We are attempting to correlate activity levels of antioxidant enzymes before and after heavy-ion exposures with cellular radiosensitivity. In preliminary feasibility experiments with human T-1 cells we are showing relatively high antioxidant enzyme levels in the unirradiated G_1 phase prior to the normal DNA synthetic phase. As a part of this effort, we have been collaborating with W.F. Blakely, K.S. Kumar, J.F. Weiss, E.V. Hollaham, and M.P. Hagan of

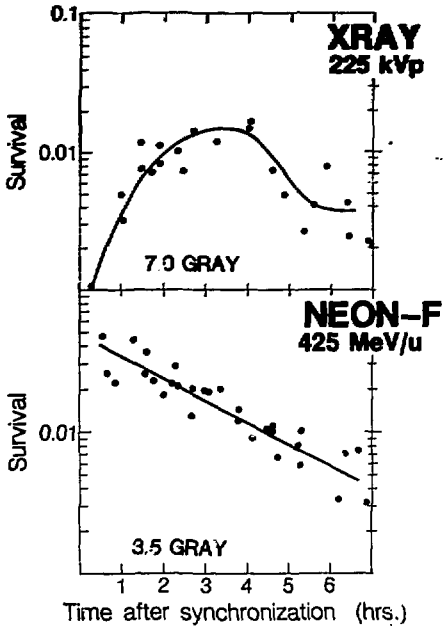

Fig. 1. Composite plot of age response experiments with synchronized human T-1 cell populations exposed to either 7 Gray x ray or 3.5 Gray neon ions. (XBL 858-3349)

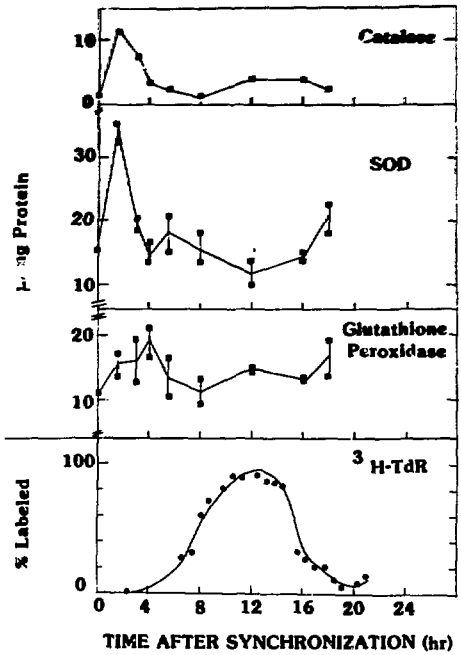

Fig. 2. Antioxidant enzyme levels measured at various ages in the unirradiated, synchronized human T-1 cell cycle. For reference, the bottom panel shows the incorporation of tritiated thymidine to identify cell cycle parameters. The three enzymes measured include: catalase, superoxide dismutase, and glutathione peroxidase. (XBL 8412-5128A)

the Armed Forces Radiobiology Research Institute (AFRRI). Endogenous cellular levels of three antioxidant enzymes are being measured at various times in the unirradiated human T-1 cell division cycle. The enzymes measured were: catalase (CAT), superoxide dismutase (SOD), and glutathione peroxidase (GSHPX).

Unlike the case in Chinese hamster V79 cells[2] the early data with the synchronized human cell show that in very early G_1 phase (e.g., approximately 1.5 hours after mitotic selection) there are significant peaks in the levels (U/mg cell protein) of both CAT and SOD (see Fig. 2). Both enzymes show increases as the unirradiated cells progressed from mitosis into G_1 phase while the levels of GSHPX measured in duplicate samples are somewhat more variable than was the case for the other two enzymes. These measurements are currently being replicated for confirmation before progressing to radiation studies. This work will primarily be completed with x rays and the Bragg peak of the 425-MeV/u neon beam as a representative heavy ion, since we have well characterized the response of the T-1 cell to damage from these radiations.

The human cell data have prompted as more detailed analysis of enzyme levels during the ~1 hour of G_1 phase in synchronous V79 cells, and will permit a comparison of enzyme activity levels in human and rodent cell lines.[3] The findings are important to an understanding of the intrinsic cellular defense mechanisms that respond to an oxidative challenge because of the possibility of distinct cell-cycle population effects.

REFERENCES

1. Blakely, E.A., Chang, P.Y., and Lommel, L. Cell-cycle-dependent recovery from heavy-ion damage in G_1-phase cells. *Radiat. Res., 104: Supplement 8* S145–S157 (1985).
2. Blakely, W.F., Kumar, K.S., Holahan, E.V., Hagan, M.P., Weiss, J.F., Jacocks, H.M. Intrinsic cellular mechanisms of resistance to oxidative damage: age response. Radiation Research Society Meeting, Los Angeles, CA (1985). Abstract.

3. Blakely, W.F., Kumar, K.S., Blakely, E.A., Holahan, E.V., Hagan, M.P., Weiss, J.F., Chang, P.Y., Sancho, A., Lommel, L., Hollies, C.L., and Tobias, C.A. Age response for oxidative protective enzymes: comparison of a human and rodent cell line. Radiation Research Society Meeting, Las Vegas, NV (1986). Abstract.

RESPONSE OF AEROBIC AND HYPOXIC HUMAN LUNG SQUAMOUS CARCINOMA CELLS TO NEON IONS

Eleanor A. Blakely, Hiroshi Ohara, Polly Y. Chang, and Leora Lommel

During the past year we began a collaborative study of the response of human squamous carcinoma cells to high-energy (425 MeV/u) neon-ion beams. The cell line was established in Japan in 1983 from a surgical specimen taken from a tumor mass.

Using techniques developed in our laboratory,[1] monolayers of the asynchronous lung-tumor cells were grown in glass petri dishes, irradiated with either 150-kVp x rays or Bragg-peak neon ions under controlled conditions of full aeration or hypoxia, and then trypsinized and plated to evaluate clonogenic potential.

The survival results of the experiment are presented in Fig. 1. Computer-assisted fits of the data have been made with the linear-quadratic model of cellular inactivation. The calculation of the aerobic RBE at 10% survival is 1.8 ± 0.03, and the x-ray oxygen enhancement ratio (OER) is 3.0 ± 0.2, while the neon OER value is 1.3 ± 0.04. These data with the human lung carcinoma cells confirm the enhanced cell killing and reduced oxygen effect previously reported for human T-1 fibroblasts at an LET of 183 keV/μm.[1] In addition to the tumor-cell studies, experiments to measure the induction of chromosome aberrations in human blood cells in the plateau and distal end of an extended Bragg peak of a 425-MeV/u neon beam have been completed and are being analyzed. The results of both sets of experiments reported here will contribute to an evaluation of the clinical potential of heavy-ion beams for the design of a medical accelerator in Japan.

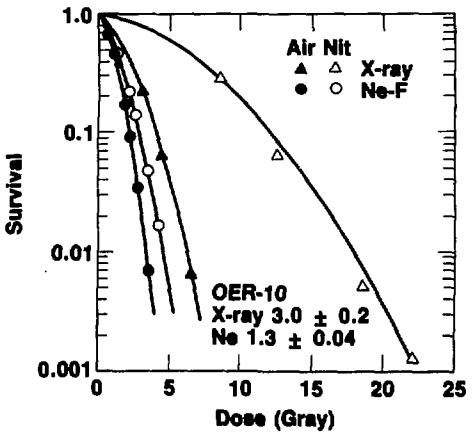

Fig. 1. Cellular survival in air or nitrogen of human lung squamous carcinoma cells exposed to 150-kVp x rays or Bragg-peak 425-MeV/u neon ions. *(XBL 854-11020)*

REFERENCES

1. Blakely, E.A., Tobias, C.A., Yang, T.C.H., Smith, K.C., and Lyman, J.T. Inactivation of human kidney cells by high energy monoenergetic heavy-ion beams. *Radiat. Res. 80,* 122–160 (1979).

MULTIPLE CHROMATIN BREAKS PRODUCED BY NEON IONS

Edwin H. Goodwin, Eleanor A. Blakely, and Cornelius A. Tobias

There is a possibility that multiple chromatin breaks will occur within a cell nucleus from the passage of a single high-LET particle, but this has been difficult to examine in interphase nuclei under a light microscope because the chromatin is too diffuse to be seen. We have used a technique known as PCC, or premature chromosome condensation,[1] to visualize interphase chromatin fragments and to score radiation-induced chromosome breaks without having to wait until the chromatin condenses at metaphase. Briefly, irradiated cells were fused to unirradiated mitotic CHO cells using polyethylene glycol in a modified version of a protocol developed by Pantelias and Maillie.[2] As the cytoplasms merge, factors from the mitotic cell act upon the interphase chromatin causing it to condense "prematurely." These chromosome-like bodies, often called PCC fragments, can be seen in an ordinary microscope after fixation and staining by a modification of the procedure of Cornforth and Bedford.[3] The unique value of the PCC technique is that it can be used to detect chromatin breaks in individual interphase cells within 30 minutes after irradiation.

Plateau-phase Chinese hamster ovary CHO-TSH1 cells were exposed to single doses (30 to 240 rad) of either 150-kVp x rays or neon ions accelerated at the Berkeley Bevalac. The particles had an initial energy of 425 MeV/u and a mean LET of 183 keV/μm near the Bragg ionization peak where the cell cultures were placed. Only those cells that were in the G_1/G_0 phase of the cell division cycle at the time of irradiation were scored. The CHO-TSH1 cell line has a modal chromosome number of 21. The unirradiated controls, as expected, had an average of 21 PCC fragments per cell, while irradiated cells showed a dose-dependent increase in fragment number with one chromosome break occurring for each 17 rad of neon-ion dose or 20 rad of x-ray dose. X-ray-induced fragments per cell had a Poisson distribution. The observed frequency of neon-ion-induced fragments was not Poisson, but rather showed multiple peaks and valleys.[4] The anomalous distribution can be explained by assuming that a single heavy ion passing through the cell nucleus is capable of producing several chromatin breaks (see Fig. 1).

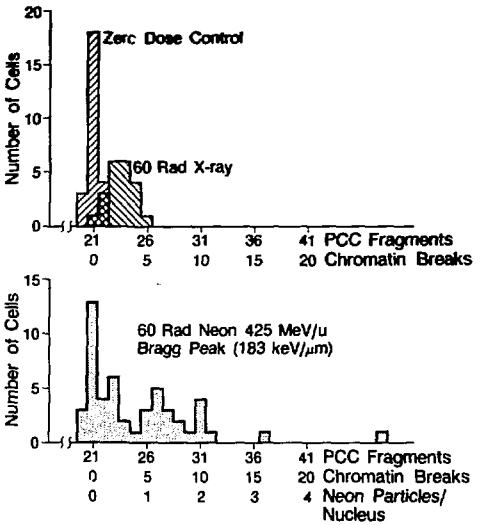

Fig. 1. Distribution of interphase chromatin fragments in Chinese hamster ovary CHO-TSH1 cells. (Upper panel) Distribution of fragments in control, unirradiated cells with a mean number of 21, and the distribution of additional fragments after 60 rad of x rays. (Lower panel) Distribution of fragments in cells irradiated with Bragg-peak neon ions. The number of chromatin breaks and the number of neon traversals per cell have been calculated. *(XBL 8511-8599)*

When a single heavy ion crosses a cell nucleus, it may produce DNA strand breaks and chromatin scissions wherever the ionizing track structure overlaps chromatin structures. The multiple yield of such lesions depends on the radial distribution of deposited energy and on the microstructure of the distribution of DNA in the cell nucleus, both of which place an upper limit on the number of lesions that can be produced by a single particle. The number of lesions per nucleus per particle can be described by a binomial distribution. The number of particles crossing a cell nucleus can be described by Poisson statistics. Combined, they yield the Neyman A distribution. Scoring chromatin breaks in CHO cells exposed to neon ions at 183 keV/μm, we have obtained results compatible with the Neyman A distribution. The maximum number of suitable crossings was found to be 5 per particle

per cell nucleus. The repair-misrepair model (RMR) has earlier suggested the occurrence of multiple DNA lesions in single heavy-ion tracks, and the current studies are in agreement with the RMR model as well as the deep-sieve model used to interpret the radiobiology of very heavy accelerated nuclei.[5]

REFERENCES

1. Johnson, R.T., and Rao, P.N. *Nature 226,* 717 (1970).
2. Pantelias, C.E., and Maillie, H.D. *Somatic Cell Genetics 9,* 5, 533 (1983).
3. Cornforth, M.N., and Bedford, J.S. *Chromosome 88,* 315 (1983).
4. Goodwin, E., Blakely, E.A., and Tobias, C.A. Multiple chromatin breaks produced by single heavy ions. Abstract, Radiation Research Society Meeting, Las Vegas, NV (1986).
5. Tobias, C.A., Goodwin, E.H., and Blakely, E.A. Theoretical distributions of DNA lesions in heavy-ion tracks. Abstract, Radiation Research Society Meeting, Las Vegas, NV (1986).

EFFECT OF INHIBITION OF PROTEIN SYNTHESIS ON THE DEVELOPMENT OF THERMOTOLERANCE

Polly Y. Chang, Eleanor A. Blakely, and Ileana Gonzalez-Flores*

The response of mammalian cells to nonlethal doses of elevated temperatures is modified by the development of a transient resistance to subsequent heat challenges.[1] The mechanism of this thermotolerant response is unknown but may be linked to the synthesis of a family of proteins called heat-shock proteins.[2,3]

We became interested in studying the response of a protein synthetic mutant cell line to hyperthermia.[4] Published investigations of the role of protein synthesis in the development of thermotolerance to heat killing have used either chemical inhibitors or environmental factors to modulate synthetic activity. We, however, have chosen to use a temperature-sensitive mutant line, CHO-TSH1,[5] which shuts down protein synthesis at nonpermissive temperatures of 40°C and above by the inactivation of its cytoplasmic nonmitochondrial leucyl-transfer RNA (t-RNA) synthetase enzyme. The parent cell line, CHO-SC1, was used as the control for these experiments. Exponentially growing, asynchronous CHO-TSH1 and CHO-SC1 cell populations were treated for times up to 8 hours at 41.5°C, 42°C, and 42.5°C (Fig. 1a). The wild-type cells showed the development of tolerance to heat killing at 41.5°C, 42°C, and possibly at 42.5°C, although the survival level at which tolerance developed at 42.5°C was too low to be statistically significant. The CHO-TSH1 mutant cell showed no tolerance at any of those temperatures (Fig. 1b).

We measured the rate of total protein synthesis in both cell lines in pulse-labeling experiments with ^{3}H-leucine under the conditions of our experiment. Results indicated that the rate of synthesis dropped precipitously within the initial hour of exposure to 42°C and remained low during the 3 hours of 42°C treatment (Fig. 2). When each cell line was returned to 35°C after the 3-hour treatment at 42°C, protein synthesis immediately resumed and eventually returned to control levels after 7 hours at 35°C.

We have also looked at the effect of resumption of protein synthesis on cellular survival by using split-temperature treatments. The cells were exposed to 42°C for 3 hours and then returned to the permissive temperature (35°C) for 20 hours. The cells were then subjected to additional time at 42°C (Fig. 3). The wild-type cell response to the split-temperature treatment is identical to that obtained with the single heat treatment, indicating that incubation at 35°C between 42°C heat treatments is not necessary for the development of tolerance. Interestingly enough, the temperature-sensitive mutant cell appears also to have developed a small amount of tolerance under split-dose conditions. When the incubation time at 35°C between split-42°C exposures was increased to 44 hours, we observed a decay of tolerance in both cell lines.

In summary, we have demonstrated loss of thermotolerance in a temperature-sensitive protein synthetic mutant. We hope to extend this work

*Participant in the Ana G. Mendez Educational Foundation Program, LBL.

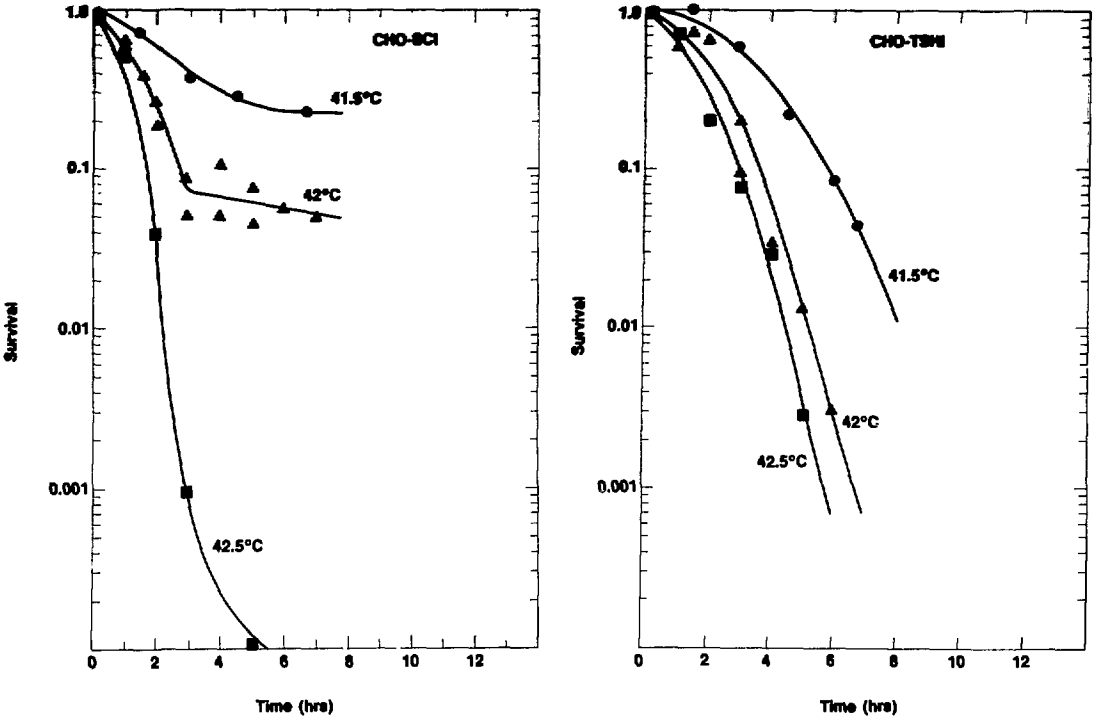

Fig. 1. CHO-SC1 (wild-type) cells show thermotolerance at 41.5°C and 42°C. At 42.5°C these cells show tolerance but at a lower level of survival than could be accurately measured. CHO-TSH1 (temperature-sensitive mutant) cells show no thermotolerance at 41.5°C, 42°C, and 42.5°C. 42°C survival experiments were done with and without post-heat-treatment trypsinization and show no differences in survival fractions. (XBL 854-11072A)

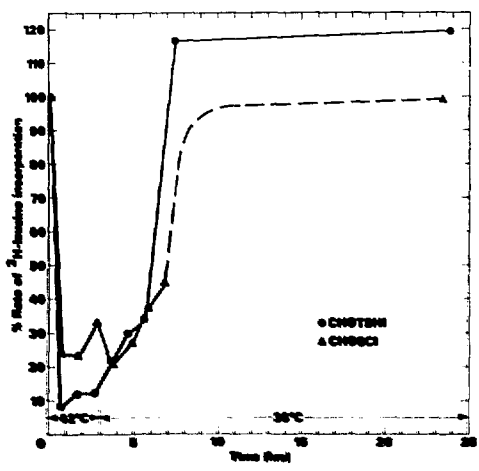

Fig. 2. Cells are treated for 3 hr at 42°C and returned to 35°C for 23 hr. Protein synthesis, as measured by ^{3}H-leucine uptake, is shut down immediately after both cell types were exposed to 42°C. After shifting the temperature back to 35°C, protein synthesis is immediately resumed, eventually reaching control levels after 7 hr at 35°C. (XBL 854-8274)

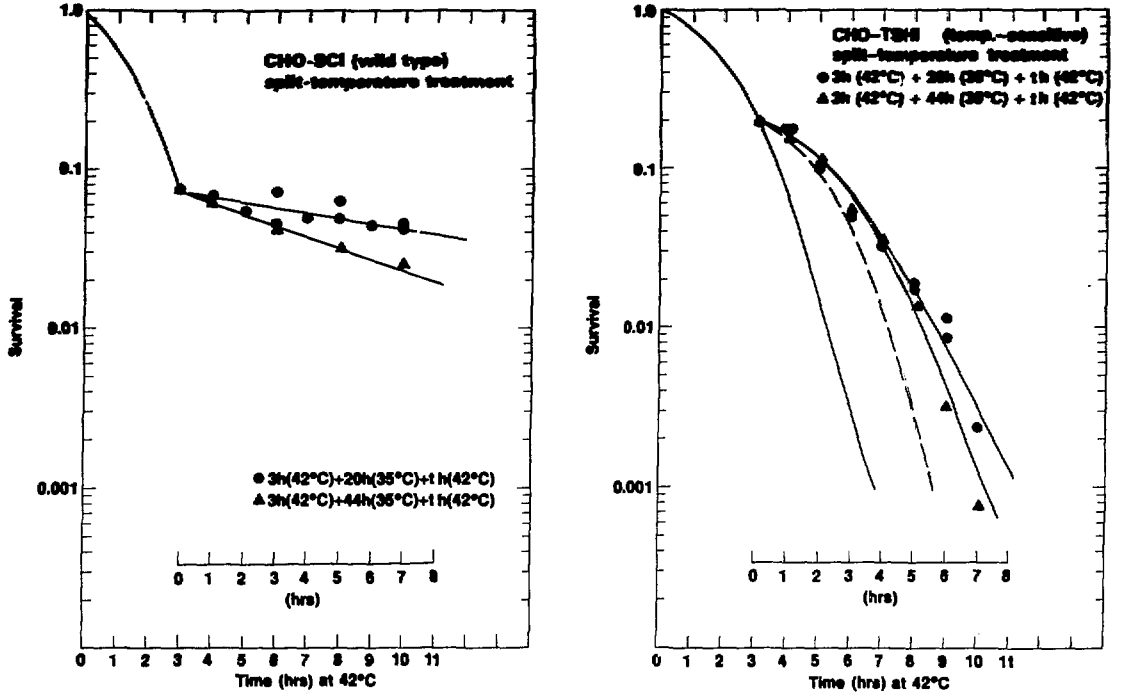

Fig. 3. Split-temperature studies are done where cells are exposed to 42°C for 3 hr, returned to 35°C for 20 hr or 44 hr, and then exposed to a second 42°C dose for the times indicated on the abscissa. CHO-SC1, when allowed to recover for 20 hr, demonstrate a tolerant curve identical to that of the single temperature treatment. After 44 hr of incubation at 35°C between doses, a slight decay in tolerance is observed. CHO-TSH1 did not show thermotolerance to the extent that the wild-type cells did, but survival data is obviously higher than if complete recovery from sublethal damage had taken place (as shown by dotted line). With 44 hr of incubation at 35°C between doses of 42°C, a slight decay in tolerance is also observed. *(XBL 854-11074A)*

furthe: by examining the difference in response of tolerant versus nontolerant cells to radiation.

REFERENCES

1. Henle, K.J., and Dethlefsen, L.A. Heat fractionation and thermotolerance: A review. *Cancer Research 38*, 1843–1851 (1978).
2. Li, G.C., Petersen, N.S., and Mitchell, H.K. Induced thermotolerance and heat shock protein synthesis in Chinese hamster ovary cells. *Int. J. Radiat. Oncol. Biol. Phys. 8*, 63–67 (1982).
3. Hahn, G.M., and Li, G.C. Thermotolerance and heat shock proteins in mammalian cells. *Radiat. Res. 92*, 452–457 (1982).
4. Chang, P.Y., Gibbs, G.F., and Blakely, E.A. Loss of thermotolerance in a temperature-sensitive protein synthesis mutant. Radiation Research Society Meeting, Los Angeles, May 1985. (Abstract)
5. Thompson, L.H., Harkins, J.L., and Stanners, C.P. *PNAS 70*, 3094–3098 (1973).

CELL CYCLE KINETICS AND *IN VIVO* MICRONUCLEI INDUCTION IN RAT RHABDOMYOSARCOMA TUMORS USING A MONOCLONAL ANTIBODY TO BrdUrd AND CELL SORTING

Michael Nüsse, S.M. Javed Afzal, Betsy C. Carr, Kristina S. Kavanau, Thomas S. Tenforde, and Stanley B. Curtis

Redistribution of tumor cells within the cell cycle after irradiation is an important factor affecting the speed of tumor regrowth. Therefore measurement of the movement of both the total and the clonogenic population of tumor cells *in vivo* through the cell cycle as a function of time after irradiation is of special interest. Blocks at certain stages of the cycle, recruitment of resting cells into the proliferating compartment, and variations in the length of the G1-, S- and G2-phases are important effects induced in the tumor cell population by irradiation. Knowledge of the relative importance of such effects is critical to the identification of the dynamic processes that determine how the tumor as a whole responds to irradiation.

Flow cytometric techniques as well as labeling techniques with radioactive DNA precursors are widely used to study cell cycle kinetics of cell populations in tumors. Besides technical problems, the main disadvantage of the FLM (fraction of labeled mitoses) or LI (labeling index) methods is that, in many tumors, only a fraction of the cells progress through the mitotic cycle. A similar problem occurs when the flow cytometric technique of DNA distribution analysis is applied in tumors. It is not possible to discriminate between cycling and noncycling cells.

A new flow cytometric technique was recently developed that reduces some limitations of earlier methods used for measurements of cell kinetics.[1] The method involves the use of a fluorescent monoclonal antibody to bromodeoxyuridine (BrdUrd) that attaches to BrdUrd incorporated into cells during S-phase in addition to the DNA stain propidium iodide which is used to estimate cellular DNA content. This technique allows the study of the progression of cells labeled during S-phase with BrdUrd and, in addition, discriminates between DNA synthesizing and nonsynthesizing cells in the case where both have a DNA content characteristic of S-phase cells.

The aim of the experiments reported here was to investigate the applicability of this BrdUrd/DNA technique to a rat rhabdomyosarcoma tumor system growing *in vivo* and to study radiation-induced changes in the progression of cells through the cell cycle. Details of this technique are described elsewhere.[2] In addition, the induction of micronuclei in tumor cells irradiated *in vivo* with x rays or peak neon ions was studied. Micronuclei found in interphase cells after irradiation represent genetic material that is lost from the genome of the cells during mitosis.[3] The formation of micronuclei that can mainly be ascribed to acentric chromosome or chromatid fragments occurs only after cells go through one or more cell divisions. Cycling cells in the tumors were therefore continuously labeled with BrdUrd, and micronuclei induction was measured only in tetraploid cycling tumor cells using the flow cytometric cell sorting technique.

THE RHABDOMYOSARCOMA TUMOR: DIPLOID HOST CELLS AND TETRAPLOID TUMOR CELLS

To analyze the cell cycle kinetics of the rhabdomyosarcoma tumors (subline R2C5 of the rhabdomyosarcoma R-1 tumor which was implanted subcutaneously into syngeneic WAG/Rij rats) using incorporation of BrdUrd, the composition of the various cell populations in this tumor was studied with DNA distribution analysis. It was known from observations of metaphase chromosomes that the tumor cells growing *in vitro* have a tetraploid DNA content. A possible contamination of the dissociated tumor cell suspension from tumors *in vivo* by diploid host cells could be easily measured using DNA distribution analysis. Figure 1 A (*insert*) shows a typical DNA distribution of the dissociated cells from this tumor. Using diploid lymphocytes from the spleen of the tumor-bearing rats, which were also stained and measured under the same conditions, it could be shown that the first peak in the DNA distribution in Fig. 1A represented diploid host cells in G1-phase (2c DNA content). The tetraploid tumor cells in G1-phase had 4c DNA content. Fig. 1A shows the proportion of tetraploid tumor cells, N_T/N_{total}, in growing tumors as a function of tumor weight. Very small tumors were found to contain only about 8% of the tetraploid tumor cells. The fraction of tetraploid tumor cells increased to a maximum of about 20% of the total cell number in large tumors. A possible contamination of the tetraploid G1-peak by diploid G2-cells has been neglected. However, using incorporation

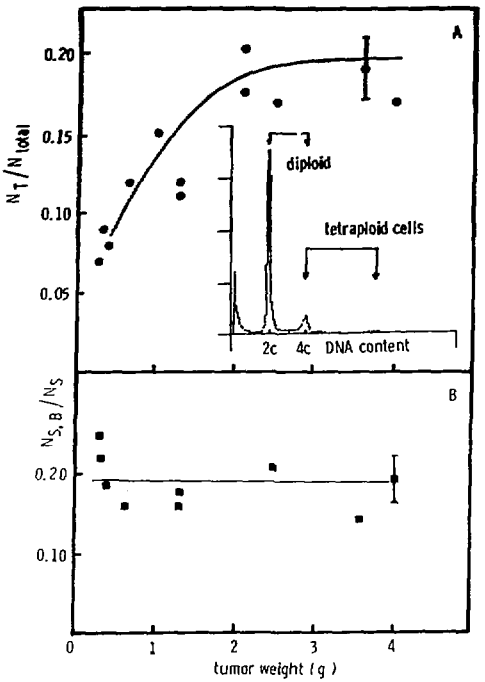

Fig. 1. (A) Fraction of tetraploid tumor cells N_T/N_{Total} in dissociated suspensions of rat rhabdomyosarcoma cells as a function of tumor weight. Insert: DNA distribution of the dissociated cells of the tumor showing peaks for diploid host cells and tetraploid tumor cells. (B) Fraction of tetraploid tumor cells in S-phase ($N_{S,B}/N_S$) that have incorporated BrdUrd at 2 hours after an intraperitoneal injection of BrdUrd (160 mg/kg body weight) as a function of tumor weight. (XBL 8510-8542)

of BrdUrd in tumor cells growing *in vitro*[2] the fraction of diploid G2-cells within the tetraploid G1-peak could be estimated. A maximum of 20% of cells in the tetraploid G1-peak were actually diploid G2-cells. The reason for the high contamination of the tetraploid tumor cells by diploid host cells and the characteristics of these host cells are unknown at present. Probably the good vascularization of this tumor line was responsible for the observed effect. The results show that a study of cell cycle kinetics and of micronuclei induction in these tumors were hampered by the contamination with host cells. In the experiments described below, only the behavior of tetraploid tumor cells is discussed.

PULSE LABELING AND CONTINUOUS LABELING OF TUMOR CELLS WITH BrdUrd

For pulse labeling experiments with BrdUrd, tumor-bearing animals were injected intraperitoneally with 160 mg BrdUrd per kilogram body weight. For continuous labeling experiments a *"mini osmotic pump"* (*Model 2001*, Alzet Co., Palo Alto, CA) was used. The pump, containing 200 µl of 0.3 mol/l bromodeoxycytidine was implanted subcutaneously into the animal's back. Bromodeoxycytidine is converted intracellularly into BrdUrd in the organism. The advantage of bromodeoxycytidine is that it can be dissolved at a much higher concentration than that of BrdUrd, thus allowing a higher level of BrdUrd in the organism compared to that produced by a single or by repeated injections of BrdUrd.

Figure 2 (insert) shows a typical BrdUrd/DNA scatter plot of the tetraploid tumor cells (the diploid host cells were cut off for clarity) two hours after injecting 160 mg BrdUrd per kg body weight. The cells were examined in the LBL FACS IV flow cytometer after staining the DNA of the cells with propidium iodide, and then defining the BrdUrd content of the cells using a monoclonal antibody to BrdUrd and a second fluorescein-conjugated goat anti-mouse antibody. The data were accumulated to form a bivariate 64×64 channel distribution (scatter plot) of DNA (red fluorescence from propidium iodide, abscissa) and BrdUrd (green fluorescence from fluorescein, ordinate) among the cells of the population.

From scatter plots such as the one shown in Fig. 2, the fraction of cells in S-phase that could incorporate BrdUrd after a single injection of BrdUrd ($N_{S,B}/N_S$) was calculated. Figure 1B shows this fraction as a function of tumor weight in unirradiated control tumors. Only about 20% of the S-phase cells were labeled with BrdUrd 2 hours after BrdUrd injection, and this percentage was independent of the tumor size. Figure 2 shows the fraction of labeled S-phase cells as a function of time after injecting BrdUrd. Four hours after injection, $N_{S,B}/N_S$ reached a plateau at a value of 0.25. If tumors were irradiated with 20 Gy of 225-kVp x rays, the fraction of labeled S-phase cells was even lower, probably because of a radiation-induced retardation of DNA-synthesis. This effect was also observed in experiments performed *in vitro*. Through observations of the scatter plots, we found

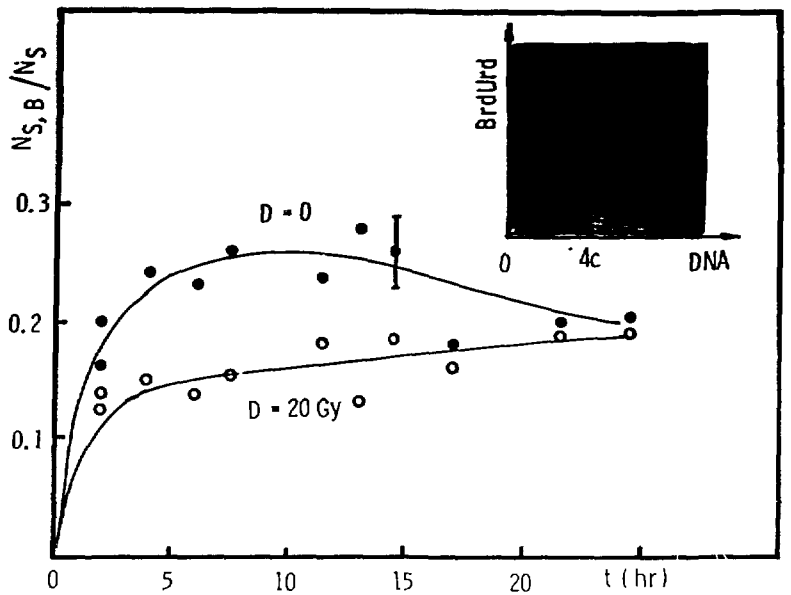

Fig. 2. Fraction of tetraploid tumor cells in S-phase ($N_{S,B}/N_S$) that have incorporated BrdUrd as a function of time after an intraperitoneal injection of BrdURD (160 mg/kg bodyweight). Closed circles are unirradiated tumors; open circles are irradiated tumors (20 Gy of 225-kVp x rays). The inserted scatter plot shows DNA and BrdUrd content of the tetraploid tumor cells 2 hours after injection of BrdUrd. (XBL 8510-8543)

that, over 2 to 10 hours, the labeled cohort of S-phase cells moved into (G2+M)-phase. The fraction of labeled S-cells decreased at later times because some of these cells divided.

The rather low fraction of labeled S-phase cells in tumors is in contrast to similar experiments with these tumor cells growing *in vitro* which showed that all S-phase cells could incorporate BrdUrd after a 1-hour pulse of BrdUrd. Probably those cells in the *in vivo* tumor were not labeled because they were either resting or slowly synthesizing DNA. Some cells in S-phase may also not be labeled as a result of limitations in the transport of BrdUrd via blood vessels or through diffusion. The main disadvantage of the pulse labeling technique with BrdUrd in this rat rhabdomyosarcoma tumor is that it is not possible to distinguish whether cells in S-phase do not incorporate BrdUrd because they do not perform DNA synthesis or because there is no BrdUrd available to them. Therefore, experiments studying continuous labeling of tumor cells using an osmotic pump were performed.

Figure 3A demonstrates the combined fraction of labeled S- and (G2+M)-phase cells as a function of time after implantation of the pump. A continuous increase of labeled cells as a function of time was observed. The fact that only 60% of S- and (G2+M)-phase cells were found to be labeled even after 50 hours demonstrates that a rather large fraction of cells in this tumor is not cycling. These cells are probably resting cells or very slowly dividing cells in the tumor. Unfortunately, the fraction of resting G1-phase cells could not be measured by this technique because of the overlap with a much higher fraction of diploid host cells in (G2+M)-phase that were also able to incorporate BrdUrd.[2]

In irradiated tumors (10 and 20 Gy of 225-kVp x rays, Fig. 3) the fraction of labeled S- and (G2+M)-phase cells reached a higher plateau than that of the controls. This effect is presumably caused by the radiation-induced G2-block in those cells of the tumor that were able to progress into the cell cycle. Figure 3C shows the fraction of labeled (G2+M)-phase cells for control tumors and irradiated tumors (20 Gy). Between 30 and 50 hours after irradiation, about 85% of G2-phase cells became labeled in the irradiated tumors whereas only 70% of these cells were labeled in the control

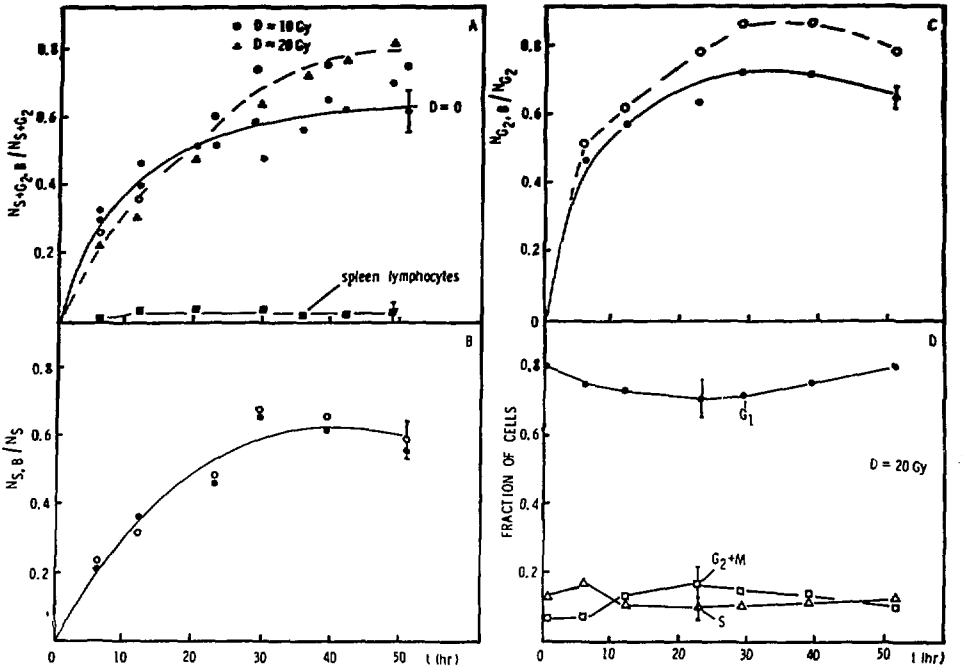

Fig. 3. (A) Fraction of cells in (S+G2)-phase ($N_{S+G2,B}/N_{S+G2}$) of tetraploid tumor cells that have incorporated BrdUrd as a function of time after implanting an osmotic pump. Closed circles are unirradiated control tumors; open circles and triangles are irradiated tumors. Closed squares represent fraction of cells in (S+G2)-phase in spleen lymphocytes of the same animals. (B) Fraction of tumor cells in S-phase ($N_{S,B}/N_S$) that have incorporated BrdUrd, as a function of time after implanting an osmotic pump. (C) Fraction of cells in (G2+M)-phase ($N_{G2,B}/N_{G2}$) that have incorporated BrdUrd as a function of time after implanting an osmotic pump. (D) Fraction of tetraploid tumor cells measured by DNA distribution analysis in G1- (closed circles), S- (open triangles) and (G2+M)-phase (open squares) as a function of time after irradiation with 20 Gy of 225-kVp x rays. (XBL 8510-8544)

tumors. Whereas in the control tumors the labeled G2-phase cells divide, the labeled cycling G2-phase cells in irradiated tumors are arrested in G2-phase for a certain time interval. Using DNA distribution analysis alone, the radiation-induced G2-block cannot be easily observed in this tumor because a large fraction of cells either do not progress into the cell cycle or are only progressing very slowly (Fig. 3D).

MICRONUCLEI INDUCTION IN CYCLING *IN VIVO* TUMOR CELLS

The experiments discussed above show that it is possible to discriminate between cycling and noncycling cells in solid tumors after continuous incorporation of BrdUrd by analyzing the dissociated cells in a flow cytometer using a monoclonal antibody to BrdUrd. The same technique in combination with cell sorting was used to study micronuclei induction in irradiated tumors *in vivo*. Because micronuclei can only be observed in cells that have gone through at least one cell division after irradiation, cycling tumor cells were sorted according to their tetraploid DNA content and high BrdUrd content at 52 hours after irradiation, when most of the cycling cells had divided. Figure 4 (insert) shows BrdUrd/DNA scatter plots of cells in the tumor without BrdUrd (left panel showing control data to demonstrate the position of unlabeled cells) and after continuous incorporation of BrdUrd using an osmotic pump (right panel, where the sorted cells are indicated by the square). The cells were sorted with the High Speed Cell Sorter of the Lawrence Livermore National Laboratory (the help of Dr. Joe Gray is gratefully acknowledged). The fraction of micronucleated cells N_{mn}/N in these sorted cells was measured in a fluorescence microscope. Figure 4 shows N_{mn}/N as a function of dose for x rays

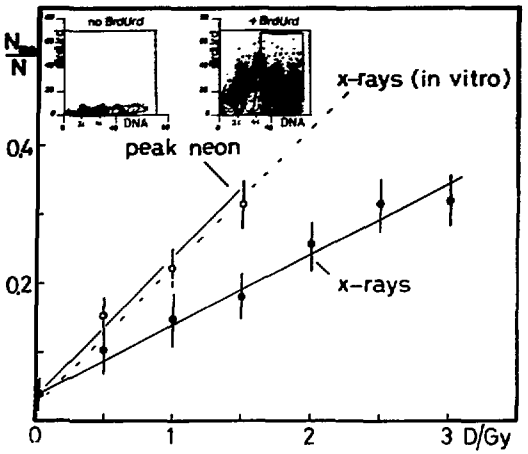

Fig. 4. Fraction of micronucleated cells (N_{mn}/N) as function of dose in cells that were sorted from dissociated tumor cells according to tetraploid DNA content and high BrdUrd content (cycling tetraploid tumor cells). Closed circles are tumors irradiated with x rays. Open circles are tumors irradiated with neon ions in the distal region of a 4-cm spread peak. Dotted line represents exponentially growing cells irradiated in vitro. Insert: BrdUrd/DNA scatter plots of dissociated tumor cells. Left: no BrdUrd treatment, right: 52 hours after implanting the osmotic pump. The cells within the rectangular region denote those selected for micronucleus determination.

(XBL 8510-8545)

and in the distal region of a 4-cm spread peak of a neon-ion beam accelerated at the Bevalac (initial energy of 557 MeV/u). A linear increase with dose was observed, similar to previous observations on micronuclei induction in exponentially growing *in vitro* cells.[3] Comparing the *in vivo* x-ray results with those from *in vitro* experiments (dotted line) it can be seen that cycling tetraploid tumor cells growing *in vivo* are less sensitive compared to *in vitro* cells. This is in accordance with cell survival data that also show a lower radiation sensitivity of tumors irradiated *in vivo*. The RBE value for neon ions in the distal portion of a 4-cm spread peak is 2.2 ± 0.5, a value that is similar to that measured with *in vitro* cells.[3]

In conclusion, it has been shown that by using the BrdUrd/DNA technique in combination with cell sorting it was possible to study micronuclei induction *in vivo* in irradiated tumors, although this rhabdomyosarcoma tumor line had a large fraction of diploid host cells and contained both cycling and noncycling cells.

REFERENCES

1. Dolbeare, F., Gratzner, H., Pallavicini, M.G., and Gray, J.W. Flow cytometric measurement of total DNA content and incorporated bromodeoxyuridine. *Proc. Natl. Acad. Sci. USA 80*, 5573 (1983).
2. Nüsse, M., Afzal, S.M.J., Carr, B., and Kavanau, K. Cell cycle kinetic measurements in an irradiated rat rhabdomyosarcoma using a monoclonal antibody to bromodeoxyuridine. *Cytometry 6*, 611–619 (1985).
3. Nüsse, M., and Curtis, S.B. A test for micronuclei induction in rat rhabdomyosarcoma tumors after irradiation with x rays and heavy charged particles. Biology and Medicine Division Annual Report 1983–1984, p. 114, Lawrence Berkeley Laboratory report LBL-18393 (1985).

TUMOR RADIOBIOLOGY STUDIES WITH HEAVY CHARGED PARTICLE BEAMS

Stanley B. Curtis, Thomas S. Tenforde, and S.M. Javed Afzal

The response of a rat rhabdomyosarcoma tumor system to irradiation with heavy charged particles is being evaluated from experiments conducted both *in vivo* and *in vitro*. The radiobiological end points studied include tumor volume response, cellular survival after tumor irradiation *in situ*, and cell-kinetic parameters measured by flow cytometry. The primary emphasis of our research during the past year has been in the following areas: 1) repair of potentially lethal damage, 2) tumor repopulation kinetics following fractionated doses of neon ions, and 3) phase-specific cell survival following *in situ* x-irradiation.

REPAIR OF POTENTIALLY LETHAL DAMAGE

Rat rhabdomyosarcoma tumor cells grown as monolayer cultures exhibit substantial recovery from potentially lethal damage (PLD), but no repair can be measured in the *in vivo* tumors. As

opposed to the rapid plating technique used *in vitro*, the *in vivo* experiments involve a lengthy procedure of tumor excision, dissociation and plating, during which a substantial amount of PLD repair could occur and thereby go undetected. Using the well known PLD repair inhibitor, β-arabinofuranosyladenine (β-ara-A), we have therefore been using an alternate approach to study PLD repair *in vivo*.

PLD repair was measured for tumors irradiated *in situ* with either 225-kVp x rays or 557-MeV/u neon ions in the distal position of a 4-cm extended peak. Tumors implanted subcutaneously in syngeneic WAG/Rij rats were irradiated with 5.8 Gy of peak neon ions and 14.5 Gy of x rays. These doses were chosen to produce about the same initial survival (0.06). Addition of 50 μM β-ara-A to the tumors immediately after x-irradiation and excision reduced the ultimate survival from 0.056 to 0.018, yielding a PLD inhibition factor of 3.11 (Table 1 and Fig. 1). The delayed exposure of tumor cells to β-ara-A after 1 or 2 hr of incubation in medium lacking the inhibitor resulted in a progressive decrease of the inhibition factor to values of 1.60 and 1.47, respectively (Table 1 and Fig. 1). Addition of β-ara-A after 3 hr of incubation in β-ara-A free medium did not inhibit the repair. When the tumors were excised at 3, 6 or 12 hr postirradiation and immediately exposed to β-ara-A for 3 hr at 37°C, no effect of the inhibitor on the ultimate cell survival was observed (Table 1 and Fig. 1).

Following 5.8 Gy of peak neon-ion irradiation, significantly less PLD repair was observed as compared to 14.5 Gy of x-irradiation (Table 1 and Fig. 1). Addition of 50 μM β-ara-A to the tumors immediately after neon irradiation reduced the ultimate survival from 0.067 to 0.032, yielding a PLD

Table 1. PLD repair in neon and x-irradiated rhabdomyosarcoma tumors in the presence and absence of β-ara-A[a,b]

	5.8 Gy of peak neon ions		14.5 Gy of x rays	
Tumor treatment after irradiation	Surviving fraction	PLD repair Inhibition factor	Surviving fraction	PLD repair Inhibition factor
Immediate excision and *no* β-ara-A	0.067	—	0.056	—
Immediate excision plus immediate addition of 50 μM β-ara-A for 4 hr at 37°C	0.032	2.09	0.018	3.11
Immediate excision plus addition of β-ara-A after 1 hr	0.044	1.52	0.035	1.60
Immediate excision plus addition of β-ara-A after 2 hr	0.050	1.34	0.038	1.47
Immediate excision plus addition of β-ara-A after 3 hr	0.064	—	0.060	—
Excision 3 hr postirradiation:				
(i) no added β-ara-A	0.060	—	0.062	—
(ii) immediate addition of 50 μM β-ara-A for 3 hr at 37°C	0.052	—	0.055	—
Excision 6 hr postirradiation:				
(i) no added β-ara-A	0.072	—	0.066	—
(ii) immediate addition of β-ara-A	0.074	—	0.062	—
Excision 12 hr postirradiation:				
(i) no added β-ara-A	0.064	—	0.052	—
(ii) immediate addition of β-ara-A	0.070	—	0.054	—

[a] The 50-μM concentration of β-ara-A used in these experiments was not directly cytotoxic during the maximum incubation period of 4 hr at 37°C.

[b] The PLD repair inhibition factor is defined as the ratio of cell survival in the absence vs. the presence of added β-ara-A.

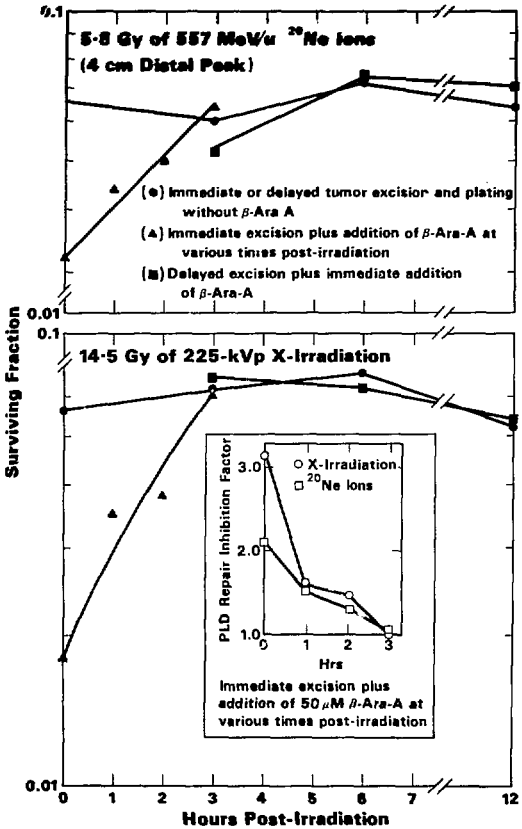

Fig. 1. PLD repair in rhabdomyosarcoma tumors irradiated in situ with 5.8 Gy of peak neon ions (upper panel) or with 14.5 Gy of 225 kVp x rays (lower panel) as a function of time between irradiation, excision, and addition of 50-μM β-ara-A. The 50-μM concentration of β-ara-A used in these experiments was not directly cytotoxic during the maximum incubation period of 3 hr at 37°C. The PLD repair inhibition factor is defined as the ratio of cell survival in the absence vs. presence of added β-ara-A. (XBL 851-8140)

repair inhibition factor of 2.09. However, as observed after x-irradiation, delayed exposure of tumor cells to β-ara-A for 1 or 2 hr resulted in a progressive decrease of the PLD repair inhibition factor to values of 1.52 and 1.34, respectively.

We interpret these results as indicating that rhabdomyosarcoma tumors do repair a considerable amount of PLD *in vivo* following both low- and high-LET radiation. Using the excision assay procedure, however, this repair cannot be detected in the absence of β-ara-A because it is already complete by the time the tumors are dissociated and plated into tissue culture medium for the assay of colony-forming ability.

Tumor Repopulation Kinetics Following Fractionated Doses of Neon Ions

In these experiments, measurements were made of the time course of survival after fractionated irradiation. Groups of rhabdomyosarcoma tumors were irradiated *in situ* with daily fractionated doses (4 fractions in 3 days) of 557-MeV/u neon ions in the distal position of a 4-cm extended peak. Based on our earlier studies of tumor volume response following fractionated doses of neon ions, doses of 1.75 Gy per fraction of neon ions were administered to achieve a cell survival of approximately 2–3% by the end of a four-fraction schedule. Cell survival was assayed daily during irradiation and then daily up to 6 days postirradiation and every second day afterwards (up to 20 days postirradiation) in order to ascertain the cellular regrowth kinetics of tumors following the fractionated radiation treatment. Groups of 3 to 4 tumors were excised and assayed for cell survival by the excision assay technique at each time point. The results are presented in Fig. 2. As observed after a single 7-Gy dose of peak neon-ion irradiation, a significant decrease in cell survival was noted 3 days following the completion of irradiation. The rate of cellular repopulation and the radiation-induced tumor growth delay (calculated as the difference in the average time for irradiated and control tumors to reach a volume twice that at irradiation) was also the same following single dose and four-fraction radiation schedules.

Phase-Specific Cell Survival Following In Vivo X-Irradiation

The survival of *in vivo* R2C5 tumor cells in different cell-cycle phases was analyzed by flow cytometry and cell sorting procedures following a 10-Gy dose of 225-kVp x rays. Cell-kinetic parameters were determined from the DNA fluorescence histograms of enzymatically dissociated tumor cells stained with a noncytotoxic 5 μM concentration of Hoechst 33342 stain. Survival data for unirradiated control cells and for cells from tumors that were excised immediately following x-irradiation are shown in Fig. 3A and 3B. The fractional survival of G1 and (G2+M) cells were comparable to the overall survival of the entire tumor cell population following a 10-Gy x-ray dose (S.F. = 0.26). However, the S-phase cells had a survival level that was 17% and 23% lower than the survival of the G1

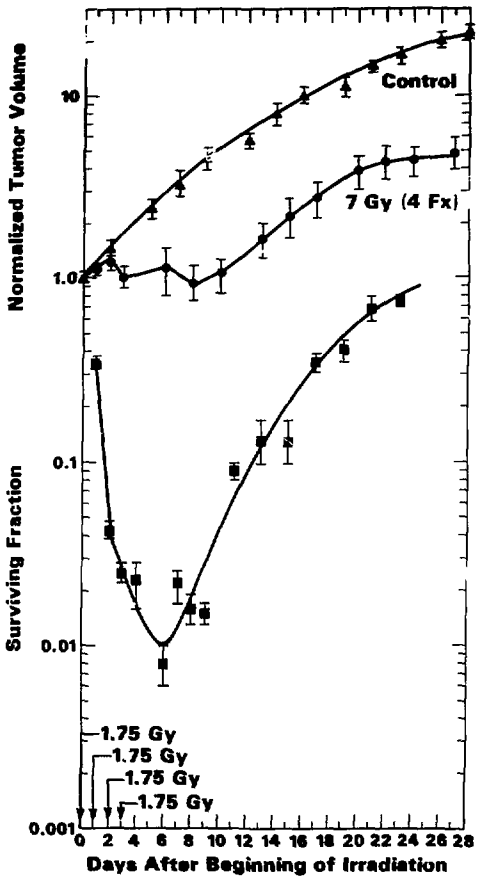

Fig. 2. Average tumor volumes are plotted as a function of time for control rhabdomyosarcoma tumors and for tumors exposed to daily fractionated doses of 1.75 Gy (4 fractions in 3 days) of 4-cm extended-peak neon ions (upper panel). All tumor volumes were normalized to unity on the first day of irradiation. Surviving fraction of tumor cells as a function of time during and after exposure to daily fractionated doses of 1.75 Gy (4 fractions in 3 days) of 4-cm extended peak neon ions is plotted in the lower panel. Groups of 3 to 4 tumors were assayed at each time point. Error bars represent ± 1 SEM.
(XBL 851-8139)

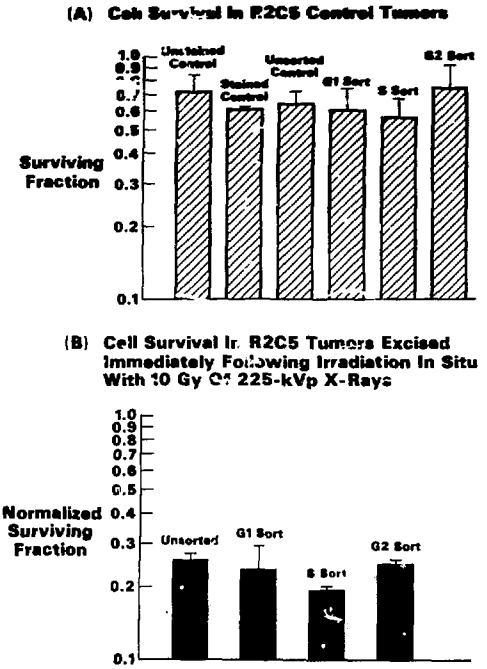

Fig. 3. Phase-specific cell survival data are presented for unirradiated R2C5 tumors (panel A) and for tumors that received a 10-Gy dose of 225-kVp x rays (panel B). The enzymatically dissociated cells were stained with Hoechst 33342 (5 μM, 2 hr, 37°C) and sorted on the basis of DNA fluorescence using a uv laser intensity of 150 mW. The survival fractions of x-irradiated cells in each phase of the cell cycle were normalized to the survival of control cells in the corresponding cell-cycle phase. No statistically significant decrease in cell survival occurred in the control tumors as a result of the staining or cell sorting procedures. In the irradiated tumor cell populations, the unsorted cells passed through the laser beam exhibited a 40.2% lower survival than the stained cells that were not subjected to flow cytometry. The phase-specific survival of the irradiated tumor cells was renormalized to correct for the laser cytotoxicity.
(XBL 851-8142)

and (G2+M) cell populations, respectively. Using the survival data shown in Fig. 3B and the fractions of tumor cells in different cell-cycle phases determined from the DNA fluorescence profile, it was calculated that the relative percentages of surviving tumor cells that were in the G1, S, and (G2+M) cell-cycle phases at the time of irradiation were 78.2, 8.7 and 13.1%, respectively.

Tumor cell kinetics and phase-specific cell survival were analyzed by flow cytometry and cell sorting procedures at 0, 1, 2.5, 4 and 8 days following irradiation *in situ* with 10 Gy of 225-kVp x rays. As shown in Fig. 4A, the percent of host diploid cells within the tumors increased from approximately 70% to 85% of the total cell population at 2.5 days postirradiation. The higher percentage of diploid host cells relative to tetraploid tumor cells was also observed at 4 and 8 days postirradiation. Figure 4B shows the relative distributions of G1, S and (G2+M) cells in irradiated tumors at times ranging from 0 to 8 days following a 10 Gy dose of x rays. At 1 day postirradiation there was a twofold increase in the percentage of G2 cells (from 12.0 to

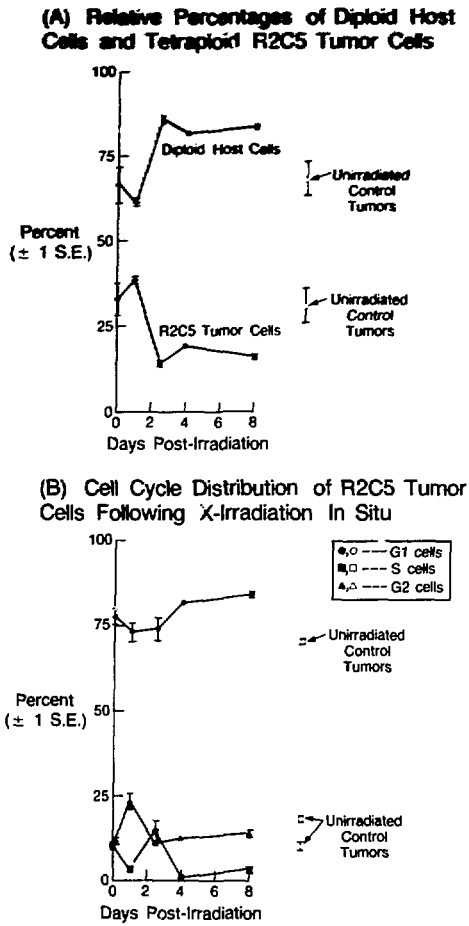

Fig. 4. The relative percentage of diploid host cells and tetraploid tumor cells (panel A) and the cycle distribution of the tumor cell population (panel B) are shown during the period from 0 to 8 days following a 10-Gy dose of 225-kVp x rays.
(XBL 859-8474)

23.5%) as a result of the radiation-induced G2 block. Corresponding decreases in both the G1 and S cell populations were observed at 1 day following irradiation. At 2.5 days postirradiation the relative percentage of G2 cells decreased to 11.3%, while the S-phase population showed a transient increase to 14.6% and the G1-phase population remained constant. This transient increase in S-phase cells may reflect the traversal of a cohort of cells into cycle following release from the postirradiation G2 block. Between 2.5 and 8 days postirradiation the relative percentage of G2 cells remained nearly constant, while the percent of G1 and S cells increased and decreased, respectively.

The cell survival fractions in unsorted and sorted tumor cell populations at 0 to 8 days following a 10-Gy dose of x rays are plotted in Fig. 5. Tumor cells stained with 5 μM Hoechst 33342 and passed through the FACS IV unit without sorting showed a significant 25-fold drop in survival at 2.5 days postirradiation, similar to that previously observed in cellular repopulation studies following a 20-Gy dose of x rays.

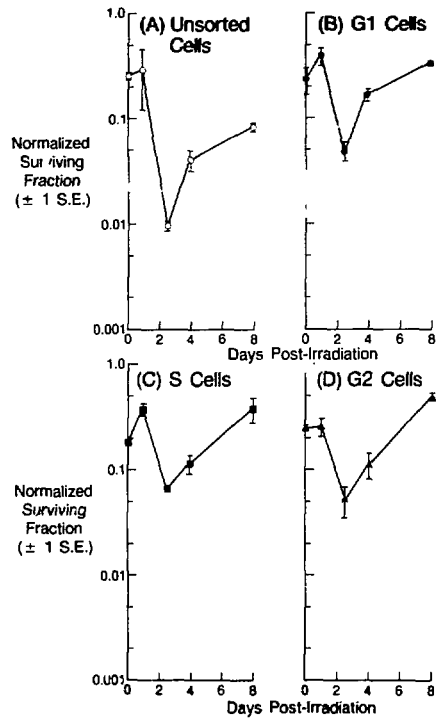

Fig. 5. Survival data are presented for unsorted (panel A) and sorted G1, S, and G2+M populations (panels B,C,D) of R2C5 tumors at 0 to 8 days following x-irradiation in situ. The enzymatically dissociated cells were stained with Hoechst 33342 (5 μM, 2 hr, 37°C) and sorted on the basis of DNA fluorescence using a uv laser intensity of 150 mW. The survival fractions of x-irradiated cells in each phase of the cell cycle were normalized using survival data for unirradiated cells in the corresponding cell-cycle phase. In the irradiated tumor cell populations at the five time points studied, the unsorted cells passed through the laser beam exhibited a survival that was 17.0% ± 7.5% (S.E.) lower, on the average, than the survival of Hoechst-stained cells that were not subjected to flow cytometry. For each individual experiment, the phase-specific survival of the irradiated tumor cells was renormalized to correct for the laser cytotoxicity measured in the same experiment. *(XBL 859-8473)*

The sorted tumor cell populations in G1, S and (G2+M) phases of the cycle exhibited 8-, 6-, and 5-fold decreases, respectively, in their survival at 2.5 days relative to 1 day postirradiation. At 8 days postirradiation the survival of the unsorted tumor cells was only one-third of the value measured immediately following irradiation (S.F. = 0.26 ± 0.02), whereas sorted cells in the G1, S and (G2+M) phases had respective survival levels that were 41, 97, and 98% greater than the values determined immediately after x-irradiation. The unsorted cells thus exhibited a greater dip in survival and a slower rebound at 2.5 to 8 days postirradiation than the sorted tumor cell populations. Because an unsorted cell population contains a very large number of diploid host cells relative to sorted tumor cell populations, the possibility exists that the large dip in survival of unsorted cells may be mediated partly or wholly by the cytotoxicity of host cells that infiltrate the tumor beginning at 2 to 3 days following irradiation (see Fig. 4A).

Using the data presented in Fig. 4B on cell-cycle distributions and the data shown in Fig. 5B, 5C and 5D on the survival of G1, S, and (G2+M) tumor cells, calculations were made of the percentage of surviving cells in each phase of the cell cycle at 0 to 8 days following a 10-Gy dose of 225-kVp x rays. These results are presented in Table 2. Throughout the 8-day postirradiation period, tumor cells in the G1 cycle phase constituted 70 to 90% of the surviving cell population. Fewer than 20% of the surviving tumor cells were measured in either the S or the (G2+M) phases at any time up to 8 days following irradiation.

Table 2. Percent of surviving tumor cells in each cycle phase at 0 to 8 days following irradiation in situ with 10 Gy of 225-kVp x rays.

Days postirradiation	Percent G1 ± S.E.	Percent S ± S.E.	Percent (G2+M) ± S.E.
0	78.2 ± 21.4	8.7 ± 0.2	13.1 ± 0.5
1	79.4 ± 15.8	3.7 ± 0.5	16.9 ± 3.1
2.5	69.6 ± 16.4	18.6 ± 0.6	11.8 ± 3.8
4	90.4 ± 12.8	0.5 ± 0.1	9.0 ± 2.5
8	76.8 ± 3.2	3.4 ± 0.9	19.8 ± 1.4

COMPARATIVE ANALYSIS OF MODELS DESCRIBING GLUCOSE UPTAKE IN THE BRAIN

Hugo A. Massaldi

Several alternatives arise when the problem of building a model for glucose exchange between cerebral capillaries and tissue is considered. Among them, a version of the lumped-compartment model has been receiving increased use for describing the uptake and breakdown of glucose and glucose analogues in the brain, by means of imaging techniques.[1-4] Although the inherent simplicity of this model justifies its use, few attempts have been made to challenge its assumptions[5] or evaluate its methodology.[6] This report presents the preliminary analysis of an attempt to contribute in this respect. It has been intended to put the lumped model into a more general context, by pointing out the scope, limitations and implicit assumptions of this and other available or new models that can be proposed with the same purpose. The different expressions and mechanisms used to present the glucose transport step constitute an essential—and not less controversial—aspect of the modeling problem. Although these elements may influence the model organization and assumptions to some extent, for the present purposes it is sufficient to adopt the simple notation of rate constants, as used in classical pharmacokinetics. A more thorough discussion of this problem is presented elsewhere.[7,8]

MAIN RELATED MODELS

Capillary Exchange, Axial Gradient in Vascular Space

Figure 1a shows a scheme of this model, which incorporates an axial flow and varying concentration along the capillary length as essential components. The assumptions with respect to the tissue compartment may vary widely and give rise to different solutions. A system of the type shown in Fig. 1a has been considered and solved[9,10] under various conditions, mainly in connection with the multiple-indicator technique and early washout curves. The

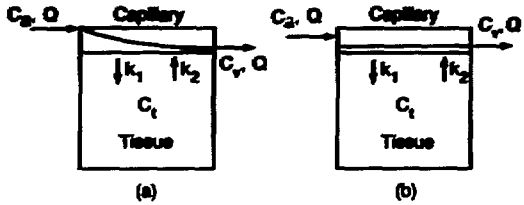

Fig. 1. Comparative analysis of models. a) Distributed model of capillary exchange, showing concentration gradient along capillary. b) Well-stirred model of capillary exchange, with uniform concentration in vascular compartment. (XBL 8511-8583)

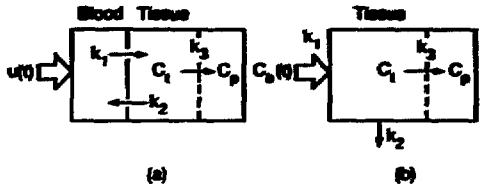

Fig. 2. Comparative analysis of models. a) Lumped-compartment model for exchange between blood and tissue. b) Compartment model scheme used in positron emission tomography (PET) of glucose analogues. (XBL 8511-8569)

situation described is perhaps the most real one for solute exchange in a capillary that does not have interconnections with other elements of the capillary bed. Its usefulness, however, and the benefits of this more detailed description, are limited to short-time experiments where the injection and sampling sites are rather close to the organ under study, since no consideration is given to the dynamics of flow.

Well-Stirred Vascular Compartment

Solutions to this model have been obtained.[11,12] Figure 1b illustrates that the well-stirred approximation implies the assumption of instantaneous mixing of the entrance solute within the compartment, which is assumed to operate at the exit concentration. Jacquez[5] has recently challenged this assumption in favor of a distributed capillary model, of the type discussed above. However, his results do not show a substantial improvement and, probably because of the low extraction fraction of glucose and glucose analogues, the well-mixing assumption may not constitute an important drawback of the model. It should be mentioned, however, that the ignorance of the dynamics of flow, which depend on recirculation effects and the choice of the injection/sampling sites, still remains in this version, and therefore, it may not be adequate to represent the data of runs longer than a first-pass experiment.

Lumped Compartment Model

This is the type of model used in compartmental analysis and classical pharmacokinetics to describe tracer distribution, obtain plasma disappearance curves, or estimate clearance rates for drugs in different regions of the organism. A scheme of this model and related parameters is shown in Fig. 2a. Again, its major limitation is the lack of allowance for the dynamics of flow, which are explicitly ignored, both in the model scheme and in writing the balance equations. The well-known solution to this model for a bolus injection in the blood compartment has the form of a summation of two exponential terms, and can be found in many classical textbooks (cf., Refs. 13,14).

The lumped model also makes use of the well-mixing condition, by implicitly assuming that, upon injection, the solute instantaneously distributes uniformly in the blood compartment. With these approximations, the model may be adequate for fitting data and for simulating the behavior of an injected solute within a rather large vascular volume over time periods longer than those for the capillary distributed models. However, the situation is different when the precise estimation and correct interpretation of the kinetic constants are required. In this respect, and concerning its application to hepatic transport kinetics, it has been shown[15] that the lumped model systematically underestimates the values of constants k_1 and k_2, and particularly, that the values of k_1, obtained from the earlier time data, may be incorrect by as much as 50–70%.

The PET Model

The conventional lumped model, discussed above, not only ignores the general dynamics of flow and recirculation, but it also neglects the flow term in the balance for the vascular compartment, $Q(C_a - C_v)$. The PET model, shown in Fig. 2b, is a varient of the lumped model that is designed to cope with the flow problem by estimating and treating the concentration function in the brain capillary region as the input function to the tissue.

Thus, regarding the question of flow effects, this model represents an improvement with respect to the classical lumped model. However, several problems, associated with the precise determination of the actual input function in the brain capillary region, still remain.[6] These make uncertain the

estimation of the transport constants k_1 and k_2, particularly from data taken at the shorter times, when the impulse input function changes more rapidly.

Step input/"Constant Infusion" Model

Another varient of the lumped model can be proposed to circumvent the problem of flow effects. It essentially consists of the same scheme as that of Fig. 2b, except that the input function, $C_b(t)$, is experimentally constructed so that it approaches a step function, as in the constant infusion experiment. The basis for this is the observation that, even in the PET model, where the solute is initially injected as a bolus, a quasi-constant slightly decreasing level is rapidly approached after the pass of the initial wave. Bischoff[16] has also pointed out this finding for the brain vascular region, in a simulation study of solute distribution in the organism. The required constancy in C_b may therefore be accomplished by a slow initial injection and one or more complementary, also slow injections of solute conveniently separated in time, all administered in the peripheral circulation.

The solution to this model, for a step-input function $C_b(t) = D$, is, for the total activity of labeled solutes in the tissue:

$$\frac{C_t + C_p}{D} = \frac{k_1}{k_2 + k_3} \left\{ k_3 t + \frac{k_2}{k_2 + k_3} [1 - \exp(-(k_2 + k_3)t)] \right\} \quad (1)$$

Several curves corresponding to Eq. (1), for various values of the parameters, are shown in Fig. 3. The trends of the uptake activity curves are similar to those observed in experimental studies[3,4] where a bolus is injected in the peripheral circulation. This can be considered as an indication that the step input condition, assumed by the proposed model, may represent a good approximation to the actual situation.

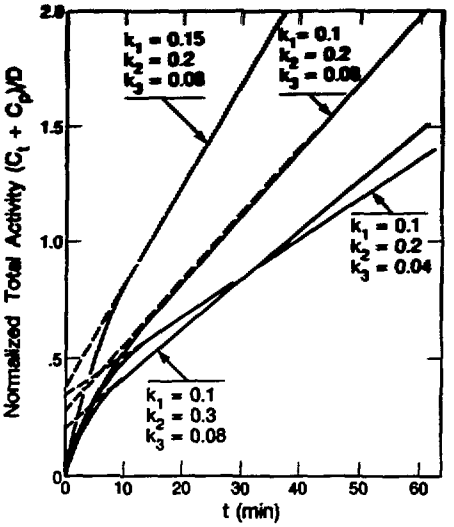

Fig. 3. Uptake curves of normalized total activity as a function of time, from "constant infusion" model. Eq. (1).

(XBL 8511-8568)

CONCLUSIONS

Despite strong limitations and apparently gross over-simplifications, the possible variants of the lumped model remain as convenient, and probably the best alternatives to describe glucose tracer distribution in the brain by means of noninvasive imaging techniques.

The final answer to the problem of model adequacy and parameter estimation has to be provided by a comprehensive model that takes into account the mentioned effects of flow dynamics, recirculation, and delay in a consistent manner. Although a model like this will probably not be amenable to direct use with the present methodology, its results would allow the parameters of the simpler models discussed here to be estimated and contrasted by simulation. Work is in progress along this line.

REFERENCES

1. Sokoloff, L., Reivich, M., Kennedy, C., Desrosiers, M.H., Patlak, C.S., Pettigrew, K.D., Sakurada, O., and Shinohara, M. The [^{14}C] deoxyglucose method for the measurement of local cerebral glucose utilization: theory, procedure and normal values in the conscious and anesthesized albino rat. *J. Neurochem. 28*, 897–916 (1977).
2. Phelps, M.E., Huang, S.C., Hoffman, E.J., Selin., C., Sokoloff, L., and Kuhl, D.E. Tomographic measurement of local cerebral glucose metabolic rate in humans with [^{18}F]-Fluoro-2-deoxi-D-glucose: validation of method. *Ann. of Neurol. 6*, 371–388 (1979).
3. Knittel, B. Kinetic analysis of dynamic PET data, Master's thesis, UC Berkeley, 1983.
4. Heiss, W.D., Pawlik, G., Herholz, K., Wagner, R., Goldner, H., and Wienhard, K. Regional kinetic constants and cerebral metabolic rate

for glucose in normal human volunteers determined by dynamic positron emission tomography of [^{18}F]-2Fluoro-2-deoxy-D-glucose. *J. Cereb. Blood Flow Metabol. 4,* 212–223 (1984).
5. Jacquez, J. Red blood cell as glucose carrier: significance for placental and cerebral glucose transfer. *Am. J. Physiol. 246,* R289–R298 (1984).
6. Budinger, T.F., Huesman, R.H., Knittel, B., Friedland, R.P., and Derenzo, S. Physiological modeling of dynamic measurements of metabolism using positron emission tomography. In *The Metabolism of the Human Brain Studied with Positron Emission Tomography,* T. Greitz et al. Eds., New York, Raven Press, 1985.
7. Massaldi, H.A. Channel model and parameters of the glucose transporter. *Nature,* submitted for publication. Nov. 5, 1985.
8. Massaldi, H.A. Scope, limitations and applicability of models describing glucose uptake in the brain. A simulation study. *Am. J. of Physiol.,* to be submitted for publication.
9. Levitt, D.G. Evaluation of the early extraction method of determining capillary permeability by theoretical capillary and organ models. *Circ. Res. 27,* 81–95 (1970).
10. Groresky, C.A., Ziegler, W.H., and Bach, G.G. Capillary exchange modeling, barrier-limited and flow-limited distribution. *Circ. Res. 27,* 739–764 (1970).
11. Middleman, S. *Transport Phenomena in the Cardiovascular System,* Wiley-Interscience, New York, pp. 193–194 (1972).
12. Huang, S.H., Phelps, M.E., Hoffman, E.J., and Kuhl, D.E. A theoretical study of quantitative flow measurements with constant infusion of short-lived isotopes. *Phys. Med. Biol. 24,* 1151–1161 (1979).
13. Atkins, G.L., *Multicompartment Models for Biological Systems,* Methiem and Co., London (1969).
14. Gibaldi, M., and Perrier, D. *Pharmacokinetics,* Dekker, New York, (1975).
15. Forker, E.L., and Luxon, B.A. Hepatic transport kinetics and plasma disappearance curves: distributed model vs. conventional approach. *Am. J. Physiol. 235,* E638–E660 (1978).
16. Bischoff, K.B. Applications of a mathematical model for drug distribution in mammals. In *Chemical Engineering in Medicine and Biology,* D. Hershey, Ed., Plenum, New York (1967).

HOLISTIC BIOPHYSICS OF RED BLOOD CELL MEMBRANE SYSTEMS

Howard C. Mel, Gary V. Richieri, Hugo A. Massaldi, and Robert Bridwell

Biological membranes may be viewed as a next step upward from the molecular level in organizational complexity, providing a foundation-setting for macrolevel properties, and for behavior of two-dimensional structures. Such properties include *semipermeability, porosity, stretchability, tear resistance, insulating ability,* and other thermal, electrical, mechanical, osmotic and geometrical qualities. The *holistic* nature of this project resides in the fact that many of these features can be related to each other and to the lower level molecular properties of ionic permeability and transport, as well as to the higher level physiology of the whole animal—*most* notably that associated with the circulation of the whole blood. Our experimental and theoretical work, then, is aimed not only at learning new facts about membranes of whole-cell systems but also at elucidating underlying mechanisms "...emphasizing the organic or functional relation between parts and whole..." (a dictionary definition of holism).

We report this year on advances in both experimental and theoretical domains. First, the whole-cell and membrane electrical resistivity and dielectric breakdown properties are exploited to lead to an improved measure of the electrical resistivity of the *cytoplasm* of the cell—an entree to information on the normal or abnormal state of hemoglobin. Secondly, new results are presented relevant to thermal responses of the membrane surface and the recently discovered phenomenon of "membrane stretch."[1,2] We conclude with a summary of a new theoretical model-study that can predict osmotic fragility properties from cell size distributions determined by resistive pulse spectroscopy (RPS).

MEMBRANE BREAKDOWN AND CYTOPLASMIC RESISTIVITY

A relatively simple improvement in the electrical components of the instrumentation for resistive pulse spectroscopy (RPS), now allows precise measurement of the electric field strength at which the red blood cell membrane will begin to pass current, the so-called *membrane breakdown potential.* We can now also measure, to a much higher degree of accuracy than previously, the internal cytoplasmic resistivity of red blood cells (and presumably other cell types as well). The procedure is as follows. Red cells, in dilute suspension, are examined under both low and high electric field strength conditions. An example of the resulting data is presented in Fig. 1 (the circles are actual data from normal blood). A low applied electric field results in a line such as (a), while a high field leads to lines such as (b), (c) or (d), depending upon the internal resistivities of the cells. The *membrane breakdown potential* is seen simply as the crossover point between the low and high electric field lines.

The determination of *cytoplasmic resistivity* is somewhat more complicated. It requires the following equations:

$$\rho_{cyto} = \rho_{medium} \cdot w$$

$$w = 1 + \frac{f_E \times M_r}{1 - M_r}$$

where ρ_{cyto} = cytoplasmic resistivity, ρ_{medium} = medium resistivity, f_E = shape factor of cells (varies from 1.0 to 1.5, and for normal isotonic red cells equals about 1.2), M_r = ratio of slope of the high electric field line to that of the low field line.

The technique to determine the shape factor has recently been published.[3]

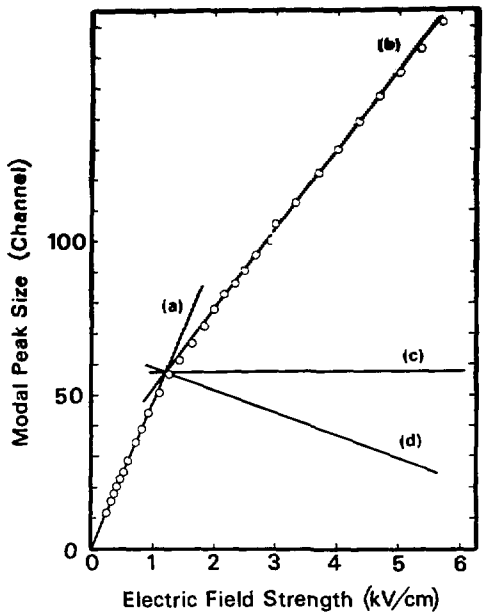

Fig. 1. Relationships between modal peak size (in channels) and applied field strength for various conditions of membrane and cytoplasmic resistivity. The circles represent experimental data for normal red blood cells in isotonic medium.

(XBL 8511-11474)

The above approach has now been applied to several different kinds of blood cell samples. The values for membrane-breakdown potential and cytoplasmic-resistivity for 8–15 normal (AA), 5–11 heterozygous sickle cell trait (AS), and 15–20 homozygous sickle cells (SS) are included in Table 1. For these samples the membrane-breakdown values do not differ significantly amongst the three groups. However, the cytoplasmic-resistivity

Table 1. The average and standard error of the multiple cellular parameters measured by the RPS technique for normal, sickle cell trait, and sickle red blood cells.

	Volume			Surface		Deformability		Fragility		Membrane	Cytoplasmic
	Modal (μm^3)	Mean (μm^3)	C.V.	area (μm^2)	Shape factor	B.I.	F.S.	50% (mOsm)	Slope	breakdown (V/cm)	resistivity (ohm-cm)
AA	89.8	93.5	16.0	129.2	1.201	1.08	11.2	127.8	5.0	1151	147.6
	±0.88	1.03	0.46	1.39	0.002	0.02	0.31	1.11	0.15	32.5	2.12
AS	85.5	88.9	16.3	125.0	1.199	1.04	11.5	115.4	4.3	1190	148.7
	±2.23	2.41	0.45	2.62	0.002	0.02	0.42	1.42	0.33	10.7	1.79
SS	87.6	91.6	23.4	144.3	1.160	0.65	8.5	98.5	2.0	1154	166.6
	±1.63	1.90	0.76	2.26	0.004	0.04	0.69	1.99	0.11	33.0	7.49

values, and the population heterogeneity in this parameter are significantly higher for the SS cells.

Different information is available when the data of Fig. 1, the unnormalized raw data, are plotted in another way. If they are replotted normalized to line (a) (i.e., taking each point along line (a) equal to 100%) we obtain Fig. 2 wherein the dashed lines correspond to lines (a) and (b) from Fig. 1. In this figure the breakdown potential appears to occur at a much lower value as compared to the single point of intersection in Fig. 1 (800 V/cm compared to 1235 V/cm). This difference is ascribed to the *heterogeneity* of the cell population, heterogeneity either in size or in membrane breakdown characteristics, which leads to a lower breakdown potential than that applicable to the population average.

SICKLE CELL TRAIT AND SICKLE CELLS

Expanding upon the data presented last year,[1] we present in Table 1 the values for eleven parameters measured by the RPS technique for the same three classes of normal, sickle trait, and sickle cells. New parameters provided are the *true* modal and mean cell volumes, surface area, shape factor, membrane breakdown potential, and cytoplasmic resistivity.

Small differences exist for certain of the properties, and large, significant differences for others. For example, these latter are found in the osmotic fragility for the AS samples, and in all but the mean and modal sizes and the membrane breakdown potential for the SS samples. In our previous report[1] we showed how a multiparameter-index approach could provide an alternative kind of holistic evaluator for purposes of comparing cell populations characterized by arrays of properties such as these. Refinement of this approach to take account of the new (or revised) measurements, and the added sample type (AS) is currently under scrutiny.

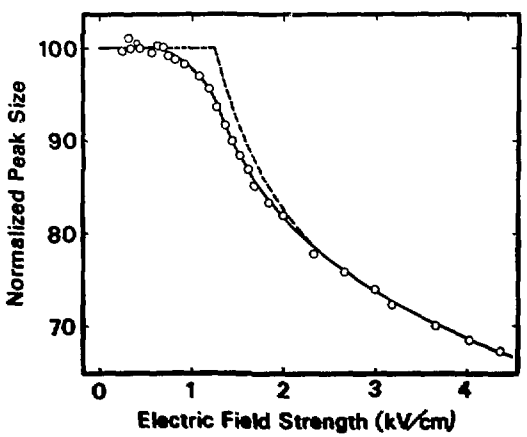

Fig. 2. Data of Fig. 1, recalculated and normalized to: 100% = the pre-breakdown apparent size at each field strength (corresponding to infinite membrane resistivity). The dashed lines are the values calculated for the solid lines (a) and (b) of Fig. 1. (XBL 8511-11475)

TEMPERATURE AND OSMOTIC RESPONSES OF CELL VOLUME AND MEMBRANE SURFACE

We previously reported on the phenomenon of "membrane stretch" and related temperature-dependent volume responses of ghost membranes.[1] These were produced at various osmotic pressures and temperatures (so as to assure formation of about 95% ghosts) in order to test the stability and reversibility of such membrane-surface area changes. Subsequent to their formation, two-way transfers were then carried out between higher and/or lower temperatures. Results suggested that the reversibility was not complete for ghosts produced at 0°C, but was almost complete for those produced at 40°C.

A new question arose out of these findings, namely the extent to which the results depended upon the specific osmotic pressures at which the cells were hemolysed and measured. New experiments were therefore carried out wherein the ghosts were first resuspended in a series of intermediate osmotic pressures (175, 200, 250 mOsm), and then subjected to temperature changes. The results (Fig. 3) indicated that these ghost membranes behaved very much like intact-cell membranes, displaying almost complete reversibility in all samples. That is, the ghost volumes were equally able to respond reversibly to changes of temperature and of osmotic pressure.

An additional series of experiments was designed to sort out the separate (but interacting) effects of osmotic pressure and temperature on membrane integrity and volume responsiveness. Ghosts were produced to the 95% level at the requisite, respective osmotic pressures and temperatures. After 30 to 60 min samples were centrifuged, then all resuspended to the common conditions of 300 mOsm and 25°C. Following this equilibration they were resuspended (at 25°C) in a series of osmotic media ranging from 100 to 300 mOsm, and their volumes were measured.

The preliminary results (Fig. 4) suggest that for the ghosts originally made at 0° and 25°C, their past history has little effect on their ability to

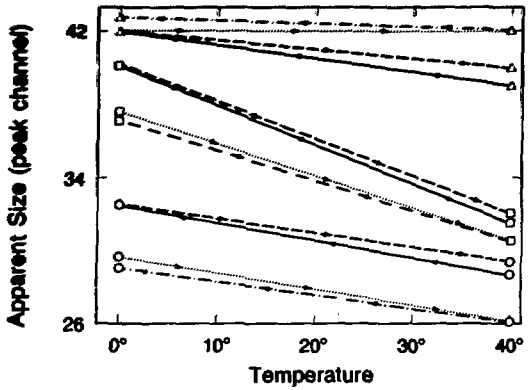

Fig. 3. Temperature reversibility of ghost volume changes. (Triangle, restored to 175 mOsm; square, restored to 200 mOsm; and circle, restored to 250 mOsm.) (XBL 8511-11477)

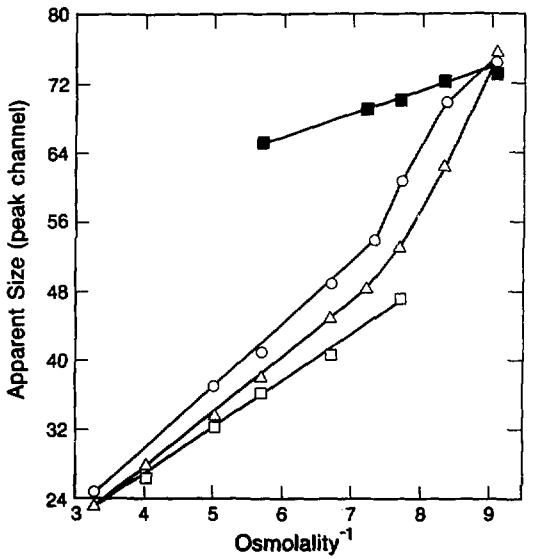

Fig. 4. Volume osmotic responses at 25°C for restored ghosts made under different conditions (Δ triangles, made at 0°C, 130 mOsm; circles made at 25°C, 120 mOsm; and squares, made at 40°C, 100 mOsm). (XBL 8511-11470)

respond osmotically—it is only the final condition that determines the results. However, for the 40°C ghosts an unexpected new phenomenon appeared: a double population—one responding well osmotically and the other (larger in volume) responding very little, indicating two classes of membrane state. A unifying explanation for these new results is being sought in our current investigations.

MEMBRANE FAILURE BY OSMOTIC FRAGILITY

A model that predicts the osmotic fragility curve of a red-cell population has been developed by combining the classic equation of Ponder with experimental size-distribution information of cell populations, as determined by resistive pulse spectroscopy. Two of the parameters involved, namely a *normalized osmotic volume correction*, B, and a *swelling index*, k, are determined from the experimental, *average properties of the population.*

The equation derived for the equilibrium-value critical osmotic pressure (the condition where the membrane will first fail osmotically) as a function of cell size is:

$$\pi_i^* = \frac{1 - B/V_i^*}{k(V_i^*)^n - B/V_i^*} \qquad (1)$$

where $V_i^* = V_{iso,i}/\hat{V}_{iso}$ is the ratio of a variable cell volume to the median cell volume at isotonicity, and the other parameters are:

$$B = \frac{b}{\hat{V}_{iso}}$$

(normalized cell volume correction for the average $\hat{V}_{iso}$ population)

b = nonosmotically active cell volume;

k = $V_c/\hat{V}_{iso}$ (swelling index for the average population)

n_e = surface area distribution index. The n_e value was theoretically found to be linked to B and k by the following expression:

$$n_e = -\log k/\log B \qquad (2)$$

Figure 5 shows the envelope of cumulative relative size distributions, percent frequency vs. V_i^*, of blood samples obtained from ten healthy donors. The data all fall within the two limiting broken lines, with average values represented by the full continuous line.

Figure 6 shows fragility curves, simulated according to Eq. (1), using the *average* size distribution shown in Fig. 5. It can be observed that, for increasing values of the swelling index, k, or the volume correction parameter, B, the curves are shifted to the left, i.e., to the region of less fragile populations. The values of the parameter n_e, calculated from Eq. (2), are also indicated in Fig. 6 for each curve. For the curve with B = 0.48, the effect of using values of n above and below n_e is to

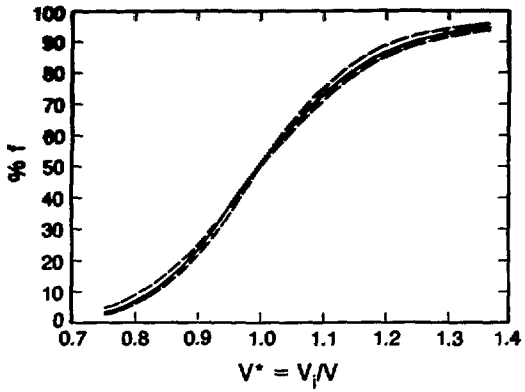

Fig. 5. The average (solid curve) and range-envelope (dashed curves) of cumulative frequency size distributions of 10 normal blood-cell samples. (XBL 8511-11473)

change only the slope of the curve; it does not alter the location of the 50% fragility point.

Figure 7 shows five sets of RPS fragility data, three of which belong to the healthy-donor samples, whose size distributions belong to those in Fig. 5. The remaining two data sets correspond to the hemoglobin SS blood samples from donors with sickle cell disease, whose cell size distributions (not shown) were found to be much broader than the normal ones. The solid lines in Fig. 7 are the result of fitting the data with Eq. (1), by using the parameters indicated for each curve along with the corresponding size distributions. The only adjustable parameter is the index n, whose experimental values are also indicated in this figure.

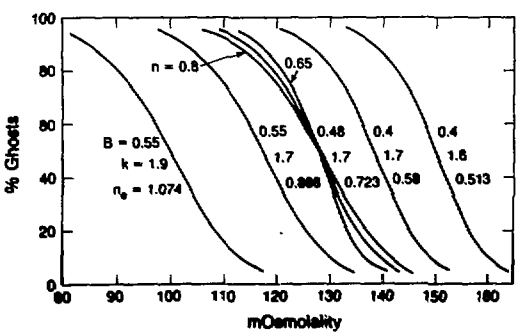

Fig. 6. Dependence of theoretical fragility curves on B, k and n_e. (XBL 8511-11469)

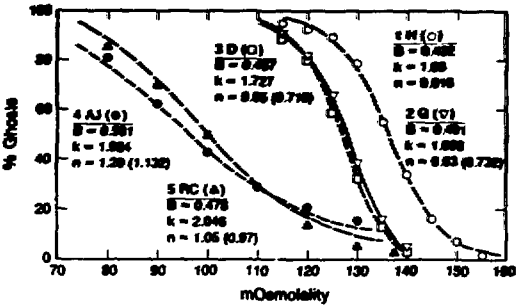

Fig. 7. The actual fragility data of five samples are matched by theoretical fragility curves with specific values of B, k and n_e or n. (XBL 8511-11476)

We interpret these results as providing good support to the use of the present model, based on the experimental size distribution of a given cell sample. Another interesting consequence of the present model is that the distribution of excess surface areas follows closely the distribution of cell sizes for normal cells. This renders an essentially constant value for the surface-to-volume ratio of all cells, in agreement with experimental observations reported in the literature.[4]

REFERENCES

1. Mel, H.C., Richieri, G.V., Massaldi, H., and Bridwell, R. Red blood cell biophysics: osmotic fragility and related membrane phenomena. Biology and Medicine Division Annual Report 1983–1984, Lawrence Berkeley Laboratory report LBL-18393, p. 139 (1985).
2. Richieri, G.V., and Mel, H.C. Temperature effects on osmotic fragility, and the erythrocyte membrane. *Biochim. Biophys. Acta 813*, 41–50 (1985).
3. Richieri, G.V., Akeson, S.P., and Mel, H.C. Measurement of biophysical properties of red blood cells by resistive pulse spectroscopy: volume, shape, surface area, and deformability. *J. Biochem. Biophys. Methods 11*, 117–131 (1985).
4. Linderkamp, O., and Meiselman, H.J. Geometric, osmotic, and membrane mechanical properties of density-separated human red cells. *Blood 59*, 1121–1127 (1982).

Tissue Effects of Heavy Charged Particle Beams

LATE RADIATION DAMAGE IN THE MOUSE KIDNEY

Edward L. Alpen, Patricia Powers-Risius, Kristina S. Kavanau, and Randy J. DeGuzman

Late radiation damage to the kidney is a dose-limiting factor for human cancer therapy when the treatment field is in the upper abdomenal region. The Berkeley Bevalac beams are being used for cancer radiotherapy, and information about the time-course and severity of renal damage following heavy-ion irradiation is of clinical and radiobiological importance.

We are studying the late effects in the mouse kidney after irradiation with single and fractionated doses of x rays or heavy charged particles. The repair capacity of the renal functional unit (glomerulus and tubule) is examined with respect to the number of dose fractions and the dose per fraction. Keeping the length of time constant between the first and last fraction, i.e., 25 days, the mice are given 1, 2, 4, 8, or 16 fractions of radiation. This regimen enables us to conform to the current radiotherapy schedule of 4 consecutive days a week.

The kidney offers the opportunity for the separate examination of at least three functional elements, each of which is thought to have limited capacity for proliferation and repair. These sytems are 1) the functional secretory and absorptive epithelial cells of the post-glomerular reabsorption apparatus (the tubule), in which one can examine the functional status of both secretory and absorptive activity, 2) the glomerular apparatus in which ultrafiltration of the plasma is the functional endpoint as measured ultimately in the filtration rate and, 3) the rate of perfusion of the kidney by plasma presenting itself for filtration in the glomerular apparatus. The latter two are, of course, closely interrelated because in any given set of circumstances, reduced plasma flow to the glomerular apparatus (in the presence of a normally functioning glomerulus), will lead to a reduced filtered volume. On the other hand, alteration of the "filterability" of the glomerular tuft may produce reduction of the glomerular filtration rate while renal glomerular perfusion remains unaltered.

Recent work by Williams and Denekamp,[1] Stewart et al.,[2,3] and Alpen and Stewart[4] have provided some methods to assess the functional status of the irradiated mouse kidney. The methods that have been fully developed include those for the measurement of glomerular filtration rate and tubular secretory function. In addition, hematocrit values will be a measure of the anemia of renal insufficiency. The functional tests are run at 8- to 10-week intervals during the year following bilateral kidney irradiation.

The method to estimate the glomerular filtration rate is based on the rate of clearance of ^{51}Cr-labeled EDTA from the plasma. This label acts as does inulin in that it is filtered at the glomerular surface and is neither secreted nor reabsorbed in the tubules. Therefore, its rate of disappearance from plasma is an estimate of the glomerular filtration rate (GFR). The method is used clinically in humans and also works well, with minimum adjustment, in the mouse. Williams and Denekamp[1] describe the method in detail. Twenty microcuries of ^{51}Cr-EDTA are injected into a mouse, and 40 minutes later a blood sample is taken from the retro-orbital sinus. The radioactivity in 20 μl of plasma is counted. High residual ^{51}Cr levels in the plasma indicate a decreased GFR. Figure 1 shows the plasma activity of ^{51}Cr-EDTA at times after an IP injection into a nonirradiated mouse.

We are using a modification of the urinary frequency apparatus developed by Stewart et al.[5] to assess tubular function. Mice are individually housed in small chambers with wire floors. Voided urine falls onto absorbent paper that is continuously drawn beneath the cages. The number of urine spots in 24 hours correlates with total urine output. The time course of the change in urination frequency as a function of dose is recorded.

We have begun to study the feasibility of using ^{131}I-hippuran to measure the effective renal plasma flow (ERPF) in mice. Hippuran is actively secreted into the tubular fluid and is removed during a single passage through the kidney. The basic method is similar to the ^{51}Cr-EDTA clearance test, and from the ratio of the EDTA/hippuran clearance we will devise a parameter proportional to the filtration fraction that represents the glomerular function independent of the perfusion rate. The renal

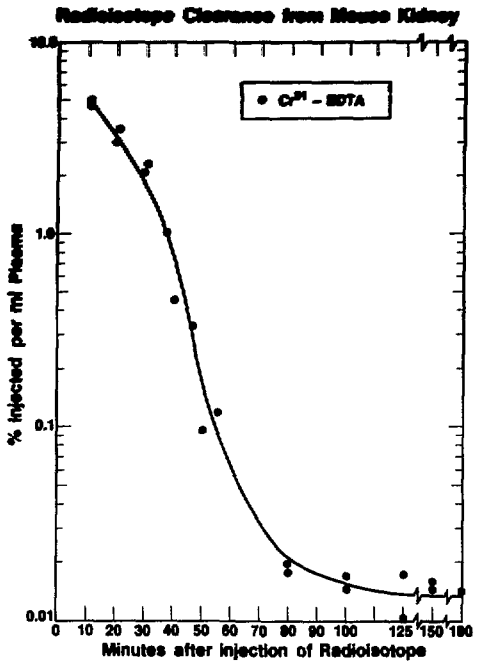

Fig. 1. The clearance curve of ^{51}Cr-EDTA (New England Nuclear) injected into LAF$_1$ mice. (XBL 857-8399A)

plasma flow itself is an important measure of the vascular state of the kidney.

Alpen and Stewart[4] observed that an anemia similar to the anemia of acute renal insufficiency in man develops as a result of radiation nephropathy in the mouse. The simple end point of the peripheral hematocrit was shown to be even more sensitive than the ^{51}Cr-EDTA clearance in detecting early radiation nephropathy. The functional significance of this end point remains to be explained. It is known that the anemia of acute renal insufficiency in man has at least two components: an increase in red cell hemolysis, possibly but not certainly in the kidney, and a decrease in the production of erythropoietin, the red cell regulating hormone that is mostly produced in the extraglomerular tuft in the kidney. The anemic changes have special significance because the effects probably arise from changes outside of the vascular or glomerular endothelium. We want to demonstrate the time relationship between the endothelial changes of glomerular damage and the onset of anemia.

One of the factors in late radiation damage to the kidney is fibrosis, which may contribute to renal failure.[6] Fibrosis is characterized by excessive connective tissue proliferation, of which collagen is the main component. Using the hydroxyproline assay, Meistrich et al.[7] have shown that significant increases in total collagen content in mouse kidneys *can be detected by 9 months after x-irradiation.* The concentration of hydroxyproline, an amino acid specific to collagen, may be a sensitive measure of late kidney damage. We are using a modification of the Woessner method[8] to measure the hydroxyproline concentration at 1 year after single and fractionated doses of irradiation.

Using the results of these experiments, we will compare the radiation response to x rays with that to the high-energy Bevalac beams. A given biological response is produced by different doses for each type of radiation, and these differences are expressed as the relative biological effectiveness, or RBE. The RBE values for kidney, a late-responding tissue, may be higher than the RBE for acute-responding tissues, such as intestine. The fractionation experiments will also provide RBEs for the amount of repair between doses. Several preliminary experiments are in progress: 1 and 4 fractions of 670-MeV neon, 1, 2 and 4 fractions of 670-MeV silicon and 1 fraction helium. The 1, 2, 4, 8 and 16 fraction x-ray experiment is completed. Figure 2 compares the dose response curves for ^{51}Cr-EDTA and ^{131}I-hippuran activity, urinary frequency and plasmacrit (100-hematocrit). Each of these systems appears to be modified in a very similar way with respect to dose fractionation. As the number of fractions is increased, the total dose needed to obtain the same response level (i.e., 12 urine spots per 24 hours) is greater.

In Fig. 3 the reciprocal total x-ray dose required for an isoeffect level is plotted as a linear function of dose per fraction. The estimate of the ratio of the y intercept (α) to the slope of the line (β), the α/β ratio, is a relative measure of cell killing. This α/β ratio is derived from the linear-quadratic model equation: ln (response) = $n(\alpha d + \beta d^2)$, where d is the dose per fraction, and n is the number of fractions. The α/β ratio is used to relate changes in biological effectiveness to the dose per fraction. This can be a guide to radiotherapists in choosing the optimum size of dose per fraction. The α/β ratios for the kidney function responses (Fig. 2) are between 4.0 and 4.65 Gray; the α/β ratio for wet kidney weight is 5.1. When the heavy-ion irradiation experiments are completed, we will compare those α/β ratios to those of x rays to assess the fractionation effects on kidney tissue of both types of radiation.

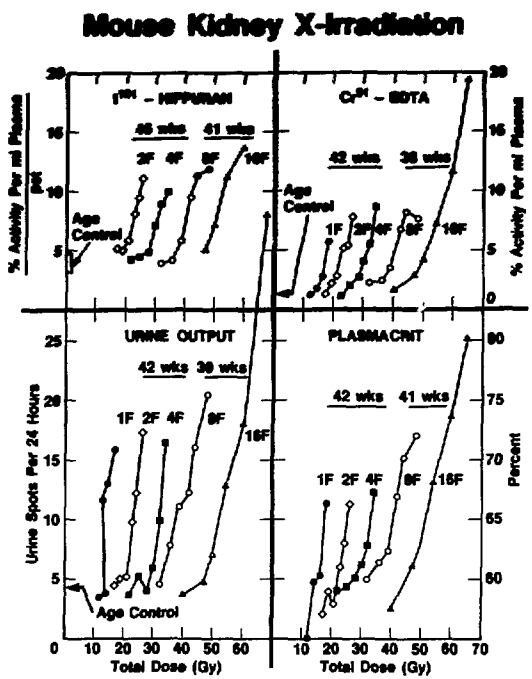

Fig. 2. Dose response curves for plasmacrits and three kidney function tests in mice. The curves are labeled with the fraction number and the number of weeks after the first dose that the test was done. (XBL 857-8393A)

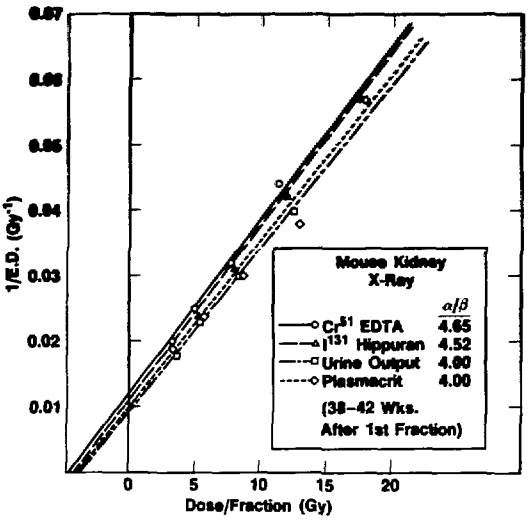

Fig. 3. The reciprocal total x-ray dose required for an isoeffect level versus the dose per fraction of x rays. α is the value of the Y intercept, and β is the slope of the line. The data points represent isoeffect levels from 1, 2, 4, 8 and 16 fractions of x rays. (XBL 857-8394)

REFERENCES

1. Williams, M.V., and Denekamp, J. Sequential functional testing of radiation-induced renal damage in the mouse. *Radiat. Res. 94,* 305–317 (1983).
2. Stewart, F.A., Soranson, J.A., Alpen, E.L., Williams, M.V., and Denekamp, J. Radiation-induced renal damage. The effect of hyperfractionation. *Radiat. Res. 98,* 407–420 (1984).
3. Stewart, F.A., Soranson, J.A., Haughan, R., Alpen, E.L., and Denekamp, J. The RBE for renal damage after irradiation with 3 MeV neutrons. *Br. J. Radiol. 57,* 1009–1021 (1984).
4. Alpen, E.L. and Stewart, F.A. Radiation nephritis and anemia. *Br. J. Radiol. 57,* 185–186 (1984).
5. Stewart, F.A., Michael, B.D., and Denekamp, J. Late radiation damage in the mouse bladder as measured by increased urinary frequency. *Radiat. Res. 75,* 649–659 (1978).
6. Chauser, B.M., Hudson, F.R., and Law, M.P. Renal function in the rat following irradiation. *Radiat. Res. 67,* 86–97 (1976).
7. Meistrich, M.L., Williams, M.V., Soranson, J., Fowler, J.F., and Denekamp, J. Increased collagen and fluid content of mouse kidneys at 9 months after single or fractionated x irradiation. *Radiat. Res. 99, 185–201 (1984).*
8. Woessner, J.F. The determination of hydroxyproline in tissue and protein samples containing small proportions of this imino acid. *Arch. Biochem. Biophys. 93,* 440–447 (1961).

HELIUM IRRADIATION OF THE RAT SPINAL CORD

Adrian Rodriguez, Edward L. Alpen, Randy J. DeGuzman, and John C. Prioleau

The spinal cord is a relatively radioresistant nonproliferative tissue that is of interest because it is often within the treatment volume during heavy-ion radiotherapy. The spinal cord exhibits long-term or late effects from radiation damage that we are studying with respect to repair after dose fractionation. Fractionation studies of spinal cord will allow us to test the hypothesis that RBE values for late effects are much higher than RBE values for acute responses of tumors and proliferating tissue. These studies will also provide RBE values for repair. This information will provide a basis for choosing the appropriate ion species, energy, and tolerance dose for radiotherapy of tumors that are adjacent to the spinal cord. Studies with neutrons as a model of high-LET radiation indicate that more than four dose fractions do not provide added protection by repair processes. If this relationship holds for heavy ions, we can expect the RBE to increase with large fraction numbers.

In the present study with helium ions, we have repeated and expanded earlier studies by Leith et al.[1] The helium ions will be used as the reference/low-LET radiation for comparison with heavy-ion responses in future studies.

The helium experiments include single dose, and 2, 4, and 8 fractions, given within 4 weeks (25 days). The dose schemes are designed to follow therapy treatment protocols: irradiations 4 days per week for 4 weeks, with a 3-day break each Friday through Monday.

White male CD-rats (approximately 10 weeks old and weighing 200–250 g) from the Charles River Breeding Laboratories, Wilmington, MA, were used. The rats were irradiated in the thoracolumbar region of the spinal cord (after anesthesia with methoxyflurane, an inhalation anesthetic, and placement in restraining holders). They were positioned in the plateau region of ionization, and an 11 × 16 mm semielliptical field was used for spinal cord exposure. The animals are maintained for 300 days and observed on a weekly basis for development of paralysis. After the animals begin to show decrements in hindlimb reflexes and leg strength, they are observed twice a week. The scoring system is the same as that used by Leith and is shown in Table 1. Radiation-induced myelopathy is considered to have occurred if the animal reaches a score of S-2 or greater.

Table 1. Grading system for assessment of radiation-induced myelopathy.

Grade	Description of gross impairment
S-O	No difference from controls
S-1	Delay in eliciting hindlimb-kick response upon pressure to limbs
S-2	Definite but mild impairment in hindlimb-kick response with obvious curling of toes
S-3	Impairment of kick moderately severe, and rats walk with slight hunchback, or flatfooted
S-4	Severe impairment, marked hunchback, rats walk on toes
S-5	Limb(s) completely useless, total paralysis (either uni- or bilateral)

RESULTS AND DISCUSSION

Irradiated rats begin to exhibit loss in hindlimb reflexes and performance within 12 to 20 weeks postirradiation. The latency of onset of paralysis is dose dependent as is the mean severity score for each dose group. Figure 1 shows the helium irradiation results as percent paralysis versus total dose for single doses and 2, 4, and 8 fractions. With increasing numbers of fractions, the total dose required to reach a particular isoeffect (50% paralysis) is greater, indicating that there has been

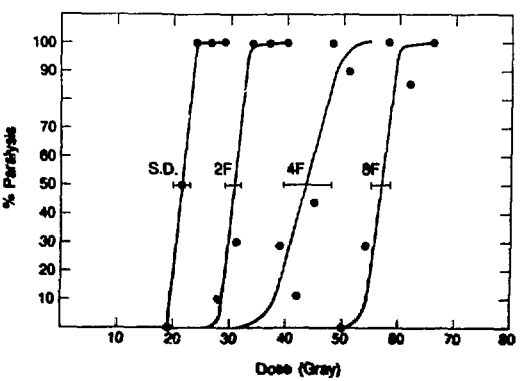

Fig. 1. Helium irradiation (plateau) with single doses and 2, 4, and 8 fractions delivered over 4 weeks (25 days). The ED_{50} for paralysis is indicated with 95% confidence limits.

(XBL 857-11236)

substantial repair. The ED_{50} doses for the single dose and the 2, 4, and 8 fractions are 22.3, 30.6, 43.6, and 56.9 gray, respectively. The single dose paralysis data is comparable to previous results of Leith et al.[1] with helium irradiation and gives an RBE of 1.08.

The isoeffect doses (ED_{50}) were evaluated with the use of the multifraction linear-quadratic model: ln (E[effect]) = n (α d + β d^2), where d is the size of the dose per fraction, and n is the number of dose fractions. We can obtain the α/β ratio from the multifraction isoeffect data, which is a relative measure of cell killing in a tissue via the linear (single event) and quadratic (double event) modes and can be used as a parameter describing the response of a tissue to dose fractionation. The linear-quadratic model can be transformed to

$$\frac{1}{nd} = \frac{\alpha}{E} + d\,\frac{\beta}{E}$$

and the data plotted as in Fig. 2. The slope of the line is an estimate of $\beta(\beta/E)$, and the intercept is an estimate of $\alpha(\alpha/E)$. The α/β value obtained for the spinal cord data is 2.43. This value is comparable to published tissue α/β values and is within the range for x-ray spinal cord data of 5.4.[1,2] In comparison, fractionated neutron (15 MeV/amu) data[3] have an α/β value of 77.4. There is little repair of neutron damage, and the high value indicates a large α component of linear cell inactivation. The repair capacity of a tissue after fractionation can be assessed by plotting the value of ΔDr against dose per fraction, as is shown in Fig. 3. ΔDr is the increase in dose per fraction needed for an isoeffect when the number of dose fractions is increased from n to n':

$$\Delta Dr = \frac{Dn' - Dn}{n'}$$

This parameter may be of value to the radiotherapist in determining the dose per fraction and fraction number beyond which there is no further advantage or sparing, since there is no further repair (i.e., increase in dose per fraction). In Fig. 3 helium plateau radiation, x rays, and 15-MeV/amu neutrons are compared. For helium and x rays the intercept on the x axis is approximately the same (1.5 — 1.6 Gy), and for neutrons it is about 4 Gy. There is no advantage in going to lower doses per fraction with neutron radiation because there is less repair than for x-ray and helium radiation.

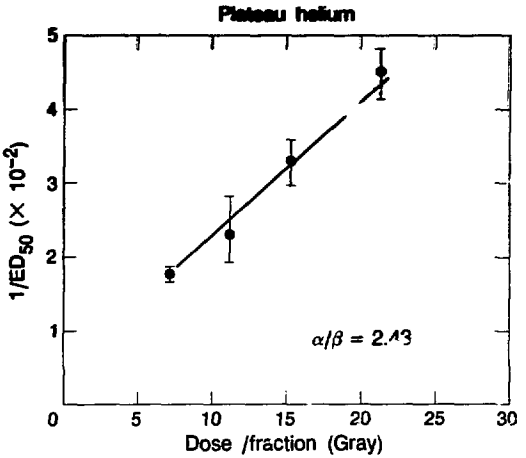

Fig. 2. Isoeffect plot ($1/ED_{50}$) versus dose per fraction of helium radiation. (XBL 857-11234)

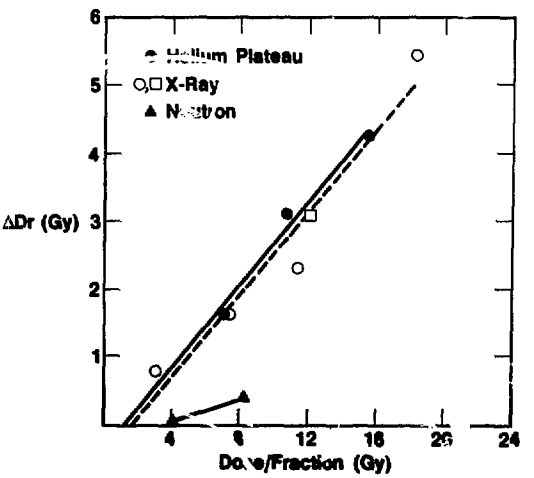

Fig. 3. Thoraco-lumbar spinal cord repair (ΔDr) as a function of dose per fraction when the number of fractions is increased from n to n'.

$$\Delta Dr = \frac{D_{n'} - D_n}{n'}$$

$D_{n'}$ and D_n are isoeffect doses. (XBL 857-8403)

REFERENCES

1. Leith, J.T., Lewinsky, B.L., Woodruff, K.H., Schilling, W.A., and Lyman, J.T. Tolerance of the spinal cord of rats to irradiation with cyclotron accelerated helium ions. *Cancer 35*, 1692 (1975).
2. White, A. and Hornsey, S. Radiation damage to the rat spinal cord: The effect of single and fractionated doses of x rays. *Br. J. Radiol. 51*, 515–523 (1978).
3. Van der Kogel, A.J., and Barendsen, G.W. Late effects of spinal cord irradiation with 300 kV x rays and 15 MeV neutrons. *Br. J. Radiol. 47*, 393–389 (1974).

INACTIVATION OF MOUSE MARROW STEM CELLS BY HEAVY CHARGED PARTICLES

E. John Airsworth, Lynn J. Mahlmann, and John C. Prioleau

A fundamental question of biophysics concerns relationships between the physics and chemistry of energy deposition and biological effect. Charged particles provide an excellent tool to explore these relationships because different patterns of energy deposition may be achieved by varying atomic number, the energy of the particle, or both. We previously explored relationships between linear energy transfer (LET) and inactivation of bone marrow colony-forming units (CFU-S) where the experiments were performed using, primarily, spread Bragg curves similar to those used in radiation therapy.[1] Under those conditions extensive fragmentation is produced by the brass spiral ridge filters, and the range of LET's to which cells are exposed is large. The purpose of the present study was to extend our work on relationships between LET and relative biological effectiveness (RBE), using the plateau portion of the Bragg curve because primary particle fragmentation is minimized, LET can be estimated more confidently, and the physics of energy deposition can be expressed in quantities of either dose or particle fluence. Because of the complex nature of energy depositions by charged particles, including the possibility of recombination of free radicals near the particle trajectory as well as a broad spectrum of delta ray energies, charged particle dose reflecting total energy deposition may be a less than wholly appropriate means by which to express the physical characteristics of charged particles. Inferences concerning the effect per particle can be derived confidently when the LET distribution is small, and, as would be predicted on physical grounds, interpretation of results on biological effects of different particles is influenced significantly depending upon whether dose or fluence is used. The present work extends our earlier studies on CFU-S inactivation[1] and on cataract production,[2] and complements ongoing studies on Harderian gland carcinogenesis[3] and life-span shortening in mice.[4]

The methods of irradiation and measurement of CFU-S survival have been described in detail elsewhere.[1] In brief, hybrid CB6F1 mice were given total-body exposure to various charged particle beams in the plateau portion of the Bragg curve, marrow was harvested between 30 and 90 minutes following irradiation, marrow-cell suspensions were prepared, and appropriate aliquots were injected into supralethally gamma-irradiated recipients. Recipient mice were sacrificed 8–10 days following irradiation; spleens excised and fixed in alcohol, acetic acid, and formalin (AAF); and surface colonies greater than 0.5 mm were counted with the aid of a dissection microscope. Survival curves and associated statistical parameters were computed by standard methods.

Figure 1 represents a summary of our current and past results. The lower curve describes the relationship between RBE at 10% survival and LET. RBE_{10} is defined as the ratio of doses, in cGy, that produces 10% survival. The triangular symbols indicate data collected using the plateau portion of the Bragg curve in recent experiments and the circles indicate estimates from previously published measurements made using spread Bragg peaks. The curve drawn through these points is eye fitted and probably adequately describes RBE-LET relationships for inactivation of CFU-S. Note that the RBE achieves a maximum value of about 1.8 in the range of 80–100 keV per micron and declines at lower and higher LETs. The one point that departs significantly from the curve is for spread-peak argon particles where LET was estimated at approximately 600 keV/μm. The RBE of about 1.1 was the result of a computed extrapolation number n of 0.7, so

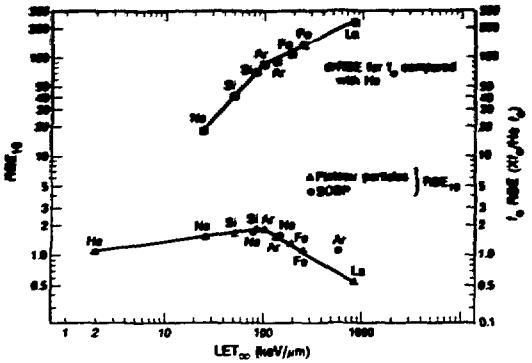

Fig. 1. Relative biological effectiveness (RBE) of charged particles for inactivation of mouse narrow colony-forming units (CFU-S). The lower curve indicates RBE at 10% survival, compared with ^{60}Co gamma radiation (left ordinate); the upper curve indicates RBE based on particle fluence, compared with helium, to reduce survival by 1/e (right ordinate). CFU-S inactivation measurements are based on replicate experiments.
(XBL 8511-8567)

the RBE value of 1.1 is probably spuriously high; based on D_0 estimates of 122 cGy for gamma rays and 151 cGy for argon particles, the RBE would be 0.8, and provide a better fit to the curve.

The upper curve in Fig. 1 shows f_0 RBE where f_0 is defined as the particle fluence that reduces survival by 1/e. The relationship between D_0 and f_0 is that D_0 is in units of dose in cGy and f_0 is based on particle fluence. The f_0 RBE indicates the relative effectiveness per particle for inactivation in comparison with helium particles. Helium particles are the lowest-LET particle for which we have collected data and for which we can confidently convert from dose to fluence. It is quite clear that estimates of RBE based on dose and/or fluence are quite different. In the case of lanthanum the lower curve in Fig. 1 shows the RBE, in terms of dose, was approximately 0.5, a value appreciably less than for helium; whereas, in terms of effectiveness per particle for inactivation, lanthanum is approximately 200 times more effective than helium. We have also estimated the number of particle traversals for helium and lanthanum in a nuclear area of approximately 50 μm, and preliminary calculations show that at the f_0 value the number of traversals is of the order of 0.6 for lanthanum and approximately 140 for helium.

Figure 2 further summarizes our results in terms of both inactivation cross section σ and f_0 in relation to LET. We have followed the lead of Dr. Gerhard Kraft at GSI in evaluating the results based on inactivation of cross section,[5] and we are greatly indebted to him and to S.B. Curtis of our Laboratory in connection with the analysis of these results in terms of σ and f_0. In the cross-section analysis we have assumed the nuclear diameter of a CFU-S to be approximately 8 microns, a value we infer from the nuclear size of a small mouse marrow lymphocyte. The curve describing σ with LET relates to the left ordinate and shows that cross section increases linearly, possibly with a slope slightly greater than 1.0, up to a LET of approximately 100 keV/μm, but at higher levels of LET a diminished rate of increase occurs. The dotted line represents an extrapolation of the curve over the LET range of 2 to 100 keV/μm, and the difference between the dotted curve and the curve fitted to the points between 100 and 1000 keV per micron indicates the extent to which energy is wasted at energy deposition rates in excess of 100 keV/μm. The descending curve in Fig. 2 relates to the right ordinate and indicates how f_0 decreases with increasing LET. For example, with helium at approximately 2 keV/μm, the f_0 is approximately *280 particles* $\times$ $10^6/cm^2$, and for lathanum, the comparable value is 1.3 $\times$ $10^6/cm^2$. The quotient of these two values indicates the RBE of approximately 200 plotted in the upper curve in Fig. 1.

The relationship between the present results obtained CFU-S and results obtained by Dr. Kraft and his co-workers at GSI is a subject of a manuscript in progress.

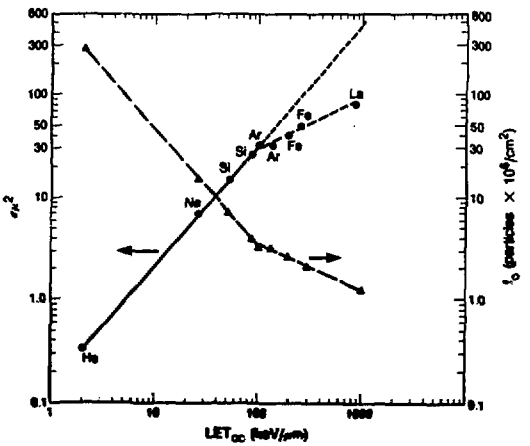

Fig. 2. Inactivation cross section (σ) and particle fluence (f_0) to reduce survival of mouse marrow CFU-S by 1/e. The geometric cross section of the mouse marrow CFU-S is estimated at about 50 microns based on the size of a small mouse marrow lymphocyte.
(XBL 8511-8566)

REFERENCES

1. Ainsworth, E.J., Kelly, L.S., Mahlmann, L.J., Schooley, J.C., Thomas, R.H., Howard, J., and Alpen, E.L. Response of colony-forming-units-spleen to heavy charged particles. *Radiat. Res. 96*, 180–197 (1983).
2. Jose, J.G., and Ainsworth, E.J. Cataract production by heavy charged argon, neon, and carbon particles. *Radiat. Res. 94*, 513–528 (1983).
3. Alpen, E.L., Powers-Risius, P., Fry, R.J., and Ainsworth, E.J. Harderian gland carcinogenesis from high LET, high Z, charged particles. In *Pion and Heavy Ion Radiotherapy: Pre-Clinical and Clinical Studies*. (L.D. Skarsgaard, Ed.), Elsevier Biomedial, New York, Amsterdam, Oxford, pp. 335–341 (1983).
4. Ainsworth, E.J., Prioleau, J.C., and Mahlmann, L.J. Life shortening effects of heavy charged particles: A status report. Biology and Medicine Division Annual Report 1981–1982, Lawrence Berkeley Laboratory report LBL-14986, p. 72 (1982).
5. Kraft, G., Blakely, E.A., Hieber, L., Kraft-Weyrather, W., Miltenburger, H.G., Muller, W., Schuber, M., Tobias, C.A., and Wulf, H. HZE effects on mammalian cells. *Adv. Space Res. 4*, No. 10, pp. 219–226 (1984).

ACUTE RADIATION LETHALITY IN MICE EXPOSED TO HEAVY CHARGED PARTICLES

E. John Ainsworth, John C. Prioleau, and Lynn J. Mahlmann

Relationships between relative biological effectiveness (RBE) and linear energy transfer (LET) are a fundamental aspect of the Biomedical Program at the Bevalac. Such relationships have been determined using various *in-vivo* and *in-vitro* model systems, and in general, the peak RBE appears to occur at a lower dose-averaged LET for *in-vivo* systems than is the case for the various *in-vitro* systems studied.[1] The response of mouse bone marrow stem cells (CFU-S) is among the several *in-vivo* systems studied, and we have determined RBE-LET relationships using charged particle beams modified by ridge filters, such as are used in radiation therapy, as well as under conditions in which mice are exposed to high-energy particles in the plateau portion of the Bragg curve.[2,3] Because we had demonstrated previously that sensitivity to the hematopoietic syndrome, reflected by acute lethality within 30 days, could be predicted based on inactivation of mouse marrow CFU-S,[4] a small program was undertaken to determine if the same relationship would hold for mice exposed to heavy charged particles. We are unaware of any previous measurements of acute radiation lethality made with heavy charged particles, but information is available for helium particles (Chong, 1971—see footnote to Table 1). The results from our acute lethality measurements may be compared with our previous marrow and activation data as well as with the responses of intestinal crypt survival reported by Alpen et al.[5]

Mice were given total body exposures to either ^{60}Co gamma radiation or to various heavy charged particles. Our initial studies on CFU-S inactivation, as well as our acute lethality measurements, were based on LAF_1 mice, but because of availability problems, the studies were extended with $CB6F_1$ mice, the latter strain being used also in our life-span studies.[6] The animals used in these studies ranged in age from approximately 3 to 6 months, and our general method of procedure was to extend our LD_{50} studies when the age of our mice exceeded the realms that were suitable for our life-span studies, and/or under circumstance when Bevalac beam time became available due to cancellation of another experiment or optimized use of beam time that provided a few extra hours for such short-notice experiments. The results were obtained between 1978 and 1982 by exposing as few as 8 to 12 animals per day under the circumstances where Bevalac beam time became available. The exposure configurations for heavy charged particles or gamma rays are the same as were described for studies on inactivation of CFU-S.[2] Most of the results were collected using spread Bragg peaks, but in 1983 we extended the study to include animals that were exposed to higher energy argon particles in the plateau portion of the Bragg curve. Mice were exposed at various times of da(or night, housed 4–5 per cage, and deaths checked

Table 1. Acute radiation lethality in mice given whole body exposures to photons or charged particles.

Strain	Radiation	$LD_{30/30}$ (cGy)	$LD_{30/7}$	No. Mice	Doses	Sex	RBE
$CB6F_1$	^{60}Co-γ	1013 (983–1038)	—	296	13	M	—
		1082 (1030–1150)	—	201	11	F	—
$CB6F_1$	^{12}C 400 MeV/n 4cm SOBP ~52 keV/μm	802 (780–827)	—	96	6	F	1.35
$CB6F_1$	^{20}Ne 670 MeV/n 10cm SOBP ~150 keV/μm	832 (795–960)	—	66	8	M	1.22
$CB6F_1$	^{40}Ar 330 MeV/n plateau ~136 keV/μm	585 (337–645)	—	153	9	F	1.85
		—	630 (576-705)	108	6	F	—
LAF_1	^{60}Co-γ	995 (972–1025)	—	78	6	M	—
		1029 (952–1083)	—	185	11	F	—
		—	1374 (1230–1463)	204	14	F	—
LAF_1	^{12}C 400 MeV/n 4cm SOBP ~52 keV/μm	706 (x–794)	—	247	14	F	1.46
		—	857 (758–942)	263	15	F	1.60
LAF_1	^{20}Ne 425 MeV/n 4cm SOBP ~117 keV/μm	758 (x–800)	—	105	6	F	1.35
		—	802 (x–897)	121	6	F	1.71
LAF_1	^{60}Co-γ[a]	863 (842-884)	—	180	9	F	—
			1461 (1457–1497)	160	8	F	—
LAF_1	^{4}He 80 MeV/n[a] 5CM SOBP 10 keV/μm	746 (731–760)	—	120	6	F	1.16
			1087 (1058–1115)	120	6	F	1.34
LAF_1	^{4}He 910 MeV/n[a] plateau ~1.5 keV/μm plateau	775 (757–794)	—	120	6	F	1.11
		—	1266 (1229–1302)	120	6	F	1.15

[a] C.Y.-L. Chong, "In-Vivo Radiobiological Studies of a 910 MeV Helium Ion Beam," submitted in partial satisfaction of the requirements for the degree of Doctor of Philosophy in Medical Physics, University of California, Berkeley, 1971 (LBL-314, 1971).

daily for at least 30 days. Diagnostic bacteriology was performed on heart blood, spleen, and liver of some animals that died, especially within the first week after irradiation. The purpose of the bacteriology was to determine the extent to which *Pseudomones aeruginosa* might contribute to the threat of lethality or to the overall estimation of LD_{50}. Mice were maintained on acidified tap water (pH 2.5) and *P. aeruginosa* was not detected bacteriologically; the most frequent organism found as a systemic invader in our postmortem cultures was a swarming Proteus species. Dose rates for charged particles were typically several hundred rad per minute, and for ^{60}Co gamma radiation, range from 20–40 rad per minute.

Table 1 is a summary of all the acute lethality data collected. Also included are old data collected by Claude Y-L. Chong and documented only in his 1971 Ph.D. thesis. The dose ranges selected were such that $LD_{50/30}$ could be estimated, and in a few instances sufficient mortality occurred before 7 days that $LD_{50/7}$ could also be estimated. The presentation of complete information on mean survival time is beyond the scope of this report, but suffice it to say that the frequency of deaths before 8–9 days was typically higher among animals exposed to charged particles than was the case for animals exposed to gamma rays. This fact made it possible to estimate $LD_{50/7}$ adequately in some cases. The gamma radiation response of the two strains used showed no significant differences between strains or between sexes based on $LD_{50/30}$. Based on $LD_{50/30}$ the RBE's and LAF_1 are slightly higher than for $CB6F_1$ mice, but the differences are probably not significant. Note that the lower 95% confidence limits for LAF_1 mice exposed to neon or carbon particles could not be estimated confidently because too few points provided low levels of mortality. The RBEs based $LD_{50/30}$ for carbon and neon are generally consistent with the RBEs of about 1.4 for these two particles based on the ratios of D_0 for photons/D_0 for charged particles. The $LD_{50/30}$ for high energy argon particles was significantly lower than for neon or carbon particles, and the LD_{50} is probably significantly elevated in comparison with the other two particles. This would indicate that the $LD_{50/30}$ response has a generally similar pattern in terms of RBE-LET relationships as does the CFU-S in activation response, since in both cases the maximum RBE occurs at a LET of the order of 80–100 keV/μm. Although RBEs based on $LD_{50/7}$ are of appreciable interest and can be compared with the previously published data by Alpen et al.,[5] adequate estimates were made in only two cases for animals exposed to heavy charged particles. In the LAF_1 mouse the RBE for $LD_{50/7}$ appears to be in the range of 1.6–1.7. While the trend is that the RBE for $LD_{50/7}$ is higher than the RBE for $LD_{50/30}$, the difference in $LD_{50/30}$ is not statistically significant in those cases where an adequate comparison can be made, mainly, for LAF_1 mice exposed to carbon particles and for CB6F1 mice exposed to plateau-argon particles. No estimate of RBE for $LD_{50/7}$ can be made confidently in CB6F1 mice because no measurement was made for gamma radiation. Assuming that the measurement made in female LAF_1 mice or $LD_{50/7}$ would be applicable to the $CB6F_1$, the RBE would be approximately 2.0 for plateau argon particles based on $LD_{50/7}$. If such an $LD_{50/7}$ estimate is valid, maximum values of RBE based on $LD_{50/30}$ and $LD_{50/7}$ are inferred from the present results at a LET of the order of 100 keV/μm. Based on the $LD_{50/6}$ for low-energy helium particles the RBE is 1.3, and 1.1 for high-energy helium, both values being significantly above 1.0.

Comparison of the present results with earlier data obtained with fission spectrum neutrons is informative. Even with the maximally effective argon particles, the estimates of RBE for $LD_{50/30}$ and $LD_{50/7}$, namely about 1.9 and 2.2, are below values published previously for fission spectrum neutrons where the comparable estimates are the order of 2.1 and 2.5 respectively.[2] With carbon and neon particles at higher or lower LETs than 100 keV/μm, the RBE estimates for $LD_{50/30}$ and $LD_{50/7}$ are appreciably lower than for fission spectrum neutrons.

Because no other data on acute lethality responses on animals given total-body exposure to charged particles are available, a useful purpose is served by documenting the present results. However, it should be duly noted that these results were collected over a period of several years, involved animals from many different shipments from a commercial supplier, and the bacteriological sample was small in scale. While the proximity of the $LD_{50/7}$ to the $LD_{50/30}$ is well known for animals exposed to high-LET neutrons, the number of deaths before 8 or 9 days observed in our animals exposed to charged particles indicates that more complete bacteriology should be done if such studies were to be repeated in the future. Although no *Pseudomones aeruginosa* was detected in these animals, it is well known that other intestinal organisms can produce early death, and more information is needed in this regard to confidently provide meaningful estimates for $LD_{50/30}$ and $LD_{50/7}$ after total body exposure to heavy charged particles.

REFERENCES

1. E.A. Blakely, Ngo, F.Q.H., Curtis, S.B., and Tobias, C.A. Heavy Ion Radiobiology—Cellular Study (J.T. Lett, Ed.). *Advances in Radiobiology 80*, 295–388 (1984).
2. Ainsworth, E.J., Kelly, L.S., Mahlmann, L.J., Schooley, J.C., Thomas, R.H., Howard, J., and Alpen, E.L. Response of colony-forming units—spleen to heavy charged particles. *Radiat. Res 96*, 180–197 (1983).
3. Ainsworth, E.J., Mahlmann, L.J., and Prioleau, J.C. Inactivation of mouse marrow stem cells by heavy charged particles, in this annual report.
4. Ainsworth, E.J., and Larsen, R.J. Colony-forming units and survival of irradiated mice with AET or endotoxin. *Radiat. Res. 40*, 149–176 (1969).
5. Alpen, E.L., Powers-Risius, P., and McDonald, M. Survival of intestinal crypt cells after exposure to high-Z, high-energy charged particles. *Radiat. Res. 83*, 677–687 (1980).
6. Ainsworth, E.J., Prioleau, J.C., and Mahlmann, L.J. Skyhook Project Progress Report. In this annual report.

SKYHOOK PROJECT: PROGRESS REPORT

E. John Ainsworth, John C. Prioleau, and Lynn J. Mahlmann

Radiation carcinogenesis remains a fundamental problem in biophysics. Much is known regarding cellular inactivation based on proliferative death as a function of radiation quality or linear energy transfer (LET), but far less is known concerning the LET dependence for injuries that persist in surviving cells that are responsible for neoplastic transformation, mutagenesis, or other alterations in functional capabilities of surviving cells. While *in-vitro* studies of neoplastic transformation are extremely informative and provide information not readily obtainable from studies with intact experimental animals,[1] prediction of *in-vivo* responses from *in-vitro* results remains a significant challenge. In the realm of external radiation studies with experimental animals, photons and fission-spectrum neutrons have been studied most extensively in comparisons of high- and low-LET radiation.[2,3] We have initiated two types of animal experiments to complement and extend the existing data base comparing low- and high-LET radiations, and our studies utilize the Harderian gland model and range-finding or pilot studies on life-span shortening after exposure to heavy charged particles characterized by different LETs. Results from our animal studies have yielded new information concerning relationships between LET and carcinogenic effects and our animal studies are of themselves complementary. The Harderian gland model yields information on *in-vivo* transformation under conditions of tumor promotion that result from excess pituitary hormones, while the life-span studies, involving no extraneous promotion, indicate interactions between tumor induction and expression. Comparison of tumorigenic results on the Harderian gland and life shortening responses are expected to be highly informative.

The purpose of the Skyhook Project was to test the hypothesis that LET was an adequate predictor for life shortening and that low-energy charged particles characterized by a LET approximately the same as that for fission neutrons would produce quantitatively similar life-shortening results after single or multifractionated doses. Another purpose was to evaluate life shortening, using comparatively high doses, over a LET range from less than 1 to approximately 200 keV/μm. Pursuant to these goals, $CB6F_1$ mice were given total-body exposures to various charged particles at the Lawrence Berkeley Laboratory Bevalac, placed in a geriatric ward under highly controlled environmental conditions, and the irradiated and control populations were permitted to live out their normal life spans. The entry of various experimental groups into the Skyhook Project was described previously.[4] A point to be emphasized is that the Skyhook Project is considered a pilot experiment that will yield significant results on single and fractionated doses of various charged particles under circumstances where the doses administered were relatively high. When these studies were initiated, it was obvious that the effectiveness of the various particles was

unknown, and the experiments were designed assuming that LET would have predictive value. The ultimate objective was to produce a data base that would permit the ultimate design of a minimum number of low-dose studies where the goal is to determine the slope of the dose-response curve over a range of low doses that are relevant for radiation protection in terrestrial as well as space radiation environments.

Table 1 summarizes the present mortality status of the various groups in the Skyhook Project. The columns indicate the array of single total-body doses administered and the fractions represent the number of animals surviving in relation to the total number of animals irradiated. The columns to the left indicate single-dose experiments, and the three columns to the right indicate fractionated weekly doses given over 24 weeks. When mortality is complete among the various groups, the Skyhook Project will contribute significant new information on the following points: 1) life-span shortening as a function LET after single doses where the LET range explored is from 1 to approximately 200 keV/μm; 2) the extent of sparing when doses of low-energy carbon particles are given as a single dose or in 24 weekly fractions; and 3) the extent of sparing when high-energy neon particles are given as a single dose or in 22–24 weekly fractions. Results of our studies with low-energy carbon particles and gamma rays were reported earlier[5,6] and show: 1) carbon is appreciably less effective than our fission-spectrum neutrons, although both are characterized by a LET of the order of 70–80 keV/μm; 2) dose fractionation produced little or no sparing effect on life shortening at those doses where the degree of life shortening produced by carbon particles was appreciable, and 3) the absence of a significant sparing effect does not occur only under circumstances where RBE or life-span shortening is high.

New information has become available during the last year concerning RBE-LET relationships as mortality has been completed in test populations exposed to high-energy plateau ^{20}Ne particles and low-energy ^{20}Ne particles where the estimated dose-averaged LETs are approximately 30 and 130 keV/μm, respectively. Tables 2 and 3 and Figs. 1 and 2 summarize the life-shortening results from these groups, together with preliminary results based on incomplete mortality among animals

Table 1. Skyhook groups: Doses and current mortality.[a]

Single dose							24 fractionation doses		
Gamma	^{12}C SOBP	^{20}Ne SOBP	^{20}Ne Plat.	^{40}Ar Plat.	^{28}Si Plat.	^{56}Fe Plat.	Gamma	^{12}C SOBP	^{20}Ne Plat.
Total N 99 % dead 61	Total N 33 % dead 100 MAS[b] 795.53 S.D.[c] 160.48	Total N 58 % dead 100 MAS 782.57 S.D. 208.89	Total N 63 % dead 78	Total N 41 % dead 83	Total N 117 % dead 58	Total N 35 % dead 57	Total N 121 % dead 46 MAS 872.56 S.D. 150.34	Total N 41 % dead 100	Total N 20 % dead 45
Dose	Dose	Dose	Dose	Dose	Dose	Dose	Dose	Dose	Dose
143 0/83[d]	40 0/78	40 0/79	40 0/88	40 18/122	40 1/79	40 50/115	17.3 0/69	1.6 0/74	17 26/70
200 40/88	80 0/49	80 0/46	80 0/48	80 2/48	80 0/63	80 33/110	20.8 49/70	3.3 0/37	22 17/70
268 0/52	120 0/42	120 0/40	120 0/47	120 1/69	120 0/47	160 19/75	23.7 0/45	5.0 0/39	31 5/70
350 28/73	160 0/46	160 0/48	160 0/47	160 1/26	160 0/61		31.3 38/68	6.6 0/39	42 2/69
450 44/50	240 0/44	240 0/47	240 0/40	240 1/52	240 0/41		35.0 0/43	10.0 0/27	
417 0/59	320 0/44	320 0/47	320 35/135	360 0/6	320 0/52		41.7 39/70	13.3 0/46	
500 17/44	440 0/24		400 0/48		400 0/6		54.2 31/69		
569 0/40			450 24/94		450 44/50		60.0 0/38		
600 41/50			500 0/47				79.0 0/44		
700 25/47			600 7/131						
745 0/4			750 0/7						
788 0/43									
Total: 195/639[d]	0/327	0/307	66/732	23/323	45/399	102/300	157/516	0/262	50/279

[a] Mortality status on 9/16/85.

[b] MAS indicates mean after survival.

[c] S.D. indicates standard deviation.

[d] Fractions indicate number surviving over the total number in the dose groups or for each radiation condition.

Table 2. Skyhook life-shortening estimates: Single doses.

Argon†			Silicon†				Iron†			Carbon*			
Dose	MST	L.S.	Dose	MAS	±S.D.	L.S.	Dose	MST	L.S.	Dose	MAS	±S.D.	L.S.
40	803	—	40	780	201	13	40	830	—	40	773	170	—
80	775	18	80	775	183	17	80	818	—	80	734	205	42
120	746	46	120	703	177	90	—	—	—	120	752	204	25
160	772	21	160	725	187	67	160	811	—	160	696	276	80
240	736	57	240	649	228	144				240	675	192	101
		320	693	183	100					320	695	176	81
										440	591	175	186

Gamma*				Neon Plateau†				Neon SOBP†			
Dose	MAS	±S.D.	L.S.	Dose	MAS	±S.D.	L.S.	Dose	MAS	±S.D.	L.S.
				40	773	192	19	40	766	197	27
				80	714	203	79	80	802	194	—
				120	687	172	105	120	739	184	54
143	751	175	25	160	753	194	40	160	716	184	77
				240	732	187	61	240	689	165	103
268	703	191	74					320	686	186	107
417	670	185	107	400	626	204	151				
569	668	201	108	500	585	243	191				
788	527	201	250								

MST = median survival time.
MAS = mean after survival.
L.S. = days lost.
* = compared with controls of 776 days; survival N = 211.
† = controls of 793 days; survival N = 168.

Table 3. Skyhook life-shortening table: Fractionated doses.

^{12}C SOBP*				Gamma*				Neon plateau**		
Dose(s)	MAS	±S.D.	L.S.	Dose(s)	MAS	±S.D.	L.S.	Dose(s)	MST	L.S.
0	776	184	—	0	776		—	0	793	—
1.6(40)	790	186	—	17.3(415)	730	186	46	17.0(408)	704	89
3.3(80)	787	151	—	23.7(569)	735	170	42	22.0(528)	630	163
5.0(120)	703	211	74	35.0(840)	676	138	101	31.0(744)	474	319
6.6(160)	806	179	—	60.0(1440)	569	185	207	42.0(1008)	355	437
10.0(240)	712	204	64	79.0(1896)	529	176	248			
13.3(320)	667	194	109							

*Used controls N = 211.
**Used controls N = 168.
MST = (50%) median survival time.
MAS = mean after survival.

exposed to high-energy silicon and iron particles. While rigorous statistical evaluation of the results is not yet complete, large and consistent differences between the various groups is not apparent. This may mean that the curve that describes relationships between RBE and LET for life shortening is relatively flat over the LET range of approximately 30–130 keV/μm, as has been described previously for the response of mouse marrow stem cells (CFU-S). While the scatter is great and firm con-

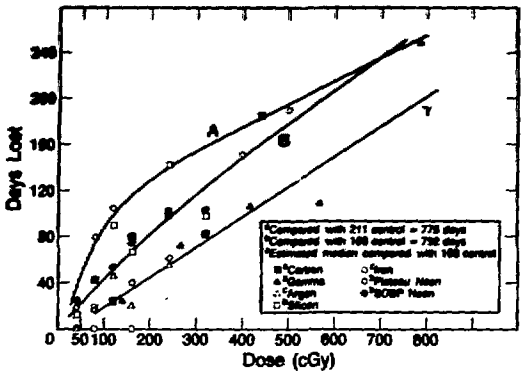

Fig. 1. Days of life span lost after single doses of photons or heavy charged particles. Estimates of days lost in male B6CF$_1$ mice given single doses of fission neutrons from the Janus reactor are as follows: 20 cGy—59 days, 80 cGy—124 days, 120 cGy—159 days, 240 cGy—216 days.[8] Heavy charged particles appear less effective than fission neutrons. (XBL 8511-8579)

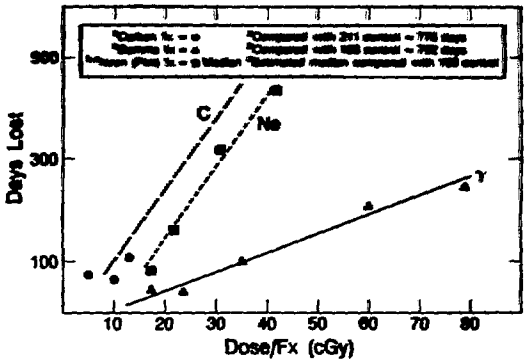

Fig. 2. Days of life span after 24 weekly fractionated doses of stopping carbon particles, high-energy neon particles, or photons. The data for high-energy neon are based on estimated median survival time and are considered preliminary. Estimates of days lost in male B6CF$_1$ mice exposed to 24 weekly fractionated doses of fission neutrons from the Janus reactor are as follows: 3.3 cGy—183 days, 5.0 cGy—262 days, 10 cGy—316 days, 13.3 cGy—417 days.[8] Carbon and neon particles appear less effective than fission neutrons. (XBL 8511-8578)

clusions about curve shapes cannot be drawn now, the trend is that life-shortening effects of high-energy neon and silicon particles tends to be higher than for stopping carbon or neon particles, perhaps as a result of fragmentation produced by ridge filters. The curves drawn through the single disc results in Fig. 1 represent possible fits to the data where RBE for 100 days of life shortening could be in the range of 2 to 4. In the case of 24 weekly fractionated doses, the results with carbon are inadequate for curve fitting because RBE was overestimated. The speculative curve drawn parallel to interim results for stopping carbon indicates a possible fit to provide an RBE of no more than 4 at 100 days of life shortening. With high-energy neon, the curve eye-fitted to the points provides an RBE estimate of about 2 for 100 days of life shortening. Preliminary results with two other particle species have become available recently, based on early replicates, involving small sample sizes in which mortality is complete.

Figure 3 compares cumulative mortality curves for mice given 160 cGy of argon or iron particles. At this dose level it is likely that significant life shortening is produced, and these results provide no evidence that iron is more effective than argon for production of life shortening where the estimated LETs are approximately 130 and 200 keV/μm, respectively. These preliminary results are consistent with the interpretation that iron could be less effective than argon, indicating saturation of effects at an LET of approximately 200 keV/μm based on life shortening. Should this prove to be the case when mortality is complete in the iron and argon groups, the results would be different than those obtained using the Harderian gland model system. Caution is prudent at this stage, and it is important to note that all the comparisons among the particles described here are based on dose rather than fluence. Were fluence used, and assuming equal life shortening for the various particles described, the relationship would be that the life-shortening effect, on a per particle basis, would increase with atomic number.

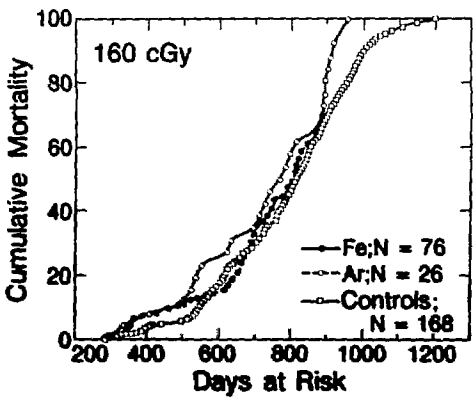

Fig. 3. Cumulative mortality among mice given 160 cGy of high-energy argon or iron particles. (XBL 8511-8580)

A fundamental issue in radiation risk assessment concerns the effects of protracted or low-rate exposures. All of our studies conducted so far have involved fractionated or single doses administered at comparatively high rates, namely, in the range of several hundred rad per minute for single doses and in the range of 2–10 rad per minute for fractionated doses. In contrast to the results described above for fractionated doses of low-energy carbon particles, where little or no sparing effect was detected, a marked sparing effect has been detected for fractionated doses of high-energy neon particles characterized by an LET of approximately 30 keV/m. The hypothesis tested in the neon experiment was that the sparing effect of fractionation would be as high for neon particles as for cobalt-60 gamma radiation, but results in Fig. 2 require rejection of this hypothesis. The life-shortening effect of fractionated neon doses is appreciably greater than for cobalt-60 gamma radiation. The dose fractionation data are consistent with the hypothesis that the RBE is higher for carbon than for neon, where the LETs are about 70–80 and 30 keV/μm, respectively.

The definition of the most scientifically productive extension of the Skyhook Project is currently under assessment. Mortality will be complete in all groups currently under study in approximately two years, including all unirradiated control animals. Because of the fundamental importance of fractionated or low dose rates for radiation risk assessment purposes, the highest priority should be given to extension of our long life in term fractionation studies. The objective would be to evaluate RBE-LET relationships under conditions of long-term dose fractionation and testing the hypothesis that under those conditions, RBE will vary over a LET range of approximately 20–150 keV/μm. If RBE-LET relationships for inhibition of repair or damage to critical repair systems vary independently from RBE-LET relationships of processes that contribute to life shortening after single exposures, this fact should be revealed by expanding our current dose-fractionation studies. The following expansions of our dose fractionation studies are under consideration: 1) evaluation of sparing effects at an LET below 30 keV/μm with which we currently have experience, for which purpose we are considering using high-energy carbon particles in the plateau portion of the Bragg curve, where the LET is of the order of 10 keV/μm, or high-energy helium or protons; and 2) long-term dose-fractionation studies that should be performed at at LET in the range of 130 keV/μm, in which we will propose to use high-energy argon particles. By addition of these dose-fractionation groups and some small supplementation of the current single-dose studies with the same particles, many full estimates of sparing effects under dose-fractionation conditions could be obtained. The dose-fractionation studies proposed would directly complement *in-vitro* studies of neoplastic transformation under conditions of short-term fractionated exposures planned by our colleague T. Yang, thus providing further direct comparisons between *in-vivo* and *in-vitro* results directly relevant to the question of radiation carcinogenesis.

The Skyhook Project will achieve its original goal of providing at least qualitative estimates of RBE for life shortening after single or fractionated doses over a broad range of dose-averaged LETs. This information from our pilot studies will place us in a position to design the most critical experiments to define RBE over a range of low doses, a range directly relevant to radiation risk assessment. Since the goal of our pilot life-span studies is being achieved, we plan to terminate those studies when mortality is complete and initiate new studies on leukemogenesis using the mouse model system for myeloid leukemia. While the mechanism of mouse and human leukemia may not be the same, myeloid leukemia is a disease of considerable interest in terms of radiation hazards to man, and we would propose to use the mouse model to explore the effects of dose fractionation over a selected range of dose-averaged LETs. The most critical question concerns the extent to which dose fractionation produces sparing or even enhancement of leukemic risk, and our proposed studies would focus on this question. Another advantage of the murine leukemia model is that tumor expression is promoted by hormone injection, much as is the situation with our Harderian gland model system, and animals are sacrificed at 600–800 days so that the information loss is minimal and considerable savings accrue in animal maintenance costs. Although the experiments to be conducted are not yet specified, we propose to initiate pilot studies with photons and at least a single heavy charged particle in the near future to determine the feasibility of using this model more extensively in low-dose studies. Because of our interest in radiation hazards in a space environment, we feel that it is important also to explore the extent to which environmental factors in a space environment could influence susceptibility to or expansion of myeloid leukemia. Hemodynamic changes are well known under these circumstances, and the likelihood appears great that bone marrow cell kinetics will be in influenced significantly. Earlier results have

demonstrated clearly that the life-time incidence of leukemia in mice is influenced by the microbial environment, and by inference, by bone marrow cell kinetics.[7] It is our strong feeling that these matters should be explored more fully in order to ensure that leukemic risks in the space environment will not be seriously underestimated. Pursuant to this goal, we plan to initiate comprehensive studies on alterations in marrow cell kinetics and to determine the extent to which such alterations influence leukemogenic risk following photon irradiation.

REFERENCES

1. Yang, T.C., Craig, L.M., Mei, M., and Tobias, C.A. Neoplastic cell transformation by heavy ion radiation. In this annual report.
2. Ainsworth, E.J., Fry, R.J.M., Williamson, F.S., Brennan, P.C., Stearner, S.P., Yang, V.V., Crouse, D.A., Rust, J.H., and Bovak, T.B. Dose-effect relationships for life shortening, tumorigenesis and systemic injuries in mice irradiated with fission neutron or ^{60}Co gamma radiation. In *Proc. IVth International Congress*, International Radiation Protection Ass'n., Vol. 4, pp. 1143–1151 (1977).
3. Ullrich, R.L. Tumor induction in BALB/c mice after fractionated or protracted exposures to fission-spectrum neutrons, *Radiat. Res. 97*, 587–597 (1984).
4. Ainsworth, E., Prioleau, J.C., and Mahlmann, L.J. Life-shortening effects of heavy charged particles: A status report. Biology and Medicine Division Annual Report, Lawrence Berkeley Laboratory report LBL-14986 (1983).
5. Ainsworth, E.J., Prioleau, J.C., and Mahlmann, L.J. Life span studies on mice exposed to heavy charged particles: A Status Report, Biology and Medicine Division Annual Report, Lawrence Berkeley Laboratory report LBL-16840 (1984).
6. Ainsworth, E.J., Life span studies in mice exposed to heavy charged particles: Objectives and experimental design. In *Proceedings of the 7th International Congress of Radiation Research*, Amsterdam, July 1983.
7. Walburg, H.E., Jr., Cosgrove, G.E., and Upton, A.C. Influence of microbiological environment on development of myeloid leukemia in x-irradiated RFM mice. *International J. of Cancer 1*, 595–572 1968.
8. Thomson, J.F., Williamson, F.S., Grahn, D., and Ainsworth, E.j. Life shortening in mice exposed to fission neutrons and γ rays. 1. Single and short-term fractionated exposures. *Radiation Research 86*, 559–572 (1981).

Heavy Ion Therapy and Related Physics and Biology

HEAVY CHARGED PARTICLE RADIOTHERAPY TRIAL

Joseph R. Castro, Theodore L. Phillips, David E. Linstadt, J. Michael Collier, Samuel Pitluck,* William T. Chu,† Sheri D. Henderson, Tim R. Renner,† Robert E. Walton,‡ Jacquelyn J. Iler, Marilyn A. Fowler, Marc L. Kessler, and Monica M. Reimers

During the past year, patients have continued to receive helium, neon, and silicon heavy-charged-particle irradiation as part of Phase I/II/III trials of the following sites:

*Engineering Division (Electronics R&D), LBL.
†Accelerator and Fusion Research Division, LBL.
‡Engineering Division (Mechanical Technology), LBL.

STUDY	PROTOCOL
Phase II Studies of dose localization (base skull, juxtaspinal tumors, etc.)	NCOG 0R81/RTOG 79-11
Phase I–II Locally advanced carcinoma of the lung	NCOG 0R81/RTOG 79-11
Phase I–II Locally advanced carcinoma of the prostate	NCOG OR81/RTOG 79-11
Phase I–II Selected, advanced head and neck tumors	NCOG OR81/RTOG 79-11
Phase I–II Locally advanced carcinoma of the pancreas	NCOG OR81/RTOG 79-11
Phase I–II Malignant glioma of the brain	NCOG OR81/RTOG 79-11
Phase I–II Locally advanced, miscellaneous tumors (biliary, gastric, soft tissue sarcoma, etc.)	NCOG OR81/RTOG 79-11
Phase I RBE studies (skin and subcutaneous metastases)	NCOG OR81/RTOG 79-11
Phase II Locally advanced carcinoma of the esophagus	NCOG 3E81/RTOG 79-08
Phase II Uveal melanoma	NCOG 7081/RTOG 79-09
Phase III Uveal melanoma	NCOG 7O85

The Phase I–II studies in NCOG 7081 (eye), 3E81 (esophagus) and 0R81 (all sites) have been closed as of September 30, 1985. A total of 550 patients were accrued in these protocols.

Successor Phase II and III protocols for lung, prostate, eye, soft-tissue and bone sarcoma, skull and juxtaspinal tumors, Phase I silicon, and pancreas have been opened or are being developed. The results of the previous studies are briefly summarized here.

DOSE LOCALIZATION STUDIES

Through mid-1985, a total of 49 patients received heavy-charged-particle irradiation for chordoma, chondrosarcoma, meningioma, or neurilemmoma of the base of skull or juxtaspinal area. The mean tumor dose was 68 Gray-equivalent, ranging from 26 to 80. Control within the irradiated area was obtained in 35 of 49 (70%). The median follow up in all 49 patients is 21 months, with a range from 3–90 months. Serious complications were seen in a small number of patients, with cranial nerve injury in two, transverse myelitis in one, and brain necrosis in three patients.

In 42 patients with tumors of other histologies and/or sites, including tumors of paranasal sinuses, retroperitoneum, soft tissue and miscellaneous other sites, heavy charged particles were also used to deliver a higher tumor dose than possible with standard irradiation techniques. In this group, 21/42 (50%) have had local tumor control, also a good result considering the extent and the range of tumor types treated. We believe that there are a number of sites in addition to the juxtaspinal/base of skull tumors that will show long term benefit from treatment with heavy charged particles.

UVEAL MELANOMA

The results in helium irradiation of uveal melanoma continue to be excellent. A tumor control rate of 95% with follow up from 3 to 90 months is seen (median: 28 months). Two hundred and five patients were accumulated in the Phase I–II study. Three dose levels of 60, 70 and 80 Gray-equivalents (GyE) given in five fractions over 7–10 days were utilized. A small group of selected patients with tumors arising in the macula were treated to a lower dose of 50 GyE in an attempt to control these tumors and preserve some vision, as an alternative therapy to enucleation. Considerable experience has been gained from this study in terms of treatment techniques, doses, results, and side effects of treatment. As with protons, the local control results are very good with a low level (5%) of metastatic disease. At all dose levels we see about 15% of patients with neovascularity in the eye, often leading to difficult-to-treat glaucoma. Other complications occur less often, including perforated sclera, severe keratitis, painful or dry eye, with the result that 9/205 patients required enucleation for complications, in addition to five for tumor progression. Lens opacification has occurred in at least 25/205 patients, with several having had successful lens extractions. Overall, about 55% of patients have retained vision of 20/400 or better, more often in patients with small tumors and/or tumors more than 3 mm from the fovea or optic disc. For the randomized Phase III study (NCOG 7O85) we have selected 70 GyE in five fractions over 7–12 days as the optimal

current helium technique. This is being compared to iodine-125 plaque therapy for appropriately sized and located tumors that can be treated by either technique.

CARCINOMA OF THE LUNG

The Phase I–II trial of advanced unresectable nonsmall-cell cancer of the lung has accrued 12 patients with primary untreated lung tumors. Treatment techniques and doses have been refined to permit acceptable toxicity, the chief being radiation pneumonitis, which has been seen at a moderately severe level in two patients. The tumor doses have ranged from 60 to 76 GyE and survival from 2–15 months; four patients appear to have local control. A Phase III study (NCOG 2N84) comparing low-LET x rays with heavy charged particles has been opened. The goal of the study is to determine whether the more precise dose distribution of neon and its high LET characteristics will provide higher local control and survival than standard radiotherapy.

CARCINOMA OF THE PROSTATE

We have begun a Phase III study (NCOG 4P85) for locally advanced carcinoma of the prostate based partly on the fact that the results in neutron and proton therapy of these tumors suggest that the local control rate and survival can be improved in patients with advanced tumors. This study tests whether the improved dose localization and high LET of neon particles allow a higher and more effective dose to the prostate with better local control and survival as as evidenced by posttreatment biopsy and long term follow up.

OTHER SITES

The results of treatment of other sites have suggested the following sites for additionally planned protocol studies:

1. RTOG 10-52: A collaborative protocol with the MGH-Harvard group for the treatment of base-of-skull and cervical chordoma-chondrosarcoma with charged particles has been submitted as an intergroup study with RTOG.
2. NCOG/RTOG: Phase I–II trials with silicon ions will be designed to study normal tissue effects and tumor response in skin and subcutaneous metastatic nodules, and in enlarged unresectable lymphatic masses.
3. NCOG/RTOG: A Phase II trial of neon heavy charged particles for sites other than cervical and base-of-skull will be designed for patients with sarcoma of bone or soft tissue.
4. NCOG/RTOG: A new Phase I and II trial of combined chemotherapy and heavy-charged-particle neon irradiation will be designed for locally advanced carcinoma of the pancreas, employing sequential infusions of methotrexate and 5-fluorouracil.

ESTIMATING RADIATION THERAPY COMPLICATION PROBABILITIES

John T. Lyman

Treatment planning optimization involves selection of an acceptable plan that controls the local and regional spread of cancer without causing normal tissue complications.[1] Clearly to accomplish this task it is desirable to have a means to estimate the complication probability of a given plan. While there are a number of factors that contribute to the probability of complication, it is well established that dose, volume, and fractionation are important factors.[2–5] To obtain adequate information about the irradiated volume of different normal structures and the dose delivered to them it is necessary to calculate dose-distributions for the entire irradiated volume, not just for a few selected slices through the volume.

This type of planning requires that a large number of depth-dose distribution data be analyzed for a single treatment plan. Dose-volume histograms for individual normal structures are a good augmentation to the dose distributions because they provide a summary of the dose-distribution from a series of CT slices for the individual normal structures.

Minimizing the dose to the normal structures always involves some trade-offs. To spare one tissue, it may be necessary to increase the dose to another; therefore compromises must be made with consideration of the estimated risk to the different

tissues. Frequently a decision must be made as to which is the better plan; to irradiate a smaller volume of an organ to a higher dose or to irradiate a larger volume to a smaller dose. The problem of identifying the more desirable of two dose distributions and the balancing the risk to the different organs is frequently a difficult task since there are no suitable data available to predict the consequences of using either plan. The desired data to aid this decision would be a library of dose-volume histograms with the associated complication probabilities for each normal structure. Lacking this data, if one is to effectively use the dose-volume histograms, some method must be devised to rank the histograms. Since the histograms may have dissimilar shapes, a subjective visual inspection may not be adequate. The integral dose is not adequate since it does not address the volume dependence of the complication probability. A ranking that is based on clinical relevance would be better than one based on a subjective scale.

An alternative to a library of complications correlated with dose-volume histograms is to use some method to identify different histograms that have the same complication probabilites. The development of such a method would then allow the identification of an equivalent histogram for which the tolerance dose data is available. Such a method of estimating the complication probability is being developed, based on the concept of the tolerance dose.[6] The tolerance dose is a function of the portion of the normal structure irradiated. The probability of complication is a function of the dose and the tolerance dose and is reasonably represented by a sigmoid curve. Guidelines for tolerance dose for different normal structures are obtained from the literature.[6-8] The values given are generally assumed to relate to the uniform partial volume irradiation of the structure with a conventional fractionation schedule (1.8 to 2.0 Gy per fraction and five fractions per week). When sophisticated treatment planning is done (three-dimensional calculations or a series of two-dimensional calculations using adjacent slices of CT data[9,10]) it is very apparent that most of the normal structures receive a non-uniform irradiation. Therefore the guidelines are not easily applied since they presumably apply to a different radiation distribution.

An algorithm has been written that can be used to obtain an interpolated estimate of the complication probability from three possible single-step histograms that bound a two-step histogram. The algorithm can then be recursively applied to reduce an arbitrary n-step histogram to an equivalent single-step histogram with the same estimated complication probability.

This method has been adopted by the Working Group for the Evaluation of Particle Treatment Planning Intercomparison as the preferred method for the evaluation of normal tissue effects.

Results of using this ranking method are as follows: 1) For simple cases, approximated by a uniform partial volume irradiation, the method predicts a complication probability consistent with the tolerance dose data. 2) For alternate treatment plans that have similarly shaped histograms or integral dose-volume histograms that do not intersect, the algorithm gives the best ranking to the histogram that represents to smallest volume and lowest dose to the structure. 3) For alternate treatment plans with dissimilarly shaped histograms (integral dose-volume histograms have at least one intersection), the best ranking is more difficult to ascertain visually because of the volume dependence of the tolerance dose which must be considered. Not all tissues have the same volume dependence, but the alogrithm will consistently use the assigned volume dependence, even though this model may not hold true for a human.

Two studies,[11,12] that compared treatment complications with dose-volume histograms for heavy charged-particle treatment plans in a limited number of cases have been used as a preliminary test of the algorithm for the estimate of the complication probability. For the two different normal tissues studied, in all cases where a complication has been observed, there was a high estimate for the complication probability. When no complications were reported, the estimates were for a low complication probability in over 90% of the cases. These studies have been too limited to identify different shaped histograms that may lead to similar complication probabilities.

Further work is required to establish which tissues are suitable for this analysis and the validity of the numeric value of the estimates of the complication probability, which is affected by the normal tissue tolerance data used by the algorithm.

REFERENCES

1. Stewart, R.R., and Gibbs, F.A. Prevention of radiation injury: Predictability and preventability of complication of radiation injury. *Ann. Rev. Med. 33*, 385-395 (1982).
2. Barendsen, G.W. Dose fractionation, dose rate and iso-effect relationships for normal tissue responses. *Int. J. Radiat. Oncol. Biol. Phys. 8*, 1981-1997 (1982).

3. Cohen, L. The tissue factor in radiation oncology. *Int. J. Radiat. Oncol. Biol. Phys. 8,* 1771–1774 (1982).
4. Schultheiss, T.E., Orton, C.G., and Peck, R.A. Models in radiotherapy: Volume effects. *Med. Phys. 10,* 410–415 (1983).
5. Withers, H.R., Thames, H.D., and Peters, L.J. Dose fractionation and volume effects in normal tissues and tumors. *Cancer Treatment Symposia 1,* 75–83 (1984).
6. Rubin, P., and Casarett, G.W. A direction for clinical radiation pathology: The tolerance dose. In *Frontiers of Radiation,* Vol 6, J.M. Vaeth, Ed., pp. 1–16, University Park Press, Baltimore, MD (1972).
7. Rubin, P., Cooper, R.A., and Phillips, T.L. Eds., *Radiation Biology and Radiation Pathology Syllabus, Set R.T.1: Radiation Oncology,* pp. 2–7, Am. College of Radiology, Chicago (1975).
8. Cohen, L. *Biophysical Modeling in Radiation Oncology.* CRC Press, Boca Raton (1983).
9. Goitein, M. The utility of computed tomography in radiation therapy: An estimate of outcome. *Int. J. Radiat. Oncol. Biol. Phys. 5,* 1799–1807 (1979).
10 Goitein, M., and Abrams, M. Multidimensional treatment planning: I. Delineation of anatomy. *Int. J. Radiat. Oncol. Biol. Phys. 9,* 777–787 (1983).
11. Zink, S.R., Castro, J.R., Chen, G.T.Y., Collier, J.M., Lyman, J.T., and Saunders, W.M. Treatment planning study compares heavy ion radiotherapy with photons for carcinoma of the esophagus. *Int. J. Radiat. Oncol. Biol. Phys.* (submitted for publication, 1985).
12. Austin-Seymour, M.M., Chen, G.T.Y., Castro, J.R., Saunders, W.M., Pitluck, S., Woodruff, K.H., and Kessler, M. Dose volume histogram analysis of liver radiation tolerance. *Int. J. Radiat. Oncol. Biol. Phys.* (accepted for publication, 1985).

CLINICAL AND CELLULAR RADIOBIOLOGICAL STUDIES OF SILICON ION BEAMS

Eleanor A. Blakely, Joseph R. Castro, Mary M. Austin-Seymour, George T.Y. Chen, Leora Lommel, Michael Yezzi, Polly Y. Chang, and Cornelius A. Tobias

This is a report of our continuing studies to characterize the potential therapeutic significance of accelerated particle beams of silicon produced at the Berkeley Bevalac. We have previously reported radiobiological data *in vitro* that indicated that these heavy-ion beams can be used to deliver improved depth-dose distributions and enhanced biological effectiveness to tumors at depth.[1] As a part of Phase I studies involving treatment of two patients with metastatic lung nodules using silicon beams, we have undertaken an evaluation of the acute reaction of skin exposed incidental to the treatment of the lung disease. Parallel biological measurements of cellular survival were made. Our work, therefore, had three major objectives:

First, to measure the single-dose survival response of human fibroblasts *in vitro* to silicon or helium particle beams under conditions identical to those in which human skin was irradiated incidental to the treatment of lung nodules.

Second, to conduct Phase I skin studies with silicon particle beams in order to determine clinical relative biological effectiveness (RBE) values relative to helium ion beams for use in future Phase II-III clinical trials.

And, third, to attempt to correlate the relative acute response of human skin to a fractionated course of treatment with silicon or helium ions, with the single dose survival response of human fibroblasts *in vitro.*

Figure 1 illustrates the dual treatment fields used for the first patient. This is a 64-year-old man with multiple, slowly growing lung nodules that appeared about 10 years after resection of a renal cell carcinoma. Silicon and helium ions were selected for palliative irradiation of the metastatic nodules identified in the lower left lung. As shown here, a left lateral port was used for treatment, with the silicon beam having an initial extraction energy of 670 MeV/u to a depth in the patient of approximately 14 cm, which was required to cover the target volume. A silicon dose of 12.0 physical Gray was selected to irradiate the lung nodules, and this dose was administered in six fractions over nine days. Ion chamber measurements indicated that the dose to the surface of the skin was 11.7 physi-

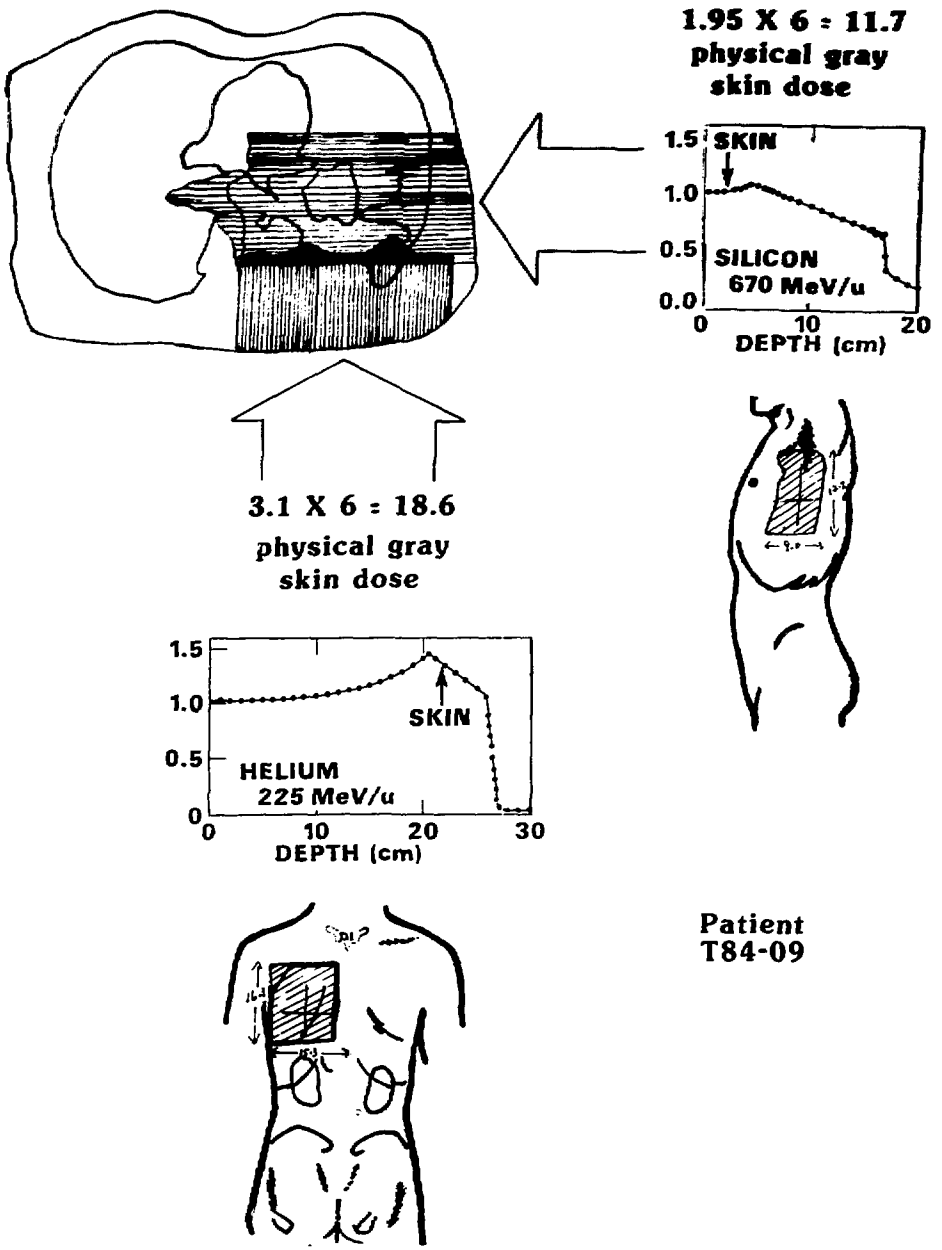

Fig. 1. Schematic representation of particle treatment plan for palliative treatment of lung nodules. Two ports were used, each with a different particle beam. A left lateral port was treated with the silicon beam, and a left posterior field was treated with the helium beam. The absorbed dose levels to the skin surfaces (that were irradiated incidental to the treatment) are given.

(XBL 8412-5119)

cal Gray. The area of skin exposed was approximately 150 cm^2.

The skin was located in the plateau of the silicon 12-cm extended Bragg peak, and particle-sensitive plastic detectors exposed at the surface of the skin, analyzed by Eugene Benton of the University of San Francisco, indicated that the dose-average LET was 46 keV/μm. The other area of lung nodules was treated with 225-MeV/u helium ions produced at the Berkeley 184-Inch Cyclotron. In the left posterior field used to treat these nodules, the superficial skin received a total of 18.6 physical Gray in six fractions, again delivered over nine days. The area of skin exposed to helium ions was approximately 250 cm^2, somewhat more than the area of skin exposed to silicon ions. The helium treatment penetrated approximately 4.6 cm deep, and, therefore, the silicon field within the lung overlapped only to a small degree, as indicated. Neither skin surface received more than one particle species.

At the time this patient was treated, two biological experiments were set up for each ion field. We used two biological methods to measure the cell killing effects of the beams with exponentially growing human T-1 cells for these experiments. A small cylindrical glass chamber was set up with the appropriate amount of material upstream to duplicate the density of the three-dimensional compensation used in the treatment plan. The center of the 1.5-cm chamber was, therefore, straddling the approximate location of the skin surface. A magnetic bar kept the cells in a stirred suspension. Cell samples were taken out before beginning the exposures and after a sequential set of doses in order to generate a complete dose-survival response. In addition, cells were grown in a monolayer attached to the inside of tissue culture flasks that were arranged in a linear array. Just prior to irradiation, the flasks that were completely filled with medium. Some flasks, filled with water, were used as blanks in order to distribute the biological sampling to areas of major interest. We call this configuration the *submarine*. The cells are later trypsinized and plated for survival.

Figure 2 summarizes the biological results for the first patient. The upper left panel represents the helium Bragg curves. Only the deepest range of the beam was used, with the tumor lying in the distal region, and the skin ending up in the proximal peak area. The physical dose distribution has been deliberately sloped down, due to the greater effectiveness of the particles with higher LET in the distal peak. And, in fact, the submarine survival

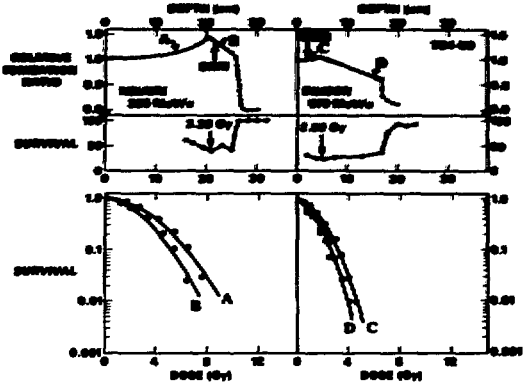

Fig. 2. Bragg curves and survival measurements for the patient treatment plan described in Fig. 1. See text for further details.
(XBL 849-7965)

experiment for this setup, which is plotted below the Bragg curve, indicates the relatively flat isoeffectiveness that can be achieved after a single proximal dose of 3.23 Gy. In the lowest panel are plotted the whole-dose curves from the glass chamber. Curve A was measured in the early plateau of the Bragg curve and is rather resistant. Curve B was measured very close to the location of the skin and shows more effectiveness. The LET here has been measured by Luxton and Fessenden of Stanford to be approximately 10 keV/μm.[2] On the right upper panel is a similar set of data for the silicon beam. Again, the physical slope of the dose appears to be well designed for uniform cell killing at a dose fraction of 2 Gy to the proximal peak. The C curve indicates survival effects at the plateau of the silicon Bragg curve. As expected, there is greater killing for C at 46 keV/μm than for the helium curve B. Still greater killing is possible at position D, as indicated for the tumor mass. The location of the skin in the plateau of the silicon beam, or in the peak of the helium beam, was purely a function of the most appropriate treatment plan for the tumor.

There are difficulties associated with determining skin RBE values with particle beams. Even in Phase I trials, it is difficult to find patients in whom, for example, multiple nodules would permit a dose response study. Therefore, accuracy at determining a skin RBE with a new modality is highly dependent on a fairly accurate estimate of an equivalent-dose level of the test radiation to the control radiation. If there is an equal skin effect, then one can be confident that the predicted RBE is relatively accurate. However, if there is less skin reaction at the

test dose selected, then the true response lies on a more resistant dose-effect curve, which would yield a lower RBE, but which is highly dependent on one's knowing the shape of the dose-response curve. Of course, the opposite could also be true, and a more severe test radiation reaction would lie on a more sensitive curve with a greater RBE. Unfortunately, we were only able to score the skin reactions on this patient out to three weeks, because the extent of the patient's disease required additional therapy, and this could not be done with silicon. Approximately equal skin reactions were scored at three weeks posttreatment between the upper silicon fields and the lower helium fields, with possibly a little more reaction for helium, which was the larger of the two fields.

Palliative irradiation of the lung nodules of a 40-year-old woman with recurrent lung nodules following initial resection for bronchoalveolar carcinoma allowed the opportunity to compare skin reactions to silicon- and helium-ion irradiation in Phase I trials. Two nonoverlapping fields were selected. As shown in Fig. 3, the upper field was treated with 15.8 physical Gray of Bragg-peak silicon ions in 10 fractions over 16 days. The tumor in each case was in the distal region of the Bragg peak. The skin surface, therefore, ended up in the proximal-peak region. Particle sensitive plastic, analyzed by Benton, indicated that the LET at the level of the skin surface was 84 keV/μm. The lower field was treated with a total dose of 26.8 physical Gray of helium ions. The helium field for this case and also for the first patient ended up being in the proximal to midpeak region of the 6-cm helium extended Bragg peak. Treatment plans were prepared for the helium and for the silicon fields.

Biological measurements made for this patient are depicted in Fig. 4. The (F) curve at the helium skin location is almost identical to the helium (B) curve from the first patient. The (H) curve representing the silicon skin exposure shows a greater reaction. After three weeks, the skin reactions in the two fields were approximately equal with perhaps the silicon field showing a little more color. However, at two months the skin reaction

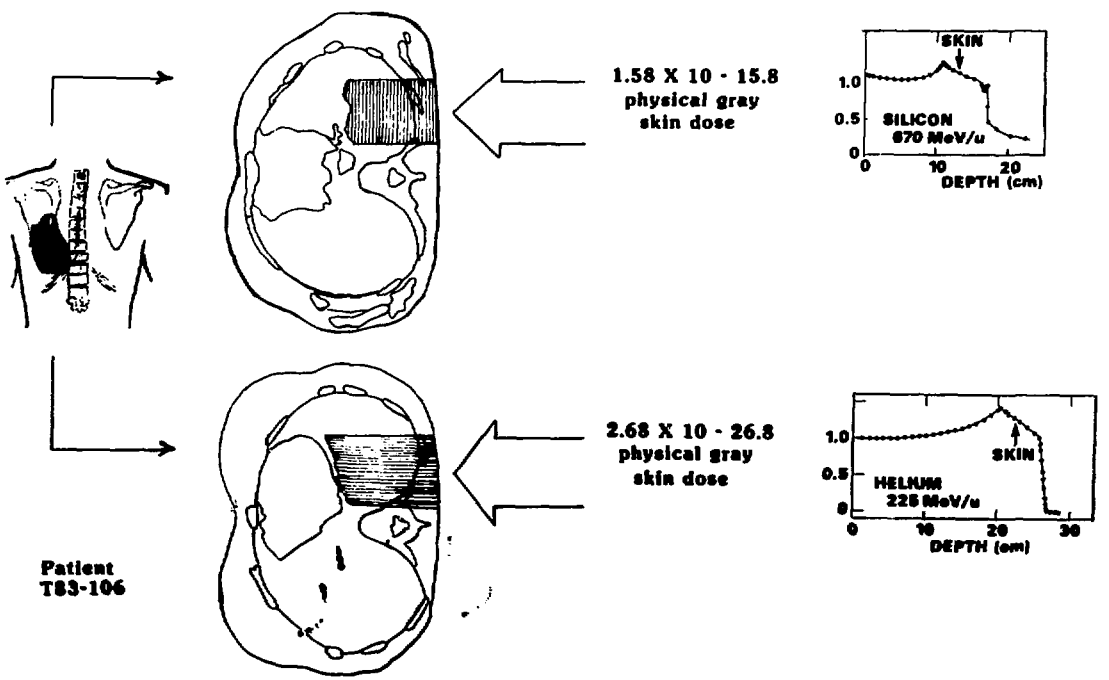

Fig. 3. Schematic representation of particle treatment plan for palliative treatment of lung nodules. Two nonoverlapping ports were used, each with a different particle beam. The upper left posterior field was treated with silicon ions, the lower left posterior field was treated with helium ions. The absorbed dose levels to the skin surfaces (that were irradiated incidental to the treatment) are given. *(XBL 8412-5117)*

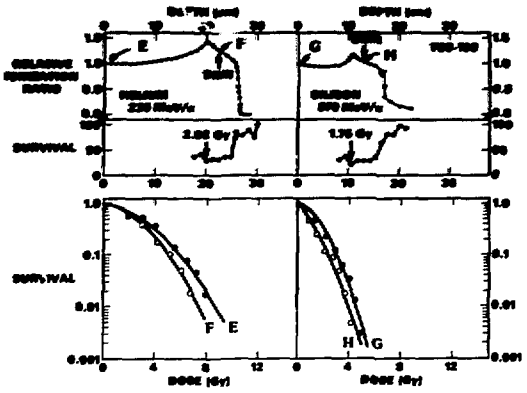

Fig. 4. Bragg curves and survival measurements for the patient treatment plan described in Fig. 3. See text for further details. (XBL 849-7964)

in the silicon field developed a significantly greater reaction. Figure 5 presents the actual LET spectra for the first patient in the top panel and for the second patient in the bottom panel. In the silicon Bragg peak, the LET distribution is broader and has the higher peak value of 84 keV/μm.

Table 1 summarizes the cellular *in-vitro* RBE values at 50% survival calculated for the ratio of doses of the two radiations to which the skin was exposed for each patient. This means the reference radiation is the helium Bragg peak radiation. For the first patient irradiated with plateau silicon ions, the RBE was 1.6 ± 0.2. For the second patient irradiated with Bragg peak silicon ions, the RBE was 3.2 ± 0.4. Although our skin RBE data are inadequate to permit a quantitative comparison with the biological data *in vitro*, there appears to be at least qualitative agreement between the two systems. We have, therefore, reached two tentative conclusions from this study:

First, the preliminary skin reaction observed in a patient exposed to Bragg peak silicon ions indicates that the reaction has an enhanced severity and an altered sequence relative to helium ions. Under ideal conditions silicon Bragg peak exposures should be limited to the tumor and should not include skin in the field. We have shown that effects that are usually seen one or two years after low-LET radiation may appear as early as sixty days after high-LET radiation. We are in the process of examining these effects in animal systems and have more experiments planned.

And, secondly, more radiobiological measurements made in parallel with clinical silicon Phase I trials are needed to evaluate the predictive value of *in-vitro* work for acute skin reactions.

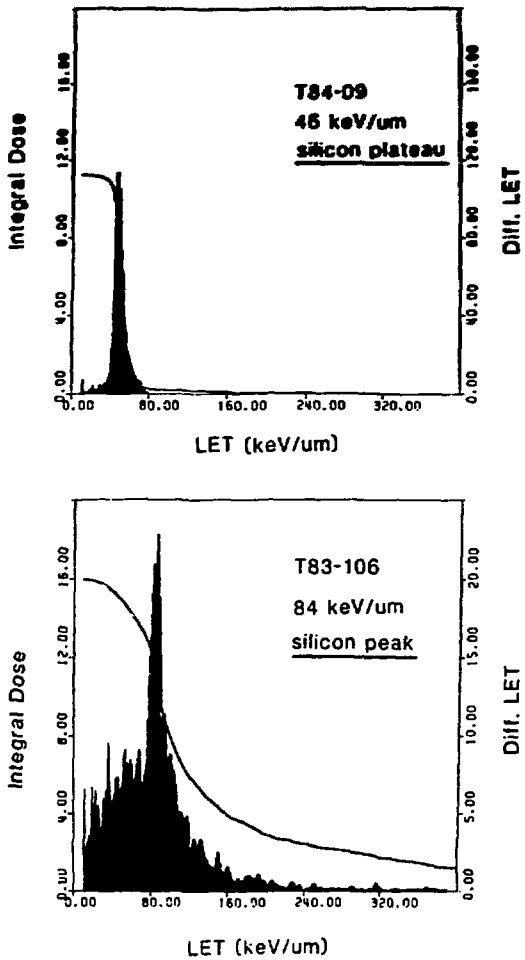

Fig. 5. Linear-energy-transfer (LET) distributions for silicon ion exposure of skin. (Upper panel) Silicon ions in the plateau of the Bragg curve from Fig. 1. (Lower panel) Silicon Bragg peak field from Fig. 3. (XBL 8512-4950)

Table 1. Relative silicon RBE values.

	Cells *in vitro* at 50% survival
Helium peak / silicon plateau	1.6 ± 0.2
Helium peak / Silicon plateau	3.2 ± 0.4

REFERENCES

1. Blakely, E.A., Ngo, F.Q.H., Curtis, S.B., and Tobias, C.A. Heavy-ion radiobiology: Cellular studies. *Adv. Radiat. Biol. 11*, 295–389 (1984).
2. Luxton, G., Fessenden, P., and Hoffman, W. *Radiat. Res. 79*, 256–272 (1979).

PLANNING CANCER TREATMENT WITH RADIOACTIVE BEAMS

Aloke Chatterjee, Joseph R. Castro, Edward L. Alpen, Jorge Llacer, George T.Y. Chen, and William T. Chu

When a heavy charged particle penetrates a medium, it deposits a very small dose along most of its path except at the end just before its stopping point. The dose in this region peaks dramatically, this phenomenon being called the Bragg peak. In radiation therapy with heavy charged particles the goal is to superimpose the Bragg peak on the tumor volume.

The availability of high-energy radioactive beams at the Bevalac, such as ^{11}C and ^{19}Ne, has provided a new dimension in optimizing cancer treatment with heavy charged particles. The diagnostic information available with these beams may preclude a large amount of uncertainty in localizing Bragg peaks on tumor volumes. It is well recognized that a slight error in placing the Bragg peak may result in severe underdosing of the tumor region and overdosing of nearby critical organs.

For precise localization of the Bragg peak, one requires an experimentally measured value of the water-equivalent thickness (thickness in a patient measured by using water as a standard) between the point of entry (of the beam particles) in a patient and the target (tumor) volume. Between these two end points there can be unknown amounts of bone, tissue, sinus, air, etc. and hence one may not be able to control precisely the incident energy of a heavy particle for the Bragg peak to coincide with the location of the tumor. In a technique that uses high-energy radioactive beams and a sensitive positron camera, the desired accuracy can be achieved through measurements in the actual treatment position, just before and immediately after the therapy.

In this technique energetic radioactive particles such as ^{11}C or ^{19}Ne are used. These particles decay by emitting positrons, which then annihilate with the medium electrons to produce two gamma rays, separated by 180°. These gamma rays can then be detected in coincidence mode by a positron camera to locate their origin in space.

By adjusting the energy of the radioactive particles (^{19}Ne has been used most commonly) they can be stopped at the location of the tumor as verified by the positron camera. This method provides a direct measure of the required water-equivalent thickness. Radioactive particles have penetration properties that are very similar to those of the heavy charged particles used in the Bragg-peak therapy. The value of the water-equivalent thickness measured by a radioactive beam is then directly applicable for treatment planning with heavy charged particles.

Through numerous studies and measurements in human phantoms, it has been realized that for the success of the technique, the following requirements for a radioactive beam are extremely important: 1) accepted minimum flux is 10^7 particles per pulse, 2) the energy spread must be as little as possible, and 3) at the location of the isocenter, the beam should be focused as tightly as possible. With respect to these requirements, some progress has been made in the last two years, as described below.

Radioactive beams are composed of secondary particles that are produced as a result of nuclear fragmentations of a suitable primary beam. For example, ^{19}Ne is produced from the accelerated stable isotope ^{20}Ne by getting rid of a neutron in a nuclear collision. Similarly, ^{11}C is produced from ^{12}C.

Accelerated heavy ions from the Bevalac are brought to a focus and made to traverse a low-Z target material (usually 2.5- or 3.8-cm-thick Be). Through nuclear reactions in the target, the projectile ion has a probability of being stripped of a neutron and emerging as a radioactive ion. The nuclear reactions take place over the entire thick-

ness of the target with an energy spread due to the difference of the energy loss rates of the primary and the secondary particles through the target material. For example, in the reaction of 400-MeV/nucleon $^{20}Ne - {}^{19}Ne$ through a 2.5-cm-thick Be target, ^{19}Ne, created near the entrance and exit of the target, will show a range difference of about 1.4 mm of water. A larger energy spread is introduced by the contribution of Fermi momentum (due to motion of nucleons inside a nucleus) of particles in nuclei involved in the nuclear reactions. Taking into account a Fermi momentum of approximately 100 MeV/c, the resulting energy spread in the ^{19}Ne beam is estimated to introduce a spread of stopping ranges of the beam of approximately 1.5 cm in water. The measured Bragg peaks of ^{20}Ne and ^{19}Ne show the increase of about 2.3 cm for ^{19}Ne over that of ^{20}Ne. The energy spread of the radioactive beam through the charged-particle transport system of the Bevalac is manifested in the experimental area as lateral dispersion of the beam, which contributes to a lower dose rate in a given irradiation volume. If the particles with different momentum were refocused, the stopping region becomes elongated. To make a spatially narrow radioactive beam with a sharp range, first the momentum spread of the beam must be reduced, and the resulting "monochromatized" beam must be refocused.

For reducing the momentum spread, a wedge made of lucite with a thickness variation from 0 to 1 in. over the base distance of 2 in. is placed in the ^{19}Ne beam between two bending magnets, upstream of a wire chamber. Since the higher-energy portion of the ^{20}Ne beam goes through the wider section of the wedge, the emerging beam has a much smaller energy spread. Such a procedure has been extremely successful in reducing the spread in the momentum of a secondary radioactive beam, and with ^{19}Ne it has now been possible to obtain 1-cm-size beam at the isocenter. In order to provide a greater flexibility, a large dial has been placed in the vacuum line of the Bevatron ring that contains wedges of different dimensions. For example, we have now four wedges having different wedge angles of 10.9°, 14.1°, 17.4°, and 25.7°. Depending upon the primary beam characteristics, we can select any one of the wedges and get a relatively suitable (tighter focus and reduced energy spread) radioactive beam for diagnostic applications. In order to improve the flux of the radioactive particles we have added a 20-ft-long vacuum pipe inside the therapy cave and directly along the optical bench. The pipe connects to the ring of the Bevatron and is generally operated at 10^{-6} torr. By adopting this procedure the scattering of the radioactive particles has been reduced significantly, helping us achieve a greater flux of the secondary beam.

These improvements have made the radioactive beam adequate for diagnostic procedures in clinical therapy of cancer patients. In Fig. 1 an arrangement of the positron camera with a patient's head between the banks of detectors is shown for localizing ^{19}Ne beam on a tumor volume in the brain. To date we have verified the water-equivalent thicknesses for Bragg-peak localization in three cancer patients, two of whom had brain tumors and the third a tumor in the thorax adjacent to the spinal cord. There was a very good agreement between the CT data and the measurements made with ^{19}Ne except in the two brain tumor patients. The measurement in the third patient involved beam transmission through lung and hard bone as well as soft tissue. The patient's original treatment setup was in a seated position. However, the positron camera required the patient to be in a horizontal (supine) position. For compatiblity with the previous treatment setup, the patient's arms were raised over his head during measurement with the positron camera. In addition to this measurement, the patient was then rescanned in the supine posi-

Fig. 1. A patient with a brain tumor is positioned on a treatment table. Through x-ray imaging (vertical and horizontal) the tumor has been located at the isocenter (a very stable reference point). The two banks of the positron camera are placed in such a way that the patient's head is immobilized between them. When a radioactive beam is stopped at the isocenter as determined by the camera, the exact water-equivalent thickness for a heavy-particle beam to penetrate can be determined. This information helps in localizing the Bragg peak on the tumor volume. (CBB 851-463)

tion and the water-equivalent path length determined from the CT scan was found to be greater than the measurement by the radioactive beam by 5 mm. Such a difference, if verified further, can be serious, and must be integrated in the treatment planning.

More patients have been scheduled for further comparison of the diagnostic procedures using the CT scanner and the radioactive beam. It is hoped that such procedures will prove of great utility and form a part of routine clinical procedures in the future.

ISOSURVIVAL TESTING OF BAR RIDGE FILTERS FOR WOBBLED NEON ION BEAMS

Stanley B. Curtis, Adrian Rodriguez, Tracy C-h. Yang, and Eleanor A. Blakely

An extensive series of experiments has been performed to test new bar filters that were designed in collaboration with the Heavy-Ion Radiobiology Related to Oncology Program Project. The filters were constructed to produce constant cell survival across the spread Bragg peak region in preparation for phase III therapeutic trials with the magnetically "wobbled" neon-ion beam. Three different filter designs (designated 3E1, 3E2 and 3E3) were studied. Each design produced a different slope in the spread peak region of the Bragg ionization curve. The three design curves calculated by C.A. Tobias for an 8-cm spread-peak region are shown in Fig. 1. Initially, three different thicknesses for the filters were chosen (4, 8, and 12 cm) for each of two of the designs (designated 3E2-4, 3E2-8, 3E2-12, 3E3-4, 3E3-8, and 3E3-12), and the filters were tested for iso-cell survival in neon-ion beams of two different energies (585 and 456 MeV/amu).

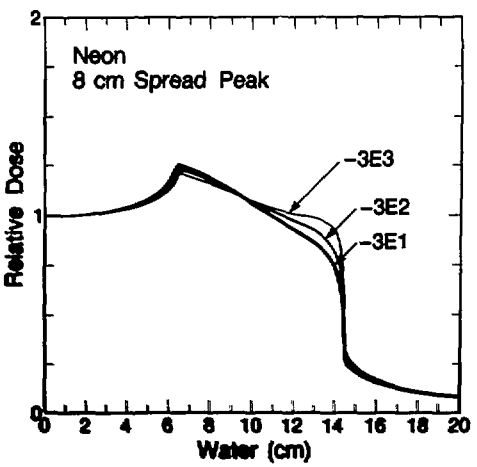

Fig. 1. Design curves for 8-cm spread-peak regions for a neon-ion beam. The three different designs 3E1, 3E2, 3E3 are indicated. The 3E3 design has the shallowest slope and the 3E1 design, the steepest slope. (XBL 8510-8520)

Cell survival curves were obtained by standard techniques in the plateau, proximal, distal, and tail portions of the Bragg ionization curve. The data were analyzed by a computer-assisted least-squares-fit to the linear quadratic (α,β) model of cellular inactivation. The best-fit parameters to the data provided RBE estimates for the proximal and distal spread Bragg peak regions for each of the filters tested. Isoeffectiveness within the spread Bragg peak was analyzed by comparing survival as a function of the dose delivered in the *plateau* entrance region of ionization. Peak-to-plateau dose ratios were obtained from the Bragg ionization curves of each filter and ion energy and used to convert the doses delivered in the Bragg peak to *plateau doses*. Examples for selected filters and energies are shown in Fig. 2. The survival curves are linear quadratic least-square-fits to the survival data in the proximal and distal spread Bragg peak regions, plotted here as a function of *plateau dose*. Thus, a superposition of the data points for the proximal and distal positions on such a plot indicates isosurvival for that filter design.

From analysis of the data, it was decided to construct a series of filters at 1-cm increments from 4 to 14 cm using the 3E3 design. The general conclusion of this analysis was that the design producing the flattest slope (3E3) produced the most constant cell survival across the peak region in the clinically important dose range.

Survival data obtained in the proximal-peak position of the Bragg curves for the already completed 3E3 filters have been useful in developing RBE tables for the upcoming phase III trials. Proximal peak RBEs are used along with other data, including cell survival measurements as a function of depth after a single exposure, to determine the physical doses to be delivered to the patients.

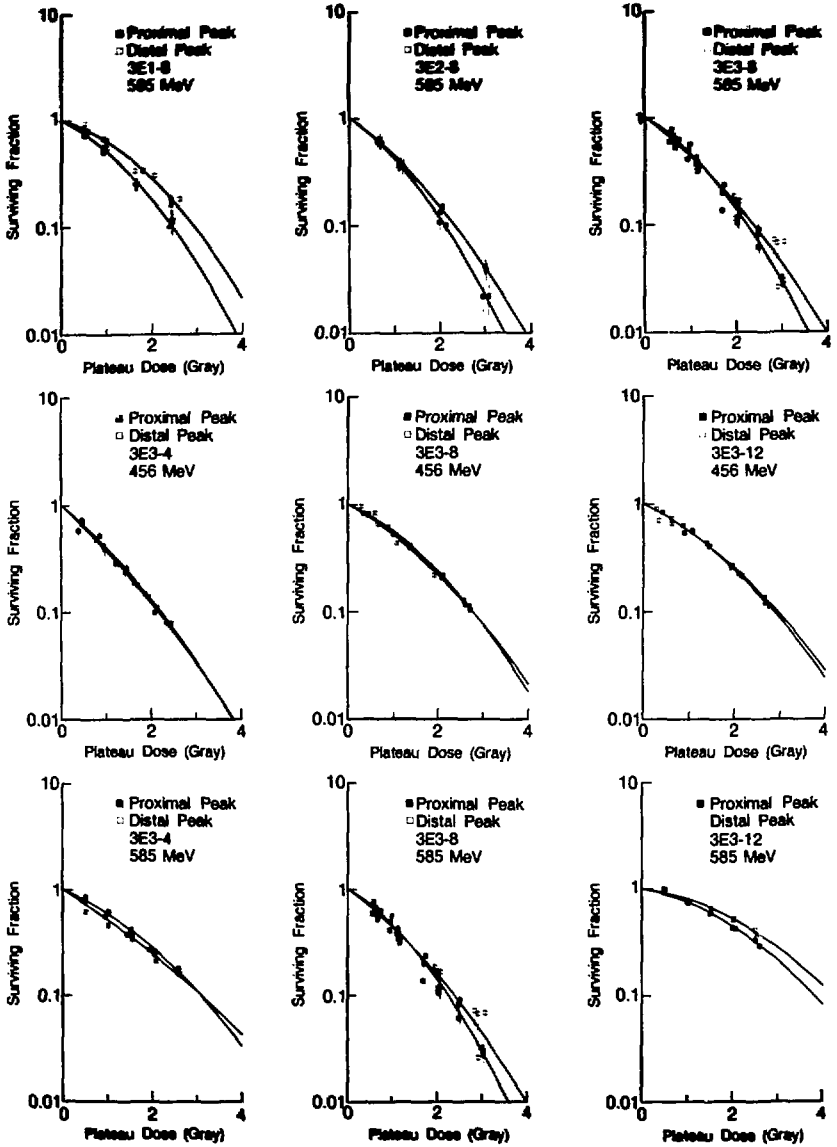

Fig. 2. Comparisons of survival of human T1 cells in the proximal and distal regions of the spread Bragg peak as a function of the dose in the plateau. Filter designs are compared that differ in the degree of slope in the spread Bragg peaks (3E1, 3E2, and 3E3) and in their widths (4, 8, and 12 cm). Filters were tested with neon-ion beams with initial energies of 456 MeV/amu and 585 MeV/amu. Survival in the proximal peak is indicated by the closed symbols, and open symbols indicate distal peak survival. The top row compares the different designs for the 8-cm spread peak at 585 MeV/amu. The middle row compares the 3E3 design for three widths of spread peaks at the lower energy (456 MeV/amu). The bottom row compares the same design for the same three widths at the higher energy (585 MeV/amu). *(XBL 8510-8521)*

RADIOBIOLOGICAL STUDIES FOR HELIUM ION THERAPY OF UVEAL MELANOMA

Eleanor A. Blakely, John T. Lyman, George T.Y. Chen, Joseph R. Castro, Polly Y. Chang, Leora Lommel, Frederick Yeater,* George J. Hampton,* Nina C. Wong, and Shari-Lyn K. Baba*

A review of the literature reporting relative biological effectiveness (RBE) of helium ions shows that there is considerable variation in values reported by several authors from different institutions (for a summary see Ref. 1). RBE values at the beam entrance or dose plateau of the Bragg curve when calculated relative to 225 kVp x rays are, in general, very close to unity. Average RBE values in the Bragg peak region are around 1.3 but, depending on the cell system and the width of the extended Bragg peak, range from 1.0 to 2.5.

This report summarizes part of the radiobiology that has been done at Berkeley's 184-Inch Cyclotron with helium-ion beams, which are currently being used to successfully treat uveal melanoma.[2] There were two main objectives to this study. The first was to confirm the adequacy of ridged filter design to achieve uniform cell killing across narrowly collimated and narrowly extended Bragg peaks of only a few centimeters in depth of range, which primarily involved measuring the RBE *in vitro* by two independent types of experiments. The second objective was to compare the physical and biological usefulness of a 308-MeV/u Bevalac-accelerated carbon beam for its potential application to the treatment of small localized volumes near critical structures.

Figure 1 demonstrates how the unmodified sharp Bragg peak, which is illustrated at the extreme right of the upper panel, can be broadened to wider and wider dose distributions with a rotating variable absorber that spreads the stopping particles over broader ranges. The dose has been deliberately sloped to be greater in the proximal peak and smaller in the distal peak where the particles are more effective. The end result is to achieve isoeffective killing across the width of the filter. Most large brain or abdominal tumors require the 12-, 8-, and 4-cm filters (also shown in the upper panel of Fig. 1). The special eye filters are shown in the lower panel of the same figure. The widths of these filters by comparison are much smaller, covering only 1.5 to 2.6 cm. The variable absorber filters used to produce the small beams are made of stacked lucite sheets. They rotate on a central axis, giving them the appearance of a propellor. The beam is aligned so that it passes through the center of each vane.

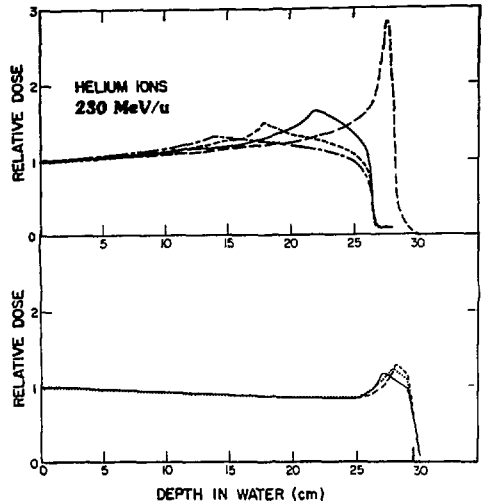

Fig. 1. 230-MeV/u helium Bragg ionization curves. (Top panel) unmodified, 4-cm , 8-cm, and 12-cm extended peaks. (Bottom panel) 1.5-cm, 2.0-cm, and 2.6-cm eye filters.
(XBL 859-4055)

Two biological methods were used to measure the cell killing effects of these beams. Exponentially-growing human T-1 cells were plated into either 25 cm^2 tissue culture flasks or in a circular area approximately 2 cm in diameter at the center of 35-mm plastic petri dishes. After the cells attached to the bottom of the petri dish, they were covered with 1 ml of culture medium. The cells in the petri dishes were prepared approximately 24 hours before irradiation, the cells in the flasks only approximately 5–6 hours before exposure. The flask experiments were not trypsinized after exposure and thereby provided two kinds of information. When the monolayer of irradiated cells was stained with methylene blue eleven days later, the pattern of cell killing permitted a check on the collimation and depth of penetration of the beam, and knowing the number of cells plated, the multiplicity of the cells at the time of exposure and the plating efficiency of control cultures, it was also possible to score surviving colonies within the 2.5-cm diameter area irradiated. In the petri dish experiment, the

*Accelerator & Fusion Division (accelerator operations) LBL.

cells are inserted into a special aluminum chamber that assures reproducible alignment in the beam. After exposure, the cells are trypsinized, resuspended, counted, plated, and incubated at 37°C for eleven days. Colony forming ability was scored by staining the cultures with 1% methylene blue and by counting surviving clones having at least 100 cells.

The petri dishes were exposed to a range of heavy-ion doses to generate a complete dose-response survival curve for an accurate calculation of RBE at several depths of range. The tissue culture flasks were irradiated at a physical dose of 8 Gy to the proximal peak in pairs behind variable amounts of polyethylene tissue-equivalent absorber. The flasks were filled with tissue culture medium at the time of exposure, and, thus, 1.8 cm of water-equivalent material was present between each exposed cellular monolayer. Depending on the width of the eye filter, six to eight pairs of flasks were irradiated to measure cell killing across the several-centimeter depth of penetration for each filter. The proximal-peak dose of 8 Gy was selected because it was similar to the dose fraction size to be used in the clinic.

Figure 2 shows an enlargement of the three eye filters of 1.5, 2.0 and 2.6 cm. Arrows on the curves designate the proximal and distal peak positions where survival curves were measured with the cells growing in the petri dishes. Survival data as a function of depth from two replicate experiments are plotted in the middle panel. The two data points plotted for the 1.5-cm filter were taken from the whole-survival curves measured with that beam. Within the limitations of the biological scatter, there appears to be isosurvival across the three filters with this system.

For reference, survival was measured in the entrance of the beam in each experiment for an RBE calculation using cells from the same population used for each experiment on the same day. The data were computer-fit to a linear-quadratic expression and the RBE values as a function of dose level were calculated by a program written by Norman Albright.[3] Figure 3 summarizes the survival results from the largest and smallest eye filters. The helium plateau data show a radiosensitivity that is intermediate between x-ray and gamma-ray survival, which makes cell survival in the beam entrance a good low-LET radiation reference for RBE calculations. Cell killing is slightly greater in the proximal peak of the 1.5-cm filter compared to the 2.6-cm filter. The survival curves measured in the distal peak positions of the filters were virtually identical. The distal peak position of the helium beam with an estimated average LET value of approximately 10 keV/μm is most effective for cell killing. At a position only a few centimeters upstream, the killing effectiveness is slightly less. The proximal-peak RBE value in the 1.5-cm beam is 1.4 ± 0.14, whereas the 2.6-cm beam value is 1.3 ± 0.12. The distal-peak RBE value for both filters is 1.6 ± 0.12. Most eye tumors require the larger filter. For simplicity of practical use in the clinic, the single RBE value of 1.3 in the proximal peak is cited as the helium-ion RBE value. Higher RBE

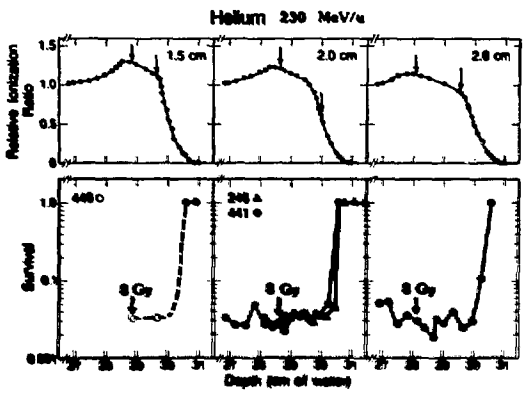

Fig. 2. Human T-1 cell survival as a function of depth in water for three eye filters using the 230-MeV/u helium beam after an 8-Gy proximal peak dose. (XBL 859-8486)

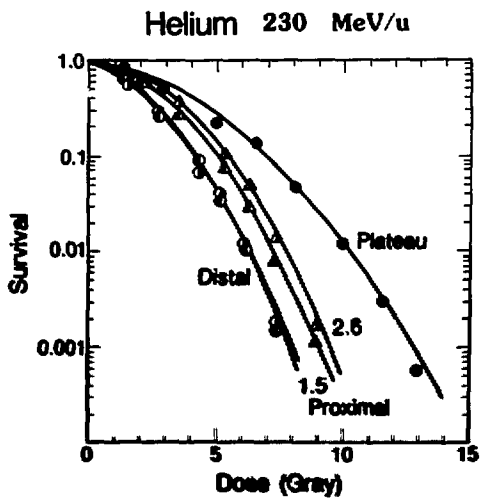

Fig. 3. Helium dose-survival response of human T-1 cells in the plateau and proximal and distal peaks of the 1.5-cm and 2.6-cm eye filters. (XBL 859-8488)

values are measured in the distal peak, but the downward slope of the Bragg curve in the distal peak is designed to ensure uniform cell killing across the filter at the desired dose level.

In summary, we have drawn two conclusions from this work:

1. The RBE measured *in vitro* in the 230 MeV/u helium-ion extended Bragg peak is 1.3–1.6.
2. Isoeffective biological response can be achieved with variable absorber filters that produce narrowly collimated Bragg peaks extended only a few cm for treatment of uveal melanoma.

REFERENCES

1. Raju, M.R. *Heavy-particle Radiotherapy,* Academic Press, New York (1980).
2. Blakely, E.A., Lyman, J.T., Chen, G.T.Y., Castro, J.R., Chang, P.Y., and Lommel, L. Radiobiological studies for helium-ion therapy of uveal melanoma. Presented at the meeting of the American Society of Therapeutic Radiologists, Miami Beach, Florida, 1985. *Int. J. Radiat. Oncol. Biol. Phys. 11,* Suppl. 1, 134 (1985).
3. Albright, N.W. Computer programs for the analysis of cell survival data. Abstract presented at the Radiation Research Society, Los Angeles, California, 1985.

SECTION 5. LIPOPROTEIN AND STRUCTURAL BIOLOGY

INTRODUCTION

The Lipoprotein and Structural Biology Group was formerly known as the Structural Biophysics Group. The new group title provides a more coherent description of the activities of investigators in the group; a major research effort is in lipoprotein metabolism and its relationship to cardiovascular disease, and another is on structural-functional correlates of biologically important macromolecules. In both areas, members of the group are internationally recognized in their respective areas of research.

Lipoprotein research has been ongoing in the Biology and Medicine Division for more than 30 years. The lipoprotein research group, under the leadership of Alex Nichols, has recently been awarded a program project grant to continue their innovative studies on plasma lipoproteins. The investigators in lipoprotein metabolism have been instrumental in developing and applying new techniques that measure and define lipoprotein levels and subclasses and provide new insights into the role of lipoproteins in health and disease. The summaries in this section indicate the breadth of research in lipoproteins from their importance in the newborn to the genetic basis of lipoprotein patterns in adults.

The internationalism of lipoprotein research is exemplified by the report of Alex Nichols, who has been carrying out a collaboration with investigators in Milan, Italy. These investigators have been examining lipoproteins in several families who have an unusual genetic defect in which a single amino acid substitution is found in the major protein (apolipoprotein AI) transported by high-density lipoproteins (HDL). Patients with the defect have unusually low levels of plasma HDL. Nichols and his colleagues were able to show that this defect is associated with a shift in HDL subpopulations to smaller denser particles than those of the normal adult. Identification of these unusual HDLs will provide a stepping stone for further studies on regulation of lipoprotein metabolism in cases where HDL subpopulations are abnormal.

In the past few years, Ronald Krauss and his associates have noted that adult LDL fell into several distinct subpopulations of particles based on size and density. Some subjects tended to have larger LDLs while others had smaller ones; the latter case was often associated with elevated plasma triglycerides. This led Ronald Krauss and Melissa Austin to ask the question whether the HDL pattern or phenotype is genetically controlled. Although the reported studies are ongoing, the results are very intriguing and suggest that indeed LDL-subpopulation distribution may be genetically controlled and that a single gene locus with two alleles may be involved. The genetic regulation of human lipoproteins is a new and developing area in the Lipoprotein Research Group and promises to be an important area for the future.

Analysis of HDL and LDL-subclass distribution using high resolution nondenaturing gradient gels was developed by Alex Nichols and Ronald Krauss. This technology is now used throughout the lipoprotein research community but has lacked a direct method for quantitation of lipoprotein subclasses. Resolution of this important methodological problem has been undertaken by Frank Lindgren who, as the present report indicates, has initiated a program to quantitate gradient-gel data. His approach using analytic ultracentrifugation as a measure of mass for discrete subclasses and relating these data to chromogenicity in the gel looks promising and is extremely important to the field. The precision of analytic ultracentrifugation mass and density measurements for lipoproteins such as LDL is dependent on precise determination of the partial specific volume and hydration of these particles. In this report, Talwinder Kahlon and Frank Lindgren and their colleagues have shown that LDL measurements are very sensitive to the solvent background and that all physical parameters must be controlled before LDL molecular weight can be measured.

In a continuing effort to understand developmental aspects of lipoprotein metabolism, Trudy Forte and colleagues investigated apolipoprotein E (apoE) distribution and plasma concentration in human umbilical cord blood. ApoE is recognized by cell receptors that also recognize LDL apoB; hence apoE may potentially regulate cholesterol metabolism in cells. ApoE concentration in the newborn was almost twofold higher than that of adults even though the newborn plasma cholesterol level was only one-third that in adults. ApoE in the fetus probably plays a significant role in cholesterol metabolism during development because the other

major cholesterol-transporting lipoprotein, LDL, is low in the fetus.

Members of the Lipoprotein and Structural Biology Group who are investigating molecular aspects of biological structures are in the forefront of their field. If one were to express a unifying theme in this area of research it is that each investigator is seeking to unravel the three-dimensional structures of macromolecules and to relate these structures to the regulation of biological processes.

Studies on the structure of biologically important molecules often includes the development of unique techniques and approaches for visualization and preservation of structural information. Kenneth Downing and Robert Glaeser developed a new approach for enhancing contrast and image information in high-resolution transmission electron microscopy. Ordinarily high-resolution transmission electron microscopy is accompanied by degradation of the image during electron irradiation. They reasoned that this was due to bending and lateral motion in the sample brought about by beam irradiation. To circumvent the problem they have developed a sophisticated computer-controlled system that takes a series of photographs of a sample irradiated by a very small electron-beam spot size. The composite image shows remarkable contrast without sacrificing structure. This Downing and Glaeser work heralds the way of the future for generating high-quality images of biological molecules for analysis of three-dimensional structure.

Bing Jap and Seok-Hwan Kong have initiated studies on the secondary structure of halorhodopsin (hR). This retinal protein functions as a light-driven electrogenic chloride pump in the bacteria *H. halobium*. Jap and Kong found that this transmembrane protein is similar in molecular weight and amino acid composition to that of the light-driven proton pump of bacteriorhodopsin. Circular dichroism indicates that both proteins have similar secondary structure; however, they lack immunological cross-reactivity. From the compositional studies they have calculated that the hR protein contains five helices that transverse the membrane. In the future, they plan to unravel the three-dimensional structure of hR to see whether this protein has structural features in common with other ion transport proteins such as bacteriorhodopsin. Another major breakthrough for Bing Jap was the isolation and crystallization of PhoE, a transmembrane protein that forms pores regulating phosphate diffusion in *E. coli* outer membranes. The PhoE protein is atypical of most integral membrane proteins in that it consists mainly of anti-parallel pleated strands instead of helical segments. Reconstitution of large highly symmetric crystals of PhoE by Jap will permit him to carry out three-dimensional structural analysis of this unusual biological macromolecule.

Thomas Hayes and his associates are well known for their development of a mechanism for examining frozen hydrated tissue in the scanning electron microscope. This technology has profoundly affected our conception of lung structure as outlined in the present report by Jacob Bastacky, Hayes, and their colleagues. Examining lung tissue in the frozen-hydrated state prevents critical point drying artifacts and reveals that the liquid surfactant interface in the lung alveoli is continuous. Until this elegant demonstration of surfactant intactness, it was thought that the alveolar aqueous surfactant layer contained pores or regions of discontinuities.

Not all studies on the macromolecular structure of biologically important molecules depend on electron microscopic visualization. This point is very aptly made in the innovative differential polarization imaging microscope developed and described by Marcos Maestre. With this microscope he is able to see differences in hemoglobin structure such as that of normal versus sickled hemoglobin. This new form of imaging has the potential for providing information on both concentration and spatial orientation of biological polymers.

A rapidly developing area in the field of macromolecular structure and interaction is that of antibody-antigen interactions. In the present report, Jack Owicki and Aaron Kantor describe a sophisticated artificial model system with which to study the molecular basis of agglutination. Phospholipid liposomes carrying an antigenic hapten (fluorescein) were produced and interacted with different monoclonal antibodies to the hapten. Their studies thus far reveal that there is little correlation between agglutination ability of the various monoclonal antibodies and affinity of antibody for antigen. Such a phenomenon may be related to conformational flexibility or geometric distribution of antigen on model membranes. It is definitely a promising new concept to be explored in future studies.

Lipoproteins

THE AI-MILANO HDL PARTICLES

Alex V. Nichols, Guido Franceschini,* Cesare R. Sirtori,* and Elaine L. Gong

Interest in the structure and function of human high density lipoproteins (HDL) derives in major part from epidemiologic observations of their inverse correlation with the risk of arterial disease.[1,2] Based on such observations, an increased incidence of premature disease would be expected in individuals with very low levels of HDL. Surprisingly, several rare familial disorders characterized by decreased levels of HDL do not show the presence of premature vascular lesions.[3,4] One such disorder appears to be the apolipoprotein variant designated AI_{Milano} or AI_M, which is generally associated with reduced plasma levels of HDL and elevated levels of triglyceride.[5] The mutant apolipoprotein AI is characterized by a single cysteine-for-arginine replacement at position 173.[6] The apolipoprotein is capable of forming intermolecular disulfide bonds that can produce dimers and mixed disulfide complexes. Since AI is the major apolipoprotein component of normal HDL and thereby plays a crucial role in determining both the lipid-binding capacity and the ultimate particle size properties of HDL, considerable change in HDL particle properties and distribution might be expected from participation of AI_M dimers and mixed disulfide complexes in HDL structure.

Franceschini et al.[7] have shown that HDL from affected carriers (designated AI_M^+) are characterized by a predominance of HDL_3 (d 1.125–1.20 g/ml) which are enriched in triglyceride and low in cholesterol content. By means of chemical crosslinking, at least three apparent HDL_3 subspecies with differential apolipoprotein composition of the protein moiety were identified by these investigators.

In the present investigation, the particle polydispersity of HDL in plasma of ten AI_M^+ and six AI_M^- (nonaffected kindred) was evaluated (Table 1). For determination of HDL particle size distribution, gradient gel electrophoresis (protein stain) was performed on the ultracentrifugal $d \leq 1.20$ g/ml fraction isolated from plasma of all of the above subjects.[8] For determination of the flotation rate distribution of HDL, the same ultracentrifugal fraction isolated from a smaller subgroup (six AI_M^+ and four AI_M^-, see Table 1) of the above subjects was analyzed by analytic ultracentrifugation.[9] Total HDL and HDL-subclass levels determined by analytic ultracentrifugation are listed in Table 1. Total plasma HDL of the group of AI_M^+ subjects ranged from 18 to 238 mg/dl and showed a predominance of HDL_3 as gauged by the pattern area within the flotation interval of $F^o_{1.20}$ 0–3.5. HDL material in the flotation interval of $F^o_{1.20}$ 3.5–9.0, corresponding to the HDL_2 subclass, was observed in AI_M^+ with higher plasma HDL-C levels. Plasma concentrations of HDL_2 in these subjects ranged from 0 to 55 mg/dl. The analytic ultracentrifugal results were consistent with the rate zonal ultracentrifugal data reported by Franceschini et al.[7]

As indicated above, the particle size distributions of HDL of AI_M^+ and AI_M^- were determined directly by gradient gel electrophoresis. By means of this technique, we previously described the occurrence in normal human plasma of at least five major subpopulations: three within the HDL_3 subclass ($(HDL_{3a})_{gge}$, $(HDL_{3b})_{gge}$, and $(HDL_{3c})_{gge}$) and two within the HDL_2 subclass ($(HDL_{2b})_{gge}$ and $(HDL_{2a})_{gge}$).[10] Peak maxima of the above subpopulations fall within specific particle size intervals that define the subpopulations: 12.9–9.7 nm, $(HDL_{2b})_{gge}$; 9.7–8.8 nm, $(HDL_{2a})_{gge}$; 8.8–8.2 nm, $(HDL_{3a})_{gge}$; 8.2–7.8 nm, $(HDL_{3b})_{gge}$; and 7.8–7.2 nm, $(HDL_{3c})_{gge}$.

Gradient gel electrophoresis patterns of AI_M^+ HDL were characterized by two major peaks with maxima located primarily within the particle size intervals of the $(HDL_{3a})_{gge}$ and $(HDL_{3b})_{gge}$ subpopulations (Fig. 1). Compared to AI_M^- HDL (Fig. 2), the AI_M^+ HDL were unique in consistently exhibiting a distinct peak within the $(HDL_{3b})_{gge}$ interval. Peaks with maxima in the $(HDL_{2b})_{gge}$ interval, which in normal subjects contains the larger species of the HDL_2 subclass, were either minor or nondetectable. Patterns of AI_M^- HDL were similar to patterns previously reported for normal subjects.[8] They were characterized by a major peak with maximum in the $(HDL_{3a})_{gge}$ interval and by peaks of varying

*Center Ennica Grossi Paoletti University of Milan, 20129 Milan, Italy.

Table 1. Identification and characteristics of AI_M carriers (AI_M^+) and nonaffected kindred (AI_M^-).

Case No.	Age (yr)	Sex	TG	HDL-C	$F^o_{1.20}$ 0–9 (total HDL)	$F^o_{1.20}$ 0–3.5 (HDL_3)	$F^o_{1.20}$ 3.5–9 (HDL_2)
AI_M^+							
445	48	M	476	9	25	25	0
456	22	M	96	10	na	na	na
447	56	M	126	10	na	na	na
449	41	M	250	11	47	47	0
487	12	M	60	15	na	na	na
454	35	M	65	21	138	119	19
444	33	F	316	8	18	18	0
455	14	F	96	18	88	75	13
458	16	F	93	20	na	na	na
473	66	F	170	35	238	183	55
AI_M^-							
17	75	M	115	42	201	197	4
18	56	M	78	51	na	na	na
21	56	M	105	70	288	164	124
22	36	F	110	50	na	na	na
19	60	F	220	61	309	214	95
20	38	F	64	76	305	172	133

Abbreviations: TG, triglyceride; HDL-C, HDL cholesterol; $F^o_{1.20}$ 0–9, 0–3.5, and 3.5–9: flotation rate intervals measured by analytic ultracentrifugation; na, not analyzed by analytic ultracentrifugation. All values in mg/dl.

amplitude in the $(HDL_{2b})_{gge}$ interval. The latter peaks, when present, were correlated with the presence of material in the HDL_2 flotation interval $F^o_{1.20}$ 3.5–9.0 in corresponding analytic ultracentrifugal patterns. In some patterns of control subjects, a shoulder on the major $(HDL_{3a})_{gge}$ peak was noted, indicating the occurrence of material within the $(HDL_{3b})_{gge}$ interval.

In HDL patterns of all AI_M^+, the mean particle sizes of the major components, with peaks in the $(HDL_{3a})_{gge}$ and $(HDL_{3b})_{gge}$ intervals (sizes at peak maxima: 8.55 ± 0.09 and 7.97 ± 0.02 nm, respectively), were similar to those (8.44 ± 0.07 and 7.88 ± 0.02 nm, respectively) observed in AI_M^-. The mean particle size of the major component in the $(HDL_{2b})_{gge}$ interval, however, was smaller (9.85 ± 0.02 vs. 10.34 ± 0.29 nm) in the AI_M^+ compared with that in the AI_M^-. Thus, the particle sizes of the major HDL_3 subpopulations in AI_M^+ were not significantly different from sizes of their counterparts in AI_M^-. It should be noted that the mean particle sizes of the major components of HDL in AI_M^- compared closely with those of a large number (n = 191) of subjects studied by us in the U.S.A.[8]

AI_M^+ HDL exhibited three characteristic gradient gel electrophoresis patterns (patterns I, II, and III, Fig. 1) that reflected the relative contributions of the two major peaks. The main distinguishing feature among the three patterns was the relative content of the smaller and larger HDL subpopulations that had peak maxima in the $(HDL_{3b})_{gge}$ and $(HDL_{3a})_{gge}$ intervals, respectively. Pattern I had the highest relative content of smaller subspecies, and pattern III had the highest relative content of larger species. In addition, it should be noted that the group of AI_M^+ with pattern I exhibited the lowest mean HDL-C value (I: HDL-C, 9.3 ± 1.5 mg/dl) compared with that of AI_M^+ with patterns II and III (II: HDL-C, 14.6 ± 4.6 mg/dl, and III: HDL-C, 28.0 ± 9.9 mg/dl). Thus, it appears that as HDL-C levels are reduced, the particle size pattern becomes relatively enriched in the smaller HDL subpopulations. Such progressive relative enrichment of HDL patterns with species of smaller particle size as a function of decreasing plasma concentration of HDL-C was also observed in normal subjects. The correlation coefficient relating the percent of the total HDL pattern area in the particle size interval of the small subpopulation $(HDL_{3b})_{gge}$

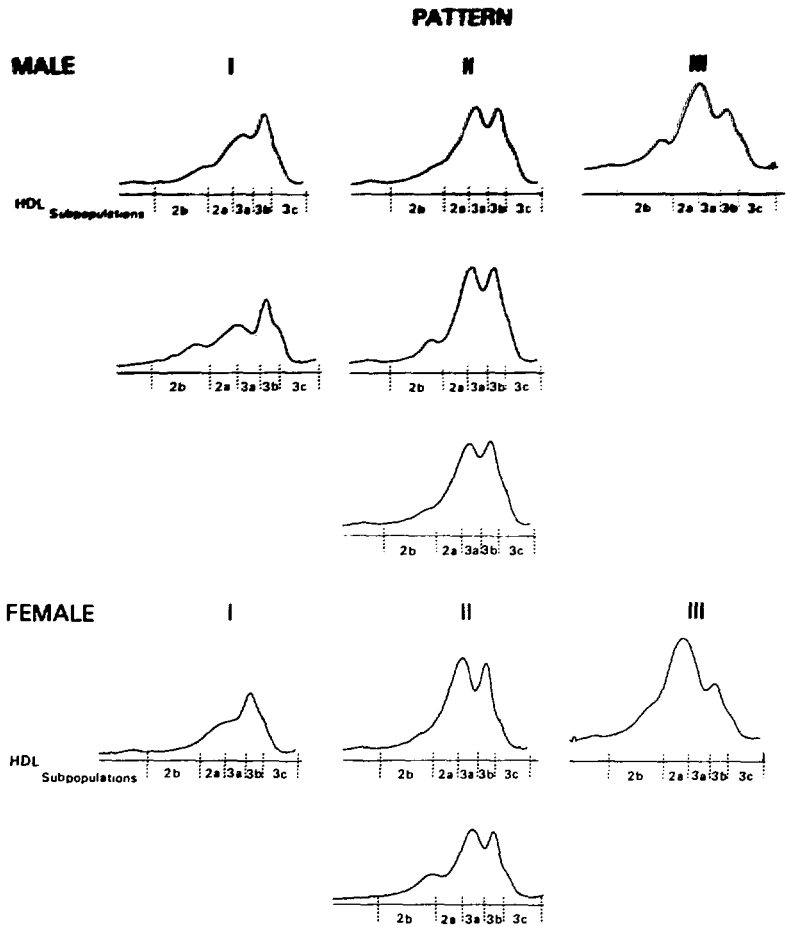

Fig. 1. Gradient gel electrophoresis patterns of male and female AI_M^+.. Patterns are obtained by densitometry of protein-stained gradient gels (4–30% polyacrylamide).[6] Intervals corresponding to particle size ranges of HDL subpopulations in normal human plasma are indicated below patterns. See text for numerical values of particle size intervals corresponding to the HDL subpopulations. Numbers appearing at lower left of each pattern designate AI_M^+ described in Table 1. *(XBL 859-3975)*

vs. HDL-C was -0.79 ($p < 0.001$) for normal male adults (age range: 35–59 yr; $n = 91$).[11] The correlation coefficient between the same parameters for an admittedly small sample of ten AI_M^+ subjects was -0.90 ($p < 0.001$). The mean HDL-C plasma levels in the above ten AI_M^+ subjects was 15.7 ± 8.3 mg/dl, while the mean level in the 91 normal male subjects was 44.0 ± 11.6 mg/dl.

Furthermore, it is well established that low levels of HDL-C are frequently associated with elevated plasma triglyceride levels and this also appeared to be the case for AI_M^+. Thus, for 33 AI_M^+,[12] the correlation coefficient for plasma triglyceride level vs. HDL-C was -0.30 ($p = 0.05$); for 91 normal males cited above, the correlation coefficient for the same variables was -0.49 ($p < 0.001$). When values of plasma triglyceride (TG) and HDL-C were plotted for the ten AI_M^+ and six AI_M^- whose HDLs were analyzed by electrophoresis, the group of AI_M^+ with pattern I exhibited the lowest mean HDL-C value and the highest mean TG value, relative to those of AI_M^+ with patterns II

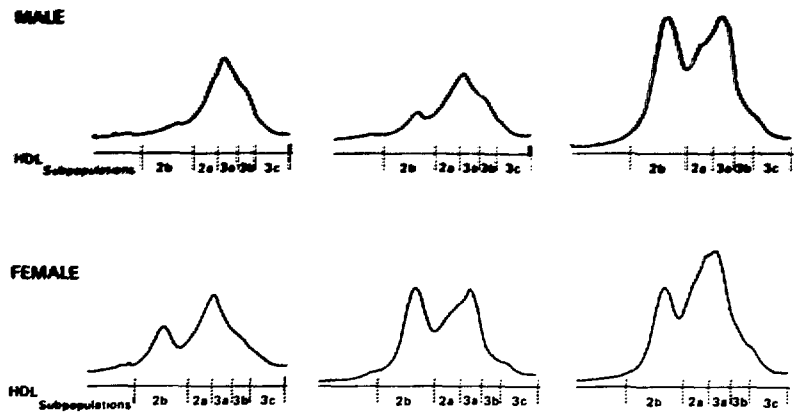

Fig. 2. Gradient gel electrophoresis patterns of male and female AI_M^- (see caption of Fig. 1 and Table 1).
(XBL 859-3976)

and III (Fig. 3). These data suggest that the pattern I distribution, in which the relative content of the smaller $(HDL_{3b})_{gge}$ subpopulation was increased, reflected the presence of both elevated plasma TG levels and very low levels of HDL-C. The observation of the relative enrichment of HDL with smaller sized particles in the presence of hypertriglyceridemia (222–2500 mg/dl) and reduced HDL-C levels (22–30 mg/dl) has been previously reported by Eisenberg et al.[13]

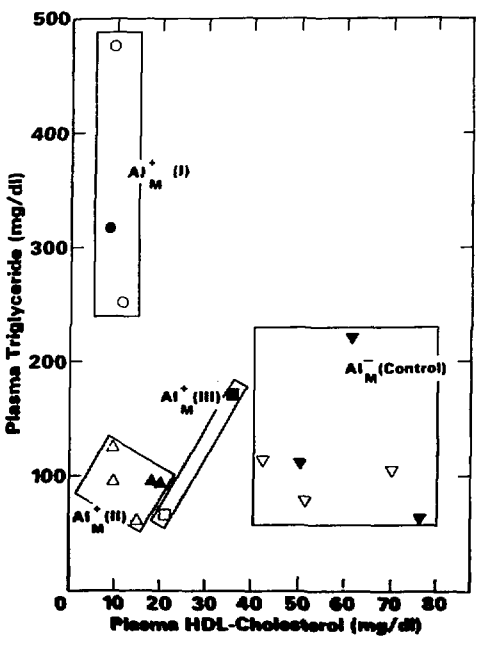

Fig. 3. Plot of triglyceride and HDL-cholesterol levels in plasma of AI_M^+ and AI_M^-. Data points for AI_M^+ of the same pattern type (I, II, and III) and for AI_M^- control are enclosed by solid lines. Sex of subjects is indicated. Subjects in this figure are those described in Table 1 and in Figs. 1 and 2. (XBL 8510-8541)

In conclusion, our investigation of HDL particles in AI_M^+ indicates the following: 1) the AI_M^+ HDL particle size distribution consists mainly of two major components, one broad peak (mean size, 8.55 nm) in the $(HDL_{2a+3a})_{gge}$ interval and one sharp peak (mean size, 7.97 nm) in the $(HDL_{3b})_{gge}$ interval; 2) the mean particle sizes of the major HDL_3 components are similar to those observed within the same HDL subpopulation intervals in AI_M^- and normal subjects; 3) three pattern types of HDL distribution can be identified in AI_M^+ that reflect the relative contribution of the two major HDL components; 4) the pattern type with greatest relative build-up of smaller HDL particles is observed in a group of AI_M^+ with highest mean TG and lowest mean HDL-C values; and 5) the statistical relationship between plasma TG and HDL-C levels in AI_M^+ is inverse as observed in normal and hypertriglyceridemic subjects.

REFERENCES

1. Miller, G.J., and Miller, N.E. Plasma high-density lipoprotein concentration and development of ischaemic heart disease, *Lancet 1*, 16 (1975).
2. Gordon, T., Castelli, W.P., Hjortland, M.C., Kannel, W.B., and Dawber, T.R. High density lipoprotein as a protective factor against

coronary heart disease: the Framingham study, *Am. J. Med.* 62:707 (1977).
3. Assmann, G., Herbert, P.N., Fredrickson, D.S., and Forte, T. Isolation and characterization of an abnormal high density lipoprotein in Tangier disease, *J. Clin. Invest. 60*, 242 (1977).
4. Carlson, L.A. Fish eye disease: a new familial condition with massive corneal opacities and dyslipoproteinemia, *Eur. J. Clin. Invest. 12*, 41 (1982).
5. Franceschini, G., Sirtori, C.R., Capurso, A., Weisgraber, A.H. and Mahley, R.W. A-I_{Milano} apoprotein: decreased high density lipoprotein cholesterol levels with significant lipoprotein modifications and without clinical atherosclerosis in an Italian family, *J. Clin. Invest. 66*, 892 (1980).
6. Weisgraber, K.H., Rall, S.C., Bersot, T.P., Mahley, R.W., Franceschini, G., and Sirtori, C.R. Apolipoprotein AI_{Milano}: detection of normal AI in affected subjects and evidence for a cysteine for arginine substitution in the variant AI, *J. Biol. Chem. 258*, 2508 (1983).
7. Franceschini, G., Frosi, T.G., Manzoni, C., Gianfranceschi, G., and Sirtori, C.R. High density lipoprotein-3 heterogeneity in subjects with the apo-AI_{Milano} variant, *J. Biol. Chem. 257*, 9926 (1982).
8. Nichols, A.V., Blanche, P.J., and Gong, E.L. Gradient gel electrophoresis of human plasma high density lipoproteins. In *Handbook of Electrophoresis, Vol. III*, L.A. Lewis, ed., CRC Press, Boca Raton, Florida (1983).
9. Lindgren, F.T., Jensen, L.C., and Hatch, F.T. The isolation and quantitative analysis of serum lipoproteins. In *Blood Lipids and Lipoproteins*, G.J. Nelson, ed., Interscience, New York (1972).
10. Blanche, P.J., Gong, E.L., Forte, T.M., and Nichols, A.V. Characterization of human high-density lipoproteins by gradient gel electrophoresis, *Biochim. Biophys. Acta 665*, 408 (1981).
11. Lindgren, F.T., Nichols, A.V., Wood, P.D., Adamson, G.L. Austin, A.M., Glines, L.A., Martin, V., and Krauss, R.M., in preparation.
12. Franceschini, G., Sirtori, C.R., Gianfranceschi, G., Menotti, A., Cerrone, A., Orsini, G., and Gualandri, V. A-I_{Milano} apoprotein: identification of the complete kindred and evidence of a dominant genetic transmission, *Amer. J. Human Genetics*, in press (1985).
13. Eisenberg, S., Gavish, D., Oschry, Y., Fainaru, M., and Deckelbaum, R.J. Abnormalities in very low, low, and high density lipoproteins in hypertriglyceridemia, *J. Clin. Invest. 74*, 470 (1984).

GENETIC STUDIES OF LDL SUBCLASSES

Melissa A. Austin and Ronald M. Krauss

The clustering of cardiovascular disease in families has been observed in many studies and may be due, at least in part, to genetic abnormalities of lipid and lipoprotein metabolism. Among the plasma lipoproteins, those of low density (LDL) and intermediate density (IDL) have been related directly to the development of coronary heart disease, while levels of high-density lipoproteins (HDL) are inversely related to cardiovascular disease risk. Genetic abnormalities leading to high-risk lipoprotein levels have been identified to date in only a small number of disease entities, such as the LDL-receptor defect responsible for hypercholesterolemia in 0.2% of the population.

Over the last several years, work in our laboratory has established the existence of considerable heterogeneity within LDL and IDL, and the existence of a number of distinct subpopulations within these classes. It is possible that previously unrecognized genetic traits could affect levels of particular LDL or IDL subclasses that are preferentially involved in the development of cardiovascular disease. To assess the genetic contribution to levels of LDL subclasses, we have initiated studies of normal kindreds and have used mathematical modeling techniques to identify phenotypes among the family members.

To date, we have screened 17 nuclear families from 8 large Mormon kindreds living in the Bay area. Mormons were chosen because they often have large families with good geneological records. A total of 78 family members have participated in the study by supplying a blood sample for lipoprotein analyses and completing a medical interview.

One of the most sensitive means of identifying LDL subclasses is gradient gel electrophoresis (GGE). This procedure separates lipoprotein particles by size, and examples of the resulting curves for low-density lipoprotein (LDL) are shown in Fig. 1. To identify subclasses within the LDL range based on these data, we have developed a mathematical modeling technique using nonlinear regression. The component curves identified by this technique are indicated by dotted lines and correspond to subclasses of LDL particles. The sum of the component curves approximates the total LDL gradient gel scan. The peak particle diameters of the curves are then calculated using calibration data from protein standards. The use of the mathematical modeling has allowed us to identify quantitatively two distinct LDL GGE patterns, A and B, and we have proposed that these patterns actually represent genetic phenotypes. Pattern A is more common, and is characterized by a major peak of large LDL subclasses, and a minor peak of smaller LDL subclasses. In contrast, pattern B, present in about 10–15% of individuals studied to date, has a single major peak of small LDL particles, with skewing to the left.

The evidence from the families studied so far is consistent with a single locus, two allele, genetic polymorphism controlling the LDL subclass patterns. One of the most intriguing findings is that there appears to be a threshold effect at about age 40. That is, individuals with a "B" allele at the proposed locus may only express the B phenotype once they have reached age 40. An example of a pedigree for a family carrying this trait is shown in Fig. 2. The parents, sample numbers 8628 and 8627, are both 70 years of age and their children range from age 44 to 29. The two youngest sons, sample numbers 8714 and 9005, are identical twins. The father in this family has pattern A, as do two of the children with sample numbers 8715 and 8904. However, the mother has pattern B and has apparently passed it on to her oldest son, sample number 8709. The twins have patterns somewhat intermediate between the usual A and B patterns. They may carry the B allele, but do not express the B phenotype because they are under age 40.

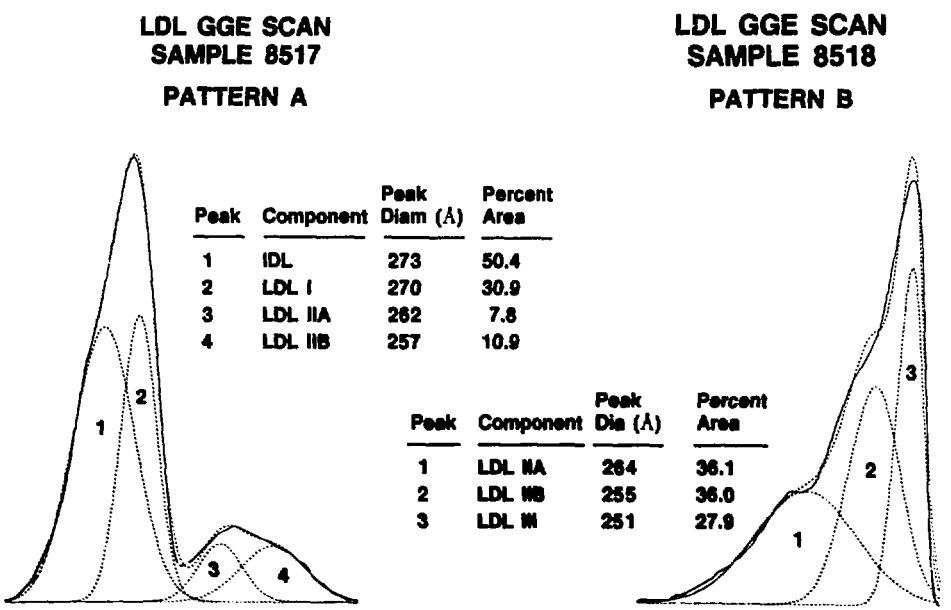

Fig. 1. Gradient gel electrophoresis scans of low density lipoproteins. Two patterns, A and B, have been identified in the genetic studies. Solid lines are the actual gradient gel data. The dotted component curves were identified by mathematical modeling using non-linear regression and correspond to LDL subclasses. The peak particle diameters of the component curves were determined from calibration data from protein standards, and the relative area under each curve was calculated. *(XBL 853-8233)*

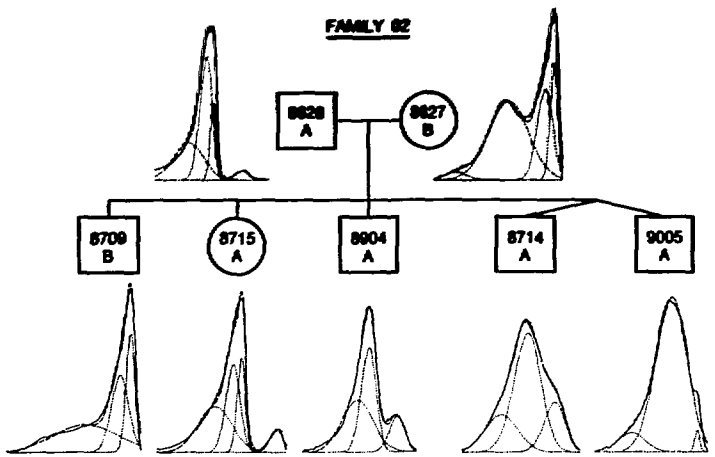

Fig. 2. Pedigree of an informative family in the genetic study. The sample number and phenotype of each subject are given, and the LDL GGE scan with component curves from the mathematical modeling is shown.
(XBL 8510-8539)

In addition to the genetic results, interrelationships between these phenotypes based on LDL and other lipids and apoproteins have been found. After statistical adjustment for age, sex, and obesity as needed, subjects with phenotype B were found to have relatively increased triglyceride and apoprotein B levels. HDL cholesterol and HDL_2 mass were also significantly lower in subjects with phenotype B compared to those with phenotype A. These differences are all in directions that suggest a higher risk of coronary disease in phenotype B than in phenotype A.

This initial study of LDL GGE subclass patterns in families has provided preliminary evidence that LDL subclasses are genetically controlled. The phenotype characterized by a predominance of small LDL particles may predispose subjects to elevated triglyceride and apo B levels and decreased HDL levels. As part of our upcoming program project, 150 to 200 additional families will be studied, and possible dietary and environmental influences on the phenotypes will be considered. If the genetic hypothesis is confirmed, we will have identified a relatively common genetic trait that may predispose the development of coronary heart disease.

INTERCORRELATIONS OF SUBCLASSES OF LDL AND HDL BY GRADIENT GEL ELECTROPHORESIS (GGE) AND ANALYTIC ULTRACENTRIFUGATION (ANUC)

Frank T. Lindgren, Alex V. Nichols, Peter D. Wood,* Gerald L. Adamson, Melissa A. Austin, Laura A. Glines, Vera Martin, and Ronald M. Krauss

The relationships between LDL and HDL subclasses as determined by gradient gel electrophoresis and analytic ultracentrifugation were determined in a normal human male population of 120, ages 35 to 39 years.

The R_f intervals relative to albumin on Pharmacia 4/30 gradient gels between R_f 0.45–0.63, 0.63–0.71, 0.71–0.78, and 0.78–0.84, defined as HDL_{2b}, HDL_{2a}, HDL_{3a}, and HDL_{3b} respectively, were highly correlated to AnUC intervals F 4–9, 3–4, 2–3, and 0–2 respectively. Mean correlation coefficients were 0.84 (all $p < 0.0001$). Similarly,

*Stanford LRC Laboratory, Stanford University Medical Center.

GGE subclasses of LDL with R_f intervals relative to apoferritin on Pharmacia 2/16 gradient gels between R_f 0.22–0.30, 0.30–0.36, 0.36–0.38, 0.38–0.41, 0.41–0.45, and 0.45–0.49 corresponded to S_f 10–20, S_f 8–10, S_f 6–8, S_f 4–6, S_f 2–4, and S_f 0–2 respectively, as measured by AnUC. Mean correlation coefficients were 0.62 (all $p < 0.0001$).

At the time this study were done, LDL and HDL cholesterol values had been determined on 91 of the 120 plasma samples. Total lipoprotein LDL and HDL mass in mg/dl were calculated on each sample (LDL cholesterol = 0.333 × total LDL; HDL cholesterol = 0.168 × total HDL). These calculated values, when compared to lipoprotein mass values from the AnUC, gave correlations of $r = 0.90$, $p < 0.0001$ (LDL) and $r = 0.85$, $p < 0.0001$ (HDL).

More exact calculation of GGE subclass concentration requires evaluation of relative dye uptake per unit mass of each subclass (Coomassie Blue stain). The initial densitometer scan of each sample on GGE is saved in data files on the PDP-11 34-A computer disc, and may be recalled for further analysis when desired.

PARTIAL SPECIFIC VOLUME AND PREFERENTIAL HYDRATION OF LOW DENSITY LIPOPROTEIN SUBFRACTIONS

Talwinder S. Kahlon, Gerald L. Adamson, Laura A. Glines, Joseph R. Orr, and Frank T. Lindgren

Partial specific volume ($\bar{v}$) and preferential hydration of low-density lipoprotein (LDL) subfractions need to be determined in order to characterize these highly atherogenic components of the human plasma lipoprotein spectra. Molecular weights of LDL subfractions have been determined by sedimentation equilibrium,[1] using an estimated $\bar{v}$, as given by $\bar{v} = 1/\rho$, where ρ is the corresponding background gradient density of isolation. However, for accurate molecular weight determinations of LDL subfractions by sedimentation equilibrium valid determination of $\bar{v}$ is essential. Preferential hydration of LDL has not been thoroughly investigated; however, no values of preferential hydration have been reported.[2]

We have determined $\bar{v}$ for five LDL subfractions ($n = 5–7$) and evaluated preferential hydration ($n = 2$) for LDL subfraction 3 in normolipoproteinemic subjects in order to characterize these highly atherogenic components of the human plasma lipoprotein spectra. Mean values for $\bar{v}$ were 0.9757 ± 0.0019 ml/g; 0.9701 ± 0.0007 ml/g; 0.9674 ± 0.0016 ml/g; 0.9616 ± 0.0016 ml/g; and 0.9550 ± 0.0025 ml/g for subfractions 1, 2, 3, 4, and 5, respectively. However, molecular densities (σ) obtained from $\rho = 1/\bar{v}$ for respective LDL subfractions were 1.0249, 1.0308, 1.0337, 1.0399, and 1.0471 g/ml, respectively. The preferential hydration of lipoprotein subfraction 3 in NaCl-H_2O solution was 2.9 to 4.8 wt%, whereas values were much lower (0.3–0.6 wt%) in 0.196 M NaCl-Xm NaBr-H_2O solvent system (Fig. 1). It was observed that the linearity of $\eta F°$ vs. ρ may not be valid for solvents NaCl-NaBr-H_2O of density as high as 1.4744 g/ml. Thus, flotation velocity data using extreme salt concentrations (1.4744 g/ml and higher) may be viewed with caution.

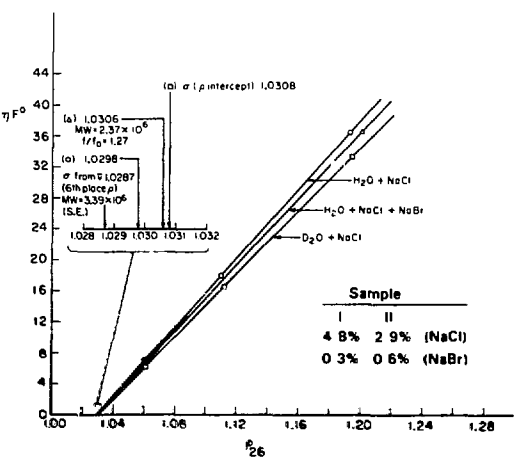

Fig. 1. $\eta F°$ vs ρ plots, LDL subfraction 3, sample 11. Preferential hydration is given by $\Gamma° = (\bar{v}_u - LDL - \bar{v}H - LDL)/(\bar{v}H - LDL - v_{H_2O})$ where $\bar{v}_u$ and v_H are the unhydrated and hydrated partial specific volumes of LDL subfraction 3, obtained from ρ intercept D_2O and ρ intercept H_2O-salt, respectively.

(XBL 832-3631B)

REFERENCES

1. Kahlon, T.S., Adamson, G.L., Shen, M.M.S., and Lindgren, F.T. *Lipids 17*, 323–330 (1982).
2. Fisher, W.R., Granade, M.E., and Mauldin, J.L. *Biochem. 10*, 1622–1629 (1971).

SERUM LIPID AND LIPOPROTEIN CONCENTRATIONS FOLLOWING EXPOSURE TO OZONE

William J. Vaughan, Gerald L. Adamson, Frank T. Lindgren, and John C. Schooley

The effects of exposure to ozone (O_3) on concentrations of serum lipids and lipoproteins were investigated. Male and female guinea pigs were exposed to O_3 at 1 ppm for two weeks. Serum concentrations of cholesterol, triglycerides, low-density (LDL) and very-low-density (VLDL) lipoproteins were elevated after O_3 exposure, particularly in the males. During O_3 exposure the food intake per day decreased (for a constant body weight), suggesting that metabolic rate and possibly basal metabolic rate was lower. Lung wet weights increased during O_3 exposure by 87% for males and 45% for females. When individual lung-weight/body-weight ratios were correlated with cholesterol and LDL values from the same animal, a high correlation is found for males ($r = 0.81$, $P < 0.05$), suggesting that there may be a relationship between lipoprotein elevations and lung damage for males. Because elevated concentrations of lipids and lipoproteins in humans increase the risk of coronary heart disease (CHD), the lipoprotein results suggest that an epidemiological study of the incidence of CHD with metropolitan O_3 levels may be warranted.

APOLIPOPROTEIN (APO) E LEVELS AND DISTRIBUTION IN HUMAN CORD BLOOD

Trudy M. Forte, Paul A. Davis,* and Conrad B. Blum†

Apo E is a protein of 35,000 molecular weight that plays an important role in the catabolism of lipoproteins, particularly those of dietary origin (chylomicron remnants). Apo E is a ligand recognized by both the apo B-E and apo E receptors on cells. Apo E-containing particles are internalized through the receptor mechanism, thus delivering cholesterol to cells. In adult plasma a majority of apo E is associated with very low density lipoproteins (VLDL), and the remainder is associated with high density lipoproteins (HDL). There is one inherited lipoprotein abnormality in which this pattern is drastically altered. This abnormality is abetalipoproteinemia, in which plasma of afflicted subjects contains no chylomicrons, VLDL, or low density lipoproteins (LDL), but does contain HDL. Apo E, in this case, is circulated solely on apo E-rich HDL, which may functionally substitute for the absent apo B and thus transport cholesterol to cells via the receptor mechanism.

The lipid and lipoprotein patterns of newborn infants in some respects are similar to those in abetalipoproteinemia. In the newborn, plasma cholesterol is low, and VLDL and LDL moieties are extremely low. This observation suggested that apo E transport in the newborn may not be primarily in the less dense lipoproteins but rather in HDL. This question was examined in cord-blood samples.

Plasma concentrations of apo E and lipids (cholesterol, triglyceride, HDL-cholesterol, and LDL-cholesterol) in 95 cord blood samples and in 49 adult plasma samples are shown in Table 1. The apo E level in cord blood is 60% greater than adult plasma, while the newborn cholesterol level is only 40% that of the adult. LDL in the cord blood is extremely low and represents less than 25% that of adult values.

*Department of Medicine, University of California, Davis.

†Department of Medicine, Columbia University, College of Physicians and Surgeons, New York.

Table 1. Plasma concentrations (Mean ± S.D.) of apo E, cholesterol, triglyceride HDL cholesterol, and LDL cholesterol.

	Normal neonates (n = 95)	Adults (n = 49)
Apo E (μg/dl)	58.1 ± 26.5	35.8 ± 10.4
Cholesterol (mg/dl)	72.1 ± 21.3	185.1 ± 33.0
Triglyceride (mg/dl)	37.8 ± 16.9	97.6 ± 36.1
HDL-cholesterol (mg/dl)	39.7 ± 12.4	54.7 ± 11.2
LDL-cholesterol (mg/dl)	24.8 ± 13.6	110.4 ± 29.7

To determine the distribution of apo E relative to cholesterol, plasma samples (cord blood and adult) were applied to 6% agarose columns and fractions eluted with phosphate buffer. The elution profiles are shown in Fig. 1. Cord blood apo E (Fig. 1A) shows a very pronounced peak in fractions 60–80, which is the recovery region for HDL. Adults, on the other hand, have a distinct bimodal distribution, with larger amounts of apo E in the larger-sized, triglyceride-rich region (fractions 40–60) as well as in the HDL region. Quantitation of apo E in the major column fractions (Table 2) reveals that only 13% of total apo E in cord blood is associated with the less dense, larger-sized particles, which are also rich in triglyceride, while 87% is in the HDL fraction. In contrast, adult plasma contains a major fraction of its apo E in the triglyceride-rich fraction (Table 2).

The results of the column fractionation for cord blood apo E are similar to those seen in subjects with abetalipoproteinemia,[1] which is consistent with our observation that, in cord blood, VLDL levels are extremely low and LDL levels are also considerably reduced. These two classes of lipoproteins carry apo B, which is recognized by the apo B-E receptor and is responsible for the major transport of cholesterol into cells in the adult. However, since apo B levels are depressed in the fetus, it is probable that apo E plays a more significant role in cholesterol transport in the developing human. Since most of the apo E in the neonate is in the HDL fraction, it is this fraction that is an important supplier of cholesterol to cells and tissues in the rapidly growing fetus.

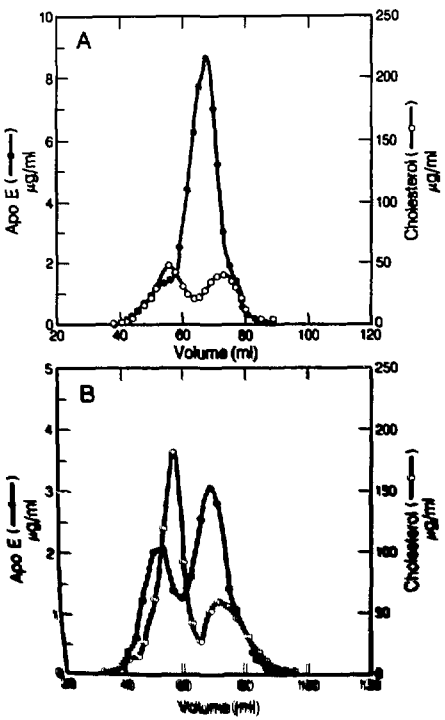

Table 2. Lipoprotein fractionation of apo E in cord blood and adult human plasma by agarose column chromatography.

	Triglyceride-rich lipoproteins		High density lipoproteins	
	%	μg/ml	%	μg/ml
Cord blood[a]	13	7.4	87	49.5
Adult blood[a]	42	15.0	58	20.3

[a] Data for cord blood plasma are the mean of two experiments, each using pooled plasma. Data for normal adult plasma are the means obtained from 30 individuals.

REFERENCES

1. Blum, C.B., Deckelbaum, R.J., Witte, L.D., Tall, A.R., and Cornicelli, J. *J. Clin. Invest. 70*, 1157–1169 (1982).

Fig. 1. *Agarose column chromatography of neonatal (A) and adult (B) human plasma. Cholesterol and apo E concentrations were measured in each fraction. The first peak of the cholesterol curve represents LDL, while the second peak is HDL. In the adult (B) elution profile, there is a small shoulder preceding the LDL peak; the former is the VLDL region. In cord blood, most of the apo E coincides with the HDL-cholesterol peak, while in the adult, apo E peaks in the region preceding the LDL peak and in the HDL region as well.* (JDL #411-8067)

FORMATION OF PHOSPHOLIPID RICH HDL WITH UNUSUAL PHYSICAL PROPERTIES: POSSIBLE MODEL FOR INTERSTITIAL FLUID HDL

Trudy M. Forte, Robert W. Nordhausen, C. Luming Ren, and Alex V. Nichols

We have previously shown that sheep lung lymph[1] and human lymphedema interstitial fluid[2] contain a unique high density lipoprotein (HDL) particle that forms square-packing arrays during negative-staining electron microscopy. In contrast, plasma HDL contains spherical, hexagonal-packing particles. The unusual square-packing particles isolated from interstitial and/or lymph fluid are characterized by a relative increase in both phospholipid and free cholesterol moieties. Overall, the particles are larger and more buoyant than their plasma counterpart. To test the hypothesis that incorporation of excess phospholipid into HDL may be responsible for the altered physical properties of the particles, an *in-vitro* model system was developed. This consisted of bovine HDL_2 incubated with dimyristoylphosphatidylcholine (DMPC). HDLs were incubated with increasing amounts of DMPC and the products were examined by gradient gel electrophoresis and electron microscopy.

Figure 1 shows the changes in particle size as determined by gradient gel electrophoresis following incubation of HDL_2 with HDL phospholipid to DMPC mole ratios of 1:0.5, 1:1, and 1:2. The major peak at 12.5 nm in control HDL (A) progressively becomes larger as indicated by a shift to smaller R_f values. A second component of smaller size (9.4 nm) is present at the 1:0.5 ratio and increases with increasing DMPC. This second component is constant in particle size as indicated in Table 1, which shows particle diameters for the various peaks. The electron microscopic structures of HDL-DMPC incubation products are seen in Fig. 2A-D. With increasing DMPC, there is an increase in particle diameter and an alteration in the shape of particles. The change in HDL packing is most pronounced at a ratio of 1:2 where particles form extensive square-packing arrays (Fig. 2D). For comparison, HDLs with similar structural properties but isolated from native biological sources are also shown. Large HDLs from a patient with abetalipoproteinemia have a tendency to form square-packing arrays. This structural anomaly is even more pronounced in the sample of sheep lung lymph (Fig. 2F) and in human interstitial fluid (not shown).

Chemical analysis of the phospholipid-enriched HDL generated after incubation of bovine HDL_2 with DMPC at a ratio of 1:2 revealed that the percent of phospholipid in the particle doubled. On the other hand, the percent protein in the particle decreased to almost 50% of the control value. Analysis of the protein moiety revealed that the major protein of bovine HDL was apo AI. Based on the composition of the particles and their estimated molecular weights, we calculated that the

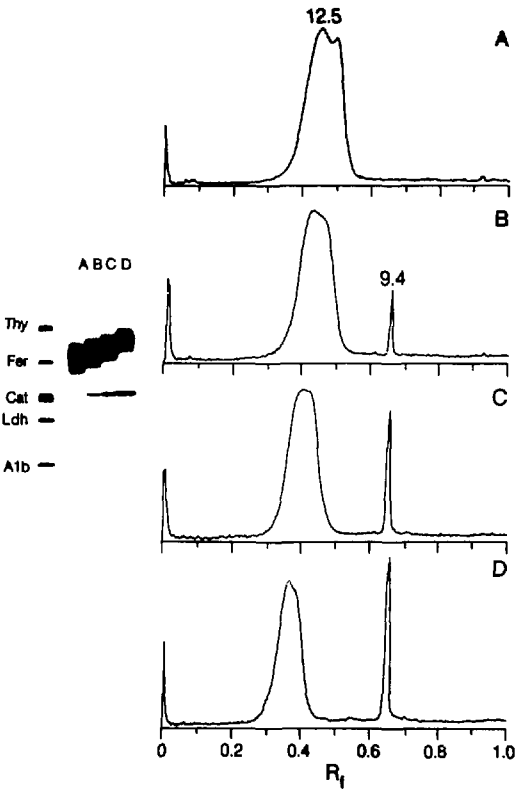

Fig. 1. Gradient gel (Coomassie-stained gel in inset) and corresponding scans of fraction I-HDL incubated with increasing amounts of DMPC. (A) HDL-control; (B) HDL-phospholipid /DMPC, 1:0.5; (C) HDL-phospholipid/DMPC, 1:1; (D) HDL-phospholipid/DMPC, 1:2. In the presence of increasing DMPC, the HDL peak (12.5 nm for control) shifts to larger diameters; concomitantly, a product of smaller diameter is also generated. The numbers over the peaks indicate particle diameter in nm.
(XBB 849-7226)

Table 1. Effect of DMPC incubation on bovine fraction I-HDL particle size distribution as determined by gradient GEL electrophoresis. Fraction I-HDL was incubated at 37°C, 12–16 hr, with increasing amounts of DMPC. Values represent mean ± S.D. for four determinations.

Mole Ratio HDL-phospholipid:DMPC	Large Particle nm ± S.D.	Small Particle nm ± S.D.
0	12.3 ± 0.1	—
1:1.05	12.9 ± 0.08	9.5 ± 0.1
1:1	13.7 ± 0.1	9.4 ± 0.08
1:2	14.6 ± 0.08[a]	9.4 ± 0.08

[a] These particles form square-packing arrays upon negative-staining electron microscopy.

control HDL possesses three molecules of apo AI. The major larger-sized product formed after incubation at the HDL-phospholipid to DMPC ratio of 1:2, however, contained only two molecules of apo AI. This suggests that during incubation DMPC is incorporated into the HDL particle until a critical phospholipid to protein ratio is reached; when this ratio is exceeded, apo AI is displaced from the surface. The resulting phospholipid lipid-rich but protein-poor particle is stable. Two factors may be responsible for the appearance of square-packing arrays during negative staining:

1) the particles may be spherical, but the distribution and conformation of surface molecules, especially apoprotein, are altered so that they are favorably disposed to foster particle-to-particle interaction. Because of the nature of the particle-to-particle interactions, particles are organized into square lattices.
2) Free-standing particles may be square (or cuboidal) and, at appropriate concentrations during negative staining, form square arrays. Square shapes of free-standing human interstitial-fluid HDL have recently been seen in our laboratory (work in progress); hence, this possibility cannot be excluded.

The ability of HDL to incorporate a large amount of polar lipids, (phospholipid and free cholesterol) into its surface is probably of functional importance. HDL entering the interstitial space may remove excess phospholipid and cholesterol from peripheral tissues and hence play an important role in reverse cholesterol transport.

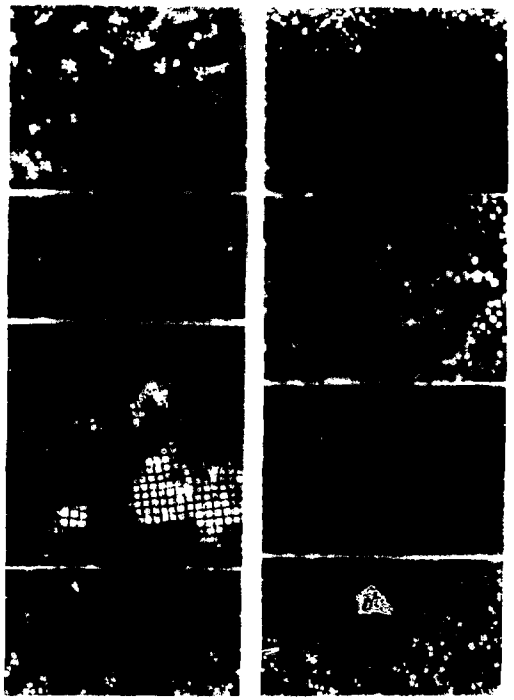

Fig. 2. Electron micrographs of negatively stained fractions. (A) HDL incubated without DMPC. (B) Product of HDL incubated with DMPC (ratio 1:0.5); note occasional rectangular or square particles (arrow). (C) Product of HDL incubated with DMPC (ratio 1:1); a few square-packing particles are apparent (arrow). (D) Large molecular-weight product of HDL incubated with DMPC (ratio 1:2); note characteristic square-packing particles. (E) HDL particles of d ≤ 1.063 g/ml isolated from the plasma of a patient with abetalipoproteinemia; particle size 12.8 ± 0.7 nm on a side. Note similarity of square-packing geometry to that produced in (D). (F) Square-packing particles, d = 1.057–1.063 g/ml fraction, isolated from sheep lung lymph; particle size is 14.9 ± 2.1 nm on a side. Bars represent 100 nm. (XBB 853-1951)

REFERENCES

1. Forte, T.M., Cross, C.E., Gunther, R.A., and Kramer, G.C. *J. Lipid Res.* **24**, 1358–1367 (1984).
2. Forte, T.M., Reichl, D.R., Hong, J.L., and Ruda, D.N. *Arteriosclerosis* **4**, 564a (1984).

Structural Biology

DIFFERENTIAL POLARIZATION IMAGING MICROSCOPY

Marcos F. Maestre, William Mickols,* Ignacio Tinoco, Jr.,* and Stephen H. Embury†

In this report we describe the development of a differential polarization imaging microscope. The technique is shown to be a logical extension of the research on the interaction of circularly polarized light with structures whose dimensions are large with respect to the wavelength of light.[1] The polarized light technique used initially to study these biological structures was circular dichroism. Circular dichroism is the difference in the extinction coefficient when a sample is illuminated by two different forms of circularly polarized light:

$$\Delta\epsilon = \epsilon_L - \epsilon_R$$

where ϵ_L and ϵ_R are the specific extinction due to left and right circularly polarized light respectively. Recently this technique has been extended to the measurement of single microscopic particles by the development of a circular dichroism (CD) microscope.[2]

The CD microscope has been used to study the circular dichroism and circular intensity differential scattering (CIDS) spectra of Chinese Hamster tissue culture cells as a function of the life cycle of the cells.[3] There are distinct spectra associated with the different states in the life cycle of the cell, and correlations exist with the amount of DNA in the cell as monitored by absorbance at 260 nm in the CD microscope.

In the CD microscope, the objective lens in the instrument only serves to collect the transmitted light through the microscopic object plus some fraction of the scattered light, depending on the aperture of the lens. The collected light is not used to form an image but instead is measured by a standard photomultiplier detector to give spectral curves. In the next section we describe the instrument that produces differential images obtained from incident illumination of specific polarization.

THE DIFFERENTIAL IMAGING MICROSCOPE

If an imaging system (a lens or a microscope) is placed between the chiral sample and the detector, an image can be formed (Fig. 1). For a chiral sample the image produced by illumination with one polarization form of light can be different from the image produced when the illumination is of another polarization form. The difference between these two images when using circularly polarized light is called the circular differential image. With the proper detection system and associated electronics, we can use the imaging properties of the microscope to form a differential image with a spatial distribution of information. The information in the image is now a point by point measurement of the

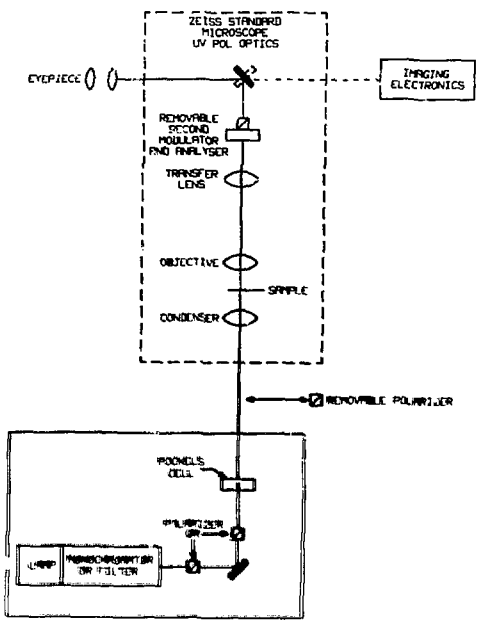

Fig. 1. A diagram of the differential imaging microscope as presently configured. (XBL 851-968)

*Department of Chemistry, UCB, and Laboratory of Chemical Biodynamics, LBL.

†University of California San Francisco

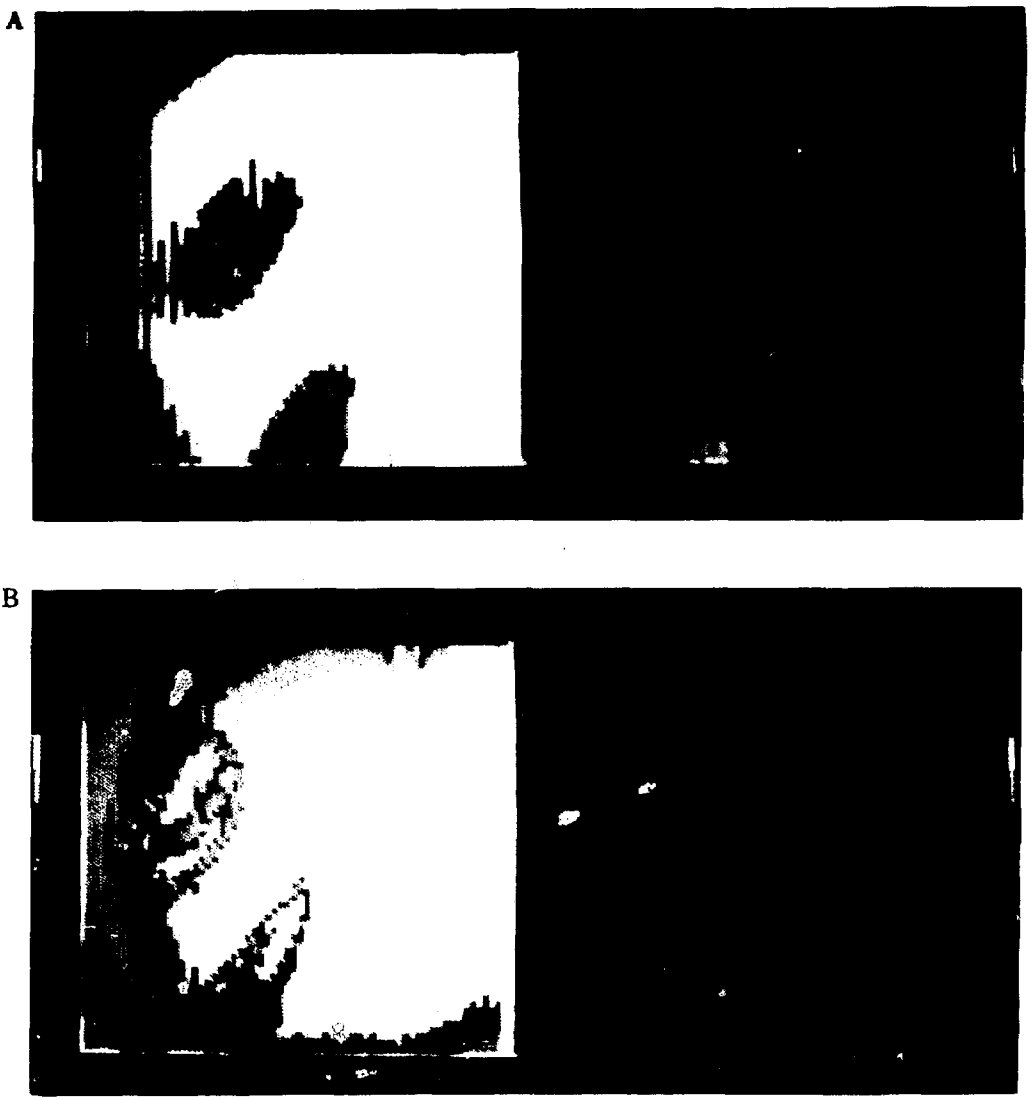

Fig. 2. *These photographs are black and white copies of color coded images of fixed deoxygenated red blood cells from a patient with sickle cell anemia. The left hand image is the intensity image. Maximum-intensity is white (top of the left hand code bar), minimum intensity is black (bottom of left code bar). The right hand image is the linear dichroism image. The maximum positive value is the top of the right hand code bar, largest negative is the bottom of the right hand code bar. The top cell is an irreversibly sickled cell, and the bottom cell is a reversibly sickled cell. Figure 2A was taken on the hemoglobin absorbance band at 415 nm and shows a large amount of aligned hemoglobin polymer in the reversibly sickled cell. Little if any aligned hemoglobin is seen in the irreversibly sickled cell. Figure 2B shows the same two cells measured at a wavelength of 450 nm, which is outside the absorption band of the hemoglobin. This figure shows images dominated by the edges of the cells. In the linear dichroism image, reflection polarization is seen at the edges of the cells.* *((A) XBC 848-6533, (B) XBC 848-6535)*

circular dichroism, in the case of transmitted light measurement, or circular differential scattering contribution to the image cross-section in the case of dark-field illumination.[4] The spatial resolution of the measurement is limited by the lens resolving power, pixel geometry in the detector, and available light intensity.

The information contained in the circular differential image will not be the same information as that of the image produced using unpolarized light. In the latter case the optical contrast that distinguishes one feature of the sample from another is provided by differences in the absorption and in the index of refraction of the various parts of the sample. In a circular differential image the contrast is provided by differences in the interaction of different parts of the sample with left and right circularly polarized light.

Preliminary studies (with a differential imaging microscope using linearly polarized light) on the polymer formation of hemoglobin S in the sickling of intact red blood cells have shown that the technique works, as can be seen in Fig. 2.[5] Two images are presented in each of the figures, the left image represents the total intensity, and the right represents the differential image. This direct comparison of the images allows the identification of regions within cells containing aligned chromophores. Information on the spatial distribution and concentration of the polymer has been obtained, on both sickled and irreversibly sickled cells. The technique shows promise as a new way of measuring the spatial distribution of chirality and orientation inside microscopic biological materials. This information can then be used to construct possible models of the biological organization.

REFERENCES

1. Tinoco, I., Jr., Bustamante, C., and Maestre, M.F. *Ann. Rev. Biophys. Bioeng 9,* 107–41 (1980).
2. Maestre, M.F., and Katz, J. *Biopolymers 21,* 1899 (1982).
3. Maestre, M.F., Salzman, G.C., Tobey, R.A., and Bustamante, C. *Biochemistry 24,* 5152–5157 (1985).
4. Keller, D., Bustamante, C., Maestre, M.F. and Tinoco, I., Jr., *Proc. Nat. Acad. USA 82,* 401–405 (1985).
5. Mickols, W., Maestre, M.F., Tinoco, I., Jr., and Embury, S. *Proc. Nat. Acad. Sci. USA 82,* 6527–6531 (1985).

ABSORPTION FLATTENING IN THE CIRCULAR DICHROISM SPECTRA OF SMALL MEMBRANE FRAGMENTS

Robert M. Glaeser and Bing K. Jap

The inhomogeneous distribution of chromophore occurring in a particulate suspension can result in a reduction in the apparent molar ellipticity recorded in circular dichroism (CD) spectra. The possibility of such a systematic error has often been a matter of concern when CD spectra of cell membrane proteins are recorded. The recent publication of CD spectra for bacteriorhodopsin in native membranes, in sonicated membranes, and in detergent-solublized form[1] gives a unique opportunity to apply the theoretical analysis of Gordon and Holzwarth[2] so as to provide a definitive answer to the question of whether absorption flattening is significant for membrane particles. We show here that the data of Mao and Wallace can be combined with the theoretical analysis of Gordon and Holzwarth to rule out significant absorption flattening effects over the range 200–240 nm for submicrometer-sized membranes. In addition, the results show that absorption flattening can be disregarded even at 190 nm for membranous material in the size range below 100 nm. The demonstration that there are no major flattening effects in the CD spectra of bacteriorhodopsin, particularly in the region of 200–240 nm, means that the experimental spectra are incompatible with the proposal that this transmembrane protein contains seven transmembrane helices.

The CD spectra between 200 and 240 nm presented by Mao and Wallace for native purple membrane, sonicated purple membrane, and bR solubilized in octyl glucoside are nearly identical, as can be seen from the published curves as they are redrawn in Fig. 1. The ellipticity of the native

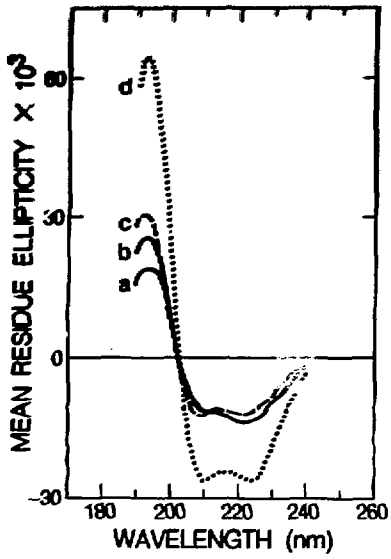

Fig. 1. CD spectra of bacteriorhodopsin redrawn in simplified form from Mao and Wallace.[1] Curves (a) and (b) represent the spectra obtained with native purple membrane, sonicated purple membrane and bR solubilized in octylglucoside; these three spectra are very similar between 200 nm and 240 nm and are shown here as a single curve, but the curve for native membrane, (a), is significantly lower at 190 nm than the average value of the curves for sonicated purple membrane or octylglucoside solubilized bR, shown as (b). Curve (c) is the spectrum of bR incorporated into SUVs, and it shows small differences from (b) over the whole range of wavelengths. Curve (d) is the theoretical spectrum calculated by Mao and Wallace for a protein containing 80% α-helix, 10% β-turn, and 10% random coil. (XBL 8411-8061)

membrane patches at 190 nm is about 0.75 times that of the other types of specimen preparation, indicating that absorption flattening is significant for intact purple membrane sheets at the shorter wavelengths. The ratio of "true" solution absorbance to the average number of particles per optical path [cf. Gordon and Holzwarth, Ref. 2] has its most extreme value at 190 nm, and thus the absorption-flattening effect cannot be any greater at longer wavelengths than it is at 190 nm.

The experimental data presented by Mao and Wallace are therefore inconsistent with their suggestion that there is a significant absorption-flattening effect in the CD spectra over the range 200–240 nm. The data of Mao and Wallace do show, however, that there can be a significant absorption-flattening effect at 190 nm for native membranes. The latter effect can be avoided by the use of sonicated membrane pieces or by the use of detergent-solubilized proteins. While Mao and Wallace suggest that octyl glucoside might cause a change in bR conformation, this suggestion is not consistent with the fact that the CD spectrum of octyl-glucoside-solubilized bR is nearly identical with that of sonicated membrane sheets.

The theoretical analysis of Gordon and Holzwarth can be used to show quantitatively that the spectra obtained by Mao and Wallace with native and sonicated purple membranes are not consistent with there being a significant amount of absorption flattening at 221 nm. Mao and Wallace calculate that the mean residue ellipticity of bR at 221 nm would be about −28000 if the helix content were as high as 80%. The measured ellipticity of sonicated purple membrane patches is only −14000, however, which would require that the CD be flattened by a factor of Q_B (notation of Gordon and Holzwarth) equal to 0.5. This degree of flattening corresponds for the model of spherical shells to a value of $A_{sol}/qm = 0.5$, where, in the notation of Gordon and Holzwarth, A_{sol} is the absorbance of an ideal solution of protein and qm is the average number of absorbing particles per centimeter. The value of qm must increase as $N^{1/3}$ where N is the total number of particles per cubic centimeter. N, in turn, must be inversely proportional to the area of the membrane patches because the total amount of membrane area is conserved upon sonication. Taking the size of native membranes to be, conservatively, no smaller than 2500 Å and the size of the sonicated membranes to be 250 Å (as reported by Mao and Wallace), the value of A_{sol}/qm of the native membrane suspension ought to be equal to 2.3. According to Fig. 3 of Gordon and Holzwarth, Q_B would then be less than 0.1 for the native membranes, i.e., 5 times smaller than for the sonicated membranes. Experimentally, the molar ellipticity of native purple membranes is hardly distinguishable from that of sonicated membranes at 221 nm, implying that there must be very little absorption flattening in either case at that wavelength.

That membrane patches in the submicrometer size range should have very little absorption flattening is further supported by the fact that Gordon and Holzwarth give an empirical estimate of $Q_B = 0.7$ for red blood cell ghosts at 221 nm. This value corresponds to $A_{sol}/qm = 0.21$. Assuming that the ghosts have a size equal to 5 μm, one finds that A_{sol}/qm should be no larger than 0.045 for vesicles that are smaller than 0.5 μm. The corresponding value of Q_B for submicrometer pieces of membrane is only about 0.9.

We believe that the arguments presented above show that absorption flattening has no significant effect at 221 nm in any of the spectra presented by Mao and Wallace. The data of Mao and Wallace confirm earlier estimates[3,4] that the helix content of bR represents only about 50% of the peptide chain. If the helix content is as little as 50%, then there can only be a maximum of five transmembrane α-helices as opposed to the seven helices predicted from electron microscopy. We will not repeat here the evidence that has been presented[4,5] in support of a structural model that would contain five helices and four strands of β-sheet. We believe that it is only important to stress two points: 1) the experimental CD spectra of bR differ greatly in amplitude from the theoretical spectrum of a protein containing seven helices, each of which is 30 Å or greater in length; and 2) light scattering and absorption flattening do not produce experimentally significant distortions of the CD spectra of native membranes, particularly in the region 200–240 nm, and therefore they are unable to explain the discrepancy between experimental results and the seven-helix model.

REFERENCES

1. Mao, D., and Wallace, B.A. *Biochemistry 23,* 2667–2673 (1984).
2. Gordon, D.J., and Holzwarth, G. *Arch. Biochem. Biophys. 142,* 481–488 (1971).
3. Becher, B., and Cassim, J.Y. *Biophys. J. 16,* 1183–1200 (1976).
4. Jap, B.K., Maestre, M.F., Hayward, S.B., and Glaeser, R.M. *Biophys. J. 43,* 81–89 (1983).
5. Glaeser, R.M., and Jap, B.K. *Biophys. J. 45,* 95–97 (1983).

CONTRAST IMPROVEMENT WITH SMALL SPOT ILLUMINATION FOR HIGH RESOLUTION ELECTRON MICROSCOPY OF BEAM SENSITIVE SPECIMENS

Kenneth H. Downing and Robert M. Glaeser

The contrast observed in images of beam-sensitive crystalline specimens is found to be significantly less than one would predict based on observations of electron diffraction patterns of the specimens.[1] Factors such as finite coherence, inelastic scattering, and the limited MTF of the photographic emulsion account for some of the decrease in contrast. It appears, however, that most of the loss in signal is caused by motion of the specimen during exposure to the electron beam. The introduction of point and other defects in the crystal, resulting from radiation damage, causes bending and lateral motion that degrade the contrast in the image. We have therefore sought to determine whether the beam-induced specimen motion can be reduced by reducing the area of the specimen that is illuminated at any one time. Not only should the total stress be decreased in proportion to the area that is illuminated, but the constraint against motion should be increased by the smaller perimeter of the illuminated area.

Our electron microscope installation at LBL provides a unique opportunity for testing this hypothesis. Using a field-emission-gun (FEG) illumination system, we can record images with a beam diameter of 400–2000 Å while retaining the high spatial coherence required for good phase contrast. Under computer control, a series of specimen areas can be irradiated in order to expose a large fraction of the photographic film. We have tested this scheme experimentally by recording images of the 3.7–4.2 Å lattice of monolayer crystals of paraffin ($C_{44}H_{90}$). These images show contrast that is consistently higher, by factors of 2–5, than obtained with a beam of normal diameter of 1–3 μm.

Figure 1 is an electron micrograph of a paraffin crystal. This micrograph was obtained by stepping a beam of diameter less than 1000 Å through a 5 × 5 array, exposing a number of discrete areas within the crystal. The paraffin lattice is resolved in each of the exposed areas. Within the small illuminated areas, we often find a significant variation in the contrast of the lattice image, as illustrated in Fig. 2. In order to investigate this effect further, an optical bench was used to obtain optical dark-field images of large areas of electron micrographs. Figure 3 shows three independent dark-field images obtained from the micrograph in Fig. 1. Variations in intensity within each of the illuminated

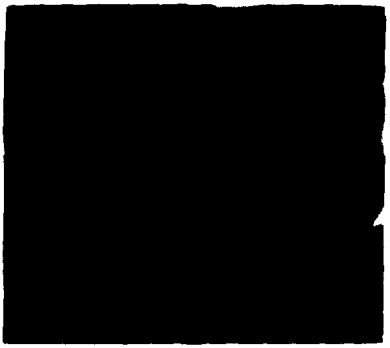

Fig. 1. Micrograph of paraffin crystal. Beam was stepped through 5 × 5 array of positions under computer control, down vertical columns starting at left. Bar = 1000 Å. Beam shape is due to residual astigmatism of illumination system.
(XBB 853-2151A)

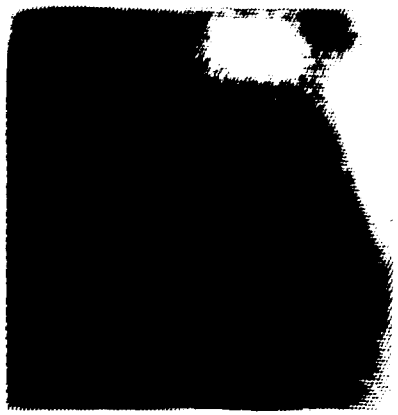

Fig. 2. Computer-filtered image of small section of one of the images as in Fig. 1. A 7 × 7-element box was masked around each diffraction spot in the 512 × 512-element Fourier transform of the micrograph, and this image obtained by inverse Fourier transform.
(XBB 850-8716)

areas, corresponding to variations in contrast in the micrograph, are caused by changes in the angle of illumination within the small areas. This problem can be minimized by the use of small illumination apertures.

The improvement in image contrast provided by this technique should be immediately applicable in the solution of atomic structures by electron crystallography. Already, the structure of purple membrane from *Halobacterium halobium* has been determined in projection to a resolution of 3.5 Å,[2] by applying advanced computational processing to conventional electron micrographs obtained at LBL, EMBL (Heidelberg), and the Fritz-Haber Institute (Berlin). The use of images recorded with the small-spot illumination system should greatly speed up the extension of this work to the determination of the three-dimensional structure.

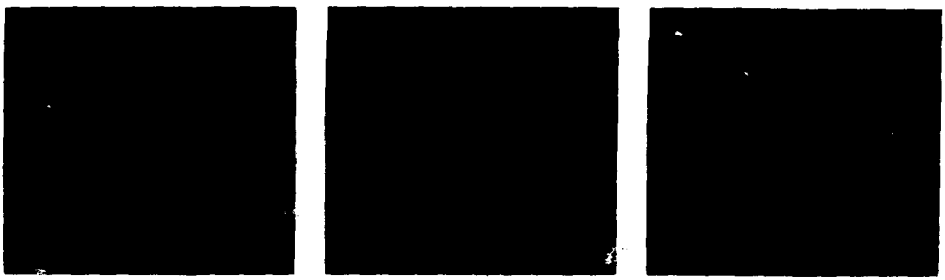

Fig. 3. Dark field images of micrograph in Fig. 1 obtained on optical bench. (a), (b), and (c) correspond to three diffraction spot pairs.
(XBB 853-2151B)

REFERENCES

1. Henderson, R., and Glaeser, R.M. Quantitative analysis of image contrast in electron micrographs of beam-sensitive crystals. *Ultramicroscopy, 16*, 139 (1985).

2. Henderson, R., Baldwin, J.R., Downing, K.H., Lepault, J., Zemlin, F. Structure of purple membrane from *Halobacterium halobium*: Recording, evaluation, and measurement of electron micrographs at 3.5 Å resolution. *Ultramicroscopy* (in press 1986).

SECONDARY STRUCTURE OF HALORHODOSPIN

Bing K. Jap and Seok-Hwan Kong

Halorhodopsin (hR) is one of three retinal-containing proteins found in *Halobacterium halobium*. The biological function of hR is to serve as a light-driven electrogenic chloride pump, transporting chloride ions inward across the membrane. Halorhodopsin has many similarities and dissimilarities when compared to bacteriorhodopsin (bR), a light-driven proton pump. Both proteins contain a retinal moiety that is apparently in a similar environment, as suggested by Raman spectroscopy, indicating that structures surrounding the retinal in both of these proteins are very similar. On SDS gel electrophoresis, hR shows a slightly greater mobility than that of bR, suggesting that hR has a similar molecular mass (i.e., 26000 daltons). The amino acid compositions of hR and bR are quite similar when residues are grouped as being hydrophobic, neutral, and polar. Proteolytic fragments of hR and bR are also similar when the proteins are partially digested with *Staphylococcus aureus* V8 protease. However, hR also shows distinct spectroscopic and photochemical properties. For example, in contrast to the case of bR, the photocycle intermediates and kinetics, as well as the position of hR absorption maximum, are affected by the presence of chloride ions. There is evidence that hR has a distinct chloride binding site, involving a sulfhydryl group. Furthermore, hR and bR lack immunological cross-reactivity, suggesting a significant difference in the primary sequences of bR and hR.

We have obtained ultraviolet circular dichroism (CD) spectra of bR and hR solubilized in a detergent solution containing 15 mM octylglucoside and 20 mM sodium phosphate (pH 7) as shown in Fig. 1. The spectra are very similar in magnitude and in their detailed shapes, suggesting that hR and bR have very similar secondary structure contents. The CD spectra of hR in buffer containing 3 M NaCl and 20 mM sodium phosphate (pH 7) were also measured to see if any conformational change was induced by an increase in ionic strength. The spectra of hR with and without 3 M NaCl are virtually identical, indicating that low ionic strength and the absence of chloride ions have no significant effect on the secondary structure of hR. Least-square curve fitting of the CD spectrum of hR in octylglucoside, using the basis functions of Chen et al.[1] yields an α helical content of 51% and β structure

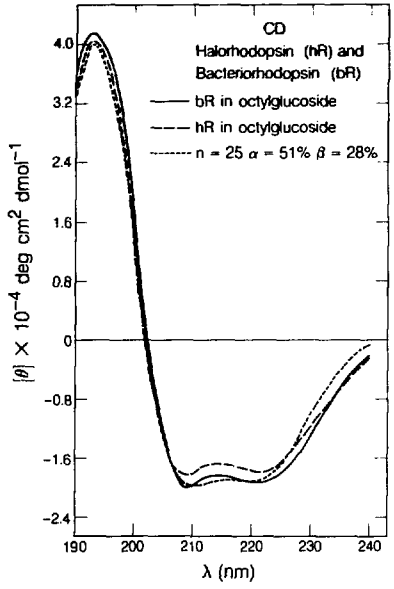

Fig. 1. The CD spectra of hR and bR solubilized in a detergent solution containing 15 mM octylglucoside and 20 mM sodium phosphate (pH 7). The theoretical curve was obtained from a least-square best fit between the hR spectrum and basis functions for helical chain lengths of 25 residues (Ref. 1). The spectra of hR and bR show a substantial similarity, indicating that their secondary structural contents are similar.

(XBL 856-8341A)

content of 28%, assuming that the helices in hR have an average length of 25 residues. The theoretical curve obtained from the least-square fitting is in acceptable agreement with experimental data (Fig. 1). Assuming that the molecular masses of hR and bR are indeed similar, the number of helical strands in hR that can transverse across a membrane of 45Å thickness is no more than five, similar to that of bR.[2]

It is intriguing to know whether there is a similarity in the pumping mechanism between hR and bR, since hR pumps chloride ions and bR pumps protons. It is not yet known whether the chemical species being transported by bR is protons (H^+), hydroxyls (OH^-), or H_3O^+, etc. If bR indeed transports hydroxyl or H_3O^+ through a channel, it is then quite possible that the molecular mechanisms of operation are quite similar for bR and for hR. The current evidence that the ultraviolet CD spectra of these two proteins are very similar is consistent with—but does not prove—that the folding of these two proteins is similar. If the similarity in the three-dimensional molecular structures of these proteins does indeed exist, these proteins may share a common mechanism of ion transport. It is, therefore, important to determine the three-dimensional molecular structures of hR directly by diffraction techniques. Crystallization of hR into two-dimensional ordered arrays for subsequent electron crystallographic structure determination is currently in progress.

REFERENCES

1. Chen. Y.H., Yang, T.J., and Chan, K.H. Determination of the helix and β form of proteins in aqueous solution by circular dichroism. *Biochemistry 13,* 3350–3359 (1974).
2. Jap, B.K., Maestre, M.F., Hayward, S.B. and Glaeser, R.M. Peptide-chain secondary structure of bacteriorhodopsin. *Biophys. J. 43,* 81–89 (1983).

STRUCTURAL ANALYSIS OF PhoE PORIN, AN OUTER MEMBRANE PROTEIN FROM *ESCHERICHIA COLI*

Bing K. Jap

The outer membrane of gram-negative bacteria such as *Escherichia coli* and *Salmonella typhimurium* generally plays at least two different roles in biological processes. It acts as a molecular sieve for hydrophilic solutes, and it serves as a part or all of the receptor for bacteriophages. The outer membrane contains a high density of porins, which are pore-forming proteins, that are specific for passive diffusion of small molecules. Furthermore, the closing and opening of these pores appear to be subject to biochemical regulation.

The outer membrane contains a variety of porins of similar molecular weight and similar amino acid composition, which nevertheless have substantially different chemical specificities for restricting free diffusion of aqueous solutes, and which show different patterns of gene expression under different physiological conditions. The predominant porin in wide-type *E. coli* is called OmpF. A similar member is called OmpC; it has a somewhat larger molecular weight but smaller pore diameter (as measured from diffusion studies). Under growth condition of high osmotic strength, expression of OmpF is turned off and that of OmpC is turned on. Another protein of the pore-forming family, PhoE porin, is preferentially expressed when cells are starved for phosphate. PhoE porins show some selectivity of the type of molecules that can diffuse through the pores.

The primary and secondary structures of a number of pore-forming proteins have some surprising features. The primary sequences show a uniform distribution of polar and hydrophobic residues along the entire peptide chain. Hydropathic profiles of the proteins show no stretches of hydrophobic segments long enough to transverse the lipid bilayer as helical rods similar to those found in many other integral membrane proteins. Even more surprising are the secondary structure data of OmpF porin, which exhibit a high content of β structure with no evidence for α helical domains. Furthermore, recent results from total attenuated reflection infrared spectroscopy and from large-angle diffuse x-ray diffraction studies indicate that anti-parallel β-pleated strands span the membrane with a mean length of 10–12 residues oriente approximately normal to the membrane plane. In view of this information it has become intriguing to

know how these proteins are folded in the hydrophobic interior of the membrane, and how they are secreted across the inner membrane and then inserted into the outer membrane.

Our proteolytic digestion study of PhoE proteins indicates that there are only a small number of proteolytic sites accessible for papain digestion. Digestion of PhoE with papain for 2 hours gives two new bands as observed by SDS-PAGE (Fig. 1). The apparent molecular weight of each of these bands is about 18,000 daltons. These results are consistent with the conclusion drawn from the studies of hybrid gene products, which indicate that the region located between residue 142 and 267 is surface exposed.[1] Prolonged digestion with papain (2 days) produces two additional bands in the gel, suggesting that there are additional exposed sites that nevertheless are not easily accessible to papain. Interestingly, the cleaved PhoE protein normally remains as a single unit that migrates at a rate identical to that of the intact trimer in SDS-PAGE. The cleaved peptides, like the intact monomers, are observed only when the specimen is boiled in the sample buffer before electrophoresis. This shows the unusual stability of the porin trimer, indicating that the cooperative involvement of many residues may play an important role in the formation of trimers. Similar observations have also been reported for bacteriophage λ receptor (maltoporin) by the Rochenbusch group.[2]

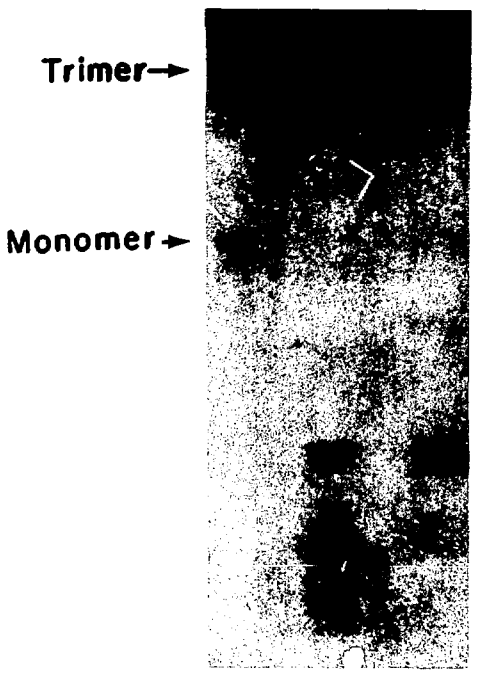

Fig. 1. Coomassie brilliant blue stained 15% polyacrylamide/SDS gel of PhoE before and after digestion with papain. Lane 1 shows a mixture of monomer and trimer of PhoE protein. Samples of PhoE were digested with papain for 2 hours and were then applied to the gel with and without boiling in the SDS sample buffer (lanes 5 and 4, respectively). Before electrophoresis, the papain was inactivated. Two bands with approximate mass of 18,000 daltons were observed when the sample was boiled in sample buffer. When papain treatment was extended to 2 days, additional bands with apparent masses of 15,000 and 10,000 daltons appeared (lanes 3 and 2 with and without boiling, respectively). *(XBB 846-4591)*

Our initial attempt to reconstitute PhoE protein from detergent solution into two-dimensional crystalline sheets was not very successful. Only a small percentage of the protein formed sheet-like patches, and the patch sizes obtained were rather small. The negatively stained images of these patches did show crystalline order as judged from their optical diffraction. However, images of the crystalline patches occasionally showed a different space group and a different lattice constant. This kind of polymorphism has also been observed for crystalline OmpF.[3] Improvement over the initial attempts was made by using a slow dialysis procedure in the removal of detergent and by making sure that the proteins were completely free of lipopolysaccharide. To obtain the required level of purity in the protein, we have used an additional column-chromatography step in our purification procedure.

The reconstituted PhoE crystalline patches now have an average diameter larger than 1 μm. A typical image of a negatively stained PhoE patch is shown in Fig. 2 together with its optical diffractogram. The optical diffraction pattern shows a rectangular lattice, with lattice constants, a = 72 Å and b = 125 Å. The images of PhoE show that the crystals are superior to those of OmpC. The coherent crystalline order of PhoE appears to extend to the entire patch, while that of OmpC is limited to small domains. Furthermore, our PhoE crystals show a single rectangular crystal form while those of OmpC show polymorphism.[4] Work is currently in progress to determine the three-dimensional structure of PhoE porin by electron crystallographic techniques.

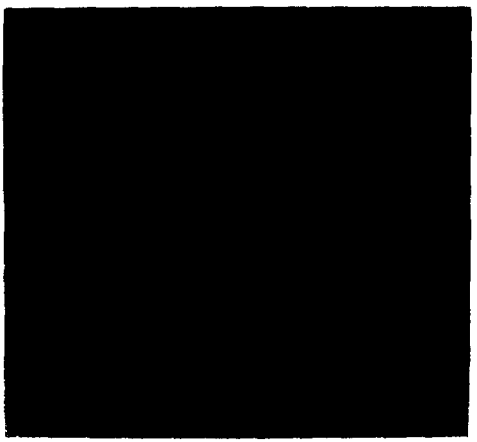

Fig. 2. A typical image of a reconstituted PhoE porin negatively stained with uranyl acetate and its optical diffraction pattern.
(XBB 859-7383)

REFERENCES

1. Tommassen, J., van der Ley, P., van Zeijl, M., and Agterberg, M. Localization of functional domains in *E. coli* K-12 outer membrane porins, *EMBO J. 4*, 1583–1587 (1985).
2. Schenkman, S., Tsugita, A., Schwartz, M. and Rosenbusch, J.P. Topology of phage λ receptor protein, *J. Biol. Chem. 259*, 7570–7576 (1984).
3. Dorset, D.L., Engel, A., Haner, M., Massalski, A., and Rosenbusch, J.P. Two-dimensional crystal packing of matrix porin. A channel forming protein in *Escherichia coli* outer membranes. *J. Mol. Biol. 165*, 701–710 (1983).
4. Chang, C.-F., Mizushima, S., and Glaeser, R.M. Projected structure of the pore-forming *OmpC protein from Escherichia coli* outer membrane. *Biophys. J. 47*, 629–639 (1985).

LOW TEMPERATURE SCANNING ELECTRON MICROSCOPY OF FROZEN HYDRATED LUNG

Jacob Bastacky, Gregory R. Hook, Gregory L. Finch, and Thomas L. Hayes

Water makes up most of the tissue portion of the lung, the remainder of the lung being filled with air. Each cell is 50–80% water, and these cells are organized into a system of airways, that are covered with an aqueous layer. Water makes up approximately 98% of the mucus in the larger airways, and the surface lining layer of the air sacs in the small airways is hypothesized to be mostly water.

Since electron beams require a vacuum for propagation, electron microscopy has required the removal of this water from the lung prior to examination. Biological samples, in general, have had to be dried for examination in the scanning electron microscope (SEM), by either air drying, freeze drying, or most commonly, critical point drying. These procedures are effective in preventing water vapor from contaminating the vacuum of the microscope and in reducing surface-tension effects, but they still cause samples to shrink. In a recent study[1] we found that lung tissue shrank almost 20% linear dimension with critical point drying or to about 50% of its original volume.

It is possible, using technology developed at LBL, to completely avoid drying the sample and to preserve the vacuum in the microscope by freezing the lung, transferring it to the microscope, and keeping it frozen at approximately −180 °C during examination. This reduces the vapor pressure of water to negligible levels that do not interfere with the electron beam.

There are a number of advantages to low temperature scanning electron microscope (LTSEM) analysis: 1) Fixation by freezing can be faster than the several seconds it takes for intracellular motion to stop with a chemical fixative such as glutaraldehyde. Freezing can stop action in a small fraction of a second in very thin pieces of tissue. 2) Freezing can eliminate the shrinkage of biological samples associated with critical point drying (20% linear dimension) and freeze drying (7%). 3) Cells that change configuration during dehydration and drying due to elution of solvent-extractable components (such as lipids) are better maintained by freezing since no cell constituents are lost 4) Cells such as intraluminal macrophages washed out of the lung or translocated within the lung by aqueous fixatives are preserved *in situ* by freezing. 5) Mucus and surfactant are preserved *in situ* with their native air/liquid interface. 6) Freezing allows

inhaled particles embedded in mucus or surfactant or phagocytosed by macrophages to be kept in place. 7) X-ray microanalysis can be quantitative without loss of extractable components or masking by heavy metal fixative/stains. 8) Electron-beam damage to the specimen is reduced by keeping the sample cold during examination. 9) Freezing is a one-step specimen preparation process, quicker and with fewer procedural variables than the usual alternative of combined chemical fixation, dehydration, and critical point drying.

Freeze-fixation and LTSEM also have certain disadvantages: Ice crystals form during freezing, distorting cells and displacing ions; handling of samples at −196 °C requires special tools and procedures to avoid warming and surface contamination with condensed ice; and a specialized SEM stage is required. However, these disadvantages are ameliorated in that micrometer-sized crystals do not interfere with the structural information we need at the alveolar level, procedures to avoid ice contamination are routine in cryobiology, and several LTSEM stages are now commercially available.

Since water is preserved as ice in frozen-hydrated samples one can examine cells with their cytoplasm and organelles still-hydrated and the surface of airways with its aqueous blanket intact. The important interface between air and the liquid lining airways and alveoli can be imaged *en face* at magnifications up to 10,000× in the frozen-hydrated state in the LTSEM. This is the first imaging technique that has made this possible (see Fig. 1). We will use this technique to resolve the current controversy as to whether the aqueous layer in the alveoli is continuous or discontinuous. The alveoli are tiny (1/4 mm) spherical outpouchings along the last few millimeters of the airway where gas exchange occurs. Surface-tension forces are important determinants of respiratory mechanics at the alveolar level, and these forces are reflected by the configuration of the liquid surface of the alveoli. We hypothesize that the aqueous lining layer is continuous, and that there are no dry areas on the alveolar wall. This continuity would allow surface forces to distribute over the surface of the alveolus and this hypothesis would be consistent with the physical model of the alveolus as an expandable major portion of a sphere. The liquid layer lining the alveolus is topped by a layer of surface-active material that, like a detergent, lowers the surface tension of the alveoli and thus reduces their tendency to collapse. Clinically, the liquid in the alveoli is important in a number of diseases. For example, the premature baby's inability to make surfactant causes respiratory distress syndrome, the major cause of hospitalization and death in intensive care nurseries in the United States. Major advances in therapy for this problem have been made. Current efforts to introduce artificial surfactant into the alveoli require an understanding of the normal configuration of the liquid lining the alveoli.

The major instrument used in our research studies is a scanning electron microscope with a special cold stage and a cryo-specimen preparation chamber as an integral part of the microscope. It was designed by James Pawley, of our laboratory, and John T. Norton, of the AMRay Corporation,* and was built by the AMRay Corporation. The prototype is in use in our group at the Donner Laboratory, and the instrument is now commercially available (AMRay 1000A SEM with biochamber). The cold stage operates with a Joule-Thomson refrigerator that cools to −190°C utilizing 1200 psi dry nitrogen gas. The stage has full 360° rotation, 0–45° tilt and ±1°C temperature control. The vacuum of the specimen preparation chamber attached to the microscope is continuous with that of the microscope, which allows us to fracture a clean, fresh surface and coat for electrical conduction under vacuum, and then to examine the surface with the low-magnification stereo-light microscope. All the necessary manipulations to prepare a frozen sample for microscopy can be performed within the vacuum of the microscope, and the lung can be routinely examined in the microscope in the frozen-hydrated state.

We have demonstrated that the LTSEM can be used to study the shape of alveoli in the hydrated state, the patency of the pores of Kohn in the alveolar wall, the shrinkage and distortion of the lung with drying, the configuration of the mucus layer in the airways, and the thickness of the pleural space, all matters of import in the functioning human lung.

---

*AMRay Corporation, 160 Middlesex Turnpike, Bedford, MA 01730

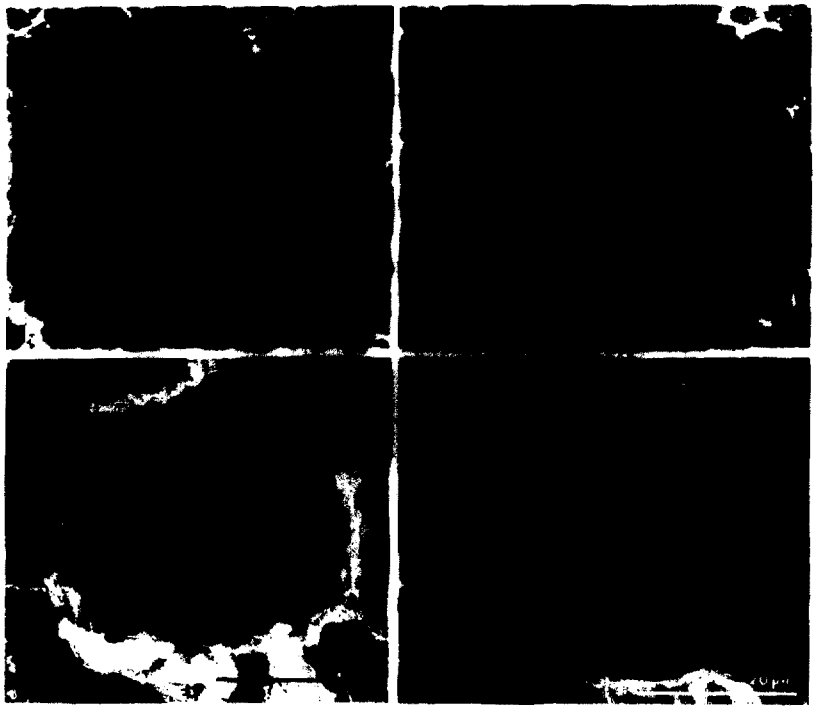

Fig. 1. *Comparison of scanning electron microscopy of dried lung (a,c) and low temperature scanning electron microscopy (LTSEM) of frozen-hydrated lung (b,d) from the mouse. The frozen-hydrated lung has retained all of its water as ice during photography at −190°C in the LTSEM. The open pores (of Kohn) in the alveolar wall seen in conventional critical point dried lungs are not evident in alveoli frozen with their liquid in place. Note also the worm-like capillaries bulging from the surface of the critical point dried alveolus as compared to the rounded contour of the frozen-hydrated alveolus. The alveolar wall is typically folded in critical point dried lungs possibly due to the almost 20% shrinkage that accompanies critical point drying. The bar in each picture represents 20 μm. Variation in x and y magnification of Figs. 1a and 1b is less than 1%; deviation from orthogonality is also less than 1% so that alveolar shape can be directly compared in the frozen-hydrated and critical point dried states in Figs. 1a and 1b.* *(XBB 850-10131)*

REFERENCE

1. Bastacky, J., Hayes, T.L., and Gelinas, R.P. Quantitation of shrinkage during preparation for scanning electron microscopy: human lung. *Scanning 7*, 134–140 (1985).

IMMUNE RECOGNITION OF MEMBRANES

Aaron B. Kantor and John C. Owicki

Recent work in our laboratory has concentrated on the molecular mechanisms of interactions involving biological surfaces. Of particular interest to us is the immune system, many of whose functions are mediated by specific ligand-receptor recognition interactions at the cell membrane.

One example is the binding of antibodies to antigen-bearing membranes, which can have at least two effects. First, the mere presence of bound antibodies marks the antigen-bearing cell as a candidate for destruction. Second, multivalent antibodies may cross-link the antigenic cells, which agglutination may itself inactivate the cells or may make them more susceptible to destruction by phagocytes.

Prior to this year we have primarily studied a model system for the binding of antibodies to isolated cells. We have now begun to investigate aggulination in the same model system. The rest of this report will describe the model system and some of our preliminary observations on molecular mechanisms of aggulation.

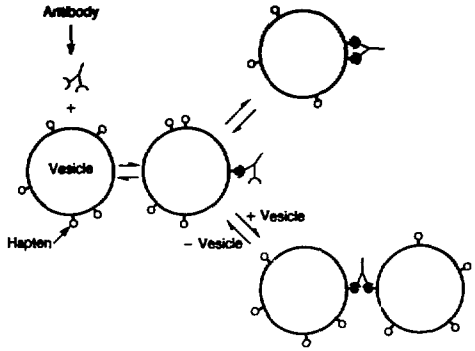

Fig. 1. Schematic representation of the interactions of bivalent antibodies with vesicles (liposomes) bearing monovalent haptens. An antibody in solution first binds monovalently to the liposome (center). Further (bivalent) binding can be either intravesicle (top right) or intervesicle (bottom right). A competition exists between the two modes of bivalent binding, and only intervesicle binding produces aggregation. (XBL 8510-8513)

MODEL SYSTEM

The system consists of phospholipid vesicles (liposomes) rendered antigenic by the attachment of a hapten (fluorescein) and monoclonal antibodies (MABs) directed against the hapten. The possible antibody-hapten interactions are detailed schematically in Fig. 1.

The liposomes are composed of phosphatidylcholines, sometimes with cholesterol, and are 50–100 nm in diameter. We have synthesized[1] a haptenated peptidyl-phospholipid of the form fluorescein-tryglycine-phosphatidylethanolamine, which is incorporated into the liposomes typically at 0.1 to 1 mole % of total phospholipid. The tripeptide spacer projects the hapten out from the membrane far enough for antibodies to bind. The MABs, murine immunoglubulin G's (IgG's) of varying isotype and affinity for hapten, have been obtained from E.W. Voss, Jr.

Fluorescein was chosen as a hapten because its brilliant fluorescence is substantially quenched upon antibody binding. This permits the convenient fluorometric assay of the binding kinetics and equilibrium down to subnanomolar hapten concentrations. Since the hapten fluorescence is sensitive to its environment, it also permits analysis of the state of the hapten prior to antibody binding, e.g., the absence of complications like hapten-hapten aggregation. Previous studies have established the basic behavior of the hapten in the liposomal membrane[2] and characterized the binding of antibodies to these membranes.[3]

STUDIES OF MEMBRANE AGGREGATION

The aggregation of particles, either by nonspecific colloidal forces or specific ligand-receptor interactions, has long been studied by biological and physical scientists. Experimental studies have been largely phenomenological, and the process is complicated enough that theorists have been forced to make great simplifying approximations.

Our model system promises to be of fundamental use in this field for two reasons. First, the behavior of the components of the system is well defined, understood, and controllable. For example, the haptens diffuse freely on the liposomal surface and their lateral density is readily controlled and varied. Second, by monitoring fluorescence quenching, it is possible to measure the number of ligand-receptor bonds as well as the amount of aggregation.

Figure 2 shows the results of an initial experiment on the ability of different concentrations of

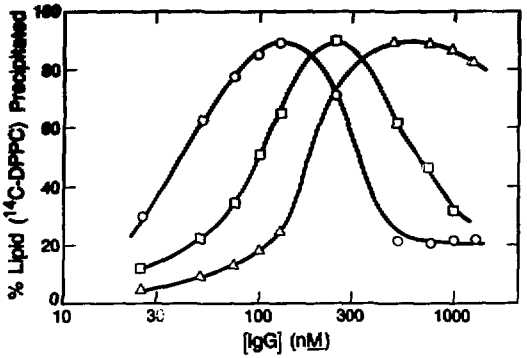

Fig. 2. Precipitation of antigenic liposomes by varying concentrations of antibody, MAB 6-19-1 (IgG_1). The liposomes were labeled with ^{14}C-phospholipid and were centrifugally precipitated (12,000 × g, 5 min) after two hours of incubation with antibodies at 25°C. The bulk lipid concentration of the liposomes was dipalmitoyl-phosphatidylcholine: cholesterol 2:1 on a molar basis. The three sets of data represent different mole fractions of hapten-bearing phospholipid in the liposomes: circles, 2%; squares, 1%; triangles, 0.5%. The three-dimensional concentration of hapten was the same (1670 nM) in all cases, so the concentration of liposomes was highest in the 0.5% hapten preparation. The observed biphasic response resembles the classical immunological precipitin reaction. (XBL 8510-8511)

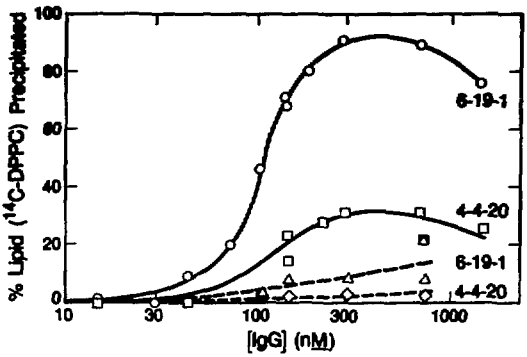

Fig. 3. Differences in the ability of two monoclonal antibodies to precipitate liposomes under conditions similar to those in Fig. 2, but with a 10-min centrifugation. The two antibodies are MAB 6-19-1 (IgG_1) and 4-4-20 (IgG_{2b}). Solid curves, 1 mole % hapten; dashed curves, 0.1 mole %; hapten concentration 1670 nM in both cases. See text for a discussion of the differences between the behavior of the antibodies. (XBL 8510-8512)

antibodies to precipitate vesicles. Results are given for three vesicle preparations with different lateral densities of hapten. In each case there is an optimum concentration of antibody: too little, and not enough is bound to cross-link; too much, and not enough free hapten is left to permit cross-links when antibody-coated liposomes encounter one another. This picture is qualitatively in accord with the classical precipitin reaction.

Figure 3 demonstrates that antibodies differ in their abilities to aggregate antigenic structures. Analysis of antibody binding to the vesicles (by fluorescence quenching) suggests that this does not reflect differences in antibody binding. The more efficient aggregator, MAB 6-19-1 (IgG_1), in this case has a lower affinity for hapten than the other antibody, MAB 4-4-20 (IgG_{2b}), (4/μM vs. 500/μM). In fact, we generally observe surprisingly little correlation of aggregating ability with affinity. We believe that the variability in aggregation reflects differences in the competition between intra- and inter-liposome bivalent binding (see Fig. 1). These difference in turn must reflect differences in properties such as the conformational flexibility and the geometric disposition of hapten binding sites on the IgG molecules.

We are presently pursuing the molecular mechanisms involved in the aggregation phenomena.

ACKNOWLEDGEMENTS

We gratefully acknowledge useful discussions with M. Carlson, K.-D. Lee, A. Petrossian, and S. Stanton. A.B.K. is an N.I.H. Predoctoral Trainee. This research was supported by N.I.H. grant AI19605 to J.C.O.

REFERENCES

1. Petrossian, A., Kantor, A.B., and Owicki, J.C. Synthesis and characterization of a highly fluorescent peptidyl-phosphatidylethanolamine. *J. Lipid Res. 26*, 767–773 (1985).

2. Stanton, S.G., Kantor, A.B., Petrossian, A., and Owicki, J.C. Location and dynamics of a membrane-bound fluorescent hapten: a spectroscopic study. *Biochim. Biophys. Acta 776*, 228–236 (1984).

3. Petrossian, A., and Owicki, J.C. Interaction of antibodies with liposomes bearing fluorescent haptens. *Biochim. Biophys. Acta 776*, 212–227 (1984).

SECTION 6. CELLULAR AND MOLECULAR BIOLOGY

INTRODUCTION

The major research emphasis in the Cellular and Molecular Biology Group continues to be the study of all aspects of carcinogenesis and mutagenesis. An important development during the past year has been the initiation of a more integrated, multi-investigator approach to fundamental research in cancer biology at the biochemical, molecular, and cellular levels. The Cellular and Molecular Biology Group consists of individual scientists with related research interests: increasing our understanding of carcinogen action by examining DNA damage, repair, and recombination events, cellular transformation, and gene expression in cancerous and normal cells. This multidisciplinary approach encompasses use of a wide variety of experimental systems (purified enzymes, bacteriophage, bacteria, yeast, mammalian, and human cells) and of experimental techniques (genetics, protein chemistry, molecular biology, immunology, biochemistry, and tissue culture). The presence of this depth and breadth of background, when focused on a particular area of investigation (such as carcinogenesis and mutagenesis), can provide a unique integrated and coordinated assault on a research problem. Such a focused approach is particularly appropriate for a national laboratory that can bring together scientists from several disciplines to work interdependently on a common project. Our goal is to take advantage of the multidisciplinary nature of our group by fostering specific collaborations among the members. The development of a deliberately organized interactive network of investigators should produce research of higher quality and greater imagination because the pooled expertise will facilitate transfer of information and techniques among the different experimental systems.

The increased understanding of carcinogen action, which is the central question of the research of this group, is an important aspect of the energy-related research supported by DOE at LBL. The by-products of energy production, e.g., radiation and chemical pollutants, have serious biomedical implications, one of which is the initiation, promotion, and progression of cancer. A multi-investigator approach is particularly valuable for a disease like cancer that clearly involves a multiplicity of factors related to numerous areas of science. Furthermore, these factors act in a series of interlocking stages that are not definable in terms of a single scientific discipline.

The response of the Cellular and Molecular Biology Group to the multidisciplinary aspects of cancer research is to set up interacting groups that do not necessarily conform to traditional scientific disciplines but are appropriate for studying specific cellular and molecular aspects of cancer. This approach has evolved the following four collaborative groups: DNA Replication/Recombination, DNA Repair, Carcinogenesis, and Differentiation. The descriptions of current research are presented in the order of the four collaborative groupings, except that each investigator's contributions are presented together to retain the integrity of individual programs. Because most investigators have research projects and/or collaborations in more than one subgoup, group barriers melt in this presentation, leaving a continuum of research programs from the more molecular to the more cellular aspects of carcinogenesis/mutagenesis. This is as it should be in integrated, multi-investigator research efforts. These reports are by no means comprehensive of all the research going on in the group but act as samples of current investigative approaches.

In the area of DNA replication and recombination, Junko Hosoda has utilized a phage system for isolation and investigation of DNA binding proteins. Here, she and her coworkers use mutations in two specific phage genes to clearly demonstrate the importance of protein-protein interactions in DNA replication. By collaborations with Michael Esposito, Hosoda has expanded her studies to include eukaryotic systems, namely yeast. In their initial studies, they have used a clever double column technique to resolve several DNA binding proteins from a series of yeast mutants. These proteins have specific demonstrable enzymatic activity. Libby Holbrook, a postdoctoral scholar in Esposito's group, is responsible for characterizing one of these enzymes, a resolvase. The Esposito/Hosoda collaboration is clearly making good progress toward their stated goal of last year: to use purified proteins to reconstitute recombination and replication systems *in vitro* from defined components. Dimitrios Maleas of Esposito's group is responsible for

characterization of specific recombination defective mutants of yeast. These basic genetic studies will continue to yield new grist for the Hosoda protein purification mill. Robert Mortimer's group is also involved in DNA studies in yeast. They describe here their compilation of established genetic maps for yeast and a genealogy of yeast strains currently in use. Keeping such a compilation up to date and accurate is absolutely essential to high quality research in yeast systems. Mortimer also maintains a Yeast Genetic Stock Center as a service to investigators throughout the world.

In the area of DNA repair, Mortimer and his associates have been using clones of specific genes involved in DNA repair to test whether expression of these genes is inducible by DNA damage. Recently, they have applied a new technique (orthogonal field alternating gel electrophoresis) for isolating large strands of DNA, including whole chromosomes, to DNA repair studies. This technique has a tremendous potential in conjunction with specific yeast mutants for investigating DNA damage and genes involved in DNA repair. Priscilla Cooper has used *E. coli* as a model system to study the DNA repair processes that promote survival. Cooper has developed the hypothesis that damage in the vicinity of the DNA replication fork poses a special problem but repair-competent cells can effectively repair such lesions. To test this hypothesis she and Vincent Ling developed a two-dimensional gel system to isolate replication forks from the main body of DNA. The success of this approach has been verified by transmission electron microscopy. The stage is now set for the testing of her hypothesis. Tony Leadon, who joined LBL and our group only a few months ago, is concentrating his research attention on repair of specific DNA sequences in mammalian cells. This overall experimental strategy is to simplify the analysis by using defined DNA sequences and specific, sensitive probes for DNA damage so that the processing of damage can be analyzed at the molecular level. In conjunction, he has developed several immunoassays for measuring DNA damage and repair that employ monoclonal antibodies to specific base modifications. Using these methodologies in primate cells in culture he has been able to measure DNA damage and its repair within specific sequences. He has found that DNA damage is preferentially repaired in the integrated and actively transcribed chimeric plasmid, pSV2-*gpt*, compared with the bulk of the genome while repair is deficient in the heterochromatic alpha DNA sequences in the same monkey cells. He is extending these initial observations by using an integrated plasmid that contains an inducible promoter so that repair can be studied in the same gene when it is expressed at a basal and after induction. He is also examining repair of damage in endogenous genes to determine to what extent the efficiency of repair is dependent on the transcriptional activity of the gene. We know that Tony Leadon will be an asset to the Division and his avidity for collaboration will promote the interactions desired by the group members.

In the area of carcinogenesis, the name of Bea Singer is well known on the Berkeley campus. She joined our group last spring and continues her fine work on chemically defining all of the modifications in DNA resulting from direct-acting carcinogens. Her current interest is the mechanism(s) for repair-specific DNA lesions and the importance of each lesion in mutagenesis. Goth-Goldstein reports on studies with direct-acting carcinogens in cells deficient or proficient in repair of DNA damage. Her goal is to investigate at the genetic level the mechanism(s) for induction of resistance to DNA damage. Although studies at the level of DNA are of paramount importance in understanding how an inheritable change in DNA results in cancer, another important aspect is attempting to evaluate the potential health risk of environmental carcinogens to the population as a whole. To this end Lois Gold, Bruce Ames and their associates have developed a numerical index of carcinogenic potency and application to an ever increasing data base has, to date, verified its value in risk assessment.

Carcinogenesis, of course, is more than modification of DNA. It has many stages; for example, initiation and promotion, all with many facets. Experiments by Mina Bissell, in conjunction with Anthony Howlett and Betsey Cullen, demonstrate that viral infection, the first step in virally induced transformation, is dependent upon the developmental stage of the host cell. Using the same viral system, Bissell and her coworkers have provocative evidence that the promotional stages of viral carcinogenesis, whether induced by wounding or chemical promoters, all involve inflammatory reactions.

As indicated by Bissell's first report and many to follow, there is an increasing interest in the relationship between normal cellular differentiation and development and carcinogenesis. In order to understand how aberrations in modulation of differentiation fit into the carcinogenic puzzle, we must first define how normal differentiation is regulated in a given cell type. Bissell and associate present their work in this regard in the murine mammary epithelial cell. From their work examin-

ing expression of genes related to milk proteins and to a specific protein, transferrin, it is clear the extracellular matrix composition and cell shape are factors in normal modulation of differentiation. The investigation of transferrin expression may have special significance in that this protein has been related to one of the proto-oncogenes. Collagen is the differentiated product of fibroblasts, the cells being studied by Richard Schwarz and Nancy Owens with respect to differentiation and the carcinogenic process. Their research has provided evidence for a unique means of controlling cellular activity. By an as yet incompletely understood mechanism, collagen gene expression is modulated by secretion of the collagen molecule. In efforts directed toward understanding the relationship between differentiation and carcinogenesis in the human mammary epithelial cells, Gordon Parry's group has developed a series of monoclonal antibodies to cell surface proteins. They are using these antibodies to address such questions as their role in cell polarity, their expression in malignancy and the implications of this expression in tumor biology and clinical medicine. This same approach is now being applied to the normal, tumor-derived and transformed human mammary cells being grown by Martha Stampfer. Stampfer's group reported last year on the first successful attempt to induce transformation in human epithelial cells in culture with a chemical carcinogen. This year Stampfer and Bartley describe distinct differences in growth control in normal and transformed cells. In conjunction with Gerri Levine, these investigators present their efforts to define modulation of differentiation in human mammary epithelial cell. The results of these studies will provide a basis for dissecting the role of perturbations of differentiation in the development of transformed and malignant cells. The final paper from our group presents Glenn Hall's efforts to apply a molecular approach to identify subspecies of bees. Such identification is basic to setting up an effective eradication program for the impending invasion of African bees.

The Cellular and Molecular Biology Group has had a scientifically fruitful year. Collaborations and interactions have been formalized and valuable new associates have been assimilated. The group members have recognized and acted upon the unique contribution that program development possible in a national laboratory system can make in the field of carcinogenesis and mutagenesis.

BACTERIOPHAGE T4 GENE 32 PROTEIN AFFINITY COLUMN CHROMATOGRAPHY

Junko Hosoda, Herbert W. Moise, Maren Bell, and Midori Hosobuchi

We have previously shown that a large number of T4 early proteins bind to columns made from gene-32 protein covalently bound to agarose. This protein-protein interaction, for a number of proteins that are involved with replication-recombination, involves the A region (a 51-residue stretch of the peptide chain including the carboxy terminus) of gene-32 protein. Experiments done with amel, an amber peptide of gene-32 protein lacking 15–20 residues from the A region, have demonstrated that most of the proteins that had affinity for the gene-32 protein columns also had affinity for the amel columns. In some cases the binding affinity was reduced to the amel column; in other cases, e.g., gene-61 protein, the binding affinity remained the same. The gene-32 amel mutant, isolated by T. Minagawa from a pseudo revertant of 49 tsC9, is not a lethal mutation. When grown in *E. coli* B^1, it has a slightly reduced burst size, increased uv-sensitivity, and a slightly reduced recombination efficiency when compared to wild-type phage (T4D). These defects are more pronounced when amel is grown in *E. coli* B40 su1 hosts (Table 1).

We found, however, that when a mutation in gene 61 (amE219) was added to gene-32 amel and the double mutant was grown in a su1 host, the combined mutations become lethal—the relative plating efficiency dropped to $< 3.7 \times 10^{-3}$ as shown in Table 1. The gene-61 product is an RNA primase essential for starting DNA replication in the reverse direction from the replication fork movement. Figure 1 shows that the rate of DNA synthesis in *E. coli* B40 su1 infected with the double mutant was greatly reduced when compared to infection with the single mutant in gene 61, which showed the normal rate of DNA synthesis, or to infection with gene-32 amel, which showed a slightly reduced rate.

To determine if there was an alteration in the interaction between amel and gene-61 protein in

Table 1.

Host	Phage	Relative plating efficiency	Burst size
B^E	am^+		172.0
B40su1	am^+	1.00	180.0
B^E	32 ame1		37.2
B40su1	32 ame1	0.45	10.8
B^E	61 amE219×2		2.8
B40su1	61 amE219	1.00	36.0
B^E	32 ame1—61 amE219×2		2.0
B40su1	32 ame1—61 amE219×2	$>3.7 \times 10^{-3}$	0.0

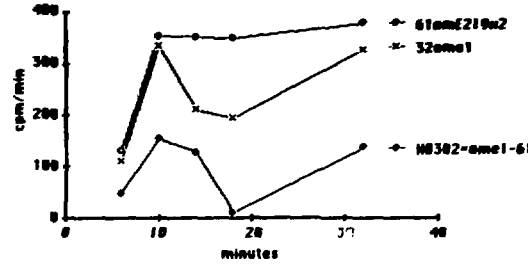

Fig. 1. TdR incorporation rates in E. Coli ..40/su1.
(XBL 8511-8571)

the su1 suppressed cells, columns were prepared by covalently coupling either ame1/B^E (ame1 grown in *E. coli* B^E) or ame1/su1 (ame1 grown in *E. coli* B40 su1) to agarose. ^{14}C-labeled extracts from either T4D or 61 amE219 grown in B40 su1 were applied to the columns in buffer containing 0.05 M NaCl and 0.01 M $MgCl_2$. Bound proteins were eluted with NaCl; and fractions were analyzed by two-dimensional gel electrophoresis. Gene-61 protein from T4D eluted from the ame1/B^E and ame1/su1 columns at 0.6 M NaCl, which is the same concentration needed to elute gene-61 protein from a gene-32 protein column. From the ame1/su1 column the T4D gene-61 protein eluted with 0.6 M NaCl. However, the gene-61 protein from 61 amE219 did not elute with any NaCl concentration tried (including 2.0 M). This suggests that the lethality and inhibition of DNA replication seen with the suppressed double mutant is caused by the irreversible binding of gene-61 protein/su1 to ame1.

FRACTIONATION OF DNA METABOLIC PROTEINS OF *SACCHAROMYCES CEREVISIAE* BY DNA CELLULOSE CHROMATOGRAPHY: SSB-1, SS-DNA DEPENDENT ATPase, DNA POLYMERASE, DNA PRIMASE, TOPOISOMERASE I, AND RESOLVASE

Junko Hosoda, Libby L. Holbrook, Herbert W. Moise, Kathleen A. Bjornstad, Dimitrios T. Maleas, Midori Hosobuchi, Maren Bell, and Michael S. Esposito

We are continuing a collaborative program to characterize the DNA binding proteins of wild-type yeast strains and mutants exhibiting defects in DNA repair and recombination. Last year we analysed the single stranded DNA (SS-DNA) cellulose binding proteins of a recombination proficient yeast strain (LBL1) and coisogenic rec mutants derived from it, and demonstrated by two-dimensional gel electrophoresis and fluorography that several *rec* mutants exhibit deficits in discrete DNA binding proteins.[1] In the present study we have employed a double stranded DNA (DS-DNA) cellulose column coupled to a SS-DNA cellulose column to separate the binding proteins that have affinity for double stranded DNA from those specific for single stranded DNA. The upper DS-DNA cellulose column and lower SS-DNA cellulose column were connected in series. Proteins which have relatively strong affinity for DS-DNA remain on the DS-DNA cellulose column. Those which have little or no affinity for DS-DNA, but bind to SSDNA, are collected on the SS-DNA cellulose column. The two columns were separated and proteins bound to each column were eluted employing a NaCl gradient. Our aim was to determine whether DNA cellulose columns would, in fact, bind a variety of DNA metabolic activities and achieve sufficient fractionation of them to warrant use of DNA cellulose column chromatography as a method for screening mutants for enzymatic defects. To this end, we have shown that NaCl gradient elution on DS-DNA cellulose columns fractionates single

stranded DNA dependent ATPase and topoisomerase I, that NaCl gradient elution of SS-DNA cellulose columns fractionates DNA polymerase, primase and SSB-1, and that a previously unreported resolvase activity of mitotic yeast cells binds to both DS- and SS-DNA cellulose columns. The SSB-1 protein was further purified to near homogeneity.

DNA CELLULOSE CHROMATOGRAPHY

For this study we have employed a haploid strain BJ2168 (*MATa prb1 pep4 prcl.* constructed by Dr. Elizabeth W. Jones of Carnegie-Mellon University) that exhibits minimal proteolytic activity due to mutations in the genes governing proteinase B, proteinase C, and processing of precursors of vacuolar hydrolases. The use of this strain together with inhibitors of proteolytic enzymes minimizes degradation of DNA metabolic enzymes and proteins by endogenous proteases. Proteins were extracted by methods similar to those of LaBonne and Dumas[2] and applied to a DS-DNA cellulose column connected in series to a denatured SS-DNA cellulose column. The columns were uncoupled and eluted separately. One-dimensional sodium dodecyl sulfate polyacrylamide gradient gel electrophoresis (1D SDS-PAGE) was employed to identify fractions from the SS-DNA cellulose column containing the yeast single stranded DNA specific binding protein SSB-1, which was then purified to near homogeneity by hydroxylapatite chromatography. The remaining fractions from DS- and SS-DNA cellulose columns were pooled, concentrated, and assayed for single stranded DNA dependent ATPase, DNA polymerase, DNA primase, resolvase, and topoisomerase I activities.

SS-DNA DEPENDENT ATPASE ACTIVITY

Enzymes and proteins exhibiting SS-DNA dependent ATPase activity comprise a large group of species that play key roles in DNA replication, repair, and recombination. Column fractions were surveyed for both SS-DNA dependent and SS-DNA independent ATPase activities (Fig. 1). Fraction ds-5 (eluted with 0.32–0.34 M NaCl) of the DS-DNA cellulose column exhibited the highest level of SS-DNA dependent ATPase activity. DS-DNA cellulose column fractions exhibited little SS-DNA independent ATPase activity. By contrast, fractions ss-2 (eluted with 0.17–0.19 M NaCl) and ss-6 (eluted with 0.30–0.33 M) from the SS-DNA cellulose column contained high levels of SS-DNA independent ATPase activity.

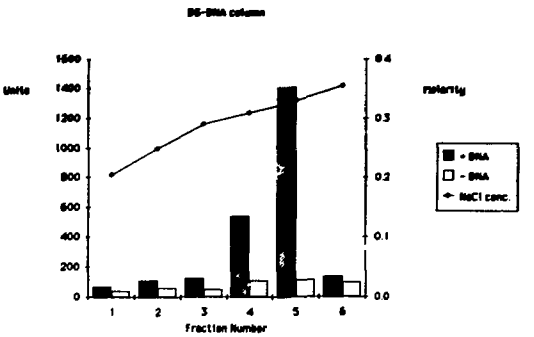

Fig. 1. SS-DNA dependent ATPase and SS-DNA independent ATPase activities of DS-DNA cellulose pooled column fractions. The ATPase activity was monitored by the conversion of [^{3}H]-ATP(30,000 cpm/nmole) into [^{3}H]-ADP which were separated by thin layer chromatography on Cellulose PEI with 1 M formic acid and 0.5 M LiCl. One unit of activity corresponds to the conversion of 1 nM ATP into ADP in 45 minutes at 37°C. To assay ATPase in the presence of DNA, 10 μg/ml of fd-viral DNA was added. (XBL 8510-4462)

DNA POLYMERASE ACTIVITY AND DNA PRIMASE ACTIVITY

Saccharomyces cerevisiae has at least two DNA polymerases, I and II. DNA polymerase I is a true DNA replicase representing about 90% of the total activity present in exponential phase yeast cells[3] while DNA polymerase II, a minor activity, exhibits proofreading 3'-exonuclease activity thus resembling prokaryotic DNA polymerases. We surveyed fractions from both the DS-DNA cellulose and SS-DNA cellulose columns for polymerase activity employing both activated calf thymus DNA and poly(dA-dT)/poly(dA-dT) as primer-templates. We did not observe significant levels of activity in fractions from the DS-DNA cellulose column. However, pooled fractions ss-3 and ss-6 from the SS-DNA cellulose column exhibited peak levels of DNA polymerase activity (Fig. 2). The observed synthesis is due to DNA polymerase activity and not terminal transferase activity.

A DNA primase activity copurifies with DNA polymerase I activity in a structural complex that may partially dissociate during DNA-cellulose chromatography.[4] We therefore assayed fractions ss-2 and ss-6 for DNA primase activity using the single-stranded closed circular fd-DNA as template in the presence and absence of a ribonucleotide triphosphate mixture (DNA polymerase cannot utilize closed circular single stranded fd-DNA as a template for DNA synthesis in the absence of primase activity or ribonucleotide triphosphates). The

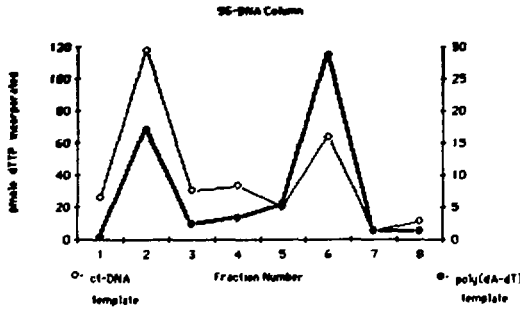

Fig. 2. DNA polymerase activity of pooled SS-DNA cellulose column fractions. The polymerase reaction was monitored by incorporation of [^{3}H]-dTTP into acid precipitable material. Either 150 μg/ml of activated calf thymus DNA or 0.5 A_{260nm} unit/ml of poly(dA-dT)/poly(dA-dT) was used as a template.
(XBL 8510-4463)

results shown in Table 1 demonstrate that fraction ss-2 contains DNA primase activity.

SINGLE STRANDED DNA SPECIFIC DNA BINDING PROTEINS

Several investigators have reported the isolation of single stranded DNA specific DNA binding proteins of *Saccharomyces cerevisiae* that stimulate *in vitro* DNA synthesis by homologous DNA polymerase I. We followed the SSB-1 isolation procedure of LaBonne and Dumas[2] because it yielded the largest protein. Two-dimensional gel electrophoresis showed that our SSB-1 protein is an acidic protein (pI 5.5 ± 0.2) with a molecular weight of 40,000 daltons, which agrees with the value given by LaBonne and Dumas.[2]

Preliminary experiments indicate that our SSB-1 preparation stimulates DNA polymerase activities in both the ss-2 and ss-6 fractions, but the optimal SSB-1/DNA ratio is apparently different for each. The activity in the ss-2 fraction, which contains primase activity, requires a higher SSB-1/DNA ratio than the one in the ss-6 fraction (Table 2).

Table 1. DNA primase activity associated with DNA polymerase activity fractioned by SS-DNA cellulose chromatography.[a]

Fraction number	rNTP's Present + Absent −	Time of incubation (min)	Percent of template replicated	Percent of total replication dependent upon primase activity
ss-2	+	5	1.7	88.2
	+	15	8.4	85.7
	+	30	14.1	80.2
ss-2	−	5	0.2	
	−	15	1.2	
	−	30	2.8	
ss-6	+	5	0.2	0.0
	+	15	0.6	0.0
	+	30	0.4	0.0
ss-6	−	5	0.1	
	−	15	0.6	
	−	30	0.9	

[a]The primase assay conditions were essentially the same as the polymerase assay except that fd-viral DNA (5 μg/ml) was used as the template in place of activated calf-thymus DNA. The assay was done in pairs: one member received 200 μM each of CTP, GTP and UTP (rNPTs) and the other received none.

RESOLVASE AND TOPOISOMERASE I ACTIVITIES

The fractions obtained from chromatography of strain BJ2168 on DS- and SS-DNA cellulose were also assayed for resolvase and topoisomerase I activities using the pBR322 dimer as a substrate (see next report by L.L. Holbrook et al.). Topoisomerase I binds to DS-DNA cellulose and elutes in fractions ds-4, ds-5, and ds-6 (0.3– 0.37 M NaCl) and fractions ss-2 to ss-8 (0.17–0.38 M NaCl) and to a lesser degree ds-2 and ds-3 (0.22–0.30 M NaCl), contain an activity that cleaves the supercoiled dimer, to linear dimer, and therefore this activity can be identified as the resolvase. A restriction-type reaction that is sequence-dependent and would give linear monomer products is not observed. (See L.L. Holbrook et al., next report.)

Table 2. Stimulation of DNA polymerase activity by SSB-1.[a]

Pooled fraction number	SSB-1 concentration μg/ml	SSB-1/DNA ratio (w/w)	Incubation time (min)	c.p.m. incorporated per 8 μl	Percent Stimulation by SSB-1
ss-2	0.0	0.0	15	165	
			30	519	
	5.1	0.5	15	177	7.6
			30	741	42.8
	10.2	1.0	15	228	38.6
			30	717	38.3
	20.4	2.0	15	318	93.3
			30	933	80.0
ss-6	0.00	0.00	15	847	
			30	2063	
	5.1	0.5	15	1422	67.8
			30	3877	87.9
	10.2	1.0	15	1540	81.8
			30	3573	73.2
	20.4	2.0	15	2026	139.3
			30	3033	62.6

[a]The assay procedure was the same as the polymerase assay with the poly(dA-dT)/poly(dA-dT) template except that the polymer template concentration was reduced to 0.25 A_{260nm} unit/ml (approximately 10 μg/ml). All ingredients except SSB-1 were first mixed on ice and then SSB-1 was added. The reaction tube was then placed in a 30°C bath to start the reaction.

REFERENCES

1. Esposito, M.S., Hosoda, J., Golin, J., Moise, H., Bjornstad, K., and Maleas D. Recombination in *Saccharomyces cerevisiae*: REC-gene mutants and dNA-binding proteins, *Cold Spring Harbor Symp. Quant. Biol. 49*, 41 (1984).
2. LaBonne, S.G., and Dumas, L.B. Isolation of a yeast single-strand deoxyribonucleic acid binding protein that specifically stimulates yeast DNA polymerase I, *Biochemistry 22*, 3214 (1983).
3. Chang, L.M.S. DNA polymerase from Baker's yeast, *J. Biol. Chem. 252*, 1873 (1977).
4. Singh, H., and Dumas, L.B. A DNA primase that copurifies with the major DNA polymerase from yeast *Saccharomyces cerevisiae*. *J. Biol. Chem. 259*, 7936 (1984).

IN VITRO RESOLUTION OF HOLLIDAY JUNCTIONS BY CELL-FREE PROTEIN EXTRACTS OF *SACCHAROMYCES CEREVISIAE*: RESOLVASE ACTIVITY OF HAPLOID AND DIPLOID CELLS

Libby Litzenberger Holbrook, Kathleen A. Bjornstad, Dimitrios T. Maleas, and Michael S. Esposito

A central feature of molecular models of genetic recombination is the formation and resolution of Holliday junctions.[1] Our previous studies of the properties of spontaneous mitotic recombination in *Saccharomyces cerevisiae* led to the prediction that mitotic yeast cells possess resolvase activity.[2] Detection of resolvase activity in yeast extracts has been facilitated by the previous studies of Mizuuchi et al.[3] and Lilley and Kemper,[4] which demonstrated that the resolvase (endonuclease VII) controlled by gene 49 of T4 cleaves Holliday junctions formed by cruciform extrusion at sites of inverted repeats. In our initial studies, mitotic cell populations of both haploid and diploid recombina-

tion proficient strains were surveyed for resolvase activity toward plasmids containing cruciforms.

Plasmids ColE1 and pBR322 contain inverted repeats of 13 and 11 bases respectively[5,6] which can assume cruciform structures as demonstrated by S1 nuclease sensitivity.[7,8] These plasmids were used to screen yeast extracts for resolvase activity. The assay is based on conversion of the supercoiled form to the linear form by cleaving at the site of cruciform extrusion as diagrammed in Fig. 1. Once the cruciform is resolved, the plasmid is no longer a substrate for resolvase.

The Rec$^+$ haploid strains[9] NLBL1 (*MATα ade5 met13-c cyh2^r trp5 LEU1 ade6 cly8 his7-1 tyr1-2 lys2-2 ade2-1 ura3-1 CAN1^s*) and NLBL3 (*MATa ADE5 met13-d CYH2^s TRP5 leu1 ADE6 CLY8 his7-2 tyr1-1 lys2-1 ade2-1 ura3-1 can1^r*) as well as the diploid NLBL1 X NLBL3 express resolvase activity toward either substrate. A time course of the reaction on ColE1 catalyzed by proteins in the NLBL1 extract is shown in Fig. 2. Production of linear plasmid is observed upon incubation from 15 to 90 minutes. The supercoiled form disappears at 15 to 30 minutes. The open circular form is also observed which presumably is not a substrate for resolvase since it no longer contains a cruciform structure. At longer incubation times the substrate is degraded (by nonspecific nucleases also present in the crude preparation). As is the case for endonuclease VII of T4,[10] yeast resolvase activity is dependent on the presence of $MgCl_2$ and does not require ATP. The yeast activity is also inhibited by concentrations of NaCl or KCl greater than 50 mM (not shown).

While assaying crude extracts, an ATP-independent topoisomerase I activity was detected. This is most likely that previously described by Goto et al.[11] since both are ATP-independent and resistant to coumermycin.

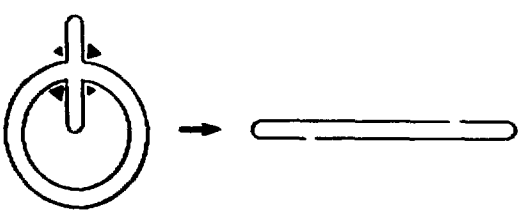

Fig. 1. Endonucleolytic resolution of a Holliday junction formed by cruciform extrusion of inverted repeat sequences contained in a supercoiled plasmid. Resolvase cleaves either the two single DNA strands marked by the small pair of arrowheads or the two single DNA strands marked by the large pair of arrowheads. Both modes of cleavage linearize the supercoiled plasmid. (XBL 8510-4460)

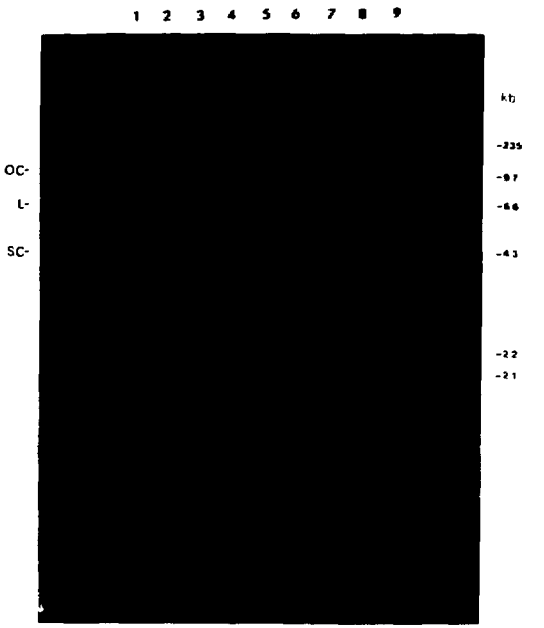

Fig. 2. Time course of resolvase reaction catalyzed by extracts of NLBL1. Cells were grown at 24°C. Resolvase was assayed in 2M ammonium sulfate pellets prepared by a modification of a published procedure[15] using ColE1 DNA (6.6 kb) in the reaction described in the legend to Fig. 3 and incubating for the following minutes: 0 (lane 3), 15 (lane 4), 30 (lane 5), 60 (lane 6), 90 (lane 7), and 120 (lane 8). Lane 1 - ColE1 DNA. Lane 2 - linear ColE1 DNA produced by EcoR1 restriction of the plasmid. Lane 9 - linear standards generated by HindIII digestion of lambda DNA. Sizes are indicated in kilobases. OC: open circular DNA. L: linear DNA. SC: supercoiled DNA. (XBB 850-8642)

The supercoiled dimer form of pBR322 was used to distinguish the resolvase activity from a restriction enzyme. Whereas both resolvase and a restriction enzyme that cuts the DNA once will produce linear DNA from a monomeric plasmid, they will produce fragments of different sizes from a dimeric plasmid. Resolvase recognizes a structural feature whose presence is dependent upon supercoiling (cruciform) and introduces one endonucleolytic scission at a Holliday junction thereby producing a linear dimer DNA product. A restriction enzyme recognizes a specific sequence and therefore will make two cuts in the dimer plasmid to give the linear monomer product. These species are easily distinguished by agarose gel electrophoresis.

Four *rec* mutants (*rec490, rec413, rec467, rec46*) isolated in this laboratory[12] (Table 1) were screened for both resolvase and topoisomerase I

Table 1. Properties of recombination mutants isolated in strain LBL1.[a]

	Median frequencies per 10^5 c.f.u.[b]				
	Leu⁺Trp⁺Cyh^r inter. rec.	Leu⁺Trp⁺Cyh^r convert.	Total Cyh^r	Resolvase activity[c]	In vitro recombination[d]
rec754[e]	0.00	0.00	0.82		—
rec780	0.00	0.00	0.00		
rec416	0.00	0.00	0.00		
rec490[e]	0.00	0.00	0.00	+	—
rec413[f]	0.00	1.12	2.50	+	—
rec336[f]	0.00	1.88	6.85		—
rec467[f]	0.00	3.02	4.71	+	+
rec141	0.11	5.20	30.69		
rec100	0.17	0.82	1.23		+
rec234	0.37	0.00	0.62		++
rec139	1.10	0.00	263.33		
rec201	1.18	0.16	14.29		
rec146	8.80	0.57	27.87		+++
rec276	10.74	1.12	157.77		+++
rec952	12.69	1.94	25.40		
rec395	16.90	1.60	123.20		
rec193	23.73	2.20	123.60		+++
rec409	54.48	5.36	48.20		
rec46[e]	243.48	19.95	1715.17	+	+++
rec199[e] (cdc9)	369.84	36.41	2025.00		+
LBL1	1.34	0.72	15.46	+	+

[a]Spontaneous mitotic gene conversion of *CYH2*^{s} to *cyh2*^{r} in the chromosome VII disomic strain LBL1 (*MATα ade5/ADE5 met13-c/met13-c cyh2^r/CYH2^s trp5/TRP5 leu1/LEU1 ade6/ADE6 cly8/CLY8 his7-1 tyr1-2 lys2-2 ade2-1 ura3-1 CAN1*^{s}) and mutants derived from it results in red Leu⁺ Trp⁺ cycloheximide resistant (Cyh^r) segregants. Spontaneous intergenic recombination in the interval *CYH2 - TRP5* results in white Leu⁺ Trp⁺ Cyh^r segregants. The ensemble of conversional, exchange, and chromosomal loss events contributes to total Cyh^r resistant segregants.[9,19] Median frequencies are based upon analyses of 25 colonies of the control Rec⁺ strain LBL1 and a minimum of five colonies of each mutant.[12] All of the mutants characterized with respect to dominance versus recessivity exhibit meiotic defects when studied in diploid *MATa/MATα* cells. The recessive mutations complement one another. The recombinational defects of *rec490* and *rec413* are temperature sensitive; *rec336* and *rec199 (cdc9)* are conditional lethals.

[b]c.f.u. = colony forming units.

[c]Resolvase activity was measured as described in Fig. 3. The *rec413* and *recr490* strains were grown at both permissive and restrictive temperatures for recombination. Rec⁺ haploids and diploids grown at 24°, 29°, and 36°C exhibit resolvase activity.

[d]Assayed by *in vitro* plasmidic recombination (L.S. Symington and R. Kolodner, personal communication).[14]

[e]Recessive mutation.

[f]Dominant or semidominant mutation.

activities. The temperature sensitive mutants (*rec490, rec413*) were grown at both the permissive and the restrictive temperatures for recombination. All mutants assayed expressed both resolvase and topoisomerase I activities, implying that their recombinational defects are not due to mutations in the structural or regulatory genes controlling these activities. Assays on crude extracts prepared from strains heterozygous and homozygous for the *rec46* mutation (see report by D.T. Maleas et al.) as well as the Rec⁺ diploid are shown in Fig. 3. All crude extracts contain resolvase activity that catalyzes

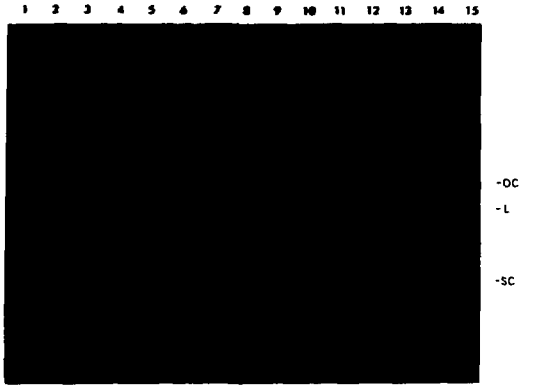

Fig. 3. Resolvase and topoisomerase I assays of diploids containing the rec46 mutation. Lanes 1 through 8 - 2M ammonium sulfate pellets. Lanes 9 through 14 - 3M ammonium sulfate pellets. Pairs were assayed as described below for 1 and 2 hours respectively. Lanes 1,2,9, and 10 - Rec⁺ diploid. Lanes 3,4,11,12 - rec46 heterozygote. Lanes 5 and 6 - a second rec46 heterozygote. Lanes 7, 8, 13, 14 - rec46 homozygote. Lane 15 - pBR322 dimer plasmid (8.7 kb). Mitotic cell populations of control and rec mutant strains were grown at 29°C in 100 ml YPD cultures supplemented with 100 mg/liter adenine sulfate and harvested at a density of 5 × 10^7 cells/ml. The cell pellet was resuspended in 50 mM Tris-HCl, pH 7.5 1 mM EDTA, 10% (w/v) sucrose and stored at −70°C. The thawed cells were treated at 37°C for 30 minutes with 0.5-mg/ml zymolyase, 5 mM 2-mercaptoethanol, 1 mM PMSF, and 2 μg/ml Pepstatin A. The cells were then treated on ice for 60 minutes with 0.4 M KCl, 0.1 mM protamine sulfate, and 10% streptomycin sulfate, briefly sonicated, and cleared by centrifugation. The supernate was successively brought to 2 M and then 3 M ammonium sulfate by the addition of 3.8 M ammonium sulfate, pH 7. The precipitated proteins in each fraction were collected by centrifugation and stored at −70°C. A protein pellet was resuspended in 20 mM Tris HCl, pH 7.5, 0.1 mM EDTA, 10% (v/v) glycerol. Resolvase activity was detected by the conversion of supercoiled to linear DNA in a 10 μl reaction mix consisting of 20 mM Tris-HCl, pH 7.5 1 mM dithiothreitol, 10 mM $MgCl_2$, 0.25 mg/ml bovine serum albumin, 0.1 μg pBR322 supercoiled DNA and yeast proteins. After incubation for 1–2 hours at 30°C, the reaction was stopped by the addition of 20 mM EDTA. DNA species were separated by electrophoresis through 0.8% agarose in TAE (40 mM Tris-HCl, 20 mM acetate, 0.5 mM EDTA, pH 8.0) buffer and visualized by ethidium bromide fluorescence under uv transillumination. Topoisomerase I activity was assayed in the same manner by detecting the formation of topoisomers from supercoiled DNA. OC: open circular DNA, L: linear dimer DNA, SC: supercoiled DNA. (X88 850-9216)

production of linear dimer from supercoiled pBR322 dimer DNA (2M ammonium sulfate fraction, lanes 1–8) and topoisomerase I activity that relaxes the supercoiled DNA to a ladder of topoisomers (predominantly in 3M ammonium sulfate fraction, lanes 9–14). No bands corresponding to linear monomer or smaller products were observed, suggesting the absence of a restriction reaction.

The fractions obtained from DNA cellulose chromatography (see report by J. Hosoda et al.) of a protease deficient strain (BJ2168, *MATa prb1 pep4 prc1*) were also assayed for resolvase and topoisomerase I activities (Figs. 4 and 5) using the pBR322 supercoiled dimer as a substrate. Topoisomerase I bound to native DNA cellulose and eluted at 0.3 - 0.37 M NaCl (fractions ds-4, ds-5, and ds-6, Fig. 4). Resolvase bound predominantly to single-stranded DNA cellulose under the conditions used and eluted at 0.17 - 0.38 M NaCl (fractions ss-2 to ss-8, Fig. 5). Some activity was also observed to elute from native DNA cellulose at 0.22 - 0.30 M NaCl.

The resolvase protein(s) that we have identified will be purified to homogeneity and used to obtain mutations in the resolvase gene(s). We wish to inquire whether mitotic and meiotic yeast cells

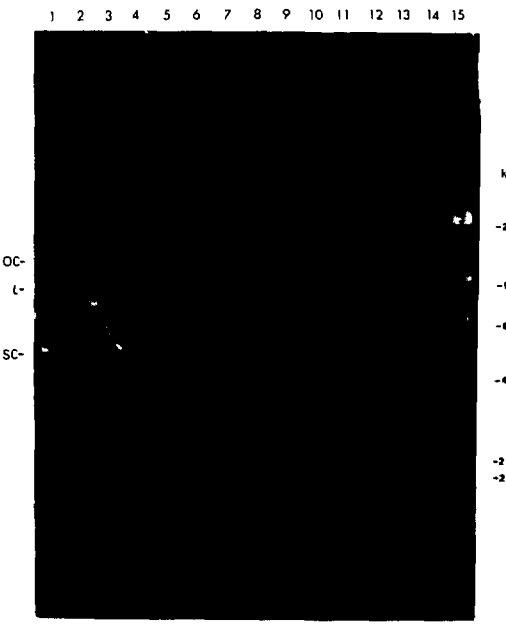

Fig. 4. Topoisomerase I activity eluted from the native DNA cellulose column. Fractions ds-1 to ds-6 were assayed as described in Fig. 3 using the pBR322 dimer (8.7 kb) substrate. Lane 1 - pBR322 DNA. Lanes 2,4,6,8,10, and 12 - ds-1 to ds-6 respectively, incubated for 60 minutes. Lanes 3,5,7,9,11 and 13 - ds-1 to ds-6 respectively, incubated for 120 minutes. Lane 14 - extract from NJBL1 × NJBL3 diploid incubated for 60 minutes. Lane 15 - linear standards as in Fig. 2. OC: open circular DNA, L: linear dimer DNA, SC: supercoiled DNA.

((illegible))

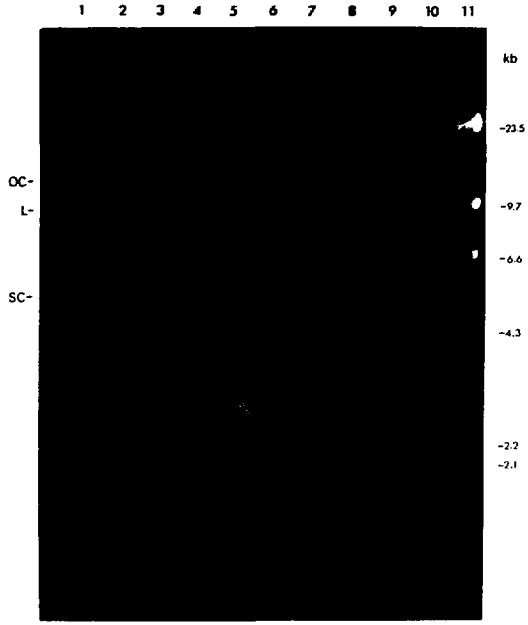

Fig. 5. *Resolvase activity eluted from the single-stranded DNA cellulose column. Fractions ss-1 to ss-8 were assayed as described in Fig. 3 using the pBR322 dimer (8.7 kb) and incubating for 60 minutes. Lane 1 - no yeast proteins added. Lanes 2 through 9 - ss-1 to ss-8 respectively. Lane 10 - as in Lane 14 of Fig. 4. Lane 11 - linear standards as in Fig. 2. OC: open circular DNA. L: linear dimer DNA. SC: supercoiled DNA.*
(XBB 850-8641)

defective in resolvase activity are viable, and to determine their recombinational phenotypes both *in vivo* and *in vitro*. In the case of mitotic diplcid cells we will ascertain whether resolvase defective cells (if viable) exhibit the hyperrecombination phenotype predicted by the prereplicational model of mitotic recombination[13] or the hyporecombination phenotype predicted by alternative models.[2]

REFERENCES

1. Holliday, R.A. Mechanism for gene conversion in fungi. *Genet. Res. 5,* 282–304 (1964).
2. Esposito, M. S., and Wagstaff, J. Mechanisms of mitotic recombination, in *The Molecular Biology of the Yeast Saccharomyces: Life Cycle and Inheritance*, Strathern, J.N., Jones, E.W., and Broach, J.R., Eds., Cold Spring Harbor Laboratory, Cold Spring Harbor, New York, pp. 341–370 (1981).
3. Mizuuchi, K., Kemper, B., Hays, J., and Weisberg, R.A. T4 endonuclease VII cleaves Holliday structures. *Cell 29,* 357–365 (1982).
4. Lilley, D.M.J., and Kemper, B. Cruciform-resolvase interactions in supercoiled DNA. *Cell 36,* 413–422 (1984).
5. Oka, A., Nomura, N., Morita, M., Sugisaki, H., Sugimoto, K., and Takanami, M. Nucleotide sequence of small ColE1 derivatives: Structure of the regions essential for autonomous replication and colicin E1 immunity. *Mol. Gen. Genet. 172,* 151–159 (1979).
6. Sutcliffe, J.G. Complete nucleotide sequence of the *E. coli* plasmid pBR322. *Cold Spring Harbor Symposia of Quantitative Biology 42,* 77–90 (1978).
7. Lilley, D.M.J. The inverted repeat as a recognizable structural feature in supercoiled DNA molecules. *Biochemistry 77,* 6468–6472 (1980).
8. Panayotatos, N., and Wells, R.D. Cruciform structures in supercoiled DNA. *Nature 289,* 466–470 (1981).
9. Esposito, M.S., Maleas, D.T., Bjornstad, K.A., and Bruschi, C.V. Simultaneous detection of changes in chromosome number, gene conversion and intergenic recombination during mitosis of *Saccharomyces cerevisiae*: Spontaneous and ultraviolet light induced events. *Current Genet. 6,* 5–11 (1982).
10. Kemper, B., and Garabaett, M. Studies of T4-head maturation. I. Purification and characterization of gene-49-controlled endonuclease. *Eur. J. Biochem. 115,* 123–131 (1981).
11. Goto, T., Laipis, P., and Wang, J.C. The purification and characterization of DNA topoisomerases I and II of the yeast *Saccharomyces cerevisiae*. *J. Biol. Chem. 259,* 10422–10429 (1984).
12. Esposito, M.S., Hosoda, J., Golin, J., Moise, H., Bjornstad, K., and Maleas, D. Recombination in *Saccharomyces cerevisiae*: REC-gene mutants and DNA-binding proteins. *Cold Spring Harbor Symposia on Quantitative Biology 49,* 41–48 (1984).
13. Esposito, M.S. Evidence that spontaneous mitotic recombination occurs at the two-

strand stage. *Proc. Natl. Acad. Science USA 75,* 4436–4440 (1978).
14. Symington, L.S., Morrison, P.T., and Kolodner, R. Genetic recombination catalyzed by cell-free extracts of *Saccharomyces cerevisiae. Cold Spring Harbor Symposia on Quantitative Biology 49,* 805–814 (1984).
15. Symington, L.S., Fogarty, L.M., and Kolodner, R. Genetic recombination of homologous plasmids catalyzed by cell-free extracts of *Saccharomyces cerevisiae. Cell 35,* 805–813 (1983).

THE *REC46* GENE OF *SACCHAROMYCES CEREVISIAE* CONTROLS MITOTIC CHROMOSOMAL STABILITY, RECOMBINATION AND SPORULATION: CELL-TYPE AND LIFE CYCLE STAGE SPECIFIC EXPRESSION OF THE *rec46-1* MUTATION

Dimitrios T. Maleas, Kathleen A. Bjornstad, Libby L. Holbrook, and Michael S. Esposito

Studies of chromosomal recombination during mitosis and meiosis of *Saccharomyces cerevisiae* have demonstrated that recombination at these two distinct stages of the yeast life cycle proceeds by mechanisms that appear similar bu. involve discrete mitosis-specific and meiosis-specific properties. We are employing *rec* mutants as a genetic tool to identify the partial reactions comprising recombination and the involvement of individual *REC* gene products in mitotic and meiotic recombination. The sequence of molecular events that results in genetic recombination in eukaryotes is presently ill-defined. Genetic characterization of *REC* gene mutants and biochemical analyses of them for discrete defects in DNA metabolic proteins and enzymes (in collaboration with the laboratory of Junko Hosoda) are beginning to remedy this gap in our knowledge.

In this report we summarize the genetic properties of the *rec46-1* mutation.

PROPERTIES OF THE *rec46-1* MUTANT

We have isolated a broad spectrum of ultraviolet light-induced hyperrecombination and hyporecombination mutants affecting spontaneous mitotic gene conversion and intergenic recombination of markers on chromosome VII in an n+1 *MATα* strain (LBL1, see Fig. 1 and Table 1) disomic for this chromosome.[1,2] Several of the *rec* mutations isolated, including *rec46-1*, exhibit analogous phenotypes with respect to *in-vitro* recombination between DNA plasmids catalyzed by mitotic cell-free extracts. The *rec46-1* mutation was chosen for further analysis since its hyperrecombinational phenotype both in vivo and *in vitro* is among the most extreme observed to date. In the experiments described below we have characterized *rec46-1* strains for mitotic chromosomal stability, mutability, intragenic recombination, intergenic recombination, sporulation, and *HO* directed interconversion of mating-type alleles. The genetic analysis of *rec46-1* demonstrates it to be a recessive mutation that enhances mitotic chromosomal loss and mitotic recombination. The hyperrecombinational activity of *rec46-1* has been observed in genetic intervals tested on three chromosomes (II, V, and VII). *MATa* and *MATα HO rec46-1* haploids are proficient in *HO* directed interconversion of mating type alleles and their survival is not detectably affected by presence of the *HO* gene. *MATa/MATα rec46-1/rec46-1* diploids are sporulation deficient and lose colony forming ability following exposure to sporulation medium, indicating that the *REC46* gene is essential for normal meiosis.[3]

The *rec46-1* mutation was recovered among survivors of ultraviolet light mutagenesis (65% survival) of the LBL1 n+1 hyperhaploid strain disomic for chromosome VII.[1,2] The LBL1 strain (Fig. 1) forms red colonies on both chemically defined and complex glucose nutrient media owing to the *ade2*

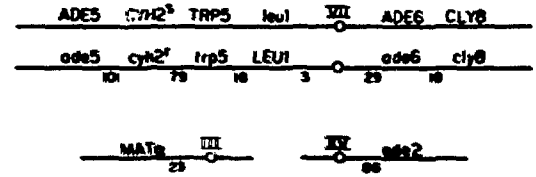

Fig. 1. Genotype of the chromosome VII disomic strain LBL1. The map distances shown are the standard meiotic values.

(KBL 824-3774)

Table 1. Spontaneous cycloheximide resistant mitotic segregants recovered on cycloheximide complete medium and leucineless-tryptophanless cycloheximide medium.

Strain	Colony Number	Plated on cycloheximide complete medium: White/ 10^3 cfu	Red/ 10^3 cfu	Total/ 10^3 cfu	Plated on leu⁻ trp⁻ cycloheximide medium: White/ 10^3cfu	Red/ 10^3 cfu	Total/ 10^3 cfu	cfu/colony $\times 10^{-6}$
Rec46	1	1,732	22	1,754	247	19	266	5.8
	2	2,152	4.3	2,156	283	11	294	5.8
	3	1,192	6.8	1,199	279	6.8	286	5.8
	4	2,465	9.1	2,474	244	9.2	253	4.6
	5	1,276	189	1,465	71	155	226	4.3
Median Frequency		1,732	9.1	1,754	247	11	266	
Rate			$1.73 \pm 0.82 \times 10^{-5}$	$1.69 \pm 0.48 \times 10^{-3}$	$2.88 \pm 0.16 \times 10^{-4}$	$1.73 \pm 0.82 \times 10^{-5}$		
LBL1[a] Median Frequency		14	0.54	16	1.4	0.86	2.7	
Rate			$1.45 \pm 0.77 \times 10^{-6}$	$2.44 \pm 0.47 \times 10^{-3}$	$3.30 \pm 0.81 \times 10^{-6}$	$2.08 \pm 0.59 \times 10^{-6}$		

[a]The values shown for the parental Rec⁺ strain, LBL1, are based upon previously published analyses of 25 2.5 mm colonies grown on synthetic complete medium at 24°C (Ref. 4).

LBL1 *MATα REC46* *ade5 met13-c cyh2ˢ trp5 LEU1 ade6 cly8*
ADE5 met13-d CYH2ˢ TRP5 leu1 ADE6 CLY8
his7-1 tyr1-2 lys2-2 ade2-1 ura3-1 CAN1ˢ

Rec46 *MATα rec46-1* *ade5 met13-c cyh2ˢ trp5 LEU1 ade6 cly8*
ADE5 met13-d CYH2ˢ TRP5 leu1 ADE6 CLY8
his7-1 tyr1-2 lys2-2 ade2-1 ura3-1 CAN1ˢ

mutation that confers adenine auxotrophy and accumulation of a cell-limited red pigment. The chromosome VII disomic pair is heterozygous at six loci distributed on both sides of the centromere (Fig. 1). The *trans* arrangement of markers at the *LEU1* and *TRP5* loci ensures maintenance of the disomic condition since rare haploid segregants (resulting from chromosomal loss or mitotic nondisjunction) are unable to grow on omission media lacking both leucine and tryptophan. Gene conversion of *CYH2ˢ* to *cyh2ʳ* and intergenic recombination in the interval *CYH2-TRP5* can be monitored selectively and simultaneously by plating cells on leucineless-tryptophanless cycloheximide medium. Gene conversion of *CYH2ˢ* to *cyh2ʳ* yields red cycloheximide resistant *cyh2ʳ/cyh2ʳ* disomic recombinants heterozygous at the other five chromosome VII loci and occurs at a rate of $1.7 \pm 0.70 \times 10^{-6}$/cell division in strain LBL1.[3] Intergenic recombination in the interval *CYH2-TRP5* results in white cycloheximide resistant *cyh2ʳ/cyh2ʳ* recombinants that are also homozygous for the *ade5* mutation. They form white colonies because the *ade5* mutation blocks red pigment formation. Such segregants are heterozygous at the four remaining chromosome VII marker loci and arise at a rate of $3.30 \pm 0.81 \times 10^{-6}$/cell division in strain LBL1.[4] The ensemble of mitotic events resulting cycloheximide resistant segregants including restitution of haploidy, intergenic recombination between the *CYH2* locus and the centromere of chromosome VII, and conversion of *CYH2ˢ* to *cyh2ʳ* can be recovered by plating cells on cycloheximide synthetic complete medium. Genetic analysis of cycloheximide resistant segregants recovered in this manner from strain LBL1 demonstrates that cycloheximide resistant restituted haploids exhibiting no detectable recombination on chromosome VII comprise 62% of all cycloheximide resistant segregants and arise at a rate of 1.37×10^{-5}/cell division.[4]

The *rec46-1* disomic strain yields cycloheximide resistant segregants at a rate per cell division that is approximately 50 times greater than that of the parental LBL1 strain. Conversion of *CYH2ˢ* to *cyh2ʳ* occurs at a rate approximately 10 times greater than in LBL1. Intergenic recombination in the interval *CYH2-TRP5* occurs at a rate approximately 100 times greater than in LBL1 (Table 1).

A sample of 100 white segregants from cycloheximide complete medium were characterized to determine the fraction of cycloheximide resistant segregants that had lost the *CYH2ˢ* bearing chromosome, i.e., *ade5 cyh2ʳ trp5 LEU1 ade6 cly8* restituted haploids. The white segregants were tested for growth at 36°C on YPD medium to

detect segregation of the temperature sensitive lethal *cly8*, growth on tryptophanless and leucineless media, and were mated with *MATa ade5* and *ade6* tester strains to monitor segregation of *ade5* and *ade6*. A total of 86/100 tested exhibited restitution of haploidy. These data indicate that restitution of haploidy in the *rec46-1* disomic strain occurs at a rate per chromosome per cell division of 1.45×10^{-3} (i.e., $1.69 \pm 0.48 \times 10^{-3} \times 0.86$) which is 100 times greater than that of the LBL1 strain (1.37×10^{-5} per chromosome per division).

MITOTIC RECOMBINATION IN *rec46-1/rec46-1 MATa/MATα* HYBRIDS

REC46/REC46, REC46/rec46-1/rec46-1 and *rec46-1/rec46-1* hybrids (RX38, RX26 and RX64, respectively, see Table 1) having chromosome VII genotypes that allow one to distinguish red Cyh^r gene convertants from while Leu$^+$ Trp$^+$ Cyh^r intergenic recombinants arising from recombination in the *CYH2 - TRP5* interval were analyzed further. The hybrids employed are also heteroallelic at *LYS2* and *HIS7* (chromosome II) and were employed to determine whether the *rec46-1* mutation enhances intragenic recombination of heteroalleles resulting in prototrophy. The mitotic rates/cell division of events resulting in red Leu$^+$ Trp$^+$ Cyh^r gene convertants, while Leu$^+$ Trp$^+$ Cyh^r intergenic recombinants, Can^r resistant segregants, Lys$^+$ prototrophs, and His$^+$ prototrophs are shown in Table 2. Red Leu$^+$ Trp$^+$ Cyh^r gene convertants and white Leu$^+$ Trp$^+$ Cyh^r intergenic recombinants occur in *MATa/MATα rec46-1/rec46-1* diploids (RX64) at rates that are only five-fold greater than those of *MATa/MATα REC46/REC46* diploids (RX38). Can^r segregants and total Cyh^r resistant segregants in *MATa/MATα rec46-1/rec46-1* diploids (RX64) occur at rates that are ten-fold higher than those of *MATa/MATα REC46/REC46* diploids (RX38).

Lys$^+$ and His$^+$ prototrophs are recovered 10 to 15 times more frequently from the *rec46-1/rec46-1* hybrid (RX64) than from the *REC46/REC46* (RX38) and *REC46/rec46-1* (RX26) hybrids (Table 2), indicating that the *rec46-1* mutation stimulates intragenic recombination resulting in prototrophy. We analyzed the lysine prototrophs recovered from each of the three hybrids to determine whether the *rec46-1* mutation confers mutator activity. The *ade2-1, lys2-1 and lys2-2* alleles are *ochre* nonsense mutations that are suppressed by dominant forward mutations, *sup*$^+$ to *SUP ochre*. The *SUP* mutants contain anticodon mutations of tyrosyl t-RNA genes that cause tyrosine to be inserted at the position of m-RNA *ochre* codons. Diploid *ade2-1/ade2-1* cells heterozygous for such *SUP* muta-

Table 2. Spontaneous mitotic gene conversion, intragenic recombination and intergenic recombination in REC46/REC46, REC46/rec46-1, and rec46-1/rec46-1, MATa/MATα hybrids.[a]

Genotype[b]	Hybrid	Median No. Red Leu$^+$Trp$^+$ Cyh^r/10^6 cfu	Median No. White Leu$^+$Trp$^+$ Cyh^r/10^6 cfu	Median No. Lys$^+$/ 10^7 cfu	Median No. His$^+$/ 10^7 cfu	Median No. Total Cyh^r/ 10^5 cfu	Median No. Can^r/ 10^5 cfu
REC46 REC46	RX38	7.2	44.6	15.4	10.0	8.8	34.4
	Rate	$2.14 \pm 0.80 \times 10^{-6}$	$7.46 \pm 2.36 \times 10^{-6}$	$9.56 \pm 3.78 \times 10^{-8}$	$1.24 \pm 0.47 \times 10^{-7}$	$1.83 \pm 0.50 \times 10^{-5}$	$5.94 \pm 1.38 \times 10^{-5}$
REC46 rec46-1	RX26	10.7	81.9	13.0	15.0	24.7	30.0
	Rate	$4.69 \pm 1.68 \times 10^{-6}$	$1.52 \pm 0.44 \times 10^{-5}$	$1.58 \pm 0.77 \times 10^{-7}$	$2.10 \pm 0.99 \times 10^{-7}$	$2.08 \pm 9.46 \times 10^{-5}$	$5.27 \pm 1.34 \times 10^{-5}$
rec46-1 rec46-1	RX64	70.9	640.5	102.5	165.0	99.2	473.2
	Rate	$7.83 \pm 2.76 \times 10^{-6}$	$7.63 \pm 1.72 \times 10^{-5}$	$1.34 \pm 0.06 \times 10^{-6}$	$2.14 \pm 0.09 \times 10^{-6}$	$1.11 \pm 0.24 \times 10^{-4}$	$4.10 \pm 1.39 \times 10^{-4}$

[a]Rates shown (±2 standard deviations) are based upon analysis of 15 2.5 mm colonies grown on synthetic complete medium and three liquid YPD cultures of each hybrid. *SUP* mutations that suppress *ade2-1, lys2-1, and lys2-2* resulting in white Ade$^+$Lys$^+$ colonies occur at the same rates in RX38 ($2.35 \pm 1.14 \times 10^{-8}$, RX26 ($3.12 \pm 1.89 \times 10^{-8}$, and RX64 ($4.63 \pm 3.11 \times 10^{-8}$).

[b]

RX38	MATa	REC46	ADE5	met13-d	CYH2	TRP5	leu1	ADE6	CLY8	his7-2	lys1-1	lys2-1	ade2-1	ura3-1	can1^r
	MATα	REC46	ade5	met13-c	cyh2^r	trp5	LEU1	ade6	cly8	his7-1	lys1-2	lys2-2	ade2-1	ura3-1	CAN1^s
RX26	MATa	REC46	ADE5	met13-d	CYH2	TRP5	leu1	ADE6	CLY8	his7-2	lys1-1	lys2-1	ade2-1	ura3-1	can1^r
	MATα	rec46-1	ade5	met13-c	cyh2^r	trp5	LEU1	ade6	cly8	his7-1	lys1-2	lys2-2	ade2-1	ura3-1	CAN1^s
RX64	MATa	rec46-1	ADE5	met13-d	CYH2	TRP5	leu1	ADE6	cly8	his7-2	lys1-1	lys2-1	ade2-1	ura3-1	can1^r
	MATα	rec46-1	ade5	met13-c	cyh2^r	trp5	LEU1	ade6	cly8	his7-1	lys1-2	lys2-2	ade2-1	ura3-1	CAN1^s

tions fail to accumulate the red pigment normally accumulated by *ade2-1* strains and grow slowly on adenineless medium. The very same suppressors fully restore lysine prototrophy in *lys2-1/lys2-2* heteroallelic diploids, and are readily detected as white Lys$^+$ colonies that exhibit partial restoration to adenine prototrophy. Suppressor mutations of this type account for approximately 20% of the events resulting in Lys$^+$ segregants of the *lys2-1/lys2-2* heteroallelic control *MATa/MATα REC46/REC46* hybrid (Table 2). The *rec46-1/rec46-1* diploid does not exhibit mutator activity for this class of mutations.

SPORULATION DEFICIENCY OF *rec46-1/rec46-1* DIPLOIDS

Diploids homozygous for the *rec46-1* mutation exhibit very low levels of sporulation when compared with coisogenic *REC46/REC46* and *REC46/rec46-1* controls (Table 3). Exposure of *rec46-1/rec46-1* diploids to sporulation medium eventually results in death of both nonsporulated and sporulated cells. These results indicate that the *REC46* gene is essential for sporulation (meiosis and ascospore formation).

HOMOTHALLIC INTERCONVERSION OF MATING TYPE ALLELES BY *rec46-1 HO* MEIOTIC SEGREGANTS

The *MATα rec46-1* haploid test strain, a heterothallic *ho* haploid, was mated with ascospores of a homothallic (*HO/HO*) diploid strain. The resultant hybrid was sporulated at 24°C and tetrads were analyzed to monitor segregation of the *rec46-1* mutation and *HO* directed interconversion of mating type alleles among *rec46-1 HO* meiotic segregants. *HO* ascosporal colonies consisting primarily of *MATa/MATα HO/HO* diploids were recognized by their failure to mate with heterothallic haploid *MATa* and *MATα* test strains. Heterothallic *ho MATa* and *MATα* ascosporal colonies were recognized by their ability to mate with heterothallic test strains of opposite mating type. A total of 53 tetrads in which all four spores survived were analyzed. There were two *MATa/MATα HO/HO* diploidized ascosporal colonies per tetrad: 43 were *MATa/MATα, rec46-1/rec46-1, HO/HO* and 63 were *MATa/MATα, REC46/REC46, HO/HO.* The *rec46-1* mutation thus does not block *HO* directed interconversion of mating type alleles.

Table 3. Sporulation deficiency of rec46-1/rec46-1 hybrids.

Hybrid	Genotype	% Four and three-spored asci	% Two and one-spored asci	% Non-sporulated cells	Total % asci
RX38	*REC46* REC46	72.2	19.5	8.3	91.7
RX62	*REC46* rec46-1	72.8	16.6	10.6	89.4
RX66	*REC46* rec46-1	87.4	5.8	6.8	93.2
RX67	*REC46* rec46-1	76.1	19.4	4.5	95.5
RX68	*REC46* rec46-1	80.5	12.5	7.0	93.0
RX61	*rec46-1* rec46-1	1.0	0.7	98.3	1.7
RX63	*rec46-1* rec46-1	0.5	0.9	98.6	1.4
RX64	*rec46-1* rec46-1	2.2	1.8	96.0	4.0
RX65	*rec46-1* rec46-1	0.3	3.5	96.2	3.8

The data presented above demonstrate that the *REC46* gene controls mitotic chromosomal stability, gene conversion, intragenic recombination, and intergenic recombination. The chromosomal instability and hyperrecombinational phenotype exhibited by *rec46-1* strains suggests that the *REC46* gene product modulates recombination and prevents accumulation of DNA damage leading to chromosomal loss. This interpretation of the function of the *REC46* gene product is consistent with the observation that *rec46-1* strains exhibit enhanced sensitivity to killing by x rays and ultraviolet light and are defective in meiosis.[2]

The phenotypes of *MATα rec46-1* n+1 chromosome VII disomics and *MATa/MATα rec46-1/rec46-1* diploids differ significantly. Both exhibit a five- to ten-fold enhancement of the rate of mitotic gene conversional events. In contrast, the *MATα rec46-1* n+1 chromosome VII disomic exhibits a one-hundred-fold enhancement in the rates of intergenic recombination and restitution of haploidy while *MATa/MATα rec46-1/rec46-1* diploids exhibit only a ten-fold enhancement of the rate of intergenic recombination and no evidence of mitotic chromosomal loss resulting in 2n-1 monosomic segregants.

Previous studies have demonstrated that *MATa/MATα* cells are more resistant to the killing effects of x rays than are *MATa/MATa* and *MATα/MATα* diploids, and thus *MATa/MATα* diploids may possess a pathway for repair of x-ray damage that is not present in *MATa* and *MATα* haploids or in *MATa/MATa* and *MATα/MATα* diploids. Operation of this pathway in *MATa/MATα rec46-1/rec46-1* diploids may result in repair of the class of prerecombinational lesions, e.g., double strand breaks, that result in chromosomal loss and high levels of intergenic recombination in *MATα rec46-1* n+1 chromosome VII disomics. Persisting prerecombinational lesions may account for the ten-fold enhancement in the spontaneous rate of gene conversion, intragenic recombination, and intergenic recombination exhibited by *MATa/MATα rec46-1/rec46-1* hybrids. Tests of this hypothesis are in progress.

REFERENCES

1. Esposito, M.S. Molecular mechanisms of recombination in *Saccharomyces cerevisiae*; Testing mitotic and meiotic models by analysis of hypo-rec and hyper-rec mutations. In *Controlling Events in Meiosis*, C.W. Evans, H.G. Dickinson, Eds., *Soc. Exptl. Biol. Symp.*, The Company of Biologists Ltd. Scarborough, North Yorkshire, *38*, pp. 123 (1984).
2. Esposito, M.S., Hosoda, J., Golin J., Moise, H., Bjornstad, K., and Maleas, D. Recombination in *Saccharomyces cerevisiae: REC* gene mutants and DNA-binding proteins. *Cold Spring Symp. Quant. Biol. 49*, 41-48 (1984).
3. Esposito, M.S., Maleas, D.T., Bjornstad, K.A., and Holbrook, L.L. The *REC46* gene of *Saccharomyces cerevisiae* controls mitotic chromosomal stability, recombination and sporulation: cell-type and life cycle stage-specific expression of the *rec46-1* mutation. *Curr. Genet.* in press (1986).
4. Esposito, M.S., Maleas, D.T., Bjornstad, K.A., and Bruschi, C.V. Simultaneous detection of changes in chromosome number, gene conversion, and intergenic recombination during mitosis of *Saccharomyces cerevisiae*: Spontaneous and ultraviolet light induced events. *Curr. Genet. 6*, 5–11 (1982).

THE GENETIC MAP OF YEAST AND THE GENEALOGY OF LABORATORY STRAINS

Robert K. Mortimer, David Schild, John R. Johnston, and Rebecca Contopoulou

The yeast *Saccharomyces cerevisiae* is currently widely used for biochemical, molecular and genetic research. Besides its traditional importance in the baking and brewing industries, it is increasingly being used for industrial production of recombinant DNA products. The ease by which this yeast can be genetically and molecularly manipulated, coupled with its extensive genetic map, have made it particularly suitable for use in both research and industry. During the past year we have been involved in several areas of yeast research, the goals of which are to improve yeast as a general organism for study. These areas include collating and publishing a new edition of the yeast genetic

map, developing a new mapping method for yeast, constructing a detailed genealogy of many commonly used laboratory strains, and maintaining the Yeast Genetic Stock Center.

Genetic maps of many organisms have been constructed and are frequently being updated as more genes are studied and mapped. The yeast *Saccharomyces cerevisiae* has one of the most extensive maps with over 500 genes mapped. This map is useful in many ways, including 1) estimating the number of chromosomes, since they cannot be reproducibly counted by cytological means, 2) determining that most functionally related genes are not clustered, and 3) examining whether two mutations with different phenotypes are alleles of a pleiotropic gene. In the area of yeast recombinant DNA, genetic mapping has recently gained significance both in cloning genes or regions of the genome by chromosome walking from a closely mapped gene, and in determining that a particular gene has been cloned.

The new recently published genetic map of *Saccharomyces cerevisiae*[1] describes the location of 568 genes distributed over 16 metacentric chromosomes plus a single gene, *KRB1*, located on a seventeenth chromosome (Fig. 1). Since our last major review in 1980, 251 genes have been added to the genetic map. In addition, several linkages that had been established only by mitotic or aneuploid analyses have been confirmed by tetrad analysis. Only chromosomes VIII, IX, X, XI, XII, and XVI remain with regions not confirmed by tetrad analysis. Assuming a minimum of 100 cM for these regions, the total minimum length of the yeast map is now 4500 cM, which is 100 cM less than our estimate made five years ago. This, and the fact that the total number of mapped genes has increased by 79% argues that the current lengths of the yeast chromosomes are close to their actual lengths.

Mapping in *S. cerevisiae* has proved more complex than in most genetically studied organisms because of the high level of meiotic recombination (> 100 crossover events per meiosis) and the large number of chromosomes. Several methods, have been developed to simplify mapping in yeast and recently several new methods based on chromosome loss, non-disjunction and chromosome transfer have been reported. We have developed a method based on chromosome loss in diploid strains homozygous for a mutation (*rad52*) involved in DNA repair.

Saccharomyces cerevisiae diploids homozygous for the *rad52-1* mutation have previously been shown in our laboratory to lose chromosomes mitotically. Spontaneous events and events following low levels of x-ray or methyl-methanesulfonate treatment result in monosomic diploids, while higher levels of treatment result in near haploidization. This *rad52-1* dependent chromosome loss has been used to develop a new mapping method[2] which can be used to assign a previously unmapped gene to a chromosome. This mapping method and subsequent tetrad analyses have been used to locate *hom6* on chromosome X, *ade4* on chromosome XIII, and *cdc31* on chromosome XV, and to demonstrate that *met5*, previously assigned to chromosome V, actually maps to chromosome X; the met$^-$ marker on chromosome V has been shown to be *met6*. *GAL80 and SUP5*, previously assigned to an unmapped fragment, have now been mapped to the right arm of chromosome XIII.

The recent explosion of interest in the genetics and molecular biology of the yeast *Saccharomyces cerevisiae* has resulted in rapid expansion of our knowledge of this organism. Several lines of evidence have recently shown various heterogeneities among strains in, for example, the distribution of restriction sites, in position and numbers of transposable elements, and in chromosome polymorphisms. To assess the relative contributions to these heterogeneities from recent events, as opposed to differences introduced in the development of the initial breeding stocks, we have developed a pedigree of some of the most common laboratory strains.[3]

We have constructed a genealogy of strain S288C, from which many of the mutant and segregant strains currently used in studies on the genetics and molecular biology of *Saccharomyces cerevisiae* have been derived. We have determined that its six progenitor strains were EM93 (Mrak), EM126 (Mrak), NRRL-210 (Wickerhan) and the three baking strains Yeast Foam, FLD, and LK. We have estimated that approximately 88% of the gene pool of S288C is contributed by strain EM93. The principal ancestral genotypes were those of segregant strains EM93-1C and EM93-3B initially distributed by C.C. Lindegren to several laboratories. We have analyzed an isolate of a lypholized culture of strain EM93 and determined its genotype as *MATa/MATα SUC2/SUC2 gal2/GAL2 mal/mal mel/mel CUP1/cup1 FLO1/flo1*. Strain EM93 is therefore the probable origin of genes *SUC2, gal2, CUP1* and *flo1* of S288C. We give details of the current availability of several of the progenitor strains and propose that this genealogy should assist in elucidating the origins of several types of genetic and molecular heterogeneities in *Saccharomyces*.

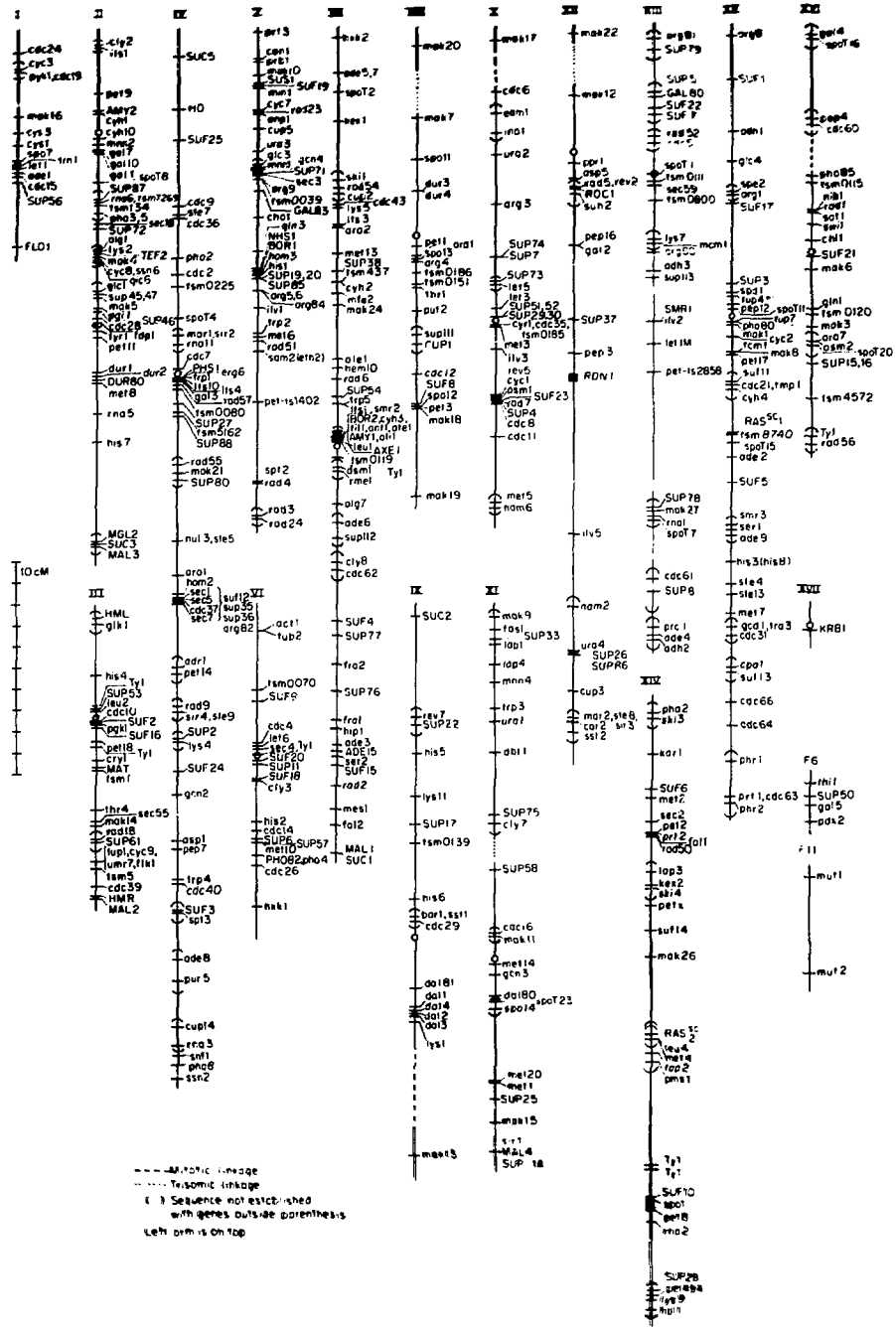

Fig. 1. *Genetic map of Saccharomyces cerevisiae (compiled by Robert K. Mortimer and David Schild).*

(RBL 829-4132C)

Our laboratory maintains the Yeast Genetic Stock Center, which tests, stores, and sends out strains of *Saccharomyces cerevisiae*. The current collection contains approximately 700 different strains, 100 of which have been added during the last year, and over 1000 strains a year are sent out. These strains are distributed to both academic institutions (~80%) and industries (~20%), throughout the world (~40% to foreign countries). The fifth edition of the Yeast Genetic Stock Center Catalogue was issued in 1984.[4]

REFERENCES

1. Mortimer, R.K., and Schild, D. Genetic map of *Saccharomyces cerevisiae*, Edition 9. *Microbiol. Rev. 49*, 181–213 (1985).
2. Schild, D., and Mortimer, R.K. A mapping method for *Saccharomyces cerevisiae* using *rad52*-induced chromosome loss. *Genetics 110*, 569–589 (1985).
3. Mortimer, R.K., and Johnston, J.R. Genealogy of principal strains of the yeast genetic stock center. *Genetics*—in press.
4. Mortimer, R.K., and Contopoulou, R. *Yeast Genetic Stock Center Catalogue*, Fifth Edition (1984), Department of Biophysics and Medical Physics, UC Berkeley.

ISOLATION AND MOLECULAR CHARACTERIZATION OF YEAST DNA REPAIR GENES AND THE USE OF A NEW GEL SYSTEM TO STUDY DNA REPAIR

Robert Mortimer, John Game, David Schild, Mari Aker, Gary Cole, Rebecca Contopoulou, Vincent Cook, Minh Dang, Leslie Kay, Susan Lovett, and Karen Sitney

STUDY OF DNA REPAIR GENES

We have previously reported the isolation and characterization of several genes involved in the recombinational repair of DNA damage in yeast. Mutations in these genes, *RAD50* to *RAD57*, result in sensitivity to ionizing radiations, recombination deficiencies, and meiotic problems. These studies have shown that 1) the size of some of these genes are: *RAD51* – 1.4 kb, *RAD52* – 1.6 kb, *RAD54* – 2.8 kb, *RAD55* –1.5 kb. Disruptions of several of these genes have been isolated (*RAD51, RAD52, RAD54, RAD55* and *RAD57*) and since these null alleles are viable, it demonstrates that none of these genes code for essential functions. The null alleles have also allowed us to more accurately determine the phenotypes of mutations in these genes. For example, using a null allele *RAD54* we have recently shown that this gene is necessary for meiosis; previous studies using a leaky mutation in *RAD54* indicated incorrectly that this gene played no major role during meiosis. Null alleles of *RAD57* have been shown to have much stronger effects on DNA repair at 23°C than at 30° or 36°C, demonstrating that this gene is normally necessary for repair primarily at lower temperatures; similar results were reported last year for *RAD55*.

To characterize these genes better at the molecular level, we are continuing to sequence the cloned genes. We have established the DNA sequence of *RAD54* and have determined most of the sequences of *RAD51* and *RAD55*. *RAD52* has been sequenced by another group. We are examining the 5′ sequences of these and other repair genes for possible common promoter sequences.

Using the cloned genes we are now determining whether any of these genes are inducible. Using both quantitative Northern hybridization and studies of lacZ-fusions with these genes, we have determined that *RAD54* is induced by DNA damage but that *RAD52* is not inducible. The *RAD54* gene has been found to be induced both by x rays and uv light, but not by heat shock. *RAD54* has also been found to be highly inducible by entry of cells into meiosis. Preliminary experiments indicate that *RAD51* also is inducible and experiments are underway to confirm this and to determine which, if any, of the other genes in this group are inducible.

In addition to the *RAD50* to *RAD57* genes, we have worked on another gene involved in x-ray repair in yeast that is in a different *rad* mutant series and is designated *RAD24*. The *RAD24* gene has been cloned and its map position on chromosome V has been more precisely defined. The only known mutant in this gene confers uv- and x-ray

sensitivity and blocks the cell's ability to undergo meiosis. The gene is very closely linked to another *RAD* gene (*RAD3*) on chromosome V, and we have determined both the order of these two genes on the chromosome, and the genetic distance between them. Using Southern hybridization and genetic complementation tests we have confirmed that the two loci are separate and do not overlap. The original *RAD24* clone has been subcloned and gene activity is conferred by an approximately 3-kb fragment, which has itself been subcloned into an M13-related vector suitable for DNA sequencing. In addition, the plasmid-encoded *RAD24* gene has been disrupted *in vitro* and will shortly be used to transform wild-type cells to make *RAD24* deletion mutants for biological characterization.

ORTHOGONAL FIELD ALTERNATING GEL ELECTROPHORESIS (OFAGE) FOR STUDYING DOUBLE STRAND BREAK REPAIR

One of the major effects of ionizing radiation on the chromosomes of cells is the induction of DNA double strand breaks. These breaks result in chromosome aberrations and very frequently in cell death. The standard procedures for assaying double strand breaks have been through the use of neutral sucrose gradients and neutral elution procedures. These methods, while informative, yield only average information about the effects on the DNA complex of an organism. They record a decrease in a average molecular weight and, if repairs occur, a corresponding increase in molecular weight. Recently, a procedure has been developed for electrophoretically separating individual yeast chromosomes (200–2000 kb) based on alternating field orthogonal gel electrophoresis,[1] and we have adapted this new technique for studying double-strand break repair and chromosome rearrangements (Fig. 1). We have shown that a dose of x rays (48,000 rad) decreases the intensity of individual chromosome bands due to breakage; the relative decrease increases with chromosome size. The fragments produced by chromosome breakage appear as a broad smear in the 100kb-1000kb region. The distribution of fragments agrees very well with target theory predictions about breakage of the different chromosomes. If a period of repair is allowed before assay, wild-type cells show a return to a near normal distribution of chromosome intensities. However, three x-ray sensitive mutants, *RAD51, RAD52, and RAD54,* failed to repair the damage and, in fact, degraded the broken fragments. We are currently further adapting the OFAGE technique for studying double strand break repair in mammalian cells.

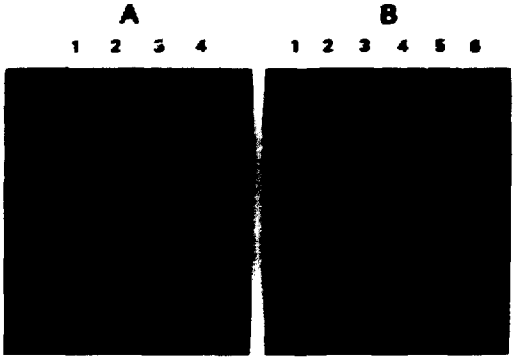

Fig. 1. *(A) Effect of irradiating wild type diploid cells with 48 krad and allowing for repair at 30°C; samples:*
1. 0 krad, t - 0,
2. 48 krad, t = 0,
3. 48 krad, t = 5 hr,
4. 0 krad, t = 5 hr.
(B) Effect of irradiating rad54-3 mutant dipoid cells with 48 krad and allowing for repair at 23°C and at 36°C; (rad54-3 mutants are sensitive to x rays at 36°C, but less so at 23°C). Samples:
1. 0 krad, t = 0,
2. 48 krad, t = 0,
3. 0 krad, t = 5 hr, 23°C,
4. 48 krad, t = 5 hr, 23°C,
5. 0 krad, t = 5 hr, 36°C,
6. 48 krad, t = 5 hr, 36°C. *(XBL 850-10247)*

REFERENCE

1. Carle, G.F., and Olson, M.V. An electrophoretic karyotype for yeast. *Proc. Natl. Acad. Sci. (USA) 82,* 3756–3760 (1985).

ISOLATION OF DNA FRAGMENTS CONTAINING REPLICATION FORKS BY TWO DIMENSIONAL AGAROSE GEL ELECTROPHORESIS

Priscilla K. Cooper and Vincent Ling

The fundamental goal of our research program is to understand on a molecular level the interaction between DNA repair processes that promote survival after damage and other processes that affect mutation resulting from such damage. In *Escherichia coli*, and probably in eucaryotic cells as well, the mutagenic or lethal consequences of any particular lesion in DNA depend on cellular processing of that lesion. Our particular interest is in those processes in *E. coli* that are facets of regulatory networks of genes induced by the damage itself, especially the SOS regulatory network, which is induced by a variety of DNA-damaging treatments that interfere with replication, and the adaptive response, which is induced by DNA damage from exposure to chemical alkylating agents.

Our previous work has identified and characterized on SOS-regulated inducible repair process, long patch excision repair, and suggested that it may be the primary process effecting resistance both to uv irradiation and to alkylation damage. We are currently investigating the nature of the small fraction of damage sites where long patch repair occurs as one approach to understanding the means by which inducible processes promote survival. Results of a variety of experiments have suggested that one requirement for the induced long patch process may be in repair of lesions introduced in the vicinity of DNA replication forks. In principle, such lesions would be expected to pose special problems for the constitutive excision repair process because of the unwinding and separation of the complementary strands. In order to test the hypothesis that the induced excision repair process *is* able to effectively repair such lesions, a method is required that would allow resolution of DNA fragments containing replication forks from the rest of the genome. We have recently developed such a technique, which is described here.

Two-dimensional agarose gel electrophoresis has previously been used to separate branched DNA molecules arising as intermediates in recombination from linear forms of DNA.[1] The separation is based on the fact that the mobility of branched structures in agarose differs from that of linear double-stranded molecules as a function of voltage and gel concentration. In principle this altered mobility should be true for three-armed replication forks as well as for model X structures. However, the situation is more complex when analyzing genomic DNA for replication forks, since the forks will exist randomly throughout the genome, i.e., they will be contained in DNA fragments of a range of molecular weights. In addition, any given DNA fragment can be expected to have varying amounts of fork structure depending on how far the replication fork has traversed through that segment of DNA at the time of isolation. A further complication is that replication forks from a variety of sources have been shown to possess varying degrees of single-stranded character. Since single-stranded DNA has higher mobility in agarose than native DNA but a branched structure should retard migration, the expected behavior of replicating DNA during electrophoresis is not entirely obvious from *a priori* considerations. Nevertheless, we have succeeded in adapting the two-dimensional gel technique to achieve resolution of nascent DNA as an arc, identified by the autoradiographic detection of a pulse label, distinct from the arc containing the bulk of the DNA.

The technique we are using is as follows. Exponentially growing cells are briefly labeled with a high specific activity of ^{3}H-thymidine and either harvested immediately into ice-cold "stop mix" or filtered to remove the label and then grown for a period in unlabeled medium before harvesting. The cells are washed, lysed, digested with proteinase K, and the DNA is purified by phenol extraction followed by chloroform-isoamyl alcohol and ether extractions. The DNA is then restricted to completion with Eco RI and electrophoresed through a 0.3% or 0.7% agarose horizontal slab gel at 1 V/cm. The lanes are excised and each is set into a second dimension gel of 1.5% agarose with 0.5 μg/ml of ethidium bromide and electrophoresed at 2 V/cm. After photographing, the gels are immersed in a fluorographic enhancer, dried, and autoradiograms are prepared from them.

Figure 1 is a photograph of the ethidium fluorescence in the first and second dimension gels, with a ladder of molecular weight markers run in the first dimension shown at the top of the photograph. As can be seen from the ethidium fluorescence in the second dimension gel, the bulk of the DNA migrates in a single arc. However, the autoradiogram of the DNA from cells harvested immediately after pulse labeling (Fig. 2A) reveals that a

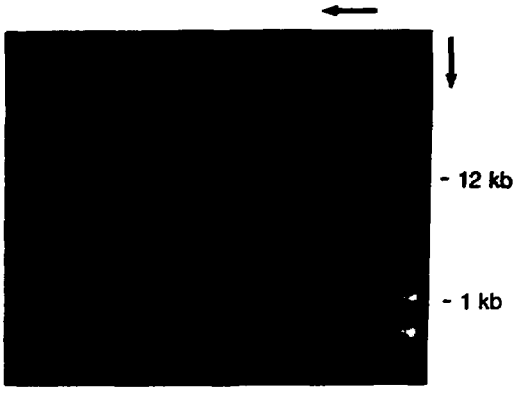

Fig. 1. *Ethidium fluorescence of Eco RI restricted genomic DNA of E. coli electrophoresed in first and second dimension agarose gels as described in text. Top lane: size markers in the first dimension.* *(XBB 850-9933)*

large proportion of the radioactive label is contained in a second arc of DNA, invisible by ethidium fluorescence and therefore representing a very small proportion of the total genomic DNA. This second arc must be derived from replicating DNA, since interposing a period of growth in unlabeled medium between the pulse label and the harvest causes essentially all of the radioactive label to "chase" into the main arc (Fig. 2B). In fact, even inadequate stopping conditions prevent visualization of the second arc, emphasizing its nascent nature. We have reproducibly obtained the second arc from a number of different DNA preparations and after restriction with a variety of different enzymes having six-base recognition sequences, and also after restriction with Dph I, which cuts at fully methylated GATC sequences. In addition, various combinations of altering gel concentration and voltage between the two dimensions have allowed resolution of the nascent DNA.

Visual inspection of the relationship between the two arcs suggests that the nascent DNA has a higher mobility than the main arc. In fact, reconstruction experiments using heat-denatured restriction digests of labeled DNA have shown that the second arc migrates with single-stranded DNA, and digestion with S1 nuclease prior to electrophoresis removes the second arc. There are two possible interpretations of these findings: 1) the arc of nascent DNA is composed of single-stranded fragments arising from disruption of replication forks during purification; or 2) it includes replication forks having single-stranded regions, and the mobility of a large proportion of the material in it results from the combination of effects of branched structure and of single-strandedness. The apparent size distribution of the DNA in the second arc, which includes material migrating even more slowly than a single-stranded 23-kb fragment, is very difficult to

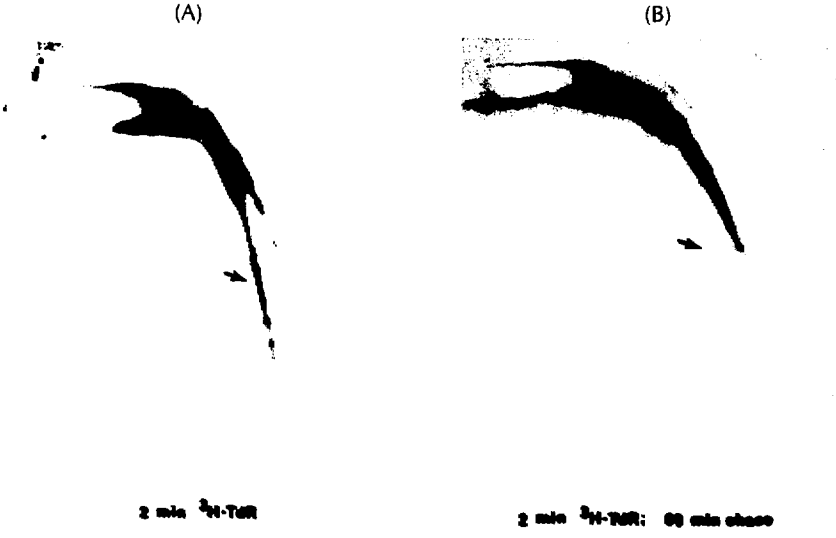

Fig. 2. *Autoradiograms of second dimension gels of (A) DNA from pulse-labeled sample and (B) DNA from pulse-labeled and "chased" sample.* *(XBB 850-9934)*

reconcile with the first interpretation. Indeed, as would be predicted if the second possibility were correct, after S1 digestion at least a portion of the label from the nascent DNA is transferred to the main arc rather than disappearing. Moreover, the second arc persists after digestion with a single-strand exonuclease (exonuclease I), as would be expected if at least some of the single-stranded regions are internal to double-stranded structures. We have also employed binding to nitrocellulose filters as a sensitive means of detecting small single-stranded regions in DNA to further assess the structure of the nascent DNA. While 20–25% of the pulse label in the restricted DNA sample is single-stranded by the criterion of sensitivity to digestion by S1 nuclease, we find that this relatively small fraction of the newly synthesized DNA that is single-stranded results in retention on nitrocellulose of 60–65% of the pulse label. This result confirms the interpretation that the S1-sensitive nascent DNA represents single-stranded regions covalently attached to predominantly double-stranded structures of newly synthesized DNA rather than consisting of single-stranded fragments.

Analysis by electron microscopy of the structure of replication forks in a variety of systems ranging from bacteriophage lambda to *Drosophila* cleavage nuclei has established the frequent occurrence of single-stranded connections both at branch points and on daughter arms but distal to the branch point. Types of structures observed are illustrated in the diagram of Fig. 3, taken from Kriegstein and Hogness.[2] Structures B and C, in which a single-stranded "whisker" protrudes from the fork, are presumed to arise by branch migration of structure A. In order to allow EM verification of the structure of the nascent DNA that we are resolving electrophoretically, we have taken advantage of the preferential binding to nitrocellulose of the nascent DNA fraction to enrich our DNA restriction digest for pulse-labeled DNA. The restricted pulse-labeled DNA that bound to nitrocellulose under high salt conditions was eluted, dialyzed, and concentrated, and a portion of it was analyzed by two-dimensional gel electrophoresis as described. After the enrichment procedure, *all* of the labeled DNA was found to migrate in the position of the arc of nascent DNA. Another portion of the enriched DNA was examined by electron microscopy, with restricted genomic DNA (i.e., not enriched for nascent structures by filter binding) serving as a control comparison. Figure 4 shows representative examples of the types of forked molecules seen with much higher frequency in the enriched sample than in the control; these are analogous to the structures diagrammed in Fig. 3.

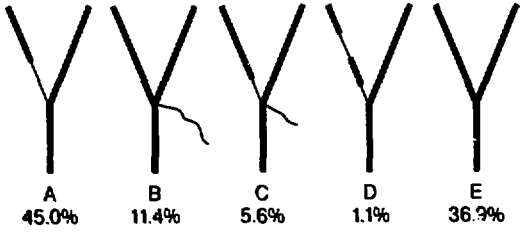

Taken together, these results make it clear that the two-dimensional gel system that we have developed does resolve DNA replication forks from linear DNA fragments. We now plan to apply this technique to testing the hypothesis that induced long patch repair occurs in replicating DNA. The technique will also allow us to directly determine the fate after DNA damage of pre-existing replication forks in both SOS induced and noninduced cells, thus providing a test of the model that induction enhances postdamage replication ability by promoting release of blocked forks. When combined with enrichment of the starting DNA preparation for nascent structures followed by hybridization of the electrophoretically isolated replicating DNA with appropriate cloned probe DNAs, this technique will also allow us to detect the replication of specific genes under a variety of circumstances.

Fig. 3. *Classes of replication forks observed in previous work in a variety of systems ranging from bacteriophage lambda to Drosophila. Frequencies are from Kriegstein and Hogness.[2]*
(XBL 8511-8594)

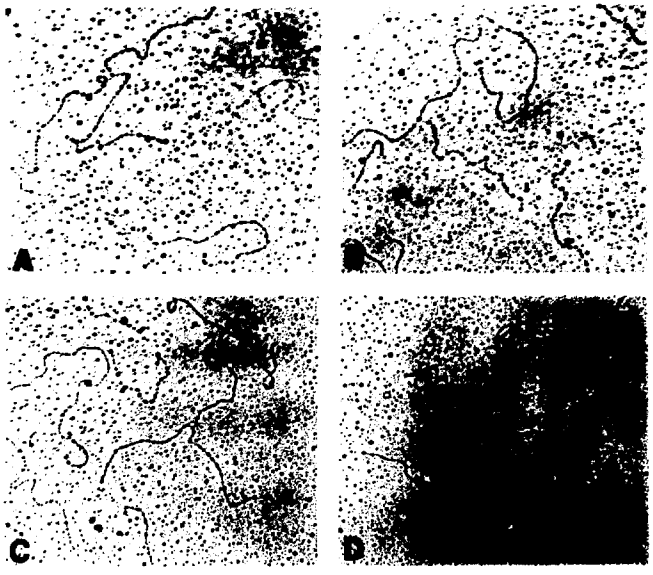

Fig. 4. Representative electron micrographs of replication forks observed in DNA migrating in the position of the pulse label in the autoradiogram of Fig. 2A. Structures shown are: (a) all or nearly all double-stranded; (b) single-stranded arm; (c) single-stranded connection at the fork; and (d) all double-stranded but with single-stranded "whisker." (XBB 8512-9911A)

REFERENCES

1. Bell, L., and Byers, B. Anal. Biochem. *130*: 527–535 (1983).

2. Kriegstein, H., and Hogness, D. *Proc. Natl. Acad. Sci. USA 71*, 135–139 (1974).

ALKYLATION OF POLYNUCLEOTIDES *IN VITRO* AND *IN VIVO*

Bea A. Singer, Sylvia J. Spengler, Frank Chavez, and Heinz Fraenkel-Conrat

The work done under this grant for the last 15 years has explored multiple aspects of how simple non-metabolically activated animal (and human) carcinogens exert their biological effects. We found that all nitrogens and oxygens can react, to varying extents, in model systems, in human cells in culture, and in whole animals.[1,2] Subsequent work has investigated not only the formation of the 13 possible adducts and 16 possible phosphotriesters, but also their persistence, mechanisms of repair, and mutagenic potential.

This report of work at LBL since April 1985 focuses on the effect of a series of O^4-alkylthymidines on the extent and fidelity of replication using *E. coli* DNA polymerase I (Pol I) under conditions that enhance rather than diminish fidelity.

We originally proposed, based on data of DNA from ethylnitrosourea-treated rats, that O^4-ethyl dT was likely to be an initiating event in carcinogenesis.[2] More recently, work from the Swedberg Laboratory[3,4] has indicated the persistence of both

O^4-methyl dT and O^4-ethyl dT as implicated in the initiation of hepatocellular tumors from animals treated with similar carcinogens.

We synthesized the deoxynucleoside triphosphates with methyl, ethyl, or isotropyl groups on the O^4 of thymidine. Using a poly(dA-dT) template as a model for B-form DNA, or activated DNA as a template, we found that all three alkyl-dTTPs could substitute for dTTP to a high extent when dTTP was present. Extensive synthesis occurred, although the rate was slower than when dATP and dTTP were used with Pol I alone. The synthesized poly(dA-dT,O^4-alkyl dT) polymers were then used as templates for misincorporation studies. In contrast to the level of misincorporation directed by Pol I from poly(dA-dT), which was 1 dG/80,000 nucleotides synthesized, the polymers containing O^4-alkyl dT caused misincorporation ranging from 1 dG/600 nucleotides (methyl) to 1 dG/5000 nucleotides (isopropyl).[5]

The next question was how effective were the O^4-alkyl dTTPs in the absence of any other source of dTTP. Both the rate of polymer elongation and the K_ms were examined, and it was found that the size of the alkyl group played a major role. The rates at three temperatures and the K_m data are shown in Figs. 1 and 2.

The temperature studies were undertaken to test whether the early termination of synthesis shown in Fig. 1(a) could be due to the formation of a frayed and ineffective 3'-OH primer terminus. If this were true, then lower temperatures of synthesis should favor stabilization of the terminus and allow synthesis to proceed further. This was, in fact, the case, since at 0°–10° the relative extent of synthesis with the O^4-derivatives was significantly higher than at 30°–40°. The high K_m values for the alkyl triphosphates indicated that they would not complete well with dTTP. Thus, the effect of this type of adduct is likely to arise from formation of the specific adduct in DNA rather than incorporation of a carcinogen-modified dTTP from the nucleotide pool.

We have also constructed a model for the probable structure of DNA that permits the insertion of the modified dTs opposite dA while apparently maintaining the normal structure and appropriate energy of the helix (Fig. 3). This propped-open structure which allows formation of a single hydrogen bond is suggested to explain proton nmr data on O^4 exchange rates.[6]

Another plan designed to test the effect of O^4-lkyl dTTPs in a biological system is a cooperative project with Dr. L. Loeb in the Department of

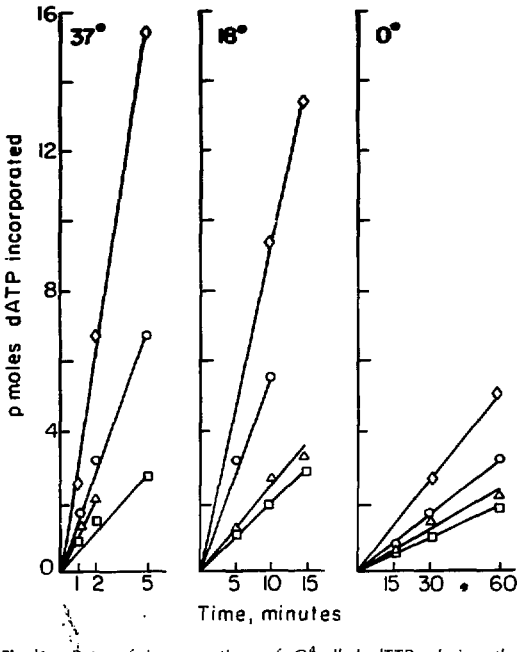

Fig. 1. Rate of incorporation of O^4-alkyl dTTPs during the linear portion of synthesis by Pol I at (a) 37°, (b) 18°, and (c) 0°. ◇, dTTP; ○, m^4dTTP; △, e^4dTTP; □, ipr^{4}dTTP. The level of incorporation in the absence of any dTTP has been substracted from these points. (XBL 8510-8528)

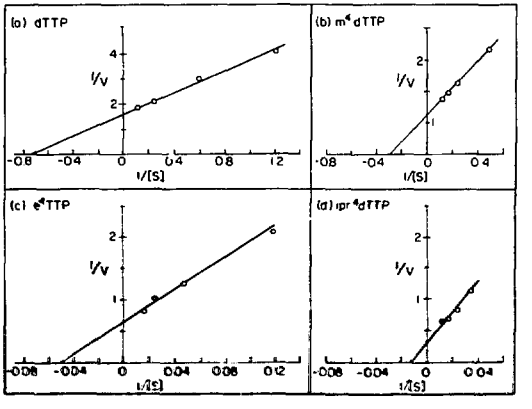

Fig. 2. K_m for (a) dTTP, (b) m^4dTTP, (c) e^4dTTP and (d) ipr^{4}dTTP were determined using poly(dA-dT) and Pol I. The Lineweaver-Burk plot is shown, although intercepts were determined by the direct linear plot of Eisenthal and Cornish-Bowden. Units: 1/V, mm/10^{-12} moles; 1/S, 10^6 M. (XBL 8510-8529)

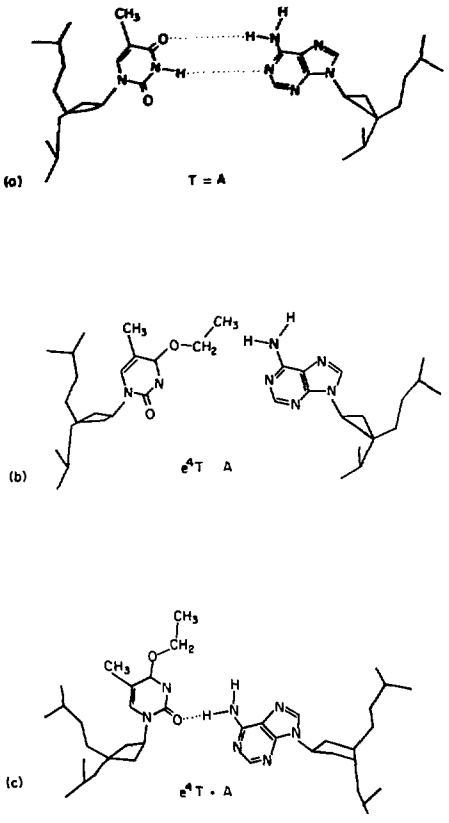

Fig. 3. *Base-pairing of dT or O^4-ethyl dT with dA. (a) Watson-Crick T-A base pair; (b) e^4T (syn) and A in the Watson-Crick positions; (c) e^4T (syn) and A in an open-helix position in which one H-bond can be formed. The position (syn to N3) and the size of the ethyl group are based on data of Birmbaum (p.c.).* *(XBL 8510-8530)*

Pathology, University of Washington. This work utilizes methods for site-directed insertion of the desired alkyl-dTTP within an amber codon of ϕX174 and subsequent biological assay for revertants in *E. coli* spheroplasts. Preliminary data indicate that the kinetics of incorporation opposite dA of the O^4-alkyl dTTPs follow the same dependence on size shown in the poly(dA-dT) experiments.

Similarly designed experiments that compare the properties of various O^2-alkyl dTTPs are in progress. In an earlier report, we found the O^2-methyl dTTP would be substituted for dTTP, but the miscoding of the resulting polymer was lower than that observed for polymers containing O^4-methyl dT.[7]

REFERENCES

1. Singer, B. *Nature 264*, 333–336 (1976).
2. Singer, B., Spengler, S.J., and Bodell, W.J. *Carcinogenesis 2*, 1060–1073 (1981).
3. Swenberg, J.A., Dyroff, M.C., Bedell, M.A., Popp, J.A., Huh, N., Kirstein, J., and Rajewsky, M.F. *Proc. Natl. Acad. Sci. (USA) 81*, 1692–1695 (1984).
4. Richardson, F.C., Dyroff, M.C., Boucheron, J.A., and Swenberg, J.A. *Carcinogenesis 6*, 625–629 (1985).
5. Singer, B., Spengler, S.J., Fraenkel-Conrat, H., and Kuśmierek, J.T. *Proc. Natl. Acad. Sci. (USA) 82*, in press (1986).
6. Mirau, P.A. and Kearns, D.R. Biopolymers 24, 711–724 (1985).
7. Singer, B., Sági, J., and Kuśmierek, J.T. *Proc. Natl. Acad. Sci. (USA) 80*, 4884–4888 (1983).

EFFECTS OF ALKYLATING CARCINOGENS ON HUMAN TUMOR CELLS IN CULTURE

Regine Goth-Goldstein and Mildred Hughes

Chemicals that can induce tumors at various sites in experimental animals are useful tools to examine the process of carcinogenesis. The initial interaction of a carcinogenic agent with cells can be studied in cell culture systems. It is primarily the reaction of a carcinogen with cellular DNA that results in the expression of biological damage such as cell killing, chromosomal alterations, mutations, and malignant transformation. Cells possess, however, various defense mechanisms to cope with the damage induced by carcinogens, and the initial DNA damage can be modified by various DNA repair processes. Alkylating carcinogens like N-methyl-N'-nitro-N-nitrosoguanidine (MNNG) are the best-studied carcinogens with regard to their reactivity with cellular components and particularly with DNA. They produce a wide variety of lesions in DNA. The biological relevance of some of these lesions could be identified in bacteria through studies with mutants that are defective in the repair of specific alkylated DNA bases. Thus, it could be concluded that alkylation of the N3 position of adenine or guanine produces a lethal lesion, whereas alkylation of exocyclic oxygens of DNA bases leads to mutagenic lesions with 06-methylguanine (06-MG) being the major contributor to the mutagenic effects of methylating agents. In mammalian cells, the absence of defined mutants in DNA repair of alkylation damage has hindered the evaluation of the biological effect of alkylation lesions. A good correlation exists between the amounts of 06-MG formed by different agents and their mutagenicity or carcinogenicity. Further, the persistence of this lesion and of 04-alkylthymine in various tissues correlates well with tumor incidence in these tissues. It is less clear what DNA lesions contribute to cell killing. A group of human tumor cell strains fail to support the growth of MNNG-damaged adenovirus. Cells of this phenotype, which has been termed Mer−, have other characteristics in common, among them that they are hypersensitive to the cytotoxic effects of alkylating agents, and that they are unable to repair 06-MG. From this it has been concluded that in human cells 06-MG is not only a mutagenic lesion as in bacteria, but also a lethal lesion. The widely studied HeLa S3 cell line that originated from a human tumor, has the Mer+ phenotype, but a Mer− variant (HeLa MR) has arisen in one laboratory. This offers the possibility to study Mer− and Mer+ cells of otherwise similar genetic background. Our work in the last year has concentrated on comparing the response of HeLa Mer+ and Mer− variants to alkylating agent.

HeLa MR cells are extremely sensitive to the cytotoxic effect of MNNG as measured by their colony-forming ability after a 1-hour exposure to MNNG. The ratio of the D_{10} (the dose that reduces survival to 10%) of the two variants is 30 (see Fig. 1, open symbols). We found previously that Chinese hamster ovary (CHO) cells that survive a highly toxic dose of MNNG have a permanently increased resistance to the cytotoxic effects of this agent. We wanted to determine if this change in sensitivity is unique to the CHO cell line or if it is a general response, also occurring in HeLa cells. The finding was surprising. When the two HeLa variants were treated with a highly toxic dose of MNNG, the surviving population of HeLa S3 cells was equally or even slightly more sensitive to a second exposure of MNNG, whereas the surviving HeLa MR population was much more resistant to MNNG with a survival dose-response similar to that of HeLa S3 (see Fig. 1, closed symbols). From a number of clones derived from single cells of the pretreated HeLa MR population, the majority had the Mer+ phenotype in respect to MNNG sensitivity. These clones were also more resistant to methylnitrosourea and ethylnitrosourea, but they were as sensitive as the untreated HeLa MR cells to chloroethylnitrosourea (CNU), the parent compound of various chemotherapeutic alkylating agents.

The lethal lesions of CNU are DNA crosslinks which are formed from monofunctional DNA-adducts. These precursors of DNA crosslinks can be repaired by the same enzyme that repairs 06-MG. Mer+ cells that have this enzymatic activity can prevent the formation of DNA crosslinks, whereas in Mer− cells that are deficient in this repair enzyme, lethal crosslinks are formed. The finding that pretreated HeLa MR cells are sensitive

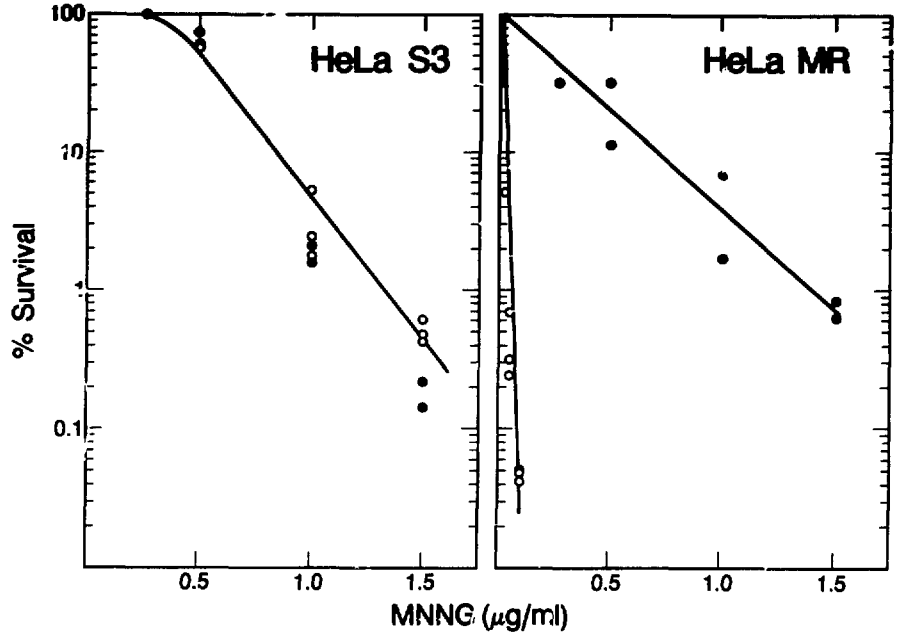

Fig. 1. Cell survival of HeLa S3 (left panel) and HeLa MR (right panel) after a 1-hr treatment with MNNG; o, survival of nonpretreated cells; •, survival of cell population that survived a highly toxic dose of MNNG (2μg/ml in case of HeLa S3, 0.2μg/ml in case of HeLa MR) 3 weeks prior to second exposure. (XBL 8511-8586)

to CNU indicates that these cells are lacking the 06-MG repair enzyme. We could show that this is in fact the case. When DNA methylated with ^{14}C-MNNG was incubated with cell extracts of the HeLa variants and the methylated DNA bases quantified by HPLC separation, 06-MG was removed only during incubation with HeLa S3 extract.

This shows that the two characteristics of the Mer− phenotype, hypersensitivity to alkylating agents and inability to repair 06-MG, can be uncoupled, and indicates that 06-M6 is not a lethal lesion.

CARCINOGENIC POTENCY

Lois Swirsky Gold, Bruce N. Ames, Renae I. Magaw, Catherine Wright, Joan Schwalbe*, Georganne Backman, Mark Blumenthal, and Thomas H. Slone

Efforts to use animal bioassays in the evaluation of the potential health risk of chemicals to humans have been hampered by the lack of a standardized method of comparing experimental results. Experimental protocols as well as the type of information reported in the literature are quite diverse. Moreover, quantitative estimates of carcinogenic potency have not been made for large numbers of chemical

*Department of Biochemistry, UCB.

carcinogens. Our Carcinogenic Potency Database is an attempt to quantify and standardize the animal bioassay literature and to organize it systematically.

TD_{50}: A NUMERICAL INDEX OF CARCINOGENIC POTENCY

As an index of carcinogenic potency, we have recommended the TD_{50}, or tumorigenic dose rate for 50% of the test animals. Briefly, the TD_{50} is defined as the chronic dose rate to induce tumors in half the test animals (in the absence of tumors in the control group). TD_{50} can be calculated for any single category of neoplasm or any combination of neoplasms. This numerical index permits comparisons of diverse test results and improves past efforts to estimate carcinogenic potency in two ways. First, our calculation takes into account whatever spontaneous tumor incidence occurs in control animals. Second, where data are available about the time of death and tumor incidence of each animal, we estimate a TD_{50} using this information. This is important because animals given high doses of a chemical frequently die early owing to chemical toxicity rather than to tumors, and failure to account for this early mortality could lead to under-estimates of the true potency. A full statistical description of TD_{50} is given in Sawyer et al.[1] and Peto et al.[2] We have found that the range of TD_{50}s is more than 10-million-fold. For male rats, the range in values is from 101 ng for 2,3,7,8-tetrachlorodibenzo-p-dioxin (TCDD) to 5.98 g for Food, Drug & Cosmetic (FD&C) Green No. 1.

THE CARCINOGENIC POTENCY DATABASE

The database of test results reported in the literature prior to July 1981 was published in a plot format in 1984.[2,3] A supplement that includes experimental results published through December 1982 will appear in the same journal in 1986. The two published databases together contain results of approximately 3,200 experiments on 835 chemicals.

The database is readily accessible for qualitative and quantitative analysis. All positive and negative experiments that fit a set of standard criteria based on suitability for estimation of potency have been included in the database, i.e., tests in which 1) exposure was chronic, 2) the route of administration was likely to result in the whole body being exposed, 3) a single compound was administered to the animals, and 4) a control group was used. Some chemicals for which there is otherwise sufficient evidence of carcinogenicity are not included if, for example, the route of administration was skin painting or subcutaneous injection, or if the dose level could not be measured in mg/kg/day.

We have included in the database information about a variety of factors that are important in interpreting bioassays, such as 1) the TD_{50} and its statistical significance, 2) the species and strains that have been tested chronically, 3) the route and duration of compound administration, 4) the tumor types, 5) the proportion of animals with specific types of tumors in dosed and control groups, 6) the shape of the dose-response curve, and 7) the author's opinion about carcinogenicity.

During the past year we have been updating the database to include experimental results published through December 1983. We have also added several tests that were published in earlier years but that were only identified recently in our ongoing literature search.

FREQUENCY OF CARCINOGENIC RESPONSE IN ANIMAL TESTS AND COMPARISON OF RESULTS IN RATS AND MICE

We are currently compiling a summary of the database in terms of 1) the proportion of chemicals tested in long-term bioassays that have been determined to be carcinogens in at least one experiment, 2) the common sites of tumor induction for these chemicals in different species, and 3) the distribution of the carcinogenic potency of these test agents. This summary has importance both as historical information and as specific background data for other analyses. Table 1 summarizes the prevalence of carcinogens among various groups of chemicals in the database; 49% of all chemicals were carcinogenic in at least one experiment, and this proportion varies slightly among the subgroups of chemicals examined. Chemicals tested in rats and chemicals tested in mice usually have similar proportions of carcinogens. The proportion of chemicals tested in both rats and mice that was found to be carcinogenic was generally higher than that found among chemicals tested in only one species.

In a related analysis we focus on the chemicals tested in both rats and mice, and investigate interspecies extrapolation in the following ways: 1) a comparison of the carcinogenic response of rats and mice to the same chemicals, 2) the importance of the target sites in one species to the prediction of the carcinogenic response to the same chemical in the other species, and 3) the relationship between the carcinogenic potency of a chemical in one species and its carcinogenicity in the second. By examining how well tests in rats and mice predict one another we hope to gain insight into

Table 1. Proportion of chemicals in the Carcinogenic Potency Database found to be carcinogenic.

Set of chemicals[a]	Animal species tested: Any species	Rats	Mice
I. All Chemicals in Database			
All chemicals	379/765 (49%)	252/538 (47%)	225/524 (43%)
NCI/NTP bioassay chemicals[b]	88/186 (47%)	62/180 (34%)	71/180 (39%)
Literature chemicals	307/632 (49%)	198/387 (51%)	163/381 (43%)
II. Chemicals Tested in Both Rats and Mice			
All chemicals	179/306 (59%)	132/306 (43%)	150/306 (49%)
NCI/NTP bioassay chemicals	84/174 (48%)	59/174 (34%)	70/174 (40%)
Literature chemicals	96/146 (66%)	74/146 (51%)	81/146 (55%)
III. Chemicals Tested in Both Sexes of Rats and Mice			
All chemicals	123/226 (54%)	89/226 (39%)	104/226 (46%)
NCI/NTP bioassay chemicals	83/168 (49%)	58/168 (35%)	70/168 (42%)
Literature chemicals	37/67 (55%)	30/67 (45%)	31/67 (46%)

[a] Results given as the number of carcinogens/number of chemicals tested, with associated percentages.

[b] NCI/NTP bioassays refer to experiments conducted by the National Cancer Institute/National Toxicology Program.

the feasibility of interspecies extrapolation of bioassay results, which ultimately includes extrapolation between rodents and man.

ASSOCIATION BETWEEN CARCINOGENIC POTENCY AND TUMOR PATHOLOGY IN RODENT CARCINOGENESIS BIOASSAYS

During the past year we have used the NCI/NTP bioassays to investigate the association between carcinogenic potency and tumor pathology. Since the TD_{50} is only one measure of potency, it cannot fully summarize the results of animal cancer tests on a particular chemical. We have, therefore, investigated other measures of hazard, including 1) whether a chemical induces tumors of more than one type in a single-sex species group of test animal, 2) whether the tumors caused the death of the animal or whether they were discovered incidentally at necropsy after terminal sacrifice, and 3) whether metastases of the induced tumor occurred. The latter two characteristics are indicative of the malignancy and biology of the tumor. We show that there is no obvious relationship between carcinogenic potency as measured by TD_{50} and the particular target organ in which tumors were induced, i.e., for the chemicals that cause tumors at a particular site, the calculated TD_{50} values span a wide range.

We also find that the three hazard indicators described above are sometimes interrelated, but that the TD_{50} values for each hazard vary considerably. In Table 2, we report the distribution of TD_{50} values for chemicals that produce tumors at multiple sites within a single-sex species group, and indicate the groups in which tumors were induced at multiple sites. We observe that multiple-site carcinogens span a broad range of potency. The frequency distribution of potency values for multiple-site chemicals is similar to the distribution for other carcinogens. However, multiple-site carcinogens are significantly more likely than other chemicals to induce tumors in both rats and mice (71% vs. 39%) rather than in only one of the species.

A variety of chemical classes are represented among the multiple-site compounds. It is especially noteworthy that chlorinated compounds are underrepresented, since most of them induced only liver tumors. Of 17 chemicals containing only carbon, hydrogen, chlorine, and optionally oxygen, only 3

Table 2. Carcinogenic potency (TD_{50}) in mg/kg body wt/day of 40 chemicals that induced tumors at more than one target site in a sex species group.

Chemical	TD_{50}[a]	Multiple site groups[b]	
		Most potent	Other
23,7,8-tetrachlorodibenzo-p-dioxin	256 (ng)	FM	
1,2-dibromo-3-chloropropane (inhalation)	0.11	MR	(FM,MM,FR)
Lasiocarpine	0.14	FR	(MR)
Thio-tepa	0.15	MR	(FR,MM)
Procarbazine.HCl	0.19	FM	(MM,FR,MR)
Phenesterin	0.21	FM	(MM)
Acronycine	*0.50*	MR	(FR)
Estradiol mustard	0.68	FM	(MM)
1,2-dibromo-3-chloropropane (gavage)	0.86	FR	
1,2-dibromoethane (inhalation)	1.10	MR	(FM,MM,FR)
1,2-dibromoethane (gavage)	1.26	FR	(FM,MM,MR)
2,4-diaminotoluene	1.43	FR	
Hydrazobenzene	3.55	MR	(FR)
Cupferron	5.33	MR	(FM,FR)
4,4'-thiodianiline	5.52	MR	(FM,MM,FR)
5-nitroacenaphthene	5.98	FR	(ME,MR)
1,2-Dichloroethane	11.50	MR	(FM)
3-amino-9-ethylcarbazole mixture	11.80	MR	(FR)
Azobenzene	19.20	MR	(FR)
2,4,5-trimethylaniline	20.40	FR	
Dapsone[c]	22.40	MR	
o-Toluidine.HCl	23.30	MR	(FR)
5-nitro-o-anisidine	28.10	MR	(FR)
o-Anisidine,HCl	31.90	MR	
1-amino-2-methylanthraquinone	34.10	MR	
Selenium sulfide	46.80	FM	
1,1,2-trichloroethane	47.60	FM	
1,5-naphthalenediamine	50.80	FR	(FM)
p-Cresidine	69.00	FM	(FR,MR)
2,4-diaminoanisole sulfate	72.60	MR	(FR)
Tris(2,3-dibromopropyl)phosphate	80.10	FM	(MM)
Nitrofen[c]	85.30	MM	
Aniline.HCl	126.00	FR	
1,4-dioxane	126.00	FR	
5-chloro-o-toluidine	134.00	MM	(FM)
4-chloro-o-phenylenediamine	197.00	MR	(FR)
5-nitro-o-toluidine	242.00	FM	(MM)
Trifluraline[c]	330.00	FM	
Nitrilotriacetic acid, trisodium salt monohydrate	511.00	MR	(FR)
3,3'-dimethoxybenzidine-4,4'-diisocyanate	742.00	MR	(FR)
Nitrilotriacetic acid	1450.00	FR	(MR)
2-aminoanthraquinone	1490.00	FM	

[a] The TD_{50} value listed is for the combination of all tumors evaluated in the NCI/NTP Technical Reports as treatment-related. For chemicals causing tumors at multiple sites in more than one sex species group, the lowest composite TD_{50} value is listed followed by the appropriate sex species group. The other sex species groups are given in parentheses. TD_{50} values are calculated to three significant figures.

[b] FM = Female Mouse, MM = Male Mouse, FR = Female Rat, MR = Male Rat.

[c] For these experiments, carcinogenicity at multiple sites was evaluated using pooled controls, and no composite TD_{50} was calculated. The reported TD_{50} values are those calculated on the basis of the most potent individual target site.

(18%) induced multiple tumors, compared to 37 of the 71 (52%) other carcinogens.

OTHER ANALYSES OF PROGRESS

Several other analyses using the results of the Carcinogenic Potency Database are in progress. We have identified "near-replicate" carcinogenesis bioassays by selecting from the entire database those cases in which a single compound was tested more than once in a particular species, strain, and sex of rodent by the same route of administration, and have examined the extent of reproducibility of the results in these different tests. We are comparing several methods for summarizing the potency of a carcinogen when several experiments have been conducted and a number of different TD_{50} values have been estimated for this same chemical. In addition, we have developed a crude index of potential human hazard by comparing the estimated human exposure levels for a compound to the carcinogenic potency in laboratory animals; we are applying this index to occupational exposures in order to determine which compounds stand out and therefore should have high priorities for some sort of regulatory action. In earlier analyses we have examined the relationship in carcinogenic potency between rats and mice[4] and compared two methods of estimating TD_{50}—one based on summary incidence data and the other on life-table data.

REFERENCES

1. Sawyer, C., Peto, R., Bernstein, L., and Pike, M.C. Calculation of carcinogenic potency from long-term animal carcinogenesis experiments. *Biometrics 40*, 17–40 (1984).
2. Peto, R., Pike, M.C., Bernstein, L., Gold, L.S., and Ames, B.N. The TD_{50}: A proposed general convention for the numerical description of the carcinogenic potency of chemicals in chronic-exposure animal experiments. *Environmental Health Perspectives 58*, 1–8 (1984).
3. Gold, L.S., Sawyer, C.B., Magaw, R., Backman, G.M., de Veciana, M., Levinson, R., Hooper, N.K., Havender, W.R., Bernstein, L., Peto, R., Pike, M.C., and Ames, B.N. A carcinogenic potency database of the standardized results of animal bioassays. *Environ. Health Perspect. 58*, 9–319 (1984).
4. Bernstein, L., Gold, L.S., Ames, B.N., Pike, M.C., and Hoel, D.G. Some tautologous aspects of the comparison of carcinogenic potency in rats and mice. *Fundam. Appl. Toxicol.*, to be published in Vol. 5 (1985).

TEMPORAL EXPRESSION OF ROUS SARCOMA VIRUS IN MICROINJECTED EMBRYONIC CHICK LIMBS

Anthony R. Howlett, Betsey Cullen, and Mina J. Bissell

Rous Sarcoma Virus (RSV), is an acutely oncogenic avian retrovirus that can induce the transformation of cultured chick embryo fibroblasts (CEF) and lead to the formation of rapidly growing sarcomatous tumor in neonate and adult birds.[1,2] In contrast, the introduction of RSV into the limb buds of stage 21–24 chick embryos does not lead to the appearence of tumors within a similar time frame despite the fact that viral spread and proviral integration is generally apparent.[3]

The transforming capacity of RSV has been shown to be accounted for by the activity of a phosphokinase ($pp60^{src}$), that can specifically phosphorylate tyrosine residues and thereby alter the pattern of phosphorylation of cellular proteins that may be involved in the maintenance of cell structure and the control of cell proliferation. It is believed that the activities of the virus, as mediated by integrated *src* oncogene, are alone sufficient to drive the transformation process, although increasing evidence to the contrary has been accumulating over the years to suggest that the process may be more complex. Tumor promotors have been shown to induce the transformation of CEF cells that have been infected with temperature sensitive (ts) mutants of RSV and cultured at the nonpermissive temperature,[4] and recently studies into the effects of wounding on tumor development in adult birds has strengthened the concept that additional factors that may be of physiological relevence may play role in the multistage process of viral carcinogenesis.[5] The possibility that additional host-related

factors are required for the transformation of embryonic tissue infected *in ovo* is of considerable interest. We have undertaken further studies aimed at providing a greater understanding of the developmental regulation of virus-host interactions through an analysis of the process of viral spreading and viral-oncogene expression in the first semester of chick development.

Using a monoclonal antibody directed against a viral structural protein (designated P19^{gag}), kindly provided by T. Pawson, we have determined the kinetics of viral infection and spread following inoculation with 10^4–10^5 ffu of RSV into the upper right limb bud of day-4 embryos. P19 positive cells could be detected in coverslip cultures of dissociated limb buds fixed 2 hours after seeding. Using the 2-hour cultures as an approximate measure of viral infection *in ovo*, the spread of the virus in the embryo was characterized by a saltatory kinetic with two rapid bursts of infectious spread and intervening periods of stasis (Table 1 and Fig. 1). Very low levels (<1%) of viral P19^{gag} positive cells were apparent from freshly dissociated limbs of 5-, 6- and 7-day old embryos. A sharp rise in the number of infected cells was demonstrable on day 8 to give a value of 12%, which was approximately sustained until day 11, when a second sharp increase was observed.

The subsequent spread of virus in the dissociated limb bud cultures was assessed after 24 and 48 hours and after 7 days. Two contrasting patterns, were apparent (Fig. 2). The low levels of virus that were found in the early (5-, 6- and 7-day) embryos remained low through 48 hours in culture and rose to approximately 10% after 7 days in culture. A similar pattern of infectivity was demonstrated in day-7 embryo cultures up to 48 hours, whereafter the percent of P19^{gag} positive cells increased to 70% within 7 days. Limb bud cultures of days 8, 9, 10, and 11 were all found to be mass transformed by 7 days. The major difference in the kinetic of viral spreading between these day-8, -9, -10 and -11 cultures appeared to be the rapidity with which they approached the maximally infected level (Fig. 2).

In conclusion, it has been shown that the spreading of RSV in infected limb tissue follows two

Table 1. Kinetics of viral spread in ovo and in culture.

Embryo age prior to limb dissociation (days)	Time elapsed after RSV inoculation (days)	Percentage cells expressing viral P19^{gag} Hours in culture 2	24	48	(7 days)
5	1	<1	2	2/3	10
6	2	<1	N/D	N/D	13
7	3	1	2/3	4	68
8	4	12	18	69	100
9	5	12	21	86	100
10	6	17	69	98	100
11	7	50	100	100	100

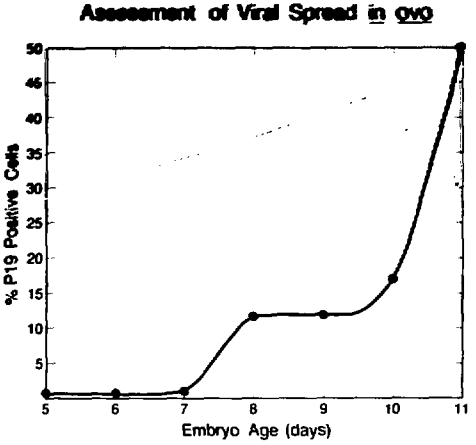

Fig. 1. Infectious spread of RSV in ovo as determined by measurement of viral antigen P19^{gag} expression in dissociated day-5 through day-11 embryos (1–7 days post infection). *(XBL 8510-8509)*

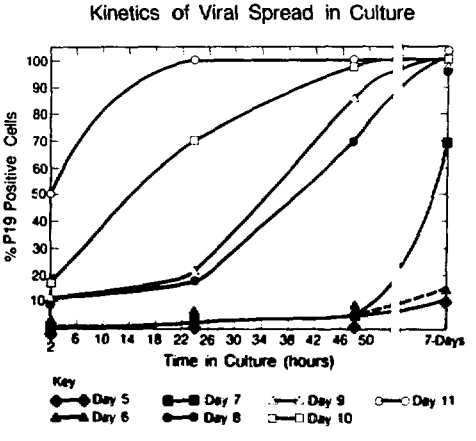

Fig. 2. Quantitation of the transmission of RSV in cultures of limb bud cells dissociated from day-5 through day-11 embryos (1–7 days post infection). *(XBL 8510-8510)*

distinguishable patterns *in ovo* and in culture. The data would indicate that viral susceptability is developmentally regulated and may be linked to the program of differentiation of the various component cells of the limb. Preliminary data of P19 localization in frozen sections of day-10 limbs (5 days post-infection) show that viral uptake is not ubiquitous. P19 staining was not apparent in epidermal structures or the cartilagenous component of the limb but was found in areas corresponding to muscle and fibrous connective tissue differentiation. We are now determining the nature of the cell types that are the initial targets of RSV and whether the early transmission of the virus in the limb buds occurs vertically along defined lineages in a developmentally related manner or horizontally by cross infection of other cell types that become susceptible as development proceeds.

REFERENCES

1. Purchase, H.G., and Burmester, B.R. In *Diseases of Poultry*, Hofsted, Ed., Iowa State University Press, pp. 502–568 (1972).
2. Hanafusa, H. In *Comprehensive Virology, Vol. 10, Fraenkel-Conrat, H., and Wagner, R., Eds. Plenum Press, New York, pp. 401–482 (1977).*
3. Dolberg, D.S., and Bissell, M.J. *Nature 309,* 552–556 (1984).
4. Bissell, M.J., Hatie, C., and Calvin, M. *Proc. Natl. Acad. Sci. 76,* 348–352 (1979).
5. Dolberg, D.S., Hollingsworth, R., Hertle, M., and Bissell, M.J. *Science,* in press (1985).

TUMOR PROMOTERS CAUSE RSV-MEDIATED TUMORS ONLY WITH CONCOMITANT LOCAL IRRITATION

Mark D. Hertle, David S. Dolberg, Robert E. Hollingsworth, and Mina J. Bissell

We have established previously that wounding is required for Rous Sarcoma Virus (RSV) to cause sarcomas in young chickens.[1,2] Tumors were induced by the intramuscular injection of 10^7 focus forming units (ffu) in one wing, which yielded the primary tumor within 7 days, and by clipping with a stainless steel clip in the other wing. Tumors due to circulating virus formed at the clip 1-2 days after the primary tumor. We then asked two further questions. Could the virus cross the epithelial layer of the gut, and in the absence of a primary tumor, could circulating virus cause a tumor if the bird were wounded? To answer these questions, we gave 5-day old chicks 5×10^6 ffu of RSV by mouth as an aerosol, and clipped the chicks in both wings as previously described.[1,2] Tumors formed in about 20% of the chicks (7 out of 39). Chicks that received the virus but no clip did not develop tumors.

This aerosol experiment demonstrates that RSV is capable of effectively crossing the epithelial barrier of the lung and/or gut. Furthermore, the nonmalignant hemorrhagic lesions that frequently occur in these animals demonstrate that the endothelial barrier of the capillaries can be breached without subsequent tumor formation. Even if injury were to alter the compartmentalization of the virus, wounding and wound healing are, in addition, good candidates for a more active role in tumor formation for several reasons. It is suspected, for instance, that wounding is a first-stage promoter in chemical carcinogenesis[3] and, in some animal models, tumors are found to develop at wounding sites[4] regardless of the method of carcinogen application. Some human tumors are also found at sites of wounding,[5] and the process of wound healing involves factors that have been implicated in the process of tumorigenesis and tumor promotion.

Since wounding has been proposed to have tumor promoting activities, we asked whether other known tumor promoters such as phorbol esters might be able to substitute for the co-carcinogenic effect of wounding. In order to ask this question, however, we needed to first minimize the wounding involved in the delivery of the substances being tested. Our approach was to implant a 1-mm

Table 1. Correlation of tumor induction with local irritation. Polyethylene catheters, 1 mm in diameter, were inserted into the wing webs of 7-day-old chicks. The catheters were attached with sutures and allowed to heal for 10 days. Solutions to be tested were then injected through the catheter in 0.1-ml volumes every other day for a total of three injections. Virus was injected in the opposite wing at the time of the first catheter injection. The extent of the local reaction was judged by the relative amounts of swelling, scabbing, and tissue necrosis and is shown as −, no reaction; ±, minimal reaction; and +, ++, and +++, increasing necrosis; a slash indicates that some animals showed a reaction and others did not. Tumors are indicated by the percentage of animals with tumors in the wing containing the catheter, and n is the number of chickens tested. TPA is 12-O-tetradecanoylphorbal 13-acetate; PDD and 4αPDD are phorbol and 4-α phorbol 12,13-didecanoate, respectively.

Treatment	n	Extent of local reaction	Tumors (%)
Medium containing <10% methanol	5	−	0
Methanol[a]	6	++/−	50
TPA in medium containing <10% methanol (0.1 to 0.5 μg)[b]	4	−	0[c]
TPA in methanol (<0.2 μg)	8	+	50
TPA in methanol (>0.2 μg)	4	+++	100
PDD and 4αPDD in medium (<10% methanol) (0.1 to 2 μg)	0	−	0
PDD and 4αPDD in medium (<10% methanol) (5 μg)	0	±/−	0
PDD in methanol (0.2 to 1 μg)	10	++	50
4αPDD in methanol (0.2 to 1 μg)	24	++	50
Mezerin in medium (0.1 to 5 μg)	3	−	0
Mezerin in medium (10 μg)	3	+++	67
Mezerin in methanol (0.05 to 0.5 μg)	6	+++	83

[a] Tumors associated with methanol occurred almost exclusively when there was a local reaction. When there were no reactions, there were no tumors.

[b] The amount refers to the total dose administered through the catheter in each application (total of 3 in the course of 6 days).

[c] In some cases, the catheters were pulled out by chickens in the middle of the experiment, and these chickens are not included.

polyethelyene tube, approximately 5 cm in length, into one wing of an eight-day-old chick. The wing was allowed to heal for 10 days with the catheter in place. Various tumor promoters were then administered through the catheter while the opposite wing was injected with RSV in the usual manner. Tumor promoters dissolved in a minimum amount of solvent (less than 10% methanol in water) caused tumors only at high concentrations (Table 1) and only when they were accompanied by necrosis and local inflammatory reactions. When the amount of methanol was increased, inflammation and necrosis became evident at the site of administration even with lower concentrations of the tumor promoters. Increasing the concentration of tumor promoters in the presence of high levels of solvent resulted in more prominent inflammation and necrosis with subsequent appearance of tumors (Table 1). Methanol (100%) also caused tumors in 50% of chickens. When tumors occurred, they were also preceded by inflammation and edema. We conclude that inflammation, as well as mechanical puncture or laceration, can act as co-carcinogens in RSV-mediated tumor formation. Furthermore, at least in this system, irritation and local injury appear to be the mode by which tumor promoters allow the induction of tumors.

REFERENCES

1. Dolberg, D.S., Hollingsworth, R.E., and Bissell, M.J. Wounding and its role in RSV-mediated tumor formation. *Annual Report 1983–1984, Biology & Medicine Division,* Lawrence Berkeley Laboratory report LBL-18393, p. 216 (1985).
2. Dolberg, D.S., Hollingsworth, R., Hertle, M., and Bissell, M.J. Wounding and its role in RSV-mediated tumor formation. *Science 230,* 676–678 (1985).
3. Slaga, T.J. *Environ. Health Perspec. 50,* 3–14 (1983).
4. Rous, R., and Kidd, J.G. *J. Exp. Med. 73,* 365 (1941).
5. Haddow, A. *Adv. Cancer Res. 16,* 181–234 (1972).

ROLE OF EXTRACELLULAR MATRIX AND HORMONES IN MODULATION OF TISSUE SPECIFIC FUNCTION IN COMMA-1-D, A MOUSE MAMMARY EPITHELIAL CELL LINE

Ming-Liang Li, Li-How Chen, and Mina J. Bissell

Synthesis of mouse milk proteins in mammary gland epithelial cells is regulated not only by lactogenic hormones but also by the extracellular matrix (ECM) and its components.[1,2] Previously, we have shown that the rate of milk protein synthesis and the level of β-casein message are increased remarkably in primary mammary epithelial cells from the pregnant gland cultured on floating collagen gels when compared to the same cells cultured on a plastic surface.[3,4] Recently, we have obtained a mouse mammmary gland cell line, COMMA-1-D (C-1-D) that has retained a degree of milk protein expression and hormonal response,[5] allowing us to investigate more easily and economically the mechanisms by which hormones and ECM modulate gene expression.

Milk protein gene expressions in the cell line are monitored at both transcriptional and translational levels. Quantitation of specific mRNA is performed by hybridization of purified cytoplasmic RNA to various ^{32}P-labeled cDNA probes using RNA dotting method. Separation and specificity determination of milk proteins are carried out using SDS-poly-acrylamide gel electrophoresis followed by reaction to specific antibodies using Western transfer technique. ECM materials, either extracted from a mouse chondrosarcoma tumor (EHS) as a complex mixture or the purified individual components of ECM, are utilized as substrata on which cells are grown for comparison.

Mouse mammary gland cell line C-1-D was grown on plastic or collagen substrata in the presence or absence of prolactin. Figure 1 shows the comparison of cytoplasmic RNA isolated from C-1-D cells grown on plastic (numbers 1 and 2), on attached gels (numbers 3 and 4) and on floating gel (numbers 5 and 6). Odd numbers are from cells grown in the absence of prolactin and even numbers are from cells grown in the presence of prolactin. Amounts of RNA dotted are based on an equal amount of DNA present in the cell. The second row and third row of dots are 2-fold and 4-fold dilutions of the first dot. Results from this experiment indicate that C-1-D cells grown in the presence of prolactin are generally synthesizing 4- to 8-fold more β-casein mRNA than those grown in the absence of prolactin. Regarding the effect of substratum, when prolactin is present, cells grown on floating collagen gel produce 8-fold more of β-casein message than those on the attached collagen gel and 16-fold more than those on the plastic surface. β-casein gene expression in the C-1-D cell, therefore, is modulated not only by hormones but also by the ECM. When milk protein synthesis was measured on polyacrylamide gels, β-casein synthesized on the floating collagen gel (number 3) amounted to least 5-fold more than on the plastic surface (number 4) as judged from the intensity of staining in the Western blot (see Fig. 2). These characteristics of C-1-D are similar to the cultures of primary mammary epithelial cells reported previously.

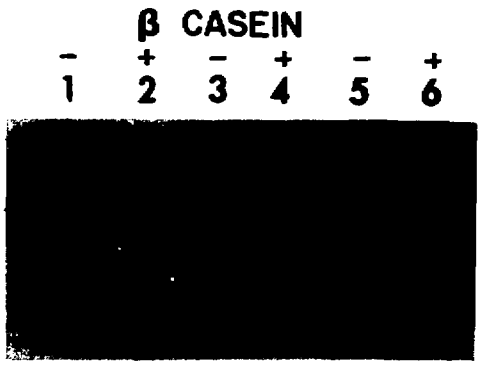

Fig. 1. Quantification of β-casein mRNA in COMMA-1-D cells. RNA was extracted and processed from cultures grown for 4 days on plastic (1,2), on flat gels (3,4) and on floating gels (5,6). Cultures 2, 4, and 6 contained prolactin. All cultures contained insulin and cortisol. RNA equivalent to 15 μg of DNA was dotted (top). Second and third dots are 1/2 dilutions.

(XBB 857-5669)

We extended our study of relation between milk protein gene expression and ECM to include other major components of ECM besides collagen (CI), such as hyaluronic acid (HA), laminin (L), heparin (H), heparan sulfate (HS), and fibronectin (F). The complete basal lamina extract from the EHS tumor is also included for comparison. Figure 3 shows levels of β-casein message in C-1-D cells grown on either plastic dishes coated with various ECM components (Fig. 3A) or grown on thick collagen gels coated with various ECM components (Fig. 3B). The latter were floated 2 days after seeding. Cytoplasmic RNA extracted from pregnant mammary gland (MG) and from C-1-D cells grown

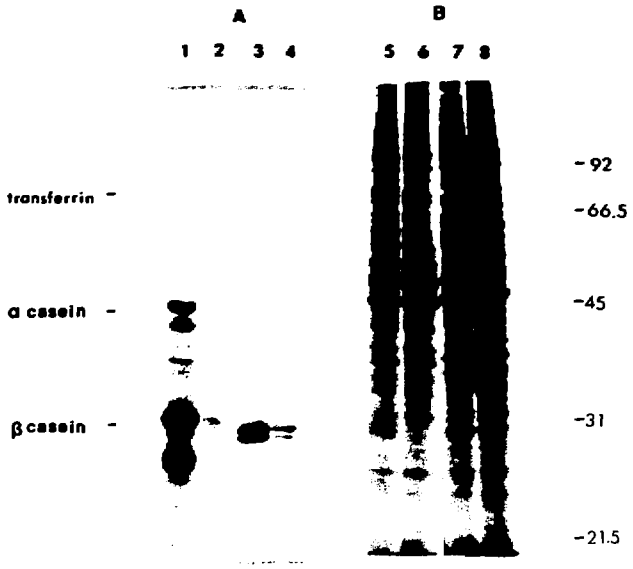

Fig. 2. A comparison of milk proteins and total protein synthesis in primary mouse mammary epithelial cells (PMME) and COMMA-1-D cultures: PMME (1,2,5,6) and COMMA-1-D (3,4,7,8) were grown on either plastic (2,4,6,8) or floating gels (1,3,5,7) in the presence of the three lactogenic hormones. (XBB 856-6398)

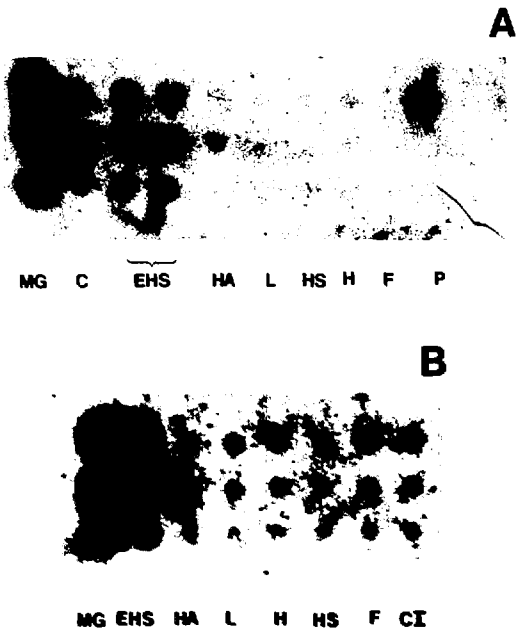

on the plastic surface (P) are used as controls in this experiment. In general, cells grown on collagen gel (Fig. 3B) regardless of the coating material synthesize more β-casein message than those on the plastic surface (Fig. 3A). However, the most important finding of this experiment is that individual components such as laminin, hyaluronic acid, heparin, heparan sulfate or fibronectin do not produce any discernible effect on β-casein gene expression. In contrast, C-1-D cells grown on EHS complex produce a large amount of β-casein message, up to 70% of that produced in the pregnant mammary gland. Since, EHS complex probably contains all the major and minor components of ECM essential for differentiated gene expression, it

Fig. 3. β-casein mRNA levels in COMMA-1-D cells grown on different substrata. (A) Cells grown on either plastic (P) or plastic coated with different substrata. MG is equivalent RNA isolated from late pregnant gland. ECM = extracellular matrix, NMUMG = "normal" murine mammary gland cell line, L = laminin, F = fibronectin, HS = heparan sulfate, H = heparan, CI = collagen I, HA = hyaluronic acid, WAP = whey acidic protein. (B) Sister cultures were plated on top of coated thick collagen gels. Two days after plating, the gels were floated and cells were harvested two days later. After collagenase treatment, cytoplasmic RNA levels over plastic in all cultures including those grown on EHS-coated collagen gels. (XBB 857-5667)

is not surprising to find that EHS is the best substratum for high expression of β-casein gene. On the other hand, the absence of measurable effect of individual ECM components on the differentiated gene expression does not preclude their involvement in this process. It is possible that either a concurrent action of two or more components of ECM is required for such activation or that a three-dimensional structure of the right components is required. The mechanism by which differentiated gene expression is modulated by the ECM is undoubtedly very complex and is being investigated further in our laboratory.

In conclusion, we have found that mouse mammary gland cell line COMMA-1-D behaves similarly to the cultures of primary mouse mammary epithelial cells with regard to their specified gene expression in response to hormones and substrata. We also find that the mechanism of gene expression modulated by the ECM is complex and the individual major components of ECM elicit little or no effect on β-casein gene expression. We propose that ECM activates gene expression in the mammary cells by a concurrent action of major components of ECM, by a change in cell shape, or by a minor, as yet unidentified component of the ECM.

REFERENCES

1. Emerman, J.T., and Pitelka, D.R. *In Vitro 13,* 316–328 (1977).
2. Bissell, M.J., Hall, G.H., and Parry, G. *J. Theoret. Biol. 99,* 31–68 (1982).
3. Lee, E.Y-H., Parry, G., and Bissell, M.J. *J. Cell Biol. 98,* 146–155 (1984).
4. Lee, E.Y-H., Lee, W.-H., Kaetzel, C.S., Parry, G., and Bissell, M.J. *Proc. Natl. Acad. Sci. USA 82,* 1419–1423 (1985).
5. Danielson, K.G., Oborn, C.J., Durban, E.M., Butel, J.S., and Medina, D. *Proc. Natl. Acad. Sci. USA 81,* 3756–3760 (1984).

CLONING OF MOUSE TRANSFERRIN cDNA

Li-How Chen, Ming-Liang Li, and Mina J. Bissell

Transferrin (Tf), an iron-binding protein of molecular weight 80 kDa, is one of the major components of milk.[1] In our study of the regulation of mouse milk protein, we have shown that Tf is synthesized and secreted by mammary epithelial cells themselves in addition to being synthesized by the liver. Our data also indicate that there is a large increase of Tf in mouse mammary gland in pregnancy compared to the virgin state (Fig. 1).

Besides providing iron to the cells, new lines of evidence[2,3] indicate that Tf may be involved in mediating proliferation and differentiation during developmental processes. An additional role as a growth factor for cultured cells has also been suggested for Tf. To study the regulation of Tf in mammary gland, we decided to clone the mouse Tf.

A mouse mammary tumor cDNA library was constructed using λ gt10 vector system (2.5×10^5 independent clones; the library was kindly provided by T. Fung and H. Varmus). A total of 1.0×10^6 phage was plated out and screened by a rat-partial Tf cDNA probe (the rat clone kindly provided by M. Griswald). Positive clones were identified and further purified. The suitable cDNA inserts were then subcloned into plasmid Puc18. Three such clones were obtained. pMTf-5 contains the longest cDNA inserts (2.2 kb) of clones with one internal EcoR1 site; pMTf-01 and pMTF-03 each contain an adjacent EcoR1 fragment of pMTf-5 insert. Restriction digestion analysis was carried out and the respective maps of these three clones were generated as shown in Fig. 1.

A Northern blot experiment was performed to determine the size of Tf message. Cellular RNA isolated from mammary gland was fractionated on MOPS gel, fixed onto nitrocellulose paper and hybridized to pMTf-5 and pRTF. The rat cDNA clone was used for comparison. As shown in Fig. 2, a band of 2.4 kb was detected in each case. The size of these bands were close to the known size of human serum Tf message (2.3 kb). This result further confirms that Tf is synthesized by mouse mammary gland cells.

Using pMTf-5, we looked at the level of Tf message at different developmental stages of mouse

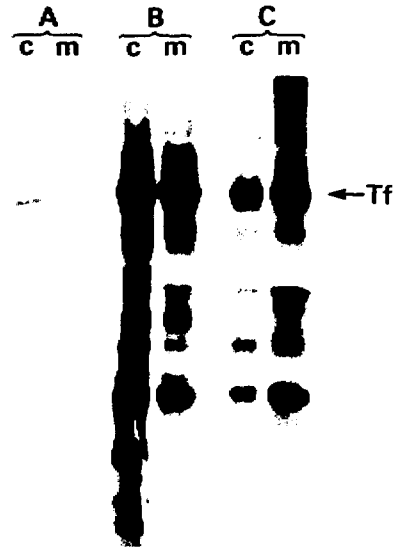

Fig. 1. Production and secretion of Tf in mouse mammary gland. Mammary gland from virgin (A), pregnant (B) and lactating (C) mice were minced and incubated with ^{35}S-methionine for 3 hours. Cells (c) and media (m) were immunoprecipitated by a polyclonal antimouse milk serum and separated by SDS-PAGE. Equal amounts of samples (based on equal amounts of DNA) were applied to the gel. While virgin gland makes the transferrin, the level increases dramatically in pregnancy and lactation. (This experiment was performed by Eva Y-H. Lee when she was at the laboratory.) *(XBB 840-8546A)*

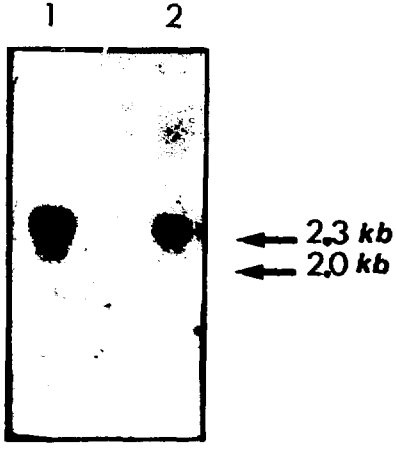

Fig. 2. Size of mouse mammary gland Tf message. Cellular RNA from mouse mammary gland probed with: 1) MTf-5, 2) oRTf as described in the text. *(XBB 850-9906)*

mammary gland. Total cellular RNA were prepared from mammary gland, lung, and liver of virgin and lactating mice, and were dotted and probed with pMTf-5. The result (Fig. 3) indicated a 20-fold increase in the level of Tf message between virgin and lactating glands.

In summary, we have cloned mouse Tf cDNA and have used it to show TF mRNA is modulated at different stages of mouse mammary gland differentiation. We now have subcloned mouse Tf cDNA into M-13 and are sequencing the necessary clones to provide unambiguous proof of the identity of the clones.

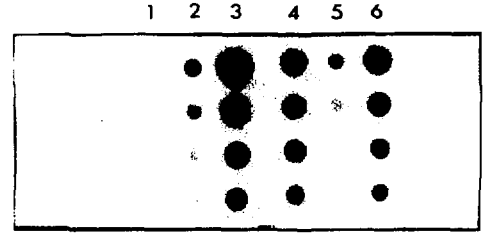

Fig. 3. Comparison of Tf message levels in various tissues. Virgin mice (1,2,3); lactating mice (4,5,6). Cellular RNA from mammary gland (1 and 4), lung (2 and 5), liver (3 and 6). Amounts of RNA dotted were based on equal amounts of DNA of the tissue. Each lane represents a series of 2-fold dilutions. *(XBB 850-9907)*

REFERENCES

1. Massan, P.L. and Hereman, J.F. *Comp. Biochem. Physiol. 39B*, 119–129 (1971).

2. Beach, R.L., Popiela, H., and Festaff, B.W. *FEBS 156*, 151–156 (1983).

3. Mescher, A.L., and Munaim, S.I. *J. Exp. Zool. 230*, 485–490 (1984).

PROCOLLAGEN SECRETION—A CRITICAL STEP IN THE REGULATION OF PROCOLLAGEN SYNTHESIS

Nancy Owens and Richard I. Schwarz

Regulation of protein synthesis in eucaryotic cells is generally thought to occur at the level of RNA transcription. Support for this view comes from a comparison with procaryotes where some of the best examples of protein regulation are at the level of gene transcription. Additionally, since many eucaryotic genes are present in the genome as a single copy, high protein production from these genes would require amplification by the mechanism of accumulating mRNA transcripts. In some ways, regulation of procollagen synthesis in primary avian tendon (PAT) cells appears to fit this common model. On addition of ascorbate, an inducer of procollagen synthesis, procollagen mRNA levels rise by 6-fold, reflecting the similar increase in procollagen production. Such data would strongly support a transcriptional control model if it were not for kinetic studies.

Understanding the kinetics of an induction process can localize the rate-controlling step in a pathway. This step needs to be shifted early in the induction process so that it can then trigger other steps in the pathway to alter their rates. Increased transcription is kinetically the last step in the pathway to change after ascorbate induction and this all but rules out the possibility of it being the controlling step.[1] The secretion rate of procollagen from the cell, on the other hand, changes rapidly (<1 hr) with ascorbate (Fig. 1) and by the same 6-fold increase seen later for translation rates and mRNA levels.[2] For this and other reasons enumerated elsewhere,[1,2] the rate of procollagen secretion is very likely the rate-controlling step.

This raises the important question of how procollagen is secreted from the cell. For the sake of clarity one can reduce this question to distinguishing between a path through the Golgi on its way to secretory vesicles, or alternatively, by a more direct route from the endoplasmic reticulum to the plasma membrane. This question is not new; quite to the contrary, the mechanism of procollagen secretion has been actively debated for many years.[2–4] PAT cells are an ideal system for this type of study because, when fully induced by ascorbate, they produce half of their total protein synthesis as procollagen[5] and secrete it rapidly from the cells with a half-life of 20 min.[1] One might expect that a cell dominated by its need to secrete procollagen would readily reveal its secretory mechanisms. This is not the case. For instance, visualization of the Golgi apparatus in the electron microscope is difficult with fibroblasts.[3] Alternatively, using specific enzymes one can track the migration of a secreted glycosylated molecule through the Golgi by changes in the sugar configuration occurring in that organelle: glycosylated groups on the secreted protein become resistant to the enzyme endoglycosidase H. However, we have observed as have oth

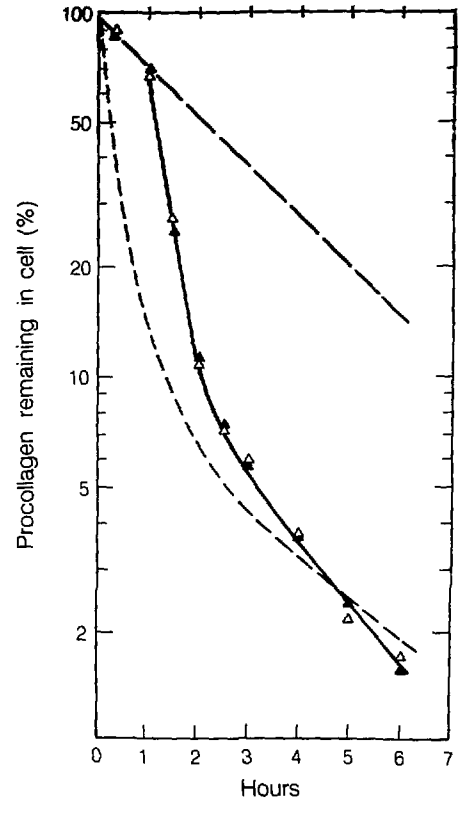

Fig. 1. Secretion of procollagen into the medium for PAT cells given ascorbate at 0 time (triangles). PAT cells were labeled with ^3H proline for 2 hr and then chased at 0 time with 100× excess cold proline. The data for cells without ascorbate (long dash; 120-min half-life) and cells given ascorbate at the time of the pulse (short dash; 20-min half-life). (XBL 8510-4390)

ers[6] that procollagen remains sensitive to this enzyme even after being secreted. So transit through the Golgi can not be proven by this method.

Other researchers have taken advantage of the fact that secretion appears to be energy dependent and as such might show a strong temperature dependence. In other systems a change of only 5°C has slowed secretion rates by about 3-fold making it easier to trace the secretory pathway. Procollagen, however, is remarkably temperature insensitive (Table 1). This result raises questions about the type of secretory mechanism that would be so temperature independent.

Similarly, one might expect that if secretory vesicles are involved in procollagen secretion their transport would require a system capable of directed motion. A likely candidate for this would be the microtubules, which have been shown in other cell types to affect procollagen secretion. While an inhibitor of microtubules, cholchicine, does reduce procollagen secretion rates, the effect is not dramatic—from 20-min half-life inside the cell to 45 min. Such a limited change is more likely to be a result of a secondary effect because loss of microtubules can alter multiple cellular processes.

Another approach has been to use electron microscopy and autoradiography. In this case cells were labeled with ^3H proline, then chased with cold proline. Assuming a vesicular transfer, one would expect to observe "hot spots" of multiple tritium tracks over the vesicles during the chase period that would be predicted to contain large amounts of labeled procollagen. No hot spots were observed (Fig. 2 and Ref. 2), but negative data are never conclusive.

In summary, procollagen secretion is an important step in the regulation of procollagen synthesis in tendon cells. The mechanism by which procollagen leaves the endoplasmic reticulum and crosses the plasma membrane is still uncertain. Attempts to establish either Golgi or vesicle involvement in the process have been negative. The possibility that another transport mechanism could be involved in procollagen secretion remains an alternative explanation and one that we continue to explore.

Table 1. Temperature sensitivity of secretion half-lives (t 1/2).

°C	t 1/2 procollagen − ascorbate	t 1/2 procollagen + ascorbate	t 1/2 noncollagen
41	120	*	70
39	120	20	75
32	120	20	140
29	*	36	*
25	*	*	*

*Not secreted with first-order kinetics.

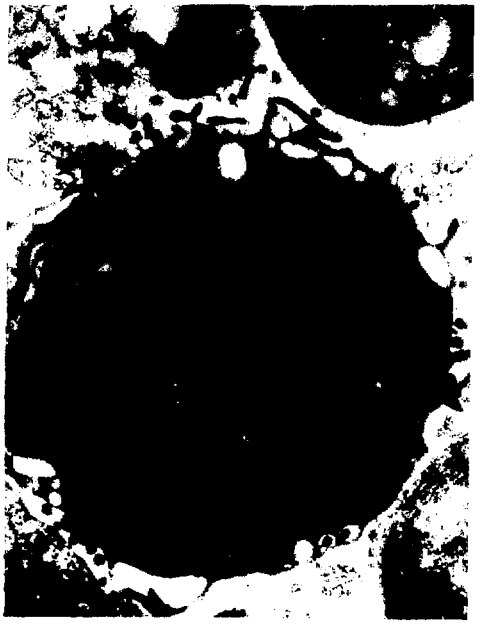

Fig. 2. *Electron autoradiograph of PAT cells labeled for 1 hr and then chased with excess cold proline for 10 min.*
(XBB 850-8605)

REFERENCES

1. Rowe, L.B., and Schwarz, R.I. *Mol. Cell. Biol. 3,* 241 (1983).
2. Schwarz, R.I. *J. Biol. Chem. 260,* 3045 (1985).
3. Olsen, B.J. In *Cell Biology of Extracellular Matrix,* Hay, E. Ed., Plenum Press, New York, pp. 139–177 (1 ?1).
4. Pierce, G.B., Jones, A., Orfanakis, N.G., Nakane, P.K., and Lustig, L. *Differentiation 23,* 60 (1982).
5. Schwarz, R.I., and Bissell, M.J. *Proc. Natl. Acad. Sci. USA 74,* 4453 (1977).
6. Clark, C.C. *J. Biol. Chem. 254,* 10798 (1979).

AN ANALYSIS OF THE ANTIGENIC STRUCTURE AND MODE OF REGULATION OF A DIFFERENTIATION ANTIGEN ON THE SURFACE OF NORMAL AND MALIGNANT HUMAN MAMMARY EPITHELIAL CELLS

Lenny Moss, Betsey Cullen, and Gordon Parry

The composition and properties of the apical plasma membrane of mammary epithelial cells is modulated extensively according to the stage of cellular differentiation. In the lactating gland the membrane is specialized to deal with the secretory activity of the cell, including the secretion of fat droplets into the milk. This is a process that involves budding of lipid droplets surrounded by apical plasma membrane from the cell surface into the milk. Several lactation-specific proteins and glycoproteins have been identified in this membrane, and monospecific and monoclonal antibodies have been prepared against some of these components. Studies utilizing such antibodies have revealed that mammary carcinoma cells express significant quantities of some of these membrane antigens. One such antigen is a high-molecular-weight mucin-like glycoprotein containing a large number of O-linked carbohydrate chains. Several groups have raised monoclonal antibodies against this molecule and have utilized them in a variety of diagnostic and clinical studies of tumorigenesis. This antigen appears to be expressed in a large number of mammary carcinomas as well as on the surface of carcinomas of ovarian and intestinal origin. In one study, monoclonal antibodies raised against this antigen were used with apparent success to treat a patient suffering from ovarian cancer.

While many clinical studies of antigen expression have been reported, basic knowledge of the structure of this molecule and the mechanisms regulating its expression have not been examined. Prompted by the possible clinical significance of the antigen and by our major interest in understanding mechanisms regulating the expression of cell surface glycoproteins, we have undertaken a study of antigen expression in normal human lactating breast tissue and in a human mammary carcinoma cell line, 734B.

IDENTIFICATION OF THE MAJOR ANTIGENIC DOMAINS OF THE MUCIN

A panel of monoclonal antibodies was generated against purified human milk fat globule membrane (the membrane that is derived from the apical surface of normal lactating epithelial cells), and monoclonal antibodies that recognized the high-molecular-weight mucin molecule were selected by screening anitbodies using Western blotting procedures. A total of 13 hybridomas were selected and propagated on this basis. Consistent with what has been reported by others, the mucin was found in both the membrane and in the soluble fraction of milk (the skimmed milk fraction). Interestingly, when skimmed milk components were resolved by SDS-polyacrylamide gel electrophoresis and the nature of the binding components examined by Western blotting (Fig. 1), it was found that some monoclonal antibodies bound to only the high-molecular-weight mucin bands while others bound to lower-molecular-weight components as well as to the large species. Some of these lower-molecular-weight molecules were also found in the milk fat globule membrane. Based upon a large number of experiments, we were able to categorize the panel of antibodies into four classes according to the number of molecular species they identified and their apparent affinity for these resolved molecules. As the antibodies in each of these classes clearly had different specificities, it was apparent that there were at least four antigenic epi-

Fig. 1. *Western blots of human skimmed milk proteins, blotted with monoclonal antibodies reactive against human milk fat globule membranes. All tracks of the gell contained the same sample of skimmed milk but were blotted with one of 13 separately isolated monoclonal antibodies. The samples are gouped into categories on the basis of the number of bands staining and the relative intensities with which they are stained.* *(XBB 850-9098)*

topes associated with the high-molecular-weight mucin. Additionally, as all 13 of the monoclonal anitbodies fell into one or other of these classes, it appeared that these four epitopes represented the major antigenic epitopes of the mucin. Competetive ELISA assays utilizing carbohydrate material derived from membranes by exhaustive proteolytic digestion revealed that these epitopes probably represented different carbohydrate structures.

STRUCTURAL RELATIONSHIPS AMONG THE MAJOR EPITOPES

Procedures were developed for immunoprecipitating the mucin from membranes and from skimmed milk. When immunoprecipitates were resolved by SDS-poly-acrylamide gel electrophoresis and then analyzed by Western blotting procedures utilizing anitbodies against different epitopes from those that were immunoprecipitated, cross-reactivity was observed. This implied that the four epitopes were associated with a single molecular species in the membranes and that there was not a family of mucin-like molecules that each expressed a different epitope.

Immunoprecipitation experiments also demonstrated that some of the lower-molecular-weight antibody binding species, notably a component with a molecular weight of 140 kDa, was associated with the mucin in the membrane. When monoclonal antibodies that bound only to the high-molecular-weight mucin bands were used for immunoprecipitation and the immunoprecipitates were then probed by Western blotting using a monoclonal antibody that recognized the 140-kDa component as well, it was found that this was indeed associated with the high-molecular-weight species. Not all the lower-molecular-weight antibody-binding components behaved in this way, however, and it is not clear whether all these are mucin-derived or whether the epitopes are expressed on other molecular species in addition to the mucin.

EXPRESSION OF MUCIN LIKE ANTIGENS ON HUMAN MAMMARY CARCINOMA CELLS

Immunofluorescence and immunoelectron microscopy revealed that all the monoclonal antibodies bound to 734B cell cultures. However, not all the cells were stained by the antibodies. The basis of this heterogeneous staining was probed further by deriving five clonal variants of the 734B cultures and then determining the extent of heterogeneous staining. It was found that there was considerable heterogeneity, even in the clones, in that only a certain proportion of the cells were stained. This implied that antigen expression in individual cells was not constant but was subject to variation in culture.

An additional interesting feature was that some of the epitopes were expressed independently in the clonal populations. Thus, for example, as is shown in Table 1, 50% of the cells of clone 1 stained with monoclonal antibody P2C1, but only 5% stained with P2A1 and P3B1. In the case of clone 3 cultures, 50% of the cells stained with antibody BC4, but fewer than 5% with P2C1. It is not

Table 1. Monoclonal antibody binding to clones of 734B cells.

734B Cell clone	P2A1	P3B1	P2C1	BC4	BC6	BC10	Mix of all 6
	(% Cells stained)						
1	5	5	50	5	20	10	80
2	5	<5	20	<5	20	<1	n.d.
3	40	20	<5	50	40	20	80
4	10	<5	20	10	10	5	60
5	25	20	60	10	10	5	70
Uncloned population	65	60	30	70	70	60	70

yet clear whether this is associated with the malignant phenotype of the cell or it is associated with maintaining the cells in culture. Experiments are in progress, in collaboration with J. Bartley and M. Stampfer, that will illuminate this point.

These immunofluorescence experiments studying antibody binding to clones of the 734B cells also revealed that the number of epitopes recognized by the antibodies might be greater than four. Three antibodies BC4, BC6, and BC10, reacted similarly in Western blotting experiments, but reacted somewhat differently with clones of the 734B cells. We conclude that there may be up to six different epitopes composing this mucin. More detailed biochemical experiments will, of course, be necessary to clarify this point.

THE ROLE OF TIGHT JUNCTIONS AND CELL SUBSTRATUM INTERACTIONS IN CONTROLLING MEMBRANE POLARITY IN CULTURED HUMAN MAMMARY EPITHELIAL CELLS

Gordon Parry, Lenny Moss, and Betsey Cullen

The plasma membrane of epithelial cells is segregated into two distinct domains: an apical domain and a basolateral domain. Tight junctions form the boundary between the two domains. The polarity is established relative to the attachment substratum, which is usually the basement membrane *in vivo* or the culture dish in cell culture experiments (Fig. 1). A variety of experiments carried out by others using several different model systems have suggested that both the attachment substratum and tight junctions play an important role in regulating membrane polarity. However, many conflicting sets of data have been published, particularly for experiments using virally infected cells as a model system, and the real role of each of these factors remains to be clarified.

To this end we have used a monoclonal antibody raised against a differentiation antigen on apically derived milk fat globule membranes to study regulation of membrane polarity in cultured human mammary epithelial cells. Immunofluorescence procedures were used for most of these experiments, and these were complemented whenever necessary by immuno-electronmicroscopy analysis.

The experiments monitored membrane polarity at different cell densities. The idea underlying this approach was that cell-substratum interactions would be constant and independent of cell density, while cell-cell interactions would be very different

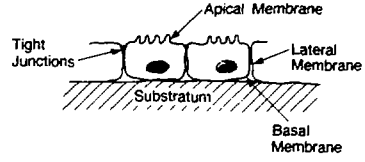

Fig. 1. Diagram illustrating the organization of the plasma membrane in epithelial cells. (XBL 8511-8584)

at low and high cell densities. We found that the antigen was highly polarized at high cell density and was clearly detectable in the apical microvilli. At very low cell densities, however, it was not polarized and was found in the lateral membranes as well as the apical membranes. This result clearly demonstrated that cell-substratum interactions in themselves were not sufficient to establish membrane polarity, and that cell-cell interactions were very important. An interesting situation was observed at intermediate cell densities when the cells formed small distinct islands of cells (see Fig. 2). Antibody staining of these islands revealed that the cells all exhibited distinct apical polarity, but cells on the edge of the islands exhibited distinct staining on the free lateral membrane. As the lateral membrane did not contain a tight junction, this observation was consistent with the view that

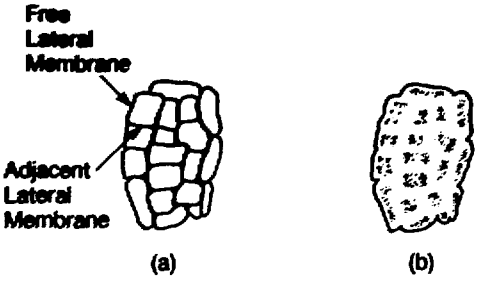

Fig. 2. (a) Diagram illustrating the organization of cells in a typical "island" of epithelial cells. Cells on the edge of the island have a free lateral surface, whereas cells in the center of the island are completely surrounded by other cells, and all lateral surfaces are in contact with other cells. (b) Diagram illustrating the distribution of fluorescently labeled antibodies bound to the surfaces of cells in an island such as that in (a): the antibody stains the face lateral membranes strongly, but not the lateral membranes of cells in the center of the island nor the adjacent lateral membranes of edge cells. (XBL 8511-8585)

in the absence of a tight junction the apical antigen was able to diffuse into the lateral zone. Notably, however, staining of the lateral membranes at the interface of adjacent cells was never detected. By using an antibody against Na^+/K^+, ATPase, a baso-

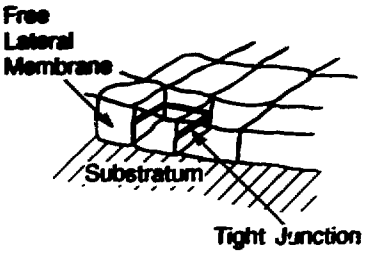

Fig. 3. Diagram illustrating the organization of the tight junction in edge cells of a small island of epithelial cells. (XBL 8511-8581)

lateral component of these cells, it was possible to show that access of the antibody to these regions, and indeed to all the internal cells of these small islands, was not a problem. As is illustrated in Fig. 3, it should be possible for antigen to diffuse beneath the tight junctions in these edge cells and to label all the lateral surfaces, not just the free one. To account for this finding, it would appear that factors other than the tight junctions contribute to the development of membrane polarity. These factors clearly involve cell-cell interactions of an unknown nature, and experiments are currently underway to identify them.

GROWTH CONTROL IN HUMAN MAMMARY EPITHELIAL CELLS

Martha Stampfer and Jack Bartley

Our laboratory has developed culture systems for the growth of human mammary epithelial cells (HMEC). Mammary tissues from both normal and tumor-bearing breasts are readily available as discard material from reduction mammoplasties and mastectomies. These cells are of particular interest for the study of human cellular carcinogenesis and differentiation since 85 to 90% of all human cancers, and 99% of breast cancers, originate from the epithelial cell type, and the breast epithelial cell *in vivo* is capable of many specialized, differentiated functions.

Two different media have been used in our laboratory for the growth of HMEC: MM, which contains the undefined elements of fetal calf serum and conditioned media as well as several growth factors and hormones, and MCDB170 (developed in Dr. Richard Ham's laboratory at the University of Colorado), which contains bovine pituitary extract (BPE) as its only undefined element. Over 70 different HMEC specimens have been grown in MM. HMEC derived from nontumor tissues typically grow for 10–15 population doublings. The cells initially maintain a uniform, cobblestone epithelial appearance. At senescence, cellular morphology is still epithelioid, but more heterogeneous, with large vacuolated cells that can no longer divide. No cells have displayed an indefinite growth potential. We have now been able to examine growth in MCDB170 of 23 cell specimens from 19 different individuals. In all cases, at second to fourth passage, the vast majority of the cell population terminally differentiates; growth ceases and the cell morphology appears myoepithelial. However, a small subpopulation that maintains the cobblestone epithelial morphology is capable of long-term active growth in culture—about 35 to 65 population doublings. At senescence, the cell morphology remains

epithelial. In several cases HMEC from the same individual have been followed to senescence 5 to 10 separate times. Each time, cell growth consistently decreases around the same passage level (12 to 22, depending upon the individual) and no cells have acquired an indefinite growth potential. These results with human epithelial cells differ greatly from those seen with cells of rodent origin, where spontaneous transformation to immortality is common.

The growth of HMEC in both MM and MCDB170 is stimulated by insulin, hydrocortisone, and epidermal growth factor. Additionally some factor(s) in the BPE are also required for growth in MCDB170. However, removal of these growth factors does not lead to an immediate cessation of division, or a G_o growth arrest, as is often the situation for cells of fibroblastic origin. In collaboration with other laboratories, we have observed that TGFβ which can be growth stimulatory for fibroblastic cells, rapidly inhibits the growth of normal HMEC. In other systems, TGFβ has been shown to be an inhibitor of normal epithelial cell growth, while tumor-derived cells may be unaffected. It may therefore prove a useful tool in the selection of variant transformed cells from a normal cell population.

We have demonstrated that the usual pattern of HMEC growth and senescence can be altered by the exposure of cells to the chemical carcinogen benzo(a)pyrene (BaP). HMEC from specimen 184, grown in MM and exposed to BaP in primary culture, displayed many cells capable of around twice the usual number of population doublings. From this extended life population, two immortal cell lines (184A1 and 184B5) have emerged. We have begun testing the effect of BaP on cells grown in MCDB170. Thus far two individuals have been examined; an increased growth potential can be seen, but we do not yet know if cells with an indefinite life span have appeared. However, we have obtained a new immortal cell line (184W1) from cells that have never been exposed to BaP. Cells from specimen 184 were grown in MCDB170 for 8 passages, and then switched to MM. Although most cells senesced by passage 15, one clonal patch has continued growing. We do not know what caused the transformation to immortality in this case.

The immortal cell lines, besides having aberrancies in the normal pathway to senescence, display other properties that distinguish them from their normal parental cells. They are all aneuploid; yet, unlike immortal cell lines derived from tumor tissues or tumor virus infection, they maintain a near diploid karyotype and show only a few chromosomal changes after 100 to 200 population doublings. They may thus be extremely useful for experimentation in which a relatively stable karyotype is desired. Neither 184A1 nor 184B5 is tumorigenic in immunosuppressed mice. At low passage levels 184A1 shows no, and 184B5 shows very little anchorage-independent growth. However, introduction of tumor virus genetic material can render both lines tumorigenic, and 184A1 anchorage independent. The possible role of known oncogenes in the transformation of these HMEC is currently being examined. Both 184A1 and 184B5 show some differences in growth factor requirements from their parent cell, and they also contain TGFβ-resistant populations. These cell lines, as well as the normal long term cell cultures, should provide useful substitutes for examining the mechanisms and factors controlling growth and senescence of human epithelial cells in culture.

EXPRESSION AND MODULATION OF DIFFERENTATION IN HUMAN MAMMARY EPITHELIAL CELLS

Jack Bartley, Gerri Levine, and Martha Stampfer

All mammalian cell types undergo stages of maturation in which a stepwise process produces highly differentiated cells with special functions. Because disruptions in this progression may be related to carcinogenesis, a complete understanding of it takes on special significance. We have been using the culture systems developed in our laboratory for growing human mammary epithelial cells (HMEC) to study regulation of differentiation in these cells.

Mammary epithelial cell maturation and differentiation is complicated by superimposition upon the maturation process of the hormonal influences accompanying puberty, the estrous cycle, meno-

pause, and those of pregnancy, lactation, and involution. Thus, unlike skin epithelial cells, the pathway of functional differentiation in mammary epithelial cells is not necessarily coincidental with that for terminal differentiation. Studies *in vivo* and in organ culture have helped to clarify the maturation stages in rodents, but the relationship between these stages and systemic hormonal influences remains obscure. Even less is known about these processes in humans. Tissue culture systems offer the possibility for experimental examination of these questions. This potential, however, would be restricted, if, as has been suggested, cells placed in culture lose the ability to express tissue-specific traits. On the other hand, several studies in epithelial cell systems have indicated that cells in culture, while not displaying tissue-specific properties, have not lost their capacity for expression; e.g., rat mammary epithelial cells growing in monolayer cultures for up to 20 days will grow into normal gland when transplanted *in vivo* into abdominal fat pads cleared of their mammary elements, and rat tracheal epithelial cell lines and normal cells in culture for one week regain the ability to form mucociliary epithelium when placed on tracheal grafts *in vivo*. It is more likely that current culture conditions are either not sufficient to support expression of functional differentiation or are selecting for a stage characterized by proliferation. In this context, it is important to note that systems for studying mammary function in culture have been successful at maintaining the functions typical of prelactation and lactation, but not in inducing any of these functions in cells from quiescent glands. Additionally, given the complexity of mammary cell maturation and differentiation, cells from quiescent glands may be present in a stage of maturation not readily recognizable because our knowledge of mammary function is largely based on the highly differentiated cells present during lactation. With this concept in mind, we are developing markers for evaluating differentiation in HMEC that are based on properties not necessarily linked to lactation.

HMEC grown in the MM vs. the MCDB170 medium invariably undergo senescence after far fewer cell divisions. The selection and proliferation properties of the post-selection cells in the MCDB170 serum-free medium might be due to their being less differentiated progenitor cells, while those in MM are more committed to differentiated function, thereby being unable to express long-term proliferation. This concept of a basic difference in expression of differentiated function by HMEC grown in each medium is supported by the pattern of glucose utilization and protein synthesis and secretion. HMEC grown in MM have a distinctly different pattern of glucose utilization from that of cells from the same specimen in MCDB170. Most notably, the syntheses of glycogen and lactate are increased. These increases correspond to changes observed in murine mammary epithelial cells during the transition from the virgin to the pregnant state. Because of the regulatory significance of glycogen synthesis in mammary epithelial cells in late pregnancy, it is likely that increased glycogen synthesis is a reliable indicator of the prelactational stage of the mammary epithelial cell. We therefore suggest that HMEC in MM are apparently in a metabolically differentiated state resembling cells present during mid-pregnancy, whereas HMEC in MCDB170 are metabolically less differentiated. This contention is supported by autoradiograms of electrophoretic gels demonstrating synthesis and secretion of a casein-related protein by cells in MM but not in MCDB170.

To further test the possibility that postselection cells in MCDB170 are progenitor cells, we transferred cells grown for eight passages in MCDB170 to MM. Syntheses of glycogen, lactate, and milk proteins were examined 4 to 24 hours later (Table 1). Control cells remained in fresh MCDB170. Syntheses of glycogen and lactate are increased at the earliest time point. In a second experiment, a xyloside was added to one set of cells to inhibit glycosylation of protein. This treatment did not affect glycogen and lactate synthesis.

We have partially purified β-casein, the major protein in human milk, to aid in the analysis of proteins secreted into the medium in these experiments. This preparation was used to produce polyclonal antibodies, and hybridomas are currently being screened for monoclonal antibody production. The polyclonal antibody preparation has been used for detection of milk proteins secreted into the medium. The proteins were precipitated from the media in replicate plates examined for glycogen and lactate synthesis. After separation by polyacrylamide gel electrophoresis, the proteins were transferred to nitrocellulose and probed with the polyclonal antibody for the presence of casein-related proteins (Western blot technique).

Comparison of proteins secreted by postselection cells to those in human milk revealed that a protein produced by cells switched to MM comigrated with a protein in human milk (Fig. 1). This protein was not recovered in medium from cells remaining in MCDB170, and its synthesis and/or secretion was severely and specifically inhibited by the addition of xyloside. The action of the

Table 1. Effect of medium on glucose metabolite pattern.

Switching from MCDB170 to MM	Glucose Incorporation (nm/mg protein):				
Time in 2nd medium (hrs)	Glycogen		Lactate		Lipid
	1st Expt.	2nd Expt.	1st Expt.	2nd Expt.	1st Expt.
0	6.4	9.0	340	415	2.30
4	14.1	18.3	995	489	3.95
8	10.4	29.1	815	763	3.61
24	141.6	25.6	407	717	2.02
24+xyloside	—	23.0		836	
Switching from MM to MCDB170					
0	70.2		1075		3.29
4	11.5		498		2.98
8	16.2		501		2.34
24	8.9		365		1.92

Cells growing eighth passage from specimen H161 in medium MCDB170 for 8 passages were fed with MM and H161 cells in second passage in MM were shifted to MCDB170 at 0-time. At 3, 7 and 23 hr later [U-^{14}C]-glucose was added and the incorporations into glycogen, lactate and lipid were determined 1 hr later as described in the text. A replicate experiment going from MCDB170 to MM was repeated several months later. In this experiment a replicate MCDB170-MM plate was treated with xyloside for 24 hr. Replicate plates acting as controls were fed with the same type of fresh medium at 0-time and incorporation of glucose into products determined at the same time intervals as the test plates.

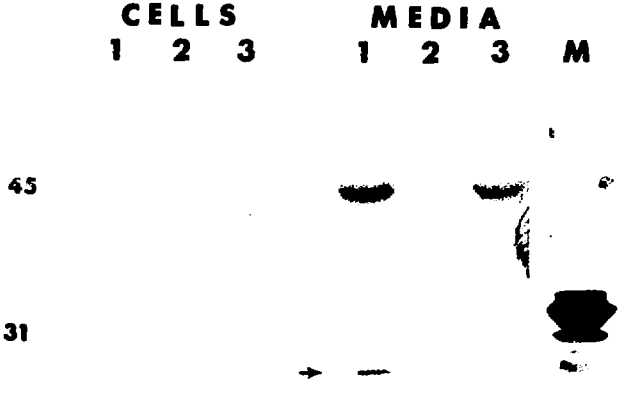

Fig. 1. Western blots using an antibody to human casein of proteins in cell lysates and media from HMEC. The experiment is the same as experiment 2 in Table 1. Lanes 1 and 3 represent results from cells grown in MM; those in lane 3 received xyloside. Lane 2 contains proteins from control cells remaining in MCDB170. Lane M contains casein purified from human milk. No positively reacting proteins were found in any cell lysates or in medium from cells in MCDB170. Addition of xyloside specifically inhibited production of a casein-related protein.

(XBB 850-8533)

xyloside in this case is likely due, in part, to inhibition of secretory vesicle formation which would, in turn, inhibit secretion of milk proteins. The specific protein in question is not β-casein but a casein-related protein that may arise from incomplete processing within the cell or from partial postsecretion degradation.

From these preliminary studies, it appears that MCDB170 supports growth of progenitor cells that can express some differentiated functions when placed in MM, and this stage appears to be comparable in many ways to rodent mammary epithelial cells from animals in early to mid-pregnancy.

In contrast to rodent systems, HMEC have not required artificial matrices, such as collagen gels, to express some differentiated functions. There are several possible explanations for this fact. First, we are dealing with cells at a physiological stage in which changes in cell shape (cuboidal to columner) and polarization are not rigorously required. Secondly, because HMEC apparently synthesize and/or accumulate sufficient matrix for long-term growth and for the specific modulations of phenotypic expression demonstrated here, it is possible that modulation of matrix formation can occur within 4 hours after the switch to medium. The source of matrix material might be different for cells in each medium. In the case of cells in MM, some matrix components might be synthesized, and other underfined factors from the medium might be organized into matrix. In MCDB170, it is more likely that HMEC are able to form the matrix necessary for growth because this medium has been optimized for growth of these cells. The experiments with xyloside are compatible with this explanation. Inhibition of matrix processing by xyloside could alter the cell's ability to synthesize and/or secrete protein.

The next steps in evaluating the functional potential of normal postselection cells are: 1) to continue development of markers for detecting stages of HMEC maturation, and 2) to attempt induction of the prelactational and lactational states. In light of the work in this field in other species, we anticipate that induction of the lactational state will likely require a prepared matrix to provide proper cell orientation and/or allow for changes in cell shape. A reduction in intracellular cAMP and specific changes in the complement of hormones and growth factors in the medium are also anticipated. The ability to grow HMEC under defined conditions presents an advantageous starting point for such studies.

The expert technical assistance of Linda Hayashi, Annie Pang, and Annette Drew in the conduct of these studies is gratefully acknowledged.

EVALUATION OF NORMAL AND TRANSFORMED HUMAN MAMMARY EPITHELIAL CELLS WITH MONOCLONAL ANTIBODIES TO CELL SURFACE ANTIGENS

Martha Stampfer, Gordon Parry, and Jack Bartley

The composition of the cell surface molecules of mammary epithelial cells may vary with the state of cellular differentiation and as a result of malignant or immortal transformation. Monoclonal antibodies (MAb), capable of recognizing the cell surface antigens that vary under these conditions, can be valuable tools both for detecting cells at different stages of differentiation and transformation and for probing the underlying biochemical processes. We have utilized six MAb's raised against human milk-fat globule antigens (HMFGA) to determine if any of them can distinguish states of differentiaion or transformation in our human mammary epithelial cell (HMEC) cultures. Data from other mammary epithelial systems have shown that some MFGA are found in greatest amounts in cells derived from lactating breasts, and also that tumor-derived cells may show increased amounts of specific HMFGA. Thus far, we have examined cells mainly by indirect immunofluorescence, which allows the cell surface properties of individual cells in the population to be visualized. Studies recently initiated will identify the proteins involved by gel electrophoresis and Western blots.

Our experiments thus far have yielded the following results:

1. The six different MAb's (designated 1–6) display four different patterns of binding.

2. Normal HMEC grown in MCDB170 show almost no binding of MAb's 2 and 3, and, depending upon the individual, 10 to 50% of cells display a punctate pattern of fluorescence with MAb's 1

and 5. When transferred to MM, 100% of the cells are now punctate positive for MAb's 1 and 5, and some cells (1–10%) are positive for MAb 2. This result is consistent with the other data we have obtained, which suggests that MCDB170 maintains the cells in a less differentiated state than the MM medium.

3. Cells derived from mastectomy tissues, and atypical reduction mammoplasty specimens, may show increased expression of MAb's 1, 2, and 5 when grown in MCDB170 compared to normal tissues.

4. The two cell lines derived from normal tissues after treatment with benzo(a)pyrene had distinct patterns of HMFGA expression. The more differentiated line, 184B5, had increased expression (~100%) of MAb's 1 and 5 in MCDB170, as well as some expression of MAb's 2 and 3 (5–20%). The less differentiated line, 184A1, had a decreased percentage of cells positive for MAb's 1 and 5, but a small (< 5%) number of cells positive for MAb's 2 and 3.

5. Treatment of cells with neuraminadase, to remove sialic acid residues, rendered all cells 100% positive for MAb's 1, 2, and 5, and had no effect on expression of MAb 3.

These results are consistent with the data of others that suggest that HMFGA may be markers of both differentiation and transformation. From these preliminary results, it is likely that MAb's 1 and 5 are more sensitive to states of differentiation, whereas MAb's 2 and 3 may be more indicative of cellular transformation.

USE OF DNA RESTRICTION FRAGMENT LENGTH POLYMORPHISMS FOR THE IDENTIFICATION OF HONEYBEE RACES

H. Glenn Hall

Honeybees of African descent (*Apis mellifera scutellata*, formerly *A.m. adansonii*),[1] accidently released from experimental hives in Brazil 28 years ago, have populated most of South and Central America, now as far north as Honduras, where they have largely displaced the honeybees of European descent.[2] The bees are a problem mainly because of their ferocious stinging. Isolated introductions of the Africanized bees have already occurred in this country, a notable case this past summer in California,[3] which have been largely contained. However, based on the bees' migration rate through Central America, they are expected to arrive in the US *en masse* within five years. In 1972, the National Academy of Science Committee on the African Honey Bee correctly concluded that the African bees' entry into the United States was inevitable and would be an environmental danger to the population and catastrophic to the commercial beekeeping and pollination industries.[4] By USDA estimates, the beekeeping industry will lose from $26 to $58 million annually.[5] The same report calculates that $19 billion worth of agricultural products are dependent upon honeybee pollination. Thus, the total loss as a result of the African bee could be immense.

Possible methods of control include quarantine and extermination, stock certification, and selective breeding for a gentle hybrid. All of these approaches are dependent upon a reliable identification method to distinguish the African bee from the European bee. Establishing a precise means of identification was a major recommendation by the National Academy Committee, but current methods are inadequate. Presently, the most effective method of identification of the African bee is through morphometric statistical analysis.[6] However, the method is subject to environmental influences and cannot reliably distinguish hybrids past one generation. Allozyme analysis is both uncertain and impractical as a means of identification because of the limited allozyme variability in bees.[7]

Until now, all efforts to identify bees have been limited to phenotype or, at best, allozyme analysis. This study is the first effort to directly utilize genetic material for identification and certification of bees. The identification is based on DNA fragments generated by restriction endonucleases. I have established a library of honeybee DNA probes and have begun their testing against two lines of European bees. The initial results encourage further development of this method.

Fragments of honeybee nuclear DNA, generated with PstI, were randomly inserted into the PstI site of the *E. coli* plasmid pBR322.[8] From the bacterial colonies transformed by the plasmids, those carrying inserts of honeybee DNA of about 4 Kb or greater and not containing repetition sequences were selected (Fig. 1).[9] DNA was isolated from two samples of honeybees: one designated as Italian (*A.m.ligustica*), and the other as Carniolan (*A.m.carnica*). The DNA was digested with eight separate restriction enzymes, the fragments separated by agarose gel electrophoresis, blotted onto membranes, and hybridized with the denatured radioactively labeled probes.[10] So far, 17 probes have been tested. Between the DNA of the two samples, six additional fragments were found in the Carniolan line, some of which are shown in Fig. 2.

The European honeybees in this country, although designated as different races, were derived from a limited number of founding populations and probably have a similar hybrid genotype. Genetic differences between African and European bees are likely to be much greater, with a higher frequency of restriction fragment polymorphisms than found here among the European bees. Africanized samples have recently been obtained from Costa Rica and will soon be tested with the same probes. Restriction site differences at many, preferably widespread, loci can potentially be found, so that after several generations and multiple recombinational events, the alleles found in hybrids will quantitatively reflect the degree of crossbreeding. Probe and enzyme combinations that reveal distinctive differences will first be sought and selected among a few samples of European and Africanized bees, and the selected probes will then be tested against many more samples. It must be determined which polymorphisms just represent variability within populations and those that show significant gene frequency differences among the populations.

Restriction fragment length polymorphisms characteristic of, and hopefully diagnostic for Africanized bees and their hybrids will provide a reliable means of identification that will be especially needed when major expensive decisions to exterminate or quarantine large numbers of colonies are to be made. Genotype identification by restriction

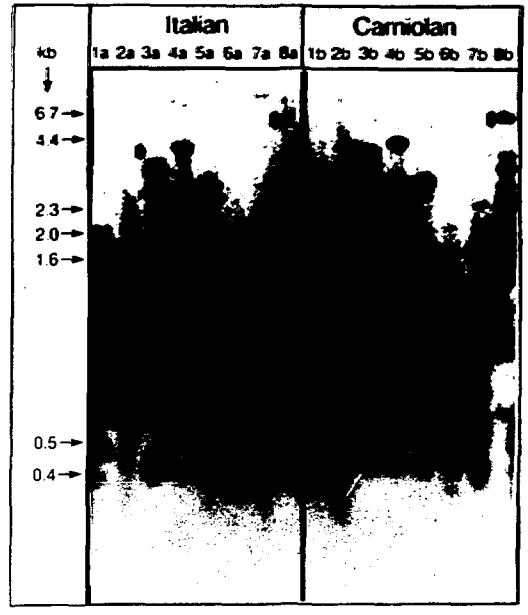

Fig. 2. Southern blot of total honeybee DNA hybridized to a mixture of four probes. The discrete bands demonstrate that the strategy for obtaining unique sequence probes was successful. Lanes 1a through 8a each contain DNA from the Italian line digested with a different restriction enzyme listed below. Lanes 1b through 8b each contain DNA from the Carniolan line digested with the corresponding restriction enzymes in lanes 1a through 8a. Lambda phage DNA digested with HindIII and pBR322 digested with HinfI were used as molecular weight standards. Arrows indicate differences in the fragments. Note that the lack of bands in lanes 3a and 8a are accompanied by an increase in the density of the next lower major bands compared to the corresponding bands in lanes 3b and 8b. 1 = MspI, 2 = TaqI, 3 = AluI, 4 = HaeIII, 5 = HhaI, 6 = MboI, 7 = HinfI, 8 = NciI. (XBB-850-10249)

Fig. 1. Colonies, already selected for containing plasmids with inserts, were hybridized to total labeled honeybee DNA. Because of the high concentration of repetitive sequences and the very low concentration of single-copy sequences, colonies containing inserts of repetitive DNA exhibit intense hybridization, whereas those with inserts of unique sequences do not. (XBB-850-10248)

fragments will be very applicable for certification of breeder stocks as non-African or as acceptable hybrids. Certification of stocks should aid selective breeding for gentle African bees. Beyond the identification of Africanized bees, the results of this research as it develops further will enhance future studies of basic honeybee genetics, such as in determining gene linkage and following gene flow and variability in populations.

REFERENCES

1. Ruttner, F. African races of honeybees. *Proc. 25th Int. Congress on Apiculture* (1976).
2. Michener, C.D. The Brazilian bee problem. *Ann. Rev. Entomol. 20*, 399–416 (1975).
3. Cobey, S., Lawrence, T. Status of the Africanized bee find in California. *Amer. Bee J. 125*, 607–711 (1985).
4. *Final Report of the committee on the African honeybee.* NAS-NRC, Washington, D.C. (1972).
5. McDowell, R. The Africanized honey bee in the United States. What will happen to the U.S. beekeeping industry? *USDA Agricultural Economic Report* No. 519 (1984).
6. Daly, H.V., Balling, S.S. Identification of Africanized honeybees in the western hemisphere by discriminant analysis. *J. Kansas Ent. Soc. 51*, 857–869 (1978).
7. Rinderer, T.E., Sylvester, H.A. Identification of Africanized bees. *Amer. Bee J. 121*, 512–516 (1981).
8. Maniatis, T., Fritsch, E.F., Sambrook, J. *Molecular Cloning. A Laboratory Manual.* Cold Spring Harbor Laboratory (1982).
9. Grunstein, M., Hogness, D. Colony hybridization: a method for the isolation of cloned DNAs that contain a specific gene. *Proc. Natl. Acad. Sci. 72*, 3961–3965 (1975).
10. Southern, E. Gel electrophoresis of restriction fragments. *Methods Enzymol. 68*, 152–176 (1979).

APPENDICES

APPENDIX A. List of Contracts and Grants Supporting Portions of Work Presented in This Annual Report

INVESTIGATOR	CONTRACT OR GRANT
E.J. Ainsworth	NASA P.O. T3516-G Life-Shortening Effects of HzE Particles on Mice/Heavy Ion Cell Transformation
E.J. Ainsworth	PHS Grant TW 00980 Killing Mouse Marrow Stem Cells by Heavy Atomic Nuclei
E.L. Alpen	PHS Grant CA 30236 Advanced Design Research Heavy Ion Medical Accelerator
E.L. Alpen	PHS Grant RR 05918 Biomedical Research Support Grant
J.C. Bartley	PHS Grant CA 38889 Human Mammary Cells: Modulation of Differentiated States
G. Brecher	PHS Grant AM 27454 Kinetics of Transfused Stem Cells in Normal Mice
T.F. Budinger	PHS Grant HL 25840 Cardiovascular Flow and Metabolism
T.F. Budinger	PHS Grant AG 05890 Cerebral Blood Flow Patterns in Alzheimer's Disease
T.F. Budinger	PHS Grant HL 07367 Quantitative Cardiovascular Research, Training Grant
T.F. Budinger	IBM Instruments P.O. 4521310 NMR Imaging Project
J.R. Castro	PHS Grant CA 19138 Treatment of Cancer w/Heavy Charged Particles
A. Chatterjee	PHS Grant CA 27024 Bragg Peak Localization by Radioactive Beams
G.K. Clemons	PHS Grant HL 22469 Radioassay of Erythropoietin
P.K. Cooper	PHS Grant CA 32986 Inducible Responses to Carcinogenic DNA Damage
S.B. Curtis	PHS Grant CA 17411 Response of Rat Tumor Cells to Heavy Ions

P.W. Durbin	NRC IAG 60-85-012 Development of Metabolic Models for Alkaline Earth and Actinide Radionuclides
P.W. Durbin	PHS Grant ES 02698 Biological Testing of New Actinide-Chelating Agents
S.N. Ebbe	PHS Grant AM 21355 Kinetics of Megakaryocyte and Platelet Turnover
M.S. Esposito	PHS Grant GM 29002 Comparative Analysis of Mitotis and Meiotic Recombination
M.S. Esposito	PHS Grant ES 02756 Genetic Effects of Carcinogens in Mitosis and Meiosis
T.M. Forte	PHS Grant HL 07279 Lipoprotein Methodology, Structure and Function Training Grant
R.M. Glaeser	PHS Grant GM 23325 Biological Structure Analysis by Electron Microscopy
R.M. Glaeser	PHS Grant RR 02246 Precision Scanning Microdensitometer Facility
L.S. Gold	PHS IAG 222-Y01-ES-10066 Quantitative Species Extrapolation in Carcinogenesis
R. Goth-Goldstein	PHS Grant ES 01916 Alkylating-Carcinogens Mutagenesis in Mammalian Cells
R. Goth-Goldstein	PHS Grant ES 03603 Inducible Resistance to Alkylating Carcinogens
H.G. Hall	PHS Grant HD 17892 Extracellular Matrix and Eptithelial Lumen Morphogenesis
J. Hosoda	PHS Grant GM 16841 Structure and Function of Helix Stabilizing Protein
R.H. Huesman	PHS Grant CA 38086 Scatter Compensation in Emission Tomography
R.M. Krauss	PHS Grant HL 33577 Plasma Lipoproteins in Coronary Artery Disease
S.A. Leadon	PHS Grant CA 40453 DNA Repair in Specific Sequences of Mammalian Cells
R.P. Liburdy	ONR Contract N00014-84-F-0186 Mechanisms of Microwave Interactions with Liposome Membranes
R.P. Liburdy	PHS Grant RR 02570 Radio Frequency Assisted HPLC
J.T. Lyman	PHS IAG Y01-CM-20110 Evaluation of Treatment Planning for Particle Beam Radiotherapy

J.T. Lyman	PHS Grant CA 22286 AAPM B682-19 Charged Particle Beam Dosimetry Task Group: Dosimetry Protocol
M.F. Maestre	PHS Grant AI 08427 Physical Structure of Viruses, Chromosomes and Cell Nuclei
R.K. Mortimer	PHS Grant GM 30990 Yeast RAD Genes in Repair, Recombination and Meiosis
A.V. Nichols	PHS Grant HL 18574 Lipoprotein Methodology and Biomedical Applications
T.W. Sargent	PHS Grant MH 36801 Transmethylation Kinetics in Schizophrenia
T.W. Sargent	V.A. Medical Center, Martinez V612P-1194 Cerebral Metabolic Indices of Dementia Pathophysiology
W. Schimmerling	PHS Grant CA 23247 Physical Characteristics of Heavy Ion Beams
W. Schimmerling	NASA P.O. L22395A To Measure the Production of Neutrons by High Energy Heavy Ions
R.I. Schwarz	PHS Grant CA 37958 Manipulation of the Differentiated State by Oncogenesis
B.A. Singer	PHS Grant CA 42736 Alkylation of Polynucleotides *in vitro* and *in vivo*
M.R. Stampfer	PHS Grant CA 24844 Characterization of Human Mammary Cells
M.R. Stampfer	PHS Grant CA 30028 (R.Ham, Univ. Colorado) P.O. 426881 Defined Medium for Human Mammary Epithelial Cells
T.S. Tenforde	EPRI Contract RP 799-21 Microprocessor-Controlled Personal Dosimeter for Recording Low-Intensity Power Frequency Magnetic Fields
T.S. Tenforde	EPRI Contract RP 2572-5 Assessment of Biological Effects Associated with Magnetic Fields from a Superconducting Magnet Energy Storage System
C.A. Tobias	PHS Grant CA 15184 Heavy Ion Radiobiology Related to Oncology

APPENDIX B: 1985 Publications

CONTRIBUTIONS TO JOURNALS

Alpen, E.L., Saunders, W., Chatterjee, A., Llacer, J., Chen, G.T.Y., and Scherer, J. A Comparison of water equivalent thickness measurements: C.T. method vs. heavy ion beam technique. *Brit. J. Radiology 58,* 542–548 (1985).

Bartley, J.C., and Stampfer, M.R. Factors influencing benzo(a)pyrene metabolism in human mammary epithelial cells in culture. *Carcinogenesis 6,* 1017–1022 (1985).

Bastacky, J., Hayes, T.L., and Gelinas, R.P. Quantitation of shrinkage during preparation for scanning electron microscopy: human lung. *Scanning 7,* 134–140 (1985).

Bastacky, J., and Hayes, T.L. Safety in the scanning electron microscope laboratory. *Scanning 7,* 255–272 (1985).

Beer, M., Caspar, D.L.D., and Glaeser, R.M. Introduction, Papers from EMSA Symposium on Electron Crystallography of Macromolecules. *Ultramicroscopy 13,* vii (1984).

Bialek, W., and Schweitzer, A. Quantum noise and the threshold of hearing. *Phys. Rev. Lett. 54,* 725–728 (1985).

Blum, C.B., Davis, P.A., and Forte, T.M. Elevated levels of apolipoprotein E in human cord blood plasma. *J. Lipid Res. 26,* 755–760 (1985).

Brown, M.S., Garcia, J.F., Phibbs, R.H., and Dallman, P.R. Decreased response of plasma immunoreactive erythropoietin to "available oxygen" in anemia of prematurity. *J. Pediatrics 105,* 793–798 (1984).

Brown, M.S., Phibbs, R.H. Garcia, J.F., and Dallman, P.R. Postnatal changes in erythropoietin levels in untransfused premature infants. *J. Pediatrics 103,* 612–617 (1983).

Budinger, T.F., and Huesman, R.H. Ten precepts for quantitative data acquisition and analysis. *Circulation 72 (Suppl. IV),* 53 (1985).

Bustamante, C., Maestre, M.F., and Keller, D. Simplified expressions for the circular intensity differential scattering of chiral aggregates. *Biopolymer 12* 1595–1612 (1985).

Calderon, I.L., Contopoulou, C.R., and Mortimer, R.K. Isolation of a DNA fragment that is expressed as an amber suppressor when present in high copy number in yeast. *Gene 29,* 69–76 (1984).

Carr, K.E., Hayes, T.L., McKoon, M., Bastacky, S.J., and Kamel, H.M.H. Etched surfaces of plastic embedded and frozen hydrated gastrointestine. *J. Submicroscopic Cytology 16,* 219–226 (1984).

Castro, J.R., Chen, G.T.Y., Pitluck, S., Cartigny, A., Phillips, T.L, Saunders, W.M., Collier, J.M., Woodruff, K.H., Friedman, M., and Austin-Seymour, M. Helium charged-particle radiotherapy of locally advanced carcinoma of the esophagus, stomach, and biliary tract. *Am. J. Clin. Oncol. (CCT) 6,* 629–637 (1983).

Chandra, M., Miller, M.E., Garcia, J.F., Mossey, R.T., and McVicar, M. Serum immunoreactive erythropoietin levels in patients with polycystic kidney disease as compared with other hemodialysis patients. *Nephron 39,* 26–29 (1985).

Chang, C.-F., Mizushima, S., and Glaeser, R.M. Projected structure of the pore-forming OmpC protein from *Escherichia coli* outer membrane. *Biophys. J. 47,* 629–639 (1985).

Chang, C.-F., Ohno, T., and Glaeser, R.M. The fatty acid monolayer technique for preparing frozen-hydrated specimens. *J. Electron Microscopy Technique 2,* 59–65 (1985).

Char, D.H., Saunders, W.M., Castro, J.R., Irvine, A.R., Stone, R.T., Crawford, J.B., Barricks, M., Lonn, L.I., Hilton, G.F., Schwartz, A., Chen, G.T.Y., Lyman, J.T., Collier, J.M., Salit, H., Straatsma, B.R., and Kaminski, A. Charged particle therapy for choroidal melanoma. *Ophthalmology 90,* 1219 (1983).

Cohen, R.A., Clemons, G.K., and Ebbe, S. Correlation between bioassay and radioimmunoassay for erythropoietin in human serum and urine concentrates. *Proc. Soc. Exptl. Biol. Med. 179,* 296–299 (1985).

Costello, M.J., Viitanen, P., Carrasco, N., Foster, D.L., and Kabach, H.R. Morphology of proteoliposomes reconstituted with purified *lac* carrier protein from *Escherichia coli*. *J. Biol. Chem. 259,* 15579–15586 (1985).

Dolberg, D.S., Hollingsworth, R., Hertle, M., and Bissell, M.J. Wounding and its role in RSV-induced tumor formation. *Science 230,* 676-678 (1985).

Dukes, P.P., Ma, A., Clemons, G.K., and Meytes, D. Measurement of human erythroid burst promoting activity (BPA) by a specific cell culture assay. *Exp. Hematol. 13,* 59–66 (1985).

Durbin, P.W., and Schmidt, C.T. The U.S. Transuranium Registry report on the ^{241}Am content of a whole body. Part V. Implications for metabolic modelling. *Health Physics 49,* 623-661 (1985).

Ebbe, S., Adrados, C., and Phalen, E. Independence of megakaryocyte number and size in long term cultures of normal mouse marrow. *Exp. Hematol. 13,* 817–820 (1985).

Eckleman, W.C., Reba, R.C., Rzeszotarski, W.J., Gibson, R.E. Hill, T., Holman, B.L., Budinger, T.F., Conklin, J.J., Eng, R., and Grisson, M.P. External imaging of cerebral muscarinic acetylcholine receptors. *Science 223,* 291–293 (1984).

Finch, G., McNeil, K., Democko, C., Lai, C., Bastacky, J., Hayes, T.L., and Fisher, G. A technique permitting correlative microscopy (light microscopy, scanning electron microscopy, transmission electron microscopy and high voltage electron microscopy) of cultured alveolar macrophages. *J. Electron. Microsc. Tech. 2,* 69–70 (1985).

Forte, T.M., Ren, C.L., Nordhausen, R.W., and Nichols, A.V. Formation of phospholipid-rich HDL: A model for square-packing lipoprotein particles found in interstitial fluid and in abetalipoproteinemic plasma. *Biochim. et Biophysica Acta 834,* 386–395 (1985).

Frankel, K.A., Bistirlich, J.A., Bennington, R., Bowman, H.R., Crowe, K.M., Martoff, C.J., Murphy, D.L., Rasmussen, J.O., Sullivan, J.P., Yoo, E., Zajc, W.A., Miller, J.P., Hashimoto, O., Koike, M., Peter, J., Benenson, W., Crawley, G.M., Kashy, E., Nolen, Jr., J.A., and Quebert, J. Pion production near mid-rapidity in high-energy heavy-ion collisions. *Phys. Rev. C 32,* 975–982 (1985).

Friedland, R.P., Budinger, T.F., Koss, B., and Ober, B.A. Alzheimer's disease: Anterior-posterior and lateral hemispheric alterations in cortical glucose utilization. *Neuroscience Letters 53,* 235–240 (1985).

Friedland, R.P., Prusiner, S.B., Jagust, W.J., Budinger, T.F., and Davis, R.L. Bitemporal hypometabolism in Creutzfeldt-Jakob disease measured by positron emission tomography with ^{18}F-2-fluorodeoxyglucose. *J. Comput. Assist. Tomog 8,* 978–981 (1984).

Glaeser, R.M., Jubb, J.S., and Henderson, R. Structural comparison of native and deoxycholate-treated purple membrane. *Biophys. J. 48,* 775–780 (1985).

Glaeser, R.M. Electron crystallography of biological macromolecules. *Ann. Rev. Phys. Chem. 36,* 243–275 (1985).

Goldberg, I.J., Mazlen, R.G., Rubenstein, A., Gibson, J.C. Paterniti, Jr., J.R., Lindgren, F.T., and Brown, W.V. Plasma lipoprotein abnormalities associated with acquired hepatic triglyceride lipase deficiency. *Metabolism 34,* 832-835 (1985).

Goodman, J.W., Hall, E.A., Miller, K.L., Shinpock, S.G. Interleukin 3 promotes erythroid burst formation in "serum-free" cultures without detectable erythropoietin. *Proc. Natl. Acad. Sci. USA 82,* 3291–3295 (1985).

Greiner, D.E., Crawford, H., Lindstrom, P.J., Kidd, J.M., Olson, D.L., Schimmerling, W., and Symons, T.J.M. Uranium nuclear reactions at 900 MeV/nucleon. *Phys. Rev. C 31,* 416–420 (1985).

Hanson, W. R., and Ainsworth, E.J. 16,16-dimethyl prostaglandin E_2 induces radioprotection in murine intestinal and hematopoietic stem cells. *Radiation Res. 103,* 196–203 (1985).

Henderson, R., and Glaeser, R.M. Quantitative analysis of image contrast in electron micrographs of beam-sensitive crystals. *Ultramicroscopy 16,* 139–150 (1985).

Herbert, P.N., Hyams, J.S., Bernier, D.N., Berman, M.M., Sartelli, A.L., Lynch, K.M., Nichols, A.V., and Forte, T.M. Apolipoprotein B-100 deficiency: intestinal steatosis despite apolipoprotein B-48 synthesis. *J. Clin. Invest. 76,* 403–412 (1985).

Hlatky, L., and Alpen, E.L. Two-dimensional diffusion limited system for cell growth. *Cell Tissue Kinet. 18,* 597–611 (1985).

Hoeg, J.M., Segal, P., Gregg, R.E., Chang, Y.S., Lindgren, F.T., Adamson, G.L., Frank, M., Brickman, C., Brewer, H.B., Jr. Characterization of plasma lipids and lipoproteins in patients with beta$_2$-glycoprotein I (apolipoprotein H) absence. *Atherosclerosis 55,* 25-34 (1985).

Jansson, L.T., Perkio, M.V., Clemons, G.K., Retino, C.J., and Dallman, P. Erythropoietin concentration during the development and recovery from iron deficiency in the rat. *Blood 65,* 959–963 (1985).

Kao, W. W-Y., Kao, C. W.-C., and Schwarz, R.I. Prolyl hydroxylase production can be uncoupled from the regulation of procollagen synthesis. *Experimental Cell Research 157,* 265–270 (1985).

Keller, D., Bustamante, C., Maestre, M.F., and Tinoco, I., Jr. Model computations of differential scattering of circularly polarized light by dense macromolecules. *Biopolymers 24,* 783–797 (1985).

Keller, D., Bustamente, C., Maestre, M.F., and Tinoco, I., Jr. Imaging of optically active biological structures using circularly polarized light. *Proc. Natl. Acad. Sci. (USA) 82,* 401–405 (1985).

Kellie, S., Holme, J., and Bissell, M.J. Interaction of tumor promoters with epithelial cells in culture: an immunofluorescence study. *Exp. Cell Res. 160,* 259–274 (1985).

Koss, E., Friedland, R. P., Ober, B.A., and Jagust, W.J. Differences in lateral hemispheric asymmetries of glucose utilization between early- and late-onset Alzheimer-type dementia. *Am. J. Psychiatry 142,* 638–640 (1985).

Koss, E., Ober, B.A., Delis, D., and Friedland, R.P. The Stroop color-word test: indicator of dementia severity. *Interntl. J. Neuroscience 24,* 53–61 (1984).

Kraft, G., Hieber, L., Schuber, M., Muller, W., Kraft-Weyrather, W., Wulf, H., Miltenburger, H., Blakely, E.A., and Tobias, C.A. HZE effects on mammalian cells (COSPAR: Life Sci. Space Res.) *Adv. Space Res. 4,* 219–226 (1984).

Lee, E., Y.-H.P., Lee, W-H., Kaetzel, C.S., Parry, G., Bissell, M.J. Interaction of mouse mammary epithelial cells with collagen substrata: regulation of casein gene expression and secretion. *Proc. Natl. Acad. Sci. USA 82,* 1419–1423 (1985).

Leven, R.M., Schick, P.K., and Budzynski, A.Z. Fibrinogen biosynthesis in isolated guinea pig megakaryocytes. *Blood 65,* 501–504 (1985).

Liburdy, R.P., and Magin, R.L. Microwaves stimulated drug release from liposomes. *Radiation Research 103,* 266–275 (1985).

Liburdy, R.P., and Vanek, Jr., P.F. Microwaves and the cell membrane. II. Temperature, plasma, and oxygen mediate microwave-induced membrane permeability in the erythrocyte. *Radiation Research 102,* 190–205 (1985).

Liburdy, R.P., and Wyant, A. Radiofrequency radiation and the immune system. III. *In vitro* effects on human immunoglobulin and on murine T- and B-lymphocytes. *Int. Journal of Radiation Biology 46(1),* 67–81 (1984).

Lloyd, R.D., Bruenger, F.W., Mays, C.W., Atherton, D.R., Jones, C.W., Taylor, G.N., Stevens, W., Durbin, P.W., Jeung, N., Jones, E.S., Kappel, M.J., Raymond, K.N., and Weitl, F.L. Removal of Pu and Am from beagles and mice by 3,4,3-LICAM(c) or 3,4,3-LICAM(S). *Radiation Res. 99,* 106–128 (1984).

Lyman, J.T., Fabrikant, J.I., and Frankel, K.A. Charged-particle stereotactic radiosurgery. *Nucl. Instr. and Methods in Phys. Res. B10/11,* 1107–1110 (1985).

McCann, J., Horn, L., and Kaldor, J. An evaluation of *Salmonella* (Ames) test data in the published literature: application of statistical procedures, and analysis of mutagenic potency. *Mutation Research 134,* 1–47 (1984).

Maestre, M.F., Salzman, G.C., Tobey, R.A., Bustamante, C. Circular dichroism studies on single Chinese hamster cells. *Biochemistry 24,* 5152–5157 (1985).

Mathis, C.A., Sargent III, T., and Shulgin, A.T. Iodine-122-labeled amphetamine derivative with potential for PET brain blood flow studies. *J. Nucl. Med. 26,* 1295 (1985).

Mazoyer, B.M., Koos, M.S., and Huesman, R.H. Dead time correction and counting statistics for positron tomography. *Phys. Med. Biol. 30,* 385–399 (1985).

Mikols, W.C., Bustamante, C., Maestre, M.F., Tinoco, I. Jr., and Embury, S.M. Differential polarization microscopy: a new imaging technique. *Biotechnology 3,* 711–714 (1985).

Mickols, W., Maestre, M.F., Tinoco, I., Jr., and Embury, S.H. Visualization of oriented hemoglobin S in individual erythrocytes by differential extinction of polarized light. *Proc. Natl. Acad. Sci. USA 82,* 6527–6531 (1985).

Monteiro, P.J.M., Bastacky, S.J., and Hayes, T.L. Low-temperature scanning electron microscope analysis of the Portland cement paste early hydration. *Cement and Concrete Research 15,* 687–693 (1985).

Mortimer, R.K., and Schild, D. Genetic map of *Saccharomyces cerevisiae,* Edition 9. *Microbiological Reviews 49,* 181–213 (1985).

Nichols, A.V., Blanche, P.J., Gong, E.L., Shore, V.G., and Forte, T.M. Molecular pathways in the transformation of model discoidal lipoprotein complexes induced by lecithin: cholesterol acyltransferase. *Biochim. Biophys. Acta. 834* 285–300 (1985).

Nüsse, M., Afzal, S.M.J., Carr, B., and Kavanau, K. Cell cycle kinetic measurements in an irradiated rat rhabdomyosarcoma using a monoclonal antibody to bromodeoxyuridine. *Cytometry 6,* 611–619 (1985).

Olson, J.E., Schimmerling, W., Windsor, A., Upham, F., and Tobias, C.A. Peak-detect-and-hold circuit for instantaneous measurement of bioelectric signals. *J. Electrophysiol. Tech. 12,* 151–157 (1985).

Parry, G., Lee, E. Y.-H., Farson, D.A., Koval, M.H., Bissell, M.J. Collagenous substrata regulate the nature and distribution of glycosaminoglycans produced by differentiated cultures of mouse mammary epithelial cells. *Exp. Cell Res. 156,* 487–499 (1985).

Pennathur-Das, R., Alpen, E., Vichinsky, E., and Lubin, B.H. Evidence for a heterogeneous response to erythropoietin in the CFU_E pool of human bone marrow. *Experimental Hematology 12,* 31–37 (1984).

Pennathur-Das, R., Alpen, E., Vichinsky, E., Garcia, J., and Lubin, B.H. Evidence for the presence of CFU_E with increased *in vitro* sensitivity to erythropoietin in sickle cell anemia. *Blood 63,* 1168–71, (1984).

Perez, C.F., Botchan, M.R., and Tobias, C.A. DNA-mediated gene transfer efficiency is enhanced by ionizing and ultraviolet irradiation of rodent cells *in vitro.* 1. Kinetics of enhancement. *Radiation Research 104,* 200–213 (1985).

Phillips, M.H., Anderson, L.W., and Lin, C.C. Electron excitation cross sections for the metastable and resonant levels of $Ne(2p^53s)$. *Phys. Rev. A 32,* 2117–2127 (1985).

Roots, R., Chatterjee, A., Chang, P.Y., Lommel, L., and Blakely, E.A. Characterization of hydroxyl radical-induced damage after sparsely and densely ionizing irradiation. *Int. J. Radiat. Biol. 47,* 157–166 (1985).

Roots, R., Kraft, G., and Gosschalk, E. The formation of radiation-induced DNA breaks: The ratio of double-strand breaks to single-strand breaks. *Int. J. Radiat. Oncol. Biol. Phys. 11,* 259–265 (1985).

Salen, G., Kwiterovich, P.O., Shefer, S., Tint, G.S., Horak, I., Shore, V., and Horak, E. Increased plasma cholestanol and 5 alpha-saturated plant sterol derivatives in subjects with sitosterolemia and xanthomatosis. *J. Lipid Research 26,* 203–209 (1985).

Saunders, W.M. Radiation oncology: The use of beams of photons or particles for the treatment of tumors. *J. Radiation Physics and Chemistry 24,* 357–364 (1984).

Saunders, W.M., Char, D.H., Quivey, J.M., Castro, J.R., Chen, G.T.Y., Collier, J.M., Cartigny, A., Blakely, E.A., Lyman, J.T., Zink, S.R., and Tobias, C.A. Precision, high dose radiotherapy: Helium ion radiotherapy of uveal melanoma. *Int. J. Radiat. Oncol. Biol. Phys. 11,* 227–233 (1985).

Saunders, W.M., Chen, G.T.Y., Austin-Seymour, M., Castro, J.R., Collier, J.M., Gauger, G., Gutin, P., Phillips, T.L., Pitluck, S., Walton, R.E., and Zink, S.R. Precision, high dose radiotherapy: II. Helium ion treatment of tumors adjacent to critical central nervous system structures. *Int. J. Radiat. Oncol. Biol. Phys. 11,* 1339–1347 (1985).

Schaefer, E.J., Ordovas, J.M., Law, S.W., Ghiselli, G., Kashyap, M.L., Srivastava, L.S., Heaton, W.H., Albers, J.J., Conner, W.R., Lindgren, F.T., Lemeshev, Y., Segrest, J.P., and Brewer, H.B. Jr. Familial apolipoprotein A-I and C-III deficiency, variant II. *J. Lipid Res. 26,* 1089–1101 (1985).

Schild, D., Mortimer, R.K. A mapping method for *Saccharomyces cerevisiae* using *rad52*-induced chromosome loss. *Genetics 110,* 569–589 (1985).

Schooley, J.C., Kullgren, B., and Fletcher, B.L. Growth of murine bone marrow adherent stromal cells in culture without hydrocortisone in a low oxygen environment. *Interntl. J. Cell Cloning 3,* 2–9 (1985).

Schwarz, R.I. Procollagen secretion meets the minimum requirements for the rate-controlling step in the ascorbate induction of procollagen synthesis. *J. Biol. Chem. 260,* 3045–3049 (1985).

Shahrokh, Z., and Nichols, A.V. Interaction of human-plasma low-density lipoproteins with discoidal complexes of apolipoprotein A-I and phosphatidylcholine, and characterization of the interaction products. *Biochem. et Biophysica Acta 837,* 296–304 (1985).

Smith, H.S., Lippman, M.E., Hiller, A.J., Stampfer, M.R., and Hackett, A.J. Response to adriamycin of cultured normal and malignant human mammary epithelial cells. *J. Natl. Cancer Inst. 74,* 341–347 (1985).

Soulen, R.L., Budinger, T.F., and Higgins, C.B. Magnetic resonance imaging of prosthetic heart valves. *Radiology 154,* 705–707 (1985).

Stampfer, M.R., and Bartley, J.C. Induction of transformation and continuous cell lines from normal human mammary epithelial cells after exposure to benzo(a)pyrene. *Proc. Natl. Acad. Sci. USA: 82,* 2394–2398 (1985).

Stockman, J.A., Graeber, A.E., Clark, D.A., McClellan, K., Garcia, J.F., and Kavey, R.E. Anemia of prematurity: Determinants of the erythropoietin response. *J. Pediatrics 105,* 786–792 (1984).

Susa, J.B., Gruppuso, P.A., Widness, J.A., Domenech, M., Clemons, G.K., Sehgal, P., and Schwartz, R. Chronic hyperinsulinemia in the fetal rhesus monkey: effects of physiologic hyperinsulinemia on fetal substrates, hormones, and hepatic enzymes. *Amer. J. Obst. Gyn. 150,* 415–420 (1984).

Teng, B., Sniderman, A., Krauss, R.M., Kwiterovich, Jr., P.O., Milne, R.W., and Marcel, Y.L. Modulation of apolipoprotein B antigenic determinants in human low density lipoprotein subclasses. *J. Biol. Chem. 260,* 5067–5072 (1985).

Tinoco, I., Jr., Maestre, M.F., Bustamante, C., Keller, D. Use of circularly polarized light to study macromolecules. *Pure and Applied Chemistry 55,* 1423–1428 (1984).

Tobias, C.A. The future of heavy-ion science in biology and medicine. (Failla Memorial Lecture, February 28, 1983, San Antonio, Texas). *Radiation Research 103,* 1–33 (1985).

Widness, J.A., Clemons, G.K., Garcia, J.F., and Schwartz, R. Plasma immunoreactive erythropoietin in normal women studies sequentially during and after pregnancy. *Amer. J. Obstet. Gynocol. 149,* 646–650 (1984).

Williams, P.T., Haskell, W.L., Vranizan, K.M., Blair, S.N., Krauss, R.M., Superko, H.R., Albers, J.J., Frey-Hewitt, B., and Wood, P.D. Associations of resting heart rate with concentrations of lipoprotein subfractions in sedentary men. *Circulation 71,* 441–449 (1985).

Williams, P.T., Krauss, R.M., Wood, P.D., Albers, J.J., Dreon, D., and Ellsworth, N. Associations of diet and alcohol intake with high-density lipoprotein subclasses. *Metabolism 34,* 524–530 (1985).

Williamson, M.S., Game, J.C., and Fogel, S. Meiotic gene conversion mutants in *Saccharomyces cerevisiae.* I. Isolation and characterization of *pms1-1* and *pms1-2. Genetics 110,* 609–646 (1985).

Wolman, S.R., Smith, H.S., Stampfer, M., and Hackett, A.J. Growth of diploid cells from breast cancers. *Cancer Genetics and Cytogen 16,* 49–64 (1985).

Wrenn, M.E., Durbin, P.W., Howard, B., Lipsztein, J., Rundo, J., Still, E.T., and Willis, D.L. Metabolism of ingested uranium and radium. *Health Physics 48,* 601–635 (1985).

Yang, T.C., and Tobias, C.A. Neoplastic cell transformation by energetic heavy ions and its modification with chemical agents. *Adv. Space Res. 4,* 207–218 (1984).

Yang, T.C., and Tobias, C.A. Effects of heavy-ion radiation on the brain vascular system and embryonic development. *Adv. Space Res. 4,* 239–245, (1984).

Yano, Y., Budinger, T.F., Mathis, C.A., Singh, M., Moore, D.H., Hunter, J., Jones, R.M., and Ebbe, S.N. Gallium-68 chemistry for labeling platelets, proteins and lipoproteins. *J. Labelled Cmpds. Radiopharm. XXI,* 999–1001 (1984).

Yano, Y., Budinger, T.F., Ebbe, S.N., Mathis, C.A., Singh, M., Brennan, K.M., and Moyer, B.R. Gallium-68 lipophilic complexes for labeling platelets. *J. Nucl. Med. 26,* 1429–1437 (1985).

Yuhas, J.M., Afzal, S.M.J., and Afzal, V. Variation in normal tissue response to WR-2721. *Internti. J. Radiat. Oncol. Biol. Phys. 10,* 1537–1539 (1984).

CONTRIBUTIONS TO BOOKS AND PROCEEDINGS

Albers, J.J., Warnick, G.R., and Nichols, A.V. Laboratory measurements of HDL. Pages 381–414 in *Clinical and Metabolic Aspects of High Density Lipoproteins,* N.E. Miller and G.J. Miller Eds. Elsevier Science Publications, B.V., Amsterdam, 1984.

Albright, N.W., and Tobias, C.A. Extension of the time-independent repair-misrepair model of cell survival to high-LET and multicomponent radiation. In *Proceedings of the Berkeley Conference in Honor of Jerzy Neyman and Jack Kiefer,* U.C. Berkeley, July 1–15, 1983, Volume 1, L. LeCam, Ed. Wadsworth International Publication, 1985.

Bissell, M.J., Lee, E. Y.-H.P., Li, M., Chen, L.-H., and Hall, H.G. The role of the matrix in regulation differentiation of endocrine sensitive cells. In *Proceedings, The Second NIADDK Symposium on the Benign Prostatic Hyperplasia.* U.S. Government Printing Office, 1985.

Budinger, T.F., Huesman, and R.H., Knittel, B., Friedland, R.P., and Derenzo, S.E. Physiological modeling of dynamic measurements of metabolism using positron emission tomography. Pages 165–183 in *The Metabolism of the Human Brain Studied with Positron Emission Tomography,* T. Greitz Eds. Raven Press, New York, 1985.

Chen, G.T.Y., Austin-Seymour, M., Castro, J.R., Collier, J.M., Lyman, J.T., Pitluck, S., Saunders, W.M., and Zink, S.R. Dose volume histograms in treatment planning evaluation of carcinoma of the pancreas. Pages 264–268 in *Proceedings 8th International Conference on Computers in Radiotherapy* (Toronto, Canada, 1984). IEEE Computer Press (ISBN 81860551-6), Silver Springs, Maryland, 1984.

Chen, G.T.Y., Pitluck, S., and Richards, T. Three-dimensional graphics in treatment planning. Pages 61–65 in *Proceedings of Annual Meeting of National Computer Graphics Association* (NCGA), May 1984.

Chu, W.T., Curtis, S.B., Llacer, J., Renner, T.R., and Sorensen, R.W. Wobbler facility for biomedical experiments at the Bevalac. IEEE Trans. Nucl. Sci. NS-32: 3321-3323, 1985.

Derenzo, S. E., Budinger, T.F., and Huesman, R.H. Detectors for high resolution dynamic positron emission tomography. Pages 21–31 in *The Metabolism of the Human Brain Studied with Positron Emission Tomography*, T. Greitz, et al, Eds. Raven Press, New York, 1985.

Downing, K.H. and Glaeser, R.M. Small-spot illumination for high-resolution electron microscopy of beam-sensitive specimens. Pages 320–321 in *Proceedings of the 43rd Annual Meeting of the Electron Microscopy of Society of America*, G.W. Bailey, Ed. San Francisco Press, Inc., San Francisco, California, 1985.

Downing, K.H., and Glaeser, R.M. Simplified treatment of statistical error in electron crystallography. In *Proceedings Ninth European Congress on Electron Microscopy* (Budapest, 1984), 1985.

Esposito, M.S. Molecular mechanisms of recombination in *Saccharomyces cerevisiae*: Testing mitotic and meiotic models by analysis of hypo-rec and hyper-rec mutations. Pages 123–159 in *Controlling Events in Meiosis*, C.W. Evans and H.G. Dickinson, Ed. Soc. Exptl. Biol. Symposium *38*: The Company of Biologists, Ltd., Scarborough, North Yorkshire, 1984.

Fabrikant, J.I., Lyman, J.T., and Hosobuchi, Y. Stereotactic heavy-ion Bragg peak radiosurgery for intracranial vascular disorders. Pages 1128–1132 in *Neurosurgery*, R.H. Wilkins, S.S. Rengcharry, Ed. McGraw-Hill, New York, 1985.

Friedland, R.P., Brun, A., and Budinger, T.F. *Pathological and positron emission tomographic correlations in Alzheimer's disease. (Letter to the Editor) Lancet i:228, 1985. (January 26, 1985)*

Graves, H.B., Bracken, T.D., Griffin, J., deLorge, J., Morgan, M.G., and Tenforde, T.S. "Biological Effects of 60-Hz Power Transmission Lines" Report of the Florida Electric and Magnetic Fields Science Advisory Commission, 266 pp., March 1985.

Guzik, T.G., Wefel, J.P., Crawford, H.J., Greiner, D.E. Lindstrom, P.J., Schimmerling, W., and Symons, T.J.M. Implication of new measurements of $^{16}O + P \rightarrow {}^{12,13}C, {}^{14,15}N$ for the abundances of C, N isotopes at the cosmic ray source. Pages 80–83 in volume 2, *19th ACRC Conference Papers*. NASA, Washington, D.C., 1985.

Hall, K., Wells, S., Keller, D., Samori, B., Maestre, M.F., Tinoco, I., Jr., and Bustamante, C. CIDS Measurements of planar and focal conic orientation tions of cholesteric liquid crystals. In *Proceedings of the Workshop on Applications of Circularly Polarized Radiation*, F. Allen and C. Bustamante, Eds. (University of New Mexico, May 18–20, 1984), Plenum Press, New York, 1985.

Kaback, H.R., Carrasco, N., Foster, D.L., Garcia, M.L., Goldkorn, T., Patel, L., and Viitanen, P. The *lac* carrier protein from *Escherichia coli*. in *Electrogenic Transport: Fundamental Principles and Physiological Implications*, M.P. Blaustein and M. Lieberman, Ed. Raven Press, New York, 1984.

Lamoreaux, P., Bebbington, W.P., Duguid, J.O., Durbin, P.W., LeGrand, H.E., Matuszek, J.M., Mendelhoff, J., Schneider, A., Sherby, O.D., and Sloss, L.L. *The Management of Radioactive Waste at the Oak Ridge National Laboratory: A Technical Review.* Panel on Oak Ridge Wastes, National Research Council. National Academy Press, Washington, D.C., 1985.

Liburdy, R.P., and Magin, R.I. Microwave-stimulated drug release from liposomes. (Correspondence). Radiation Res. *103*: 266–275, 1985.

Lyman, John T. Heavy charged-particle beam dosimetry. Pages 267–280 in *Advances in Dosimetry for Fast Neutrons and Heavy Charged Particles for Therapy Applications*, Proceedings IAEA Advisory Group Meeting, (Vienna, Austria June 14–18, 1982); IAEA, Vienna, 1984.

Maestre, M.F. Circular dichroism. Pages 291–341 in *Optical Techniques in Biological Research*, D.L. Rousseau, Ed. Academic Press, New York, 1985.

Maestre, M.F., Keller, D., Bustamante, C., Tinoco, I., Jr. Circular differential microscopy. In *Proceedings of the Workshop on Applications of Circularly Polarized Radiation*; F. Allen and C. Bustamante, Eds. (University of New Mexico, May 18–20, 1984). Plenum Press, New York, 1985.

Mortimer, R.K., and Contopoulou, R. *Yeast Genetic Stock Center Catalogue*, Fifth Edition, 1984 (55 pages)

Mortimer, R.K., and Schild, D. Genetic map of *Saccharomyces cerevisiae*. Pages 224–233 in *Genetic Maps 1984*, S.J. Obrien, Ed. Cold Spring Harbor Press, New York.

Mosteller, F., Fabrikant, J.I., Fry, R.J.M., Lagakos, S.W., Miller, A.B., Saenger, E.L., Shottenfeld, D., Scott, E.L. Van Ryzin, J.R., and Webster, E.W. Assigned share for radiation as a cause of cancer. In *Review of Radioepidemiologic Tables Assigning Probabilities of Causation*. National Academy of Sciencs — National Research Council, National Academy Press, Washington, D.C., 1985.

Resnick, O.A., Chow, T., Nitiss, J., and Game, J. Changes in the chromosomal DNA of yeast during meiosis in repair mutants and the possible role of a deoxyribonuclease. Pages 639–649 in *Recombination at the DNA Level*. Cold Spring Harbor Symposia on Quantitative Biology XLIX, Cold Spring Harbor Laboratory, 1984.

Seeman, N.C., Maestre, M.F., Ma, R.I., and Kallembach, N.R. Physical characterization of a nucleic acid junction. Pages 99–108 in *Molecular Basis of Cancer*, R. Rein, Ed. Alan R. Liss, 1985.

Stampfer, M.R., and Bartley, J.C. Development of human epithelial cell culture systems and their use for studies of carcinogenesis and differentiation. In *In Vitro Models for Cancer Research*, Volume 3, M. Weber and L. Sekely,

Tenforde, T.S. Book Review of *Biomagnetism: An Interdisciplinary Approach* (S.J. Williamson, G.L. Romani, L. Kaufman, and I. Modena, Eds.). IEEE Engineering in Med. and Biol. 4: 42, 1985.

Tenforde, T.S. Mechanisms for biological effects of magnetic fields. Pages 71–92 in *Biological Effects and Dosimetry of Non-Ionizing Radiation: Static and ELF Electromagnetic Fields*. M. Grandolfo, S.M. Michaelson, A. Rindi, Eds. Plenum Press, New York, 1985.

Tenforde, T.S. Physical properties of high-voltage ELF electromagnetic fields and their interaction with living systems. Pages 195–213 in *Electric Energy Systems Research*, Proceedings of Workshop held April 24–26, 1985. National Research Council Committee on Electric Energy Systems, National Academy Press, Washington, D.C., 1985.

Tenforde, T.S. Biological effects of stationary magnetic fields. Pages 93–127 in *Biological Effects and Dosimetry of Non-Ionizing Radiation: Static and ELF Electromagnetic Fields*, M. Grandolfo, S.M. Michaelson, A. Rindi, Eds. Plenum Press, New York, 1985.

Tenforde, T.S. Biological effects of ELF magnetic fields. Pages 79–127 in *Biological and Human Health Effects of Extremely Low Frequency Electromagnetic Fields*. Report of the American Institute of Biological Sciences, Arlington, Virginia, March 1985.

Tenforde, T.S., Gaffey, C.T., and Raybourn, M.S. Influence of stationary magnetic fields on ionic conduction processes in biological systems. Pages 205–210 in *Proceedings of the Sixth Symposium and Technical Exhibition on Electromagnetic Compatibility*, T. Dvorak, Ed. Zurich, Switzerland, 1985.

Tobias, C.A., Albright, N.W., and Yang, T. C.-H. The roles of ionizing radiation in cell transformation. In *Proceedings of the Berkeley Conference in Honor of Jerzy Neyman and Jack Kiefer* (U.C. Berkeley July 1–15, 1983), Volume 1. L. LeCam, Ed. Wadsworth International Publication, 1985.

Wyke, J.A., Bissell, M.J., Gillespie, D.A., and Levantis, P. The molecular basis for phenotypic modulation in cells containing an integrated viral *src* oncogene. In *Hormones and Cell Regulation*, Volume 9 (Proceedings of the 9th European Symposium on Hormones and Cell Regulation), B. Hamprecht and J. Dumont, Eds. Elsevier, Amsterdam, 1985.

Yang, T.C.-H., and Tobias, C.A. Mechanisms of radiation-induced neoplastic cell transformation. Pages 343–371 in *Proceedings of the Berkeley Conference in Honor of Jerzy Neyman and Jack Kiefer* (U.C. Berkeley July 1–15, 1983) Volume 1, L. LeCam, Ed. Wadsworth International Publication, 1985.

LBL REPORTS ISSUED

Albright, N.W. and Tobias, C.A. Extension of the time-independent repair-misrepair model of cell survival to high-LET and multicomponent radiation. LBL-17112, July 1983, 27 pp.

Bastacky, J., and Hayes, T.L. Scanning electron microscope laboratory safety. LBL-19441, April 1985, 48 pp.

Biology and Medicine Division, LBL. Heavy charged particles in research and medicine — Abstracts/Program, presented at the Symposium on Heavy Charged Particles in Research and Medicine (Lawrence Berkeley Laboratory, Berkeley, CA, May 1–3, 1985) LBL-19352, May 1985, 51 pp.

Blakely, E.A., Chang, P.Y., and Lommel, L. Cell-cycle-dependent recovery from heavy-ion damage in G_1-phase cells (Presented at the Symposium on Heavy Charged Particles in Research and Medicine, Berkeley, CA, May 1–3, 1985). LBL-20402, May 1985, 31 pp.

Budinger, T.F., Huesman, R.H., Knittel, B., Friedland, R.P., and Derenzo, S.E. Physiological modeling of dynamic measurements of metabolism using positron emission tomography. LBL-18454, October 1984, 20 pp.

Castro, J.R., Chen, G.T.Y., and Blakely, E.A. Current considerations in heavy charged particle radiotherapy: A clinical research trial of the University of California, Lawrence Berkeley Laboratory, Northern California Oncology Group and Radiation Therapy Oncology Group (Presented at the Symposium and Heavy Charged Particles in Research and Medicine, Berkeley, CA, May 1–3, 1985). LBL-20394, May 1985, 22p.

Chatterjee, A. Discussion of the Physics Session. (Presented at the Symposium on heavy Charged Particles in Research and Medicine, Berkeley, CA, May 1–3, 1985). LBL-20395, May 1985, 6 pp.

Chu, W.T., Curtis, S.B., Llacer, J., Renner, T.R., and Sorensen, R.W. Wobbler facility for biomedical experiments at the Bevalac. LBL-18953, 1985.

Clemons, G.K. Comparison of radioimmunoassay and bioassay of erythropoietin. LBL-19861, June 1985, 23 pp.

Curtis, M.P. Cornelius A. Tobias, Symposium Honorary Chairman. (Presented at the Symposium on Heavy Charged Particles in Research and Medicine, LBL Berkeley, California, May 1–3, 1985). LBL-20390, May 1985, 4 pp.

Curtis, S.B. The LPL Model applied to low dose rates. LBL-18539, April 1985, 20 pp.

Curtis, S.B. Discussion of the Models of Biological Action Session (Presented at the Symposium on Heavy Charged Particles in Research and Medicine, Berkeley, May 1–3, 1985). LBL-20397, May 1985, 15 pp.

Curtis, S.B., and Alpen, E.L. Introduction to the Symposium on Heavy Charged Particles in Research and Medicine (Presented at the Symposium on Heavy Charged Particles in Research and Medicine, Berkeley, CA, May 1–3, 1985). LBL-20398, May 1985, 3 pp.

Derenzo, S.E., and Budinger, T.F. Advanced instrumentation for positron emission tomography. (Presented at the NATO Advanced Studies Institute Series — Physics and Engineering of Medical Imaging, Maratea, Italy, September 23–October 5, 1984). LBL-19435, April 1985, 19 pp.

Durbin, P.W., Jeung, N., and Schmidt, C.T. $^{238}Pu(IV)$ in monkeys: Overview of metabolism. LBL-20022, July 1985, 96 pp.

Fabrikant, J.I., Lyman, J.T., and Frankel, K.A. Heavy charged-particle Bragg peak radiosurgery for intracranial vascular disorders. (Presented at the Symposium on Heavy Charged Particles in Research and Medicine, Berkeley, CA, May 1–3, 1985). LBL-20393, May 1985, 28 pp.

Fry, R.J.M., Powers-Risius, P., Alpen, E.L., and Ainsworth, E.J. High-LET radiation carcinogenesis (Presented at the Symposium on Heavy Charged Particles in Research and Medicine, Berkeley, CA, May 1–3, 1985). LBL-20392, May 1985, 20 pp.

Hallowes, R., and Stampfer, M. Workshop on *in vitro* culture systems. LBL-19623, May 1985, 8 pp.

Hutchinson, M.S. Electrophoretic and biochemical studies of erythrocyte membrane structure. LBL-18458 (Ph.D. thesis), December 1984, 160 pp.

Lawton, M.S. Phase-encoded, rapid, multiple-echo (PERME) nuclear magnetic resonance imaging. LBL-20101, August 1985, 23 pp.

Lyman, J.T. Complication probability as assessed from dose-volume histograms. (Presented at the Symposium on Heavy Charged Particles in Research and Medicine; Berkeley, CA, May 1–3, 1985. LBL-19630, May 1985, 7 pp.

Maestre, M.F., Keller, D., Bustamante, C., and Tinoco, I., Jr. Circular differential microscopy. LBL-20169, August 1985, 17 pp.

Mathis, C.A., Jones, R.M., and Chasko, J.H. Overall radio-HPLC design. LBL-19433, December 1984, 45 pp.

Mazoyer, B.M., Huesman, R.H., Budinger, T.F., and Knittel, B.L. A study of factors that affect the precision of compartmental model parameter estimation using dynamic positron emission tomography. LBL-19614, May 1 985, 30 pp.

Perez, C.F. Ionizing and ultraviolet radiation enhances the efficiency of DNA mediated gene transfer *in vitro*. LBL-18303 (Ph.D. thesis), August 1984, 234 pp.

Saunders, W.M., Castro, J.R., Chen, G.T.Y., Tobias, C.A., Alpen, E.L., Collier, J.M., Zink, S.R., Pitluck, S., Char, D., Gutin, P., Ganger, G., and Phillips, T.L. Helium ion radiation therapy at the Lawrence Berkeley Laboratory: Recent results of a Northern California Oncology Group Clinical Trial (Presented at the Symposium on Heavy Charged Particles in Research and Medicine, Berkeley, CA, May 1–3, 1985). LBL-20395, May 1985, 23 pp.

Tenforde, T.S. Biological effects of ELF magnetic fields. LBL-19157, January 1985, 62 pp.

Tenforde, T.S. Physical properties of high-voltage ELF electromagnetic fields and their interaction with living systems. LBL-19710, April 1985, 21 pp.

Tenforde, T.S. Magnetic field applications in modern technology and medicine. LBL-19711, May 1985, 36 pp.

Tenforde, T.S., and Budinger, T.F. Biological effects and physical safety aspects of NMR imaging and *in vivo* spectroscopy. LBL-20053, August 1985, 57 pp.

Tenforde, T.S., Levy, L., and Veklerov, E. Monitoring of circadian waveforms in rodents exposed to high-intensity static magnetic fields. LBL-18384, October 1984, 37 pp.

Tobias, C.A. Symposium Honorary Chairman (Presented at the Symposium on Heavy Charged Particles in Research and Medicine, Berkeley, CA, May 1–3, 1985). LBL-20390, May 1985, 4 pp.

Tobias, C.A. Summary of Symposium on Heavy Charged Particles in Research and Medicine. (Presented at the Symposium on Heavy Charged Particles in Research and Medicine, Berkeley, CA May 1–3, 1985). LBL-20399, May 1985, 22 pp.

Tobias, C.A. The repair-misrepair model in radiobiology: Comparison to other models. (Presented at the Symposium on Heavy Charged Particles in Research and Medicine, Berkeley, CA, May 1–3, 1985). LBL-20400, May 1985, 45 pp.

Wulf, H., Kraft-Weyrather, W., Miltenburger, H.G. Blakely, E.A., and Tobias, C.A. Heavy-ion effects on mammalian cells: Inactivation measurement with different cell lines. (Presented at the Symposium on Heavy Charged Particles in Research and Medicine, Berkeley CA, May 1–3, 1985). LBL-20391, May 1985, 28 pp.

Yang, T.C., Craise, L.M., Mei, M.-T., and Tobias, C.A. Neoplastic cell transformation by heavy charged particles. (Presented at the Symposium on Heavy Charged Particles in Research and Medicine, Berkeley, CA May 1–3, 1985). LBL-20401, May 1985, 23 pp.

Yano, Y., Budinger, T.F., Ebbe, S.N., Mathis, C.A., Moore, D.H., Singh, M., Brennan, K., Moyer, B.R., and Nichols, A. Gallium-68 Chemistry for labeling platelets, proteins and lipoproteins. LBL-18388, 1984.

Yezzi, M.J. The role of protein synthesis in the repair of sublethal x-ray damage in a mutant chinese hamster ovary cell line. LBL-19500 (Ph.D. thesis), April 1985, 156 pp.

PATENTS

Liburdy, R.P. Method for Determining Cell Membrane Dielectric Breakdown. U.S. Patent No. 4,472,506. Granted September 18, 1984.

APPENDIX C: Biology and Medicine Division Staff September 30, 1985

The accomplishments of the Biology and Medicine Division are due in large measure to the capability and dedication of its staff. Listed below are those who have participated in the Division's programs during fiscal year 1985 as full- or part-time employees, consultants, and participating guests. The guest staff includes visiting scientists, postdoctoral trainees, resident physicians, graduate and undergraduate students, and summer research participants.

DIVISION HEAD

Edward L. Alpen
Thomas L. Hayes, Deputy

DIVISION ADMINISTRATION STAFF

Mary P. Curtis
Janice C. DeMoor
De A. Eggers
Michael B. Fizer
Wendell Hom
Allan W. Long
Georgia A. Peterson
Robert W. Springsteen
Baird Whaley
† Herbert Wiener
Mary L. Worth

DIVISION SCIENTIFIC STAFF

S. Javed Afzal
Judith Aggeler
E. John Ainsworth
* Steve P. Akeson
Julius J. Almasi
‡ Bruce N. Ames
Melissa A. Austin

John C. Bartley
John B. Bassel
S. Jacob Bastacky
* Astrid Baumgartner
‡ Alan J. Bearden
Eugene V. Benton
Peter A. Berardo
Leslie Bernstein
Stephen E. Bicknese
Mina J. Bissell
Eleanor A. Blakely
* Caridad Borras
§ George Brecher
Kathleen M. Brennan
Michael F. Bruno
‡§ Thomas F. Budinger
Ralph Buncher

*‡ Gail E. Butterfield

* Barbara E. Cahoon
Vincent P. Carabillo
§ Joseph R. Castro
* Lai-Man Chan
* Chung-Fu Chang
Aloke Chatterjee
* George T.Y. Chen
Gisela K. Clemons
John P. Cody
J. Michael Collier
Priscilla K. Cooper
* Tom L. Crisswell
Stanley B. Curtis

* Maya Das
Stephen E. Derenzo
* David S. Dolberg
Kenneth H. Downing
* Werner K. Doyle
* D.M. Driscoll
Patricia W. Durbin

§ Shirley N. Ebbe
* Herschell S. Emery
* Masahiro Endo
Michael S. Esposito

§ Jacob I. Fabrikant
* Gregory L. Finch
James Fontanesi
Trudy M. Forte
David L. Foster
Heinz Fraenkel-Conrat
Kenneth A. Frankel
‡ Michael Freeling
|| Robert P. Friedland

* Gunther Gademann
Cornelius T. Gaffey
John C. Game
§ Grant E. Gauger
Peter S. Geissler
Orsolya Genzel
* Jack R. Gerson
‡ Robert M. Glaeser
Lois S. Gold
Joseph D. Goldstein
* Joan W. Goodman
Regine Goth-Goldstein
‡ Martin H. Graham
Dale E. Greenwalt
* Gianfranco Grossi
* Raphael C. Guzman

Michael P. Hagem
H. Glenn Hall

---

*Left Biology and Medicine Division prior to September 30, 1985.
†Retired during Fiscal Year 1985.
‡Faculty UC Berkeley.
§Faculty UC San Francisco.
||Faculty UC Davis.

• Colin G. Harrison
• William R. Havender
John W. Hoffman
Eugene V. Holahan
Libby L. Holbrook
William R. Holley
§ Yoshio Hosobuchi
Junko Hosoda
Jerry Howard
Anthony R. Howlett
Mirko I. Hrovat
John P. Huberty
Ronald H. Huesman
• Philippe Hugues

‖ William J. Jagust
Bing K. Jap
Lin C. Jensen
John R. Johnston

Talwinder S. Kahlon
Leon N. Kapp
• Jerry S. Kidd
Patrice A. Koehl
• Betty Koss
§ Ronald M. Krauss

Michael La Belle
‡ John H. Lawrence
Steven A. Leadon
• Wen-Hwa Lee
Robert M. Leven
• Francine C. Levin
• Jack Levin
• Robert H. Levinson
Ming Li
Robert P. Liburdy
• Jonathan G. Lieber
Tz-Hong Lin
Frank T. Lindgren
David E. Linstadt
Helen F. Londe
Susan T. Lovett
Bernhard A. Ludewigt
John T. Lyman

Marcos F. Maestre
John L. Magee
Andrew C. Magyarosy
Neela B. Manley
• Edward K. Markell
Vera Martin
Hugo A. Massaldi
Chester A. Mathis
Bernard M. Mazoyer
Elisabeth Mazoyer
Joyce C. McCann
• Man-Tong Mei
‡ Howard C. Mel
• Kathleen L. Miller
• Alok K. Mitra
Stephen M. Moerlein
• David H. Moore
‡ Robert K. Mortimer
• John P. Mumane

Richard A. Mushlin
Thomas A. Musliner

Yen H. Nguyen
‡ Alex V. Nichols

• Hiroshi Ohara
• Rebecca C. Osborn
‡ William G. Owen
‡ John C. Owicki

Gordon Parry
• John J. Peloquin
• Carl F. Perez
Mark H. Phillips
§ Theodore L. Phillips

Gian M. Ratto
• Michael S. Raybourn
• Todd L. Richards
Gary V. Richieri
Adrian Rodriguez
Mark S. Roos
Ruth J. Roots

Thornton W. Sargent, III
*§ William M. Saunders
David Schild
Walter Schimmerling
John C. Schooley
• Stanley Schuman
• Jeffrey M. Schwartz
Richard I. Schwarz
Zahra Shahrokh
Alexander T. Shulgin
Paul H. Silverman
Bea A. Singer
‡ Jerome R. Singer
Thomas H. Slone
Sylvia J. Spengler
Martha R Stampfer
• Susan G. Stanton
Henry H. Stauffer
Thomas Swain
• Susan F. Sweigert

Thomas S. Tenforde
‡ Cornelius A. Tobias
• Conrad N. Trumbore
Sylvanus A. Tyler

• Peter E. Valk
Karen M. Vranizan

• Liang-Zhong Wang
• Klaus J. Weber
§ Philip R. Weinstein
Margaret R. White
Paul T. Williams
Kay H. Woodruff
Mervyn Wong
• Wennie H. Wu

Tracy C. Yang
Yukio Yano
• Chi-Kwan Yen

• Sandra R. Zink

DIVISION SUPPORT STAFF

Linda D. Abe
James R. Abney
Frederick E. Abrams
Gerald L. Adamson
* Myungho Ahn
Mari Aker

Kari P. Baken
* David Baker
John R. Baker
Violet Barghe-Sharghi
Josephine L. Barr
George M. Basile
Maren Bell
Sindy E. Berger
* William H. Bingham
* Patricia Biscay
Kathleen A. Bjornstad
Patricia J. Blanche
* Mark G. Blumenthal
Nicolas R. Bolo
Yvonne C. Bopp
* Jochen Braun
Mitch C. Brenner
Robert S. Bridwell
S. Kay Bristol
Gerald L. Brooks
* Erik T. Burns

Mary Cabbage
John L. Cahoon
* Denise Capra-Young
* Mark L. Carlson
Mardel M. Carnahan
Dorothy A. Carpenter
* Betsy C. Carr
Albert C. Casselhoff
Lida M. Caylor
Rosemarie L. Celli
* Dominic Chan
Polly Y. Chang
Frank Chavez
Li-How Chen
Melody L-Y Cheng
* Larry J. Chevez
Dennis Chin
Gary M. Cole
C. Rebecca Contopoulou
Vincent E. Cook
* Maria R. Costin
Laurie M. Craise
Freddie L. Crenshaw, Jr.
Christopher Cullander
Betsey L. Cullen

Kanu B. Dalal
Minh N. Dang
Randy J. Deguzman
Greg T. De Lory
Darlene J. DeMarmcor
* Susan M. Dettling
Uyen Nina Dinh
Nietha A. Dodson
* Edward T. Dowling

Annette C. Drew
Bill M. Du Four
* Katherine A. Dukes
* Dennis P. Duncan

Eva L. Edwards
Julie A. Ellison
Nina Engineer
David E. Erkenbrack

Diana E. Fajardo
Dennis Fantin
Deborah A. Farson
Sherry L. Fitzsimmons
* Brian L. Fletcher
* Ted Y. Fong
Myrtle L. Foster
Marilyn A. Fowler
Roscoe Frazier
* Carol J. Fujihara
Charlie M. Fuller
* Carla L. Fulton

* Roassana A. Garon
Lance A. Gee
John C. Gilbert
Christine Giotas
Queen E. Gipson
Brian J. Glassner
Laura A. Glines
Michael A. Glotzer
Tennessee W.-Y Gock
Elaine L. Gong
Edwin H. Goodwin
Sara P. Goolsby
* Eddy A. Gosschalk
* Robert A. Graf
* Joan M. Graham

Angela Habrek-Davidson
William A. Hare
* Ronald M. Harris
Andrew C. Hasenfeld
Carroll Hatier
Virginia C. Havens
Lilian E. Hawkins
Linda G. Hayashi
* Mark F. Henteleff
* Jeffrey V. Hernandez
Mark D. Hertle
Peter Hertz-Herskovits
Sharon A. Hibdon
* Kathleen J. Hicks
Lynn R. Hlatky
Christine S. Hong
Laura J. Horn
Midori Hosobuchi
Mildred K. Hughes
Jacquelyn J. Iler
Daniel Young-Bin Im
* Angela Ingendaay
Gayla P. Ivery

Nylan M. Jeung
* Patricia A. Johnson
* Mary Ann Jones
Reese M. Jones

- Jay S. Joseph
  James W. Judnick
  David M. Kang
  Aaron B. Kantor
  Kristina S. Kavanau
- David E. Kellog
  Marc L. Kessler
- Susan B. Klein
  Paul M. Kleinman
  Brian L. Knittel
  Seok-Hwan Kong
  Renee J. Kopa
  Lori E. Kopp
  Kari L. Koszdin
  Susanne E. Kuehl
  Birgetta R. Kullgren
  Natalia Kusubov
- Christian Labadie
  Clifford E. Lai
- Mark T. Lasartemay
- Mark S. Lawton
  Ann Lee
  Kyung-Dall Lee
  Samuel Lee
- Yue-Hwa Pan Lee
- Barbara A. Leivonen
  Gerri A. Levine
  Lynette L. Levy
  Richard P. Levy
- John P-J Lin
- Vincent Ling
  Leora Lommel
- Peggy A. Lopipero
  Janice K. Louie
- Katherine A. Louie
  Janet S. Lowe
  Karen E. Lowe
- Helen Lu
- Beverly G. McCalla
  Tommy J. McKey
- May F. McKoon
  Velma B. McNeal
- Ian S. Madfes
  Renae I. Magaw
  Lynn J. Mahlmann
  Dimitrios T. Maleas
- Missie J. Martis
- William J. Meechan
  Marc S. Mendonca
- Roy E. Mintzer
  Barbara Modlinski
  Herbert W. Moise, III
- Maureen H. Morford
  Lenny Moss
- Brian R. Moyer
  Kimberly Mulcahy
- Don L. Murphy
  Steve S. Nieben
  Trie Niemanisme
  Rocky Nievin
- Collette R. Newman
  Robert W. [illegible]
- [illegible]

  Virginia L. Obie
  Mary Lou Olbrich
  Lucinda S. Olney
- Peter A. Origenes
  Joseph R. Orr
- Lars G. Osterberg
- Nancy L. Owens
  Annie C. Pang
- Shannon S. Parr
- Elizabeth A. Phalen
  Huan N. Phan
  Patricia P. Powers-Risius
  John C. Prioleau
  Jose A. Ramirez
  Louise Ray
  Monica H. Reimers
- Johanna E. Reneke
- Gretchen A. Rothrock
- Craig D. Ruden
  Dolores J. Ruff
  Lisa R. Sawrey-Kubicek
  Janis S. Scherer
  James B. Schmidt
  Annelie D. Schumann
- Peter R. Seipel
  Janet F. Selmek
  Ajit S. Shah
  Ellen S. Sher
- Andy Shih
- Sarah G. Shinpock
  Mohindar Singh
  Karen C. Sitney
  Karen Smith
  Elmer M. Soriano
  Dorothy S. Sprague
  Karen A. Springsteen
  Lore S. Stein
- Bonnie Stern
- Paul F. Stetson
- Jeanne M. Stevens
  David P. Suchard
  Shirley C. Sutton
- Vincent V. Suzara
- John N. Takakuwa
- Cheryl L. Tanguilig
  Joseph R. Taylor
  Richard Thrift
- Scott Shen-Ta Ting
  Laura M. Tracewell
- Sophia M. Tu
  Sally P. Tubach
  Julia A. Twitchell
  Vladimir Vacata
  Dagmar D. Van Dusen
- Paul F. Vanek
- Margaret S. Vogt
  Peter J. Waliun
  Angela Y. Wang
  Marian M. Wertheimer
- Joyce T. West
  Monroe Whitney

Evelyn F Williams
- Howard S Wong
Jason Wong
Sam T.S Wong
- Sina Wong
- Catherine Wright
- Scott Y Wu

Patrick K Yang
- Filame M Yee
Marilyn Yee
Tamlyn K Yee
Michael J Yezzi

Committees

DIVISION ADVISORY COMMITTEE

Edward L. Alpen
John C. Bartley
Eleanor A. Blakely
Thomas F. Budinger
Trudy M. Forte
Thomas L. Hayes
Robert K. Mortimer
Thomas S. Tenforde
Cornelius A. Tobias
† Baird Whaley

DIVISION STAFF COMMITTEE

Shirley N. Ebbe, Chair
Aloke Chatterjee
Trudy M. Forte
John T. Lyman
Tony W. Sargent

EQUIPMENT COMMITTEE

Tony W. Sargent, Chair
John C. Bartley
Aloke Chatterjee
Shirley N. Ebbe
Cornelius T. Gaffey
Frank T. Upham
* Allan W. Long
* Herbert Wiener

SPACE COMMITTEE

Thomas S. Tenforde, Chair
Gisela K. Clemons
Michael S. Esposito
Tracy C. Yang
Yukio Yano
* Allan W. Long

SALARY COMMITTEE

Edward L. Alpen, Chair
John C. Bartley
Thomas F. Budinger
Trudy Forte
Thomas L. Hayes
Thomas S. Tenforde
Cornelius A. Tobias
* Baird Whaley

HUMAN USE COMMITTEE

Henry H. Stauffer, Chair
Thomas F. Budinger
George T.Y.Chen
Shirley N. Ebbe
Kathleen E. Handron
† Janice C. DeMoor
* Baird Whaley

RADIOACTIVE DRUG RESEARCH COMMITTEE

Jacob I. Fabrikant, Chair
Edward L. Alpen
Aloke Chatterjee
Henry H. Stauffer
Paola S. Timiras
Joseph D. Goldstein (Consultant)
† Janice C. DeMoor

ANIMAL WELFARE COMMITTEE

John C. Bartley, Chair
Herman Bonasch
Kathlenn Brennan
Joan W. Goodman
John C. Schooley
* Robert W. Springsteen
† Janice C. DeMoor

DONNER LIBRARY COMMITTEE

Ronald M. Krauss, Chair
Edward L. Bennett
Thomas F. Budinger
Stanley B. Curtis
Thomas L. Hayes
Frank T. Lindgren
Howard C. Mel
* Dorothy F. Denney
* Gloria L. Haire

DONNER SEMINAR COMMITTEE

Stephen E. Derenzo, Chair
Michael S. Esposito
Stanley B. Curtis

---

*Ex Officio, non-voting member.
†Executive Officer.